ISSI Scientific Report SR-005

The Physics of the Heliospheric Boundaries

V. V. Izmodenov and R. Kallenbach (Eds.)

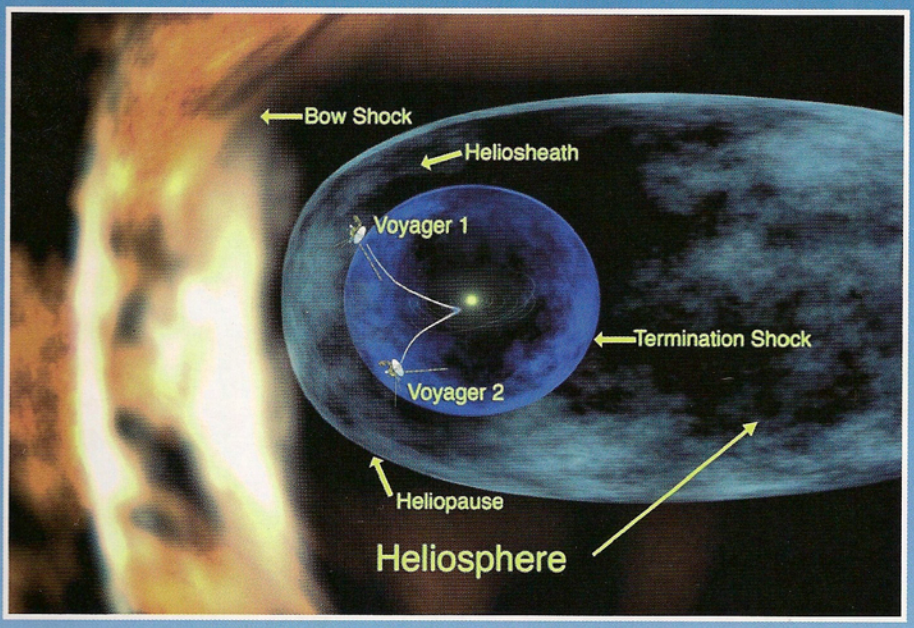

INTERNATIONAL SPACE SCIENCE INSTITUTE

Preface

This book reviews the general concepts and presents knowledge on many aspects of the physical phenomena at the heliospheric boundaries. The physical properties at the edge of the heliosphere are determined by the interaction of the solar wind with the local interstellar medium. At the present time there are no doubts that both the solar wind and the local interstellar medium have a multi-component nature and include plasma, neutral gases, magnetic fields, and energetic particles. This makes the physics of the heliospheric interface so diverse and interesting. The multi-component nature of the interface creates challenges for theoreticians to adequately describe the physical phenomena at the boundaries, in particular the solar wind termination shock and the heliopause.

The specific intent of this volume is to summarize the progress in the understanding of the physics and the global structure of the heliospheric boundaries that has been achieved in the frame of the international collaboration project "Physics of the heliosheath plasma flow and structure of the termination shock" (Principal Investigator: Reinald Kallenbach). This project had been funded by INTAS – The International Association for the Promotion of Co-operation with Scientists from the New Independent States (NIS) of the Former Soviet Union. The international consortium of the project consisted of seven teams of different institutions from France, Germany, Russia, and Switzerland:

Organization	Team
International Space Science Institute (ISSI) Bern, Switzerland	Reinald Kallenbach Johannes Geiss Rudolf von Steiger
Service d'Aeronomie (SA), CNRS, Verrieres-le-Buisson, France	Rosine Lallement Eric Quémerais
Lomonosov Moscow State University (MSU) Department of Mechanics and Mathematics, Moscow, Russia	Vladimir B. Baranov Vladislav V. Izmodenov Pavel Nemtsov
Institute for Problems in Mechanics (IPM), Moscow, Russia	Sergey V. Chalov Yury G. Malama Dmitry B. Alexashov Artyom V. Myasnikov
Max-Planck-Institut fur Aeronomie (MPIA) Katlenburg-Lindau, Germany	Martin Hilchenbach Helmut Rosenbauer
Max Planck Institute for Extraterrestrial Physics (MPIE) Garching, Germany	Rudolf Treumann Manfred Scholer
Institute of Cosmophysical Research and Aeronomy (IKFIA), Yakutsk, Russia	Eugeny G. Berezhko Leonid Ksenofontov

The leading organization and host for team-meetings was the International Space Science Institute (ISSI) in Bern. The project was also financially supported in the frame of ISSI's team program. The duration of the INTAS project was 3 years from May 2002 to April 2005.

The initiative to summarize our results in the form of this volume has been taken in spring 2005 while preparing the final report of our INTAS project for several reasons: 1) We soon realized that it was difficult to compress the outcome of 46 articles, published in international journals in the frame of our project, and of 22 talks and posters into a few pages of text. 2) We just learnt that Voyager 1 had crossed the termination shock and had entered the heliosheath in December 2004, so that direct measurements would be available on the objects we have studied theoretically. 3) The direction of the interstellar magnetic field had been constrained by SOHO/SWAN data. 4) New Mars Aspera-3 data on energetic neutral atoms created in the heliosheath became available.

We decided to carefully evaluate the most recent data and to write up summary articles in which we compare our model results to the experimental facts. The ISSI Scientific Report series seemed to be an excellent place to do this. Immediately after deciding to put together a book, we realized that it would be much more useful and interesting for a larger number of readers if the book discussed the broader context of studies on the heliospheric boundaries beyond the scope of the INTAS project. As a result we invited several authors to participate who were not formal members of our INTAS project but have close links to members of the INTAS team. Andrzej Czechowski, Len Fisk, George Gloeckler, Norman Ness, Raymond Pottelette, and Peter Wurz kindly agreed to contribute to the book.

Students and readers who are not familiar with the research field may like the introductory (or tutorial) chapters or appendices that provide some guidelines to the theoretical approaches employed in the models as well as the historical introductions to the subject.

This volume has 13 chapters. The first chapter by Vladimir Baranov is a tutorial on hydrodynamic and kinetic approaches in space plasmas. The second and third chapters give brief historical overviews of the early concepts of the heliospheric interface, where the second chapter by Vladimir Baranov reviews the history of the plasma interface models while the third chapter by Vladislav Izmodenov reviews early concepts of the hydrogen atom penetration into the heliosphere. As is seen in Chapter 4 by Izmodenov and Baranov, some of the pioneering concepts and models are still valid and their modern versions still in use. Chapter 4 summarizes the current state of the art in the modelling of the global structure of the heliospheric interface that is determined by the multi-component nature of both the local interstellar medium and the solar wind.

Chapters 5 and 6 are overviews of the results of the pioneering heliospheric missions Ulysses and Voyager. While Ulysses was the first mission to explore the three-dimensional structure of the heliosphere, the Voyager spacecraft, launched in the 1970's, have finally reached the outer boundaries of the heliosphere. Chapter 5 written by Johannes Geiss, George Gloeckler and Len Fisk reviews the observational knowledge for interstellar gas inside the heliosphere and the newest basic concepts of Anomalous Cosmic Ray acceleration. In particular, the chapter demonstrates the importance of understanding the filtration process in the heliosheath for pre-

cise determination of interstellar elemental abundances. The interstellar abundance measurements in turn put the research on the heliosphere-interstellar medium interaction into context with the studies of the galactic chemical evolution. Chapter 6 by Norman Ness reviews observations of global and microstructures of the heliospheric magnetic field obtained by the Voyager 1 spacecraft from 1977 up to the middle of 2005. These data include the remarkable event of 16 December 2004, when Voyager 1 crossed the heliospheric termination shock. This event opened a new era in the exploration of the outer heliosphere. Norman Ness discusses this event and the characteristics of the heliospheric magnetic field in the heliosheath which are fundamentally different from the characteristics in the supersonic solar wind.

Chapter 7 by Reinald Kallenbach, Andrzej Czechowski, Martin Hilchenbach and Peter Wurz and Chapter 8 by Sergey Chalov can be considered as tutorials on theoretical models of the evolution of solar wind turbulence and stochastic acceleration efficiencies with heliocentric distance, ranging from Earth's orbit beyond the termination shock to the subsonic heliosheath plasma. However, Chapter 7 also contains comparisons to data from the SOHO, ACE, Voyager, and Mars Express missions, while Chapter 8 mainly reviews the theoretical aspects of the evolution of the interstellar pickup ions from their origin toward the heliospheric termination shock, where a part of the pickup ions are accelerated to the high energies of the termination shock particles and Anomalous Cosmic Rays (ACRs). The ACR injection problem is also discussed in both Chapters 7 and 8.

Chapters 9-12 provide reviews of different remote diagnostic techniques for the heliospheric interface. Chapter 9 by Eric Quémerais discusses backscattered Lyman-α radiation measurements, which have been one of the basic diagnostics since the 1970s. Now there is no doubt that the correct interpretation of the backscattered Lyman-α requires multiple scattering. The chapter provides details of the backscattered Lyman-α radiation and can be considered as a tutorial as well. Chapter 10 by Andrzej Czechowski, Martin Hilchenbach, and Reinald Kallenbach reviews the high energy Energetic Neutral Atoms (ENAs) as a diagnostic of the inner heliosheath, i.e. the region between the heliospheric (solar wind) termination shock and the heliopause. Chapter 11 by Brian Wood discusses the Lyman-α absorption diagnostic, reviewing what kind of information these observations can provides about the outer heliosphere. It is also shown that the absorptions provide a unique tool to diagnose stellar astrospheres. Finally, Chapter 12 by Rudolf Treuman and Raymond Pottelette discusses the kHz-emission measured by the Voyager spacecraft as a possible diagnostic of the distant heliosphere. In particular, they suggest a new mechanism for the heliopause radio emission.

The additional Chapter 13 briefly summarizes all achievements in the study of the heliospheric interface made in the frame of the INTAS project. This chapter is an addition to the final report submitted to INTAS. At the end of the chapter we also discuss questions that are still open and challenging for researchers. After Voyager 1 crossed the heliospheric termination shock, more new questions arose than old questions obtained an answer.

All chapters included in the book were refereed. We thank very much Vladimir Baranov, Jean-Loup Bertaux, Iver Cairns, Sergey Chalov, Rosine Lallement, Jeffrey Linsky, Wayne Pryor, and Monica Tosi who were so kind as to serve as referees

for the different chapters. A full list of all of the authors of the book is given below in alphabetical order, including their affiliations. We are deeply indebted to these authors for investing so much effort and to their institutions for providing them the opportunity to work with us:

Vladimir B. Baranov, Institute for Problems in Mechanics,
Russian Academy of Sciences
Lomonosov Moscow State University, Department of Aeromechanics,
School of Mechanics and Mathematics, Russia
Sergey V. Chalov, Institute for Problems in Mechanics,
Russian Academy of Sciences
Andrzej Czechowski, Center of Space Research Polish Academy of Sciences,
Poland
Johannes Geiss, International Space Science Institute, Bern, Switzerland
George Gloeckler, Department of Atmospheric, Oceanic, and Space Sciences,
University of Michigan, Ann Arbor, USA
Len Fisk, Department of Atmospheric, Oceanic, and Space Sciences,
University of Michigan, Ann Arbor, USA
Martin Hillchenbach, Max-Planck-Institut für Sonnensystemforschung,
Katlenburg-Lindau, Germany
Vladislav V. Izmodenov, Lomonosov Moscow State University,
Department of Aeromechanics, School of Mechanics and Mathematics, Russia
Space Research Institute (IKI) Russian Academy of Sciences
Institute for Problems in Mechanics Russian Academy of Sciences
Reinald Kallenbach, International Space Science Institute, Bern, Switzerland
Norman Ness, The Catholic University of America, USA
Raymond F. Pottelette, CETP/CNRS, St. Maur des Fossés Cedex, France
Eric Quémerais, Service d'Aeronomie CNRS, France
Rudolf A. Treumann, Geophysics Section, Ludwig-Maximilians University
of Munich, Munich, Germany
Brian Wood, JILA and NIST University of Colorado, Boulder, Colorado, USA
Peter Wurz, Physikalishes Institut, University of Bern, Switzerland.

Last but not least the funding by INTAS is very gratefully acknowledged.

Finally, as was noted above, on December 16 2004 Voyager 1 opened up a new era in the exploration of the outer heliosphere. The Voyager data obtained in 2003-2006 not only provide important new clues for our understanding of the heliospheric boundaries, but also raise new questions that still need to be understood. The Interstellar Boundary Explorer (IBEX) scheduled for launch in 2008 will certainly provide new breakthroughs in understanding the heliosphere. Nevertheless, all models and theories as well as observational diagnostics discussed in the book are based on solid physical background and, they will remain applicable in the future. We hope that our book will be useful for the scientists working in the field as well as for the specialists in other fields of space physics, Ph.D. students, and postdoctoral researchers who are looking for a short and comprehensive introduction to the physics of the heliospheric boundaries.

— 1 —

Kinetic and Hydrodynamic Approaches in Space Plasma

Vladimir B. Baranov[1]
Institute for Problems in Mechanics, Russian Academy of Sciences;
Lomonosov Moscow State University, School of Mechanics and Mathematics,
Department of Aeromechanics and Gas Dynamics

Abstract. **This chapter provide a theoretical background for the models discussed in other chapters of this book. The derivation of the Boltzmann equation and its solution by the Chapman - Enskog method are schematically presented. The derivation of hydrodynamic and magneto-hydrodynamic (MHD) equations from the Boltzmann kinetic equation for velocity distribution function is given. The closed systems of hydrodynamic and MHD equations are formulated. Transport coefficients (coefficients of viscosity, thermal and electro - conductivities) for fully ionized hydrogen plasma obtained by this method on the basis of the kinetic equation with the integral collisions in the Landau form (Braginskii, 1965) are given. These coefficients are anisotropic in the strong magnetic field when $\omega\tau \geq 1$ (ω and τ are cyclotron frequency and mean free time of charged particles, respectively). The basic assumptions to derive the Boltzmann equation with integral collisions in the Landau form from the Liouville equation for the N-particle distribution function are presented.**

1.1 Introduction

To describe the dynamics of gas in different problems of physics and astrophysics one of the three following approaches should be chosen and employed: (i) the individual particle approach, where the motion of individual particles is studied, (ii) the kinetic approach, where the gas is described by velocity distribution functions, and (iii) the hydrodynamic (or magnetohydrodynamic) approach. The first approach is usually used to describe flows of very rarefied gases, when the interactions between individual particles can be neglected. The dynamic state of such a system is determined by known external forces and by given coordinates and momenta of all particles at the initial time. However, real situations often deal with a great quantity of interacting particles, and the individual particle approach is not satisfying for two reasons. Firstly, initial coordinates and momenta are not known for every particle. Secondly, even when initial coordinates and momenta

[1]in *The Physics of the Heliospheric Boundaries*, V. Izmodenov and R. Kallenbach (eds.), ISSI Scientific Report No. 5, pp. 1–26, ESA-ESTEC, Paris 2006

would be known, the individual particle approach requires the solution of a system of equations of particle motions for such a large number of interacting particles that it becomes computationally impossible. The dynamics of such systems can be described on the basis of the kinetic approach (ii). To get the velocity distribution function, which is a function of seven independent variables (three coordinates in space, three coordinates in velocity phase-space, and time), requires one to solve a complicated integro-differential nonlinear equation. Very often, detailed knowledge of the velocity distribution function is not necessary. In most cases experiments provide the averaged characteristics of a gas. The hydrodynamic description (iii) deals with averaged characteristics of gas such as number density, bulk velocity, temperature, and others that depend on four variables (three space coordinates and time). The hydrodynamic approach is attractive because the set of hydrodynamic equations is simpler to solve than the kinetic equation. It is valid if the mean free path of the particles is much smaller than the characteristic size of the problem, and if the frequencies of collisions between particles are much larger than the characteristic frequencies.

Construction of quantitative theoretical models for prediction and explanation of experimental data is an important goal in various branches of scientific knowledge. However, such models are only useful if they are based on reliable and physically correct theoretical concepts. This chapter reviews the foundations of kinetic, hydrodynamic (HD) and magnetohydrodynamic (MHD) approaches, because namely these approaches constitute a theoretical basement for the models of the heliospheric interface discussed in other chapters of this book. This chapter gives a derivation of the HD and MHD equations from the Boltzmann equations for the velocity distribution function and, in particular, a derivation of MHD equations for fully ionized plasma using the integral of collisions in the Landau form (Braginskii, 1965). Basic criteria for the validity of the MHD approach, and the hydrodynamic equations for a collisionless plasma are also discussed in this chapter.

1.2 The distribution function of a one-component gas and its connection with the hydrodynamic parameters

Let us consider a volume element of physical space $\mathrm{d}\mathbf{r} \equiv \mathrm{d}x\mathrm{d}y\mathrm{d}z$ (x, y, z – cartesian coordinates). This volume element should be chosen in such a way that it contains a large number of individual particles. Particles from this volume element form a cloud of particles in velocity space (v_x, v_y, v_z). It is assumed in kinetic theory that the number density of particles in this cloud is proportional to the volume element of physical space. Therefore, the number density can be denoted as $f(\mathbf{r},\ \mathbf{v},\ t)\,\mathrm{d}\mathbf{r}$, where $\mathbf{r} = (x, y, z)$ and $\mathbf{v} = (v_x, v_y, v_z)$ are the coordinates and the velocity radius vectors, respectively. Then a probable number of particles with coordinates in the range from (x, y, z) to (x+dx, y+dy, z+dz) and velocities in the range from(v_x, v_y, v_z) to ($v_x + \mathrm{d}v_x$, $v_y + \mathrm{d}v_y$, $v_z + \mathrm{d}v_z$) is equal to $f(\mathbf{r}, \mathbf{v}, t)\,\mathrm{d}\mathbf{r}\,\mathrm{d}\mathbf{v}$. Here $\mathrm{d}\mathbf{v} \equiv \mathrm{d}v_x\mathrm{d}v_y\mathrm{d}v_z$ is a volume element in velocity space. It is important to emphasize that $\mathrm{f}(\mathbf{r}, \mathbf{v}, t)\,\mathrm{d}\mathbf{r}\mathrm{d}\mathbf{v}$ represents the number of particles averaged in the

time interval between t and $t + \mathrm{d}t$. Thus, the function $f(\mathbf{r}, \mathbf{v}, t)$ is a probable number density of particles in the 6D phase space and is called the *distribution function*.

The relation between the distribution function and the number density of gas, $n(\mathbf{r}, t)$, is evident

$$n(\mathbf{r}, t) = \int f(\mathbf{r}, \mathbf{v}, t)\, \mathrm{d}\mathbf{v} \ . \tag{1.1}$$

Let us consider an arbitrary function of individual particle velocity, $\Phi(\mathbf{v})$. $\Sigma\, \Phi(\mathbf{v})$ is the sum of $\Phi(\mathbf{v})$ taken over all particles of the volume element $\mathrm{d}\mathbf{r}$ and then averaged over the time interval between t and $t + \mathrm{d}t$. It is evident that

$$\Sigma\, \Phi(\mathbf{v}) = n\, \mathrm{d}\mathbf{r}\, \langle \Phi(\mathbf{v}) \rangle \ ,$$

where the term in angle brackets is the averaged magnitude of $\Phi(\mathbf{v})$. On the other hand each of the $f(\mathbf{r}, \mathbf{v}, t)\mathrm{d}\mathbf{r}\mathrm{d}\mathbf{v}$ particles contributes a value of $\Phi(\mathbf{v})$ to the sum $\Sigma\, \Phi(\mathbf{v})$. The total contribution of all particles to the sum is equal to $\Phi(\mathbf{v}) f(\mathbf{r}, \mathbf{v}, t)\, \mathrm{d}\mathbf{r}\, \mathrm{d}\mathbf{v}$. Therefore,

$$\Sigma\, \Phi(\mathbf{v}) = \mathrm{d}\mathbf{r} \int \Phi(\mathbf{v})\, f(\mathbf{r}, \mathbf{v}, t) \mathrm{d}\mathbf{v} \ .$$

Comparing two last equations we obtain

$$n\, \langle \Phi \rangle = \int \Phi\, f\, \mathrm{d}\mathbf{v} \ . \tag{1.2}$$

The last equation is very useful to get relations of the distribution function with hydrodynamic parameters. For example, in the case when $\Phi(\mathbf{v}) = \mathbf{v}$, (1.2) gives the relation between the bulk velocity of gas $\mathbf{V}(\mathbf{r}, t)$ and the distribution function:

$$n(\mathbf{r}, t)\, \mathbf{V}(\mathbf{r}, t) = \int \mathbf{v} f(\mathbf{r}, \mathbf{v}, t)\, \mathrm{d}\mathbf{v} \tag{1.3}$$

1.3 Physical derivation of the equation for the distribution function

In this section we derive the kinetic equation for the distribution function $f(\mathbf{r}, \mathbf{v}, t)$ using a simplified physically intuitive method. An exact derivation of the kinetic equation is based on the Liouville equation for the N-particle distribution function depending on $3N$ coordinates and $3N$ velocities of N particles, which form the given system, and the time t could be found, e.g., in Bogolubov (1946).

We assume in this section that the collision time of each particle with other particles is much smaller than the time between collisions. Another assumption is that forces $\mathbf{F}(\mathbf{r}, t)$ acting on individual particles are functions of the coordinates and time only, and they do not depend on the particle velocities.

Let us consider a particle that has 6D phase-space coordinates $(\mathbf{r}, \mathbf{v})$ at the moment t, and the particle moves under the action of an external force $\mathbf{F}$ only. In this case the particle has the following coordinates at the moment $t^* = t + \mathrm{d}t$:

$$\mathbf{r}^* = \mathbf{r} + \mathbf{v}\mathrm{d}t; \quad \mathbf{v}^* = \mathbf{v} + (\mathbf{F}/m)\mathrm{d}t \ , \tag{1.4}$$

where m is the particle mass.

The phase-space volume element $\mathrm{d}\mathbf{r}\,\mathrm{d}\mathbf{v}$ has $f(\mathbf{r},\mathbf{v},t)\,\mathrm{d}\mathbf{r}\,\mathrm{d}\mathbf{v}$ particles at the moment t. The number of particles in the phase space volume $\mathrm{d}\mathbf{r}^*\mathrm{d}\mathbf{v}^*$ at the moment $t^* = t + \mathrm{d}t$ is equal to $f(\mathbf{r}^*,\mathbf{v}^*,t^*)\,\mathrm{d}\mathbf{r}^*\,\mathrm{d}\mathbf{v}^*$. In the case when collisions between particles are absent and particles move under the influence of an external force, $\mathbf{F}$, $f(\mathbf{r}^*,\mathbf{v}^*,t^*)\,\mathrm{d}\mathbf{r}^*\,\mathrm{d}\mathbf{v}^* - f(\mathbf{r},\mathbf{v},t)\,\mathrm{d}\mathbf{r}\,\mathrm{d}\mathbf{v}$ is equal to zero. However, during the time period $\mathrm{d}t$ every particle can experience collisions with other particles. In the case of collisions, the trajectories of particles will not be determined by equations (1.4) and the difference $f(\mathbf{r}^*,\mathbf{v}^*,t^*)\,\mathrm{d}\mathbf{r}^*\,\mathrm{d}\mathbf{v}^* - f(\mathbf{r},\mathbf{v},t)\,\mathrm{d}\mathbf{r}\,\mathrm{d}\mathbf{v}$ is not equal to zero.

If we denote changes of number of particles in the volume element $\mathrm{d}\mathbf{r}^*\,\mathrm{d}\mathbf{v}^*$ due to collisions in the interval of time $\mathrm{d}t$ as $-S\,\mathrm{d}\mathbf{r}\,\mathrm{d}\mathbf{v}\,\mathrm{d}t$, then we have

$$f(\mathbf{r}+\mathbf{v}\mathrm{d}t, \mathbf{v}+\mathbf{F}/m\,\mathrm{d}t, t+\mathrm{d}t,)\,\mathrm{d}\mathbf{r}^*\,\mathrm{d}\mathbf{v}^* - f(\mathbf{r},\mathbf{v},t)\,\mathrm{d}\mathbf{r}\,\mathrm{d}\mathbf{v} = -S\,\mathrm{d}\mathbf{r}\,\mathrm{d}\mathbf{v}\,\mathrm{d}t, \quad (1.5)$$

The right part of Equation (1.5) represents a difference between the number of particles which are inside the phase volume $\mathrm{d}\mathbf{r}\,\mathrm{d}\mathbf{v}$ at moment t but, due to collisions, are outside of $\mathrm{d}\mathbf{r}^*\,\mathrm{d}\mathbf{v}^*$ at moment t^*, and the number of particles which are out of $\mathrm{d}\mathbf{r}\,\mathrm{d}\mathbf{v}$ at moment t but enter the volume $\mathrm{d}\mathbf{r}^*\,\mathrm{d}\mathbf{v}^*$ at moment t^* due to collisions. The term S, which is called the *integral of collisions*, will be derived below in explicit form.

The volume elements $\mathrm{d}\mathbf{r}\,\mathrm{d}\mathbf{v}$ and $\mathrm{d}\mathbf{r}^*\,\mathrm{d}\mathbf{v}^*$ have the following relation

$$\mathrm{d}\mathbf{r}^*\,\mathrm{d}\mathbf{v}^* = J\,\mathrm{d}\mathbf{r}\,\mathrm{d}\mathbf{v}\ , \quad (1.6)$$

where J is the Jacobian of the transformation from ($\mathbf{r}$, $\mathbf{v}$) to ($\mathbf{r}^*$, $\mathbf{v}^*$). In the case that an external force $\mathbf{F}$ is a function of $\mathbf{r}$ and t, the Jacobian is equal to 1.

Expanding the left hand side (LHS) of Equation (1.5) into a Taylor series, taking into account first order terms only, and dividing both sides of Equation (1.5) by $\mathrm{d}\mathbf{r}\,\mathrm{d}\mathbf{v}\,\mathrm{d}t$ ($\mathrm{d}\mathbf{r}\,\mathrm{d}\mathbf{v} = \mathrm{d}\mathbf{r}^*\,\mathrm{d}\mathbf{v}^*$) we, finally, get the *kinetic equation* for the distribution function $f(\mathbf{r},\mathbf{v},t)$

$$\frac{\partial f}{\partial t} + \mathbf{v}\cdot\frac{\partial f}{\partial \mathbf{r}} + \frac{\mathbf{F}}{m}\cdot\frac{\partial f}{\partial \mathbf{v}} + S(f) = 0\ . \quad (1.7)$$

1.4 The equations for the moments of the distribution function

As previously, we consider $\Phi(\mathbf{v})$ as an arbitrary function of velocity $\mathbf{v}$. Upon multiplying Equation (1.7) by $\Phi(\mathbf{v})$ and integrating over velocity space we get

$$\frac{\partial}{\partial t} n\,\langle\Phi(\mathbf{v})\rangle + \sum_{i=1}^{3}\frac{\partial}{\partial x_i} n\,\langle\Phi(\mathbf{v})v_i\rangle - \sum_{i=1}^{3} F_i n\left\langle\frac{\partial\Phi}{\partial v_i}\right\rangle = -\int S(f)\Phi(\mathbf{v})\mathrm{d}\mathbf{v}, \quad (1.8)$$

where Equation (1.2) was used. We also assume that $f\Phi(\mathbf{v}) \longrightarrow 0$ for $|\mathbf{v}| \longrightarrow \infty$.

Equation (1.8) represents the transport equation for an averaged function that is in angle brackets. Let us consider three cases: $\Phi(\mathbf{v}) = 1$, $\Phi(\mathbf{v}) = m\mathbf{v}$, and $\Phi(\mathbf{v}) = mv^2/2$. It is physically evident that elastic collisions do not change the total

number density, momentum and energy of the gas particles. These conservation laws are mathematically expressed in the following form:

$$\int S(f)\,\mathrm{d}\mathbf{v} = \int S(f)\,m\mathbf{v}\,\mathrm{d}\mathbf{v} = \int S(f)\,\frac{1}{2}mv^2\mathrm{d}\mathbf{v} = 0\ . \tag{1.9}$$

Note, that these physically evident relations can be proven mathematically by using the explicit expressions for the integral of collisions $S(f)$ in the forms of Boltzmann or Landau (see, e.g., Chapman and Cowling, 1952).

The continuity equation is obtained from Equation (1.8) in the case of $\Phi(\mathbf{v}) = 1$:

$$\frac{\partial n}{\partial t} + \nabla \cdot n\mathbf{V} = 0 \ \text{ or } \ \frac{\partial \rho}{\partial t} + \bigtriangledown \cdot \rho\mathbf{V} = 0 \tag{1.10}$$

using the mass density $\rho = mn$.

The momentum equation is obtained from Equation (1.8) for $\Phi(\mathbf{v}) = m\mathbf{v}$. The projection of this equation on the i-axis is

$$\frac{\partial}{\partial t}\rho V_i + \nabla \cdot (\rho\langle v_i\mathbf{v}\rangle) - \rho F_i = 0.$$

This equation can be written in the form

$$\frac{\partial}{\partial t}\rho V_i + \bigtriangledown \cdot \rho\left[\langle \mathbf{c}\, c_i\rangle + \mathbf{V}V_i\right] - \rho F_i = 0,$$

where $\mathbf{c} = \mathbf{v} - \mathbf{V}$ is the random velocity of a particle. Taking into account the continuity equation (1.10) and introducing the static pressure p and components of the viscous stress tensor, $\pi_{ij} = (\tilde{\pi})_{ij}$ by the formula:

$$p = \rho\left\langle \frac{c^2}{3}\right\rangle; \quad \pi_{ij} = \rho\left(\left\langle \frac{c^2}{3}\right\rangle \delta_{ij} - \langle c_i c_j\rangle\right), \tag{1.11}$$

the momentum equation can be re-written in its final form:

$$\rho\frac{\mathrm{d}\mathbf{V}}{\mathrm{d}t} = -\nabla p + \nabla \cdot \tilde{\pi} + \rho\mathbf{F}\ . \tag{1.12}$$

Here

$$\frac{\mathrm{d}}{\mathrm{d}t} = \frac{\partial}{\partial t} + \mathbf{V} \cdot \nabla,$$

and the i - component of vector $\nabla \cdot \tilde{\pi}$ is

$$(\nabla \cdot \tilde{\pi})_i = \sum_{j=1}^{3} \frac{\partial}{\partial x_j}\,\pi_{ij}.$$

The energy equation is obtained from Equation (1.8) for $\Phi(\mathbf{v}) = mv^2/2$:

$$\frac{\partial}{\partial t}\left(\rho\left\langle \frac{v^2}{2}\right\rangle\right) + \nabla \cdot \left(\rho\left\langle \frac{v^2}{2}\mathbf{v}\right\rangle\right) = \rho\mathbf{F} \cdot \mathbf{V}.$$

The temperature T (in degrees Kelvin) is defined in kinetic theory as:

$$kT = m\left\langle \frac{c^2}{3}\right\rangle, \tag{1.13}$$

where k is the Boltzmann constant. Taking into account that $\langle v^2\rangle = \langle c^2\rangle + V^2$, $\langle v^2\mathbf{v}\rangle = \langle c^2\mathbf{c}\rangle + \langle c^2\rangle\mathbf{V} + V^2\mathbf{V} + 2\langle \mathbf{c}\otimes\mathbf{c}\rangle\cdot\mathbf{V}$ and introducing the temperature, the energy equation can be re-written in the following form:

$$\frac{\partial}{\partial t}\left(c_v\rho T + \rho\frac{V^2}{2}\right) + \nabla\cdot\rho\left(\left\langle\frac{c^2}{2}\mathbf{c}\right\rangle + c_vT\mathbf{V} + \frac{V^2}{2}\mathbf{V} + \mathbf{V}\cdot\langle\mathbf{c}\otimes\mathbf{c}\rangle\right) = \rho\mathbf{F}\cdot\mathbf{V},$$

where $c_v = 3k/2m$ and the components of the direct product $\mathbf{c}\otimes\mathbf{c}$ are $(\mathbf{c}\otimes\mathbf{c})_{ij} = c_ic_j$. Further transformations give:

$$\rho\frac{\mathrm{d}}{\mathrm{d}t}\left(\frac{V^2}{2} + c_vT\right) = \rho\mathbf{F}\cdot\mathbf{V} - \nabla\cdot p\mathbf{V} + \nabla\cdot(\tilde{\pi}\cdot\mathbf{V}) - \nabla\cdot\mathbf{q}\ . \tag{1.14}$$

Here $\mathbf{q} = \rho\left\langle\mathbf{c}\,c^2/2\right\rangle$ is the vector of thermal flux.

The first of equations (1.11) and equation (1.13) give an evident relation between pressure and temperature

$$p = \rho\frac{k}{m}T \tag{1.15}$$

which is known as the *equation of state*.

The equations (1.10), (1.12),(1.14) and (1.15) could form a closed system of equations for macroscopic parameters $\rho(\mathbf{r},t)$, $\mathbf{V}(\mathbf{r},t)$, $p(\mathbf{r},t)$, and $T(\mathbf{r},t)$ if the expressions for the tensor viscous stress $\tilde{\pi}$ and the vector of the thermal flux $\mathbf{q}$, which are integrals of the distribution function, could be defined. Therefore, to get expressions for $\tilde{\pi}$ and $\mathbf{q}$ one needs to solve the kinetic equation (1.7). However, the explicit form for the integral of collisions, $S(f)$, needs to be specified first.

1.5 The collision integral in the Boltzmann form

In this section we derive an explicit form for the integral of collisions S under the assumption that a gas is sufficiently rarefied that we only need to take into account the pair collisions. Let us introduce the following notations: $m_0 = m_1 + m_2$, $M_1 = m_1/m_0$, $M_2 = m_2/m_0$, where indices "1" and "2" are introduced to distinguish colliding particles. Conservation of the total momentum of two colliding elastic particles gives that $m_0\mathbf{v}_0 = m_1\mathbf{v}_1 + m_2\mathbf{v}_2 = m_1\mathbf{v}_1' + m_2\mathbf{v}_2'$, where velocities marked by primes correspond to the velocities of particles after the collision. Relative velocities are denoted as

$$\mathbf{g}_{21} = \mathbf{v}_2 - \mathbf{v}_1 = -\mathbf{g}_{12};\quad \mathbf{g}'_{21} = \mathbf{v}'_2 - \mathbf{v}'_1 = -\mathbf{g}'_{12}$$

$$(\mid\mathbf{g}_{21}\mid = \mid\mathbf{g}_{12}\mid = g;\quad |\mathbf{g}'_{21}| = |\mathbf{g}'_{12}| = g')\,.$$

Taking into account the relations above we obtain

$$\mathbf{v}_1 = \mathbf{v}_0 + M_2\mathbf{g}_{12};\ \mathbf{v}'_1 = \mathbf{v}_0 + M_2\mathbf{g}'_{12};\ \mathbf{v}_2 = \mathbf{v}_0 + M_1\mathbf{g}_{21};\ \mathbf{v}'_2 = \mathbf{v}_0 + M_1\mathbf{g}'_{21}\ .$$

From the last formula and the law of energy conservation in elastic collisions, i.e.

$$m_1\frac{v_1^2}{2} + m_2\frac{v_2^2}{2} = m_1\frac{v_1'^2}{2} + m_2\frac{v_2'^2}{2},$$

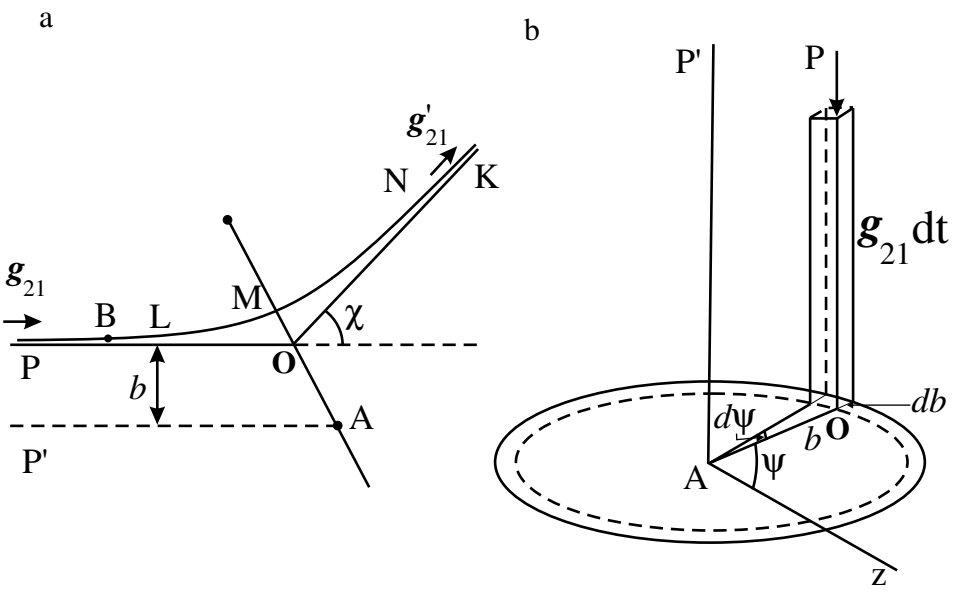

Figure 1.1: a. Scheme of a two-particle interaction. Curve LMN represents the trajectory of particle B relative to particle A. OP and OK are asymptotic lines to the trajectory of particle B. Line AP' is parallel to line OP. OA is the line that connects particle A with particle B at the moment when the distance between the particles is minimal. b. Scheme of a cylinder which is associated with each interacting particle of A-type. b is the impact parameter, ψ the azimuth angle.

we can obtain that

$$g = g',$$

i.e. the modulus of the relative velocity of the colliding particles has the same value after the collision as it had before. However, the direction of the relative velocity is changed during the collision. Let us introduce the impact parameter b that is the minimum distance of colliding particles in the case of non-interacting particles (see Fig. 1.1). From the conservation of angular momentum of the two interacting particles we have that

$$b = b'.$$

The dynamic effect of the two-particle collision is completely determined by the direction of the vector $\mathbf{g}'_{21}$. This direction is determined by the initial velocities $\mathbf{v}_1$, $\mathbf{v}_2$, the parameter b and a deviation angle χ of the relative velocity $\mathbf{g}_{21}$ (see Fig. 1.1). Knowing the interaction potential of the colliding particles one can derive a functional connection between b, g and χ.

Let us denote ψ as the azimuth angle between the plane of the trajectory of particle B (LMN in Fig. 1.1a) and the plane containing line AP' and some fixed in space direction which we denote as the Az-axis (see Fig. 1.1b). We consider particle A (Fig. 1.1) and calculate the number of collisions of this particle with

other particles having the impact parameters in the range from b to $b + \mathrm{d}b$ and angle ψ from ψ to $\psi + \mathrm{d}\psi$. We consider the collisions which occur in the time-interval from t to $t + \mathrm{d}t$. It is evident that particle A has collisions with those particles which are not farther than $g\,\mathrm{d}t$ from plane OAz (Fig. 1.1b). (Note, that it is again assumed that the time of collisions themselves are much less than $\mathrm{d}t$.)

Let us denote the particles having velocities from $\mathbf{v}$ to $\mathbf{v} + \mathrm{d}\mathbf{v}$ as A-type (like particle A in Fig. 1.1b). Particles with velocities in the range from $\mathbf{v}_1$ to $\mathbf{v}_1 + \mathrm{d}\mathbf{v}_1$ are called B-type. For each of the $f(\mathbf{r}, \mathbf{v}, t)\,\mathrm{d}\mathbf{r}\,\mathrm{d}\mathbf{v}$ A-type particles, a cylinder segment having a surface element $b\,\mathrm{d}b\,\mathrm{d}\psi$ as its base and length $g\,\mathrm{d}t$ can be drawn. Since $\mathrm{d}b$ and $\mathrm{d}\psi$ are small, it is reasonable to assume that these cylinder segments of A-type particles do not cross each other, and therefore the total volume of these cylinder segments is equal to

$$\mathrm{d}U = f\mathrm{d}\mathbf{r}\,\mathrm{d}\mathbf{v}gb\,\mathrm{d}b\,\mathrm{d}\psi\,\mathrm{d}t \tag{1.16}$$

Some of these cylinders will not have particles of B-type. Since $\mathrm{d}b$, $\mathrm{d}\psi$ and $\mathrm{d}\mathbf{v}_1$ are small, we can neglect a probability that each of these cylinders has more than one particle. Therefore, the full number of B-type particles in the volume $\mathrm{d}U$ will coincide with the number of "occupied" cylinders. Note that every "occupied" cylinder corresponds to one collision. That is why the full number of collisions is equal to $f_1(\mathbf{r}, \mathbf{v}_1, t)d\mathbf{v}_1\,\mathrm{d}U$, or using (1.16) we obtain

$$f(\mathbf{r}, \mathbf{v}, t)f_1(\mathbf{r}, \mathbf{v}_1, t)gb\,\mathrm{d}b\,\mathrm{d}\psi\,\mathrm{d}\mathbf{v}\,\mathrm{d}\mathbf{v}_1\,\mathrm{d}\mathbf{r}\,\mathrm{d}t\,. \tag{1.17}$$

Note that for the derivation of Equation (1.17), we assumed that collisions with a participation of more than two particles can be neglected. This is the so-called hypothesis of pair collisions. To get the full number of collisions of $f(\mathbf{r}, \mathbf{v}, t)\,\mathrm{d}\mathbf{r}\,\mathrm{d}\mathbf{v}$ of A-type particles for period $\mathrm{d}t$, expression (1.17) should be integrated over the full range of impact parameters, b, azimuth angles, ψ, and velocities, $\mathbf{v}_1$:

$$\mathrm{d}\mathbf{v}\,\mathrm{d}\mathbf{r}\,\mathrm{d}t \iiint f(\mathbf{r}, \mathbf{v}, t)f_1(\mathbf{r}, \mathbf{v}_1, t)gb\,\mathrm{d}b\,\mathrm{d}\psi\,\mathrm{d}\mathbf{v}_1\,. \tag{1.18}$$

All collisions accounted for in Equation (1.18) lead to a change in trajectories of A-type particles. Equation (1.18) gives the number of particles which are presented in the volume element $\mathrm{d}\mathbf{r}\,\mathrm{d}\mathbf{v}$ at the moment t, but they did not appear in the $\mathrm{d}\mathbf{r}^*\,\mathrm{d}\mathbf{v}^*$ at the moment $t + \mathrm{d}t$ due to collisions.

Now, let us consider 'reverse' collisions, i.e. collisions in which the velocities of colliding particles after the collisions are $\mathbf{v}$ and $\mathbf{v}_1$. In this case, due to the symmetry of the laws in classical mechanics, the initial velocities of the particles are $\mathbf{v}'$ and $\mathbf{v}'_1$. The number of particles which are not presented in the volume element $\mathrm{d}\mathbf{r}\,\mathrm{d}\mathbf{v}$ at t but which *do appear* in the volume element $\mathrm{d}\mathbf{r}^*\,\mathrm{d}\mathbf{v}^*$ at $t + \mathrm{d}t$ is given by

$$\mathrm{d}\mathbf{r}\,\mathrm{d}\mathbf{v}'\,\mathrm{d}t \iiint f'\left(\mathbf{r}, \mathbf{v}', t\right) f'_1\left(\mathbf{r}, \mathbf{v}'_1, t\right) g'b'\,\mathrm{d}b'\,\mathrm{d}\psi\,\mathrm{d}\mathbf{v}'_1. \tag{1.19}$$

Taking into account $\mathrm{d}\mathbf{v}'\,\mathrm{d}\mathbf{v}'_1 = \mathrm{d}\mathbf{v}\,\mathrm{d}\mathbf{v}_1$, $g = g'$, and $b = b'$ and replacing the right hand side of (1.5) by the difference between (1.19) and (1.18) we obtain *the*

kinetic equation for the distribution function f with the integral of collisions in the Boltzmann form instead of Equation (1.7):

$$\frac{\partial f}{\partial t} + \mathbf{v} \cdot \frac{\partial f}{\partial \mathbf{r}} + \frac{\mathbf{F}}{m} \cdot \frac{\partial f}{\partial \mathbf{v}} = \iiint (f' f_1' - f f_1)\, g\, b\, \mathrm{d}b\, \mathrm{d}\psi\, \mathrm{d}\mathbf{v}_1, \tag{1.20}$$

where we have introduced the designations

$$f' = f(\mathbf{r}, \mathbf{v}', t); \quad f_1 = f(\mathbf{r}, \mathbf{v}_1, t); \quad f_1' = f(\mathbf{r}, \mathbf{v}_1', t) \ .$$

In some situations (e.g. Chapter 8 of this book) the Boltzmann collision integral is convenient to write as:

$$S(f) = \iiint (f' f_1' - f f_1)\, g\, \sigma(g, \chi) \sin\chi\, \mathrm{d}\chi\, \mathrm{d}\psi\, \mathrm{d}\mathbf{v}_1 \,,$$

where $\sigma(g, \chi)$ is a function of relative velocity of the colliding particles and the scattering angle χ (see Fig.1.1a). σ is determined by the interacting potential between the colliding particles, and is called the *differential cross section*.

In the case where the gas consists of particles of different species, the Boltzmann equation (1.20) can be re-written as:

$$\frac{\partial f_\alpha}{\partial t} + \mathbf{v} \cdot \frac{\partial f_\alpha}{\partial \mathbf{r}} + \frac{\mathbf{F}_\alpha}{m_\alpha} \cdot \frac{\partial f_\alpha}{\partial \mathbf{v}} = \sum_\beta \iiint (f_\alpha' f_\beta' - f_\alpha f_\beta)\, g_{\alpha\beta}\, b\, \mathrm{d}b\, \mathrm{d}\psi\, \mathrm{d}\mathbf{v}_\beta. \tag{1.21}$$

Here the summation is taken over all particle species. The derivation of Equations (1.21) is identical to the derivation for the one-component gas given above. The kinetic equations (1.21) written for each species of particles form a system of kinetic equations, which needs to be solved in order to determine, for example, unknown functions such as the viscous stress tensor π, and the vector of thermal flux $\mathbf{q}$.

It should be noted at the end of this section that the electromagnetic force depends on the velocity $\mathbf{v}$ of the particle:

$$\mathbf{F}_\alpha = e_\alpha (\mathbf{E} + \frac{1}{c} \mathbf{v} \times \mathbf{B}),$$

where e_α is the charge of α-type particles (α=e for electrons, α=p for protons, and α=i for other ions), $\mathbf{E}$ and $\mathbf{B}$ are vectors of the electric field intensity and the magnetic field induction. In this case the Jacobian of the transformation from the volume element $\mathrm{d}\mathbf{r}\, \mathrm{d}\mathbf{v}$ to the elementary volume $\mathrm{d}\mathbf{r}^* \mathrm{d}\mathbf{v}^*$ is not exactly equal to unity, but it is easy to show that in this case J is equal to 1 within the second order of approximation, i.e. in $(\mathrm{d}t)^2$.

1.6 Basics of the Chapman-Enskog method

In this section we consider the solution of the Boltzmann equation (1.20) by the Chapman-Enskog method. This method is usually used for the derivation of gas-dynamic equations for various gases including multi-component gases. We present the basic concepts of the method only to avoid long mathematical derivations. We will assume here that

$$\frac{\tau}{t^*} << 1; \quad \frac{l}{L} << 1, \tag{1.22}$$

where t^* and L are the characteristic time and length of the problem considered, and τ and l are the mean free time and path of the particles, respectively. If we assume that the order of the left hand side (LHS) of Equation (1.20) is 1, then the order of the right hand side (RHS) of this equation is t^*/τ or L/l.

Equation (1.20) can be re-written in the following form

$$\Lambda(f) \equiv \frac{\partial f}{\partial t} + \mathbf{v} \cdot \frac{\partial f}{\partial \mathbf{r}} + \frac{\mathbf{F}}{m} \cdot \frac{\partial f}{\partial \mathbf{v}} - \iiint (f' f_1' - f f_1)\, g\, b\, \mathrm{d}b\, \mathrm{d}\psi\, \mathrm{d}\mathbf{v}_1 = 0. \quad (1.23)$$

We will search for a solution of Equation (1.23) assuming that it can be represented in the form of an infinite series:

$$f = f^{(0)} + f^{(1)} + f^{(2)} + ...$$

Applying the operator Λ to this series we get

$$\Lambda(f) = \Lambda(f^{(0)} + f^{(1)} + f^{(2)} + ...)$$
$$= \Lambda^{(0)}(f^{(0)}) + \Lambda^{(1)}(f^{(0)}, f^{(1)}) + \Lambda^{(2)}(f^{(0)}, f^{(1)}, f^{(2)}) + ...$$

It is assumed in the Chapman-Enskog method that every term of the last series is equal to zero, and:

$$\Lambda^{(0)}(f^{(0)}) \equiv \iiint (f'^{(0)} f_1'^{(0)} - f^{(0)} f_1^{(0)})\, g\, b\, \mathrm{d}b\, \mathrm{d}\psi\, \mathrm{d}\mathbf{v}_1 = 0,$$

$$\Lambda^{(1)}(f^{(0)}, f_1^{(0)}) \equiv \frac{\partial f^{(0)}}{\partial t} + \mathbf{v} \cdot \frac{\partial f^{(0)}}{\partial \mathbf{r}} + \frac{\mathbf{F}}{m} \cdot \frac{\partial f^{(0)}}{\partial \mathbf{v}} - \quad (1.24)$$

$$- \iiint (f'^{(0)} f_1'^{(1)} + f'^{(1)} f_1'^{(0)} - f^{(0)} f_1^{(1)} - f^{(1)} f_1^{(0)})\, g\, b\, \mathrm{d}b\, \mathrm{d}\psi\, \mathrm{d}\mathbf{v}_1 = 0,$$

.....

The sequence of Equations (1.24) can be obtained more exactly by expanding f into a series $f = f^{(0)} + \varepsilon f^{(1)} + \varepsilon^2 f^{(2)} + ...$, where ε is the small parameter determined by relations (1.22). Only the first and the second equation of sequence (1.24) are considered in the Chapman-Enskog method.

The first of Equations (1.24) is fulfilled if the function $f^{(0)}$ is such that

$$f'^{(0)} f_1'^{(0)} = f^{(0)} f_1^{(0)} \quad \text{or} \quad \ln f'^{(0)} + \ln f_1'^{(0)} = \ln f^{(0)} + \ln f_1^{(0)}\ . \quad (1.25)$$

The last equation means that $\ln f$ is the invariant of collision. Three independent invariants are known for elastic collisions. These are mass, momentum and energy of the interacting particles. Therefore, $\ln f$ should be a combination of these three invariants:

$$\ln f^{(0)} = a_1 \frac{mv^2}{2} + \mathbf{a}_2 \cdot m\mathbf{v} + a_3, \quad (1.26)$$

where a_1, $\mathbf{a}_2$ and a_3 are functions of $\mathbf{r}$ and t which are weakly changing over the mean free path l and during the mean free time τ of particles. The functions a_1, $\mathbf{a}_2$ and a_3 can be determined if we assume that hydrodynamic parameters such as

number density, bulk velocity, and temperature, are expressed through $f^{(0)}$ only, i.e.

$$n\,(\mathbf{r},t) = \int f^{(0)}\mathrm{d}\mathbf{v},$$

$$n\,\mathbf{V}(\mathbf{r},t) = \int \mathbf{v} f^{(0)}\,\mathrm{d}\mathbf{v}, \tag{1.27}$$

$$\frac{3}{2}kT(\mathbf{r},t) = \int \frac{(\mathbf{v}-\mathbf{V})^2}{2} f^{(0)}\,\mathrm{d}\mathbf{v}$$

From equations (1.26) and (1.27) we obtain that $f^{(0)}$ is the local Maxwell distribution function:

$$f^{(0)} = n\left(\frac{m}{2\pi kT}\right)^{3/2}\exp\left[-\frac{m}{2kT}(\mathbf{v}-\mathbf{V})^2\right], \tag{1.28}$$

where the hydrodynamic parameters n, $\mathbf{V}$ and T are slowly changing functions of coordinates $\mathbf{r}$ and time t. Comparison of Equations (1.27) with the definitions of n, $\mathbf{V}$ and T [Equations (1.1), (1.3), (1.13)] shows that for any $f^{(k)}$ $(k > 0)$ the following conditions must be satisfied:

$$\int f^{(k)}\,\mathrm{d}\mathbf{v} = \int \mathbf{v} f^{(k)}\,\mathrm{d}\mathbf{v} = \int (\mathbf{v}-\mathbf{V})^2 f^{(k)}\,\mathrm{d}\mathbf{v} = 0; \quad (k = 1, 2, ...). \tag{1.29}$$

For the local Maxwell distribution function, i.e. in the case when $f = f^{(0)}$ the viscous stress tensor and the vector of the thermal flux are zero ($\pi_{i,j} = 0$ and $\mathbf{q} = 0$). In this case, the momentum equation (1.12) can be re-written as

$$\rho\frac{\mathrm{d}\mathbf{V}}{\mathrm{d}t} = -\nabla p + \rho\mathbf{F}, \tag{1.30}$$

and the energy equation (1.14) becomes

$$\rho\frac{\mathrm{d}}{\mathrm{d}t}\left(\frac{V^2}{2} + \frac{3k}{2m}T\right) = \rho\mathbf{F}\cdot\mathbf{V} - \nabla\cdot p\mathbf{V}$$

Forming the scalar product of $\mathbf{V}$ with the momentum equation (1.30) and using the continuum equation (1.10) , the last equation can be re-written as

$$\rho c_v\frac{\mathrm{d}T}{\mathrm{d}t} + p\nabla\cdot\mathbf{V} = 0; \quad \left(c_v = \frac{3k}{2m}\right). \tag{1.31}$$

In this approximation (local Maxwell distribution function) we get a closed system of Equations (1.10), (1.30), (1.31), and (1.15) for $\rho(\mathbf{r},t)$, $\mathbf{V}(\mathbf{r},t)$, $p(\mathbf{r},t)$, and $T(\mathbf{r},t)$. These are the Euler equations of the ideal hydrodynamics without dissipation of energy. The next Chapman-Enskog approximation, which gives rise to the non-ideal hydrodynamics and the Navier-Stokes equations, requires getting a solution, $f^{(1)}$, to the second equation of the system (1.24).

Introducing the local Maxwell distribution function $f^{(0)}$ from Equation (1.28), the second equation of (1.24) for $f^{(1)}$ has the following form:

$$f^{(0)}\left\{\frac{1}{n}\frac{\partial n}{\partial t}+\frac{1}{T}\frac{\partial T}{\partial t}\left[\frac{m(\mathbf{v}-\mathbf{V})^2}{2kT}-\frac{3}{2}\right]+\right.$$

$$+\frac{m}{kT}(\mathbf{v}-\mathbf{V})\cdot\frac{\partial \mathbf{V}}{\partial t} \quad + \quad \frac{\mathbf{v}}{n}\cdot\frac{\partial n}{\partial \mathbf{r}}+\frac{\mathbf{v}}{T}\cdot\frac{\partial T}{\partial \mathbf{r}}\left[\frac{m(\mathbf{v}-\mathbf{V})^2}{2kT}-\frac{3}{2}\right]+ \tag{1.32}$$

$$\left.+\left[\frac{m}{kT}\left(\mathbf{v}\cdot\bigtriangledown\right)\mathbf{V}\right]\cdot(\mathbf{v}-\mathbf{V})-\frac{m}{kT}(\mathbf{v}-\mathbf{V})\cdot\frac{\mathbf{F}}{m}\right\}=$$

$$\iiint(f'^{(0)}f_1'^{(1)}+f'^{(1)}f_1'^{(0)}-f^{(0)}f_1^{(1)}-f^{(1)}f_1^{(0)})\,g\,b\,\mathrm{d}b\,\mathrm{d}\psi\,\mathrm{d}\mathbf{v}_1.$$

The time derivation in the RHS of Equation (1.32) can be excluded by using equations of ideal hydrodynamics that can be re-written in the form:

$$\frac{\partial n}{\partial t}=-\nabla\cdot n\mathbf{V},$$

$$\frac{\partial \mathbf{V}}{\partial t}=-\mathbf{V}\cdot\nabla\mathbf{V}-\frac{1}{mn}\nabla p+\mathbf{F},$$

$$\frac{\partial T}{\partial t}=-\mathbf{V}\cdot\nabla T-\frac{2}{3nk}p\nabla\cdot\mathbf{V},$$

$$p=nkT,$$

The function $f^{(1)}$ can be re-written as a product of $f^{(0)}$ and a function φ: $f^{(1)}=f^{(0)}\varphi(\mathbf{r},\mathbf{v},t)$. Then Equation (1.32) can be re-written for the function φ

$$f^{(0)}\left[\mathbf{c}\cdot\frac{\partial \ln T}{\partial \mathbf{r}}\left(\frac{m}{2kT}|\mathbf{c}|^2-\frac{5}{2}\right)+\sum\sum\frac{m}{kT}\left(c_ic_j-\frac{1}{3}\delta_{ij}|\mathbf{c}|^2\right)\frac{\partial V_i}{\partial x_j}\right] \tag{1.33}$$
$$=\iiint f_1^{(0)}f^{(0)}(\varphi'+\varphi_1'-\varphi-\varphi_1)\,g\,b\,\mathrm{d}b\,\mathrm{d}\psi\mathrm{d}\mathbf{v}_1,$$

where $\mathbf{c}=\mathbf{v}-\mathbf{V}$ is the random velocity.

Equation (1.33) is a non-uniform linear integral equation for the function φ that replaces the second equation of the sequence (1.24). Equation (1.33) has solutions if the LHS of this equation is orthogonal to the solutions of the corresponding homogeneous equation. It can be easily shown (see, for example, Chapman and Cowling, 1952) that this condition is fulfilled. Because Equation (1.33) is linear we can present a solution of this equation as follows:

$$\varphi(\mathbf{c})=-A(\xi)\,\mathbf{c}\cdot\sqrt{\frac{m}{2kT}}\frac{\partial \ln T}{\partial \mathbf{r}}-\frac{m}{2kT}B(\xi)\sum\sum\left(c_ic_j-\frac{1}{3}\delta_{ij}|\mathbf{c}|^2\right)\frac{\partial V_i}{\partial x_j}. \tag{1.34}$$

Here A and B are unknown functions of $\xi = m\left|\mathbf{c}\right|^2/2kT$. The first and third condition of Equation (1.27) are identically satisfied. From the second condition we get

$$\int_0^\infty \mathrm{d}\xi \xi^{3/2} e^{-\xi} A(\xi) = 0. \tag{1.35}$$

The functions A and B can be expanded in a series of orthogonal Sonin-Lager's polynomials by

$$A(\xi) = \sum_{i=0}^{\infty} a_i L_i^{3/2}(\xi), B(\xi) = \sum_{i=0}^{\infty} b_i L_i^{3/2}(\xi), \tag{1.36}$$

where a_i and b_i are unknown constant coefficients, and the polynomials L_i are determined as

$$L_i^r(\xi) = \sum_{j=0}^{i} (-1)^j \xi^j \frac{i!\Gamma(i+r+1)}{j!\Gamma(j+r+1)\Gamma(i-j+1)}, \quad \Gamma(i+\frac{1}{2}) = \frac{\sqrt{\pi}}{2^i}(2i-1)!!$$

The conditions of orthogonality of Sonin-Lager's polynomials are

$$\int_0^\infty d\xi e^{-\xi} \xi^r L_i^r(\xi) L_{i'}^r(\xi) = \delta_{ii'} i!\Gamma(i+r+1) \tag{1.37}$$

The first two polynomials of Sonin-Lager have the form

$$L_0^{3/2}(\xi) = 1, \quad L_1^{3/2}(\xi) = \frac{5}{2} - \xi, L_0^{5/2}(\xi) = 1, \quad L_1^{5/2}(\xi) = \frac{7}{2} - \xi.$$

From Equations (1.37) and (1.35) one derives $a_0 = 0$.

Replacing φ in Equation (1.33) by the expressions given in (1.34) and (1.36) one can get two independent infinite systems of algebraic equations for sequences of the coefficients $a_i$and b_i. Usually, it is sufficient to take into account only the few first coefficients of the expansion in (1.36).

As an example let us consider an algorithm for deriving the equations for the coefficients a_i. Replacing φ in Equation (1.33) by the expressions given in (1.34) and (1.36), and equating all coefficient of $\partial \ln T/\partial \mathbf{r}$ with zero we get the following equation

$$f^{(0)}\mathbf{c}\left(\xi - \frac{5}{2}\right) = -\iiint f_1^{(0)}(\mathbf{c}_1) f^{(0)}(\mathbf{c}) \sum_{i=1}^{\infty} a_i \sqrt{\frac{m}{2kT}} \times$$

$$\times \left[\mathbf{c}' L_i^{3/2}(\xi') + \mathbf{c}_1' L_i^{3/2}(\xi_1') - \mathbf{c} L_i^{3/2}(\xi) - \mathbf{c}_1 L_i^{3/2}(\xi_1)\right] g\, b\, \mathrm{d}b\, \mathrm{d}\psi\, \mathrm{d}\mathbf{c}_1$$

Multiplying this equation by $\mathbf{c}(m/2kT)L_j^{3/2}(m\left|\mathbf{c}\right|^2/2kT)$, integrating over velocities $\mathbf{c}$ and using the orthogonality condition (1.37) we obtain that the LHS of this equation is equal to

$$-\delta_{j1}\frac{15}{4}n.$$

As a result we have an infinite system of algebraic equations to determine the coefficients a_i

$$\frac{15}{4} n\delta_{j1} = \sum_{i=1}^{\infty} \alpha_{ij} a_i, \quad j = 1, 2, ..., \infty \tag{1.38}$$

where the coefficients α_{ij} are:

$$\alpha_{ij} = \int \mathrm{d}\mathbf{c}\, \mathrm{d}\mathbf{c}_1\, g\, b\, \mathrm{d}b\, \mathrm{d}\psi\, f_1^{(0)} f^{(0)} L_j^{3/2} \left(\frac{m}{2kT}\right)^{3/2} \times$$

$$\times \left[\mathbf{c}\cdot\mathbf{c}' L_i^{3/2}(\xi') + \mathbf{c}\cdot\mathbf{c}_1' L_i^{3/2}(\xi_1') - |\mathbf{c}|^2 L_i^{3/2}(\xi) - \mathbf{c}\cdot\mathbf{c}_1 L_i^{3/2}(\xi_1)\right]$$

In the simplest case, when we restrict ourselves to the first term of the expansion (1.36), a solution of system (1.38) is simple because $a_0 = 0$:

$$a_1 = \frac{15}{4}\frac{n}{\alpha_{11}}.$$

A system of equations for the coefficients b_i can be obtained in a similar way.

Therefore, the problem is now reduced to getting solutions of an algebraic system of equations. Indeed, resolving the system of Equations (1.38) we get a_i. These coefficients are then used to get $\varphi(\mathbf{c})$ from Equations (1.34) and (1.36). Thereafter, the distribution function $f(\mathbf{r}, \mathbf{v}, t)$ is determined in the first approximation by Equation (1.28) and $f^{(1)} = f^{(0)}\varphi(\mathbf{c})$.

It is important to note that the viscous stress tensor π and the vector of the thermal flux $\mathbf{q}$ are determined by the function $f^{(1)}$, only. In particular, the vector of the thermal flux can by calculated in the first approximation by the formula (see Section 1.3)

$$\mathbf{q} = \rho \left\langle \frac{c^2}{2}\mathbf{c} \right\rangle = \int \frac{m|\mathbf{c}|^2}{2}\mathbf{c}(f^{(0)} + f^{(1)})\, \mathrm{d}\mathbf{c} = \int \frac{m|\mathbf{c}|^2}{2}\mathbf{c} f^{(1)}\, \mathrm{d}\mathbf{c} = -\kappa\nabla T,$$

where κ is the coefficient of the thermal conductivity. The expression for κ can be derived from (1.34) noting that the integral of the second term of (1.34) is equal to zero:

$$\kappa = \frac{2}{3}\sqrt{\frac{2kT}{m\pi}} kn \int_0^{\infty} \mathrm{d}\xi e^{-\xi} \xi^{5/2} A(\xi)$$

An expression for the viscous stress tensor can be obtained in a similar way. The coefficients of viscosity, thermal conductivity and so on are called *transport coefficients*. Exact expressions for the transport coefficients can be calculated when the interaction potential of the colliding particles, or the differential cross section of the collisions are known.

1.7 Transport coefficients for a fully ionized magnetized two-component gas

Hydrogen is the most abundant gas in space. It can either be in partially or in fully ionized states. Such states of gas are usually called *plasma* in the case of quasi-neutral gases, i.e. gases where negative and positive charges approximately compensate each other. Unlike previous sections considering a simple gas, in this section we consider fully ionized plasma consisting of electrons and protons. In this case we have the system of Boltzmann equations (1.21) consisting of equations for electrons (index "e") and protons (index "p"):

$$\frac{\partial f_{\rm e}}{\partial t} + \mathbf{v}\cdot\frac{\partial f_{\rm e}}{\partial \mathbf{r}} - \frac{e}{m_{\rm e}}\left(\mathbf{E} + \frac{1}{c}\mathbf{v}\times\mathbf{B}\right)\cdot\frac{\partial f_{\rm e}}{\partial \mathbf{v}} = \tag{1.39}$$

$$\int\int\int \left(f'_{\rm e}f'_{\rm e1} - f_{\rm e}f_{\rm e1}\right)\, g\, b\,{\rm d}b\,{\rm d}\psi\,{\rm d}\mathbf{v}_1 + \int\int\int \left(f'_{\rm e}f'_{\rm p1} - f_{\rm e}f_{\rm p1}\right)\, g\, b\,{\rm d}b\,{\rm d}\psi\,{\rm d}\mathbf{v}_1,$$

$$\frac{\partial f_{\rm p}}{\partial t} + \mathbf{v}\cdot\frac{\partial f_{\rm p}}{\partial \mathbf{r}} + \frac{e}{m_{\rm p}}\left(\mathbf{E} + \frac{1}{c}\mathbf{v}\times\mathbf{B}\right)\cdot\frac{\partial f_{\rm p}}{\partial \mathbf{v}} = \tag{1.40}$$

$$=\int\int\int \left(f'_{\rm p}f'_{\rm e1} - f_{\rm p}f_{\rm e1}\right)\, g\, b\,{\rm d}b\,{\rm d}\psi\,{\rm d}\mathbf{v}_1 + \int\int\int \left(f'_{\rm p}f'_{\rm p1} - f_{\rm p}f_{\rm p1}\right)\, g\, b\,{\rm d}b\,{\rm d}\psi\,{\rm d}\mathbf{v}_1,$$

where the charge of the electron is $-e$, $\mathbf{E}$ and $\mathbf{B}$ are vectors of electric field intensity and magnetic field induction, respectively. Assuming that the scattering of charged particles occurs predominantly at small angles only (i.e. distant collisions dominate) the RHS of these equations can be re-written in the Landau form (see, for example, Braginskii, 1965). On the basis of the Landau integral of collisions, Braginskii (1965) calculated the transport coefficients for a fully ionized plasma having different temperatures for electrons and protons ($T_{\rm e}$ and $T_{\rm p}$, respectively). A Chapman-Enskog method, similar to the one described in the previous section, was used in these calculations. Generalizing the Chapman-Enskog method for the system (1.39) and (1.40), which replaces Equation (1.23), we get the following form of the system (1.24):

$$\frac{e_\alpha}{m_\alpha c}\left(\mathbf{c}_\alpha\times\mathbf{B}\right)\cdot\frac{\partial f_\alpha^{(0)}}{\partial \mathbf{v}} = \sum_\beta \int\int\int \left(f_\alpha^{\prime(0)}f_\beta'(0) - f_\alpha^{(0)}f_\beta^{(0)}\right)\, g\, b\,{\rm d}b\,{\rm d}\psi\,{\rm d}\mathbf{v}_\beta \tag{1.41}$$

$$\frac{\partial f_\alpha^{(0)}}{\partial t} + \mathbf{v}\cdot\frac{\partial f_\alpha^{(0)}}{\partial \mathbf{r}} + \frac{e_\alpha}{m_\alpha}\left(\mathbf{E} + \frac{1}{c}\mathbf{V}_\alpha\times\mathbf{B}\right)\cdot\frac{\partial f_\alpha^{(0)}}{\partial \mathbf{v}} = -\frac{e_\alpha}{m_\alpha c}(\mathbf{c}_\alpha\times\mathbf{B})\cdot\frac{\partial f_\alpha^{(1)}}{\partial \mathbf{v}} -$$

$$-\sum_\beta \int \left(f_\alpha^{(1)}f_\beta^{(0)} + f_\alpha^{(0)}f_\beta^{(1)} - f_\alpha^{\prime(1)}f_\beta^{\prime(0)} - f_\alpha^{\prime(0)}f_\beta^{\prime(1)}\right)\, g_{\alpha\beta}\, b\,{\rm d}\,b\,{\rm d}\psi\,{\rm d}\mathbf{v}_\beta \tag{1.42}$$

.....

Here $\mathbf{c}_\alpha = (\mathbf{v} - \mathbf{V}_\alpha)$, $\mathbf{V}_\alpha$ is the mean velocity of the α-component ($\alpha = {\rm e}, {\rm p}$) that is determined as

$$n_\alpha \mathbf{V}_\alpha = \int \mathbf{v} f_\alpha\,{\rm d}\mathbf{v}\ . \tag{1.43}$$

It can be shown (see, for example, Chapman and Cowling, 1952) that the solution of the two equations ($\alpha = e, p$) of (1.41) is Maxwellian distribution functions with the equal temperatures for electrons and protons ($T_\mathrm{e} = T_\mathrm{p} = T$):

$$f_\alpha^{(0)} = n_\alpha \left(\frac{m_\alpha}{2\pi kT}\right)^{3/2} \exp\left[\frac{m_\alpha}{2kT}\left(\mathbf{v} - \mathbf{V}_\alpha\right)^2\right] . \tag{1.44}$$

However, since the mass of the electron is much less than the mass of the proton ($m_\mathrm{e} \ll m_\mathrm{p}$), the relaxation times for the velocity distribution to become Maxwellian are much smaller for each of the two components compared with the characteristic time of exchange between energies of the two components due to collisions. This means that situations where $T_\mathrm{e} \neq T_\mathrm{p}$ are quite possible in space. In this case magnetohydrodynamic equations with two temperatures can be derived. Transport coefficients for such a two-temperature plasma were derived by Braginskii (1965) using the collision integral in the Landau form, which is

$$S_\alpha\left(\mathbf{r}, \mathbf{p}, t\right) = -\sum_\beta 2e_\alpha^2 e_\beta^2 \frac{\partial}{\partial p_i} \int Q_{ij}\left(\mathbf{v} - \mathbf{v}'\right)\left\{\frac{\partial f_\alpha}{\partial p_j} f_\beta - \frac{\partial f_\beta}{\partial p_j'} f_\alpha\right\} \mathrm{d}\mathbf{p}', \tag{1.45}$$

where

$$Q_{ij} = \pi \ln\left(\frac{r_\mathrm{d}}{r_\mathrm{min}}\right) \frac{1}{|\mathbf{v} - \mathbf{v}'|^3}\left(|\mathbf{v} - \mathbf{v}'|^2 \delta_{ij} - \left(\mathbf{v} - \mathbf{v}'\right)_i \left(\mathbf{v} - \mathbf{v}'\right)_j\right),$$

where r_d and $r_\mathrm{min} = e^2/kT_e$ are the Debye radius and the minimal distance between charged particles which was considered by Landau (1937) only taking into account small-angle scattering. The exact derivation of the kinetic equation for a fully ionized plasma with the collision integral in the form of Landau (1.45) was made, for example, by Klimontovich (1967). The derivation was done on the basis of the Liouville equation for the N-particle distribution function $f_N\left(\mathbf{r}_1, \mathbf{r}_2, ...\mathbf{r}_N; \mathbf{p}_1, \mathbf{p}_2, ...\mathbf{p}_N, t\right)$. The basic assumptions to obtain the kinetic equation with the collision integral in the form of Landau (1.45) are discussed in Section 1.8 of this chapter following Klimontovich (1967).

Here, we consider several results obtained by Braginskii (1965) for a fully ionized plasma on the basis of the Chapman-Enskog method described schematically in Section 1.6. The hydrodynamic equations were derived in the presence of the magnetic field $\mathbf{B}$ under the condition of relatively large magnetic fields such that $\omega_\alpha \tau_\alpha \geq 1$, when the left-hand side of Equation (1.41) cannot be neglected. Here $\omega_\alpha = e_\alpha B/(m_\alpha c)$ and τ_α are the cyclotron frequency and the mean free time of a charged particle, respectively. Braginskii (1965) has used the fact that the electron thermal velocity, v_{T_e} is much larger than proton thermal velocity, v_{T_p}, i.e. $v_{T_\mathrm{e}} >> v_{T_\mathrm{p}}$, and assumed that $T_\mathrm{e} \geq T_\mathrm{p}$ ($m_\mathrm{e} << m_\mathrm{p}$). In this case it is possible to simplify the collisional integrals S_ep and S_pe and to get a solution of the Boltzmann equation for the proton component separately from the electron component. As a result the first approximation of the Chapman-Enskog method (see the Equation (1.41)) gives Maxwellian distribution functions for electrons and protons, but the components have different temperatures, namely

$$f_\alpha^{(0)} = n_\alpha \left(\frac{m_\alpha}{2\pi kT_\alpha}\right)^{3/2} \exp\left[-\frac{m_\alpha}{2kT_\alpha}\left(\mathbf{v} - \mathbf{V}_\alpha\right)^2\right], \alpha = \mathrm{e}, \mathrm{p}. \tag{1.46}$$

In this approach the viscosity stress tensor π_α and the vector of thermal flux $\mathbf{q}_\alpha$ are equal to zero. In the next approximation (Equation (1.42)) the momentum equations for the bulk velocity of electrons and protons ($\mathbf{V}_\alpha$) have the following form

$$m_\alpha n_\alpha \frac{\mathrm{d}_\alpha \mathbf{V}_\alpha}{\mathrm{d}t} = -\nabla p_\alpha + e_\alpha n_\alpha \left(\mathbf{E} + \frac{1}{c} \mathbf{V}_\alpha \times \mathbf{B} \right) + \nabla \cdot \pi_\alpha + \mathbf{R}_\alpha, \tag{1.47}$$

where $\alpha = \mathrm{e}, \mathrm{p}$, $\mathbf{R}_\alpha$ is the term for the exchange of momentum between electrons and protons due to collisions ($\mathbf{R}_{\mathrm{ep}} = -\mathbf{R}_{\mathrm{pe}}$). External forces $\mathbf{F}_\alpha$ are omitted for simplicity. Expressions for viscosity stress tensors, π_α, were calculated by Braginskii (1965) in this approximation of the Chapman-Enskog method. This tensor becomes anisotropic (it depends on the magnitude and direction of the magnetic field $\mathbf{B}$). In addition, following notation was used in the equation (1.47):

$$\frac{\mathrm{d}_\alpha}{\mathrm{d}t} = \frac{\partial}{\partial t} + \mathbf{V}_\alpha \cdot \nabla. \tag{1.48}$$

The heat transfer equations have the following form in the case of $T_\mathrm{e} \neq T_\mathrm{p}$:

$$\frac{3}{2} n_\alpha k \frac{\mathrm{d}_\alpha T_\alpha}{\mathrm{d}t} + p_\alpha \nabla \cdot \mathbf{V}_\alpha = -\nabla \cdot \mathbf{q}_\alpha + \sum_{k,l} (\pi_\alpha)_{kl} \frac{\partial (\mathbf{V}_\alpha)_k}{\partial x_l} + Q_\alpha \tag{1.49}$$

with $\alpha = \mathrm{e}, \mathrm{p}$. Here $\mathbf{q}_\alpha$ are the vectors of the thermal flux of the electron and proton components, and Q_α is the heat transfer to the α-component due to collisions with particles of the other component.

According to Braginskii (1965) the terms of momentum exchange between the components can be expressed as:

$$\mathbf{R}_{\mathrm{ep}} = -\mathbf{R}_{\mathrm{pe}} \equiv \mathbf{R} = \mathbf{R}_u + \mathbf{R}_T, \quad (\mathbf{R}_{\alpha\alpha} = 0), \tag{1.50}$$

where

$$\mathbf{R}_u = -\alpha_\parallel \mathbf{u}_\parallel - \alpha_\perp \mathbf{u}_\perp + \alpha_\wedge (\mathbf{b} \times \mathbf{u}), \tag{1.51}$$

$$\mathbf{R}_T = -\beta_\parallel^{uT} \nabla_\parallel T_\mathrm{e} - \beta_\perp^{uT} \nabla_\perp T_\mathrm{e} - \beta_\wedge^{uT} (\mathbf{b} \times \nabla T_\mathrm{e}); \tag{1.52}$$

($\mathbf{u} = \mathbf{V}_\mathrm{e} - \mathbf{V}_\mathrm{p}; \mathbf{b} = \mathbf{B}/B$).

The vector of the thermal flux can be calculated as

$$\mathbf{q}_\mathrm{e} = \mathbf{q}_\mathrm{e}^u + \mathbf{q}_\mathrm{e}^T, \quad \mathbf{q}_\mathrm{e}^u = \beta_\parallel^{Tu} \mathbf{u}_\parallel + \beta_\perp^{Tu} \mathbf{u}_\perp + \beta_\wedge^{Tu} (\mathbf{b} \times \mathbf{u}), \tag{1.53}$$

$$\mathbf{q}_\mathrm{e}^T = -\kappa_\parallel^\mathrm{e} \nabla_\parallel T_\mathrm{e} - \kappa_\perp^\mathrm{e} \nabla_\perp T_\mathrm{e} - \kappa_\wedge^\mathrm{e} (\mathbf{b} \times \nabla T_\mathrm{e}), \tag{1.54}$$

$$\mathbf{q}_\mathrm{p}^T = -\kappa_\parallel^\mathrm{p} \nabla_\parallel T_\mathrm{p} - \kappa_\perp^\mathrm{p} \nabla_\perp T_\mathrm{p} + \kappa_\wedge^\mathrm{p} (\mathbf{b} \times \nabla T_\mathrm{p}) \tag{1.55}$$

The heat transfer between components due to collisions is

$$Q_{\mathrm{pe}} = \frac{3 n_e}{\tau_\mathrm{e}} \frac{m_\mathrm{e}}{m_\mathrm{p}} k (T_\mathrm{e} - T_\mathrm{p}) (Q_{\alpha\alpha} = 0), Q_{\mathrm{pe}} + Q_{\mathrm{ep}} = -\mathbf{R} \cdot (\mathbf{V}_\mathrm{e} - \mathbf{V}_\mathrm{p}). \tag{1.56}$$

The last equation of (1.56) is a consequence of conservation of energy in collisions between the components. Indexes "$\parallel$" and "$\perp$" stand for components of a

vector parallel and normal to the magnetic field, respectively. Coefficients, introduced in Equations (1.50) - (1.56), have the following form (see, Braginskii, 1965) for the hydrogen plasma:

$$\alpha_{\parallel} = 0.5129\frac{m_{\rm e}n_{\rm e}}{\tau_{\rm e}}, \alpha_{\perp} = \frac{m_{\rm e}n_{\rm e}}{\tau_{\rm e}}\left(1-\frac{6.416x^2+1.837}{\triangle}\right), \tag{1.57}$$

$$\alpha_{\wedge} = \frac{m_{\rm e}n_{\rm e}}{\tau_{\rm e}}\frac{x\left(1.704x^2+0.7796\right)}{\triangle}, \tag{1.58}$$

$(x=\omega_{\rm e}\tau_{\rm e},\quad \triangle = x^4+14.79x^2+3.7703)$

$$\beta_{\parallel}^{uT} = 0.711n_ek, \beta_{\perp}^{uT} = n_ek\frac{5.101x^2+2.681}{\Delta}, \beta_{\wedge}^{uT} = n_ek\frac{x(1.5x^2+3.053)}{\Delta},$$

$$\beta_{\parallel}^{Tu} = \beta_{\parallel}^{uT}T_{\rm e},\ \beta_{\perp}^{Tu} = \beta_{\perp}^{uT}T_{\rm e},\ \beta_{\wedge}^{Tu} = \beta_{\wedge}^{uT}T_{\rm e}.$$

The coefficients of the electron and proton thermal conductivity have the following form:

$$\kappa_{\parallel}^{\rm e} = 3.1616\frac{n_{\rm e}k^2T_{\rm e}\tau_{\rm e}}{m_{\rm e}},\ \kappa_{\perp}^{\rm e} = \frac{n_{\rm e}k^2T_{\rm e}\tau_{\rm e}}{m_{\rm e}}\frac{(4.664x^2+11.92)}{\triangle}, \tag{1.59}$$

$$\kappa_{\wedge}^{\rm e} = \frac{n_{\rm e}k^2T_{\rm e}\tau_{\rm e}}{m_{\rm e}}\frac{x(2.5x^2+21.67)}{\triangle},$$

$$\kappa_{\parallel}^{\rm p} = 3.906\frac{n_{\rm p}k^2T_{\rm p}\tau_{\rm p}}{m_{\rm p}},\ \kappa_{\perp}^{\rm p} = \frac{n_{\rm p}k^2T_{\rm p}\tau_{\rm p}\left(2y^2+2.645\right)}{\triangle_1}, \tag{1.60}$$

$$\kappa_{\wedge}^{\rm p} = \frac{n_{\rm p}k^2T_{\rm p}\tau_{\rm p}}{m_{\rm p}}\frac{y(2.5y^2+4.65)}{\triangle_1}$$

$$\left(y=\omega_{\rm p}\tau_{\rm p},\ \triangle_1 = y^4+2.7y^2+0.667\right), \tag{1.61}$$

where $\tau_{\rm e}$ and $\tau_{\rm p}$ are the times of the mean free paths of electrons and protons:

$$\tau_{\rm e} = \frac{3\sqrt{m_{\rm e}}\left(kT_{\rm e}\right)^{3/2}}{4\sqrt{2\pi}e^4n_{\rm p}\Lambda},\ \tau_{\rm p} = \frac{3\sqrt{m_{\rm p}}\left(kT_{\rm p}\right)^{3/2}}{4\sqrt{\pi}e^4n_{\rm p}\Lambda}. \tag{1.62}$$

Here Λ is the Coulomb logarithm, and e is the proton charge.

The results summarized in Equations (1.50) - (1.62) allow us to make the following conclusions:

1. The friction force $\mathbf{R}$ between electrons and protons due to collisions is rather complicated and depends on the magnitude and direction of the magnetic field.

2. The thermal conductivity is anisotropic in the case of $\omega_\alpha\tau_\alpha \geq 1$. In the presence of magnetic field the thermal conductivity does not change in the direction along the magnetic field.

3. We did not present the expressions for the viscous stress tensor because they are too awkward. However, we would like to note here that this tensor is also anisotropic in the case when $\omega_\alpha\tau_\alpha \geq 1$.

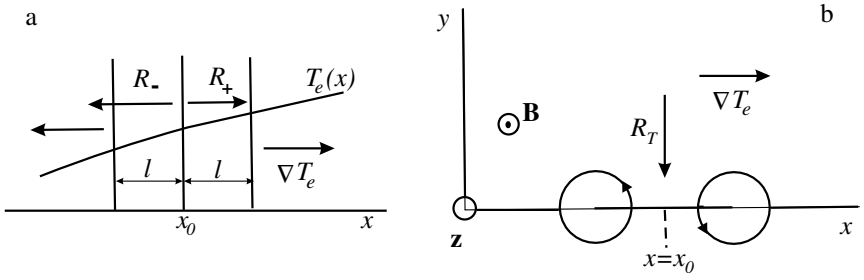

Figure 1.2: Diagrams describing the physical meaning of the thermal force $\mathbf{R}_T$ in the case of negligible magnetic field (a) and in the case of substantial magnetic field (b). In the latter case the thermal force is perpendicular to both the gradient of the temperature ($\nabla T_{\rm e}$) and the magnetic field ($\mathbf{B}$).

To illustrate results summarized in Equation (1.50) - (1.62) we consider the physical explanation of the expression (1.52) for the thermal force, $\mathbf{R}_T$, which is part of momentum transfer term $\mathbf{R}$. Let us consider the case of zero magnetic field or the case when $\mathbf{B} \parallel \nabla T_{\rm e}$ (see Fig. 1.2a). We assume a temperature gradient along the Ox-axis. Electrons colliding at $x = x_0$ arrive to this location from the right and left sides. The electrons arrive on average from a distance of the order of their mean free path $l \sim v_T \tau$ (l is the mean free path). Electrons coming from the right side arrive from a region where the temperature is larger by $\sim l\partial T_{\rm e}/\partial x$ compared with electrons coming from left. As a result the difference between forces $\mathbf{R}_+$ and $\mathbf{R}_-$ (see Fig.1.2) can be estimated as

$$R_T \sim \frac{l}{T_{\rm e}} \frac{\partial T_{\rm e}}{\partial x} \frac{m_{\rm e} n_{\rm e} v_{{\rm e}T}}{\tau_{\rm e}} \sim \frac{m_{\rm e} v_{{\rm e}T}^2}{k T_{\rm e}} k n_{\rm e} \frac{\partial T_{\rm e}}{\partial x} \sim k n_{\rm e} \frac{\partial T_{\rm e}}{\partial x}$$

and this force is directed towards the left side that corresponds to sign "$-$" in Equation (1.52).

Assume now that there is the magnetic field $\mathbf{B}$ which is large enough to be $\omega_{\rm e}\tau_{\rm e} \geq 1$ and it is directed along the Oz-axis (Fig. 1.2b). In this case electrons have the Larmor rotation with the radius $r_{\rm le} \sim v_{{\rm e}T}/\omega_{\rm e}$. Therefore, electrons arrive to the point $x = x_0$ from the left and right sides from distances of order of magnitude of $r_{\rm le}$. "Right" and "left" side electrons have different temperatures. The temperature difference is equal $r_{\rm le}\partial T_{\rm e}/\partial x$. Analogously to the previous case "left" and "right" friction forces do not compensate each other. The resulting force of friction $\mathbf{R}_T$ is normal both to the gradient of the temperature ($\nabla T_{\rm e}$) and the magnetic field ($\mathbf{B}$). This effect is described by the last term of the formula (1.52).

The physical explanation of formula (1.53) – (1.55) for the thermal fluxes could be presented analogously.

1.8 Magnetohydrodynamic equations for a fully ionized one-fluid plasma

In the previous section we considered two-fluid approximation of fully ionized plasma that consists of the system of the magnetohydrodynamic equations for electrons and protons. The number density n_α, bulk velocity $\mathbf{V}_\alpha$, partial pressure p_α, temperature T_α, tensor of viscous intensity π_α, and the vector of thermal flux $\mathbf{q}_\alpha$ were defined for each component ($\alpha = \mathrm{e}, \mathrm{p}$ for electrons and protons, respectively). However, this system of equations can be simplified by introducing total density and bulk velocity of plasma:

$$\rho = \sum_\alpha m_\alpha n_\alpha \simeq m_\mathrm{p} n_\mathrm{p}\,(m_\mathrm{e} << m_\mathrm{p},\ n_\mathrm{e} \approx n_\mathrm{p})\,;\ \rho\mathbf{V} = \sum_\alpha m_\alpha n_\alpha \mathbf{V}_\alpha, \qquad (1.63)$$

where ρ and $\mathbf{V}$ are the mass density and bulk velocity of the electron and proton mixture. Multiplying the continuum equation of the α-component by the mass of the particle, m_α, and taking the sum of the continuum equations of electron and proton components, we get the continuum equation in the one-fluid approximation:

$$\frac{\partial \rho}{\partial t} + \nabla \cdot \rho\mathbf{V} = 0. \qquad (1.64)$$

To get the momentum transfer equation we take the sum of Equations (1.47) over the components. Projection of the total (i.e. for sum of components) momentum equation on the j-axis ($j = x, y, z$) has the following form

$$\rho\frac{\mathrm{d}V_j}{\mathrm{d}t} + \frac{\partial}{\partial x_k}\sum_\alpha (p_\alpha \delta_{jk} - \pi_{\alpha jk} + m_\alpha n_\alpha u_{\alpha k} u_{\alpha j}) = \rho_\mathrm{e}(\mathbf{E})_j + \frac{1}{c}(\mathbf{j}\times\mathbf{B})_j + \rho(\mathbf{F})_j\,, \qquad (1.65)$$

where the following notations are introduced

$$\mathbf{u}_\alpha = \mathbf{V}_\alpha - \mathbf{V};\ \rho_\mathrm{e} = e\,(n_\mathrm{p} - n_\mathrm{e}) \approx 0;\ \mathbf{j} = e\,(n_\mathrm{p}\mathbf{V}_\mathrm{p} - n_\mathrm{e}\mathbf{V}_\mathrm{e}) \approx -e n_\mathrm{e}\,(\mathbf{V}_\mathrm{e} - \mathbf{V}_\mathrm{p})\,, \qquad (1.66)$$

where ρ_e is the charge density, $\mathbf{j}$ is the density of the electric current, and $\mathbf{F}$ is an external mass force. Assuming that the first term on the RHS of Equation (1.65) is much less than the second term due to the condition of quasi-neutrality, $n_\mathrm{e} \approx n_\mathrm{p}$, and that the thermal velocity $v_{\alpha T} >> |\mathbf{u}_\alpha|$ ($p_\alpha \sim v_{\alpha T}^2 >> u_\alpha^2$), we get the momentum equation in the one-fluid approximation

$$\rho\frac{\mathrm{d}\mathbf{V}}{\mathrm{d}t} = -\nabla p + \frac{1}{c}\mathbf{j}\times\mathbf{B} + \nabla\cdot\pi_\mathrm{p} + \rho\mathbf{F}, \quad (\mathbf{R}_\mathrm{ep} = -\mathbf{R}_\mathrm{pe})\,. \qquad (1.67)$$

Here $p = p_\mathrm{e} + p_\mathrm{p}$ is the total static pressure in the one fluid approach. The viscous stress tensor in the one-fluid approach is determined by proton viscosity because it is possible to show that the ratio of the viscous coefficient for electrons to the coefficient for protons is proportional to $\sqrt{m_\mathrm{e}/m_\mathrm{p}} \ll 1$. Although, the viscous stress tensor of proton component is determined through mean velocity of this component, $\mathbf{V}_\mathrm{p}$, it is necessary to note that $\mathbf{V}_p \approx \mathbf{V}$ in the case when the difference $\mathbf{V}_\mathrm{e} - \mathbf{V}_\mathrm{p}$ is not too large (see, (1.63)).

The equation of state is

$$p = \frac{k}{m_\mathrm{p}}\rho\,(T_\mathrm{e} + T_\mathrm{p})\,, \qquad (1.68)$$

because for the partial pressure we have $p_\alpha = n_\alpha k T_\alpha$ and $\rho \approx m_\mathrm{p} n_\mathrm{p}$, $n_\mathrm{e} \approx n_\mathrm{p}$.

To get a closed system of magnetohydrodynamic equations one has to add the heat transfer equations (1.49) for the electron and proton components. Assuming that $T_\mathrm{e} = T_\mathrm{p} = T$ and summing Equations (1.49) for electrons and protons we get

$$\rho c_v \frac{\mathrm{d}T}{\mathrm{d}t} + p\nabla\cdot\mathbf{V} = -\nabla\cdot\mathbf{q} + \sum_{\alpha,k,l} \pi_{\alpha kl}\frac{\partial V_{\alpha k}}{\partial x_l} + \sum_\alpha \left(\mathbf{u}_\alpha\cdot\nabla p_\alpha + Q_\alpha\right), \qquad (1.69)$$

where $\mathbf{q} = \mathbf{q}_\mathrm{e} + \mathbf{q}_\mathrm{p} + \frac{5}{2} n_\mathrm{e} k T \mathbf{u}_\mathrm{e} + \frac{5}{2} n_\mathrm{p} k T \mathbf{u}_\mathrm{p}$ is the vector of the thermal flux. The expression for $\mathbf{q}$ can be simplified to $\mathbf{q} \approx \mathbf{q}_\mathrm{e} - (5kT/2e)\mathbf{j}$ by taking into account that $|\mathbf{q}_\mathrm{e}| >> |\mathbf{q}_\mathrm{p}|$ because of $|\mathbf{q}_\mathrm{e}| \sim m_\mathrm{e}^{-1/2}$ and $|\mathbf{q}_\mathrm{p}| \sim m_\mathrm{p}^{-1/2}$ [see (1.59) – (1.62)], $\mathbf{u}_\mathrm{e} \approx -\mathbf{j}/e n_\mathrm{e}$, $\mathbf{u}_\mathrm{p} \approx 0$.

To evaluate the equation of heat transfer (1.69) further, we must get the equation for the density of the electric current. Multiplying the momentum equation (1.47) by $-e/m_\mathrm{e}$ for electrons ($\alpha = \mathrm{e}$) and by e/m_p for protons, summarizing these equations, taking into account $m_\mathrm{e} << m_\mathrm{p}$, and neglecting viscous terms and external forces (because these terms are usually small in the equation for the electric current) we obtain

$$-e n_\mathrm{e}\frac{\mathrm{d_e}\mathbf{V}_\mathrm{e}}{\mathrm{d}t} + e n_\mathrm{p}\frac{\mathrm{d_p}\mathbf{V}_\mathrm{p}}{\mathrm{d}t} = \frac{e}{m_\mathrm{e}}\nabla p_\mathrm{e} + \frac{e^2 n_\mathrm{e}}{m_\mathrm{e}}\left(\mathbf{E} + \frac{1}{c}\mathbf{V}_\mathrm{e}\times\mathbf{B}\right) - \frac{e}{m_\mathrm{e}}\mathbf{R},$$

($\mathbf{R}_\mathrm{e} = -\mathbf{R}_\mathrm{p} = \mathbf{R}$).

The LHS of this equation has the order of magnitude of $\sim |\mathbf{j}|/t^*$ (t^* is the characteristic time of the hydrodynamic problem considered) and the last term on the RHS has the order of magnitude of $|\mathbf{j}|/\tau_\mathrm{e}$. Since in the hydrodynamic approximation $\tau_\mathrm{e} << t^*$ differential terms in the LHS can be neglected compared with the last term in the RHS. As a result we obtain the generalized Ohm's law in the following form

$$e n_\mathrm{e}\left(\mathbf{E} + \frac{1}{c}\mathbf{V}\times\mathbf{B}\right) - \frac{1}{c}\mathbf{j}\times\mathbf{B} = \mathbf{R} - \nabla p_\mathrm{e}. \qquad (1.70)$$

Here we used the fact that $\mathbf{u}_\mathrm{e} = \mathbf{V}_\mathrm{e} - \mathbf{V} = -\mathbf{j}/e n_\mathrm{e}$. We must also take into account that $\mathbf{R} = \mathbf{R}_u + \mathbf{R}_T$.

Using Equations (1.56) and (1.70) the last term in the RHS of the equation (1.69) can be re-written in a form that has physical interpretation. Indeed, we have

$$Q_\mathrm{e} + Q_\mathrm{p} - \frac{1}{e n_\mathrm{e}}\mathbf{j}\cdot\nabla p_\mathrm{e} = -\mathbf{R}\cdot(\mathbf{V}_\mathrm{e} - \mathbf{V}) - \frac{1}{e n_\mathrm{e}}\mathbf{j}\cdot\nabla p_\mathrm{e} = \frac{1}{e n_\mathrm{e}}\mathbf{j}\cdot(\mathbf{R} - \nabla p_\mathrm{e})$$

Then, substituting $(\mathbf{R} - \nabla p_\mathrm{e})$ from Equation (1.70), we get the heat transfer equation (1.69) in the following form

$$\rho c_v \frac{\mathrm{d}T}{\mathrm{d}t} + p\nabla\cdot\mathbf{V} = -\nabla\cdot\mathbf{q} + \sum_{k,n}\pi_{kn}\frac{\partial V_k}{\partial x_n} + \mathbf{j}\cdot\left(\mathbf{E} + \frac{1}{c}\mathbf{V}\times\mathbf{B}\right), \qquad (1.71)$$

$$\left(c_v = \frac{3k}{m_p},\ \ \pi_{kn} \approx \pi_{pkn},\ \ \mathbf{V}_p \approx \mathbf{V}\right). \qquad (1.72)$$

The first term of the RHS of Equation (1.71) determines the heating of the plasma by thermal conductivity and diffusion, the second term determines the heating of the plasma by dissipation produced by the work of the viscous force, the last term determines the heat produced by the electric current flow.

Usually, the generalized Ohm's law is written in the literature in a simpler form compared with (1.70):

$$\mathbf{j} = \sigma \left(\mathbf{E} + \frac{1}{c} \mathbf{V} \times \mathbf{B} \right) - \frac{e\tau_{\mathrm{e}}}{m_{\mathrm{e}}} \left(\frac{1}{c} \mathbf{j} \times \mathbf{B} - \nabla p_{\mathrm{e}} \right), \tag{1.73}$$

where $\sigma = n_{\mathrm{e}} e^2 \tau_{\mathrm{e}} / m_{\mathrm{e}}$ is the electric conductivity of a fully ionized plasma and the last term of the RHS of this equation determines the Hall current, which can be neglected in the case of $\omega_{\mathrm{e}} \tau_{\mathrm{e}} << 1$. Equation (1.73) can be derived from Equation (1.70) by neglecting $\mathbf{R}_T$ and assuming that $\mathbf{R}_u = -\left(m_{\mathrm{e}} n_{\mathrm{e}} / \tau_{\mathrm{e}}\right) \left(\mathbf{V}_{\mathrm{e}} - \mathbf{V}_{\mathrm{p}}\right)$.

In case that $\omega_{\mathrm{e}} \tau_{\mathrm{e}} << 1$, the generalized Ohm's law can be written in the classic magnetohydrodynamic (MHD) form:

$$\mathbf{j} = \sigma \left(\mathbf{E} + \frac{1}{c} \mathbf{V} \times \mathbf{B} \right) \tag{1.74}$$

In this case, the last term of the RHS of Equation (1.71) is equal to j^2/σ and represents the classic Joule's heat. Note that in the case of $\omega_{\mathrm{e}} \tau_{\mathrm{e}} << 1$ the thermal fluxes, the plasma viscosity, and the electric conductivity become isotropic.

In concluding this section we would like to note that the continuity equation (1.64), the momentum equation (1.67), the equation of heat transfer (1.71), and the generalized Ohm's law in form of (1.73) (or in form of (1.70)) together with the equation of state

$$p = \frac{2k}{m_p} \rho T \tag{1.75}$$

and Maxwell's equations

$$\nabla \times \mathbf{B} = \frac{4\pi}{c} \mathbf{j}, \ \nabla \times \mathbf{E} = -\frac{1}{c} \frac{\partial \mathbf{B}}{\partial t}, \ \nabla \cdot \mathbf{B} = 0, \ \nabla \cdot \mathbf{E} = 4\pi \rho_{\mathrm{e}}, \tag{1.76}$$

(the displacement current $(1/c)\partial \mathbf{E}/\partial t$ is neglected in MHD) form the closed system of equations in the one-fluid approximation relative to the values of ρ, $\mathbf{V}$, p, T, $\mathbf{j}$, $\mathbf{E}$, $\mathbf{B}$, and ρ_{e}. The last equation of (1.76) determines the charge density.

1.9 Summary of basic assumptions made for the fully ionized collisional plasma

In this section we summarize the restrictions on plasma parameters which should be fulfilled in order to be able to use the Boltzmann equation with the collision integral in the form of Landau (see, for example, Baranov, 2000) in order to calculate the transport coefficients, as was done in Sections 1.6 and 1.7 of this chapter. We also illustrate these assumptions in Figure 1.3. The axis of abscissae of the figure corresponds to the temperature (in electron-volts). The axis of ordinates

presents the electron number density (in cm^{-3}). The lower part of the diagram in Figure 1.3 corresponds to rarified space plasmas such as in the interplanetary and interstellar medium. The upper part of this diagram corresponds to dense regions, which appear in the atmospheres of the Sun, stars, planets, etc.

The assumptions are:

1. The Debye sphere contains many particles, i.e.

$$n r_{\mathrm{d}}^3 \gg 1, \tag{1.77}$$

where

$$\frac{1}{r_{\mathrm{d}}^2} = \sum_{\alpha} \frac{4\pi e_\alpha^2 n_\alpha}{k T_\alpha}, \quad n_{\mathrm{e}} \approx n_{\mathrm{p}} = n.$$

The inequality (1.77) provides a possibility to obtain the Boltzmann equation from the Liouville equation for N-particle distribution function. The area of (n_{e}, T=$\mathrm{T_e}$ ~$\mathrm{T_p}$) of plasma for which condition (1.77) is fulfilled is the region below line 1 in Figure 1.3.

2. Independence of this collisional integral on the electric field. This applies when

$$e_\alpha \left|\mathbf{E}\right| r_{\mathrm{d}} << m_\alpha v_T^2, \tag{1.78}$$

where v_T is the particle thermal velocity. This condition is fulfilled for the regions above the lines 2 and $2'$, which are plotted for $|\mathbf{B}| \sim 10^5$G and $\sim 10^{-5}$G, respectively. Note that an increase (decrease) the value of the magnetic field by an order of magnitude would result in a parallel shift of the lines by two units up (down). For the electric field it is assumed here that $|\mathbf{E}| \sim (1/c)\ v_T\, |\mathbf{B}|$. Note that under the assumption of $B^2/8\pi \sim 2 n_{\mathrm{e}} k T$ the condition (1.78) is fulfilled to the left of line $2''$.

3. Independence of the collisional integral in the Landau form on the magnetic field. This is the case for

$$r_{\mathrm{d}} << r_l, \tag{1.79}$$

where $r_l = (m_\alpha c v_T) \,/\, (e_\alpha \left|\mathbf{B}\right|)$ is the Larmor radius. This condition is fulfilled for the regions above lines 3 and $3'$, which are plotted for $|\mathbf{B}| \sim 10^5$G and $\sim 10^{-5}$G, respectively. Note that under the assumption of $B^2/8\pi \sim 2 n_{\mathrm{e}} k T$, condition (1.79) is fulfilled to the left of line $3''$.

4. The characteristic time of the problem considered, t^*, must be much larger than the correlation time τ_{cor}, which is the characteristic time for two colliding particles to be statistically independent, i.e.

$$t^* >> \tau_{\mathrm{cor}} = r_{\mathrm{d}}/v_T = \omega_{\mathrm{p}}^{-1}, \tag{1.80}$$

where ω_{p} is the plasma frequency. This condition is not shown in Figure 1.3 because it is fulfilled for most problems of space physics.

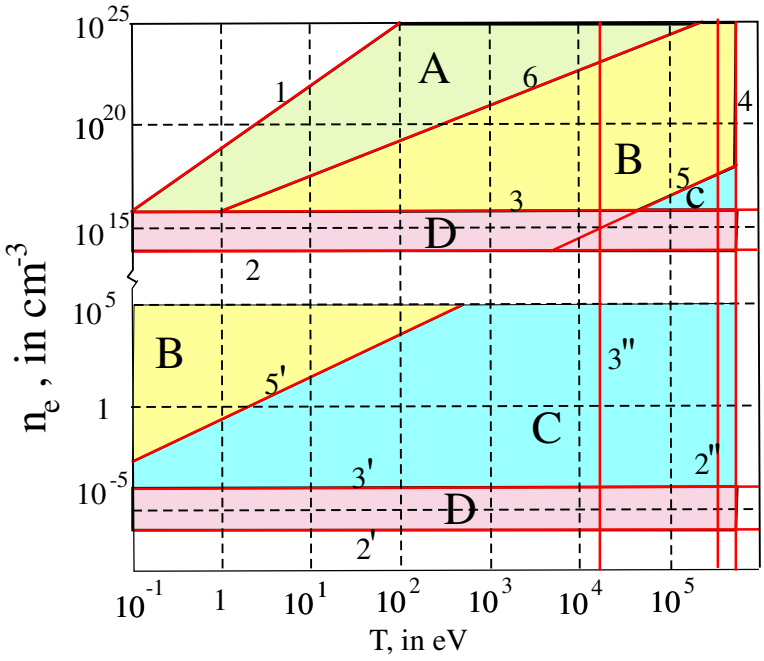

Figure 1.3: Regions where different approximations for a fully ionized plasmas can be used.

5. Finally, the following inequality must be satisfied:

$$k^2 r_{\rm d}^2 >> 1. \tag{1.81}$$

Here k is the wave number of plasma fluctuations. Physically the inequality (1.81) implies that "binary collisions" of charged particles are only taken into account in the collisional integral in the Landau form (1.45), while the interaction of the charged particles with plasma fluctuations is neglected. This condition contains the wave number of plasma fluctuations and cannot be drawn in Figure 1.3.

In addition to lines 1, 2, 2′, 2″, 3, 3′, 3′, several other lines are shown in Figure 1.3. The parameters of ($n_{\rm e}$, T), which are left of line 4, correspond to the case when $v_T^2 \ll c^2$, where c is the speed of light. In this case, relativistic effects are negligible. The area above lines 5 and 5′ satisfies the condition of validity of the continuous media approach, which is

$$Kn = \frac{l}{L} \ll 1, \tag{1.82}$$

where L is the characteristic size of the problem and l is the mean free path of Coulomb collisions. For line 5 it was assumed that $L \approx 10^5$ cm, and $L \approx 10^{10}$ cm for line 5′. To be fulfilled, the condition (1.82) requires that

$$2.26 \cdot 10^{-13} L \gg T^2/n_{\rm e}.$$

This means that the increase in characteristic size L by one order of magnitude results in the parallel transition of lines 5 and 5′ by one unit downwards.

Line 6 corresponds to the condition of $\omega_e \tau_e = 1$ adopting $|\mathbf{B}| \sim 10^5$G. The area where $\omega_e \tau_e \ll 1$ is located to the left of line 6.

Lines 1–6, 2', 2", 3', 3" separate the (n_e, T)-plane into several regions (Figure 1.3). Region A corresponds to the classical MHD situation when the transport coefficients are isotropic. Region B is the region of MHD with anisotropic transport coefficients that was described above in this chapter. Region C is the region where collisions between particles can be neglected. Region D corresponds to the situation when the collision integral in the kinetic equation depends on the magnetic field.

1.10 MHD equations for a collisionless plasma

In developing theoretical models for a problem in space physics, we are often dealing with a situation where the inequalities (1.22), i.e. $\tau \ll t^*$, $l \ll L$ (where τ and l are mean free time and path, t^* and L are the characteristic time and length of the problem) are not fulfilled. The hydrodynamic approximation can be justified even in this case for a fully ionized collisionless plasma. What does collisionless mean for a fully ionized plasma?

Firstly, let us consider a situation when condition (1.81) is not satisfied. In this case the dielectric permeability ε is not equal to unity ($\varepsilon = 1 + k^2 r_d^2 + ...$). Then instead of the collision integral in the Landau form S_{lan} ($\varepsilon = 1$) [see (1.45)] this integral can be presented as a sum of S_{lan} and an additional integral called S_{coll} (see Klimontovich, 1967). This integral S_{coll} describes the interaction of charged particles with the fluctuations of the electromagnetic field ("collective processes in plasmas"). Let us define 'collisionless plasma' as a plasma where the relaxation time τ_{rel} for the distribution function to become Maxwellian is much larger than the characteristic time of the problem, t^*, i.e. the inequality

$$\tau_{rel} >> t^* \tag{1.83}$$

is fulfilled instead of condition (1.22). Note that $\tau_{rel} \sim \tau_\alpha$, where τ_α ($\alpha = e, p$) is the mean free time of particles.

In the case that condition (1.83) is fulfilled, we can neglect S_{lan} as compared with S_{coll} because the order of magnitude of S_{coll} is determined by the characteristic time of collective processes, τ_{coll}, i.e. $S_{coll} \sim \tau_{coll}^{-1}$ while $S_{lan} \sim \tau_{rel}^{-1}$. There are three cases where the hydrodynamic approximation can be justified for a collisionless plasma.

In the first case when

$$\tau_{coll} << t^* \tag{1.84}$$

we can, in principal, use the hydrodynamic approach because Coulomb collisions are replaced by the scattering of charged particles in plasma fluctuations ("collective processes" in plasma). Condition (1.84) is analogous to the inequality (1.22). The presence of bow shocks (collisionless shocks) near the planets and comets shows that the hydrodynamic approximation works for these problems of space physics. The shocks are formed despite the fact that interplanetary plasma is collisionless

[i.e. (1.83) is fulfilled] because condition (1.84) is valid. It should be noted here that the integral $S_{\rm coll}$ is too complicated to be used for calculations of $\tau_{\rm coll}$ and the transport coefficients for such a plasma.

In the second case

$$\tau_{\rm coll} >> t^* \ , \tag{1.85}$$

and the RHS of the Boltzmann equation is equal to zero. The hydrodynamic equations for such a plasma were derived by Chew et al. (1956). This approximation is often called the CGL-approximation. To derive hydrodynamic equations it was assumed that the term $1/c\,(\mathbf{v}\times\mathbf{B})\cdot\partial f_\alpha/\partial\mathbf{v}$ is dominant in the kinetic equation. This is correct when [compare with (1.22)]

$$r_l << L. \tag{1.86}$$

Dissipative processes are absent in the CGL-approximation because the third moments (thermal fluxes) are neglected. The static pressure is anisotropic ($p_\parallel \neq p_\perp$) where $p_\parallel$ and $p_\perp$ are pressures parallel and perpendicular to the magnetic field, respectively. The distribution function of the plasma particles is assumed to be bi-Maxwellian, having parallel and perpendicular temperatures relative to the magnetic field direction. However, in this approach there is no justification for neglecting the thermal fluxes along the magnetic field. This is the reason why the hydrodynamics of Chew, Goldberger and Low lead to incorrect results for some problems.

Finally, as was mentioned in the previous section, the hydrodynamic approximation can be used in the case of a "cold" plasma when the mean thermal velocity of particles is much smaller than the bulk velocity, i.e. $v_{\rm T}^2 << V^2$. The stress tensor can be neglected in this case ($p << mnV^2$). Continuity and momentum equations constitute the closed system of hydrodynamic equations without taking into account the equation of energy. As an example, such an approximation can be used for the hypersonic solar wind.

Bibliography

Bogolubov, N.N., Problems of dynamic theory in statistical physics (in Russian), Moscow, Gostechizdat, 119 pp., 1946.

Braginskii S.I., Transport processes in plasmas. *Reviews of Plasma Physics* (Ed. M.A. Leontovich), Vol. 1, pp. 205-309, Consultants Bureau, New York, 1965.

Chapman S. and Cowling T., The mathematical theory of non-uniform gases, Cambridge, University press, 1952.

Chew,G., Goldberger, M., and Low, F., *Proc Roy. Soc.*, A236, 1204, 1956.

Landau L.D., Zh. Exp. Teoret. Fiz (in Russian), 7, No. 2, 1937.

Klimontovich, Yu.L. "The statistical theory of non-equilibrium processes in a plasma." International series of monographs in natural philosophy. Pergamon Press, 1967.

Baranov V.B., On the probem of fluid dynamics foundation in the space physics, *Astrophys. Space Sci.*, 274, 3–16, 2000.

— 2 —

Early Concepts of the Heliospheric Interface: Plasma

Vladimir B. Baranov[1]

Institute for Problems in Mechanics, Russian Academy of Sciences;
Lomonosov Moscow State University, School of Mechanics and Mathematics,
Department of Aeromechanics and Gas Dynamics

Abstract. **The construction of the early hydrodynamic models of the solar wind interaction with the local interstellar medium (LISM) was stimulated by the poor knowledge of the physical properties of the LISM. In particular, the dynamics of the interstellar gas were unknown before 1971, when experiments on scattered solar radiation at Lyman-α wavelengths, obtained on board the OGO-5 spacecraft, proved that H - atoms originating from the LISM are moving relative the Sun with a bulk velocity of $\sim$20 km/s. This is the reason why different physical properties of the LISM were considered before the beginning of the 1970s. However, the early models are interesting, first from the historical point of view, secondly because they stimulated astronomers to undertake experimental investigations of the LISM's parameters, and third because they predicted some physical phenomena discovered later on the basis of experimental data obtained by means of the spacecraft studying the outer regions of the Solar System (for example, the existence of the interface region or heliosheath). The early hydrodynamic models of the solar wind interaction with the LISM are considered in this Chapter.**

2.1 Introduction

The solar wind as the process of the solar corona's supersonic expansion was first discovered theoretically by Parker (1958). Later, this phenomenon was confirmed experimentally by means of spacecraft measurements (Gringauz et al., 1960; Neugebauer and Snyder, 1962). At Earth's orbit ($r = r_{\rm E}$), the measured solar wind velocity, on average, is equal to about $V_{\rm E} \approx 400$ km s^{-1}. This value is about ten times larger than the speed of sound. It means that the solar wind is really a highly supersonic flow.

Parker's model of a spherically-symmetric solar wind and its later developments have given rise to an asymptotic solution (with $r \to \infty$, where r is the distance from the Sun) for the supersonic flow with a constant radial velocity ($V_{\rm SW} = const$) and solar wind mass density $\rho_{\rm SW} \propto 1/r^2$. Therefore, the solar wind dynamic pressure

[1]in *The Physics of the Heliospheric Boundaries*, V. Izmodenov and R. Kallenbach (eds.), ISSI Scientific Report No. 5, pp. 27–43, ESA-ESTEC, Paris 2006

($\propto \rho_{SW} V_{SW}^2$) tends to zero at $r \to \infty$ (the static pressure p_{SW} of the solar wind also tends to zero due to the condition $p_{SW} \ll \rho_{SW} V_{SW}^2$ for supersonic flow). Since the pressure p_∞ of the interstellar gas into which the solar wind flows is finite (though very low), a new theoretical problem appeared, namely, the problem of conjugation of the solutions for the solar wind and the interstellar medium. At some heliocentric distance the solar wind pressure becomes too low to push the wind further into the interstellar medium and as a result the solar wind must be damped. The problem of the solar wind interaction with the local interstellar medium (LISM) has long been a topic of interest. In this Chapter we will consider Parker's model of the solar wind and only early concepts of the solar wind interaction with the interstellar medium.

2.2 Parker's model of the solar wind

The solar wind model has been developed by Parker (1958) on the basis of one-fluid and one-dimensional continuity, momentum and energy hydrodynamic equations (electrons and protons are the main components of the solar wind). For a steady-state spherically-symmetric flow these equations for an ideal gas have the form (see Chapter 1):

$$\rho V r^2 = const, \qquad V\frac{\mathrm{d}V}{\mathrm{d}r} = -\frac{1}{\rho}\frac{\mathrm{d}p}{\mathrm{d}r} - \frac{GM_\odot}{r^2}, \qquad \frac{\mathrm{d}}{\mathrm{d}r}\left(\frac{p}{\rho^n}\right) = 0. \tag{2.1}$$

Here ρ, V and p are the solar wind mass density, radial velocity and pressure, respectively, G is the gravitational constant, $M_\odot$ is the solar mass, r is the heliocentric distance, and n is the empirical polytropic index reflecting the lack of exact knowledge about thermal processes in the vicinity of the Sun. Under not very restrictive assumptions about the temperature dependence on the heliocentric distance, integral curves of Equations (2.1) take the form presented in Figure 2.1. Curve 1 corresponds to the solar wind, a is the sound velocity (the value a for $n = 1$ is the sound velocity for the isothermal gas), r_c is a critical distance where $V = a$. The point (r_c, a) is the singularity ("saddle").

Thus, the solar wind is the supersonic flow of the fully ionized hydrogen gas (fully ionized hydrogen plasma) which is flowing out from the solar corona with a small subsonic velocity. The gravitational force gives rise to the possibility of transition from the subsonic to supersonic flow [hydrodynamic Equations (2.1) without gravitational force have only the subsonic or supersonic solutions at whole region of the flow considered]. The solar wind will be supersonic ($M_{SW} = V_{SW}/a_{SW} \gg 1$, where M_{SW} is the solar wind Mach number) behind the Earth's orbit, i.e. $V_{SW} = V_E = const$ at $r \geq r_E$. Here, V_E is the solar wind velocity at $r = r_E$ (r_E is the distance from the Sun to the Earth).

2.3 Early models of the solar wind interaction with the interstellar gas

We see from Figure 2.1 that Parker's model of the solar wind does not resolve the problem of the solar wind interaction with the local interstellar medium. Parker

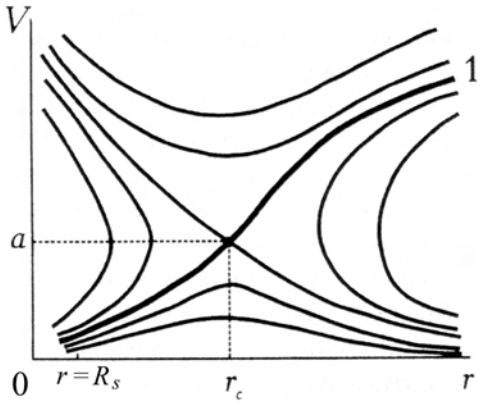

Figure 2.1: Integral curves of Equations (2.1). The curve 1 is the solar wind, r_c – critical point, where $V = a$ (V is the radial solar wind velocity, a is the thermal sound velocity). The Sun is in the origin of the coordinate system.

(1961) was the first who developed quantitative gas dynamic models of the stellar wind interaction with the interstellar medium. Since at that time there were no direct observations of the interstellar gas motion relative to stars, Parker (1961) investigated theoretically the following three possibilities: (i) the outflow of a supersonic stellar wind into an interstellar gas at rest, (ii) the supersonic stellar wind interaction with incompressible translational flow of the interstellar gas, and (iii) the outflow of the supersonic stellar wind into a homogeneous interstellar magnetic field providing the interstellar gas dynamical pressure is negligible. Later, a model of the supersonic solar wind interaction with the supersonic translational flow of the LISM was constructed by Baranov et al. (1970) in the Newtonian thin layer approximation. Let us consider these early models. First we will consider the three models by Parker (1961).

2.3.1 Solar wind outflow into the homogeneous interstellar gas at rest

Consider a stationary, spherically-symmetric solar wind outflow into a space occupied by a gas at rest. The static pressure of this gas is $p_\infty \neq 0$, and the bulk velocity is $V_\infty = 0$. In this case we must establish the next boundary conditions for the solar wind parameters

$$p \to p_\infty, \qquad V = 0 \qquad \text{at} \quad r \to \infty, \tag{2.2}$$

where r is the distance from the Sun. The relations (2.2) are valid if the interstellar magnetic field and galactic cosmic rays can be neglected. Then the transition from the supersonic solar wind to the interstellar gas at rest may be realized through a spherical shock only. The Rankine-Hugoniot relations at this shock must be satisfied. In the supersonic limit $M_1 \gg 1$, where $M_1 = V_{\rm SW}/a_1$ is the Mach number, and a_1 is the sonic velocity in front of the shock, $V_{\rm SW}$ is the solar wind

velocity at the Earth's orbit (it is constant till the shock due to the supersonic character of the flow considered), they have the form:

$$\frac{V_2}{V_{\rm SW}} = \frac{\gamma-1}{\gamma+1}, \qquad \frac{\rho_2}{\rho_1} = \frac{\gamma+1}{\gamma-1}, \qquad p_2 = \frac{2\rho_1 V_{\rm SW}^2}{\gamma+1}. \tag{2.3}$$

Here, V, ρ, p, and γ are the solar wind velocity, mass number density, static pressure and specific heat ratio, respectively. Indices "1" and "2" relate to their values in preshock and postshock, respectively. The Mach number behind the shock $M_2 \ll 1$ if $M_1 \gg 1$. Therefore, the flow behind the shock may be assumed as incompressible ($\rho = const = \rho_2$). To satisfy the boundary conditions (2.2) it is necessary to use the Bernoulli integral for an incompressible fluid in the form:

$$p + \rho_2 \frac{V^2}{2} = p_2 + \rho_2 \frac{V_2^2}{2} = p_\infty. \tag{2.4}$$

Since the solar wind velocity $V_{\rm SW} = const$ at $r \geq r_{\rm E}$ the continuity equation [first equation in (2.1)] for the supersonic solar wind will have the form:

$$\rho r^2 = \rho_{\rm E} r_{\rm E}^2 = \rho_1 r_1^2, \tag{2.5}$$

where r_1 is the heliocentric distance to the shock (below we will call it the "termination shock"). After substituting Equations (2.3) and (2.5) into (2.4) and solving the resulting equation relative to r_1 we will have finally

$$r_1 = r_{\rm E} \left[\frac{\gamma+3}{2(\gamma+1)} \frac{\rho_{\rm E} V_{\rm E}^2}{p_\infty} \right]^{1/2}. \tag{2.6}$$

This formula determines the boundary of the supersonic solar wind, i.e. the heliocentric distance to the termination shock if the interstellar gas is at rest with the static pressure p_∞. From the continuity equation for an incompressible fluid (behind the termination shock) we obtain

$$V r^2 = V_2 r_1^2 \quad \text{or} \quad V = \frac{\gamma-1}{\gamma+1} V_{\rm E} \left(\frac{r_1}{r}\right)^2,$$

i.e. the second boundary condition in Equation (2.2) is satisfied. To estimate the order of magnitude for r_1 in this case, let us take $V_{\rm E} = 4 \cdot 10^7$ cm s^{-1}, $p_\infty = 10^{-13}$ dyn cm^{-2}, $\rho_{\rm E} = 10^{-23}$ g cm^{-3}, $\gamma = 5/3$. From the formula (2.6) we obtain $r_1/r_{\rm E} \approx 350$ AU, i.e. about some hundreds of astronomical units.

Here, we considered the stationary solar wind outflow into the interstellar gas at rest. This case is not real because the boundary between the solar wind plasma and interstellar gas proved to be at infinity ($V \to 0$ with $r \to \infty$). However, the solution obtained above (Parker, 1961) may be considered as a limiting case (at $t \to \infty$, where t is the time) of the well-known problem connected with interstellar bubble formation (see, for example, Weaver et al., 1977).

2.3.2 Solar wind outflow into the interstellar gas moving with subsonic velocity

The interstellar gas motion relative to the Sun breaks the spherical symmetry of the solar wind interaction with the interstellar gas at rest considered in Subsection

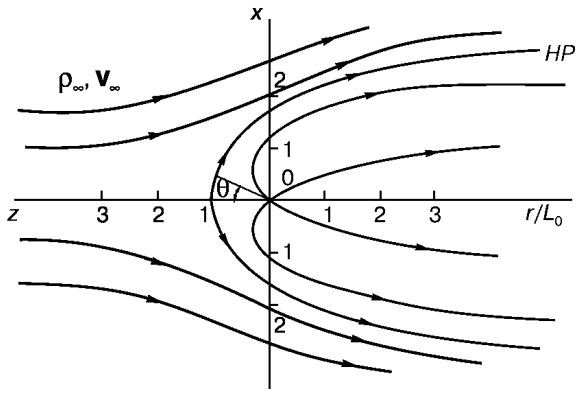

Figure 2.2: Stream lines in the model of the solar wind interaction with a subsonic interstellar wind (Parker, 1961). The Sun is in the origin of the coordinate system, HP is the heliopause (the tangential discontinuity) separating the solar and interstellar winds.

2.3.1. Assuming that the solar wind is spherically-symmetric and the undisturbed subsonic interstellar wind is characterized by constant density ρ_∞, bulk velocity V_∞, and static pressure p_∞, the resulting flow will have an axial symmetry. The main assumption made by Parker (1961) for the solution of the problem is

$$\frac{\rho_\infty V_\infty^2}{2} \ll p_\infty \quad \text{or} \quad M_\infty^2 \ll 1\,, \tag{2.7}$$

where M_∞ is the Mach number of the undisturbed interstellar wind. Evidently, in this case the termination shock can be considered as a spherically-symmetric structure due to the fact that the dynamic pressure is much less than the static pressure in the interstellar medium [see the inequality (2.7) and previous Subsection]. The general view of stream lines for such a flow is shown in Figure 2.2. In this case the characteristic length L_0 of this flow, which will be determined below, turns out to be much larger than the heliocentric distance r_1 of the termination shock ($L_0 \gg r_1$). That is why the termination shock is not shown in Figure 2.2. The subsonic interstellar wind interacts directly with the subsonic flow of the solar wind compressed at the termination shock. The tangential discontinuity separates the subsonic solar and interstellar winds.

Since the termination shock has a spherical shape due to the assumption (2.7) and the supersonic solar wind Mach number $M_1 \gg 1$ at $r = r_1$ we have $M_2 \ll 1$ behind the termination shock. Therefore, we can consider the subsonic solar wind as an incompressible and potential flow. We can also take the interstellar gas flow as incompressible and potential flow due to the inequality (2.7). The velocity potential introduced by the formula

$$\mathbf{V} = -\rho^{-1/2}\nabla\varphi \tag{2.8}$$

satisfies the Laplace equation

$$\triangle\varphi = 0. \tag{2.9}$$

We take $\rho = const = \rho_2$ for the subsonic solar wind and $\rho = const = \rho_\infty$ for the interstellar wind. The boundary conditions for Equation (2.9) follow from (2.8), namely

$$-\nabla\varphi = \rho_\infty^{1/2}\mathbf{V}_\infty \quad \text{with} \quad r \to \infty \tag{2.10}$$

and

$$-\nabla\varphi = \rho_2^{1/2}\mathbf{V}_2 \quad \text{for} \quad r = r_1. \tag{2.11}$$

The values ρ_2 and V_2 (solar wind radial velocity) are determined by the Rankine-Hugoniot relations (2.3) at the termination shock. Since the problem formulated by (2.8) – (2.11) has axial symmetry, the unknown potential can be expressed as the sum of potentials corresponding to a homogeneous flow and a spherically-symmetric source of incompressible fluids:

$$\varphi(r,\theta) = \rho_\infty^{1/2}V_\infty r\cos\theta + \rho_2^{1/2}V_2\frac{r_1^2}{r}, \tag{2.12}$$

where r is the distance from the Sun (which is in the origin of the coordinate system), θ is the polar angle counted from the Oz-axis (the vector $\mathbf{V}_\infty$ is directed along the negative Oz-axis) and r_1 is the location of the termination shock determined from the formula (2.6).

The potential (2.12) satisfies the Laplace equation (2.9), boundary conditions (2.10) and (approximately) (2.11). The latter is correct if we assume $\rho_\infty V_\infty^2 \ll \rho_2 V_2^2$. As a result the potential (2.12) is the solution of the problem considered.

Let us now determine the characteristic scale L_0 of the flow. It is determined as the distance at which the subsonic solar wind will be deflected from spherically-symmetric flow by the interstellar wind. Clearly, this is at a distance where the dynamic pressures of the solar and interstellar winds are the same order of magnitude, i.e. $\rho_2 V^2 \sim \rho_\infty V_\infty^2$ ($\rho_2 V_2^2 \gg \rho_\infty V_\infty^2$). To estimate the value V we will use the last formula of the previous Subsection. We obtain

$$\rho_2 V_2^2\left(\frac{r_1}{r}\right)^4 \approx \rho_\infty V_\infty^2 \quad \text{or} \quad r \approx r_1\left(\frac{\rho_2 V_2^2}{\rho_\infty V_\infty^2}\right)^{1/4}.$$

This gives

$$L_0 = r_1\left(\frac{\rho_2 V_2^2}{\rho_\infty V_\infty^2}\right)^{1/4} \gg r_1, \tag{2.13}$$

i.e. the characteristic length of the flow considered is much larger than the heliocentric distance of the termination shock. That is why the termination shock is not visible in Figure 2.2.

The equations for the stream lines will have the form:

$$-\frac{r^2\sin^2\theta}{2L_0^2} = \cos\theta + C \quad (C = const).$$

Evidently, through the surface separating the solar wind and the interstellar gas (this surface is a tangential discontinuity which is often called the heliopause)

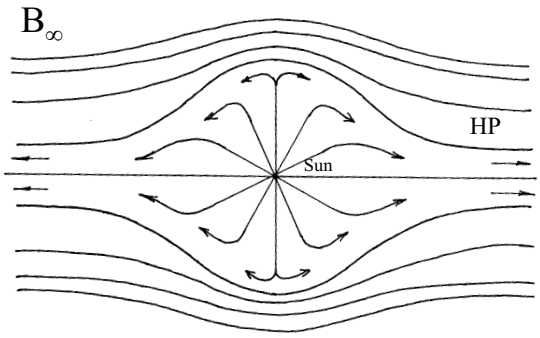

Figure 2.3: Qualitative picture of the solar wind stream lines and the interstellar magnetic field lines in the model of the solar wind interaction with the interstellar magnetic field (Parker, 1961).

the static pressure is continuous and the normal component of the bulk velocity is equal to zero. Since the tangential discontinuity coincides with a stream line and the ray $\theta = 0$ intersects it, we have $C = -1$ for this stream line, i.e. the equation of the heliopause is

$$-r^2 \sin^2\theta = 2L_0^2 (\cos\theta - 1) . \tag{2.14}$$

Hence, we see that L_0 is the heliocentric distance to the heliopause stagnation point ($\theta = 0$) and this distance is determined by the formula (2.14). At $r \to \infty$ and $\theta \to \pi$ we have $r \sin\theta \to 2L_0$, i.e. the shape of the heliopause tends to a cylindrical surface with radius $2L_0$.

2.3.3 The solar wind deceleration by the interstellar magnetic field

The third case considered by Parker (1961) relates to the possibility of the solar wind being decelerated by a homogeneous interstellar magnetic field $\mathbf{B}_\infty$ only. This is possible if the magnetic field pressure $B_\infty^2/8\pi$ is much larger than the static and dynamic pressures of the interstellar gas (p_∞ and $\rho_\infty V_\infty^2/2$, respectively). The spherical symmetry of the solar wind outflow into the interstellar medium is distorted in this case by the magnetic field due to its decelerating effect, which is different for various directions. The magnetic field of the interstellar medium is driven out by the solar wind plasma due to the "freezing-in" effect (the magnetic Reynolds number $Re_\mathrm{m} \gg 1$ in the problem considered). Thus a cavity is formed which is elongated along the magnetic field $\mathbf{B}_\infty$ and is filled by the solar wind plasma (see Figure 2.3). However, for solving this problem the following assumption was made by Parker (1961). He assumed that the solar wind deceleration from supersonic to subsonic flow takes place through a spherically-symmetric termination shock, in spite of the fact that the magnetic field, in the general case, distorts the spherical symmetry of this flow. Under this assumption a solution to

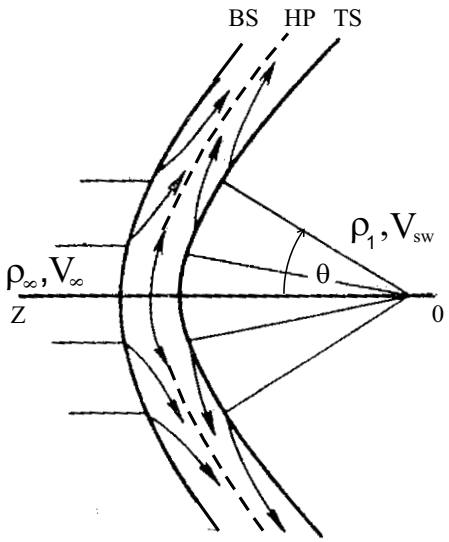

Figure 2.4: Qualitative picture of the solar wind interaction with the supersonic fully ionized interstellar wind. Here, BS is the bow shock formed in the interstellar gas, TS is the termination shock formed in the supersonic solar wind, and the heliopause HP (*dashed lines*) separates the solar and interstellar winds. The Sun is at the point O, and ρ_1 is the solar wind mass density at the TS.

the problem exists, if the solar wind stagnation pressure p_0 on the heliopause (HP in Figure 2.3) is changed in a very small interval,

$$\frac{B_\infty^2}{8\pi} \leq p_0 \leq \frac{3B_\infty^2}{16\pi}.$$

It seems to us that this solution cannot be realized in nature, and it will not be considered here.

It should be noted that the heliocentric distance to the termination shock in the direction normal to $\mathbf{B}_\infty$ could be estimated using the formula (2.6) where we must introduce the magnetic field pressure $B_\infty^2/8\pi$ instead of the static pressure p_∞. In this case the assumption concerning spherical symmetry of the shock is not important.

2.3.4 The solar wind interaction with the supersonic fully ionized interstellar wind

As was noted at the beginning of Section 2.3, the gas dynamic model of the solar wind interaction with the supersonic interstellar gas flow was developed by Baranov et al. (1970). A qualitative picture of the flow is shown in Figure 2.4. Two shocks are formed: the bow shock and the termination shock (BS and TS in Figure 2.4, respectively). The supersonic flow of the interstellar gas passes through the

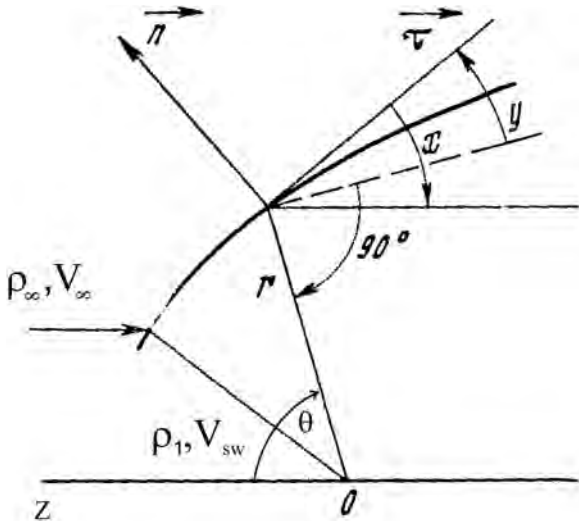

Figure 2.5: Qualitative geometrical picture of the flow in the model of the supersonic solar wind interaction with the supersonic interstellar wind in the thin layer approximation (Baranov et al., 1970). Here **n** and τ are normal and tangential directions to the surface (infinitesimal thickness of the heliosheath) separating the solar and interstellar winds.

BS decelerating due to the interaction with the solar wind. The solar wind passes through the TS decelerating due to the interaction with the interstellar gas flow. The dashed line HP shows the tangential discontinuity (heliopause) separating interstellar gas, compressed at the BS, and the solar wind, compressed at the TS. It should be noted here that the qualitative picture presented in Figure 2.4 is possible only in the hydrodynamic approximation. That is why Baranov et al. (1970) assumed that the interstellar medium is the fully ionized hydrogen plasma which can be described by hydrodynamic equations. They also assumed that the interstellar gas flow is supersonic ($M_\infty \gg 1$). The problem of the interaction between the supersonic solar wind and supersonic flow of the LISM can be solved in the Newtonian thin layer approximation (Cherny, 1959), i.e. in the case when the thickness of the layer between the BS and TS, which is now called the heliospheric interface or heliosheath, is small compared with their distance from the Sun. The latter assumption can be correct for a region which is not far from the stagnation point. In this approximation the thin layer between the BS and TS can be considered as a discontinuity surface (see Figure 2.5) across which the average velocity of the gas is constant. The momentum equations for gas in the directions normal and tangential to this layer will have the form (Baranov et al., 1970):

$$\rho_\infty V_\infty^2 = \rho_1 V_{\mathrm{En}}^2 + \frac{mV_l}{2\pi r R_\kappa \sin\theta}\,,$$

$$\frac{\mathrm{d}}{\mathrm{d}l}\left(mV_l\right) = 2\pi r \sin\theta \left(\rho_\infty V_{\infty \mathrm{n}} V_{\infty\tau} + \rho_1 V_{\mathrm{En}} V_{\mathrm{E}\tau}\right)\,. \qquad (2.15)$$

Here we consider the cylindrical symmetry of the problem using the spherical coordinate system in which the Sun is at its origin, r is the heliocentric distance and θ is the polar angle, ρ and V are the mass density and the bulk velocity, indices "E" and "∞" relate to the solar wind and the interstellar gas, ρ_1 is the solar wind mass density at the TS. It is assumed in this model that there is a relative motion of the Sun and interstellar gas due to the motion of the Sun relative to the nearest stars in the apex direction with the velocity $V_\infty \sim 20$ km s^{-1}. Therefore, the direction $\theta = 0$ (axis of symmetry) coincides with the apex direction. In Equations (2.15) m is the mass of the gas flowing into the layer per unit time, R_κ is the radius of curvature of the unknown surface replacing the compressed gas layer between the BS and TS, V_l is the average (over the area of the cross-section of the thin layer) velocity along the layer. The last term in the first equation (2.15) represents a centrifugal force, the indices "n" and "τ" are related to projections on the normal and tangential directions to the discontinuity surface. The values m and R_κ are determined by the formulae

$$m = \pi r^2 \rho_\infty V_\infty^2 \sin^2\theta + 2\pi r^2 \rho_1 V_{\rm E} (1 - \cos\theta) ,$$
$$R_\kappa = \frac{\left(r^2 + r'^2\right)^{3/2}}{r^2 + 2r'^2 - rr''} , \qquad r = r(\theta) , \tag{2.16}$$

where a prime denotes the derivative over the polar angle θ. It should be noted here that Equations (2.15) do not include the static pressure p due to the supersonic character of the flow where $\rho V^2 \gg p$. Equations (2.15) and (2.16) represent the generalization of the Newtonian thin layer approximation which is often used in hydro-aeromechanics for calculations of supersonic flows around blunt bodies (Cherny, 1959). More strictly these equations were obtained by Giuliani (1982), who generalized them for the non-stationary case and for a case with arbitrarily directed magnetic field.

Let us introduce the angle x between the vector $\mathbf{V}_\infty$ and the tangent to the unknown surface (see Figure 2.5) and the angle y between the normal direction to this surface and the radius-vector. Then excluding V_l , m and R_κ from (2.15) and (2.16), we will have the equation

$$2\pi r \sin\theta \left(\rho_\infty V_\infty^2 \sin x \cos x + \rho_1 V_{\rm E}^2 \sin y \cos y\right) \tag{2.17}$$
$$= \frac{1}{\left(r^2 + r'^2\right)^{1/2}} \left[\frac{2\pi r \sin\theta \left(r^2 + r'^2\right)^{3/2} \left(\rho_\infty V_\infty^2 \sin^2 x - \rho_1 V_{\rm E}^2 \cos^2 y\right)}{r^2 + 2r'2 - rr''}\right]'' .$$

If we take into account the relations

$$\tan x = \tan\left[\frac{\pi}{2} - \theta + \arctan\left(\frac{1}{r}r'\right)\right] , \qquad \tan y = \frac{1}{r}r' , \tag{2.18}$$
$$V_{\infty{\rm n}} = V_\infty \sin x , \;\; V_{\infty\tau} = V_\infty \cos x , \;\; V_{\rm En} = V_{\rm E} \cos y , \;\; V_{{\rm E}\tau} = V_{\rm E} \sin y ,$$

Equation (2.17) can be reduced to a complicated nonlinear differential equation of third order for the unknown function $r = r(\theta)$. In the general dimensionless form this equation can be written as

$$\xi''' = \frac{\Psi_1(\theta, \xi, \xi'', \xi'')}{\Psi_2(\theta, \xi, \xi'', \xi'')} , \qquad r = r_0 \xi , \tag{2.19}$$

where Ψ_1 and Ψ_2 are the known functions of their arguments, r_0 is heliocentric distance to the unknown surface $r = r(\theta)$ at $\theta = 0$, which is determined from the first equation (2.15) (the centrifugal force is zero at $\theta = 0$), i.e. from the equation $\rho_\infty V_\infty^2 = \rho_1 V_\mathrm{E}^2$ and using the continuity equation for the solar wind $\rho_\mathrm{E} r_\mathrm{E}^2 = \rho_1 r_0^2$ (ρ_1 is the solar wind mass number density at the unknown surface). As a result we obtain

$$\frac{r_0}{r_\mathrm{E}} = \frac{V_\mathrm{E}}{V_\infty}\sqrt{\frac{\rho_\mathrm{E}}{\rho_\infty}}. \tag{2.20}$$

Equation (2.15) was numerically solved by Baranov et al. (1970) at the following boundary conditions:

$$\xi = 1, \quad \xi' = 0, \quad \xi'' = \frac{2}{5} \quad \text{at} \quad \theta = 0. \tag{2.21}$$

The second condition is due to the symmetry of the problem and the third condition gives rise to a possibility to go out from the saddle singular point ($r = r_0$, $\theta = 0$) to present the unknown surface. It is interesting to note here that there are no dimensionless parameters in Equation (2.19). That is why the calculated curve $\xi = \xi(\theta)$ has a universal character, presented in Figure 2.6, and the surfaces $r = r_0\xi(\theta)$ are proportional to r_0, determined by the formula written above.

However, the centrifugal force in Equations (2.15) gives rise to unimportant changes in the shape and heliocentric distance to the surface considered. We can obtain an analytical formula for this surface neglecting the centrifugal force (see, for example, Dyson, 1975). In this case we will have

$$\rho_\infty V_{\infty\mathrm{n}}^2 = \rho_1 V_\mathrm{En}^2 \tag{2.22}$$

instead of (2.15). At the stagnation point 1 (Figure 2.6), Equation (2.22) becomes

$$\rho_\infty V_\infty^2 = \rho_1(r_0)\, V_\mathrm{E}^2, \tag{2.23}$$

where r_0 is determined by the formula (2.20). Dividing (2.22) by (2.23) we have

$$\frac{V_{\infty\mathrm{n}}^2}{V_\infty^2} = \frac{r_0^2}{r^2}\frac{V_\mathrm{En}^2}{V_\mathrm{E}^2} \equiv \frac{1}{\xi^2}\frac{V_\mathrm{En}^2}{V_\mathrm{E}^2}, \qquad \xi = \frac{r}{r_0}. \tag{2.24}$$

Taking into account (2.18) we have from (2.24) the equation

$$\xi\cos\theta + \frac{\mathrm{d}\xi}{\mathrm{d}\theta}\sin\theta = 1$$

for determining the shape of the unknown surface. The solution of this equation has a simple form

$$\frac{r}{r_0} = \frac{\theta}{\sin\theta}.$$

There is no difficulty to take into account an effect of the interstellar magnetic field $\mathbf{B}_\infty \parallel \mathbf{V}_\infty$ in this thin layer approximation (Baranov and Krasnobaev, 1971; Baranov, 1990). In this case we should use the equations

$$\rho_\infty V_\infty^2 + \frac{B_{\infty\tau}^2}{8\pi} - \frac{B_{\infty\mathrm{n}}^2}{8\pi} = \rho_1 V_\mathrm{En}^2 + \frac{mV_l}{2\pi r R_\kappa \sin\theta}$$

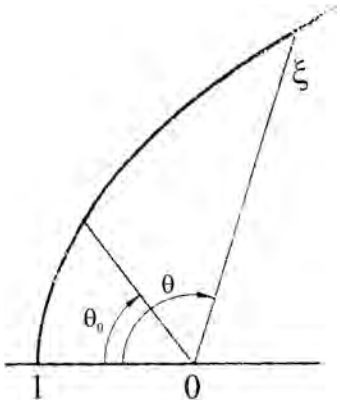

Figure 2.6: The form and location of the heliosheath (the region between BS and TS) calculated numerically by Baranov et al. (1970) in the approximation of its infinitesimal thickness. Here θ is the polar angle, $\theta_0 \sim 53^\circ$ is the angle between the apex direction ($\theta = 0$) and the ecliptic plane, $\xi = r/r_0$ is the dimensionless heliocentric distance.

$$\frac{\mathrm{d}}{\mathrm{d}l}\left(mV_l\right) = 2\pi r \sin\theta \left(\rho_\infty V_{\infty \mathrm{n}} V_{\infty\tau} - \frac{B_{\infty \mathrm{n}} B_{\infty\tau}}{4\pi} + \rho_1 V_{\mathrm{En}} V_{\mathrm{E}\tau}\right)$$

instead of Equations (2.15). Results obtained by Baranov and Krasnobaev (1971) show that the heliocentric distance of the thin surface (the heliosheath in this approximation) increases with increasing magnetic field. Obviously, this effect is due to the tension of the magnetic field lines at $\mathbf{B}_\infty \parallel \mathbf{V}_\infty$. More than 20 years later this effect was confirmed by numerical solution of the considered problem without the thin layer approximation (Baranov and Zaitsev, 1995).

2.3.5 The solar wind interaction with the supersonic partially ionized interstellar wind

The problem of the solar wind interaction with the local interstellar medium (LISM) became especially relevant at the beginning of the 1970s, when experiments on scattered solar radiation at wavelengths of $\lambda = 1216$ Å and $\lambda = 584$ Å(Bertaux and Blamont, 1971; Thomas and Krassa, 1971; Weller and Meier, 1974) and their interpretation (Blum and Fahr, 1970; Fahr, 1974) proved that H and He atoms of the LISM are moving with a supersonic velocity relative to the Sun. The direction of this motion is almost in the ecliptic plane and does not coincide with the direction of the solar motion relative to the nearest stars (apex direction) as was suggested by Baranov et al. (1970) (see Subsection 2.3.3). Besides, these experiments demonstrated the neutral atom penetration into the Solar System, whereas Baranov et al. (1970) assumed that the LISM is a fully ionized plasma. At the same time there was no doubt that the LISM is a partially ionized gas. Wallis (1975) was the first to show that plasma and neutral components can influence each other by charge exchange effects. This mutual influence has two aspects.

First, the plasma interface (heliosheath) between the bow and terminal shocks (BS and TS in Figure 2.4), introduced in Subsection 2.3.3, becomes kind of a "filter" for H atoms penetrating from the LISM into the Solar System. Second, the resonance charge exchange processes ($H^+ + H = H + H^+$) can change the plasma interface structure and its distance from the Sun due to pick-up of "new" protons (see details in Chapter 4).

The first self-consistent hydrodynamic model taking into account the mutual influence of the plasma component (electrons and protons) and H-atoms was constructed by Baranov et al. (1981, 1982). A stationary model of the supersonic spherically-symmetric solar wind interaction with the translational and uniform supersonic flow of the partially ionized hydrogen gas was considered. Such a problem is axisymmetric, i.e. all parameters depend only on the heliocentric distance r and the polar angle θ in the spherical coordinate system with the origin at the Sun and the axis of symmetry Oz coinciding with the direction opposite to that of the constant velocity vector $\mathbf{V}_\infty$ of the interstellar gas. In this case one-fluid hydrodynamic equations for the plasma components (electrons and protons) without viscosity and thermal conductivity (see Chapter 1) can be written in the form

$$\begin{aligned} v_r\frac{\partial v_r}{\partial r}+\frac{v_\theta}{r}\frac{\partial v_r}{\partial\theta}-\frac{v_\theta^2}{r}+\frac{1}{\rho}\frac{\partial p}{\partial r}&=\nu_{\rm c}U_r,\\ v_r\frac{\partial v_\theta}{\partial r}+\frac{v_\theta}{r}\frac{\partial v_\theta}{\partial\theta}+\frac{v_r v_\theta}{r}+\frac{1}{\rho r}\frac{\partial p}{\partial\theta}&=\nu_{\rm c}U_\theta, \end{aligned} \tag{2.25}$$

$$\frac{\partial\rho v_r r^2}{\partial r}+\frac{r}{\sin\theta}\frac{\partial\rho v_\theta\sin\theta}{\partial\theta}=0, \tag{2.26}$$

$$\begin{aligned} &\frac{1}{r^2}\frac{\partial}{\partial r}\left[\left(\frac{5kT}{m_p}+\frac{v_r^2+v_\theta^2}{2}\right)\rho v_r r^2\right]\\ &+\frac{1}{r\sin\theta}\frac{\partial}{\partial\theta}\left[\left(\frac{5kT}{m_{\rm p}}+\frac{v_r^2+v_\theta^2}{2}\right)\rho v_\theta\sin\theta\right]=\\ &\rho\nu_{\rm c}\left(U_r v_r+U_\theta v_\theta\right)+\rho\nu_{\rm c}\left(\frac{v_r^2+v_\theta^2}{2}+\frac{3kT_{\rm H}}{m_{\rm H}}-\frac{3kT}{m_{\rm p}}\right), \end{aligned} \tag{2.27}$$

$$p=\frac{2\rho kT}{m_{\rm p}}. \tag{2.28}$$

Here (2.25) – (2.28) are the equations of momentum, continuity, energy, and state, respectively, ρ, p, and T are mass density, static pressure and temperature of plasma, v_r and v_θ are components of the bulk velocity vector $\mathbf{V}$, index "H" relates to the H-atoms. The RHSs of Equations (2.25) and (2.27) describe (Holzer, 1972) a change in the plasma component momentum and energy due to processes of the resonance charge exchange between H-atoms and protons, where

$$\nu_{\rm c}=n_{\rm H}\sigma U_*, \tag{2.29}$$

$$U_*=\left[U_r^2+U_\theta^2+\frac{128k\left(T+T_{\rm H}\right)}{9\pi m_{\rm H}}\right]^{1/2},$$

$$U_r = -\left(v_r - v_{r\mathrm{H}}\right), U_\theta = -\left(v_\theta - v_{\theta\mathrm{H}}\right).$$

Here ν_c and σ are the frequency of collisions and the effective cross-section for the resonance charge exchange processes, n_H is the H-atom number density. These formulae for the effect of H-atoms on the plasma component were obtained by Holzer and Banks (1969) on the basis of the collision integral in the Boltzmann form (1.21) on the assumption that the distribution functions of H - atoms and protons are Maxwellian (1.28). It is necessary to add the equations for n_H, $\mathbf{V}_\mathrm{H}$, and T_H to take into account the mutual effect of neutral and plasma components. Estimations show that inequalities (1.22) are not satisfied for collisions connected with processes of resonance charge exchange ($\nu_\mathrm{c} = 1/\tau_\mathrm{c} \sim 1/t^*$ and $l_\mathrm{c} \sim L$), i.e. the hydrodynamic momentum and energy equations for H-atoms are not correct in this case. That is why the following approximation for $\mathbf{V}_\mathrm{H}$ and T_H was used in the model by Baranov et al. (1981, 1982)

$$\begin{aligned} &v_{r\mathrm{H}} = -V_\infty \cos\theta, v_{\theta\mathrm{H}} = V_\infty \sin\theta, \\ &T_\mathrm{H} = T_\infty, \\ &\frac{1}{r^2}\frac{\partial}{\partial r}\left(m_\mathrm{H} n_\mathrm{H} v_{r\mathrm{H}} r^2\right) + \frac{1}{r\sin\theta}\frac{\partial}{\partial\theta}(m_\mathrm{H} n_\mathrm{H} v_{\theta\mathrm{H}} \sin\theta\Big) = -\rho\nu_\mathrm{c}, \end{aligned} \tag{2.30}$$

where V_∞ and T_∞ are the constant bulk velocity and temperature of the LISM gas, and the RHS of the H-atom continuity equation [last equation in (2.30)] only takes into account the disappearance of the primary H-atoms moving from the LISM with constant velocity V_∞.

The following boundary conditions for the numerical solution of Equations (2.25) – (2.28) were satisfied in the model by Baranov et al. (1981, 1982): (1) Rankine-Hugoniot relations on the bow and termination shocks (BS and TS, respectively), (2) the equality of plasma pressures and vanishing normal component of the plasma bulk velocity on the tangential discontinuity (heliopause HP), separating the solar wind and the plasma component of the LISM, (3) given and constant values of solar wind parameters V_E, ρ_E, and T_E (or Mach number $M_\mathrm{E} = V_\mathrm{E}/a_\mathrm{E}$, where a is the sound velocity) at the Earth's orbit ($r = r_\mathrm{E}$), and (4) given and constant values of the undisturbed LISM parameters V_∞, ρ_∞, and T_∞ (or M_∞). The boundary condition for H-atoms is $n_\mathrm{H} = n_{\mathrm{H},\infty}$ in the LISM.

Four dimensionless parameters determine the problem

$$M_\infty = \frac{V_\infty}{a_\infty},\ K = \frac{\rho_\mathrm{E} V_\mathrm{E}^2}{\rho_\infty V_\infty^2} = \frac{n_\mathrm{E} V_\mathrm{E}^2}{n_{\mathrm{p},\infty} V_\infty^2}, q = \frac{n_{\mathrm{H},\infty}}{n_{\mathrm{p},\infty}}, \chi = \sigma r_\mathrm{E} n_{\mathrm{p},\infty}\sqrt{K}, \tag{2.31}$$

where $n_{\mathrm{p}\infty}$ is the proton number density in the undisturbed interstellar gas flow. Figure 2.7 demonstrates the geometrical pattern of the heliosheath (the region between BS and TS), calculated on the basis of the mathematical model formulated in this Subsection at $M_\infty = 2$, $\chi = 0.8$ and different values of the parameter $q = n_{\mathrm{H},\infty}/\mathrm{n}_{\mathrm{p},\infty}$. The linear dimensions in this Figure are divided by $r_\mathrm{E}\sqrt{K}$. We see the important effect of the resonance charge exchange processes. With the increase of the H-atom number density in the LISM the heliocentric distance of the heliosheath is decreasing. In particular, it is easy to obtain from Figure 2.7 that at $\mathrm{n}_{\mathrm{H},\infty} = n_{\mathrm{p},\infty} = 0.1$ cm^{-3} (q=1), $\mathrm{V}_\infty = 25$ km s^{-1}, $n_\mathrm{E} = 10$ cm^{-3}, and

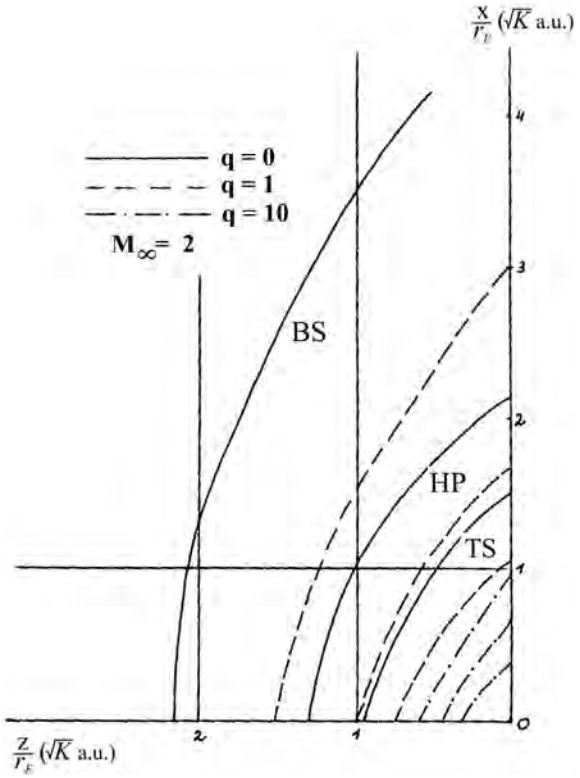

Figure 2.7: The effect of primary interstellar H-atoms on the geometrical pattern of the heliosheath in the model by Baranov et al. (1981, 1982). BS, HP and TS are the bow shock, the heliopause and the termination shock, respectively.

$V_E = 400$ km s^{-1} ($\sqrt{K} = 160$), the heliocentric distance to the termination shock (TS) along the axis of symmetry Oz is approximately equal to 100 AU. Therefore, the termination shock crossing by the Voyager-1 spacecraft in December 2004 at the heliocentric distance ∼94 AU was predicted about 25 years ago on the basis of the model considered by Baranov et al. (1981, 1982).

2.4 Conclusion

Parker's model of the solar wind considered in Section 2.2 is both stationary and spherically-symmetric. It is based on the one-fluid approximation of the ideal gas (see Chapter 1). Later, the solar wind theory has been developed to take into account (i) multi-component character of the flow due to, for instance, effects of pick-up ions (in distant solar wind) or different temperatures of electrons and protons, (ii) effect of the solar activity, (iii) inhomogeneous character of the solar wind outflow from the solar corona, etc. (see following Chapters).

The early models of the solar wind interaction with the interstellar medium (LISM) have been a reflection of our poor knowledge concerning parameters of the LISM. However, they stimulated astronomers to study experimentally the environment of the Solar System. At present, there is no doubt that the local interstellar medium is mainly partially ionized hydrogen gas moving with the supersonic bulk velocity (with respect to the thermal sound velocity a) relative to the Solar System. Therefore, the solar wind interaction with the supersonic flow of the interstellar gas cannot be considered on the basis of early models presented in Subsections 2.3.1 and 2.3.3 (interstellar gas at rest), in Subsections 2.3.2 (incompressible interstellar gas flow) and 2.3.4 (thin heliosheath layer and fully ionized interstellar gas). The early self-consistent model considered in Subsection 2.3.5 takes into account the supersonic character of the interstellar gas flow and the mutual influence of the plasma (electrons and protons) and H-atom components due to processes of resonant charge exchange. However, it has some defects, although it predicted the location and the form of the termination shock, the heliopause, and the bow shock at polar angles $0 \leq \theta \leq \pi/2$ within a good region of accuracy. These defects are as follows:

1. The most important defect is connected with the validity of the continuity equation for H-atoms [the last equation of (2.30)]. It takes into account only disappearing primary H-atoms of the LISM due to charge exchange with protons and does not take into account secondary H-atoms, "born" in this process in all regions of the flow.

2. To calculate the effect of H-atoms on the plasma component (RHSs of the momentum and energy equations (2.25) and (2.27), respectively) it is assumed that the distribution functions of H-atoms and protons are Maxwellian (Holzer and Banks, 1969; Holzer, 1972) . However, the Maxwellian distribution function for H-atoms cannot be conserved if the mean free path l_c for their collisions with protons in processes of charge exchange is comparable with the characteristic size L of the problem considered (for the solar wind interaction with the LISM $l_c \approx L$, where L is, for example, the thickness of the heliosheath). The exact theoretical calculations, where H-atoms are described by the Boltzmann equation (Chapter 4), show that all populations of H-atoms are not Maxwellian, i.e. the hydrodynamic approximation is not correct for describing the neutral component.

3. It is assumed that the bulk velocity of H-atoms and their temperature are constant, i.e. $\mathbf{V}_H = \mathbf{V}_\infty = const$, $T_H = T_\infty = const$, because the momentum and energy equations for H-atoms are not correct at $l_c \approx L$ (see Chapter 1). It should be noted here that this assumption was used many years later for the 3D MHD numerical simulation of the solar wind interaction with the LISM (Linde et al., 1998).

The kinetic gas dynamic model by Baranov and Malama (1993) without these defects will be considered in Chapter 4.

Bibliography

Baranov, V.B.: 1990, *Space Sci. Rev.* **52**, 89–120.
Baranov, V., Krasnobaev, K., and Kulikovskii, A.: 1970, *Dokl. Akad. Nauk SSSR* **194**, p. 41.
Baranov, V.B., and Krasnobaev, K.V.: 1971, *Kosmicheskie issledovaniya* **4** (in russian).
Baranov, V.B., and Zaitsev, N.A.: 1995, *Astron. Astrophys.* **304**, 631–637.
Baranov, V.B., Ermakov, M.K., and Lebedev, M.G.: 1981, *Soviet. Astron. Lett.* **4**, 206.
Baranov, V.B., Ermakov, M.K., and Lebedev, M.G.: 1982, *Fluid Dynamics* **17**, 754–759.
Bertaux, J.L., and Blamont, J.: 1971, *Astron. Astrophys.* **11**, 200–217.
Blum, P., and Fahr, H.: 1970, *Astron. Astrophys.* **4**, 280–290.
Cherny, G.G.: 1959, Techenija gaza s bol'shoi sverchzvukovoi skorost'ju (in russian), Fizmatgiz, Moskva.
Dyson, J.E.: 1975, *Astrophys. Space Sci.* **35**, 299–312.
Fahr, H.: 1974, *Space Sci. Rev.* **15**, 483–540.
Gringauz, K., Bezrukih, V., Ozerov, V., and Ribchinsky, R.: 1960, *Dokl. Akad. Nauk SSSR* **131**, 1301.
Holzer, T.: 1972, *J. Geophys. Res.* **77**, 5407–5431.
Holzer, T., and Banks, P.: 1969, *Planet. Space Sci.* **17**, 1074–1077.
Linde, T.J., Gombosi, T.I., Roe, P.L., Powell, K.G., and DeZeeuw, D.L.: 1988, *J. Geophys. Res.* **103**, 1889–1904.
Neugebauer, M., and Snyder, C.: 1962, *Science* **138**, 3545.
Parker, E.N.: 1961, *Astrophys. J.* **134** 20.
Parker, E.N.: 1958, *Astrophys. J.* **128**, 664.
Thomas, G., and Krassa, R.: 1971, *Astron. Astrophys.* **11**, 218–233.
Wallis, M.: 1975, *Nature* **254**, 207–208.
Weaver, R., McGray, R., Castor, J.: 1977, *Astrophys. J.* **218**, 377.
Weller, C., and Meier, R.: 1974, *Astrophys. J.* **193**, 471–476.

— 3 —

Early Concepts of the Heliospheric Interface: H Atoms

Vladislav V. Izmodenov[1]

Lomonosov Moscow State University,
School of Mechanics and Mathematics, Department of Aeromechanics;
Space Research Institute, Russian Academy of Sciences;
Institute for Problems in Mechanics, Russian Academy of Sciences

Abstract. **Since the 1960s the concept of the plasma heliosphere, as discussed in Chapter 2 of this book (Baranov, 2006), has been developed. Despite the fact that the role of charge exchange in the interaction between these two components was realized very early, mainly the concept of simple interstellar neutral atom penetration into the heliosphere has been pursued. This Chapter reviews early analytical (or simple numerical) models of the interstellar H atom flow in the heliosphere. Since the mean free path of H atoms is larger than the size of the heliosphere, the behaviour of the interstellar H atom flow is essentially kinetic. Historically, the modelling of the interstellar neutral hydrogen gas flow in the heliosphere was inspired by the measurements of backscattered solar Lyman-α radiation. Although this Chapter refers to the large number of papers discussing and analyzing measurements of backscattered solar Lyman-α radiation, it mainly focuses on the modelling of interstellar atoms in the heliosphere.**

3.1 Introduction

The first ideas of the presence of atomic hydrogen in the interplanetary medium were inferred from the rocket measurements of ultraviolet radiation, when a strong diffuse UV radiation at 10.5-12.25 nm was observed instead of the expected stellar point sources. In the discussion of their rocket night-flight results, Kupperian et al. (1959) interpreted this emission as due to solar Lyman-α photons scattered by interplanetary H atoms. Similarly, Shklovsky (1959) interpreted these rocket results, together with the night time H alpha measurements of Prokudina (1958), in the same way. However, he mentioned an alternate explanation ".. which cannot be excluded for the time being", in which this night time Lyman-α emission would be produced by resonance scattering of H atoms linked to the Earth, in an extended atmosphere that he called "geocorona". In order to discriminate the sources, Morton and Purcell (1962) performed a night time rocket measurement of

[1]in *The Physics of the Heliospheric Boundaries*, V. Izmodenov and R. Kallenbach (eds.), ISSI Scientific Report No. 5, pp. 45–65, ESA-ESTEC, Paris 2006

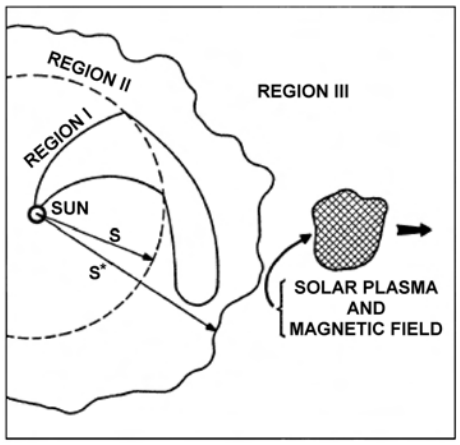

Figure 3.1: A sketch of the structure of the interaction of the solar wind with the interstellar magnetic field proposed by Axford et al. (1963). The solar wind is supersonic in Region I, and the solar magnetic field lines form Archimedes spirals co-rotating with the Sun. The termination shock occurs at a heliospheric distance S. Beyond TS, in region II (the boundary shell), charge-exchange between solar-wind protons and interstellar neutral hydrogen takes place, and dissipative effects permit oppositely directed solar wind magnetic-field lines to merge and form closed loops. S^* is the distance to the boundary between the solar magnetic field and the interstellar magnetic field. Blobs of solar plasma and magnetic field become detached from region II, and move out into region III (interstellar space), where they gradually diffuse away.

diffuse Lyman-α by using an absorption cell technique (for description of the technique see, e.g., Bertaux and Lallement, 1984). These measurements have shown that only 15% of the observed scattered Lyman-α radiation was at a wavelength shifted by more than 0.04 $\dot{A}$ from the line centre. The 85% absorbed radiation were produced by transport of Lyman-α photons from the day side to the night side by radiative transfer in an extended exosphere, while the 15% was highly Doppler shifted, possibly produced by precipitating magnetospheric protons, or of extra-terrestrial origin. In order to produce such wavelength-shifted photons, the scattering gas should be either hot (to produce a broad spectral linewidth) or should be in motion with respect to the Sun (to produce Doppler-shifted protons).

Patterson, Johnson and Hanson (1963) proposed a scenario for the hot atomic hydrogen within the heliosphere and obtained the first analytical expression for the distribution of the atomic hydrogen in interplanetary space. This work was based on the concept of the heliospheric interaction with the surrounding interstellar (or galactic) medium suggested by Axford et al. (1963) and shown schematically in Figure 3.1. It was assumed in the model that the solar wind blows continuously outward from the Sun with a nearly constant, highly supersonic velocity. Hence, the solar wind density and dynamic pressure direct radially away from the Sun and decrease as $\sim 1/r^2$. At the distance where the dynamic pressure equals the pressure

of the local interstellar medium (magnetic pressure and/or thermal pressure), the solar wind passes through a standing shock – the termination shock – beyond which it is subsonic. In the region beyond the shock front (that we call now the inner heliosheath), the individual velocities of the solar wind protons remain of the order of ∼300 km/s due to high thermal velocities. The energetic protons undergo charge exchange with neutral interstellar hydrogen. This process leaves low-energy protons in the transition region beyond the shock, and provides an *isotropic* source of high-energy neutral hydrogen atoms. Some of these atoms (now called energetic neutral atoms – ENAs) move through the TS back toward the Sun.

Patterson et al. (1963) calculated the distribution of the neutral hydrogen atoms in interplanetary space assuming that the TS is an isotropic source of the neutrals and taking into account their velocity, the ionizing solar radiation, and the charge exchange with the solar wind. It was also assumed that (1) the post-shocked solar wind protons suffer charge exchange with interstellar neutrals just in a thin shell beyond the TS, (2) half of the solar wind flux is returned into the heliosphere in the form of fast neutrals. Later, Hundhausen (1968) has shown that most of the neutral hydrogen observable in the vicinity of the Earth does not undergo charge exchange between solar wind protons and interstellar neutral hydrogen near the shock boundary of the heliosphere, as assumed by Patterson et al. (1963), but in a region far beyond the shock. Hundhausen's model predicted a much smaller atomic hydrogen density near Earth. Therefore, the neutral hydrogen density near Earth could then only be maintained in the model if the shock is near 5 AU.

An alternative approach, which actually became a commonly accepted paradigm for at least two decades, was suggested by Fahr (1968a). In the next Section we will discuss the Fahr model, but here we should point out that modern concepts of the ENAs originating in the inner heliosheath (see, e.g., Gruntman et al., 2001) are very similar to those of Patterson et al. (1963) and Hundhausen (1968).

3.2 The cold model

Fahr (1968a) pointed out that the assumption of the random motion of interstellar hydrogen made by Patterson et al. (1963) is very unlikely because the Solar System itself has a velocity of 20 km/s with respect to the local reference system of the nearby stars, and also the interstellar hydrogen clouds are moving. It was shown (Blum and Fahr, 1970; Axford 1972) that the concept of the Strömgren sphere of ionized gas around a hot star fails for the Sun, in the case that there is a relative bulk motion of the interstellar atoms with respect to the Sun. The Strömgren sphere is determined by equating the flux of ionizing photons emitted by the Sun to the total recombination rate (Strömgren, 1939). In case of the Sun, the Strömgren sphere has a radius of about 1500 AU. It was estimated (Blum and Fahr, 1970) that about 90% of the cold interstellar hydrogen with a velocity of 20 km/s will enter the heliosphere without being ionized or charge exchanged.

Fahr (1968a) has calculated the heliospheric distribution of the number density of the cold interstellar hydrogen taking into consideration the macroscopic motion of the interstellar gas and the solar gravitational field. Blum and Fahr (1970) took into account the losses of interstellar atoms due to charge exchange with the

solar wind protons and due to photoionization by the solar radiation. Therefore, in the model, the cold interstellar neutrals enter the Solar System along Kepler trajectories and suffer losses caused by charge exchange with the solar wind protons and the EUV-ionization. The charge exchange process produces the secondary fast neutrals having the velocity of the solar wind. These particles move radially outwards without any losses within the solar wind (Fahr, 1968b), and cannot be observed in Lyman-α because they are too much Doppler shifted from the centre of the solar line.

Following Fahr (1968a) and Blum and Fahr (1970) we derive the number density of the cold interstellar component in the heliosphere. The name "cold model" refers to the model assumption that all H atoms have the same velocity far away from the Sun (monocinetic velocity distribution), which is the opposite of the velocity of the Sun through the local interstellar medium. It is assumed in the model that the rates of the charge exchange and the photoionization are spherically symmetric and decrease with distance as $1/\mathrm{r}^2$:

$$\nu(r) = (\nu_{\mathrm{ce,E}} + \nu_{\mathrm{ph,E}}) \frac{r_{\mathrm{E}}^2}{r^2},$$

where $\nu_{\mathrm{ce,E}}$ and $\nu_{\mathrm{ph,E}}$ are the charge exchange and photoionization rate at Earth's orbit, r is the heliocentric distance, and $r_{\mathrm{E}} = 1$ A.U. The interstellar atoms change their trajectories in the heliosphere due to the influence of the solar gravitation and radiation pressure that can be described by a single force with potential

$$U(r) = -(1-\mu)\frac{M_{\odot} m G}{r},$$

where $\mu = F_{\mathrm{rad}}/F_{\mathrm{grav}}$ is the ratio of the solar radiation to solar gravitational forces, $M_{\odot}$ is the mass of the Sun, m is the mass of the interstellar atom, and G is the gravitational constant. The solar radiation pressure F_{rad} exerted on one H atom is due to its continuous scattering of solar Lyman-α photons. This effect was omitted in the early work of Blum and Fahr (1970), and included in Bertaux et al. (1972), which pointed out that, if $\mu > 1$, there is a zone void of H atoms (see below). Both the loss rate and force acting on the interstellar atoms are spherically symmetric. However, since interstellar H atoms move with respect to the Sun the problem considered becomes axisymmetric. Let us introduce coordinates (r, θ) (see Figure 3.2). Since all interstellar H atoms have the same velocity at infinity (i.e. in the undisturbed interstellar medium), only two particle trajectories pass through a space point. The trajectories that pass through the points with (r, θ) are characterized by two impact parameters:

$$P_{1(2)}(r,\theta) = \frac{r}{2}\sin\theta \cdot \left(1 \pm \sqrt{1 + \frac{4}{r\beta(1+\cos\theta)}}\right), \tag{3.1}$$

where

$$\beta = \frac{V_{\infty}^2}{(1-\mu) M_{\odot} G}.$$

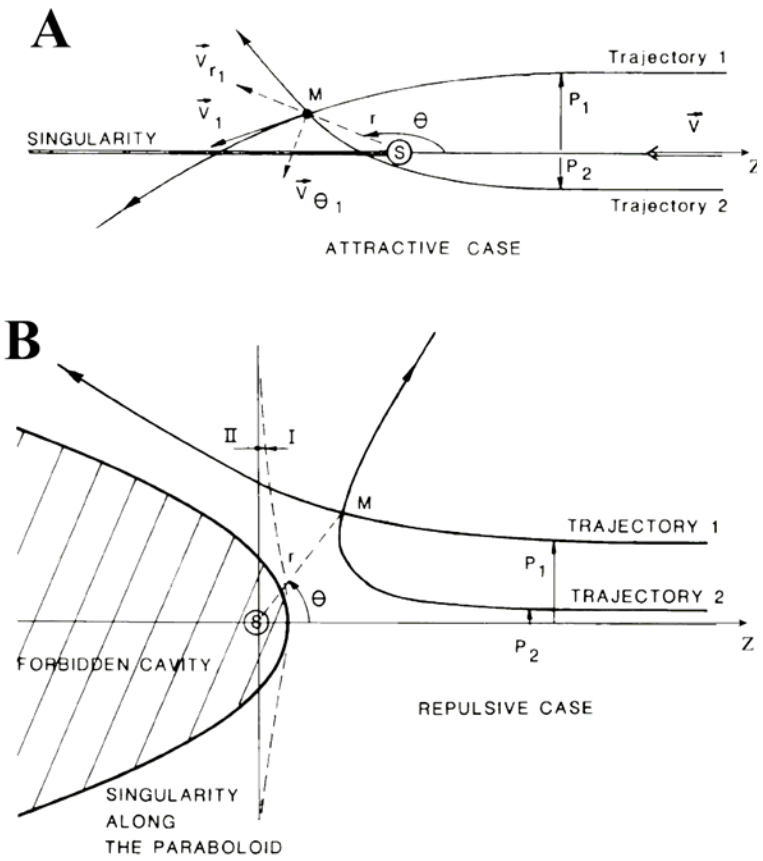

Figure 3.2: Geometry of the cold model. Each point M with coordinates (r, θ) is crossed by two hyperbolic trajectories coming from infinity with two different impact parameters P_1 and P_2. For $\mu \leq 1$ (A) one of the two orbits is direct (with $P_1 > 0$ and $\theta_1 < \pi$) and the second is indirect (with $P_2 < 0$ and $\theta_2 \geq \pi$). The local velocity components are shown for orbit 1. The density becomes infinite at Oz-axis for $z < 0$, i.e. in the so-called downwind direction. For $\mu \geq 1$ at each point M outside a paraboloidal cavity determined by inequality (3.2) there are two direct trajectories coming from infinity. Adopted from Lallement et al. (1985)

Note, that $P_1 > 0$, $P_2 < 0$ if $\mu < 1$, and $P_1 > 0$, $P_2 > 0$ if $\mu > 1$. In the case that $\mu > 1$, the stream of particles cannot penetrate inside the downwind region defined by the condition

$$r\,(1 + \cos\theta) \leq -4/\beta \tag{3.2}$$

When condition (3.2) is fulfilled the impact parameters becomes imaginary.

To calculate the number density $n(r,\theta)$ we will calculate the contribution for trajectories with one impact parameter. Then the total number density is the sum of the two contributions:

$$n\left(r,\theta\right)=\sum_{i=1,2} n_{(i)}\left(r,\theta\right)\ . \tag{3.3}$$

In the case where the loss processes are absent, the flux of particles is conserved in the flux tube:

$$n_{(i)}\left(r,\theta\right)V\left(r\right)\mathrm{d}S=n_{\infty}V_{\infty}\mathrm{d}S_{(i),\infty},$$

where $n_{(i)}(r,\theta)$ and $V(r)$ are the number density and velocity of interstellar atoms of the (i)-th component at (r,θ), n_{∞}, and V_{∞} are the number density and velocity at infinity. The flux is calculated through the surface element $\mathrm{d}S$, which is perpendicular to the particle velocities at point (r,θ). At infinity this surface element converges to become $\mathrm{d}S_{(i),\infty}$.

Since the problem considered has cylindrical symmetry (Oz is the axis of symmetry, Figure 3.2), $\mathrm{d}S$ is the surface of rotation of the element perpendicular to the velocity of particles at point (r,θ). It can be calculated as:

$$\mathrm{d}S=2\pi r\sin\theta\cdot\mathrm{d}r\cos\delta, \tag{3.4}$$

where δ is the angle between the radius-vector $\mathbf{r}$ and the normal to the trajectory at point (r,θ). It is easy to show that

$$\cos\delta=\frac{r}{\sqrt{r^2+(\mathrm{d}r/\mathrm{d}\theta)^2}}. \tag{3.5}$$

$\mathrm{d}S_{\infty}$ is equal to $2\pi P_{0,(i)}\mathrm{d}P_{0,(i)}$. Finally, in the case where loss processes are not taken into account:

$$\frac{n_{(i)}\left(r,\theta\right)}{n_{\infty}}=\frac{V_{\infty}P_{0,(i)}}{v(r)r\sin\theta\cos\delta\cdot\mathrm{d}r/\mathrm{d}P_{0,(i)}}, \tag{3.6}$$

where $v(r)$ is the velocity of the atom at distance r:

$$v(r)=\sqrt{V_{\infty}^2+\frac{2(1-\mu)GM_0}{r}}=V_{\infty}\sqrt{1+\frac{2}{r\beta}} \tag{3.7}$$

The expressions for $\mathrm{d}r/\mathrm{d}P_0$ and for $\mathrm{d}r/\mathrm{d}\theta$ in Equation (3.5) can be obtained from the trajectory equation in (r,θ) coordinates:

$$r=\frac{\beta P_{0,(i)}^2}{1+\beta P_{0,(i)}\sin\theta-\cos\theta},$$

The derivatives are:

$$\frac{\mathrm{d}r}{\mathrm{d}P_{0,(i)}}=\frac{2\beta P_{0,(i)}}{1+\beta P_{0,(i)}\sin\theta-\cos\theta}-\frac{\beta^2P_{0,(i)}^2\sin\theta}{\left(1+\beta P_{0,(i)}\sin\theta-\cos\theta\right)^2} \tag{3.8}$$

$$\frac{\mathrm{d}r}{\mathrm{d}\theta}=\frac{\beta P_{0,(i)}^2\left(\beta P_{0,(i)}\cos\theta+\sin\theta\right)}{\left(1+\beta P_{0,(i)}\sin\theta-\cos\theta\right)^2}. \tag{3.9}$$

Summarizing, in the case where there are no losses of interstellar particles in the heliosphere, the number density of the particles is determined by Equation (3.3), where $n_{(i)}$ is given by Eqsuations (3.6), (3.1), (3.7), (3.5), (3.8) and (3.9).

After transformations, Equation (3.6) can be written in the following form:

$$\frac{n_i}{n_\infty} = \frac{\sqrt{r^2H^4 + \beta^2 P_{0,(i)}^4 \left(\beta P_{0,(i)} \cos\theta + \sin\theta\right)^2}}{r^2 \sin\theta \left(2H - \beta P_{0,(i)} \sin\theta\right) \sqrt{1 + 2/\left(r\beta\right)}},$$

where $H = 1 + \beta P_{0,(i)} \sin\theta - \cos\theta$.

The probability $\mathrm{d}E$ that a particle becomes ionized or lost by charge exchange while covering the distance $\mathrm{d}s$ it its orbit is given by $\mathrm{d}E = \left(\nu_\mathrm{E} r_\mathrm{E}^2 \mathrm{d}s\right) / \left(r^2 v\right)$, where $\nu_\mathrm{E} = \nu_{\mathrm{ex,E}} + \nu_{\mathrm{phot,E}}$. Therefore, in order to take into account the losses of particles along the trajectory, the density n_∞ in Equation (3.6) should be replaced by the number density $n^*_{\infty,i}$ that takes into account losses along the trajectory:

$$n^*_{\infty,i} = n_\infty \exp\left(-\int_\infty^s \frac{\mathrm{d}s}{v} \cdot \frac{\nu_\mathrm{E} r_\mathrm{E}^2}{r^2}\right) \tag{3.10}$$

where $\mathrm{d}s = \sqrt{\mathrm{d}r^2 + \left(r\mathrm{d}\theta\right)^2} = \mathrm{d}\theta\sqrt{r^2 + \left(\mathrm{d}r/\mathrm{d}\theta\right)^2}$. Equation (3.10) can be re-written taking into account that $\mathrm{d}s/v = \mathrm{d}t$ and conservation of momentum $\mathrm{d}t/r^2 = \mathrm{d}\theta/V_\infty P_{0,(i)}$:

$$n^*_{\infty,i} = n_\infty \exp\left(-\frac{\nu_\mathrm{E} r_\mathrm{E}^2 \theta'}{V_\infty P_{0,(i)}}\right), \tag{3.11}$$

where $\theta' = \theta$ if $P_0 > 0$, $\theta' = 2\pi - \theta$ if $P_0 < 0$. Finally,

$$\frac{n\left(r,\theta\right)}{n_\infty} = \sum_{i=1,2} \frac{\sqrt{r^2H^4 + \beta^2 P_{0,(i)}^4 \left(\beta P_{0,(i)} \cos\theta + \sin\theta\right)^2}}{r^2 \sin\theta \left(2H - \beta P_{0,(i)} \sin\theta\right) \sqrt{1 + 2/\left(r\beta\right)}} \cdot \exp\left(-\frac{\nu_\mathrm{E} r_\mathrm{E}^2 \theta_i}{V_\infty P_{0,(i)}}\right), \tag{3.12}$$

where $H = 1 + \beta P_{0,(i)} sin\theta - cos\theta$, and $\theta_i = \theta$ if $P_{0,(i)} > 0$, $\theta_i = 2\pi - \theta$ if $P_{0,(i)} < 0$.

Expression (3.12) for $n(r,\theta)$ can be re-written in a simpler form (Axford, 1972; Dalaudier et al., 1984, Lallement et al., 1985):

$$\frac{n\left(r,\theta\right)}{n_\infty} = \frac{\left(1 + \sqrt{A}\right)^2}{4\sqrt{A}} \exp\left(-\frac{\nu_\mathrm{E} r_\mathrm{E}^2 \theta_1}{V_\infty |P_{0,(1)}|}\right) + \frac{\left(1 - \sqrt{A}\right)^2}{4\sqrt{A}} \exp\left(-\frac{\nu_\mathrm{E} r_\mathrm{E}^2 \theta_2}{V_\infty |P_{0,(2)}|}\right), \tag{3.13}$$

where $A = 1 + 4/[r\beta(1 + \cos\theta)]$, and θ_i (i=1,2) are defined as previously.

Figures 3.3 (A, B) show the distribution of the number density of the interstellar H atoms within the heliosphere for the cold model. The number density of interstellar H atoms is larger in the direction towards the interstellar flow, and, therefore, according to the prediction of the cold model of Blum and Fahr (1970), the observed Lyman-α emission should have a maximum, and the maximum should be toward the direction of the interstellar H atom flow. Extraterrestrial UV radiation (most likely Lyman-α) was measured from interplanetary probes Zond 1 (Kurt, 1965, 1967), of Venera 2, 3, and 4 (Kurt and Germagenova, 1967; Kurt and Syunyaev, 1968), and of Mariner 5 and 6 (Barth, 1970). These measurements

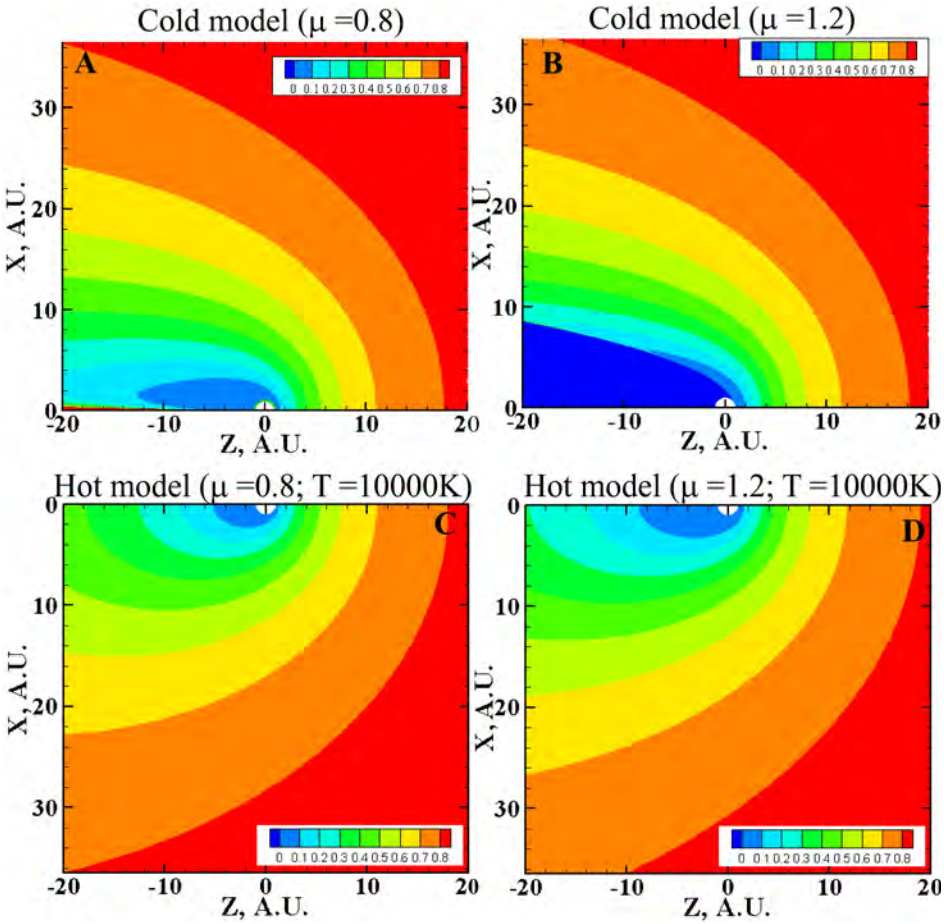

Figure 3.3: Cold (A, B) and hot (C, D) model distributions of the number density of interstellar hydrogen atoms within the heliosphere normalized to the number density at infinity. Calculations were performed for $V_\infty = 20$ km/s, $\nu = 5.35 \cdot 10^{-7}$ s^{-1}. The parameter μ is equal to 0.8 and 1.2 for panels A, C, and B, D respectively. Note that for $\mu < 1$ the number density is infinite at the z-axis for $z < 0$. For $\mu > 1$ there is a region (deep blue in panel B) of zero density, where particles cannot penetrate along the Keplerian trajectories. In the case of the hot model (C, D) $T = 10000$ K. The Y axis direction is preserved in plots C and D to provide better visual comparison with A and B.

proved that the 15% highly shifted night time Lyman-α found earlier by Morton and Purcell (1962) in their rocket flight was indeed of extra-terrestrial origin. It was found in these interplanetary probe measurements that the maximum of the backscattered Lyman-α emission exists and it is located towards the direction of the galactic centre. Because of this specific direction of the emission maximum,

a new 'galactic' source of the diffuse radiation was suggested as an alternative to Patterson et al. (1963) scenario.

The dilemma of the galactic or interstellar origin for the diffuse radiation was resolved by OGO-5 spacecraft measurements (Bertaux and Blamont, 1971; Thomas and Krassa, 1971; see the review of Lallement, 2001). The apogee of OGO-5 was out of the geocorona, i.e. geocorona emission could be ruled out at apogee. The spacecraft was spinning so that the extraterrestrial diffuse Lyman-α radiation could be mapped over the sky. A broad maximum in one direction and a minimum in the opposite direction were observed. To find the distance to the region of the maximum emissivity of the backscattered Lyman-α emission, two sky-mappings of the diffuse Lyman-α were performed on board the OGO-5 spacecraft in September 1970 and April 1970, when the Earth (and the spacecraft too) was at opposite positions in its orbit. The difference in the position of the maximum of diffuse Lyman-α emission as seen in the two maps was about 30°. This proved that the emission was from a few AU and displacement of the maximum is due to the parallax effect that would be negligibly small in the case of a galactic source for the emission. Analyzing the three sky-maps of the OGO-5 allowed one to find the direction of the interstellar H atoms approaching the Sun (Bertaux et al.,1972). Newer values of the direction of interstellar hydrogen inside the heliosphere are (252.2°, 9°) in ecliptic coordinates (Lallement et al., 2005).

Therefore, the theoretical prediction made by Fahr (1968a) and Blum and Fahr (1970), i.e. that interstellar H atoms penetrate into the heliosphere up to distances of a few AU from the Sun, was confirmed by Lyman-α measurements made by OGO-5 spacecraft instruments in 1969-1970 (Bertaux and Blamont, 1971; Thomas and Krassa, 1971; see, also, Thomas, 1972), and the 'galactic' interpretation was ruled out. An upper limit to galactic emission of 15 Rayleigh (compared to the observed 300-500 R of extra-terrestrial emission) was derived from hydrogen absorption cell measurements onboard Prognoz-5 and 6 (Lallement et al., 1984).

3.3 The hot model

Since the interstellar temperature is $\sim 10^4$ K, the real situation is drastically different from the cold model considered above. Especially the cold model fails for the downwind direction at the axis of symmetry, where it gives infinite densities for $\mu < 1$. The problem with finite temperature has been considered by Fahr (1971), Thomas (1972), Feldman et al. (1972), Bertaux et al. (1972), Fahr (1974), Blum et al. (1975), Meier (1977), Fahr (1978), and Wu and Judge (1979). Measurements of the backscattered solar Lyman-α radiation with a hydrogen absorption cell onboard the Soviet interplanetary probe Mars-7 (Bertaux et al., 1976) yielded information concerning the spectral profile of the extraterrestrial Lyman-α radiation. More accurate measurements with a hydrogen absorption cell flown on Prognoz -5, interpreted with the assumption of a Gaussian velocity distribution of H atoms, yielded a temperature of $(8.8 \pm 1) \cdot 10^3$ K (Bertaux et al., 1977). However, a more accurate interpretation of the spectral profile is only possible if the velocity distribution function of the interstellar hydrogen is taken into account, even for the simple case of μ=1, in which atom trajectories are straight lines.

Correct interpretation of the spectral profile is only possible if the velocity distribution function of the interstellar hydrogen is taken into account.

Actually, Danby and Camm (1957) were the first to solve the problem of the motion of a cloud of gas particles in the gravitational field of a point mass. They found an analytical formula for the velocity distribution function of the particles. Later, the Danby-Camm formula was applied to the interstellar atoms moving in the heliosphere and modified by including a loss function to take into account the effects of charge exchange and photoionization.

The hot model implies the solution of the kinetic equation of the velocity distribution of the interstellar atoms, $f(\mathbf{v}, \mathbf{r}, t)$:

$$\frac{\partial f}{\partial t} + \mathbf{v} \cdot \frac{\partial f}{\partial \mathbf{r}} + \mathbf{F} \cdot \frac{\partial f}{\partial \mathbf{v}} = -\nu f, \tag{3.14}$$

where $\mathbf{F} = -(1 - \mu(\mathbf{r}, \mathbf{v}, t)) GM_{\odot}\mathbf{r}/r^3$. As in the cold model, the force results from the solar gravitation and from the solar radiation pressure. The rate of loss of the interstellar atoms due to the photoionization and charge exchange processes is $\nu(\mathbf{r}, t)$. In the classical hot model it is assumed that:

1. the problem is stationary, i.e. $\partial f/\partial t = 0$,
2. the H atoms approaching the Sun are subject to the *stationary, spherically symmetric* **effective** solar gravitational force (resulting from the combined action of the solar gravity and solar radiation pressure), and therefore $\mu(\mathbf{r}, t)$ = const,
3. the H atoms approaching the Sun are subject to the *stationary, spherically symmetric* **effective** ionization (resulting from the combined action of the photoionization and the charge exchange process), i.e. $\nu(\mathbf{r}, t) = \nu_{\mathrm{E}} r_{\mathrm{E}}^2/r^2$, where ν_{E} is the rate of losses at the Earth's orbit, r_{E} is one astronomical unit, r is the distance in the heliocentric coordinate system.

Further generalizations of the hot model no longer have these limitations. These modern models will be reviewed in Section 3.4 of this Chapter.

To complete the formulation of the classical hot model the boundary condition should be added to the kinetic equation (3.14). The boundary condition is given at infinity ($r \to \infty$):

$$\lim_{r\to\infty} f(\mathbf{v}, \mathbf{r}, t) = f_{\infty}(\mathbf{v}) = \frac{n_{\infty}}{\pi\sqrt{\pi}c_{\infty}^3} \cdot \exp\left(-\frac{(\boldsymbol{V_{\infty}} - \mathbf{v})^2}{c_{\infty}^2}\right), \tag{3.15}$$

where $c_{\infty}^2 = 2k_B T_{\infty}/m$ is the thermal velocity of interstellar H atoms, n_{∞}, $\mathbf{V}_{\infty}$, T_{∞} are the number density, velocity and temperature of the interstellar atoms at infinity, m is the mass of an individual atom, k_B is the Boltzmann constant.

The kinetic equation (3.14) can be solved by the method of characteristics. According to this method, the velocity distribution function of the interstellar atoms, $f(\mathbf{v}, \mathbf{r}, t)$ changes along characteristics as follows:

$$\frac{\mathrm{d}f(\mathbf{v}, \mathbf{r}, t)}{\mathrm{d}t} = -\nu f(\mathbf{v}, \mathbf{r}, t). \tag{3.16}$$

The characteristics of Equation (3.14) in six-dimensional phase-space are

$$\frac{\mathrm{d}\mathbf{r}}{\mathrm{d}t} = \mathbf{v}, \quad \frac{\mathrm{d}\mathbf{v}}{\mathrm{d}t} = \mathbf{F}. \tag{3.17}$$

Note, that the characteristics of Equation (3.14) coincide with the trajectories of the individual particles. Equation (3.16) can be integrated over the characteristic (trajectory) from infinity to r:

$$f(\mathbf{v}, \mathbf{r}, t) = f_\infty(\mathbf{v}_\infty) \cdot \exp\left(-\int_\infty^t \nu \mathrm{d}t\right) = f_\infty(\mathbf{v}_\infty) \cdot E, \tag{3.18}$$

where

$$E = \exp\left(-r_\mathrm{E}^2 \int_{-\infty}^t \frac{\nu_\mathrm{E} \mathrm{d}t}{r^2}\right) \tag{3.19}$$

is the extinction factor that takes into account losses due to charge exchange and photoionization. The integral (3.19) is taken along the trajectory. $\mathbf{v}_\infty$ is an asymptotic solution at $r \to \infty$ and $t \to -\infty$ of Equations (3.17) that passes through point ($\mathbf{v}$, $\mathbf{r}$, t). Physically $\mathbf{v}_\infty$ means the velocity at infinity of the particle that has velocity $\mathbf{v}$ at point $(\mathbf{r}, t)$.

Note that for the classical stationary hot model the time t does not become important, because the characteristics (trajectories) are stationary. As for the cold model, Eq. (3.19) for the extinction factor E could be re-written by using the fact of conservation of momentum $r^2(\mathrm{d}\theta'/\mathrm{d}t) = v_\infty P_0$:

$$E = \exp\left(-\frac{\nu_\mathrm{E} r_\mathrm{E}^2}{v_\infty P_0} \int_0^\theta \nu_\mathrm{E} \mathrm{d}\theta'\right) = \exp\left(-\frac{r_\mathrm{E}^2 \nu_\mathrm{E} \theta'}{v_\infty P_0}\right), \tag{3.20}$$

where P_0 is the impact parameter, v_∞ is the velocity at infinity along the trajectory, and θ' is swept-angle along the trajectory.

Let us introduce a spherical coordinate system (r, θ, ϕ), where θ is the angle with respect to the upwind direction, and (v_r, v_ρ, ψ) are coordinates in velocity space, where v_r is the radial velocity, and (v_ρ, ψ) are the velocity coordinates in the plane perpendicular to the radius-vector $\mathbf{r}$. For the classical hot model both ν and μ depend on radial distance only, and the problem considered becomes axisymmetric and the velocity distribution does not depend on ϕ. Equation (3.18) can be re-written for this case in the following form (Wu and Judge, 1979):

$$f(v_r, v_\rho, \psi, r, \theta) = \frac{n_\infty}{\left(\sqrt{\pi} c_\infty\right)^3} \exp\left(-F_1 - F_2 \sin\psi\right), \tag{3.21}$$

where

$$F_1 = -\frac{V_\infty^2 + v_\infty^2 + 2V_\infty v_\infty \cos\theta}{c_\infty^2} + \frac{2V_\infty v_\infty \cos\theta}{c_\infty^2} \frac{\left(v_\infty - v_r\right)^2}{v_\infty\left(v_\infty - v_r\right) + Q^2} - \frac{\nu_\mathrm{E} r_\mathrm{E}^2 \theta'}{r v_\rho},$$

$$F_2 = \frac{2 v_\infty V_\infty v_\rho \sin\theta}{c_\infty^2} \frac{\left(v_\infty - v_r\right)}{v_\infty\left(v_\infty - v_r\right) + Q^2},$$

$$Q^2 = \frac{(1-\mu)\,GM_\odot}{r}, \quad v_\infty = \sqrt{v_r^2 + v_\rho^2 - 2Q},$$

θ' is the angle swept out by an atom moving along a Keplerian trajectory that can be expressed as

$$\theta' = \theta_0 \pm \theta_1,$$

where the plus sign is for $v_r > 0$ and the minus sign is for $v_r < 0$; θ_0 is the perihelion angle of the hyperbolic trajectory

$$\theta_0 = \tan^{-1}\left(-v_r v_\rho / Q^2\right), \ \pi/2 < \theta_0 < \pi,$$

and

$$\theta_1 = \tan^{-1}\left(\frac{\sqrt{r_0/r_1 + 2r_0/r - (r_0/r)^2}}{r_0/r - 1}\right), 0 < \theta_1 < \pi,$$

with $r_0 = r v_r^2/Q^2$, $r_1 = Q^2 r/v_\infty^2$.

Figure 3.4 presents a (v_z, v_x)-cut of the 3D (in velocity space) velocity distribution function when $v_y = 0$. (v_z, v_y, v_x) are the coordinates of the velocity vector in the coordinate system, when the z axis is directed towards the interstellar flow. It can be seen that the velocity distribution is not Maxwellian within the heliosphere due to the lack of collisions. At 1 AU in the upwind direction the velocity distribution function is symmetric with respect to $v_x = 0$, but not symmetric with respect to $v_z = V_\infty$. The asymmetry is connected with the so-called selection effect, when at a certain distance slow particles are more ionized than fast particles. This is simply because the slow particles have more time to be ionized before they reach the distances closer to the Sun. To illustrate the effect we plot the distribution function closer to the Sun at 0.125 AU (Figure 3.4B; of course, the number density of H atoms at this distance is very small). In the downwind direction, the velocity distribution function has two peaks and a minimum at $v_x = 0$. This is connected with the fact that particles can penetrate into the downwind direction only from the sides and all particles with $v_x \sim 0$ approach the small heliocentric distances and are ionized there. The two-peak distribution remains at 10 AU distance from the Sun and further.

The distribution of interstellar H atom number density can be obtained by integration of Equation (3.18) over velocity space at infinity. This can be done analytically or numerically. Figure 3.3 also presents the distribution of the number density for two cases when $\mu = 0.8 < 1$ (Fig. 3.3C) and $\mu = 1.2 > 1$ (Fig. 3.3D) and the parameters are identical to those of the cold model (see caption to Figure 3.3). The temperature at infinity was chosen as 10^4 K. It is seen from the Figure 3.3(C, D) that there is a singularity in the downwind direction (for $\mu < 1$), and the zero density cavity (for $\mu > 1$) disappeared in the case of the hot model. Note, that in the upwind hemisphere the cold and hot models give very similar results for the distribution of H atom number density.

Since the velocity distribution function of interstellar atoms is not Maxwellian the kinetic temperature and bulk velocities can only be defined as was discussed in Chapter 1. Figure 3.5 presents distributions of the kinetic radial temperature of

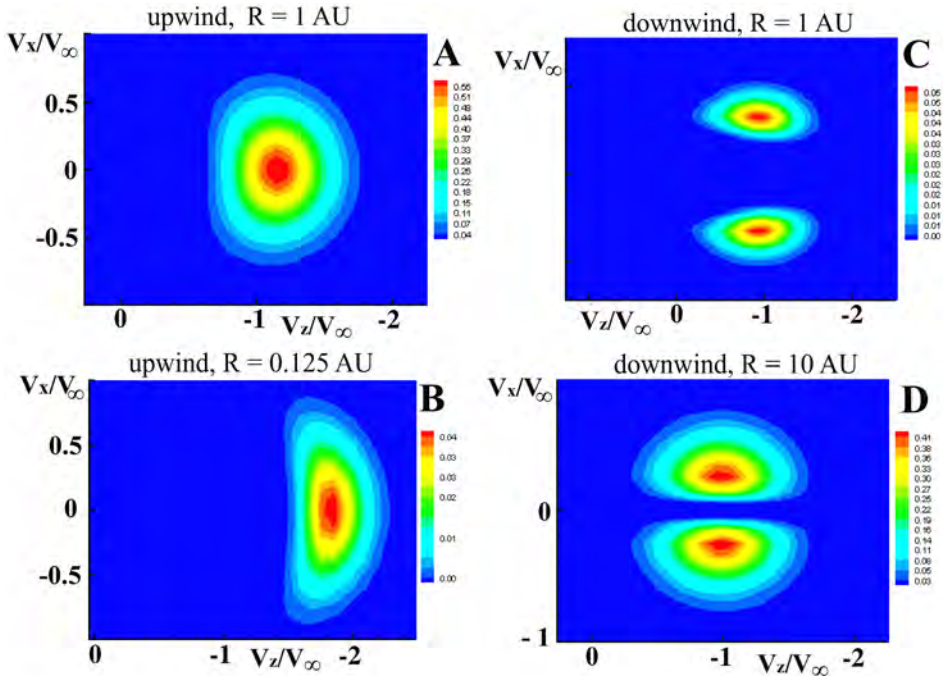

Figure 3.4: Evolution of the velocity distribution function of the interstellar H atoms within the heliosphere: A) at 1 AU in upwind direction, B) at 0.125 AU upwind, C) at 1 AU downwind, D) at 10 AU downwind, E) at 90 AU downwind. $V_\infty = 26.4$ km/s, $\mu = 0.9$, $T_\infty = 6700$ K, $\nu_{\rm E} = 10^{-7}$ s^{-1} were adopted in the calculations. Velocities are normalized to V_∞ and the velocity distribution is presented in dimensionless units. From Kolesnikov (2006).

hydrogen atoms in the heliosphere and the streamlines of the bulk atom flow. The effective radial temperature decreases slightly towards the Sun in the upwind direction. This is due to the effect of selection. The radial temperature is increased from upwind to downwind since the velocity distribution becomes relatively broader. It is interesting that the streamlines are directed toward the axis of symmetry even in the repulsive case of $\mu = 1.2$. This effect is connected with the non-symmetric ionization of particles with negative and positive v_x-components. Generally, in any given location, the particles with the positive v_x component are more ionized compared with the particles with the negative v_x component.

3.4 Further developments of the hot model

In the 1980-1990s the classical hot model was widely used to interpret backscattered solar Lyman-α measurements. However, very soon it became clear that effects connected with the heliolatitudinal and solar cycle variations of the solar wind need to be taken into account.

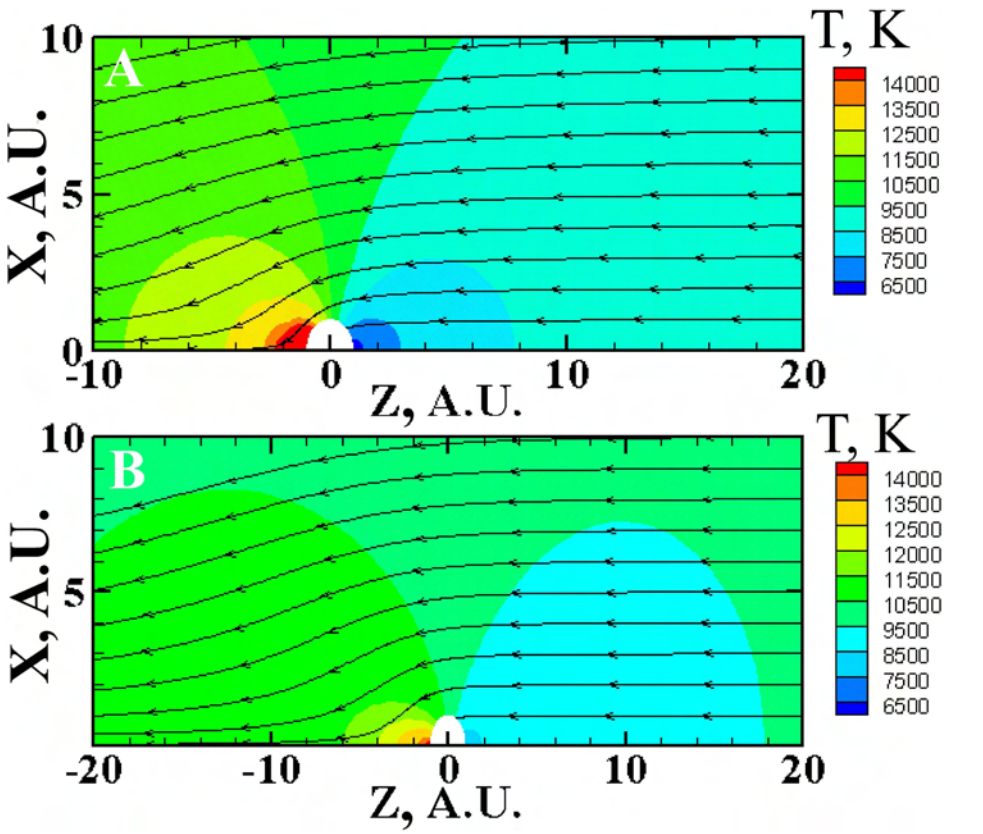

Figure 3.5: The streamlines and temperature distribution of the interstellar H atoms in the heliosphere obtained in the hot model for the $\mu = 0.8$ (A) and $\mu = 1.2$ (B) cases. The model parameters are listed in the caption to Figure 3.3.

3.4.1 Effects of latitudinal asymmetry of charge exchange and photoionization

It is assumed in the classical hot model that the charge exchange and photoionization processes are spherically symmetric, i.e. ν is a function of heliocentric distance and does not depend on heliolongitude and heliolatitude. Possible longitudinal asymmetries are averaged over the 27-day period of solar rotation, while latitudinal effects need to be considered.

It has been shown through modelling by Joselyn and Holzer (1975) that a non-isotropic solar wind would strongly affect the distribution of atomic hydrogen in the heliosphere, and that this could be observed in maps of backscattered solar Lyman-α radiation. The signatures of the latitudinal variations were observed in backscattered interplanetary Lyman-α from Mariner 10 (Kumar and Broadfoot, 1979; Witt et al., 1979, 1981), Prognoz 6 (Lallement et al., 1985b; Summanen et al., 1993), Pioneer-Venus (Ajello et al., 1987; Lallement and Stewart, 1990),

SOHO/SWAN (Bertaux et al., 1997, 1999), and by the Ulysses GAS Lyman-α measurements (Pryor et al., 2003).

As in the case of the classical stationary model Equation (3.14) is solved with the boundary conditions (3.15). The total ionization rate ν including photoionization and charge exchange is equal to $\nu_{\rm E}(r_{\rm E}/r)^2$, where $\nu_{\rm E}$ is the total ionization rate at $r_{\rm E} = 1AU$. The difference with the classical hot model is that $\nu_{\rm E}$ is not a constant anymore, but a function of heliolatitude. Kumar and Broadfoot (1978, 1979), Lallement et al. (1985b), and Pryor et al. (2003) employed the following trigonometric function for the latitude dependence of ν:

$$\nu(r,\lambda) = \nu_{0,\rm E}(1 - A\sin^2\lambda)(r_{\rm E}/r)^2, \tag{3.22}$$

where $\nu_{0,\rm E}$ represents the total ionization rate at 1 AU from the Sun in the solar equatorial plane, and A is a parameter describing the degree of anisotropy of the ionization. The use of a trigonometric function for the latitudinal dependence is very convenient because it allows one to evaluate the integral in Equation (3.19) analytically.

Lallement et al. (1985b) have performed an analysis of Prognoz 5 and 6 measurements by comparing the model results with the varying parameters $\nu_{0,\rm E}$ and A. It was shown that the best agreement between data and model is achieved for $\nu_{0,\rm E} = (5.0 \pm 0.5) \times 10^{-7}$ s^{-1} and $A = 0.4 \pm 0.1$. This means a 30-50% decrease in the ionization rate over the solar pole in comparison with the equatorial plane. The anisotropy of the total ionization was studied in much more detail by the SOHO/SWAN instrument (e.g. Bertaux et al., 1997, 1999). Studies of the total ionization rate variations with latitude and solar cycle were also performed by Pryor et al. (2003). However, description of the details of the Lyman-α analysis is beyond the scope of this Chapter.

3.4.2 Effects of the solar cycle

It follows from the classical hot model that due to the net effects of the solar gravitation, radiation pressure, the charge exchange and photoionization, the velocity distribution of the interstellar atoms is disturbed at about 15–20 AU in the upwind direction. In the downwind direction the 'solar imprint' remains up to $\sim$ 100 AU. A typical interstellar atom with a velocity of 20 km/s travels about 4 AU per year. The time needed for the atom to pass through the region where the ionization and gravitational effects are significant is comparable with the 11 year solar cycle. Since both solar radiation and solar wind flux change with the solar cycle, the time-dependent variations of interstellar atoms within the heliosphere were considered (see, e.g., Blum et al., 1993; Kyrölä et al., 1994; Bzowski and Rucinski, 1995; Rucinski and Bzowski, 1995; Summanen, 1996; Bzowski et al., 1997, 2002; Pryor et al., 2003; Quémerais et al., 2006).

The variability of the solar factors exerts a significant imprint on the hydrogen density distribution within 10–20 AU from the Sun and is most pronounced in the downwind region. Rucinski and Bzowski (1995) have modelled the number density of the interstellar hydrogen in the frame of a time-dependent hot model. As in the case of the classical stationary model, Equation (3.14) was solved with the

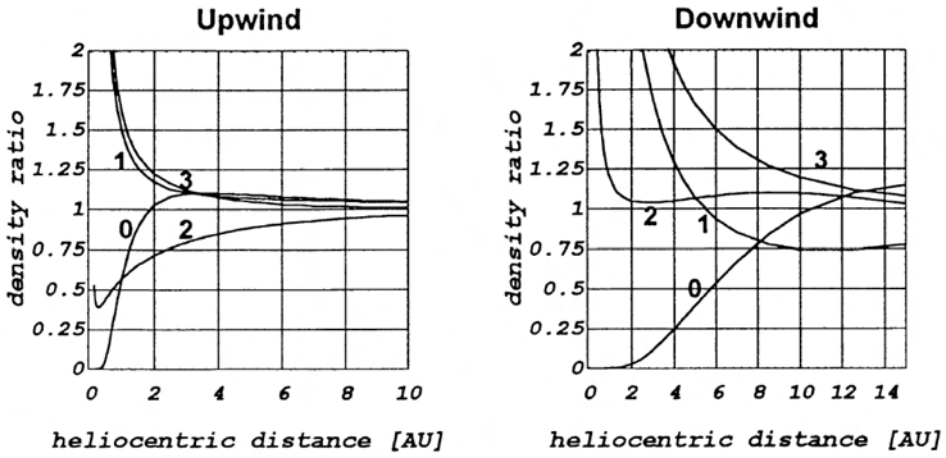

Figure 3.6: The radial profiles of the interstellar H atom density ratios of the time-dependent model compared to the stationary hot model. The radial profiles are shown in the upwind (*left panel*) and downwind (*right panel*) directions for four phases of the solar cycle, separated in time by 2.75 years. Phase 0 corresponds to the solar maximum, phase 2 to solar minimum, phases 1 and 3 are intermediate. From Rucinski and Bzowski (1996).

boundary conditions (3.15). However, parameters μ and $\nu_{\rm E}$ were chosen as the following functions of time:

$$\begin{aligned} \mu\,(t) &= \mu_0 + \hat{\mu}\cos\left(\omega t\right)\exp\left[\cos\left(\omega t\right)\right], \\ \beta\,(t) &= \beta_0 + \hat{\beta}\cos\left(\omega t + \pi\right)\exp\left[\cos\left(\omega t + \pi\right)\right], \end{aligned} \tag{3.23}$$

where $\mu_0 = 0.75$, $\hat{\mu} = 0.243$, $\beta_0 = 5.5 \times 10^{-7}$ s^{-1}, $\hat{\beta} = 10^{-7}$ s^{-1}, $\omega = 2\pi/T_{\rm solar_c ycle}$, and $T_{\rm solar_c ycle} = 11$ year. Also, $v_\infty = 20$ km/s and $T_\infty = 8000$ K were chosen in the calculations of Rucinski and Bzowski (1995). The problem was solved numerically.

Figure 3.6 demonstrates the radial profiles of the ratios of the hydrogen density at a certain phase of the solar cycle to the density calculated in the frame of a stationary model with parameters averaged over the solar cycle. The departures of the density profiles from the stationary model presented at different phases of the solar cycle are clearly visible up to 5 AU on the upwind side (approximately the same occurs in the sidewind direction) and to 15 AU in the downwind region. Further away from the Sun, the differences decrease and practically vanish beyond 15–20 AU in the upwind and 50–60 AU in downwind direction, respectively.

Bzowski and Rucinski (1995) calculated the distributions of H atom number density by using a number of stationary models with 'instantaneous' values of the radiation pressure and ionization rate for the considered phase of the solar cycle. Comparison of these distributions with the results of the non-stationary model has shown significant differences. Therefore, the time-dependent approach is essential for accurate modelling of the interstellar H atoms within the heliosphere.

3.5 Conclusions

A brief summary of the models that have described the distribution of the interstellar atoms within the heliosphere was given in this Chapter. The development of simple and more complex models was inspired by the necessity to understand the measurements of backscattered solar Lyman-α radiation. The cold and hot models described in detail in this Chapter were analytical. Despite their simplicity these models provide a quite reasonable 'first order' approximation for the interstellar H atom distribution within the heliosphere. More complex descriptions take the effects of the latitudinal and solar-cycle variations of the model parameters into account. Moreover, these effects need to be considered simultaneously (e.g. Bzowski et al., 2002; Pryor et al., 2003; Quémerais et al., 2006). Despite the fact that advanced models require numerical solution because of their complexity, the method of characteristics still reduces partial differential kinetic equations for the velocity distribution function to a set of ordinary differential equations. The solution of the latter equations is then straightforward.

At the present time, there is no doubt that the interstellar H atoms are both disturbed in the region of the heliospheric interface and influence the plasma distribution in this region by charge exchange. Therefore, any adequate modern model for the interstellar H atoms in the heliosphere should include the interaction of the neutral and plasma components self-consistently. Such self-consistent models are developed and reviewed in Chapter 4 (Izmodenov and Baranov, 2006) of this book. Despite their complexity, further employing and developing the modern versions of the hot model seems to be useful in the future for at least two reasons:

1. Interstellar helium penetrates through the heliospheric interface without being disturbed. Therefore, the advanced hot models are perfectly suited to studying the properties of the interstellar helium within the heliosphere. Such studies that allowed one to determine the local velocity and temperature of interstellar helium in the circumsolar interstellar medium were performed in the framework of the ISSI team "Physical parameters of LISM through coordinated observations of the Gravitational focussing cone at 1 AU" coordinated by E. Möbius. The results of this study are published in Möbius et al. (2004) and references therein.

2. Comparison of the results of the hot model (classical or improved by including an additional effect) with the results of a model that includes the heliospheric interface allows one to discriminate the imprints of the heliospheric interface from the local effects. This potentially helps to discover the heliospheric interface imprints in observational data (as Lyman-α maps or spectra, pickup ion spectra, etc.)

Acknowledgements

I thank Jean-Loup Bertaux and Mike Gruntman for reading of the manuscript and for very fruitful comments and suggestions. I also thank Reinald Kallenbach for editing the manuscript and for improving the English. This work was supported in part by INTAS Award 2001-0270, RFBR grants 04-02-16559, 05-02-22000(PICS), and the International

Space Science Institute in Bern. The author was also supported by the "Dynastia Foundation" and by the "Foundation in Support of Homeland Science".

Bibliography

Ajello, J.M., Stewart, A.I., Thomas, G.E., and Graps, A.: 1987, 'Solar cycle study of interplanetary Lyman-alpha variations – Pioneer Venus Orbiter sky background results', *Astrophys. J.* **317**, 964–986.

Axford, W.I., Dessler, A.J., and Gottlieb, B.: 1963, 'Termination of solar wind and solar magnetic field', *Astrophys. J.* **137**, 1268–1278.

Axford, W.I.: 1972, 'The interaction of the solar wind with the interstellar medium', in C.P. Sonett, P.J. Coleman, and J.M. Wilcox (eds.), *Solar Wind*, Scientific and Technical Information Office, National Aeronautics and Space Administration., Washington, p. 598.

Baranov, V.S.: 2006, Chapter 2, this volume.

Barth, C.A.: 1970, 'Mariner 6 measurements of the Lyman-α sky background', *Astrophys. J.* **161**, L181–L184.

Bertaux, J.L., and Blamont, J.E.: 1971, 'Evidence for a source of an extraterrestrial hydrogen Lyman-α emission: the interstellar wind', *Astron. Astrophys.* **11**, 200.

Bertaux J.L., Ammar, A., and Blamont, J.E.: 1972, 'OGO-5 determination of the local interstellar wind parameters', *Space Res.* **XII**, 1559–1567.

Bertaux, J.L., Blamont, J.E., Tabarie, N., Kurt, W.G., Bourgin, M.C., Smirnov, A.S., Dementeva, N.N.: 1976, 'Interstellar medium in the vicinity of the sun – a temperature measurement obtained with the Mars-7 interplanetary probe', *Astron. Astrophys.* **46**, 19–29.

Bertaux, J.L., Blamont, J.E., Mironova, E.N., Kurt, V.G., Bourgin, M.C. : 1977, 'Temperature measurement of interplanetary interstellar hydrogen', Nature, 270, 156–158.

Bertaux, J.L., and Lallement, R.: 1984, 'Analysis of interplanetary Lyman-α line profile with a hydrogen absorption cell – theory of the Doppler angular spectral scanning method', *Astron. Astrophys.* **140** 230–242.

Bertaux, J.L., Quémerais, E., Lallement, R., Kyrölä, E., Schmidt, W., Summanen, T., Goutail, J.P., Berthé, M., Costa, J., Holzer, T.: 1997, 'First results from the SWAN Lyman-α solar wind mapper on SOHO', *Sol. Phys.* **175**, 737–770.

Bertaux, J.-L., Kyrölä, E., Quémerais, E., Lallement, R., Schmidt, W., Summanen, T.. Costa, J., and Makinen, T.: 1999, 'SWAN observations of the solar wind latitude distribution and its evolution since launch', *Space Sci. Rev.* **87**, 129–132.

Blum, P.W., Fahr, H.J.: 1970, 'Interaction between interstellar hydrogen and the solar wind', *Astron. Astrophys.* **4**, 280–290.

Blum, P.W., Pfleiderer, J., and Wulf-Mathies, C.: 1975, 'Neutral gases of interstellar origin in interplanetary space', *Planet. Space Sci.* **23**, 93–105.

Blum, P., Gangopadhyay, P., Ogawa, H.S., and Judge, D.L.: 1993, 'Solar-driven neutral density waves', *Astron. Astrophys.* **272**, 549–554.

Bzowski, M., and Rucinski, D.: 1995, 'Solar cycle modulation of the interstellar hydrogen density distribution in the heliosphere', *Space Sci. Rev.* **72**, 467–470.

Bzowski, M., Fahr, H.J., Rucinski, D., and Scherer, H.: 1997, 'Variation of bulk velocity and temperature anisotropy of neutral heliospheric hydrogen during the solar cycle', *Astron. Astrophys.* **326**, 396–411.

Bzowski, M., Summanen, T., Rucinski, D., Kyrölä, E.: 2002, 'Response of interplanetary glow to global variations of hydrogen ionization rate and solar Lyman-α flux', *J. Geophys. Res.* **107**, SSH 2-1, CiteID 1101, DOI 10.1029/2001JA000141.

Dalaudier, F., Bertaux, J.L., Kurt, V.G., and Mironova, E.N.: 1984, 'Characteristics of interstellar helium observed with Prognoz 6 58.4 nm photometers', *Astron. Astrophys.* **134**, 171–184.

Danby, J.M.A., and Camm, G.L.: 1957, *Monthly Notices of the Royal Astron. Soc.* **117**, 50–71.

Fahr, H.J.: 1968a, 'On the influence of the neutral interstellar matter on the upper atmosphere', *Astrophys. Space Sci.* **2**, 474–495.

Fahr, H.J.: 1968b, 'Neutral corpuscular energy flux by charge transfer collisions in the vicinity of the Sun', *Astrophys. Space Sci.* **2**, 496–503.

Fahr H.J.: 1971, 'The interplanetary hydrogen cone and its solar cycle variations', *Astron. Astrophys.* **14**, 263–274.

Fahr, H.J.: 1974, 'The extraterrestrial UV-background and the nearby interstellar medium', *Space Sci. Rev.* **15**, 483–540.

Fahr, H.J.: 1978, 'Change of interstellar gas parameters in stellar-wind-dominated astrospheres: the solar case', *Astron. Astrophys.* **66**, 103–117.

Feldman, W.C., Lange, J.J., and Scherb, F.: 1972, 'Interstellar helium in interplanetary space', in C.P. Sonett, P.J. Coleman, and J.M. Wilcox (eds.), *Solar Wind*, Scientific and Technical Information Office, National Aeronautics and Space Administration., Washington, p. 668.

Gruntman, M., Roelof, E.C., Mitchell, D.G., Fahr, H.J., Funsten, H.O., and McComas, D.J.: 2001, 'Energetic neutral atom imaging of the heliospheric boundary region', *J. Geophys. Res.* **106**, 15'767–15'782.

Hundhausen, A.J.: 1968, 'Interplanetary neutral hydrogen and the radius of the heliosphere', *Planet. Space Sci.* **16**, 783–793.

Joselyn, J.A., Holzer, T.E.: 1975, 'The effect of asymmetric solar wind on the Lyman-α sky background', *J. Geophys. Res.* **80**, 903–907.

Izmodenov, V.V., Baranov, V.B.: 2006, this volume.

Kolesnikov, I.V.: 2006, *The method to find the velocity distribution function in the heliosphere*, Term paper, Moscow State University, 2006.

Kumar, S., and Broadfoot, A.L.: 1978, 'Evidence from Mariner 10 of solar wind flux depletion at high ecliptic latitudes', *Astron. Astrophys.* **69**, L5–L8.

Kumar, S., and Broadfoot, A.L.: 1979, 'Signatures of solar wind latitudinal structure in interplanetary Lyman-α emissions – Mariner 10 observations', *Astrophys. J.* **228**, 302–311.

Kurt, V.G.: 1965, 'Measurement of scattered Lyman-α radiation in the vicinity of the Earth and in interplanetary space', Space Research: Transactions of the All-union Conference on Space Physics. NASA Technical Translation – NASA TT F-389. Edited by G. A. Skuridin, et al.. Science Publishing House, Moscow, June 10-16, 1965. Translation published by NASA, Washington DC, USA, May 1966, p. 769.

Kurt, V.: 1967, *Kosmicheskie Issledovania* (in russian), **5(6)**.

Kurt, V.G., and Germogenova, T.A.: 1967, 'Scattering of solar Lyman-α radiation by galactic hydrogen', *Soviet Astronomy* **11**, 278–282.

Kurt, V.G., and Syunyaev, R.A.: 1967, 'Observations and interpretation of the ultraviolet radiation of the Galaxy', *Soviet Astronomy* **11**, 928–931.

Kupperian, J.E., Byram, E.T., Chubb, T.A., and, Friedman, H.: 1959, 'Far ultraviolet radiation in the night sky', *Planet. Space Sci.* **1**, 3–6.

Kyrölä, Summanen, T., and Raback, P.: 1994, 'Solar cycle and interplanetary hydrogen', *Astron. Astrophys.* **288**, 299–314.

Lallement, R., Bertaux, J.L., Kurt, V.G., and Mironova, E.N. : 1984, 'Observed perturbations of the velocity distribution of interstellar H atoms in the solar system with Prognoz Lyman a measurements', *Astron. Astrophys.* **140**, 243–250.

Lallement, R., Bertaux, J.L., and Dalaudier, F.: 1985a, 'Interplanetary Lyman-α spectral profiles and intensities for both repulsive and attractive solar force fields predicted absorption pattern by a hydrogen cell', *Astron. Astrophys.* **150**, 21–32.

Lallement, R., Bertaux, J.L., and Kurt, V.G.: 1985b, 'Solar wind decrease at high heliographic latitudes detected from Prognoz interplanetary Lyman-α mapping', *J. Geophys. Res.* **90**, 1413–1423.

Lallement, R., and Stewart, A.I.: 1990, 'Out-of-ecliptic Lyman-α observations with Pioneer-Venus – solar wind anisotropy degree in 1986', *Astron. Astrophys.* **227**, 600–608.

Lallement, R.: 2001, 'The interaction of the heliosphere with interstellar medium', in A.M.Bleeker, J. Geiss, and M.C.E. Huber (eds.), *The Century of Space Science*, Kluwer, 1191–1216.

Lallement, R., Quémerais, E., Bertaux, J.L., Ferron, S., Koutroumpa, D., and Pellinen, R.: 2005, 'Deflection of the interstellar neutral hydrogen flow across the heliospheric interface', *Science* **307**, 1447–1449.

Meier, R.R.: 1977, 'Some optical and kinetic properties of the nearby interstellar gas', *Astron. Astrophys.* **55**, 211–219.

Morton, D.C., and Purcell, J.D.: 1962, 'Observations of the extreme ultraviolet radiation in the night sky using an atomic hydrogen filter', *Planet. Space Sci.* **9**, 455–458.

Möbius, E., Bzowski, M., Chalov, S., Fahr, H.-J., Gloeckler, G., Izmodenov, V., Kallenbach, R., Lallement, R., et al.: 2004, 'Synopsis of the interstellar He parameters from combined neutral gas, pickup ion and UV scattering observations and related consequences', *Astron. Astrophys.* **426**, 897–907.

Patterson, T.N.L., Johnson, F.S., and Hanson, W.B.: 1963, 'The distribution of interplanetary hydrogen', *Planet. Space Sci.* **11**, 767–778.

Prokudina , V.S.: 1958, *Astronomich. Zhurnal* **35**, in russian.

Pryor, W.R., Ajello, J.M.; McComas, D.J., Witte, M., and Tobiska, W.K.: 2003, 'Hydrogen atom lifetimes in the three-dimensional heliosphere over the solar cycle', *J. Geophys. Res.* **108**, LIS 9-1, CiteID 8034, DOI 10.1029/2003JA009878.

Shklovsky, I.S.: 1959, 'On hydrogen emission in the night glow', *Planet. Space Sci.* **1**, 63–65.

Thomas, G.E., and Krassa, R.F.: 1971, 'OGO-5 measurements of the Lyman-α sky background', *Astron. Astrophys.* **11**, 218.

Thomas, G.E.: 1972, 'Properties of nearby interstellar hydrogen deduced from Lyman-α sky background measurements', in C.P. Sonett, P.J. Coleman, and J.M.

Wilcox (eds.), *Solar Wind*, Scientific and Technical Information Office, National Aeronautics and Space Administration., Washington, p. 661.

Quémerais, E., Lallement, R., Bertaux, J.-L., Koutroumpa, D., Clarke, J., Kyrölä, E., and Schmidt, W.: 2006, 'Interplanetary Lyman-α profiles: variations during solar activity cycle',Astron. Astrophys. 455, 1135-1142, 2006.

Rucinski, D., and Bzowski, M.: 1995, 'Modulation of interplanetary hydrogen density distribution during the solar cycle', *Astron. Astrophys.* **296**, 248–263.

Rucinski, D., and Bzowski, M.: 1996, 'Modelling of the interstellar hydrogen distribution in the heliosphere', *Space Sci. Rev.* **78**, 265–276.

Strömgren, B.: 1939, 'The physical state of interstellar hydrogen', *Astrophys. J.* **89**, 526–547.

Summanen, T., Lallement, R., Bertaux, J. L., and Kyrola, E.: 1993, 'Latitudinal distribution of solar wind as deduced from Lyman-α measurements – an improved method', *J. Geophys. Res.* **98**, 13,215–13,224.

Summanen, T.: 1996, 'The effect of the time and latitude-dependent solar ionisation rate on the measured Lyman α-intensity', *Astron. Astrophys.* **314**, 663–671.

Witt, N., Blum, P.W., and Ajello, J.M.: 1979, 'Solar wind latitudinal variations deduced from Mariner 10 interplanetary H /1216 A/ observations', *Astron. Astrophys.* **73**, 272–281.

Witt, N., Blum, P.W., and Ajello, J.M.: 1981, 'Polar solar wind and interstellar wind properties from interplanetary Lyman-α radiation measurements', *Astron. Astrophys.* **95**, 80–85.

Wu, F.M., and Judge, D.L.: 1979, 'Temperature and flow velocity of the interplanetary gases along solar radii', *Astrophys. J.* **231**, 594–605.

— 4 —

Modern Multi-component Models of the Heliospheric Interface

Vladislav V. Izmodenov[1]
Lomonosov Moscow State University,
School of Mechanics and Mathematics, Department of Aeromechanics;
Institute for Problems in Mechanics, Russian Academy of Sciences;
Space Research Institute, Russian Academy of Sciences

Vladimir B. Baranov
Lomonosov Moscow State University,
School of Mechanics and Mathematics, Department of Aeromechanics;
Institute for Problems in Mechanics, Russian Academy of Sciences

Abstract. **At the present time there is no doubt that the Sun is moving through a warm (∼6500 K) and partly ionized local interstellar cloud (LIC) with a velocity of ∼26 km/s. The charged component of the interstellar medium interacts with the solar wind (SW), forming the heliospheric interface. Following the discussion of the first pioneering models of the SW/LIC interaction region in Chapters 2 and 3 of this volume, this Chapter reviews the current state of the art in modelling the heliospheric interface. Both the solar wind and interstellar gases have a multi-component nature that creates a complex behaviour of the interaction region. Modern models of the interface take into account the solar wind and the interstellar plasma components (protons, electrons, pickup ions, interstellar helium ions, and solar wind alpha particles), the interstellar neutral component (H atoms), interstellar and heliospheric magnetic fields, galactic and anomalous cosmic rays, and latitudinal and solar cycle variations of the solar wind. The predictions of self-consistent, time-dependent, and kinetic/gas-dynamic models of the heliospheric interface are confirmed by available experimental data from remote diagnostic and in-situ spacecraft measurements of backscattered solar Lyman-α radiation, the heliospheric absorption of stellar light, the flux of anomalous cosmic rays (ACRs), heliospheric neutral atoms (ENAs) and pickup ions, and of the deceleration of the solar wind at large heliocentric distances by the Voyager 1/2 and Pioneer 10/11 spacecraft investigating the outer regions of the Solar System.**

[1]in *The Physics of the Heliospheric Boundaries*, V. Izmodenov and R. Kallenbach (eds.), ISSI Scientific Report No. 5, pp. 67–135, ESA-ESTEC, Paris 2006

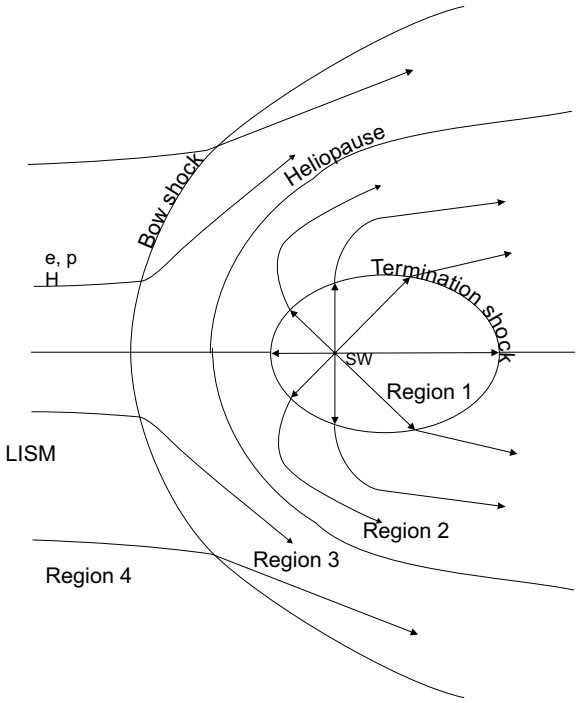

Figure 4.1: Qualitative picture of the solar wind (SW) interaction with the local interstellar cloud (LIC). The *heliopause* (HP) is a contact (or tangential) discontinuity, which separates the solar wind plasma and the interstellar plasma component. The *termination shock* (TS) is formed due to the deceleration of the supersonic solar wind. The *bow shock* (BS) may also exist if the interstellar plasma flow is supersonic. Four regions are distinguished: the supersonic solar wind (region 1); the solar wind flow between the TS and the HP (region 2 or the *inner heliosheath*); the disturbed interstellar plasma component flow (region 3 or the *outer heliosheath*); and the undisturbed interstellar gas flow (region 4).

4.1 Introduction

The structure of the outer heliosphere and the heliospheric boundary is determined by the interaction of the solar wind with the interstellar neighbourhood of the Sun – the Local Interstellar Cloud (LIC). There is no doubt that the LIC is partly ionized due to ultraviolet light from nearby stars and that the interaction of the charged component of the LIC with the solar wind plasma gives rise to the formation of the interaction region, which is often called the *heliospheric interface* or *heliosheath* (Figure 4.1). The heliospheric interface has a complex structure, where the solar wind and interstellar plasma, interplanetary and interstellar magnetic fields, interstellar atoms of hydrogen, galactic and anomalous cosmic rays (GCRs and ACRs) and pickup ions play important roles.

Although a space mission into the Local Interstellar Cloud may now become feasible, and despite the fact that Voyager 1 has recently crossed the inner boundary of the heliospheric interface (the termination shock), there are as yet no direct observations of the plasma and the H atoms inside the heliosheath. Therefore, at the present time the heliospheric interface structure and local interstellar parameters can only be explored with remote and indirect measurements.

To reconstruct the structure and the physical processes inside the interface using remote observations a theoretical model should be employed. Theoretical studies of the heliospheric interface have been performed for more than four decades, following the pioneering work by Parker (1961) and Baranov et al. (1971) as described in Chapter 2 of this volume. However, a complete theoretical model of the heliospheric interface has not yet been constructed. The basic difficulty is connected with the multi-component nature of both the LIC and the solar wind. The LIC consists of at least four main components: plasma (electrons and protons), hydrogen atoms, interstellar magnetic field and galactic cosmic rays. The heliospheric plasma consists of particles of solar origin (protons, electrons, alpha particles, etc.), pickup ions and energetic particle components that include, for example, the termination shock particles (TSP) (Stone et al., 2005; Decker et al., 2005; Burlaga et al. 2005) and the anomalous cosmic ray component (ACR). Pickup protons (or ions) are created by processes of charge exchange and photoionization, and then picked up by the magnetic field. The pickup protons modify the heliospheric plasma flow starting from ∼20-30 AU. TSPs and ACRs may also modify the plasma flow upstream of the termination shock and in the heliosheath (e.g. Chapter 8 in this volume).

The development of a theoretical model of the heliospheric interface requires the correct approach for each of the interstellar and solar wind components. Interstellar and solar wind protons and electrons can be described as fluids (see Chapter 1). However, the mean free path of interstellar H atoms is comparable with the size of the heliospheric interface. This requires a kinetic description for the interstellar H atom flow in the interaction region. For the pickup ion and cosmic ray components the kinetic approach is required as well.

This chapter focuses on theoretical numerical models of the global heliospheric interface structure. The term 'global' refers to models that describe the entire interaction region, including the termination shock, the heliopause and the possible bow shock. This chapter, however, should not be considered as a complete review of progress in the field. It is beyond the scope of this article to cite and discuss all papers having contributed to the field. We restrict ourselves to the papers that are necessary to describe the most important physical phenomena in the interface region. The structure of the chapter is the following: the next section briefly describes our current knowledge of the local interstellar and solar wind parameters from the point of view of a theorist. Section 4.3 describes the first self-consistent model of the SW/LIC interaction by Baranov and Malama (1993) and results obtained in the frame of this model. Sections 4.4 - 4.8 describe the approaches and results of the more recent models of the heliospheric interface that include effects of the interstellar helium and solar wind alpha particle components (Section 4.4), effects of the ACR and GCR components (Section 4.5), effects of the interstellar magnetic field (Section 4.6), and effects of the solar cycle variations of the solar wind (Section 4.7). The specific study of the structure of the heliotail – the tail

region of the SW/LIC interaction – is summarized in Section 4.8. The most recent advancement in theories on the heliospheric interface is the model that includes the multi-component behaviour of the charged component of the solar wind (Section 4.9). Section 4.10 reviews the predictions and interpretations of spacecraft experiments made in the frame of the Baranov-Malama model of the heliospheric interface and its subsequent advancements. Section 4.11 summarizes the Chapter.

4.2 Brief summary of observational knowledge

Choice of an adequate theoretical model of the heliospheric interface depends on the undisturbed solar wind and interstellar properties. That is why in this section we briefly review our current knowledge of the local (circumsolar) interstellar and the solar wind parameters from the point of view of a theorist.

4.2.1 Solar wind observations

At Earth's orbit the flux of interstellar atoms is quite small (due to losses via the processes of photoionization and charge exchange with protons) and the solar wind at 1 AU can be considered as undisturbed. Measurements of pickup ions and ACRs also show that these components have no dynamical influence on the original solar wind flow near Earth's orbit. Therefore, the Earth's orbit can be taken as an inner boundary in a model of the SW/LIC interaction.

The solar wind structure and behaviour evolve over the solar cycle (e.g. Gazis, 1996; Neugebauer 1999; McComas et al. 2000, 2001, 2002, 2006a). At solar minimum, high-latitude regions on the Sun have well-developed coronal holes, which are sources of high-speed ($\sim$700 km/s), low-density solar wind. At low heliolatitudes the solar wind has low speed ($\sim$400 km/s) and high density. The dividing line between the fast and slow solar wind regimes is at about 20° heliolatitude. At solar maximum the slow and dense solar wind is present at all latitudes (McComas et al., 2002). Shortly after the solar maximum, well-developed large coronal holes and, therefore, the typical high-speed solar wind streams appear again. At this stage, both coronal holes and the high-speed solar wind may appear even near the ecliptic, which results in an increased average solar wind momentum flux at low latitudes shortly after solar maxima. Spacecraft near the ecliptic at 1 AU have detected variations in the solar wind momentum flux by a factor of two (Lazarus and McNutt, 1990; Gazis, 1996). Deep space probe data obtained with Pioneer and Voyager measurements in the distant solar wind also support this conclusion (Lazarus and McNutt, 1990; Gazis, 1996). A recent update of the Voyager 2 measurements of the solar wind can be found in Richardson et al. (2005; 2006). Apparently, over the past two solar cycles the momentum flux had a minimum value at solar maximum and then a rapid increase after solar maximum reaching a peak 1-2 years later. The flux subsequently decreased until after the next solar maximum. It was unclear from the measurements in the ecliptic plane whether the variations in the momentum flux are a global effect or whether they are limited to the ecliptic. Ulysses observations from its first full polar orbit revealed that the momentum flux is diminished near the equator compared to higher latitudes. The effect is clearly

Table 4.1: Number densities, and thermal and dynamic pressures of different solar wind components

	4-5 AU		80 AU	
Component	Density $[\mathrm{cm}^{-3}]$	Pressure $[\mathrm{eV\,cm}^{-3}]$	Density $[\mathrm{cm}^{-3}]$	Pressure $[\mathrm{eV\,cm}^{-3}]$
Original solar wind protons	0.2-0.4	2.-4. (th.) ~ 200 (dyn.)	$(7-14)\cdot 10^{-4}$	10^{-3} - 10^{-4} $\sim 0.5-1.0$ (dyn.)
Pickup ions	$5.1\cdot 10^{-4}$	0.5	$\sim 2\cdot 10^{-4}$	~ 0.15
Anomalous cosmic rays				0.01 - 0.1

evident in the period near solar minimum (May 1995 – December 1997) (McComas et al., 2000). Around solar maximum the three-dimensional structure of the solar wind is remarkably different from, and more complicated than, the simple, bimodal structure observed throughout much of the rest of the solar cycle. At solar maximum, the solar wind has the same properties at all latitudes (McComas et al., 2001; 2002).

Theoretical models predict that the pickup ion and energetic particle (as ACRs) components dynamically influence the solar wind at large heliocentric distances (Fichtner, 2001; Chalov, 2006). Table 4.1 presents estimates of the dynamic importance of the heliospheric plasma components at small and large heliocentric distances. The table shows that the pickup ion thermal pressure can be up to 30-50% of the dynamic pressure of the solar wind.

4.2.2 Interstellar parameters

The local interstellar temperature and velocity can be inferred from direct measurements of interstellar helium atoms by the Ulysses/GAS instrument (Witte et al., 1996; Witte, 2004). Atoms of interstellar helium penetrate the heliospheric interface undisturbed, because of the small strength of their coupling with interstellar and solar wind protons. Indeed, due to the small cross sections of elastic collisions and charge exchange with protons, the mean free path of these atoms is much larger than the size of the heliospheric interface. Independently, the velocity and temperature in the LIC can be deduced from the analysis of absorption features in stellar spectra (Lallement, 1996; see, also, review by Lallement, 2001). However, this method provides only mean values along lines of sight toward nearby stars in the LIC. A comparison of local interstellar temperatures and velocities derived from stellar absorption with those derived from direct measurements of interstellar helium, however, show quite good agreement (see Table 4.2).

Other local parameters of the interstellar medium, such as interstellar H atom and electron number densities are not well known. In the models they can be

Table 4.2: Local Interstellar Parameters

Parameter	Direct measurements/estimations
Sun/LIC relative velocity	26.3 ± 0.4 km s^{-1} (direct He atoms [1]) 25.7 km s^{-1} (Doppler-shifted absorption lines [2])
Local interstellar temperature	6300 ± 340 K (direct He atoms [1]) 6700 K (absorption lines [2])
LIC H atom number density	0.2 ± 0.05 cm^{-3} (estimate based on pickup ion observations [3])
LIC proton number density	0.03 - 0.1 cm^{-3} (estimate based on pickup ion observations [3])
Local interstellar magnetic field	Magnitude: 2-4 μG Direction: unknown
Pressure of low-energetic cosmic rays	$\sim$0.2 eV cm^{-3}

[1] Witte (2004), Möbius et al. (2004); [2] Lallement(1996);
[3] Gloeckler (1996), Gloeckler et al. (1997), Geiss et al. (2006).

considered as free parameters. However, indirect measurements of interstellar H atoms and direct measurements of their derivatives such as pickup ions and ACRs provide important constraints on the local interstellar proton and atom densities and total interstellar pressure. The number density of the interstellar H atoms in the inner heliosphere depends on the filtration strength of hydrogen atoms in the heliospheric interface due to charge exchange. Since interstellar helium atoms are not perturbed in the interface, the local interstellar number density of H atoms can be estimated from the neutral hydrogen to neutral helium ratio in the LIC, $R(\mathrm{H\,I/He\,I})_{\mathrm{LIC}}$: $n_{\mathrm{LIC}}(\mathrm{H\,I}) = R(\mathrm{H\,I/He\,I})_{\mathrm{LIC}}\, n_{\mathrm{LIC}}(\mathrm{He\,I})$. The He - atom number density in the heliosphere has been recently determined to be very likely around 0.015 ± 0.002 cm^{-3} (Gloeckler and Geiss, 2001; see, also Witte, 2004; Gloeckler et al., 2004; Lallement et al., 2004a,b; Möbius et al., 2004; Vallerga et al., 2004). The interstellar HI/HeI ratio is likely to be in the range of 10-14. Therefore, expected interstellar H atom number densities are in the range of $0.13 - 0.25$ cm^{-3}. It was shown by modelling (Baranov and Malama, 1995; Izmodenov et al.,1999a) that the filtration factor, which is the ratio of neutral H density inside and outside the heliosphere, is a function of the interstellar plasma number density. Therefore, the number density of interstellar protons (electrons) can be estimated from this filtration factor (Lallement, 1996). Independently, the electron number density in the LIC can be estimated from abundance ratios of ions in different ionization states (Lallement, 1996).

Note also that there are other methods to estimate the interstellar H atom number density inside the heliosphere. They are based on the effect of the interstellar H atoms on the distant solar wind (Richardson, 2001; Richardson et al., 2007) or on the analysis of the ACR spectra (Stone, 2001). Data from the recent crossing

Table 4.3: Local Pressures of Interstellar Components

Component	Pressure estimation, dyn cm^{-2}
Interstellar plasma component	
Thermal pressure	$(0.6 - 2.0) \cdot 10^{-13}$
Dynamic pressure	$(1.5 - 6) \cdot 10^{-13}$
H atoms	
Thermal pressure	$(0.6 - 2.0) \cdot 10^{-13}$
Dynamic pressure	$(4.0 - 9.0) \cdot 10^{-13}$
Interstellar magnetic field	$(1.0 - 5.0) \cdot 10^{-13}$
Low-energy part of GCR	$(1.0 - 5.0) \cdot 10^{-13}$

of the heliospheric termination shock at 94 AU by the Voyager 1 spacecraft on 16 December 2004 (Stone et al., 2005) also provides strict constraints on the local interstellar parameters. However, a simultaneous analysis of different types of observational constraints has not yet been carried out. Theoretical models should be employed to accomplish such an analysis. Table 4.2 presents a summary of our knowledge of local interstellar parameters. It should be noted here that there are no direct experimental data concerning the strength and direction of the interstellar magnetic field in the vicinity of the heliosphere. The magnitude of the interstellar magnetic field presented in Table 4.2 is based on estimations (e.g. Gloeckler et al., 1997).

Using the values of the local interstellar parameters from Table 4.2, local pressures of different interstellar components are estimated in Table 4.3. As we see from this Table, pressures of all components can have the same order of magnitude. This means that theoretical models should not neglect any of these interstellar components although their effect on the heliospheric interface can be different as we will see below.

4.3 Self-consistent two-component model of the heliospheric interface

The first self-consistent stationary model of the interaction of the two-component (plasma and H atoms) LIC with the solar wind had been developed by Baranov and Malama (1993). The interstellar wind was assumed to be a uniform parallel supersonic flow, and the solar wind was assumed to be spherically symmetric at Earth's orbit. Under these assumptions, the heliospheric interface has an axisymmetric structure. The main physical process of this interaction is resonance charge exchange (H atoms with protons) although the processes of photoionization

and ionization of H-atoms by electron impact can be important in some regions of the heliosphere (for example, in the inner heliosheath or in the supersonic solar wind). The significant effect of the resonance charge exchange is connected with the large cross section of such collisions (see Chapter 1), which is a function of the relative velocity of colliding particles. However, it was discussed by some authors (Williams et al., 1997) that elastic H - H and H - proton collisions can be important in the problem of the solar wind interaction with the local interstellar medium. This specific question had been discussed in detail by Izmodenov et al. (2000), and it was shown that the elastic collisions are negligible.

The hydrodynamical equations of the one-fluid approximation (see Chapter 1) were used for describing the solar wind interaction with the plasma component of the local interstellar cloud. The equations are

$$\nabla \cdot \rho \mathbf{V} = 0, \tag{4.1}$$

$$\rho \mathbf{V} \cdot \nabla \mathbf{V} + \nabla p = \mathbf{q}_2 \tag{4.2}$$

$$\nabla \cdot \left[\rho \mathbf{V} \left(\varepsilon + \frac{p}{\rho} + \frac{\mathrm{V}^2}{2} \right) \right] = q_3 \tag{4.3}$$

$$\varepsilon = \frac{p}{(\gamma - 1)\rho}. \tag{4.4}$$

Here, as in Chapter 1, ρ ,$\mathbf{V}$ and p are mass density, vector of bulk velocity and static pressure, respectively; $\gamma = 5/3$. The right-hand sides ("source terms") of these equations determine changes of momentum and energy of the plasma component due to charge exchange of H-atoms with protons. The effects of photoionization and electron impact ionization were later included in the model (Baranov and Malama, 1996). Contrary to the early model by Baranov et al. (1981), which assumed constant H-atom temperature and bulk velocity (see Chapter 2), and the "source terms" to be in the form obtained by Holzer and Banks (1969) under the assumption of Maxwellian distribution functions of colliding particles, the kinetic approach for H-atoms allows one to calculate the source terms exactly without making any additional assumptions. The following formulae were used by Baranov and Malama (1993) to calculate $\mathbf{q}_2$ and q_3 and to take into account the charge exchange process only:

$$\mathbf{q}_2 = m_{\mathrm{H}} \int \mathrm{d}\mathbf{w}_{\mathrm{H}} \int \mathrm{d}\mathbf{w}_{\mathrm{p}} \sigma_{\mathrm{ex}}^{\mathrm{HP}} \left| \mathbf{w}_{\mathrm{H}} - \mathbf{w}_{\mathrm{p}} \right| \left(\mathbf{w}_{\mathrm{H}} - \mathbf{w}_{\mathrm{p}} \right) f_{\mathrm{H}} \left(\mathbf{r}, \mathbf{w}_{\mathrm{H}} \right) f_{\mathrm{p}} \left(\mathbf{r}, \mathbf{w}_{\mathrm{p}} \right), \tag{4.5}$$

$$q_3 = m_{\mathrm{H}} \int \mathrm{d}\mathbf{w}_{\mathrm{H}} \int \mathrm{d}\mathbf{w}_{\mathrm{p}} \sigma_{\mathrm{ex}}^{\mathrm{HP}} \left| \mathbf{w}_{\mathrm{H}} - \mathbf{w}_{\mathrm{p}} \right| \left(\frac{w_{\mathrm{H}}^2}{2} - \frac{w_{\mathrm{p}}^2}{2} \right) f_{\mathrm{H}} \left(\mathbf{r}, \mathbf{w}_{\mathrm{H}} \right) f_{\mathrm{p}} \left(\mathbf{r}, \mathbf{w}_{\mathrm{p}} \right), \tag{4.6}$$

$$n_{\mathrm{H}} = \int \mathrm{d}\mathbf{w}_{\mathrm{H}} f_{\mathrm{H}} \left(\mathbf{r}, \mathbf{w}_{\mathrm{H}} \right), \; n_{\mathrm{p}} = \int \mathrm{d}\mathbf{w}_{\mathrm{p}} f_{\mathrm{p}} \left(\mathbf{r}, \mathbf{w}_{\mathrm{p}} \right), \tag{4.7}$$

where f_{H} is the distribution function of H atoms (see Chapter 1), $\mathbf{w}_{\mathrm{H}}$ and $\mathbf{w}_{\mathrm{p}}$ are velocity vectors of individual particles of H atoms and protons, $\sigma_{\mathrm{ex}}^{\mathrm{HP}}$ is the effective cross section of collisions connected with charge exchange, and $\mathbf{r}$ is the radius-vector.

The hydrodynamic approach is not valid to describe the H-atom flow in the heliospheric interface because $l_{ex} \sim L$, where l_{ex} is the mean free path of H atoms with respect to the charge exchange collisions, and L is a characteristic length of the problem considered (for example, the heliocentric distance to the heliopause). In this case the distribution function of the H atoms cannot be supported by collisions to get the Maxwellian form. That is why the kinetic approach was used by Baranov and Malama (1993) for the calculation of f_H and the formulae (4.5) - (4.6) are used to calculate the source terms. In the model considered the Boltzmann equation for f_H has the following form:

$$\mathbf{w}_H \cdot \frac{\partial f_H}{\partial \mathbf{r}} + \frac{\mathbf{F}_r + \mathbf{F}_g}{m_H} \cdot \frac{\partial f_H}{\partial \mathbf{w}_H} =$$
$$f_p(\mathbf{r}, \mathbf{w}_H) \int \mid \mathbf{w}'_H - \mathbf{w}_H \mid \sigma_{ex}^{HP} f_H(\mathbf{r}, \mathbf{w}'_H)\, d\mathbf{w}'_H \tag{4.8}$$
$$-f_H(\mathbf{r}, \mathbf{w}_H) \int \mid \mathbf{w}_H - \mathbf{w}_p \mid \sigma_{ex}^{HP} f_p(\mathbf{r}, \mathbf{w}_p)\, d\mathbf{w}_p.$$

Here, $\mathbf{F}_r$ and $\mathbf{F}_g$ are the force of the solar radiation pressure and the gravitational force of the Sun, respectively; $f_p(\mathbf{r}, \mathbf{w}_H)$ is the local Maxwellian distribution function of protons with gas dynamic values $\rho(\mathbf{r})$, $\mathbf{V}(\mathbf{r})$ and $p(\mathbf{r})$ (see Chapter 1).

The kinetic equation (4.8) for neutrals was solved together with the Euler equations for the plasma component (4.1) - (4.4). The "source terms" are calculated directly by a highly efficient Monte Carlo method with splitting of trajectories (Malama, 1991) without calculating the distribution function f_H. The set of kinetic and Euler equations is solved by an iterative procedure, as suggested in Baranov et al. (1991). Supersonic boundary conditions were used for the unperturbed interstellar plasma and for the solar wind plasma near Earth's orbit. The distribution function of interstellar H atoms is assumed to be Maxwellian in the unperturbed LIC. The results of this model are discussed below.

4.3.1 Plasma

Interstellar atoms strongly influence the heliospheric interface structure. The heliospheric interface is much closer to the Sun when H atoms are taken into account in the model, compared to a pure gas dynamical case (Figure 4.2). The termination shock becomes more spherical and the flow in the region between HP and TS becomes subsonic (sonic lines disappear). The Mach disk and the complicated tail shock structure, consisting of the reflected shock (RS) and the tangential discontinuity (TD), disappear.

The supersonic plasma flows upstream of the bow and termination shocks are disturbed. The supersonic solar wind flow (region 1 in Figure 4.1) is disturbed by charge exchange with the interstellar neutrals. The new protons created by charge exchange are picked up by the solar wind magnetic field. The Baranov-Malama model assumes immediate assimilation of pickup ions into the solar wind plasma. The solar wind protons and pickup protons are treated as one fluid, called the solar wind. The number density, velocity, temperature, and Mach number of the solar wind are shown in Figure 4.3A. The effect of charge exchange on the solar wind is significant. By the time the solar wind flow reaches the termination shock, it is

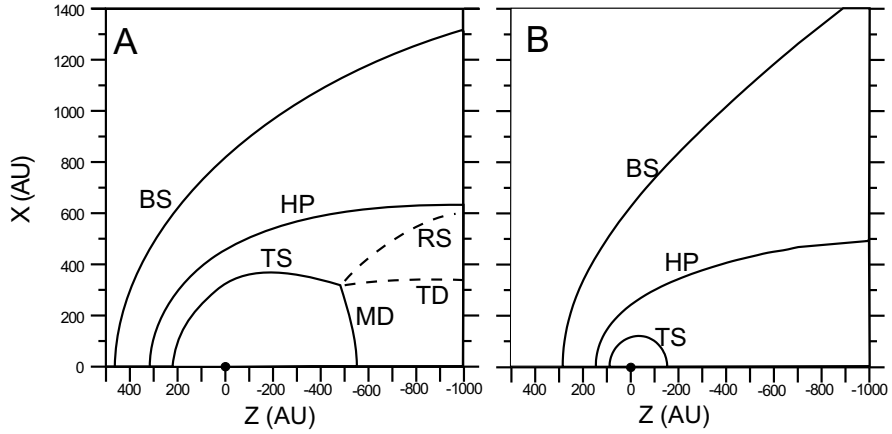

Figure 4.2: Effect of the interstellar H atoms on the geometrical pattern of the interface. (A) The heliospheric interface pattern in the case of fully ionized local interstellar cloud (LIC), and (B) the case of partly ionized LIC. Here, BS, HP, TS are the bow shock,the heliopause and the termination shock, respectively. MD, TD and RS are the Mach disk, the tangential discontinuity, and the reflected shock that are formed in the case of fully ionized plasma. The result was obtained firstly by Baranov and Malama (1993). (From Izmodenov and Alexashov, 2003).

decelerated by 15-30%, strongly heated by a factor 5-8, and loaded by the pickup proton component (approximately 20-50%).

The interstellar plasma flow is disturbed upstream of the bow shock by charge exchange of the interstellar protons with secondary H atoms. These secondary atoms originate in the solar wind. This leads to heating (40-70%) and deceleration (15-30%) of the interstellar plasma before it reaches the bow shock. The Mach number decreases upstream of the BS and for a certain range of interstellar parameters ($n_{\rm H,LIC} \gg n_{\rm p,LIC}$) the bow shock may disappear. Solid curves in Figure 4.3B correspond to a small ionization degree in the LIC ($n_{\rm p}/(n_{\rm p}+n_{\rm H}) = 1/6$); the bow shock almost disappears in this case.

Interstellar neutrals also modify the plasma structure in the heliosheath. In a pure gas dynamic case (without neutrals) the density and temperature of the postshock plasma are nearly constant. However, the charge exchange process leads to a large increase in the plasma number density and a decrease in its temperature (Figure 4.3C). The electron impact ionization process may influence the heliosheath plasma flow by increasing the gradient of the plasma density from the termination shock to the heliopause (Baranov and Malama, 1996). The influence of interstellar atoms on the heliosheath plasma flow is important, in particular, for the interpretation of the kHz-radio emissions detected by Voyager (Gurnett et al., 1993; Gurnett and Kurth, 1996; Gurnett et al., 2006; see, also, Treumann et al., 1998, and Treumann et al., 2006, in this volume) and for possible future imaging of the heliosphere using the energetic neutral atom (ENA) fluxes (Gruntman et al., 2001; McComas et al., 2004, 2006b).

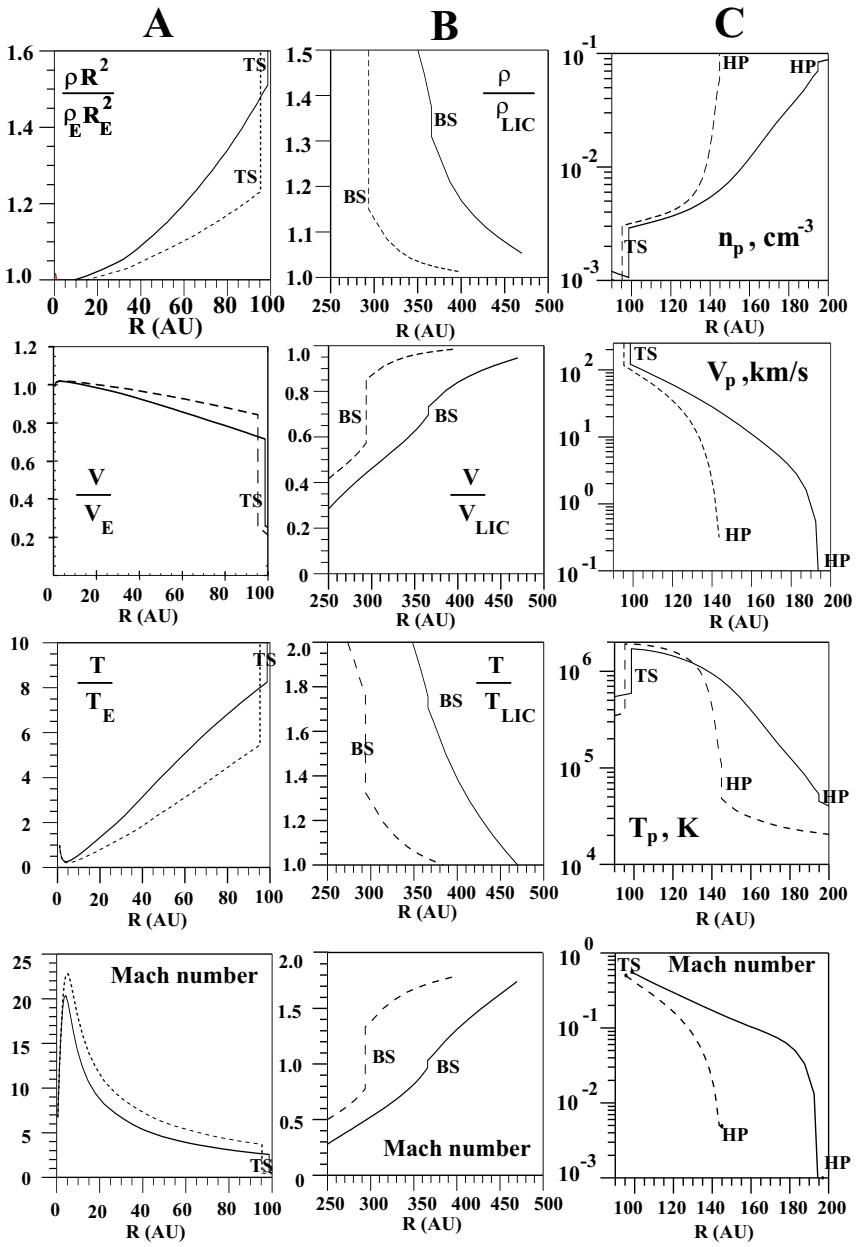

Figure 4.3: Plasma density, velocity, temperature and Mach number upstream of the termination shock (A), upstream of the bow shock (B), and in the heliosheath (C). The distributions are shown for the upwind direction. Solid curves correspond to $n_{\rm H,LIC} = 0.2$ cm^{-3}, $n_{\rm p,LIC} = 0.04$ cm^{-3}. Dashed curves correspond to $n_{\rm H,LIC} = 0.14$ cm^{-3}, $n_{\rm p,LIC} = 0.10$ cm^{-3}. $V_{\rm LIC}$=25.6 km/s, $T_{\rm LIC} = 7000$ K. (From Izmodenov, 2000).

4.3.2 Hydrogen atoms

Charge exchange significantly alters the interstellar atom flow. Atoms newly created by charge exchange have the velocity of their ion counterparts in charge exchange collisions. Therefore, the velocity distribution of these new atoms depends on the local plasma properties in the place of their origin. It is convenient to distinguish four different populations of atoms, depending on the region in the heliospheric interface where the atoms were formed. Population 1 are the atoms created in the supersonic solar wind up to the TS (region 1 in Figure 4.1), population 2 are the atoms created in the inner heliosheath (region 2 in Figure 4.1), and population 3 are the atoms created in the outer heliosheath (region 3 in Figure 4.1). The atoms of population 3 are often called the secondary interstellar atom component. We will call the original (or primary) interstellar atoms population 4. The number densities and mean velocities of these populations are shown in Figure 4.4 as functions of the heliocentric distance. The distribution function of H atoms, $f_{\rm H}\left(\mathbf{r}, \mathbf{w}_{\rm H}\right)$, can be represented as the sum of the distribution functions of these populations: $f_{\rm H} = f_{\rm H,1} + f_{\rm H,2} + f_{\rm H,3} + f_{\rm H,4}$. The Monte Carlo method allows us to calculate these four distribution functions which were presented by Izmodenov (2001) and Izmodenov et al. (2001) at the 12 selected points in the heliospheric interface. As an example, the distribution functions at the termination shock in the upwind direction are shown in Figure 4.5 for four introduced populations of H atoms. It is seen from this Figure that the distribution functions of all H-atom populations are not Maxwellian inside the heliosphere, i.e. the hydrodynamic approach is not correct for describing the motion of neutral atoms (Chapter 1). Note that the distribution function of H atoms in the heliosphere was also presented by Mueller et al. (2000). However, the different populations of H atoms cannot be considered separately in the mesh particle simulations of H atoms (Lipatov et al., 1998) which were used in that paper. (Another paper, by Heerikhuisen et al., 2006, that demonstrates the velocity distribution of H atoms was recently published).

Original (or primary) interstellar atoms (population 4) are significantly filtered (i.e. their number density is reduced) before reaching the termination shock (Figure 4.4A). The outer heliosheath is the main "filter" for these atoms. Since slow atoms have a small mean free path (due to both larger charge exchange cross section and smaller velocities) in comparison to the fast atoms, they undergo larger losses. This kinetic effect, called *selection*, results in a deviation of the interstellar distribution function from Maxwellian (Figure 4.5A). The selection also results in an $\sim$10% increase in the primary atom mean velocity towards the termination shock (Figure 4.4C).

The secondary interstellar atoms (population 3) are created in the disturbed interstellar medium by charge exchange of primary interstellar neutrals with protons decelerated in the vicinity of the heliopause. The secondary interstellar atoms collectively make up the *hydrogen wall*, a density increase at the heliopause. The *hydrogen wall* has been predicted by Baranov et al. (1991) and detected in the direction of α Cen (Linsky and Wood, 1996) on the Hubble Space Telescope (see, also, Chapter 11 of this volume). At the termination shock, the number density of secondary neutrals is comparable to the number density of the primary interstellar atoms (Figure 4.4A, dashed curve). The relative abundances

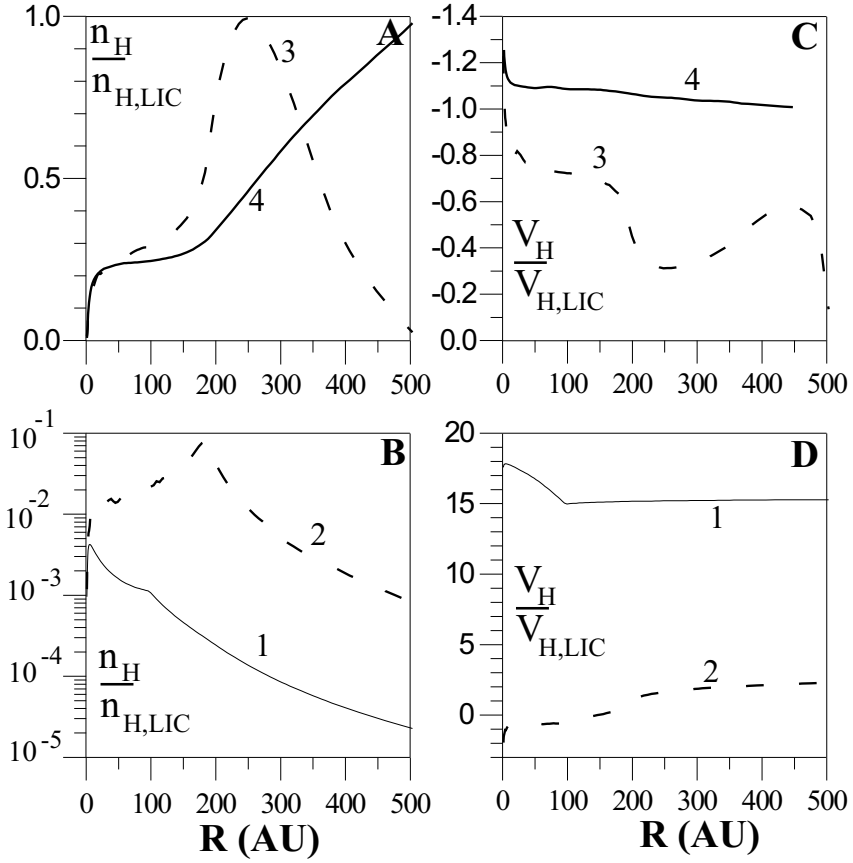

Figure 4.4: Number densities and velocities of four atom populations as functions of heliocentric distance in the upwind direction. 1 designates atoms created in the supersonic solar wind, 2 atoms created in the heliosheath, 3 atoms created in the disturbed interstellar plasma, and 4 original (or primary) interstellar atoms. Number densities are normalized to $n_{\rm H,LIC}$, velocities are normalized to $V_{\rm LIC}$. It is assumed that $n_{\rm H,LIC} = 0.2$ cm^{-3}, $n_{\rm p,LIC} = 0.04$ cm^{-3}. (From Izmodenov et al., 2001)

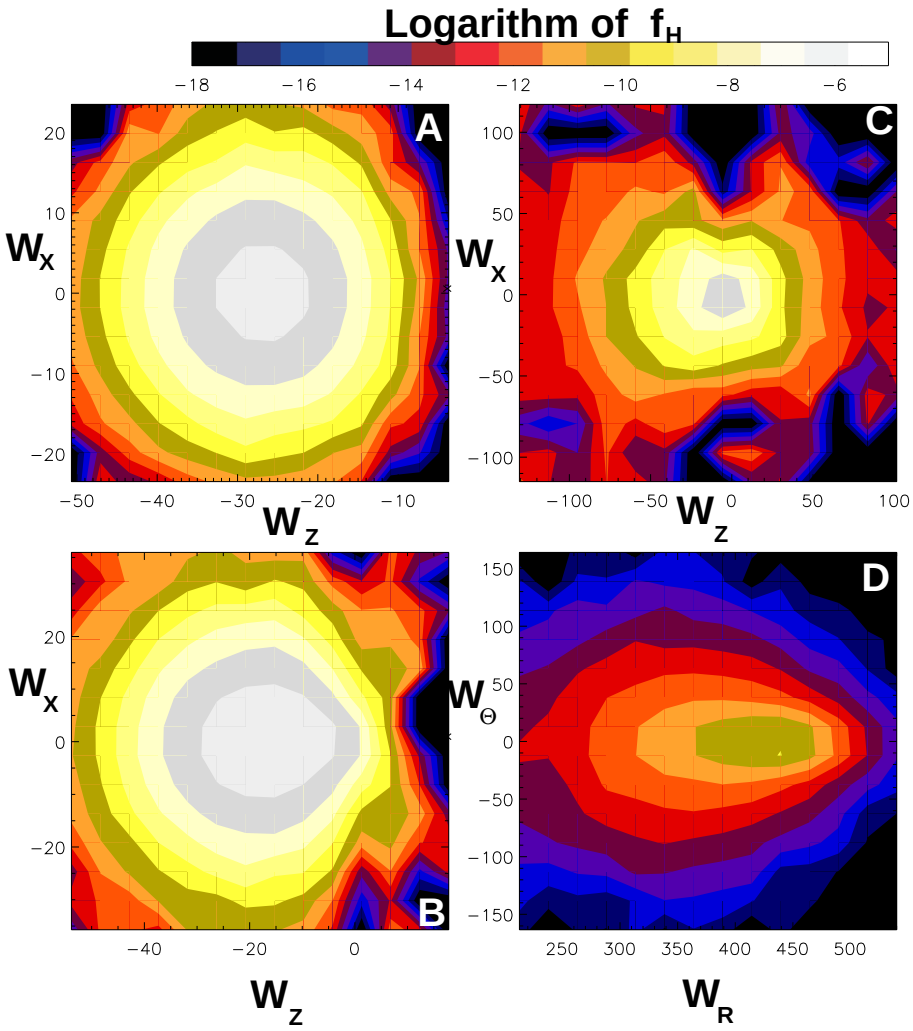

Figure 4.5: Velocity distributions of four atom populations at the termination shock in the upwind direction. (A) primary interstellar atoms, (B) secondary interstellar atoms, (C) atoms created in the heliosheath, (D) atoms created in the supersonic solar wind. w_z is the projection of the velocity vector on the axis parallel to the LIC velocity vector. Negative values of w_z indicate approach to the Sun. w_x is the radial component of the projection of the velocity vector on the perpendicular plane. w_z, w_x are in km/sec. It is assumed that $n_{\mathrm{H,LIC}} = 0.2$ cm^{-3}, $n_{\mathrm{p,LIC}} = 0.04$ cm^{-3}. (From Izmodenov et al., 2001)

of secondary and primary atoms entering the heliosphere vary with the degree of interstellar ionization. The bulk velocity of population 3 is about −18 to −19 km/s. The sign "-" means that the population approaches the Sun. One can see that the distribution function of this population is not Maxwellian (Figure 4.5B). The reason for the abrupt behaviour of the distribution function for $w_z > 0$ is that the particles with significant positive w_z velocities can reach the termination shock only from the downwind direction. The distribution functions of different H atom populations were calculated by Izmodenov et al. (2001) for different directions from upwind. The fine structures of the distribution functions of the primary and secondary interstellar populations vary with direction. These variations reflect the geometrical pattern of the heliospheric interface. The distribution functions of the interstellar atoms can be good diagnostics of the global structure of the heliospheric interface.

Another population (population 2) of the heliospheric hydrogen atoms are **the atoms created in the inner heliosheath** by charge exchange with hot and compressed solar wind and pickup protons. The number density of this population is an order of magnitude smaller than the number densities of the primary and secondary interstellar atoms. This population has a minor importance for the interpretation of Lyman-α and pickup ion measurements inside the heliosphere. Some atoms of this population may probably be detectable by a Lyman-α hydrogen cell experiment due to their large Doppler shifts (Quémerais and Izmodenov, 2002). Recently it was pointed out by Chalov and Fahr (2003) that charge exchange of these atoms with solar wind protons may produce tails in the distribution function of pickup ions that are measured at one or several AU during quiet time periods. Gruntman and Izmodenov (2004) have shown that this population of H-atoms is a major contributor to the density of interplanetary hydrogen at heliocentric distances <1 AU and could dominate in the downwind (interstellar wind) region under typical solar and interstellar conditions. Mass transport by heliospheric ENAs may become especially important for determining the origin of the pickup ions attributed to the inner source of neutral particles in the Sun's vicinity.

Due to their high energies and large mean free path, a portion of the atoms in this population penetrate upstream of the BS and disturb the pristine interstellar medium at large heliocentric distances. Inside the termination shock the atoms propagate freely. Thus, these atoms are a rich source of information on the plasma properties at the place of their birth, i.e. at the inner heliosheath. There are plans to measure this population of atoms on future missions, including the Small Explorer called Interstellar Boundary Explorer (IBEX) that was selected by NASA and is scheduled for launch in June 2008.

The last population of the heliospheric atoms are **the atoms created in the supersonic solar wind (population 1)**. The number density of this atom population has a maximum at ∼5 AU. At this distance, the number density of the population is about two orders of magnitude smaller than the number density of interstellar atoms. Outside the termination shock the density decreases faster than r^{-2}, where r is the heliocentric distance (curve 1, Figure 4.4B). The mean velocity of population 1 is about 450 km/sec, which corresponds to the bulk velocity of the supersonic solar wind. The distribution function of this population is also not Maxwellian (Figure 4.5D). The extended "tail" in the distribution function is

caused by the solar wind plasma deceleration upstream of the termination shock. This "supersonic" atom population penetrates the interface and charge exchanges with interstellar protons beyond the BS. The process of charge exchange leads to heating and deceleration upstream of the bow shock and, therefore, to a decrease in the Mach number ahead of the bow shock.

The model by Baranov and Malama (1993) takes into account essentially two interstellar components: H atoms and charged particles. To apply this model to space experiments, one needs to evaluate how other possible components of the interstellar medium influence the results of this two-component model. The effects are considered in the following sections.

4.4 Effects of interstellar and solar wind ionized helium

Recent measurements of interstellar helium atoms (Witte et al., 1996; Witte, 2004) and interstellar He pickup ions (Gloeckler and Geiss, 2001; Gloeckler et al., 2004) inside the heliosphere, as well as of the interstellar helium ionization (Wolff et al., 1999) allow us to estimate the number density of interstellar helium ions to be 0.008-0.01 cm^{-3}. Current estimates of the proton number density in the LIC fall into the range 0.04 - 0.07 cm^{-3}. Since helium ions are four times heavier than protons, the dynamic pressure of the ionized helium component is comparable to the dynamic pressure of the ionized hydrogen component. Therefore, interstellar ionized helium cannot be ignored in the modelling of the heliospheric interface. The model of the SW/LIC interaction that was used to study the effects of interstellar ionized helium for the first time was developed by Izmodenov et al. (2003b). Simultaneously with interstellar ionized helium, the model took into account solar wind alpha particles, which constitute 2.5 - 5% of the solar wind and, therefore, produce 10 - 20% of the solar wind dynamic pressure.

The model considers all plasma components (electrons, protons, pickup ions, interstellar helium ions, and solar wind α particles) as one fluid with total density ρ and bulk velocity $\mathbf{V}$. This one-fluid approximation assumes that all ionized components have the same temperature T. Although this assumption cannot be made in the case of the solar wind (see Section 4.9), the one-fluid model is based on mass, momentum, and energy conservation laws and predicts the plasma bulk velocity and locations of the shocks very well. The plasma is quasi-neutral in the model i.e., $n_e = n_p + n_{He^+}$ for the interstellar plasma, and $n_e = n_p + 2n_{He^{++}}$ for the solar wind. As in the model by Baranov and Malama (1993), the magnetic fields are ignored. While the interaction of interstellar H atoms with protons by charge exchange is important, for helium ions the process of charge exchange is negligible because of the small cross sections for the charge exchange of helium atoms. As in the Baranov-Malama model, the hydrodynamic Euler equations for the charged component are solved self-consistently with the kinetic equation for the interstellar H atom component. The system of Euler equations is as follows:

$$\nabla \cdot (\rho \mathbf{V}) = q_1, \tag{4.9}$$

$$\nabla \cdot (\rho \mathbf{V}\mathbf{V} + p\hat{I}) = \boldsymbol{q}_2 \tag{4.10}$$

$$\nabla \cdot \left[\rho \mathbf{V}\left(\varepsilon + \frac{p}{\rho} + \frac{\mathrm{V}^2}{2}\right)\right] = q_3, \tag{4.11}$$

where $\rho = \rho_\mathrm{p} + \rho_\mathrm{e} + \rho_\mathrm{He}$ is the total density of the ionized component, and $p = p_\mathrm{p} + p_\mathrm{e} + p_\mathrm{He}$ is the total pressure of the ionized component. Here, ρ_{He} denotes the He^+ density in the interstellar medium, and the He^{++} density in the solar wind; $\varepsilon = p/(\gamma - 1)\rho$ is the specific internal energy; $\hat{I}$ is the unit tensor. The term q_1 of the continuity equation takes into account the source of mass due to photoionization and electron-impact ionization processes.

The kinetic equation for the velocity distribution function of the interstellar H-atoms is as follows:

$$\begin{aligned}
&\mathbf{w}_\mathrm{H} \cdot \frac{\partial f_\mathrm{H}}{\partial \boldsymbol{r}} + \frac{\mathbf{F}_\mathrm{r} + \mathbf{F}_\mathrm{g}}{m_\mathrm{H}} \cdot \frac{\partial f_\mathrm{H}}{\partial \mathbf{w}_\mathrm{H}} = -\left(\nu_\mathrm{ph} + \nu_\mathrm{impact}\right) f_\mathrm{H}\left(\boldsymbol{r}, \mathbf{w}_\mathrm{H}\right) \\
&-f_\mathrm{H} \cdot \int |\mathbf{w}_\mathrm{H} - \mathbf{w}_\mathrm{p}| \sigma_\mathrm{ex}^\mathrm{HP} f_\mathrm{p}\left(\boldsymbol{r}, \mathbf{w}_\mathrm{p}\right) \mathrm{d}\mathbf{w}_\mathrm{p} \\
&+f_\mathrm{p}\left(\boldsymbol{r}, \mathbf{w}_\mathrm{H}\right) \int |\mathbf{w}_\mathrm{H}^* - \mathbf{w}_\mathrm{H}| \sigma_\mathrm{ex}^\mathrm{HP} f_\mathrm{H}\left(\boldsymbol{r}, \mathbf{w}_\mathrm{H}^*\right) \mathrm{d}\mathbf{w}_\mathrm{H}^*.
\end{aligned} \tag{4.12}$$

As compared with Equations (4.1)-(4.8), Equations (4.9) - (4.12) take into account the processes of photoionization and electron impact ionization. Here ν_{ph} is the photoionization rate; and ν_impact is the electron impact ionization rate. Other notations are as for Equations (4.1) - (4.8).

The source terms take into account photoionization and electron impact ionization:

$$q_1 = m_\mathrm{p} n_\mathrm{H} \cdot \left(\nu_\mathrm{ph} + \nu_\mathrm{impact}\right), \qquad n_\mathrm{H}\left(\mathbf{r}, t\right) = \int f_\mathrm{H}\left(r, \mathrm{w}_\mathrm{H}, t\right) \mathrm{dw}_\mathrm{H}, \tag{4.13}$$

$$\begin{aligned}
&\boldsymbol{q}_2 = \int m_\mathrm{p}\left(\nu_\mathrm{ph} + \nu_\mathrm{impact}\right) \mathbf{w}_\mathrm{H} f_\mathrm{H}\left(\mathbf{r}, \mathbf{w}_\mathrm{H}\right) \mathrm{d}\mathbf{w}_\mathrm{H} + \\
&\int\int m_\mathrm{p} v_\mathrm{rel} \sigma_\mathrm{ex}^\mathrm{HP}\left(v_\mathrm{rel}\right)\left(\mathbf{w}_\mathrm{H} - \mathbf{w}\right) f_\mathrm{H}\left(\mathbf{r}, \mathbf{w}_\mathrm{H}, t\right) f_\mathrm{p}\left(\mathbf{r}, \mathbf{w}, t\right) \mathrm{d}\mathbf{w}_\mathrm{H} \mathrm{d}\mathbf{w},
\end{aligned} \tag{4.14}$$

$$\begin{aligned}
&q_3 = \int m_\mathrm{p}\left(\nu_\mathrm{ph} + \nu_\mathrm{impact}\right) \frac{\mathrm{w}_\mathrm{H}^2}{2} f_\mathrm{H}\left(\mathbf{r}, \mathbf{w}_\mathrm{H}, t\right) \mathrm{d}\mathbf{w}_\mathrm{H} + \\
&\frac{1}{2}\int\int m_\mathrm{p} v_\mathrm{rel} \sigma_\mathrm{ex}^\mathrm{HP}\left(v_\mathrm{rel}\right)\left(\mathrm{w}_\mathrm{H}^2 - \mathrm{w}^2\right) f_\mathrm{H}\left(\mathbf{r}, \mathbf{w}_\mathrm{H}, t\right) f_\mathrm{p}\left(\mathbf{w}\right) \mathrm{d}\mathbf{w}_\mathrm{H} \mathrm{d}\mathbf{w} \\
&+n_\mathrm{H}\left(\nu_\mathrm{ph} E_\mathrm{ph} - \nu_\mathrm{impact} E_\mathrm{ion}\right)
\end{aligned} \tag{4.15}$$

Here $v_\mathrm{rel} = |\mathbf{w}_\mathrm{H} - \mathbf{w}|$ is the relative velocity of an atom and a proton, E_ph is the mean photoionization energy (4.8 eV), and E_ion is the ionization potential of H atoms (13.6 eV).

Note that the system of equations (4.9- 4.15) is not closed because the distribution function of protons, $f_\mathrm{p}\left(\mathbf{w}, \mathbf{r}\right)$ requires knowledge of the number density of protons. In order to determine n_p the continuity equations are solved for He^+ in

Table 4.4: Sets of model parameters and locations of the TS, HP and BS in the upwind direction

#	$n_{\mathrm{H,LIC}}$	$n_{\mathrm{p,LIC}}$	$n_{\alpha,\mathrm{sw}}/n_{\mathrm{e,sw}}$	$\frac{\mathrm{He\,II}}{\mathrm{He\,I}+\mathrm{He\,II}}$	R(TS)	R(HP)	R(BS)
	cm^{-3}	cm^{-3}	%		AU	AU	AU
1	0.18	0.06	0	0	95.6	170	320
2	0.18	0.06	0	0.375	88.7	152	270
3	0.18	0.06	2.5	0	100.7	176	330
4	0.18	0.06	2.5	0.150	97.5	168	310
5	0.18	0.06	2.5	0.375	93.3	157	283
6	0.18	0.06	4.5	0.375	97.0	166	291
7	0.20	0.04	0	0	95.0	183	340
8	0.20	0.04	2.5	0.375	93.0	171	290

the interstellar medium and for α-particles in the solar wind. Then, the proton number density can be calculated as $n_{\mathrm{p}} = (\rho + m_{\mathrm{He}} n_{\mathrm{He}})/m_{\mathrm{He}}$. (Here, as previously, n_{He} denotes the He^{+} number density in the interstellar medium, and the He^{++} number density in the solar wind.) The temperature of the plasma is determined from the equation of state $p = 2\,(n_{\mathrm{p}} + n_{\mathrm{He}^{+}})\,kT$ for the interstellar plasma and $p = (2n_{\mathrm{p}} + 3n_{\mathrm{He}^{++}})\,kT$ for the solar wind.

To evaluate possible effects of both interstellar ions of helium and solar wind alpha particles, Izmodenov et al. (2003b) performed parametric model calculations with the eight sets of boundary conditions given in Table 4.4. Calculated locations in the upwind direction of the termination shock, the heliopause, and the bow shock are given for each model in the last three columns of Table 4.4. It can be seen that the heliopause and the termination and bow shocks are closer to the Sun when the influence of interstellar helium ions is taken into account. This effect is partially compensated by additional solar wind alpha particle pressure that we also took into account in our model. The net result is as follows: the heliopause, termination and bow shocks are closer to the Sun by $\sim$ 12 AU, $\sim$ 2 AU, $\sim$ 30 AU, respectively in the model taking into account both interstellar helium ions and solar wind alpha particles (model 5) compared to the model ignoring these ionized helium components (model 1). Despite the fact that the net effect of interstellar helium ions and solar alpha particles is rather small ($\sim$7% of displacement for the heliopause, $\sim$10% of the BS and 2 % for the TS), it can still be important for interpretations and predictions of experimental data connected with the heliosheath region.

It was also found that both interstellar ionized helium and solar wind alpha particles do not significantly influence the filtration of the interstellar H atoms through the heliospheric interface.

4.5 Effects of GCRs and ACRs

An effect of the cosmic rays on the plasma flow is determined by the cosmic ray pressure $p_{\rm CR}$ which can be expressed via the cosmic ray distribution function by the formula

$$p_{\rm CR} = \frac{4\pi}{3} \int f_{\rm CR}\left(\mathbf{r}, |\mathbf{p}|, t\right) |\mathbf{p}|^4 {\rm d}|\mathbf{p}|,$$

where $\mathbf{p}$ is the individual momentum of particles. In this case terms with the gradients of the cosmic ray pressure ($\nabla p_{\rm CR}$) and the energy transfer of the cosmic rays ($\mathbf{V} \cdot \nabla p_{\rm CR}$) have to be added in the hydrodynamic equations (4.10) and (4.11), and these equations can be written as

$$\nabla \cdot \left[\mathbf{V}\mathbf{V} + \left(p + p_{\rm CR}\right) \hat{I}\right] = \mathbf{q}_2 \tag{4.16}$$

$$\nabla \cdot \left[\rho \mathbf{V} \left(\varepsilon + \frac{p}{\rho} + \frac{V^2}{2}\right)\right] = q_3 - \mathbf{V} \cdot \nabla p_{\rm CR}. \tag{4.17}$$

To close the system of equations (4.9), (4.12 - 4.15), (4.16), and (4.17) it is necessary to add the equation for $p_{\rm CR}$ which, in a stationary situation, has the form

$$\nabla \cdot \left[\kappa_{\rm CR} \nabla p_{\rm CR} - \gamma_{\rm CR} \left(\mathbf{V} + \mathbf{V}_{\rm d}\right) p_{\rm CR}\right] + \left(\gamma_{\rm CR} - 1\right) \mathbf{V} \cdot \nabla p_{\rm CR} + Q = 0. \tag{4.18}$$

Here $\kappa_{\rm CR}$ and $\gamma_{\rm CR}$ are the diffusion coefficient and polytropic index of cosmic rays, respectively, $\mathbf{V}_{\rm d}$ is the momentum-averaged drift velocity, and Q is the energy injection rate describing energy gains of ACRs from hot protons. Chalov and Fahr (1996, 1997) suggested that

$$Q = -\alpha p \nabla \cdot \mathbf{V}, \tag{4.19}$$

where α is a constant coefficient of injection efficiency defined by the specific plasma properties in the heliosphere (Chalov and Fahr, 1997), the plasma pressure p is determined by pickup protons in the distant solar wind. It should be noted that there is no injection into the GCRs ($\alpha = 0$).

The influence of the galactic cosmic rays on the heliospheric interface structure was studied by Myasnikov et al. (2000a,b). The study was done in the frame of two-component (plasma and GCRs) and three-component (plasma, H atoms and GCRs) models. For the two-component case it was found that cosmic rays could considerably modify the shape and structure of the solar wind termination shock and the bow shock and change heliocentric distances to the heliopause and the bow shock. At the same time, for the three-component model it was shown that the GCR influence on the plasma flow is negligible when compared with the influence of H atoms. The exception is the bow shock, a structure which can be modified by the cosmic rays. The model by Baranov and Malama (1993) is therefore acceptable for the interpretation of the physical processes in the heliosphere as long as the processes are not related to the bow shock structure.

The dynamical influence of ACRs on the solar wind flow in the outer heliosphere and on the structure of the termination shock has been studied by Fahr et al. (2000) and Alexashov et al. (2004a). Using the closed system of equations (4.9), (4.12)

- (4.19) (the drift velocity, $\mathbf{V}_d$, was neglected) Alexashov et al. (2004a) studied effects connected with changes in the value of the diffusion coefficient while keeping the injection rate fixed. Different values of the diffusion coefficient were considered because κ_{CR} is poorly known in the outer heliosphere and especially in the heliosheath, and, in addition, the value of the diffusion coefficient varies with the solar cycle. It was shown that:

- The effect of ACRs on the solar wind flow near the termination shock leads to the formation of a smooth precursor, followed by the subshock, and to a shift of the subshock towards larger distances in the upwind direction. This result is consistent with earlier findings based on one-dimensional spherically symmetric models. Both the intensity of the subshock and the magnitude of the shift depend on the value of the diffusion coefficient, with the largest shift (about 4 AU) occurring at medium values of κ_{CR}.

- The precursor of the termination shock is rather pronounced except for the case with large κ_{CR}.

- The post-shock temperature of the solar wind plasma is lower in the case of the cosmic-ray-modified termination shock when compared to the shock without ACRs. The decrease in the temperature results in a decrease in the number density of hydrogen atoms originating in the region between the termination shock and the heliopause.

- The cosmic-ray pressure downstream of the termination shock is comparable to the thermal plasma pressure for small κ_{CR} when the diffusive length scale is much smaller than the distance to the shock. On the other hand, at large κ_{CR} the post-shock cosmic-ray pressure is negligible when compared with the thermal plasma pressure. There is a pronounced upwind-downwind asymmetry in the cosmic-ray energy distribution due to a difference in the amount of the energy injected into ACRs in the up- and downwind parts of the termination shock. This difference in the injected energy is connected with the fact that the thermal plasma pressure is lower in the downwind part of the shock compared to the upwind part.

It has also been shown by Berezhko (1986), Chalov (1988a, b), and Zank et al. (1990) that the precursor of a cosmic-ray-modified shock is highly unstable with respect to magnetosonic disturbances if the cosmic-ray pressure gradient in the precursor is sufficiently large. The oscillations connected with the instability of the precursor have a distinctive feature: the magnetic field in more unstable modes oscillates in the longitudinal direction, while the solar wind speed oscillates in the direction perpendicular to the ecliptic plane (Chalov, 1990). The detail study of magnetic field oscillations measured by Voyager 1 in front of the termination shock allows one to determine whether it was really a strong cosmic-ray modified shock. It seems, however, that cosmic rays did not play any important dynamical role in the plasma flow near the shock during the time of the shock crossing, since measurements at Voyager 1 did not reveal evidence of local acceleration of ACRs.

4.6 The effect of the interstellar magnetic field

Before investigating any effect of the interstellar magnetic field on the plasma flow and on the distribution of H atom parameters in the interface, it is necessary to formulate the closed system of magnetohydrodynamic (MHD) equations for the plasma component and to use the Boltzmann equation (4.12). One-fluid MHD equations for the plasma component were considered in Chapter 1. Excluding the density of the electric current $\mathbf{j}$ and the intensity of the electric field $\mathbf{E}$ from the system of equations (1.67), (1.71), (1.74), (1.76) and neglecting dissipative processes (viscosity, thermal conductivity and energy dissipation due to electric current) the ideal MHD equations for a stationary problem will have the form

$$\nabla \cdot \rho\mathbf{V} = q_1 \ , \tag{4.20}$$

$$\nabla \cdot (\rho\mathbf{V}\mathbf{V} + p) = \frac{1}{4\pi}(\nabla \times \mathbf{B}) \times \mathbf{B} + \mathbf{q}_2 \ , \tag{4.21}$$

$$\nabla \times (\mathbf{V} \times \mathbf{B}) = 0 \ , \quad \nabla \cdot \mathbf{B} = 0 \tag{4.22}$$

$$\nabla \cdot \left[\rho\mathbf{V}\left(\frac{\gamma}{\gamma-1}\frac{p}{\rho} + \frac{V^2}{2} + \frac{1}{4\pi}\mathbf{B} \times [\mathbf{V} \times \mathbf{B}]\right)\right] = q_3 \ . \tag{4.23}$$

The system of Equations (4.20) - (4.23) together with Equation (4.12) and the source terms (4.13)-(4.15) was numerically solved by Alexashov et al. (2000) for the case of the magnetic field parallel to the relative Sun/LIC velocity vector. In this case, the model remains axisymmetric. It was shown that the effect of the interstellar magnetic field on the positions of the termination and bow shocks and the heliopause is significantly smaller compared to the model with no H atoms (Baranov and Zaitsev, 1995). The calculations were performed with various Alfvén Mach numbers in the undisturbed LIC. It was found that the bow shock straightens out with decreasing Alfvén Mach number $M_{\rm A} = V_{\rm LIC}\sqrt{4\pi\rho}/B_{\rm LIC}$ (increasing magnetic field strength in LIC). It approaches the Sun near the symmetry axis, but recedes from it on the flanks. By contrast, the nose of the heliopause recedes from the Sun due to the tension of magnetic field lines, while the heliopause in its wings approaches the Sun under magnetic pressure. As a result, the region of the compressed interstellar medium around the heliopause (or "pileup region") decreases by almost 30%, as the magnetic field increases from zero to 3.5×10^{-6} Gauss. It was also shown that H atom filtration and heliospheric distributions of primary and secondary interstellar atoms are virtually unchanged over the entire assumed range of the interstellar magnetic field ($0 - 3.5 \times 10^{-6}$ Gauss). The magnetic field has the strongest effect on the density distribution of population 2 of H atoms, which increases by a factor of almost 1.5 as the interstellar magnetic field increases from zero to 3.5×10^{-6} Gauss.

Izmodenov et al. (2005a), Izmodenov and Alexashov (2005a, 2006) have studied the problem assuming that the interstellar magnetic field (ISMF) is inclined to the direction of the interstellar flow. In this case the SW/LIC interaction region becomes asymmetric and the flow pattern becomes essentially three-dimensional.

Figure 4.6 presents the shapes of the termination shock (TS), heliopause (HP), and the bow shock (BS) in the xz plane along with their heliocentric distances.

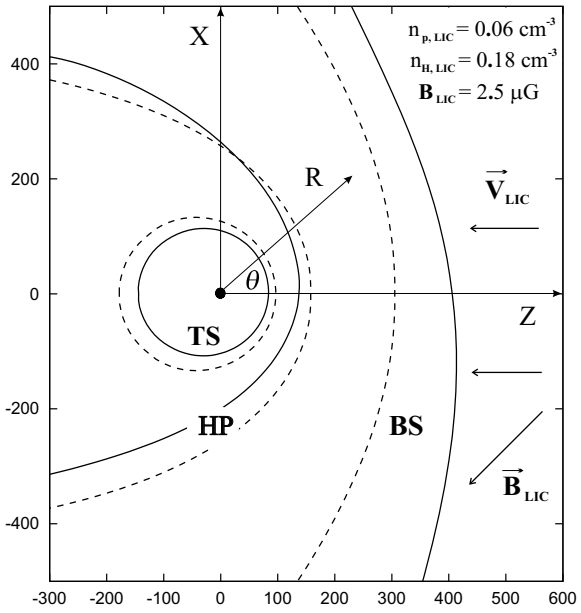

Figure 4.6: The structure of the heliospheric interface. TS is the termination shock, HP is the heliopause and BS is the bow shock. Solid curves correspond to the model, when the interstellar magnetic field is taken into account; dashed curves correspond to the model with vanishing magnetic field.

The xz plane is determined by the Sun-LIC relative velocity and the interstellar magnetic field vectors. The direction of the z axis is chosen to be opposite to the interstellar gas velocity vector. The direction of the ISMF vector is $-135°$ relative to the z axis. For the purpose of comparison, Figure 4.6 shows the TS, HP and BS for the case of vanishing ISMF (dashed curves). It can be seen that the interstellar magnetic field pressure pushes the heliopause and the termination shock towards the Sun compared to a model without magnetic field. In the upwind direction the TS and HP are closer to the Sun by ∼10 AU and ∼20 AU, respectively. The maximum and minimum of the magnetic field pressure occur in the directions of $\theta = -45°$ and $\theta = 45°$, respectively. (The definition of θ is given in Figure 4.6, and an interval $-180° < \theta < 180°$ is adopted here.) The difference in magnetic pressure creates a strong asymmetry of the heliopause with respect to the z axis. The distances to the heliopause are ∼144 AU and ∼164 AU, for $\theta = -45°$ and $\theta = 45°$, respectively. For comparison, the distance to the HP is ∼180 AU in the case of a vanishing magnetic field. The asymmetry is weaker, but still pronounced, for the TS. The distances to the TS are 87 AU for $\theta = -45°$ and 95 AU for $\theta = 45°$, respectively.

The asymmetry of the bow shock (Figure 4.6) is connected with both the asymmetry of the heliopause, which serves as an obstacle for the interstellar plasma flow, and different propagation of MHD waves along and perpendicular to the interstellar magnetic field. As a result of the discussed asymmetry, the distance between

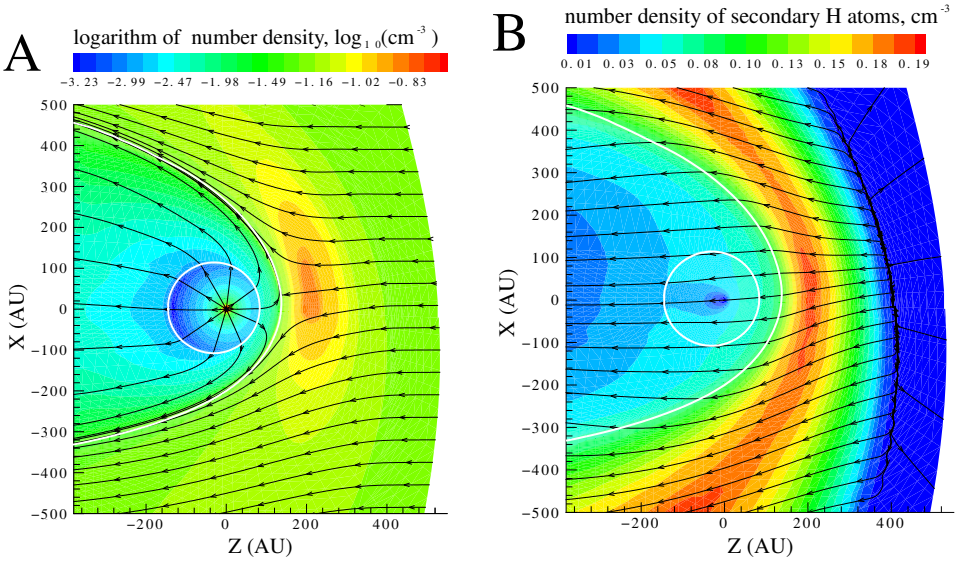

Figure 4.7: Isolines of the number density and streamlines of the plasma component (A) and secondary H atom population (B). The asymmetry of the plasma pileup region due to the ISMF is clearly seen.

the HP and BS is larger in the upper half of the zx-plane, where θ is positive, compared to the negative half of the plane. In fact, the interstellar plasma is more compressed for the positive values of θ and less compressed for its negative values (see also Figure 4.7A). The maximum of the plasma pileup region is shifted towards the upper half of the plane in Figure 4.7A. It is important to note that due to the rather strong magnetic field and the mass-loading of the interstellar plasma by charge exchange with secondary interstellar atoms, the BS becomes very weak and tends to turn into the characteristic.

Figure 4.7A also presents the streamlines of the plasma component. The stagnation point is located in the upper half of the zx plane shifted by $\sim 10^\circ$ away from the z axis. It is important to note that the velocity vector of the plasma passing through the region of maximum plasma density has a noticeable V_x component. The secondary interstellar atoms, which originate in the region between the BS and the HP, should have the properties of the plasma of this region. Figure 4.7B presents the number density of this secondary interstellar atom component. The maximum density appears in the region between the TS and the HP. This is the so-called hydrogen wall as discussed in Subsection 4.3.2 above. It is seen in the figure that the maximum of the hydrogen wall is also slightly shifted to the upper half of the xz plane and reflects the behaviour of the plasma distributions. The streamlines of the H atom component are also shown in Figure 4.7B. The streamlines were plotted based on the mean velocity field distribution of the interstellar H atoms, which was calculated in a Monte-Carlo scheme as the integral $\boldsymbol{V}_{\mathrm{H}} = \int \boldsymbol{w} f_{\mathrm{H}}(\boldsymbol{r}, \boldsymbol{w})\, \mathrm{d}\boldsymbol{w}$, where $f_{\mathrm{H}}(\boldsymbol{r}, \boldsymbol{w})$ is the velocity distribution function of the H atom component. The velocity vector $\boldsymbol{V}_{\mathrm{H}}$ determines the direction of the H

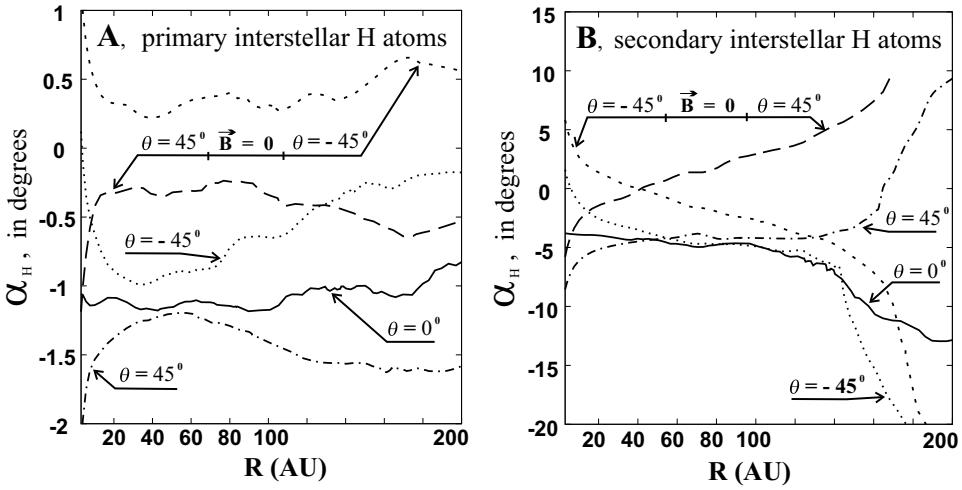

Figure 4.8: The angle $\alpha_{\rm H} = \arctan(V_{x,{\rm H}}/V_{z,{\rm H}})$ as a function of the heliocentric distance for the primary (A) and secondary (B) interstellar H atoms. $\alpha_{\rm H}$ is shown for different lines of sight and for the models with and without interstellar magnetic field.

atom flow on average. It is seen from the figure that in the heliosphere the velocity vector $\boldsymbol{V}_{\rm H}$ has a noticeable V_x component even very close to the Sun. The effect of the shift in the direction of interstellar hydrogen flow compared to the direction of the interstellar helium was observed by the SOHO/SWAN H cell instrument (Lallement et al., 2005). This effect is clearly reproduced by our numerical results. To quantify the effect we plot the angle $\alpha_{\rm H}$, which determines the direction of the H atom flow: $\alpha_{\rm H} = \arctan(V_{x,{\rm H}}/V_{z,{\rm H}})$. Figure 4.8 shows $\alpha_{\rm H}$ for the primary (right plot) and secondary (left plot) populations of the interstellar H atoms. $\alpha_{\rm H}$ is presented as a function of the heliocentric distance for three different lines of sight, which correspond to the angles $\theta = 0°$, $45°$, $-45°$. It is seen that for the upwind direction ($\theta = 0°$) $\alpha_{\rm H} \sim -5°$ for the secondary interstellar H atom population and $\alpha_{\rm H} \sim -1°$ for the primary interstellar H atoms. The small erratic variations in the curves are due to statistical uncertainties in our Monte-Carlo calculations. Dashed curves in Figure 4.8 correspond to lines of sight of $\theta = 45°$ and $-45°$. It is seen that the curves are nearly symmetric around $\alpha_{\rm H} = -5°$ for the secondary H atom component and $\alpha_{\rm H} = -1°$ for the primary interstellar component. For the purposes of comparison, Figure 4.8 also shows $\alpha_{\rm H}$ towards $\theta = 45°$ and $-45°$ lines of sight for the axisymmetric model, when the ISMF vanishes. It can be seen that the curves are symmetric around $\alpha_{\rm H} = 0$ in this case. Therefore, we conclude that for the ISMF under consideration the direction of the secondary H atom flow is $\alpha_H = -5°$ and that of the primary H atom population is $\alpha_H = -1°$. The direction of the combined H flow in the heliosphere is the averaged sum of the two populations, which is $\sim$3.5-4°. This number is in very good agreement with the results obtained by Lallement et al. (2005) from the analysis of backscattered solar Lyman-α radiation.

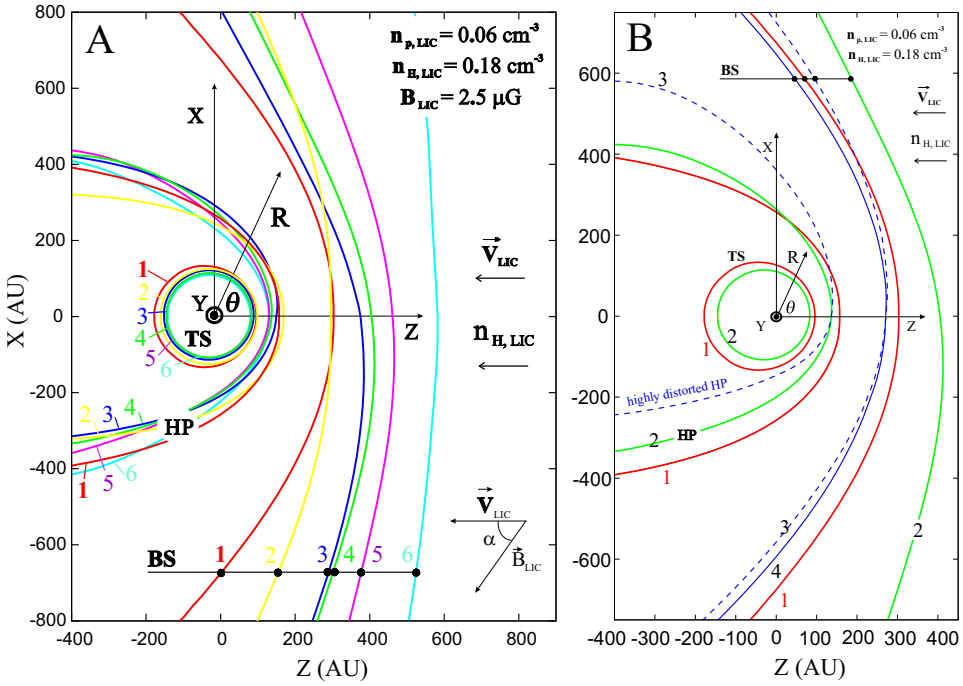

Figure 4.9: A. The termination shock, heliopause and bow shock in the ($\mathbf{V}_{\rm LIC}$, $\mathbf{B}_{\rm LIC}$)-plane for different angles α between the directions of the interstellar magnetic field and interstellar plasma flow. Curves 1 correspond to the case when $B_{\rm LIC} = 0$. For curves 2-6 $B_{\rm LIC} = 2.5\mu$G. Curves 2 show results for $\alpha = 0°$, curves 3 for $\alpha = 30°$, curves 4 for $\alpha = 45°$, curves 5 for $\alpha = 45°$, curves 6 for $\alpha = 90°$.
B. Curves 1 show the TS, BS and HP for $B_{\rm LIC}$=0. Curves 2 are for $B_{\rm LIC} = 2.5\mu$G, $\alpha = 45°$, curves 3 correspond to the test case of a highly disturbed heliopause. Curve 4 (for the BS) corresponds to the gas dynamic flow around the fixed heliopause obtained for $B_{\rm LIC} = 2.5\mu$G, $\alpha = 45°$. (From Izmodenov and Alexashov, 2006.)

Izmodenov and Alexashov (2006) performed the calculations in the frame of the 3D MHD-kinetic model for different values of the angle α between the direction of the interstellar magnetic field (ISMF) and the direction of the interstellar flow. The shapes of the termination shock (TS), heliopause (HP), and the bow shock (BS) are shown in Figure 4.9A in the xz plane along with their heliocentric distances. The xz plane is determined by the Sun-LIC relative velocity and the interstellar magnetic field vectors. The direction of the z axis is chosen to be opposite to the interstellar gas velocity vector. The direction of the ISMF vector constitutes angles: $\alpha = 0°$ (curves 2), $\alpha = 30°$ (curves 3), $\alpha = 45°$ (curves 4), $\alpha = 60°$ (curves 5) and $\alpha = 90°$ (curves 6). For the purpose of comparison Figure 4.9A shows the TS, HP and BS for the case of vanishing ISMF (curves 1).

Pogorelov and Zank (2006) pointed out that the deflection of interstellar H atom flow could be also due to the influence of the heliospheric magnetic field. To examine

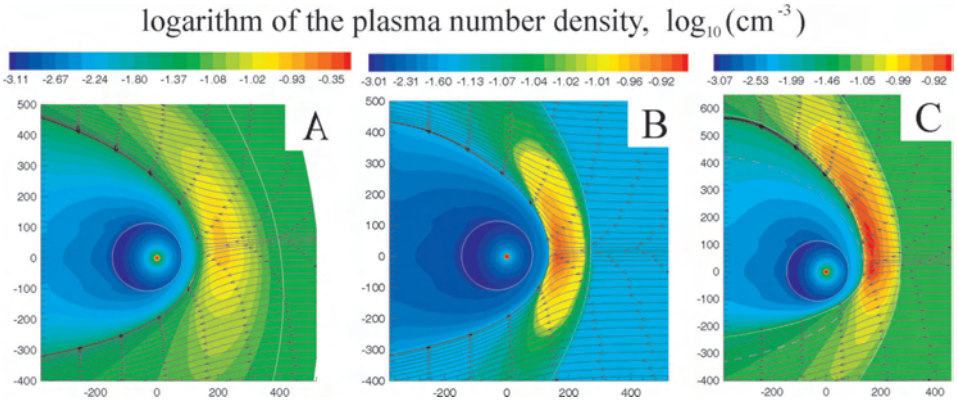

Figure 4.10: Isolines of the number density and streamlines of the plasma component. (From Izmodenov and Alexashov, 2006.)
A. 3D MHD-kinetic model with $B_{\rm LIC} = 2.5\mu$G, $\alpha = 45°$.
B. Test case of gas-dynamic flow around the fixed heliopause obtained in the case of $B_{\rm LIC} = 2.5\mu$G, $\alpha = 45°$.
C. Test case of gas-dynamic flow around the highly disturbed heliopause.

the effect of the possible deviation of H atoms caused by the heliospheric effects and to understand the nature of the deflection of interstellar H atoms better, two test calculations (Fig. 4.9B) were performed by Izmodenov and Alexashov (2006).

In the first test we fixed the shape of the heliopause to be as it was in the full self-consistent 3D MHD-kinetic calculations (curve 2 in Figure 4.9B). The plasma flow inside the heliopause was unchanged. Then the interstellar magnetic field was switched off and the gas-dynamic interstellar plasma flow around the fixed-shape heliopause was computed. Figure 4.9B shows the TS, HP and BS for this test (curves 2 for TS and HP, curve 4 for BS). It is seen that the outer heliosheath region is thinner in the gas-dynamic case compared with the MHD cases. Comparison of the plasma streamlines and number density for MHD and gas-dynamic cases can be seen from Figure 4.10A and 4.10B. The V_x component of the plasma velocity is much smaller in the test. The stagnation point is closer to axis Oz.

The difference in the plasma flows around the heliopause is pronounced in the direction of the velocity of the H atom component inside the heliosphere (Figure 4.11). Curve 3 of the figure shows the direction of H atoms for the test case. The deflection of 0.5° in the test case is smaller compared to ≈3° in the MHD case. Therefore, we conclude that the deflection is mainly caused by properties of the MHD flow of the interstellar plasma. The deflection caused by the asymmetric shape of the heliopause is relatively small.

The heliospheric effects connected with the 3D nature of the solar wind and heliospheric magnetic field may influence the region between the HP and BS indirectly by changing the shape of the heliopause. To study the possible influence of the inner heliospheric effects on the deflection of the interstellar H atoms we strongly disturb the shape of the heliopause (Figure 4.9B, curve 3). Then we consider the heliopause as an obstacle and calculate the outer and inner plasma flows

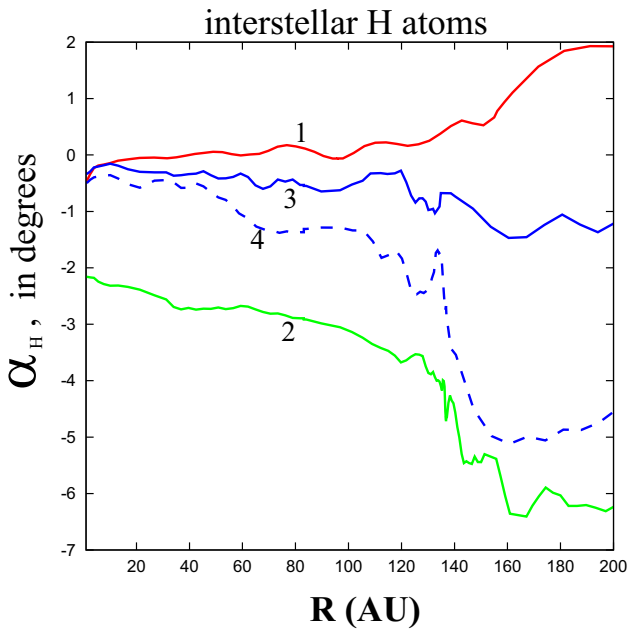

Figure 4.11: The angle $\alpha_{\rm H}$ for (1) $B_{\rm LIC} = 0$ (curve 1), (2) $B_{\rm LIC} = 2.5\mu$G, $\alpha = 45°$ (curve 2), (3) test case of gas-dynamic flow around the fixed heliopause obtained in the case of $B_{\rm LIC} = 2.5\mu$G, $\alpha = 45°$, (4) test case of gas-dynamic flow around the highly disturbed heliopause (curve 4). (From Izmodenov and Alexashov, 2006.)

around the obstacle. Figure 4.10C shows the plasma streamlines and number density in the case of the distorted heliopause. The stagnation point is shifted toward the north with respect to the line $x = 0$. However, in general the streamlines are less declined as compared with the MHD case (Figure 4.10A). The value of $\alpha_{\rm H}$ for the case of the distorted heliosphere (curve 4 in Figure 4.11A) is significantly less than in the MHD case (curve 2). In a realistic heliosphere the disturbance of the heliopause is less than considered here. Therefore, these estimates suggest that deflection of the interstellar H atoms in the heliospheric interface due to ISMF effects is larger than the possible deflection due to the effects connected with a heliospheric magnetic field or a 3D solar wind. Nevertheless, the role of the heliospheric magnetic field on the global structure of the heliospheric interface still needs to be investigated in the frame of the kinetic-MHD modelling.

4.7 Effects of the solar cycle variations of the solar wind

More than 30 years (three solar cycles) of observation of the solar wind show that its momentum flux varies by a factor of ∼2 from solar maximum to solar minimum (Gazis, 1996; Richardson, 1997). It has been shown theoretically that

such variations in the solar wind momentum flux strongly influence the structure of the heliospheric interface (e.g., Karmesin et al., 1995; Wang and Belcher, 1999; Baranov and Zaitsev, 1998; Zaitsev and Izmodenov, 2001; Zank and Müller, 2003).

Most global models of solar cycle effects have ignored the interstellar H atom component or took this component into account by using simplified fluid approximations. These simplifications were made because it is difficult to solve a 6D (time, two dimensions in space, and three dimensions in velocity-space) kinetic equation for the interstellar H atom component. Recently, the non-stationary, self-consistent model of the heliospheric interface was developed by Izmodenov et al. (2003a), Izmodenov and Malama (2004a,b), Izmodenov et al. (2005b). This model is described below.

4.7.1 Model

The model is a non-stationary version of the two-component model described in Section 4.3 above. In addition to the classical Baranov-Malama two-component consideration, both the helium components were taken into account as was described in Section 4.4 for the stationary case. The system of non-stationary governing equations is the following:

$$\frac{\partial \rho}{\partial t} + \nabla \cdot (\rho \mathbf{V}) = q_1 \ , \tag{4.24}$$

$$\frac{\partial (\rho \mathbf{V})}{\partial t} + \nabla \cdot \left(\rho \mathbf{V}\mathbf{V} + p\hat{I} \right) = \boldsymbol{q}_2 \ , \tag{4.25}$$

$$\frac{\partial E}{\partial t} + \nabla \cdot [\mathbf{V} (E + p)] = q_3 \ , \tag{4.26}$$

where $\rho = \rho_{\rm p} + \rho_{\rm e} + \rho_{\rm He}$ is the total density of the ionized component, $p = p_{\rm p} + p_{\rm e} + p_{\rm He}$ is the total pressure of the ionized component (Here, $\rho_{\rm He}$ denotes the He^+ density in the interstellar medium, and the He^{++} density in the solar wind), $E = \rho \left(\varepsilon + V^2/2 \right)$ is the total energy per unit volume, $\varepsilon = p/(\gamma - 1)\rho$ is the specific internal energy, and $\hat{I}$ is the unit tensor. As in Section 4.4, the temperature of the plasma is determined from the equation of state $p = 2(n_{\rm p} + n_{\rm He^+})kT$ for the interstellar plasma and $p = (2n_{\rm p} + 3n_{\rm He^{++}})kT$ for the solar wind, where k is Boltzman's constant; $n_{\rm p}$, $n_{\rm He^+}$ and $n_{\rm He^{++}}$ are the proton, interstellar He ion and solar wind alpha particle number densities. In addition to the Equations (4.24)-(4.26), the continuity equations were solved for He^+ in the interstellar medium and for α-particles in the solar wind. Then the proton number density was calculated as $n_{\rm p} = (\rho - m_{\rm He} n_{\rm He})/m_{\rm p}$, where $n_{\rm He}$ denotes the He^+ number density in the interstellar medium, and the He^{++} number density in the solar wind. The source terms in the right hand sides of Equations (4.24)-(4.26) have the same expressions (4.13)-(4.15) as for the stationary model.

The system of Equations (4.24)-(4.26) is solved self-consistently together with the non-stationary kinetic equation for the velocity distribution function of the interstellar H-atoms,

$$\frac{\partial f_{\rm H}}{\partial t} + \mathbf{w}_{\rm H} \cdot \frac{\partial f_{\rm H}}{\partial \boldsymbol{r}} + \frac{\mathbf{F}_{\rm r} + \mathbf{F}_{\rm g}}{m_{\rm H}} \cdot \frac{\partial f_{\rm H}}{\partial \mathbf{w}_{\rm H}} = -(\nu_{\rm ph} + \nu_{\rm impact}) f_{\rm H}(\boldsymbol{r}, \mathbf{w}_{\rm H})$$

$$-f_{\rm H} \cdot \int |\mathbf{w}_{\rm H} - \mathbf{w}_{\rm p}| \sigma_{\rm ex}^{\rm HP} f_{\rm p}\left(\boldsymbol{r}, \mathbf{w}_{\rm p}\right) {\rm d}\mathbf{w}_{\rm p} \tag{4.27}$$

$$+f_{\rm p}\left(\boldsymbol{r}, \mathbf{w}_{\rm H}\right) \int |\mathbf{w}_{\rm H}^{*} - \mathbf{w}_{\rm H}| \sigma_{\rm ex}^{\rm HP} f_{\rm H}\left(\boldsymbol{r}, \mathbf{w}_{\rm H}^{*}\right) {\rm d}\mathbf{w}_{\rm H}^{*} \ .$$

Notations used here are the same as for Equation (4.12) in Section 4.4.

Izmodenov et al. (2005b) have solved the system of equations (4.24)- (4.27) to explore the solar cycle variations of the interface. The 'ideal' solar cycle was considered in the paper. It was assumed that, at Earth's orbit, the solar wind number density oscillates harmonically, while the bulk velocity and temperature remain constant:

$$\begin{aligned} n_{\rm p;E} &= n_{\rm p;E;0}\left(1 + \delta_n \sin \omega t\right) \ , \\ v_{\rm E} &= v_{\rm p;E;0} \ , \\ T_{\rm E} &= T_{\rm E;0} = {\rm const.} \end{aligned} \tag{4.28}$$

For the solar wind disturbances determined by Equations (4.28), the ratio of the maximum to minimum momentum flux is equal to $\Delta = \left(1 + \delta_n\right) / \left(1 - \delta_n\right)$. Following Baranov and Zaitsev (1998) the calculations were performed for $\delta_n = 1/3$, so that $\Delta = 2$. As was pointed out by Zank and Müller (2003), the solar cycle effects in the heliospheric interface remain the same when the variation in the solar wind dynamic pressure is caused by the solar wind velocity variation. This paper considers variations in the solar wind density, which is sufficient for the purposes of this paper. The effects of the realistic solar cycle on the TS variation were studied (preliminary) by Izmodenov et al. (2003a).

The following solar wind parameters averaged over a few solar cycles were used by Izmodenov et al. (2005b): $n_{\rm p;E;0} = 8$ cm^{-3}, $V_{\rm p;E;0}$= 445 km/s. The following parameters of the interstellar gas in the unperturbed interstellar medium were used at the outer boundary: $V_{\rm LIC} = 26.4$ km/s, $T_{\rm LIC} = 6500$ K, $n_{\rm H,LIC} = 0.18$ cm^{-3}, $n_{\rm p,LIC} = 0.06$ cm^{-3}. These particular values of the interstellar velocity and temperature were chosen on the basis of the recent observations of the interstellar He atoms by GAS/Ulysses (Witte et al., 1996; Witte, 2004; Gloeckler et al., 2004). The choice of $n_{\rm H,LIC}$ and $n_{\rm p,LIC}$ is based on our analysis of the Ulysses pickup ion measurements (see, e.g., Izmodenov et al. 2003a,b, 2004).

Now we will explain why the study was done for "idealized" harmonic perturbations at the Earth's orbit rather than the realistic perturbations of the solar wind parameters obtained from observations. The statistical Monte-Carlo method used to obtain periodic solutions of the kinetic equation requires us to fix the time-period. The non-linear nature of the system may lead to interaction of the external 11-year fluctuations with the internal oscillations of the heliospheric interface. As a result, oscillations with periods different from 11 years may appear in the self-consistent solution of the governing equations (4.24)-(4.27) with the boundary conditions (4.28). One of the main objectives of our study was to verify whether such oscillations do appear. To do this the time-period of the Monte-Carlo calculations was increased by 6 times. If oscillations with periods different from 11 years are present in the solution this method allows us to determine these periods. If the realistic perturbations of the solar wind parameters, which are, in general,

not periodic, are used as the boundary conditions, it would be rather difficult to detect the presence of oscillations with periods different from 11 years.

To solve the Euler equations self-consistently with the kinetic equation, an iterative procedure as suggested by Baranov et al. (1991) for the stationary model was employed. In the first step of this iterative procedure the Euler equations with the constant source terms q_1, $\boldsymbol{q}_2$ and q_3 were solved with the use of the boundary conditions (4.28). The source terms were taken from the stationary solution with the average solar wind parameters. The calculations were performed over 300 solar cycles. As a result, the distribution of the plasma parameters was obtained. This distribution was analyzed and it was found that there is only the 11 year periodicity.

In the second step, the kinetic equation was solved by a Monte Carlo method with splitting of trajectories (Malama, 1991). To increase the statistical efficiency of the method, periodicity with the time period $t_{\rm period} = 66$ years was assumed. To minimize statistical errors, the statistical results were averaged over $t_{\rm mc} = 1$ year. When doing so a distribution of the plasma parameters for the last 66 years obtained in the first step was employed. As a result, the periodic (66 year) q_1, $\boldsymbol{q}_2$, and q_3 source terms were obtained. In the third step, the Euler equations were solved with the boundary conditions (4.28) and the periodic source terms obtained in the second step. Again, the gas-dynamic calculations were performed over 300 solar cycles. Analysis of the plasma distributions shows the 11 year periodicity only. Then, the kinetic equation was solved by the Monte Carlo method with the distribution of the plasma parameters for the last 66 years obtained in the third step. This process of iterations was continued until the results of two subsequent iterations were practically the same.

The method allows one to obtain the self-consistent solution of the system of the Euler equations (4.24)-(4.26) and the 6D kinetic equation (4.27) with the boundary conditions (4.28). Since the uniqueness of the solution for this system is not proven, it cannot be excluded that other solutions of this system of equations may exist. These solutions may have periods different from 11 years. The numerical method used to solve the Euler equations does not need any restricting assumptions. Remarkably, as reported in the next section, our numerical solution does not contain oscillations with periods different from 11 years.

In addition to the "ideal" solar cycle calculations, some complementary calculations were carried out. The solar wind ram pressure was increased by a factor of 1.5 during the first 11 years of our 66-year period (Figure 4.12, bottom left plot). This study was inspired by the fact that observations of the solar wind are restricted to the recent ~ 30 years. It allowed us to understand how the solar wind conditions in the past, when they were not observed, influence the heliospheric interface and observational quantities today and in the future.

4.7.2 Results

The variations in the heliocentric distances to the termination shock, heliopause and the bow shock are shown in Figure 4.12. The discontinuities vary with an 11-year time-period under the action of 11-year fluctuations of the solar wind dynamic pressure at the inner boundary of our computational grid. The termination shock oscillates around 100 AU from its minimal distance of ~ 93 AU, which is reached

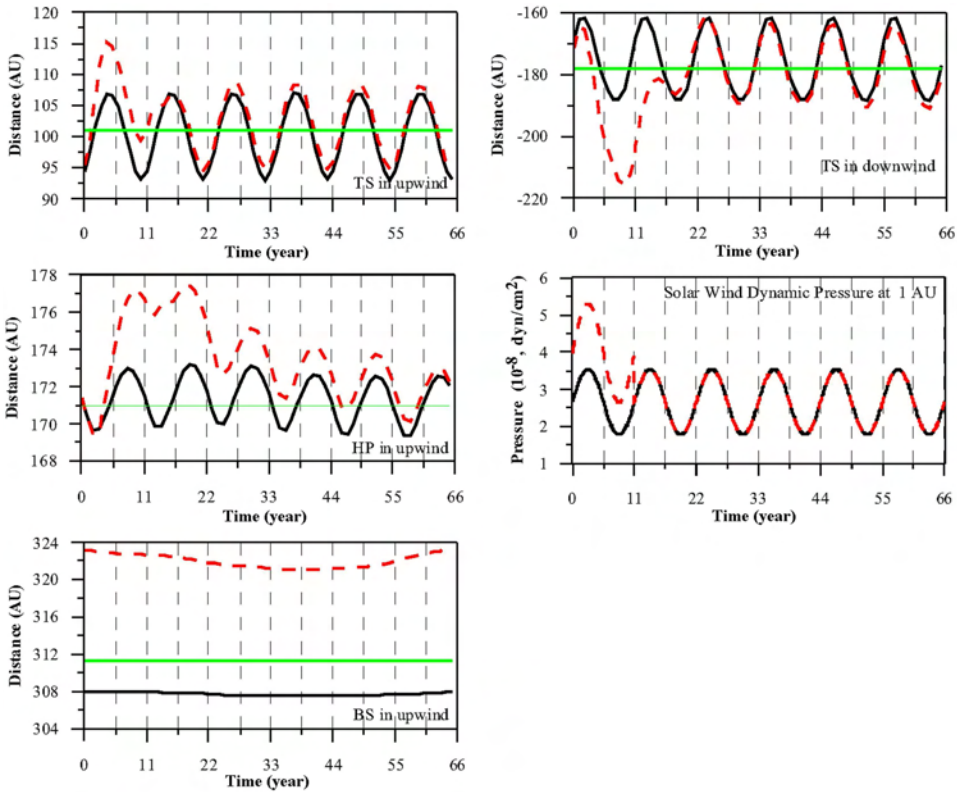

Figure 4.12: Time variations of the heliocentric distances to the termination shock, bow shock and the heliopause in the upwind direction, and to the termination shock in the downwind direction. The bottom plot shows variations in the solar wind momentum flux, $\rho_E V_E^2$, with time. Dashed curves correspond to the solution of the problem with the "broken" first of six solar cycles, when the solar wind dynamic pressure was increased by factor of 1.5 during the first 11 years of our 66-year periodic calculations. (After Izmodenov et al., 2005b.)

in the last (11th) year of the "ideal" solar cycle, to its maximum distance of ~ 107 AU, which is reached during the fourth year of the cycle. Fluctuations in the TS distance are larger in the downwind direction than in the upwind direction. By the upwind direction we mean the direction that is opposite to the direction of the relative Sun-LIC motion. The downwind direction coincides with the Sun-LIC velocity vector. The variation of the TS distance in the downwind direction is ~ 25 AU from its minimum value of ~ 163 AU during the third year of the cycle to its maximum value of ~ 188 AU in the 9th year of the cycle. In the upwind direction the most distant position of the termination shock is reached ~ 1.5 years after the maximum of the solar wind dynamic pressure has been reached at 1 AU. The variations in the solar wind dynamic pressure are shown at the bottom left

of Figure 4.12 for convenience. The phase of downwind fluctuations of the TS is shifted by ~ 3.5 years compared to the phase of the upwind fluctuations.

The strength of the TS has important consequences for the spectra of anomalous cosmic rays (ACRs) because the velocity jump at the TS is related to the spectral index β of ACRs that determines the variation of intensity of the cosmic rays j with energy E: $j \sim E^{-\beta}$. The variation of the velocity jump at the TS was computed. In the upwind direction the jump in the plasma velocity at the TS, or, in other words, the strength of the TS, varies from a minimum value of 2.92 to its maximum value of 3.09. This corresponds to a variation in β from 1.28 to 1.22. The strength of the TS varies from 2.92 to 3.17 in the downwind region. This strength variation is translated into a variation in β from 1.28 to 1.19.

The heliopause distance fluctuates with smaller amplitude as compared to the termination shock. It varies from 169 AU, which is reached during the 4th year of the solar cycle, to 173 AU reached in the 9th year of the solar cycle. The distance to the heliopause averaged over the solar cycle is $\sim$171 AU. This coincides with the stationary solution. The solar-cycle induced fluctuations of the BS is less than 0.1 AU in the upwind direction. The fluctuations are not visible in Figure 4.12. The distance to the BS averaged over the solar cycle is $\sim$308 AU, while this distance is $\sim$311 AU in the case of the stationary solution.

Dashed curves in Figure 4.12 correspond to the solution of the problem with the "broken" first of six solar cycles, when the solar wind ram pressure was increased by a factor of 1.5 during the first 11 years of our 66-year periodic calculations (bottom left plot in Figure 4.12). The termination shock in the upwind direction "feels" the increase in solar wind dynamic pressure for approximately 4-5 years after the increase ended. In the downwind direction, the "feeling" endures somewhat longer and lasts another solar cycle. The second maximum of the TS both in the upwind direction (dashed curve on the top plot in Figure 4.12) and in the downwind direction is closer to the Sun compared to the subsequent maxima.

The post-reaction of the heliopause to the 50% increase in solar wind dynamic pressure is much longer compared to the reaction of the termination shock. The heliopause does not return to its periodic fluctuations even at the end of the 66-year time-period. One can see from the figures that the heliocentric distances to the termination shock, heliopause and bow shock are always larger in the case of a "broken" solar cycle compared to our "regular" solar cycles. This is related to the fact that the solar wind ram pressure averaged over 66 years is 8% greater compared to the "regular" cycle calculations. The effect is most pronounced for the bow shock. It appears that 66 years are not enough for the BS to relax to its "regular"-cycle position. As a result, the BS is $\sim$ 10 AU further away for the "broken"-cycle calculations compared to the "regular" cycle.

Plasma parameters undergo 11-year fluctuations in the entire computation region. However, the wavelength of the plasma fluctuations in the solar wind is apparently larger compared to the distances to the TS and HP. This means that time snap-shots of the distributions of plasma parameters (density, velocity and temperature) are not qualitatively different from stationary solutions. The situation is different in the outer heliosheath, which is the region between the HP and BS. 11-year periodic motion of the heliopause produces a number of additional weak shocks and rarefaction waves (Baranov and Zaitsev, 1995). The amplitudes

of these shocks and rarefaction waves decrease while they propagate away from the Sun due to the increase in their surface areas, interaction between the shocks and rarefaction waves, and the dissipative attenuation of the shocks. To resolve the wave structure the resolution of our computational grid was increased by three times in the region. It was also checked that an additional increase in the resolution of our computational grid does not change the results. Figure 4.13 presents distributions of plasma density, velocity, pressure and temperature as functions of the heliocentric distance in the upwind direction at two different moments, $t_1 = 1$ year (curves 1), and $t_2 = 6$ year (curves 2). It is seen that the characteristic wavelength in the region is ~ 40 AU. Long-scale waves are also seen in plasma distributions in the post-shocked plasma of the downwind region (Figure 4.13, right column). The amplitudes of the waves are much less than in the upwind direction and the wavelength is ~ 200 AU.

Figure 4.13 shows a comparison of the 11-year average distributions of interstellar plasma parameters (dots) with those obtained from a stationary solution. The stationary calculations were performed with exactly the same inner and outer boundary conditions as used in the time-dependent calculations. At the Earth's orbit 11-year average values of the solar wind density were assumed. It can be seen that the two distributions practically coincide. The congruence with the stationary solution is additional evidence of sufficient resolution of our computational grid and the lack of significant numerical dissipation in our numerical calculations. These results contradict the conclusion made by Zank and Müller (2003) that "the shocks provide additional heating in the heliotail and outer heliosheath." According to our results, the heating is very small and it is not noticeable in our calculations. However, to draw conclusions on the plasma heating in the heliosheath, Zank and Müller (2003) had compared their time-dependent results with a stationary model that assumed a smaller solar wind dynamic pressure compared to the 11-year averaged value. Therefore, the observed heating could be (1) due to shock heating, or (2) due to different boundary conditions. Additional multi-fluid studies are needed to distinguish between these two mechanisms.

To better understand why the variation in the solar wind parameters does not disturb the bow shock very much, the propagation of perturbations in the outer heliosheath was studied analytically (see Appendix in Izmodenov et al., 2005b). The propagation of perturbations was studied only near the symmetry axis, and it was assumed that the wavelength is small in comparison to the characteristic scale of inhomogeneity. The latter assumption enabled the use of the WKB approximation. In addition, the interaction of the plasma perturbations with the H atoms was neglected. Then, using the reductive perturbation method, the governing equation for the plasma perturbations was derived. It is a generalization of the nonlinear equation used in nonlinear acoustics for the description of sound waves. This equation was solved assuming the boundary conditions at the heliopause corresponding to the harmonic oscillation of the heliopause with a period of 11 years and an amplitude of 2 AU. The main result of this analytical study is that, due to the nonlinear steepening, the shock forms in the wave profile about midway between the heliopause and the bow shock. The wave energy dissipation in this shock causes strong attenuation of the perturbations on their way from the heliopause to the bow shock. As a result, the wave amplitude at the bow shock is about 3

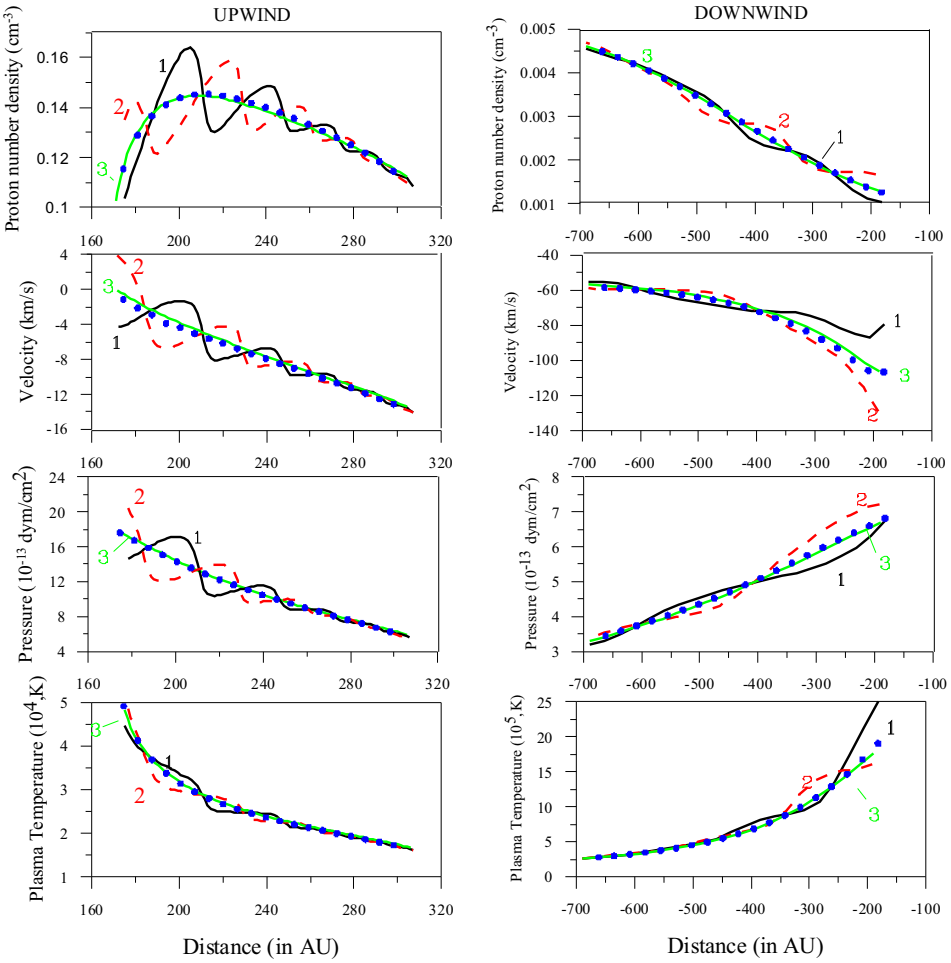

Figure 4.13: Interstellar plasma number density, velocity, pressure and temperature as functions of the heliocentric distance for two different moments in time: t_1 = 1 year (curves 1), t_2 = 6 year (curves 2). The stationary solutions (curves 3) and time-dependent solutions averaged over 11 years (dots) are shown. (After Izmodenov et al., 2005b.)

times smaller than that predicted by the linear theory. Since the wave energy flux is proportional to the amplitude squared, this implies that almost 90% of the wave energy is dissipated in the shocks. On the basis of this result it was concluded that the main reason why the solar cycle variation almost does not disturb the bow shock is that the perturbations propagating from the heliopause to the bow shock are strongly attenuated due to dissipation in the shocks.

Comparison with numerical results reveals that the attenuation of the perturbations obtained in the numerical simulation is even stronger than that predicted by the analytical solution. The most probable cause of this difference is that the interaction between the plasma perturbations and the H atoms provides additional wave dissipation.

Using the analytical solution describing the wave propagation in the outer heliosheath, the rate of the plasma heating due to wave dissipation was estimated. It was found that the mean temperature of the plasma in the outer heliosheath can be increased by about 280 K during one solar cycle. The plasma heating due to the wave dissipation is compensated by the energy loss due to convective plasma motion and due to the interaction between the plasma and the H atoms as seen from the results of our numerical calculations.

4.7.3 H atoms

The main advantage of our model compared to previously published multi-fluid models (Scherer and Fahr, 2003; Zank and Müller, 2003) is a rigorous kinetic description of the interstellar H atoms. Charge exchange significantly disturbs the interstellar atom flow penetrating the heliospheric interface. The atoms newly created by charge exchange have the velocities of their ion partners in the charge exchange collisions. Therefore, the velocity distribution of these new atoms depends on the local plasma properties at their place of origin. As was discussed in the introduction, it is convenient to distinguish four different populations of H atoms depending on the region in the heliospheric interface where the atoms originate. Figure 4.14 compares the distributions of the populations of H atoms obtained by the stationary model (dots) with the time-dependent solution averaged over 11 years. For the plasma component there is no noticeable difference between these two distributions. Although only distributions in the upwind direction are presented, the conclusion remains valid for all of the computational domain. The stationary distributions of the H atom parameters for directions different from upwind can be found in our earlier papers (see, e.g., Izmodenov 2000; Izmodenov et al. 2001).

To evaluate time-dependent features in the distribution of H atoms in the heliospheric interface we plot the number densities of the four populations of H atoms normalized to the densities obtained in the stationary solution. By doing this, spatial gradients of the densities, which are apparently larger than the time-variations of the densities, were suppressed. Figure 4.15 shows the normalized densities for two different years of the solar cycle. Solid curves correspond to $t_1 = 1$ year and dashed curves to $t_2 = 6$ years. It can be seen that the density variation is within $\pm 5\%$ of its mean value for the primary and secondary interstellar populations, and for the atoms created in the inner heliosheath. Closer to the Sun, for distances of less than 10 AU, the amplitude of the fluctuations increases up to 15%. The

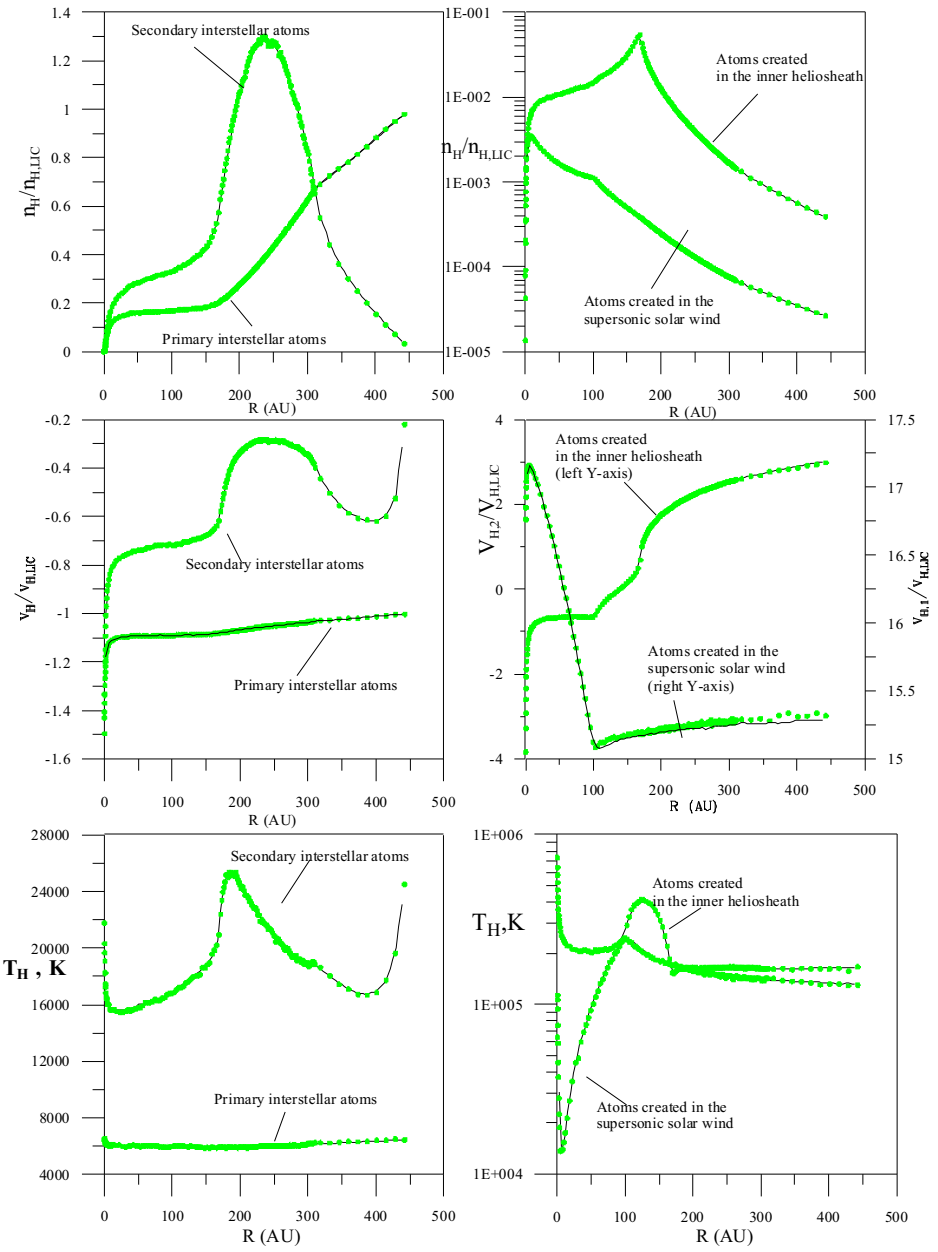

Figure 4.14: Number densities (top row), bulk velocities (middle row) and kinetic temperatures (bottom row) of primary and secondary interstellar atom populations (left column) and atoms created in the supersonic solar wind and inner heliosheath (right column) in the upwind direction as functions of the heliocentric distance. Dots, which represent the stationary solution, are practically coincident with solid curves, which represent the 11-year averaged time-dependent solution. (After Izmodenov et al., 2005b.)

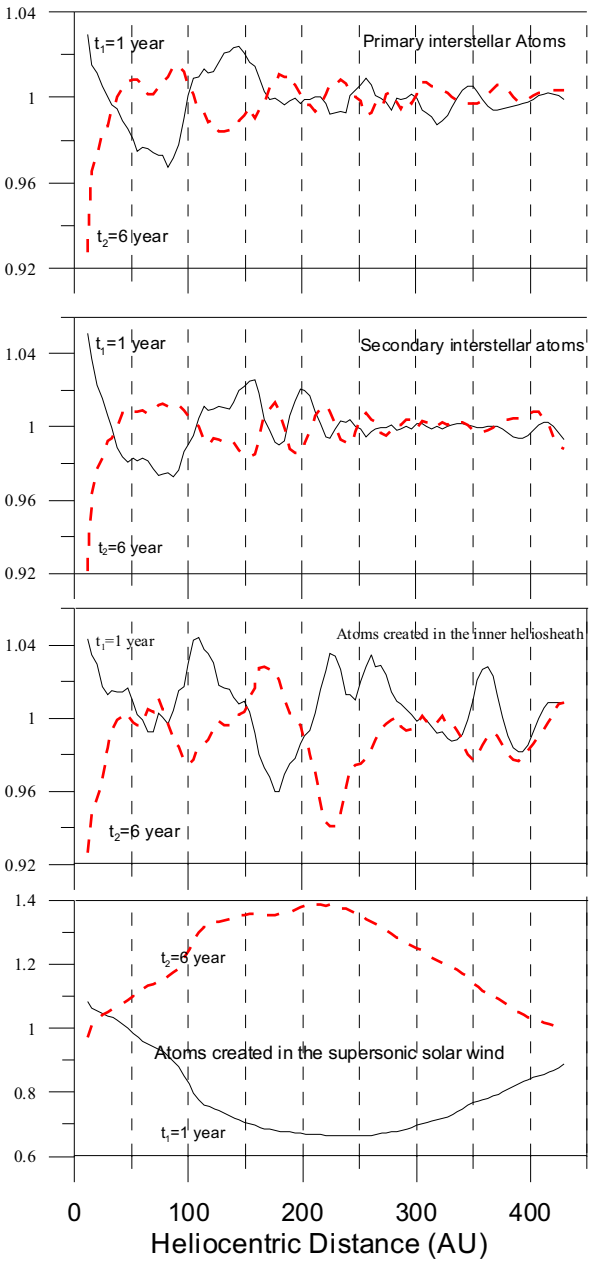

Figure 4.15: Time-variation of the number densities of primary and secondary interstellar atoms (top panels), H atoms created in the inner heliosheath and H atoms created in the supersonic solar wind (bottom panels) as functions of heliocentric distance for two different moments in the solar cycle. (After Izmodenov et al., 2005b.)

variation of the number density of H atoms created in the supersonic solar wind is ±30% about its mean value.

Figure 4.16 shows the time-variation of the number densities, bulk velocities and kinetic temperatures of three populations of H atoms at different heliocentric distances in the upwind direction. All parameters are normalized to their initial values at $t = 0$. Clear 11-year periodicity is apparent for the number densities of the atoms. Any deviation from the exact 11-year periodicity is related to the errors of our statistical calculations, which are $\sim$ 2–3%. Less than 10% variation (from maximum to minimum) is apparent for number densities of all populations at distances greater than 10 AU. At 5 AU the variations are of the order of 30%. Variations of the bulk velocity and kinetic temperature are negligibly small for both primary and secondary interstellar populations. However, the bulk velocity and kinetic temperature of atoms created in the inner heliosheath vary with the solar cycle by 10–12%. This is related to the fact that most of the H atoms of the latter population are created in the vicinity of the heliopause (Figure 4.14) and they reflect long wavelength plasma variations in this region. The correlation of parameters of the H atom population created in the inner heliosheath with the plasma parameters in the vicinity of the heliopause is illustrated in Figure 4.17.

It is important to note that number densities of all three components of H atoms fluctuate in the same phase. Such coherent behaviour of fluctuations remains in the entire supersonic solar wind region ($R < 90$ AU) for the three populations of H atoms and in the inner heliosheath for the primary and secondary atoms. The reason for such coherent behaviour of the variations of H atom densities becomes evident when the variations are compared with the plasma density variations (Figure 4.16, left column). The two quantities vary almost in anti-phase. Apparently, such a correlation is only possible when temporal variations in the H atom densities are caused by variation of the local loss of the neutrals due to charge exchange and ionization processes. The local fluctuations are not transported over large distances because the velocities of individual atoms are chaotic and their mean free path is large.

However, coherent fluctuations of different populations of H atoms disappear in the regions where the populations originate, and the process of creation dominates the losses. Indeed, in the inner heliosheath (for example, at 160 AU in the upwind direction as shown in Figure 4.16) the fluctuations in number density of H atoms created in this region are shifted with respect to the coherent fluctuations of the primary and secondary interstellar atom populations, and are in phase with the variation in the proton number density near the heliopause. Variations in the secondary interstellar atom populations are in anti-phase with variations of primaries in the outer heliosheath (see, $R = 190$ AU in Figure 4.16) and almost in phase with plasma fluctuations in the region. Again, the creation processes are dominant in the outer heliosheath for the secondary interstellar atom population.

Finally, it is important to note that the behaviour of the H atom populations in the heliospheric interface has a kinetic nature. Variations in the atom parameters are determined by the loss and creation processes rather than by the convection and pressure gradient terms, as would be the case in the fluid description. The fluid description is valid if the Knudsen number $Kn = l/L \ll 1$, where l and L are the mean free path of the particles and the characteristic spatial scale of the

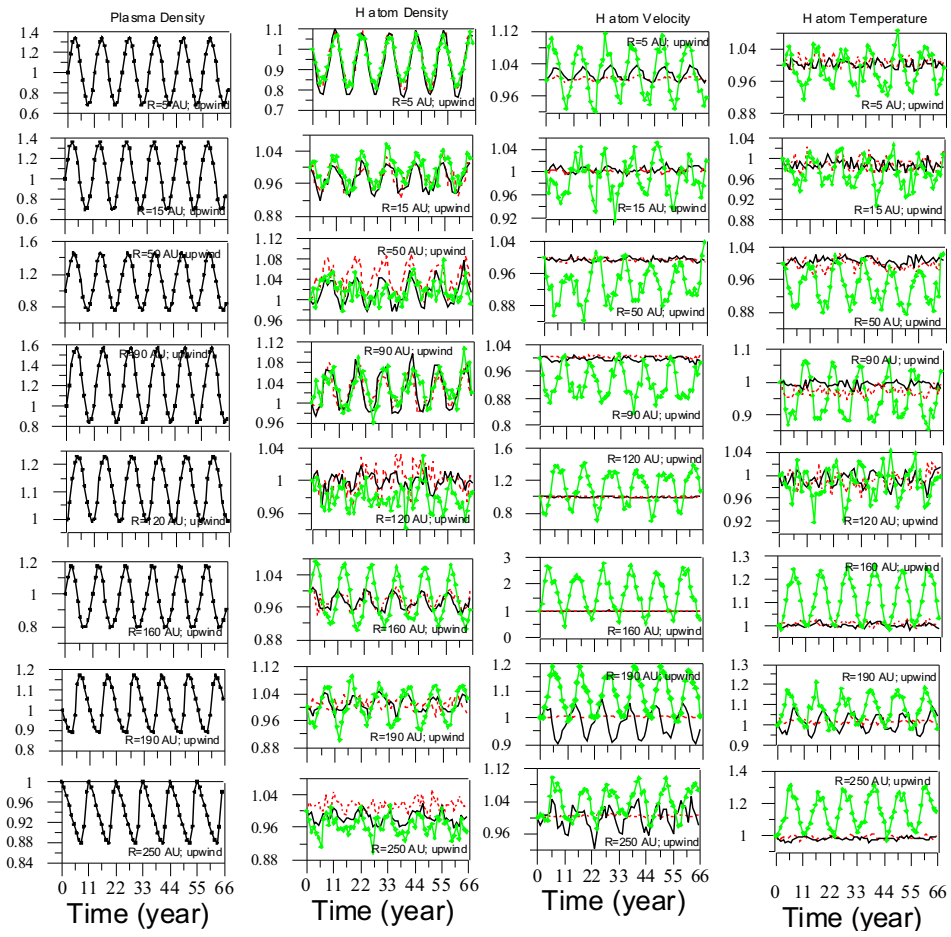

Figure 4.16: The number densities (second column from the left), bulk velocities (second column from the right) and kinetic temperatures (right column) of the primary (solid curves) and secondary (dashed curves) interstellar atom populations and the atoms created in the inner heliosheath (curves with diamonds) at different heliocentric distances in the upwind direction as functions of time. For comparison, the number density of the plasma is shown (left column). All parameters are normalized to their values at $t = 0$. (After Izmodenov et al., 2005b.)

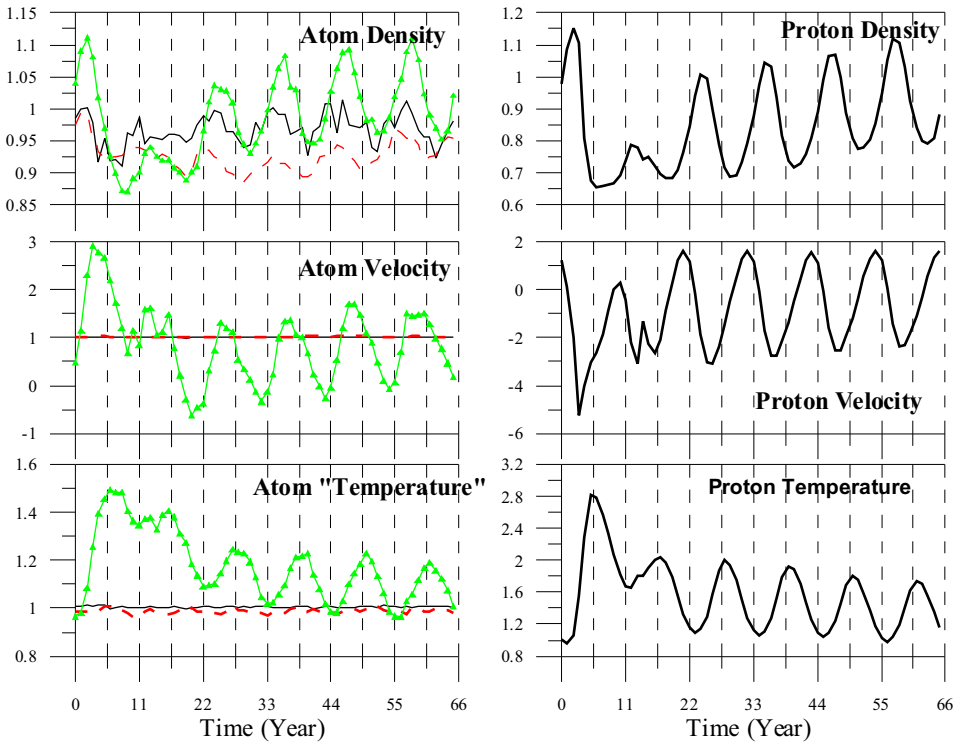

Figure 4.17: Comparison of variations in density, velocity and kinetic temperature of H atoms created in the inner heliosheath (left column, lines with triangles) with those plasma parameters (right column). The variations are shown at $R = 160$ AU in the vicinity of the heliopause in the upwind direction for 'broken' solar cycle calculations, where the solar wind ram pressure was increased by a factor of 1.5 during the first 11 years of the chosen 66-year time-period. Proton parameters are non-dimensionlized to their values at $t = 0$. H atom parameters are non-dimensionlized to the stationary solution. (After Izmodenov et al., 2005b.)

problem, respectively. For the stationary problem the distance between the HP and BS, which is approximately 100 AU, can be chosen as L. The mean free path of H atoms in the region is ~ 50 AU. Therefore, $Kn_{\rm stationary} \approx 0.5$. The results obtained on the basis of the kinetic and fluid descriptions were compared by Baranov et al. (1998), Izmodenov et al. (2001), Alexashov and Izmodenov (2005), and Izmodenov and Alexashov (2005b). This comparison has shown explicitly that the velocity distribution function of H atoms is non-Maxwellian everywhere in the interface. For the time-dependent problem considered in this paper, the characteristic size, L, is determined as a half of the wavelength of plasma fluctuations. In the region between the HP and BS $L \approx 20$ AU as follows from Figure 4.13. Therefore, $Kn_{\rm time} \approx 2$ and a fluid description is even less appropriate than for the stationary model. The fact that the fluid description is inappropriate for the atom motion is the most probable cause of the big discrepancy between our results and the

results obtained by Zank and Müller (2003) and Scherer and Fahr (2003), who used the multi-fluid and fluid approaches, respectively. It is interesting to note the qualitative difference between the Zank and Müller (2003) and Scherer and Fahr (2003) results. The reason for this discrepancy could be once again the different descriptions of H atoms used in these two papers. Scherer and Fahr (2003) used a one-fluid description for H atoms, while Zank and Müller (2003) used a three-fluid description for H atoms in the interface.

The results described above can be briefly summarized as follows. A non-stationary self-consistent model of the heliospheric interface has been developed and applied to explore the solar cycle variations in the interface. The solution of the system of Euler equations (4.24)-(4.26) for plasma, and the kinetic equation (4.27) for interstellar H atoms was found numerically with the periodic boundary conditions (4.28) for the solar wind at the Earth's orbit. The period of the solution is 11 years. The basic results for the plasma component confirm the results obtained previously:

1. The solar cycle variation in the TS location is ± 7 AU about its mean value.

2. The heliopause location varies by ± 2 AU about its mean value.

3. The variation in the bow shock location is negligible.

4. There is a sequence of additional weak shocks and rarefaction waves in the region between the heliopause and the bow shock. The additional heat of the plasma in the outer heliosheath induced by the shock waves is small and it is not observable in our calculations.

5. Our numerical results in the region between the HP and BS are confirmed by an analytical solution based on the WKB approximation.

For the interstellar H atom component, the following new results were obtained:

1. The variation in the number density of the H atoms in the outer heliosphere is within 10%. The variation increases at 5 AU up to 30% due to strong ionization processes in the vicinity of the Sun.

2. The variations in the number densities of three populations of H atoms – primary and secondary interstellar atoms, and atoms created in the inner heliosheath – are coherent in the entire supersonic solar wind region and determined by loss due to charge exchange. The coherent behaviour of fluctuations disappears in the regions where the production process is dominant.

3. There is no significant variation in the temperature and bulk velocity of the primary and secondary interstellar H atoms with the solar cycle. However, the bulk velocity and kinetic temperature of atoms created in the inner heliosheath vary with the solar cycle by 10–12%. It is shown that this variation reflects the plasma properties at the heliopause.

4. There is a qualitative difference between our results and the results obtained by using the fluid or multi-fluid description for the interstellar H atoms. It

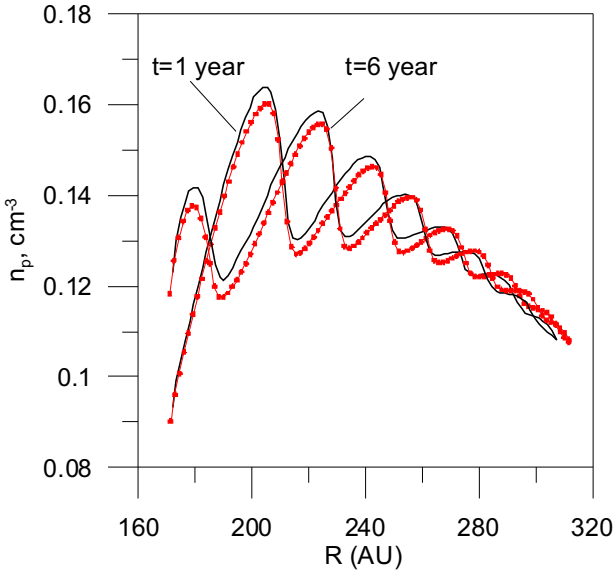

Figure 4.18: Comparison of the time-dependent self-consistent model results (solid curves) with the solution of the time-dependent Euler equation with the source terms (3) taken from the corresponding stationary solution (connected dotted). The figure presents the distribution of plasma number density in the upwind direction for two different moments in the solar cycle. The difference between the two models is a few percent. (After Izmodenov et al., 2005b.)

was shown that the multi-fluid description is less appropriate for the time-dependent case than for the stationary case because the Knudsen number is larger for the time-dependent problem.

In addition, Izmodenov et al. (2005b) have performed specific calculations of the time-dependent Euler equation with the source terms (4.13)-(4.15) taken from the corresponding stationary solution. The difference in plasma distribution with the self-consistent model is a few percent (Figure 4.18). Therefore, it was suggested that time-dependent multi-fluid models may produce results that are closer (but still different) to the kinetic time-dependent model in the case where the source terms are taken from the stationary solution.

4.8 Heliotail

Plasma and H atom distributions in the tail of the LIC/SW interaction region were not of interest until recently. However, modelling of the heliospheric interface provides answers to the two fundamental questions:

1. Where is the edge of the Solar System plasma?

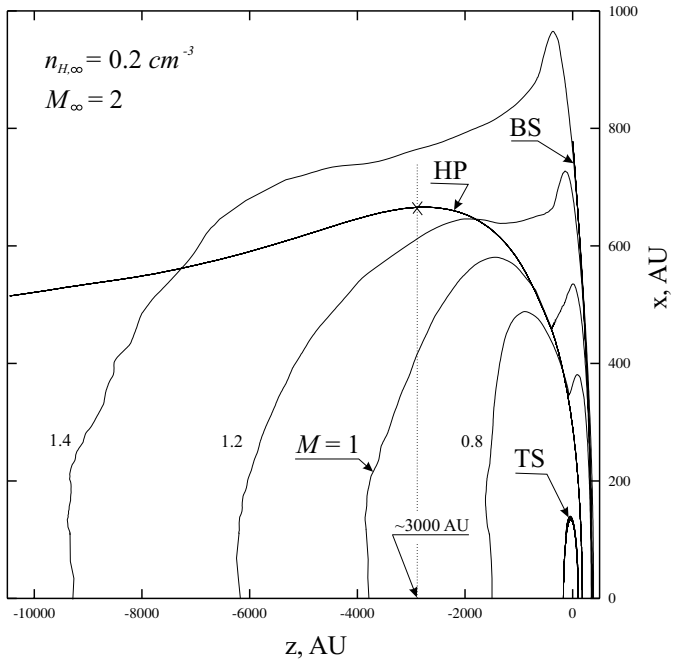

Figure 4.19: Isolines of the Mach number of the solar wind and interstellar plasma flows in the downwind direction. (After Izmodenov and Alexashov, 2003).

2. How far downstream does the solar wind influence the surrounding interstellar medium?

To supply an answer to the first question we need to define the Solar System plasma boundary. It is natural to assume that the heliospheric boundary is the heliopause which separates the solar wind and interstellar plasmas. This definition is not completely correct, because the heliopause is an open surface and, therefore, the heliosphere ends at infinity. To resolve the problem, and to address the second question, specific and detailed modelling of the structure of the tail region up to 50000 AU was performed by Izmodenov and Alexashov (2003), Alexashov and Izmodenov (2003), Alexashov et al. (2004b). It was shown that the charge exchange process qualitatively changes the solar wind – interstellar wind interaction in the tail region. The termination shock becomes more spherical and the Mach disk, reflected shock, and tangential discontinuity disappear. This result was obtained previously by Baranov ana Malama (1993), who performed calculations out to 700 AU in the heliotail. In addition, Alexashov et al. (2004b) found that the jumps in density and tangential velocity across the heliopause become smaller in the heliotail and disappear at about 3000 AU. Parameters of solar wind plasma and interstellar H atoms approach their interstellar values at large heliocentric distances. This allows an estimation of the influence of the solar wind and, therefore, the solar system size in the downwind direction to about 20000 - 40000 AU. An illustration of the results is shown in Figure 4.19. The figure shows isolines of the Mach

number up to 10000 AU. The solar wind plasma has a velocity of $\sim$ 100 km/s and a temperature of $\sim 1.5 \times 10^6$ K immediately after passing the TS. Then the velocity becomes smaller due to new protons injected by charge exchange and approaches the value of interstellar velocity. Since interstellar H atoms are effectively cooler compared with postshocked protons, the solar wind also becomes cooler. This makes the Mach number increase. At distances of $\sim$ 4000 AU the solar wind again becomes supersonic and the Mach number then approaches its interstellar value at $\sim$ 40000 - 50000 AU, where the solar wind gas-dynamic parameters become undistinguishable from undisturbed interstellar parameters. This result cannot be obtained in the absence of H atoms because the solar wind flow in the heliotail remains subsonic in that case.

4.9 New multi-component model of the heliospheric interface

The Baranov-Malama model described in Section 4.3 and more recent models described in Section 4.4-4.8 assume immediate assimilation of pickup protons into the solar wind plasma and consider the mixture of solar wind and pickup protons as a single component. However, it is clear from observations (e.g. Gloeckler and Geiss, 2004) that the pickup ions are thermally decoupled from the solar wind protons and should be considered as a separate population. Moreover, measured spectra of pickup ions show that their velocity distributions are not Maxwellian. Therefore, a kinetic approach should be used for this component. Theoretical kinetic models of pickup ion transport, stochastic acceleration and evolution of their velocity distribution function are now developed (Fisk, 1976; Isenberg, 1987; Bogdan et al., 1991; Fichtner et al., 1996; Chalov et al., 1997; le Roux and Ptuskin, 1998). However, these models are (1) restricted to the supersonic solar wind region, and (2) do not consider the back reaction of the pickup protons on the solar wind flow pattern, i.e. pickup protons are considered as test particles. Chalov et al. (2003, 2004a) have studied properties of pickup proton spectra in the inner heliosheath, but in its upwind part only. Several self-consistent multi-component models (Isenberg, 1986; Fahr et al. 2000; Wang and Richardson, 2001) were considered, but pickup ions in these models were treated in the fluid approximation which does not allow one to study kinetic effects.

Malama et al. (2006) presented a new kinetic-continuum model of the heliospheric interface. The new model retains the main advantage of the previous models, namely a rigorous kinetic description of the interstellar H atom component. In addition, it considers pickup protons as a separate kinetic component.

4.9.1 The model

Since the mean free path of H atoms, which is mainly determined by the charge exchange reaction with protons, is comparable to the characteristic size of the

heliosphere, their dynamics are governed by the kinetic equation for the velocity distribution function $f_{\rm H}(\boldsymbol{r}, \mathbf{w}_{\rm H}, t)$:

$$\frac{\partial f_{\rm H}}{\partial t} + \mathbf{w}_{\rm H} \cdot \frac{\partial f_{\rm H}}{\partial \mathbf{r}} + \frac{\mathbf{F}}{m_{\rm H}} \cdot \frac{\partial f_{\rm H}}{\partial \mathbf{w}_{\rm H}} = -\left(\nu_{\rm ph} + \nu_{\rm impact}\right) f_{\rm H}\left(\mathbf{r}, \mathbf{w}_{\rm H}\right)$$

$$-f_{\rm H} \cdot \sum_{i={\rm p,pui}} \int |\mathbf{w}_{\rm H} - \mathbf{w}_i| \sigma_{\rm ex}^{\rm HP} f_i\left(\mathbf{r}, \mathbf{w}_i\right) {\rm d}\mathbf{w}_i \tag{4.29}$$

$$+ \sum_{i={\rm p,pui}} f_i(\mathbf{r}, \mathbf{w}_{\rm H}) \int |\mathbf{w}_{\rm H}^* - \mathbf{w}_{\rm H}| \sigma_{\rm ex}^{\rm HP} f_{\rm H}(\mathbf{r}, \mathbf{w}_{\rm H}^*) {\rm d}\mathbf{w}_{\rm H}^*.$$

Here $f_{\rm p}\left(\mathbf{r}, \mathbf{w}_{\rm p}\right)$ and $f_{\rm pui}\left(\mathbf{r}, \mathbf{w}_{\rm pui}\right)$ are the local distribution functions of protons and pickup protons; $\mathbf{w}_{\rm p}$, $\mathbf{w}_{\rm pui}$ and $\mathbf{w}_{\rm H}$ are the individual proton, pickup proton, and H-atom velocities in the heliocentric rest frame, respectively; $\sigma_{\rm ex}^{\rm HP}$ is the charge exchange cross section of an H atom with a proton; $\nu_{\rm ph}$ is the photoionization rate; $m_{\rm H}$ is the atomic mass; $\nu_{\rm impact}$ is the electron impact ionization rate; and $\boldsymbol{F}$ is the sum of the solar gravitational force and the solar radiation pressure force.

All plasma components (electrons, protons, pickup protons, interstellar helium ions and solar wind alpha particles) are considered as media co-moving with bulk velocity $\boldsymbol{V}$. The plasma is quasi-neutral, i.e. $n_{\rm e} = n_{\rm p} + n_{\rm He^+}$ for the interstellar plasma and $n_{\rm e} = n_{\rm p} + n_{\rm pui} + 2n_{\rm He^{++}}$ for the solar wind. For simplicity the magnetic fields are ignored. While the interaction of interstellar H atoms with protons by charge exchange is important, this process is negligible for helium due to the small cross section. The system of governing equations for the sum of all ionized components is:

$$\begin{aligned} \frac{\partial \rho}{\partial t} + \nabla \cdot (\rho \mathbf{V}) &= q_1 \ , \\ \frac{\partial \rho \mathbf{V}}{\partial t} + \nabla \cdot \left(\rho \mathbf{V}\mathbf{V} + p\hat{I}\right) &= \boldsymbol{q}_2 \ , \\ \frac{\partial E}{\partial t} + \nabla \cdot \left([E + p]\, \mathbf{V}\right) &= q_3 + q_{3,\rm e} \ , \end{aligned} \tag{4.30}$$

Here $\rho = \rho_{\rm p} + \rho_{\rm e} + \rho_{\rm He} + \rho_{\rm pui}$ is the total density of the ionized component, $p = p_{\rm p} + p_{\rm e} + p_{\rm pui} + p_{\rm He}$ is the total pressure of the ionized component, $E = \rho\left(\varepsilon + \boldsymbol{u}^2/2\right)$ is the total energy per unit volume, and $\varepsilon = p/\left(\gamma - 1\right)\rho$ is the specific internal energy.

The expressions for the sources are the following:

$$q_1 = m_{\rm p} n_{\rm H} \cdot \left(\nu_{\rm ph} + \nu_{\rm impact}\right), \qquad n_{\rm H} = \int f_{\rm H}\left(\mathbf{w}_{\rm H}\right) {\rm d}\mathbf{w}_{\rm H},$$

$$\boldsymbol{q}_2 = \int m_{\rm p} \left(\nu_{\rm ph} + \nu_{\rm impact}\right) \mathbf{w}_{\rm H} f_{\rm H}(\mathbf{w}_{\rm H}) {\rm d}\mathbf{w}_{\rm H} +$$

$$\int\int m_{\rm p} v_{\rm rel} \sigma_{\rm ex}^{\rm HP}\left(v_{\rm rel}\right)\left(\mathbf{w}_{\rm H} - \mathbf{w}\right) f_{\rm H}\left(\mathbf{w}_{\rm H}\right) \sum_{i={\rm p,pui}} f_i\left(\mathbf{w}\right) {\rm d}\mathbf{w}_{\rm H} {\rm d}\mathbf{w},$$

$$q_3 = \int m_{\rm p}\left(\nu_{\rm ph} + \nu_{\rm impact}\right)\frac{\mathbf{w}_{\rm H}^2}{2} f_{\rm H}\left(\mathbf{v}_{\rm H}\right)\mathrm{d}\mathbf{w}_{\rm H} + \frac{1}{2}\int\int m_{\rm p} v_{\rm rel}\cdot$$

$$\cdot\sigma_{\rm ex}^{\rm HP}\left(v_{\rm rel}\right)\left(\mathbf{w}_{\rm H}^2 - \mathbf{w}^2\right) f_{\rm H}\left(\mathbf{w}_{\rm H}\right)\sum_{i={\rm p,pui}} f_i\left(\mathbf{w}\right)\mathrm{d}\mathbf{w}_{\rm H}\mathrm{d}\mathbf{w},$$

$$q_{3,{\rm e}} = n_{\rm H}\left(\nu_{\rm ph}E_{\rm ph} - \nu_{\rm impact}E_{\rm ion}\right),$$

$v_{\rm rel} = |\mathbf{w}_{\rm H} - \mathbf{v}|$ is the relative velocity of an atom and a proton, $E_{\rm ph}$ is the mean photoionization energy (4.8 eV), and $E_{\rm ion}$ is the ionization potential of H atoms (13.6 eV).

The system of equations for the velocity distribution function of H-atoms (Equation 4.29) and for mass, momentum and energy conservation for the total ionized component (Equations 4.30) is not self-consistent, since it includes the velocity distribution function of pickup protons. At the present time there is observational evidence (e.g. Gloeckler et al., 1993; Gloeckler, 1996; Gloeckler and Geiss, 1998) and theoretical estimates (e.g. Isenberg, 1986), which clearly show that pickup ions constitute a separate and very hot population in the solar wind. Even though some energy transfer from the pickup ions to the solar wind protons is now theoretically admitted in order to explain the observed heating of the outer solar wind (Smith et al., 2001; Isenberg et al., 2003; Richardson and Smith, 2003; Chashei et al., 2003; Chalov et al., 2004b), it constitutes no more than 5% of the pickup ion energy. The observations show also that the velocity distribution function can be considered as isotropic (fast pitch-angle scattering) except for some short periods in the inner heliosphere when the interplanetary magnetic field is almost radial.

So it is assumed here that the velocity distribution of pickup protons in the solar wind rest frame is isotropic, and it is determined through the velocity distribution function in the heliocentric coordinate system by the expression:

$$f_{\rm pui}^*\left(\mathbf{r}, w\right) = \frac{1}{4\pi}\int\int f_{\rm pui}\left(\mathbf{r}, \mathbf{v}\right)\sin\theta\mathrm{d}\theta\mathrm{d}\phi\ . \tag{4.31}$$

Here $\mathbf{v} = \mathbf{V} + \mathbf{w}$, $\mathbf{v}$ and $\mathbf{V}$ are the velocity of a pickup proton and bulk velocity of the plasma component in the heliocentric coordinate system, $\boldsymbol{w}$ is the velocity of the pickup proton in the solar wind rest frame, and $(w,\, \theta,\, \phi)$ are coordinates of $\mathbf{w}$ in the spherical coordinate system. The equation for $f_{\rm pui}^*\left(\mathbf{r}, w\right)$ can be written in the following general form taking into account velocity diffusion but ignoring spatial diffusion, which is unimportant at the energies under consideration:

$$\frac{\partial f_{\rm pui}^*}{\partial t} + \mathbf{V}\cdot\frac{\partial f_{\rm pui}^*}{\partial \mathbf{r}} = \frac{1}{w^2}\frac{\partial}{\partial w}\left(w^2 D\frac{\partial f_{\rm pui}^*}{\partial w}\right) + \tag{4.32}$$

$$+\frac{w}{3}\frac{\partial f_{\rm pui}^*}{\partial w}\nabla\cdot\left(\mathbf{V}\right) + S\left(\mathbf{r}, w\right),$$

where $D(\mathbf{r}, w)$ is the velocity diffusion coefficient. The source term $S\left(\boldsymbol{r}; w\right)$ can be written as

$$S\left(\boldsymbol{r}; w\right) = \frac{1}{4\pi}\int\int \nu_{\rm ion}\left(\mathbf{w}\right) f_{\rm H}\left(\mathbf{r}, \mathbf{w} + \mathbf{V}\right)\sin\theta\mathrm{d}\theta\mathrm{d}\phi \tag{4.33}$$

$$-\frac{1}{4\pi}\int\int f^*_{\rm pui}\left(\mathbf{r},w\right)\nu_{\rm H}\left(\mathbf{w}\right)\sin\theta{\rm d}\theta{\rm d}\phi\ .$$

In equation (4.33) ν_{ion} and $\nu_{\rm H}$ are ionization rates:

$$\nu_{\rm ion}=\sum_{i={\rm pui,p}}\int\int\int f^*_i\left(\mathbf{r},w_i\right)\left|\mathbf{w}_i-\mathbf{w}\right|\times$$

$$\times\ \sigma^{\rm HP}_{\rm ex}\left(\left|\mathbf{w}_i-\mathbf{w}\right|\right)w_i^2{\rm d}w_i\sin\theta_i{\rm d}\theta_i{\rm d}\phi_i+\nu_{\rm ph}+\nu_{\rm impact},$$

$$\nu_{\rm H}=\int f_{\rm H}\left(\mathbf{r},\mathbf{v}_{\rm H}\right)\left|\mathbf{w}+\mathbf{u}-\mathbf{v}_{\rm H}\right|\sigma^{\rm HP}_{\rm ex}\left(\left|\mathbf{w}+\mathbf{u}-\mathbf{v}_{\rm H}\right|\right)\ {\rm d}\mathbf{v}_{\rm H}\ .$$

Although only stationary solutions of Equation (4.32) will be sought here, it is preferred to keep the first term in the equation to show its general mathematical structure. The effective thermal pressure of the pickup ion component is determined by

$$p_{\rm pui}=\frac{4\pi}{3}\int m_p w^2 f^*_{\rm pui}\left(\mathbf{r},w\right)w^2{\rm d}w\ . \tag{4.34}$$

The continuity equations for He^+ in the interstellar medium and for alpha particles in the solar wind were solved. Then proton number density can be calculated as $n_{\rm p}=\left(\rho-m_{\rm He}n_{\rm He}\right)/m_{\rm p}-n_{\rm pui}$. Here $n_{\rm He}$ denotes the He^+ number density in the interstellar medium, and He^{++} the number density in the solar wind.

In addition to the system of equations (4.30), (4.29), (4.32), the heat transfer equation for the electron component was solved:

$$\frac{\partial\rho_{\rm e}\varepsilon_{\rm e}}{\partial t}+\nabla\cdot\left(\left[\rho_{\rm e}\varepsilon_{\rm e}\right]\mathbf{V}\right)= \tag{4.35}$$

$$-p_{\rm e}\nabla\cdot\boldsymbol{u}+q_{3,{\rm e}}+Q_{\rm e,p}+Q_{\rm e,pui}\ .$$

Here $\varepsilon_{\rm e}=p_{\rm e}/\left(\gamma-1\right)\rho_{\rm e}$ is the specific internal energy of the electron component, $Q_{\rm e,p}$ and $Q_{\rm e,pui}$ are the energy exchange terms of electrons with protons and pickup ions, respectively.

To complete the formulation of the problem one should specify: (a) the diffusion coefficient $D\left(\boldsymbol{r},w\right)$, (b) the exchange terms $Q_{\rm e,p}$ and $Q_{\rm e,pui}$, (c) the behaviour of pickup protons and electrons at the termination shock. In principle, our model allows us to make any assumptions and verify any hypothesis regarding these parameters. Moreover, the diffusion coefficient $D\left(\mathbf{r},w\right)$ depends on the level of solar wind turbulence, and the equations describing the production (say, by pickups) and evolution of the turbulence need to be added to Equations (4.29)-(4.35). This work is still in progress and will be advanced in the nearest future.

In this paper as simple a model as possible is considered. Coefficient D is chosen to be zero. While velocity diffusion is not taken into account, suprathermal tails in the velocity distributions of pickup protons are formed as will be shown below.

It is believed that the thickness of the termination shock ramp lies in the range from the electron inertial length up to the ion inertial length: $c/\omega_{\rm e}\le L_{\rm ramp}\le c/\omega_{\rm p}$, where $\omega_{\rm e,p}=\left(4\pi n_{\rm e,p}e^2/m_{\rm e,p}\right)^{1/2}$ are the electron and proton plasma frequencies

(see discussion in Chalov, 2005). Since this thickness is less than the gyro-radius of a typical pickup proton in front of the termination shock by at least a factor of 10, the shock is considered here as a discontinuity. In this case the magnetic moment of a pickup ion after interaction with a perpendicular or quasi-perpendicular shock is the same as it was before the interaction (Toptygin, 1980; Terasawa, 1979). The only requirement is that the mean free path of the ions is larger than their gyro-radius (weak scattering). For perpendicular or near perpendicular parts of the termination shock, conservation of the magnetic moment leads to the following jump condition at the shock (Fahr and Lay, 2000):

$$f^*_{2,\mathrm{pui}}(\mathbf{r}, w) = C^{-1/2} f^*_{1,\mathrm{pui}}\left(\mathbf{r}, w/\sqrt{C}\right) \tag{4.36}$$

where $C = \rho_2/\rho_1$ is the shock compression. Although the termination shock can be considered as perpendicular at their nose and tail parts only (Chalov and Fahr, 1996; 2000; Chalov, 2005), it is nevertheless assumed here for the sake of simplicity that Equation (4.36) is valid everywhere at the shock. It should be emphasized that we are forced to adopt this condition in the axisymmetric model because taking into account the real geometry of the large-scale magnetic field near the shock requires one to take into account (1) the three-dimensional structure of the interface, (2) reflection of pickup ions at the termination shock due to the abrupt change in the magnetic field strength and direction. The reflection is a very important process to inject ions into anomalous cosmic rays, and so this complication will be considered in future work. Note that the concept of magnetic moment conservation is only one of the possible scenarios for the behaviour of pickup ions at the termination shock. Other possibilities will also be considered in the future.

It is assumed also that $Q_{\mathrm{e,pui}} = 0$ and $Q_{\mathrm{e,p}}$ is such that

$$T_{\mathrm{e}} = T_{\mathrm{p}} = T_{\mathrm{He}^{++}}$$

everywhere in the solar wind. Physically this assumption means that the thermal energy exchange between the components occurs at characteristic distances that are much smaller than the characteristic scale of the problem. Because of this assumption, there is no need to solve Equations (4.35). Nevertheless, this equation is solved in order to check the numerical accuracy of our solution. Later, it is planned to explore models with more realistic D, $Q_{\mathrm{e,pui}}$ and $Q_{\mathrm{e,p}}$ and different microscopic theories can be tested.

The boundary conditions for the charged component are determined by the solar wind parameters at the Earth's orbit and by parameters in the undisturbed LIC. At the Earth's orbit it is assumed that the proton number density is $n_{\mathrm{p,E}} = n_{e,E} = 7.72$ cm^{-3}, the bulk velocity is $u_{\mathrm{E}} = 447.5$ km/s, and the ratio of alpha particles to protons is 4.6%. These values were obtained by averaging the solar wind data over the two last solar cycles. The OMNI-2 compilation of the available solar wind data was used (`http://omniweb.gsfc.nasa.gov/index.html`). The velocity and temperature of the pristine interstellar medium were recently determined from the consolidation of all available experimental data (Möbius et al., 2004; Witte, 2004; Gloeckler et al., 2004; Lallement et al., 2004a,b). $V_{\mathrm{LIC}} = 26.4$ km/s and $T_{\mathrm{LIC}} = 6527$ K are adopted in this paper.

For the local interstellar H atom, proton and helium ion number densities, it is assumed that $n_{\mathrm{H,LIC}} = 0.18$ cm^{-3}, $n_{\mathrm{p,LIC}} = 0.06$ cm^{-3} and $n_{\mathrm{He^+,LIC}} = 0.009$ cm^{-3}, respectively (for argumentation see, e.g., Izmodenov et al., 2003, 2004). The velocity distribution of interstellar atoms is assumed to be Maxwellian in the unperturbed LIC. For the plasma component at the outer boundary in the tail, soft outflow boundary conditions were used. For details of the computations in the tail direction see Section 4.8 of this Chapter and Izmodenov and Alexashov (2003) and Alexashov et al. (2004b).

To solve the system of governing Euler equations for the plasma component, the second order finite volume Godunov type numerical method was used (Godunov et al., 1979; Hirsch, 1988). To increase the resolution properties of the Godunov scheme, a piecewise linear distribution of the parameters inside each cell of the grid is introduced. To achieve the TVD property of the scheme the minmod slope limiter function is employed (Hirsch, 1988). An adaptive grid as in Malama (1991) was employed. The grid fits the termination shock, the heliopause and the bow shock. The kinetic equation (4.29) was solved by the Monte-Carlo method with splitting of trajectories following Malama (1991). The Fokker-Planck type equation (4.32) for the pickup proton velocity distribution function is solved by calculating statistically relevant numbers of stochastic particle trajectories (Chalov et al., 1995). To get a self-consistent solution of the plasma Euler equations (4.30), the kinetic equation (4.29), and the Fokker-Planck type equation (4.32), the method of global iterations suggested by Baranov et al. (1991) was employed.

4.9.2 Results

Figures 4.20-4.24 present the main results obtained in the frame of our new multi-component model described in the previous section. The shapes and locations of the termination shock (TS), heliopause (HP) and bow shock (BS) are shown in Figure 4.20. For the purposes of comparison the positions of the TS, HP, and BS are also shown for the case when pickup and solar wind protons are treated as a single fluid. Later we refer to this model as the Baranov-Malama (B&M) model. Two different cases obtained with the B&M model are shown. In the first case ionization by electron impact is taken into account, while this effect is omitted in the second case. The only (but essential) difference between the B&M model and our new model, considered in this paper, is that the latter model treats pickup protons as a separate kinetic component. As seen from Figure 4.20 the differences in the locations of the TS, HP, and BS predicted by the new and the B&M models are not very large in the upwind direction. The TS is 5 AU further away from the Sun in the new model compared to the B&M models. The HP is closer by 12 AU. The effect is much more pronounced in the downwind direction where the TS shifts outward from the Sun by $\sim$70 AU in the new model. Therefore, the inner heliosheath region is thinner in the new model compared to the B&M model. This effect is partially connected with the lower temperature of electrons and, therefore, with a lower electron impact ionization rate in this region. Indeed, new pickup protons created by electron impact deposit additional energy and, therefore, pressure in the region of their origin, i.e. in the inner heliosheath. The additional pressure pushes the heliopause outward and the TS towards the Sun. Even though our multi-

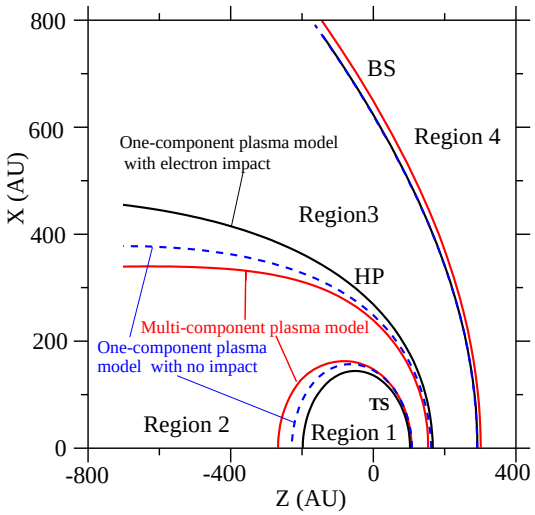

Figure 4.20: The termination shock, heliopause and bow shock shown for three models of the heliospheric interface: (1) new multi-component model, (2) Baranov and Malama model, (3) Baranov and Malama model with no electron impact.

component model takes into account ionization by electron impact, this is not as efficient as in one-fluid models (like B&M) due to the lower electron temperature in the heliosheath. Excessively high electron temperatures which are predicted by the one-fluid models in the outer heliosphere are connected with the physically unjustified assumption of the immediate assimilation of pickup protons into the solar wind plasma.

However, the HP is closer to the Sun and the TS is further from the Sun in the new multi-component model even in the case when electron impact ionization is not taken into account. This is because the solar wind protons and pickup protons are treated in the new multi-component model as two separate components. Indeed, hot energetic atoms (ENAs), which are produced in the heliosheath by charge exchange of interstellar H atoms with both the solar wind protons and pickup protons heated by the TS, escape from the inner heliosheath easily due to their large mean free paths. These ENAs remove (thermal) energy from the plasma of the inner heliosheath and transfer the energy to other regions of the interface (e.g., into the outer heliosheath). In the case of the new model there are two parenting proton components for the ENAs – the original solar protons and pickup protons. In the B&M model these two components are mixed to one. As a result, the ENAs remove energy from the inner heliosheath more efficiently in the case of the multi-component model than in the case of the B&M model. A similar effect was observed for multi-fluid models of H atoms in the heliospheric interface described in detail by Alexashov and Izmodenov (2005).

To gain a better insight into the results of the new model and its potential possibilities to predict and interpret observational data, the heliospheric protons (original solar and pickup protons) are divided into five types, and H atoms into

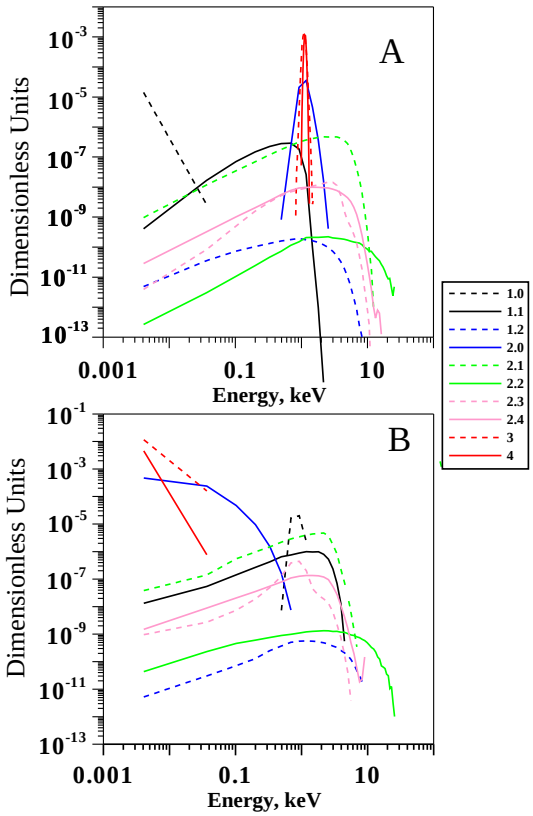

Figure 4.21: The source term S (Equation 4.33) from different populations of H atoms as a function of energy shown in the supersonic solar wind at 5 AU (A) and in the inner heliosheath (B).

ten populations described in Table 4.5. The first index in the notation of an H-atom population is the number of the region, where the population was created, i.e. populations 1.0-1.2 are the H atoms created in the supersonic solar wind (region 1, see Figure 4.20), populations 2.0-2.4 are the H atoms created in the inner heliosheath (region 2), populations 3 and 4 are secondary and primary interstellar atoms. Definitions of the two last populations are the same as in the B&M model. The second index denotes the parent charged particles (protons), i.e. from 0 to 4.

Original solar wind protons are denoted as type 0. Protons of this type are cold compared to the normal pickup protons in the solar wind. The pickup protons, which have characteristics close to the original solar wind protons, are also added to type 0. These are pickup protons created in the supersonic solar wind (region 1) from H atoms of population 1.0 (this population forms a so-called neutral solar wind, e.g., Bleszynski et al., 1992) and pickup protons created in the inner heliosheath (region 2) from H atoms of populations 2.0, 3, and 4. The type 0 is formed in such a way that (1) its thermal pressure is much less than the dynamic pressure everywhere in the heliosphere and, therefore, unimportant; (2) we are not interested

Table 4.5: Description of types of protons and populations of H atoms introduced.

Type number	Proton type description
0	'cold proton type' consisting of: original solar wind protons + protons created in region 1 from atoms of population 1.0 + protons created in region 2 from atoms of populations 2.0, 3, 4
1	pickup protons created in region 1 from atoms of populations 1.1, 2.0, 3, 4
2	pickup protons created in region 1 from atoms of populations 1.2, 2.1-2.4
3	pickup protons created in region 2 from atoms of populations 1.0, 1.1
4	pickup protons created in region 2 from atoms of populations 1.2, 2.1-2.4
Population number	**H atoms created in:**
1.0	region 1 from protons of type 0
1.1	region 1 from pickup protons of type 1
1.2	region 1 from pickup protons of type 2
2.0	region 2 from protons of type 0
2.1	region 2 from pickup protons of type 1
2.2	region 2 from pickup protons of type 2
2.3	region 2 from pickup protons of type 3
2.4	region 2 from pickup protons of type 4
3	secondary interstellar atoms (as previously)
4	primary interstellar atoms (as previously)

in details of the velocity distribution of this type of proton and assume that it is Maxwellian. The rest of the pickup protons are divided into four types: two are those pickup protons that are created in region 1 (supersonic solar wind), and the others are pickup protons created in region 2 (inner heliosheath). In each region of birth we separate pickup protons into two additional types depending on their energy (more precisely, parent atoms). For instance, type 1 is the ordinary pickup proton population which is created in the supersonic solar wind from primary and secondary interstellar atoms and then convected into the inner heliosheath. Type 2 is also created in the supersonic solar wind but, in contrast to type 1, from energetic atoms. Among pickup protons created in the inner heliosheath, type 4 are more energetic than type 3. Thus, two types of pickup protons (1 and 2) exist in the supersonic solar wind and four (1-4) in the inner heliosheath, of which types 2 and 4 are more energetic than 1 and 3. A more detailed description of the properties of the different types of pickup protons will be given below (Figures 4.22-4.23).

One should keep in mind that at any place in the heliosphere real pickup protons constitute a full distribution and they are not divided into different types as we have introduced here. However, and this is very important, the pickup protons

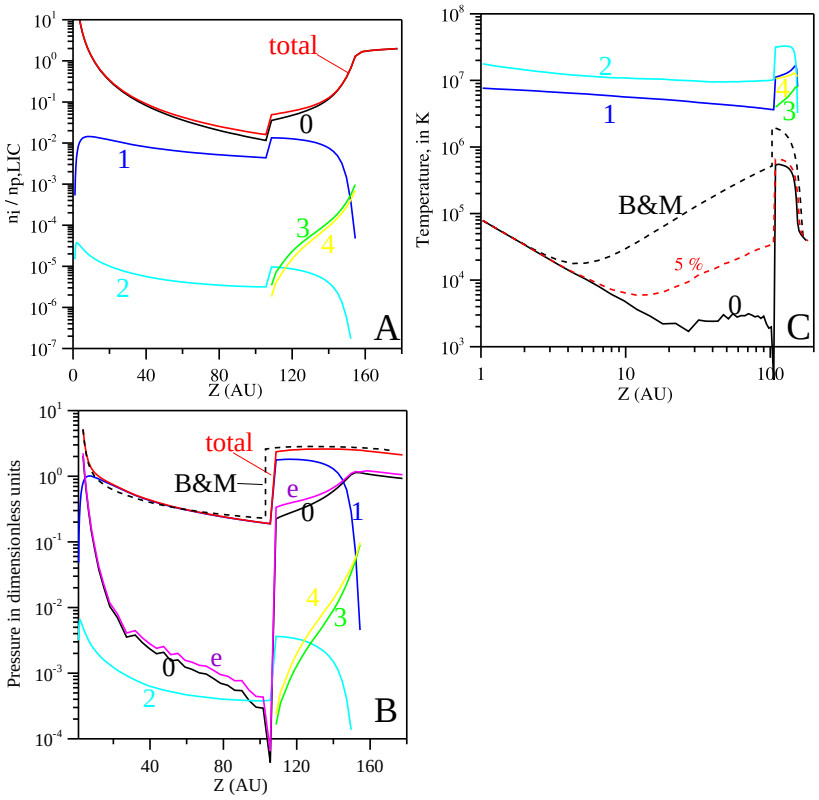

Figure 4.22: Number densities (A), thermal pressures (B), and temperatures (C) of different types of protons. Curves are labelled with proton types.

have a rather broad energy spread and, as we show below, particles with different places of birth and parent atoms prevail in a particular energy range according to our separation into the different types. The same is valid for H atoms. Thus, one of the main advantages of our new model is the theoretical possibility of predicting solar wind plasma properties in the outer parts of the heliosphere (including the inner heliosheath) through observations of pickup protons and hydrogen atoms in different energy ranges. Note that even without this rather complicated separation of particles into different types and populations but in the case when all pickup protons are treated as a distinct kinetic component (the simplest version of our model), the plasma flow pattern, positions, and shapes of the TS, HP, and BS are essentially the same.

As a useful illustration of the above, we present the calculated source term S (see Equation 4.33) of pickup protons in the supersonic solar wind and in the heliosheath in Figure 4.21. It is apparent that the relative contributions of different H atom populations to pickup protons are essentially different. In the supersonic solar wind (Figure 4.21A) narrow peaks near 1 keV are created by populations 2.0, 3, and 4. These populations are seeds for the major type of pickup protons,

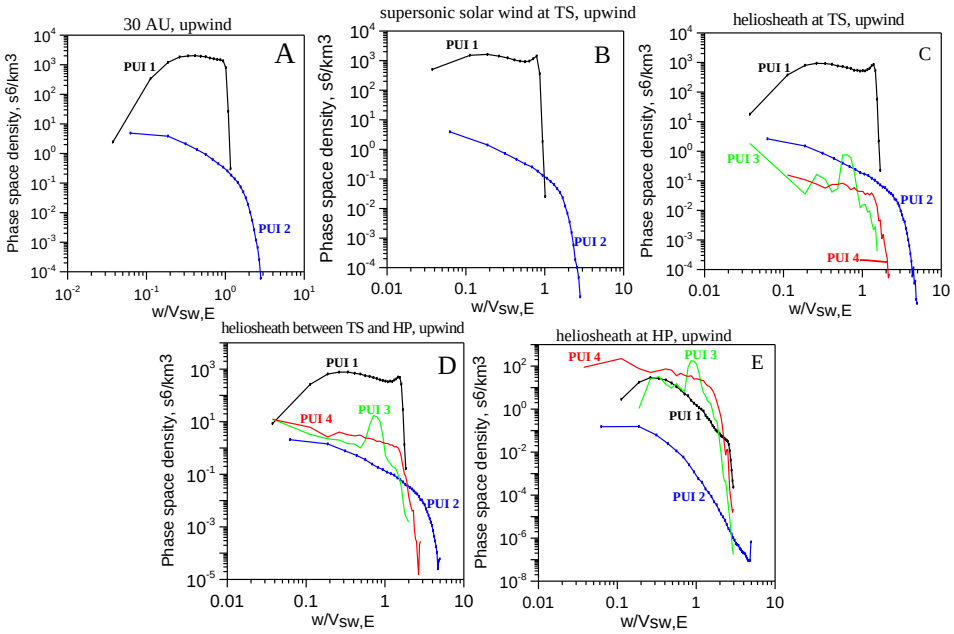

Figure 4.23: Phase space densities of different types of protons in the supersonic solar wind at 30 AU (A), upstream (B) and downstream (C) of the termination shock, inside the inner heliosheath (D) and at the heliopause (E). All curves are shown for the upwind direction.

which we denote as type 1. Pickup protons created from population 1.1 are also added to type 1 due to the lack of high energy tails in their distributions. Pickup protons created from H atoms of populations 1.2, 2.1-2.4 form type 2, which is more energetic compared to type 1 (see also argumentation above). A similar discussion can be applied to pickup protons created in the inner heliosheath.

It is important to emphasize here again that the main results of our model do not depend on the way in which we divide H atoms and pickup ions into populations and types. Such a division has two principal goals, namely, (1) to have a clearer insight into the origin and nature of the pickup ions measured by SWICS/Ulysses and ACE (Gloeckler and Geiss, 2004) and ENAs that will be measured in the near future (McComas et al., 2004, 2006b), and (2) to obtain better statistics in our Monte Carlo method with splitting of trajectories (Malama 1991) when we calculate high energy tails in the distributions of pickup protons and H atoms that are several orders of magnitude lower in density than the bulk of particles.

Number densities, pressures, and temperatures for the types of charged particles introduced are shown in Figure 4.22. It can be seen (Figure 4.22A) that the protons of type 0 (recall that these protons are mainly of solar origin) dominate by number density everywhere in the heliosphere, while type 1 pickup protons constitute up to 20% of the total number density in the vicinity of the TS. Approaching the HP, the number densities of types 1 and 2 decrease, since in accordance with our notation

these types are created in the supersonic solar wind only. When the pickup protons are convected in the regions behind the TS, types 1 and 2 experience losses due to charge exchange with H atoms. New pickup protons created in the inner heliosheath as a result of this reaction have different properties from the original pickup protons (see below), and we assign them to types 3 and 4. The number densities of these types increase towards the HP.

While the solar wind protons (type 0) are in excess in the number density, pickup protons are generally much hotter (see Figure 4.22C), and, as a consequence, the thermal pressure of type 1 dominates in the outer parts of the supersonic solar wind and in the inner heliosheath. Downstream of the TS this pressure is almost an order of magnitude larger than the pressure of type 0. As would be expected, the temperatures of types 2 and 4 are much larger than those of types 1 and 3, respectively. The temperature of the solar wind protons of type 0 decreases adiabatically out to 20 AU. Then the temperature becomes so low that the energy transferred to the solar wind by photoelectrons becomes non-negligible. This effect results in the formation of a plateau in the spatial distribution of the proton temperature in the region from 20 AU up to the TS. Figure 4.22C presents the proton temperature calculated with the B&M model for comparison. A highly unrealistic increase in the temperature is connected to the unrealistic assumption of immediate assimilation of pickup protons into the solar wind. Our new model is free of this assumption but it allows us to take into account some energy transfer between pickup and solar wind protons. The curve denoted as "5%" in Figure 4.22C shows the results of calculations, where we simply assume that 5% of the thermal energy of pickup protons is transferred to the solar wind protons (to type 0). For pickup protons it is assumed that their initial velocities (in the solar wind rest frame) of newly injected pickup protons are ∼2.5% smaller than the solar wind bulk velocity. The curve denoted as "5%" is qualitatively very similar to the Voyager 2 observations, which clearly show some increase in the proton temperature in the outer heliosphere. More prominent mechanisms of energy transfer between pickup and solar wind protons based on real microphysical background will be included in the model in the future.

Velocity distribution functions (in the solar wind rest frame) for the four types of pickup protons are shown in Figure 4.23 for different heliocentric distances in the upwind direction. All distributions are presented as functions of the dimensionless speed $w/V_{\mathrm{SW,E}}$, where $V_{\mathrm{SW,E}}$ is the solar wind speed at the Earth's orbit. In the supersonic solar wind (Figure 4.23A,B) type 1 is dominant at energies below about 1 keV ($w < V_{\mathrm{SW,E}}$), while the more energetic type 2 is dominant for energies above 1 keV ($w > V_{\mathrm{SW,E}}$). As was shown for the first time by Chalov and Fahr (2003), this energetic type of pickup proton (secondary pickup protons) created in the supersonic solar wind from energetic hydrogen atoms may contribute to the quiet-time suprathermal tails observed by SWICS/Ulysses and ACE instruments (Gloeckler, 1996; Gloeckler and Geiss, 1998). Downstream of the TS up to the heliopause (Figure 4.23C-E) the high-energy tails are more pronounced. The high-energy pickup ions form an energetic population of H atoms known as ENAs (e.g. Gruntman et al., 2001).

As we have discussed above and as can be seen from Figure 4.23, the pickup protons of type 1 prevail throughout the heliosphere except in a region near the

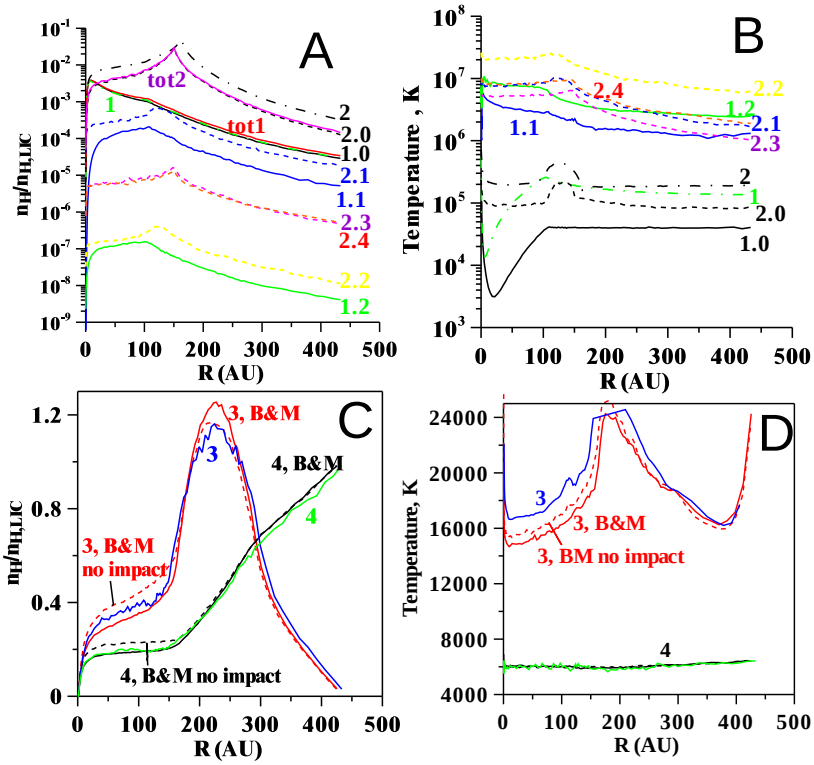

Figure 4.24: Number densities of H atom populations 1 and 2 (A) and populations 3 and 4 (C), and temperatures of these populations (B and D, respectively) as functions of heliocentric distance. Number densities and temperatures obtained with the Baranov and Malama (1993) model denoted as B&M and "B&M no impact" are shown for comparison. The sum of the number densities of populations 1.0,1.1 and 1.2 are shown as curve 'tot1'. The sum of the number densities of populations 2.0-2.4 are shown as curve 'tot2'.

HP. In the supersonic solar wind the velocity distributions of these pickup protons are close to the distributions obtained by Vasyliunas and Siscoe (1976), who also ignored velocity diffusion. However, our distributions are different, since in our model (1) the solar wind speed varies with the distance from the Sun, (2) the spatial behavior of the ionization rate is more complicated, (3) thermal velocities of H atoms are taken into account, and (4) the set of parent atoms is more varied (see Table 4.5). Note that we are forced to calculate the velocity distribution functions in the supersonic solar wind with a very high accuracy taking into account all above-mentioned effects self-consistently, since the proton temperature is several orders of magnitude lower than the temperature of the pickup protons (see Figure 4.22C) and even small numerical errors in the temperature of the pickup protons can result in negative temperatures for the solar wind protons.

Figure 4.24 presents the number densities and temperatures of H atom popula-

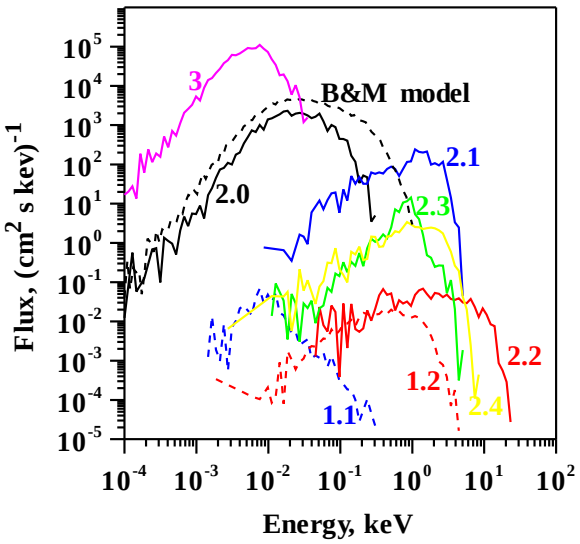

Figure 4.25: Fluxes of H atoms of populations 1.1, 1.2, 2.0-2.4, and 3 at 1 AU in the upwind direction as functions of energy.

tions created inside (Figure 4.24A and 4.24B) and outside the heliopause (Figure 4.24C and 4.24D). The sum of the number densities of populations 1.0, 1.1, 1.2 is denoted as 'tot1', the sum of the number densities of populations 2.0-2.4 is denoted as 'tot2'. For comparison we present the number densities of populations 1 and 2 of the B&M model (denoted as curves 1 and 2). Curves 'tot1' and '1' coincide, while curves 'tot2' and '2' are noticeably different. The B&M model overestimates the total number density of populations 2.0-2.4. This is connected with the fact that 'temperatures' (as measures of the thermal energy) of populations 2.1-2.4 are far above the temperature of population 2 in the B&M model. Inside 20 AU, population 1.0 dominates in the number density, while outside 20 AU population 2.0 becomes dominant. Figure 4.25 presents differential fluxes of different populations of H atoms at 1 AU. It can be seen that different populations of H atoms dominate in different energy ranges. At the highest energies above 10 keV, population 2.2 dominates. This population consists of atoms created in the inner heliosheath from hot pickup protons of type 2. Population 2.1 dominates in the energy range 0.2-6 keV. This population consists of atoms created in the inner heliosheath from hot pickup protons of type 1. Since both populations are created in the inner heliosheath, the measurements of these energetic particles as planned by IBEX will provide robust information on the properties of the inner heliosheath and, particulary, on the behaviour of pickup ions in this region. Note also that there is a significant difference in the ENA fluxes predicted in the frame of the one- and the multi-component models.

Returning to Figures 4.24C and 4.24D, the filtration factor, i.e. the amount of interstellar H atoms penetrating through the interface, and the temperature of population 3 are noticeably different in the new multi-component model than the B&M

model. This could lead to changes in interpretation of those observations, which require knowledge of the interstellar H atom parameters inside the heliosphere, say at the TS.

4.9.3 Summary

The new self-consistent kinetic-continuum model by Malama et al. (2006) includes the main advantage of our previous models, i.e. a rigorous kinetic description of the interstellar H atom flow and, in addition, takes into account pickup protons as a separate kinetic component. The new model is very flexible and allows one to test different scenarios for the pickup component inside, outside, and at the termination shock. The model allows one to treat electrons as a separate component and to consider different scenarios for this component. We have created a new tool for the interpretation of pickup ions and ENAs as well as all diagnostics, which are connected with the interstellar H atom component. The new model requires a more exact description of the physical processes involved than previous non-self-consistent models. It is shown that the heliosheath becomes thinner and that the termination shock is located further away from the Sun in the new model than in the B&M model. The heliopause, however, is closer to the Sun.

The main methodological advances made in the reported model, which were not discussed in this paper, are that we have successfully applied the Monte Carlo method with splitting of trajectories (Malama, 1991) to non-Maxwellian velocity distribution functions of pickup protons. The splitting of trajectories allows us to improve the statistics of our method and to calculate differential fluxes of ENAs at 1 AU with a high level of accuracy. We have shown that ENAs created from different types of pickup protons dominate in different energy ranges, which allows us to determine the nature of the heliosheath plasma flow.

4.10 Predictions and interpretations of spacecraft experiments

One of the main goals of theoretical studies of the heliospheric interface is to predict the results of future space experiments and to interpret the measurements already available from spacecraft exploring the outer regions of the heliosphere. The major physical phenomena that were predicted (and confirmed by space experiments later) or were explained in the frame of the kinetic-hydrodynamic models of the SW/LIC interaction, can be summarized as follows:

- The existence of the heliospheric interface itself (confirmed by many observations).

- The existence of the hydrogen wall (i.e. increased number density) around the heliosphere (confirmed by HST/GHRS and HST/STIS experiments in Lyman-α absorption, and Voyager 1 in Lyman-α emission).

- The existence and location of the termination shock at 90-100 AU depending on the solar wind conditions (confirmed by Voyager 1 crossing the TS at 94 AU in December 2004).
- The heating and deceleration of the interstellar hydrogen atoms in the heliospheric interface (confirmed by SOHO/SWAN experiments).
- The slowdown of the solar wind in the distant solar wind due to charge exchange between the solar wind protons and the interstellar protons (confirmed by Voyager 2 plasma experiment).
- The asymmetry of the heliospheric interface region due to the influence of the interstellar magnetic field (indirectly confirmed by SOHO/SWAN experiment).
- Filtration of interstellar atoms of hydrogen and oxygen in the interface.
- The fluctuations (within 10%) of H atom number density at large heliocentric distance (evidence in backscattered solar Lyman-α data from distant spacecraft Voyager 1/2, Pioneer 10).
- The disturbance of the interstellar gas in front of the termination shock by ENAs of the heliospheric origin (no space experiments that can confirm/disprove the prediction yet).
- The existence of the very distant tail in the downwind direction (no space experiments that can confirm/disprove the prediction yet).

In the next section we illustrate some physical phenomena from the list above.

The hydrogen wall

The hydrogen wall is an example where the physical phenomenon was first predicted theoretically by Baranov et al. (1991), but the experimental confirmation of its existence came only 5 years later.

As was described in Section 4.3 the "hydrogen wall" is created by the secondary interstellar H atoms. These atoms originate in the region between the bow shock and the heliopause by charge exchange. The interstellar protons are decelerated and heated in the region (compared to the local interstellar gas). The secondary H atoms are also decelerated and heated compared to the original interstellar component (e.g. Figure 4.4). The absorption produced by this secondary H atom component should be broader and Doppler-shifted (by a few km/s) as compared to the absorption in the LIC. Since the column number density of the heliospheric hydrogen is much smaller than the interstellar H column number density, one could expect to detect the heliospheric absorption only because it is Doppler-shifted and broader. This detection is possible towards nearby stars, when the interstellar absorption is not too large.

Linsky and Wood (1996) have discovered hydrogen wall absorption for the first time in the spectra measured by the GHRS instrument onboard the Hubble Space Telescope (HST) spacecraft toward α Centauri. A schematic of these observations

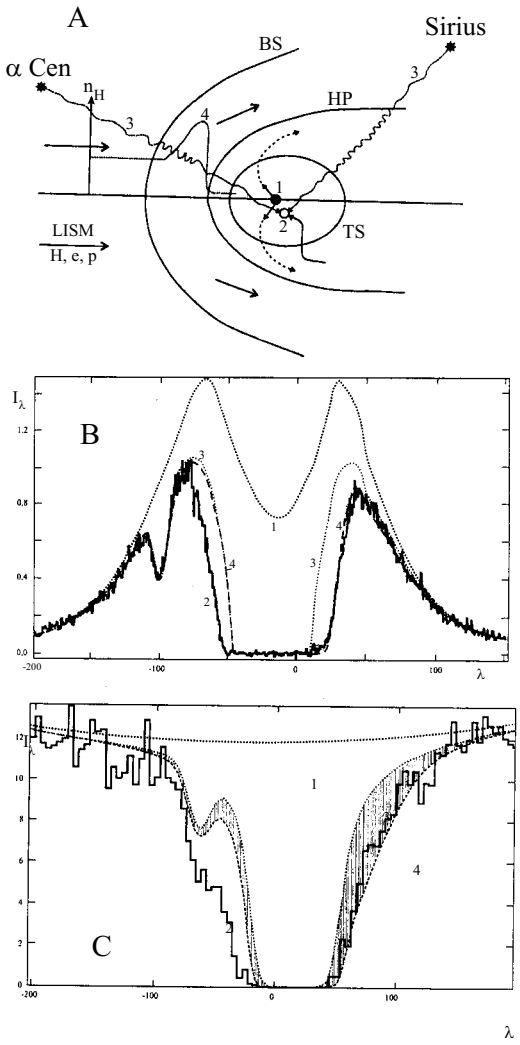

Figure 4.26: **A:** Schematics of an experiment on the Lyman-α absorption spectra measurements towards nearby stars; 1 is the Sun; 2 is an instrument that measures the spectra; 3 is the direction towards Sirius; 4 is the direction toward α Cen, and 5 is the hydrogen wall. **B:** Lyman-α absorption towards α Cen: 1 is the α Cen emission spectrum; 2 is the absorption spectrum measured by HST/GHRS; 3 is the spectrum after the absorption by hydrogen atoms in the LISM, and 4 is the spectrum obtained taking into account the heliospheric absorption in the hydrogen wall region. **C:** Lyman-α absorption toward Sirius. Designations are the same as for α Cen.

is shown in Figure 4.26A. If the emission spectrum of a star (say, α Cen) is known, then the instrument at point 2 in Figure 4.26 (point 1 coincides with the Sun)

receives spectra that include the absorption produced by the gas between the Sun and α Cen along the line of sight (line 3). This gas includes the interstellar and heliospheric atomic hydrogen. Most of the absorption occurs in the interstellar gas, while the right side of the absorption spectra (Figure 4.26B) could be attributed only to the absorption in the heliospheric hydrogen wall (4 in 4.26A) because the right side corresponds to a Doppler redshift (the motion of the interstellar H atoms is directed towards the instrument). The maximum intensity of the hydrogen wall is associated with the upwind direction. For this reason, the hydrogen wall absorption is mostly detectable in the upwind direction. HST/STIS measurements of absorption spectra toward another star, 36Oph, have confirmed the presence of the H wall (Wood et al., 2000).

The absorption spectrum obtained by HST/GHRS (Figure 4.26C) toward Sirius – the line of sight that has an angle of 139° with respect to the upwind direction – was analyzed by Izmodenov et al. (1999b). The hydrogen wall is very low in this direction and it does not produce detectable absorption. However, the heliospheric absorption exists in this direction too. Izmodenov et al. (1999b) have shown that the absorption might be produced by the atoms of population 2, originating in the region of the inner heliosheath between the TS and HP. Later, by studying absorption spectra toward other stars, it was shown (Izmodenov et al., 2002) that there is a tendency for two-component (H atom and plasma) models to overestimate the absorption from the inner heliosheath. One of the possible reasons is the one-fluid plasma approach used in the model. Wood et al. (2007) have shown that the multi-component model of Malama et al. (2006) provides better (but still not complete!) agreement between the model and data.

It is interesting to note that the left side of the absorption spectra (Figure 4.26B,C) can be attributed to the absorption in hydrogen walls around the observed stars (Wood et al., 2000; Izmodenov et al., 1999b). The heliospheric and astrospheric absorption is discussed in Chapter 11 of this volume in detail.

The hydrogen wall's existence has been inferred from the Voyager UVS Ly α data (Quémerais et al., 2000, 2003; see, also, Chapter 9 in this volume). As a matter of fact, it has become clear that the Lyman-α intensity on the upwind side is incompatible with a constant density far from the Sun: there is a need for an H density increase far from the Sun, i.e. an H wall.

Experimental evidence for the heliospheric interface

The concept of the heliospheric interface, as a region between the termination shock and the bow shock, first introduced by Baranov et al. (1971), was completely ignored by experimentalists until 1985. However, during more than 20 years the experimental data obtained by spacecraft exploring the outer regions of the heliosphere have been interpreted invoking this concept. The question arises: What are the experimental data that bear evidence of the interface?

Even on the basis of the first measurements of H and He atom number densities from the backscattered solar radiation at 1216 and 584 Å wavelengths it could be inferred that in the heliosphere the ratio of He/H is about twice as large as in the interstellar medium. This fact can easily be explained by the presence of the heliospheric interface, where the interstellar H atoms are "filtrated" due to

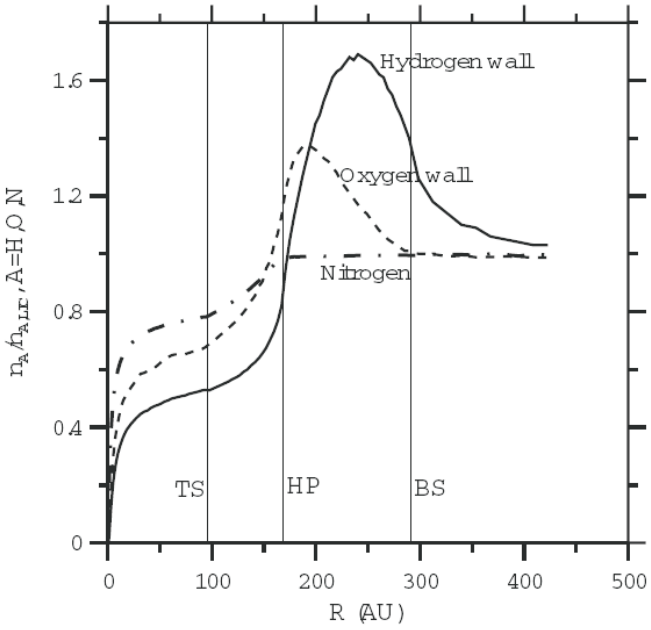

Figure 4.27: Distribution of hydrogen, oxygen and nitrogen in the upwind direction along the axis of symmetry. The penetration factor can be determined as $P = n_{\mathrm{A,TS}}/n_{\mathrm{A,LIC}}$. The filtration factor $F = 1 - P$.

their large charge exchange cross section (Figure 4.27) compared to that of He atoms which penetrate into the heliosphere from the interstellar medium without changing their parameters. However, the most weighty evidence for the presence of the interface was obtained by the SOHO and Ulysses spacecraft. For example, SOHO/SWAN measurements of backscattered solar Lyman-α with the hydrogen cells have shown (Costa et al., 1999; Quémerais et al., 1999) that in comparison with interstellar helium the mean hydrogen flow is decelerated by 3 to 5 km/s and heated by about 4000-5000 K. This is clear evidence of the secondary interstellar component (population 3 in Section 4.3.2).

The ground-based measurements of the H atom and proton number densities in the LIC usually led to estimates with an accuracy factor of 2 and 3-4, respectively. Since the proton number density in the circumsolar LISM determines to a considerable degree the interface filter efficiency, Izmodenov et al. (2003b) carried out a parametric study of the heliospheric interface structure within the model described in Section 4.4 for proton and H atom number densities ranging from 0.03 to 0.1 cm^{-1} for $n_{\mathrm{p,LIC}}$ and from 0.16 to 0.2 cm^{-3} for $n_{\mathrm{H,LIC}}$. For each ($n_{\mathrm{p,LIC}}$, $n_{\mathrm{H,LIC}}$) pair, the H atom number density $n_{\mathrm{H,TS}}$ near the termination shock can be calculated. This value can also be obtained on the basis of the measurements of the pickup protons onboard Ulysses, or on the basis of the measurement of the slow-down of the solar wind at large heliocentric distances performed onboard Voyager 2. An analysis of these measurements led to the estimate $n_{\mathrm{H,TS}} \sim 0.1000 \pm 0.005$

cm^{-3} near the TS. Comparison of this value with the results of the parametric study leads to a possible range for the ($n_{p,LIC}$, $n_{H,LIC}$) number densities. This range can be narrowed by invoking: (1) the estimate of the degree of He atom ionization obtained by the Extreme Ultraviolet Explorer (EUVE) along the lines of sight towards white dwarfs (Wolff et al., 1999), (2) the value of the He atom number density 0.015 cm^{-3} obtained by direct measurements onboard Ulysses and, (3) the interstellar H/He ratio of 10. As a result, a relation between $n_{p,LIC}$ and $n_{H,LIC}$ can be obtained; using this relation, together with the results of a parametric study (Izmodenov et al., 2003b) leads to estimates of the most probable interstellar hydrogen atom and proton number densities in the vicinity of the Sun: $n_{p,LIC} = 0.05 \pm 0.015$ cm^{-3} and $n_{H,LIC} = 0.185 \pm 0.01$ cm^{-3}.

It is interesting to note that the direct measurements of the He velocity and temperature onboard Ulysses (Witte, 2004) showed that the values of these parameters are very close to those in the LIC (Lallement, 1996; Lallement, 2001), as distinct from the hydrogen parameters changing across the heliospheric interface.

Filtration of interstellar hydrogen, oxygen, and nitrogen in the interface

The Ulysses spacecraft has also measured the pickup ions of other chemical elements. Using these measurements, data on the cosmic abundance of different elements in the local interstellar medium, independent of astronomical observations, can be obtained using the theoretical description of the filtration of different atoms due to their interaction with plasmas of outer and inner heliosheaths. The most effective filtration process for hydrogen and oxygen is charge exchange with the interstellar protons in the outer heliosheath (Izmodenov et al., 1997), but electron impact ionization may also produce noticeable filtration in the outer heliosheath (Izmodenov et al., 1999b, 2004). In Izmodenov et al. (2004) a comparative analysis of the penetration of interstellar hydrogen, oxygen, and nitrogen atoms through the interface was made. It was shown that (81±2)% and (89±1)% of the interstellar oxygen and nitrogen, respectively, penetrate into the heliosphere through the interface. Using the calculated filtration coefficients, together with data from the Ulysses measurements of pickup ions, the oxygen and nitrogen atom number densities in the LIC were determined. They turned out to be equal to $n_{O\,I,LIC} = (7.8 \pm 1.3) \times 10^{-5}$ cm^{-3} and $n_{N\,I,LIC} = (1.1 \pm 0.2) \times 10^{-5}$ cm^{-3}. Having estimates for the number densities of different elements, their relative cosmic abundances can be evaluated: $(n_{O\,I}/n_{H\,I})_{LIC} = (4.3 \pm 0.5) \times 10^{-4}$ and $(n_{N\,I}/n_{O\,I})_{LIC} = 0.13 \pm 0.01$. The ratio $(n_{O\,I}/n_{H\,I})_{LIC}$ thus obtained is only slightly different from the value $(4.8 \pm 0.48) \times 10^{-4}$ obtained on the basis of spectroscopic observations of absorption lines in stellar spectra (Linsky et al., 1995).

4.11 Summary

The interaction between the supersonic flow of partially ionized plasma of the local interstellar medium and the solar wind produces a complicated flow pattern (Figure 4.1) consisting of two shock waves (the heliospheric termination shock and the bow shock), and a contact discontinuity, the heliopause. Due to the charge

exchange process, the region between the two shocks (heliospheric interface) separating these flows plays the role of a filter for the penetration of interstellar H, O, N, and other atoms into the Solar System.

From a theoretical point of view, the interaction should be considered in the frame of kinetic-continuum models where the interstellar H atom component is described in the framework of the kinetic theory, since for hydrogen atoms the Knudsen number with respect to charge exchange is Kn ~ 1. The first self-consistent model of the SW/LIC interaction was developed by Baranov and Malama (1993). Since that time the set of kinetic-continuum models has been developed. The modern kinetic-continuum models take into account the following physical components/effects:

- the ionized interstellar helium component and the solar wind alpha particles;
- anomalous and galactic cosmic rays;
- the interstellar magnetic field;
- solar cycle variations in the solar wind parameters;
- the heliotail;
- filtration of interstellar oxygen and nitrogen;
- the multi-component nature of the heliospheric plasma.

Large efforts have also been put into the modelling of the heliospheric interface by other groups (e.g. Zank, 1999). Nevertheless, a complete time-dependent multi-component kinetic-continuum model that includes all above effects (plus the interplanetary magnetic field) simultaneously has not been developed yet. This leaves a challenge for future theoretical studies.

The numerical kinetic-continuum models of the heliospheric interface in the frame of the Baranov-Malama model led firstly to the prediction of the many physical phenomena discovered later onboard spacecraft, and secondly to the interpretation of previously obtained experimental data. This was discussed in the previous section. In December 2004, an event anticipated for more than 30 years took place, namely the Voyager 1 spacecraft has finally crossed the heliospheric termination shock at a distance of 94 AU. This was predicted (with 10% accuracy) more than 25 years ago (Baranov et al., 1981; Baranov, 1990; Baranov, 2002).

The topicality of the heliospheric interface studies is dictated by several factors: (1) it is expected that the Voyager 1 and 2 spacecraft will transmit information until the year 2020; (2) in 2008 NASA plans to launch the IBEX spacecraft which will measure the fluxes of energetic neutral atoms arriving from the inner interface at the Earth's orbit; (3) NASA and ESA are discussing plans to launch the Interstellar Probe spacecraft, which for 10 to 15 years will be at a distance of the order of 200 AU; and (4) the development of technologies that would make it possible to launch a spacecraft to α Centauri, the nearest star to the Sun, is planned.

Acknowledgements

We thank Yu. Malama, D. Alexashov, S.V. Chalov, and A.V. Myasnikov for their significant contributions to the development of the kinetic-continuum models of the interface described in this Chapter. We also thank Reinald Kallenbach for his editing of the manuscript which greatly improved it and Rosine Lallement for her fruitful comments. This work was supported in part by INTAS Award 2001-0270, RFBR grants 04-02-16559, 05-02-22000(PICS), 04-01-00594 and the International Space Science Institute in Bern. V.I. was also supported by the "Dynastia Foundation" and by the "Foundation in Support of Homeland Science".

Bibliography

Aleksashov, D.B., Baranov, V., Barsky, E., Myasnikov, A.: *Astronomy Letters* **26**, 743–749, 2000.

Alexashov., D., Izmodenov, V.: AIP Conf. Proc. 679, 218–221, 2003.

Alexashov, D., Chalov, S.V., Myasnikov, A., Izmodenov V., Kallenbach, R.: *Astron. Astrophys.* **420**, 729–736, 2004a.

Alexashov, D., Izmodenov, V., Grzedzielski, S.: *Adv. Space Res.* **34**, Issue 1, 109–114, 2004b.

Alexashov, D., Izmodenov, V.: *Astron. Astrophys.* **439**, 1171–1181, 2005.

Baranov, V.B., Krasnobaev, K.V., Kulikovksy, A.G.: *Sov. Phys. Dokl.* **15**, 791, 1971.

Baranov, V.B., Ermakov, M.K., Lebedev, M.G.: *Soviet Astron. Lett.* **7**, 206, 1981.

Baranov, V.B.: *Space Sci. Rev.* **52**, 89–120, 1990.

Baranov, V.B., Lebedev, M., Malama, Y.: *Astrophys. J.* **375**, 347–351, 1991.

Baranov, V.B., Malama, Y.G.: *J. Geophys. Res.* **98**, 15157–15163, 1993.

Baranov, V.B., Malama, Y.G.: *J. Geophys. Res.* **100**, 14755–14762, 1995.

Baranov, V.B., Malama, Y.G.: *Space Sci. Rev.* **78**, 305–316, 1996.

Baranov, V.B., Zaitsev, N.A.: *Astron. Astrophys.* **304**, 631–637, 1995.

Baranov, V., Zaitsev, N.: *Geophys. Res. Lett.* **25**, 4051–4054, 1998.

Baranov, V.B., Izmodenov, V., Malama, Y.: *J. Geophys. Res.* **103**, 9575–9586, 1998.

Baranov, V.B.: *Planet. Space Sci.* **50**, 535–539, 2002.

Baranov, V.B.: in *Physics of the heliospheric boundaries* (Eds. V. Izmodenov and R. Kallenbach), 2006.

Berezhko, E.G.: *Soviet Astron. Lett.* **12**, 352, 1986.

Błeszynski S., Grzedzielski S., Rucinski D., Jakimiec J.: *Planet. Space Sci.* **40**, 1525, 1992.

Bogdan T.J., Lee M.A., Schneider P.: *J. Geophys. Res.* **96**, 161, 1991.

Burlaga, L.F., Ness, N.F., Acuña, M.H.: *Science* **309**, 2027–2029, 2005.

Chalov, S.V.: *Soviet Astron. Lett.* **14**, 114, 1988a.

Chalov, S.V.: *Astrophys. Space Sci.* **148**, 175, 1988b.

Chalov, S. V. 1990, in *Physics of the Outer Heliosphere* (Eds. S. Grzedzielski, D.E. Page), Pergamon Press, 219, 1990.

Chalov, S.V., Fahr, H.: *Astron. Astrophys.* **311**, 317–328, 1996.

Chalov, S.V., Fahr, H.: *Astron. Astrophys.* **326**, 860–869, 1997.

Chalov, S.V., Fahr, H.J., Izmodenov, V.V.: *Astron. Astrophys.* **304**, 609–616, 1995.
Chalov, S.V., Fahr, H.J., Izmodenov, V.V.: *Astron. Astrophys.* **320**, 659–671, 1997.
Chalov, S.V., Fahr, H.: *Astron. Astrophys.* **401**, L1–L4, 2003.
Chalov, S.V., Fahr H.J.: *Astron. Astrophys.* **360**, 381, 2000.
Chalov, S.V., Fahr H.J., Izmodenov V.V.: 2003, *J. Geophys. Res.* **108**, 1266, 2003.
Chalov, S.V., Izmodenov V.V., Fahr H.J.: 2004a, *Adv. Space Res.* **34**, 99, 2004a.
Chalov, S.V., Alexashov, D.B., Fahr, H.J.: *Astron. Astrophys.* **416**, L31, 2004b.
Chalov, S.V.: *Adv. Space Res.* **35**, 2106–2114, 2005.
Chalov, S.V., in *Physics of the heliospheric boundaries* (Eds. V. Izmodenov and R. Kallenbach), 2006.
Chashei, I., Fahr, H.J., Lay, G.: *Ann. Geophys.* **21**, 1405, 2003.
Costa, J., Lallement, R., Quémerais, E., Bertaux, J.-L., Kyrola, E., Schmidt, W.: *Astron. Astrophys.* **349**, 660-672, 1999.
Decker, R.B., Krimigis, S.M., Roelof, E.C.: *Science* **309**, 2020–2024, 2005.
Fahr, H.J., Lay, G.: *Astron. Astrophys.* **356**, 327–334, 2000.
Fahr, H., Kausch, T., Scherer, H.: *Astron. Astrophys.* **357**, 268–282, 2000.
Fichtner, H., le Roux, J.A., Mall, U., Rucinski, D.: *Astron. Astrophys.* **314**, 650–662, 1996.
Fichtner, H.: *Space Sci. Rev.* **95**, 639–754, 2001.
Fisk, L.A.: *J. Geophys. Res.* **81**, 4633, 1976.
Gazis, P.R.: *Rev. Geophys.* **34**, 379–402, 1996.
Geiss, J., Gloeckler, G., Fisk, L.A., in *Physics of the heliospheric boundaries* (Eds. V. Izmodenov and R. Kallenbach), 2006.
Gloeckler, G., Geiss, J., Balsiger, H., et al.: *Science* **261**, 70–73, 1993.
Gloeckler, G.: *Space Sci. Rev.* **78**, 335–346, 1996.
Gloeckler, G., Fisk, L.A., Geiss, J.: *Nature* **386**, 374–377, 1997.
Gloeckler, G., Geiss, J.: *Space Sci. Rev.* **86**, 127, 1998.
Gloeckler, G., Geiss, J.: AIP Conf. Proc. 598, 281, 2001.
Gloeckler, G., Geiss, J.: *Adv. Space Res.* **34**, 53, 2004.
Gloeckler, G., Möbius, E.; Geiss, J., et al.: *Astron. Astrophys.* **426**, 845–854, 2004.
Godunov, S.K. (Ed.), *Resolution Numerique des Problems Multidimensionnels de la Dynamique des Gaz*, Editions MIR, Moscow, 1979.
Gurnett, D.A., Kurth, W., Allendorf, S., Poynter, R.: *Science* **262**, 199–202, 1993.
Gurnett, D., Kurth, W.: *Space Sci. Rev.* **78**, 53–66, 1996.
Gurnett, D.A., Kurth, W.S., Cairns, I.H., Mitchell, J.: AIP Conf. Proc. 858, 129–134, 2006.
Gruntman, M., Roelof, E.C., Mitchell, D.G., et al.: *J. Geophys. Res.* **106**, 15767–15782, 2001.
Gruntman, M., Izmodenov, V.: *J. Geophys. Res.* **109**, A12, CiteID A12108, 2004.
Heerikhuisen, J., Florinski, V., Zank, G.P.: *J. Geophys. Res.* **111**, A6, CiteID A06110, 2006.
Hirsch, C.: 1988, *Numerical Computation of internal and external flows*, Vol.2, John Willey and Sons, 691 pp.
Holzer, T.E., Banks, P.M.: *Planet. Space Sci.* **17**, 1074, 1969.
Isenberg, P.: *J. Geophys. Res.* **91**, 9965, 1986.
Isenberg, P.A.: *J. Geophys. Res.* **92**, 1067, 1987.
Isenberg, P.A., Smith C.W., Matthaeus, W.H.: *Astrophys. J.* **592**, 564, 2003.

Izmodenov, V., Malama, Yu. G., Lallement, R.: *Astron. Astrophys.* **317**, 193–202, 1997.
Izmodenov, V., Geiss, J., Lallement, R., et al.: *J. Geophys. Res.* **104**, 4731–4742, 1999a.
Izmodenov, V., Lallement, R., Malama, Y.: *Astron. Astrophys.* **342**, L13–L16, 1999b.
Izmodenov, V.: *Astrophys. Space Sci.* **274**, 55–69, 2000.
Izmodenov, V., Malama, Y., Kalinin, A., et al.: *Astrophys. Space Sci.* **274**, 71–76, 2000.
Izmodenov, V.: *Space Sci. Rev.* **97**, 385–388, 2001.
Izmodenov, V., Gruntman, M., Malama, Y.: *J. Geophys. Res.* **106**, 10681, 2001.
Izmodenov, V., Wood, B., and Lallement, R.: *J. Geophys. Res.* **107**, doi: 10.1029/2002JA009394, 2002.
Izmodenov, V., Gloeckler, G., Malama, Y.G.: *Geophys. Res. Lett.* **30**, doi 10.1029/2002GL016127, 2003a.
Izmodenov, V., Malama, Y.G., Gloeckler, G., Geiss, J.: *Astrophys. J.* **594**, L59–L62, 2003b.
Izmodenov, V., Alexashov, D.: *Astronomy Lett.* **29**, No. 1, pp. 58–63, 2003.
Izmodenov, V., Malama, Y.G., Gloeckler, G., Geiss, J.: *Astron. Astrophys.* **414**, L29–L32, 2004.
Izmodenov, V.V., Malama, Y.G.: *Adv. Space Res.* **34**, 74–78, 2004a.
Izmodenov, V.V., Malama, Y.G.: AIP Conf. Proc. 719, 47–52, 2004b.
Izmodenov, V., Alexashov, D., Myasnikov, A.: *Astron. Astrophys.* **437**, L35–L38, 2005a.
Izmodenov, V., Malama, Y.G., Ruderman, M.S.: *Astron. Astrophys.* **429**, 1069–1080, 2005b.
Izmodenov, V.V., Alexashov, D., in Proc. Solar Wind 11 / SOHO 16 Conf. (Eds. B. Fleck, T.H. Zurbuchen, H. Lacoste), ESA SP-592, Published on CDROM, p.55.1, 2005a.
Izmodenov, V.V., Alexashov, D., in Proc. Solar Wind 11 / SOHO 16 Conf. (Eds. B. Fleck, T.H. Zurbuchen, H. Lacoste), ESA SP-592, Published on CDROM, p.56.1, 2005b.
Izmodenov, V. V., Alexashov, D.: AIP Conf. Proc. 858, 14–19, 2006.
Izmodenov, V.V., in *Physics of the heliospheric boundaries* (Eds. V. Izmodenov and R. Kallenbach), 2006.
Karmesin, S., Liewer, P, Brackbill, J.: *Geophys. Res. Lett.* **22**, 1153–1163, 1995.
Lallement, R.: *Space Sci. Rev.* **78**, 361–374, 1996.
Lallement, R., in *The Century of Space Science* (Eds. A.M. Bleeker, J. Geiss, M.C.E. Huber), Kluwer, 1191–1216, 2001.
Lallement, R., Raymond, J.C., Vallerga, J., Lemoine, M., Dalaudier, F., Bertaux, J.-L.: *Astron. Astrophys.* **426**, 875–884, 2004a.
Lallement, R., Raymond, J.C., Bertaux, J.-L., Quémerais, E., Ko, Y.-K., Uzzo, M., McMullin, D., Rucinski, D.: *Astron. Astrophys.* **426**, 867–874, 2004b.
Lallement, R., Quémerais, E., Bertaux, J.-L., Ferron, S., Koutroumpa, D., Pellinen, R.: *Science* **307**, Issue 5714, pp. 1447–1449, 2005.
Lazarus, A.J., McNutt, R.L., Jr., in *Physics of the Outer Heliosphere* (Eds. S. Grzedzielski and D.E. Page), Pergamon, 229–304, 1990.

le Roux, J.A., Ptuskin, V.S.: *J. Geophys. Res.* **103**, 4799, 1998.
Linsky, J., Wood, B., *Astrophys. J.* **463**, 254, 1996.
Linsky J.L., Dipas A., Wood B.E., et al.: *Astrophys. J.* **451**, 335–351, 1995.
Lipatov, A.S., Zank, G.P., Pauls, H.L.: *J. Geophys Res.* **103**, 20631–20642, 1998.
Malama, Y.G.: *Astrophys. Space Sci.* **176**, 21–46, 1991.
Malama, Y.G., Izmodenov, V.V., Chalov, S.V.: *Astron. Astrophys.* **445**, 693–701, 2006.
McComas, D.J., Barraclough, B.L., Funsten, H.O., Gosling, J.T., et al.: *J. Geophys. Res.* **105**, A5, 10419–10433, 2000.
McComas, D.J., Goldstein, R., Gosling, J.T., Skoug, R.M.: *Space Science Rev.* **97**, 99–103, 2001.
McComas, D.J., Elliot, H.A., Gosling, J.T., et al.: *Geophys. Res. Lett.* **29**, 28-1, CiteID 1314, 2002.
McComas, D., Allegrini, F., Bochsler, P., et al.: AIP Conf. Proc. 719, 162, 2004.
McComas, D.J., Elliott, H.A., Gosling, J.T., Skoug, R.M.: *Geophys. Res. Let.* **33**, Issue 9, CiteID L09102, 2006a.
McComas, D.J., Allegrini, F., Bartolone, L., et al.: AIP Conf. Proc. 858, pp. 241–250, 2006b.
Möbius, E., Bzowski, M., Chalov, S., Fahr, H.-J., Gloeckler, G., Izmodenov, V., Kallenbach, R., Lallement, R., McMullin, D., Noda, H.: *Astron. Astrophys.* **426**, 897–907, 2004.
Mueller, H. R., Zank, G., Lipatov, A.S.: *J. Geophys. Res.* **105**, 27419–274388, 2000.
Myasnikov, A.V., Izmodenov, V., Alexashov, D., Chalov, S.: *J. Geophys. Res.* **105**, 5179–5188, 2000a.
Myasnikov, A.V., Alexashov, D., Izmodenov, V., Chalov, S.: *J. Geophys. Res.* **105**, 5167–5178, 2000b.
Neugebauer, M.: *Rev. Geophys.* **37**, 107–126, 1999.
Parker, E.N.: *Astrophys. J.* **134**, 20–27, 1961.
Pogorelov, N., Zank, G.P.: *Astrophys. J.* **636**, L161–L164, 2006.
Quémerais, E., Izmodenov, V.: *Astron. Astrophys.* **396**, 269–281, 2002.
Quémerais, E., Bertaux, J.-L., Lallement, R., Berthe, M., Kyrola, E., Schmidt, W.: *J. Geophys. Res.* **104**, 12585–12604, 1999.
Quémerais, E., Sandel, B. R., Bertaux, J. L., Lallement, R.: *Astrophys. Space Sci.* **274**, 123–132, 2000.
Quémerais, E.,Bertaux, J.-L., Lallement, R., Sandel, B.R., Izmodenov, V.: *J. Geophys. Res.* **108**, LIS 4-1, CiteID 8029, DOI 10.1029/2003JA009871, 2003.
Richardson, J.D.: *Geophys. Res. Lett.* **24**, 2889–2892, 1997.
Richardson, J.D., in *The Outer Heliosphere: The Next Frontiers* (Eds. K. Scherer et al.), COSPAR Colloquiua Series, 11, 301–310, 2001.
Richardson, J.D., Smith, C.W.: *Geophys. Res. Lett.* **30**, 1206, 2003.
Richardson, J.D., Wang, C., Stone, E.C., et al., Proc. Solar Wind 11 /SOHO 16 Conf. (Eds B. Fleck, T.H. Zurbuchen, H. Lacoste), ESA SP-592, Published on CDROM., p.62.1, 2005.
Richardson, J.D., Wang, C., Zhang, M.: AIP Conf. Proc. 858, pp. 110–115, 2006.
Richardson, J.D., Liu, Y., Wang, C., McComas, D.J.: *Astron. Astrophys.*, in press, 2007.

Smith, C.W., Matthaeus, W.H., Zank, G.P., et al.: *J. Geophys. Res.* **106**, 8253–8272, 2001

Scherer, K., Fahr, H.J.: *Annales Geophys.* **21**, 1303–1313, 2003.

Stone, E.C.: *Science* **293**, 55–56, 2001.

Stone, E.C., Cummings, A.C., McDonald, F.B., et al.: *Science* **309**, 2017–2020, 2005.

Terasawa, T.: *Planet. Space Sci.* **27**, 193, 1979.

Toptygin, I.N.: *Space Sci. Rev.* **26**, 157, 1980.

Treumann, R., Macek, W., Izmodenov, V.: *Astron. Astrophys.* **336**, L45–L48, 1998.

Treumann, R., Izmodenov, V., Pottelette, R., in *Physics of the heliospheric boundaries* (Eds. V. Izmodenov and R. Kallenbach), 2006.

Vallerga, J., Lallement, R., Lemoine, M., Dalaudier, F., McMullin, D.: *Astron. Astrophys.* **426**, 855–865, 2004.

Vasyliunas, V.M., Siscoe, G.L.: *J. Geophys. Res.* **81**, 1247–1252, 1976.

Wang, C., Belcher, J.: *J. Geophys. Res.* **104**, 549–556, 1999.

Wang C., Richardson J.D.: *J. Geophys. Res.* **106**, 29401, 2001.

Williams, L., Hall, D.T., Pauls, H.L., Zank, G.P.: *Astrophys. J.* **476**, 366–384, 1997.

Witte, M., Banaszkiewicz, M., Rosenbauer, H.: *Space Sci. Rev.* **78**, 289–296, 1996.

Witte, M.: *Astron. Astrophys.* **426**, 835–844, 2004.

Wood, B.E., Linsky, J.L., Zank, G.P.: *Astrophys. J.* **537**, 304–311, 2000.

Wood, B.E., Izmodenov, V.V., Linsky, J.L., Astrophys. J., in press 2007.

Wolff, B., Koester, D., Lallement, R.: *Astron. Astrophys.* **346**, 969–978, 1999.

Zaitsev, N., Izmodenov V., in *The Outer Heliosphere: The Next Frontiers* (Eds K. Scherer, H. Fichtner, H. Fahr, and E. Marsch), COSPAR Colloquiua Series, 11. Amsterdam: Pergamon Press, pp. 65–69, 2001.

Zank, G.P., Axford, W.I., McKenzie, J.F.: *Astron. Astrophys.* **233**, 275–284, 1990.

Zank, G.P., Müller, H.-R.: *J. Geophys. Res.* **108**, SSH 7-1, CiteID 1240, 2003.

Zank, G.P.: *Space Sci. Rev.* **89**, 413-688, 1999.

— 5 —

Interstellar Gas Inside the Heliosphere

Johannes Geiss[1]
International Space Science Institute
Bern, Switzerland

George Gloeckler
Department of Physics and IPST, University of Maryland, College Park, USA;
Department of Atmospheric, Oceanic, and Space Sciences,
University of Michigan, Ann Arbor, USA

Lennard A. Fisk
Department of Atmospheric, Oceanic, and Space Sciences,
University of Michigan, Ann Arbor, USA

Abstract. **Interstellar neutral gas flows into the heliosphere as a result of the motion of the Sun relative to the Local Interstellar Cloud (LIC), and it provides information on elemental and isotopic abundances as well as on physical conditions in the LIC. Interstellar hydrogen undergoes charge-exchange near the heliopause, where the solar wind merges with the LIC, thus enabling studies of physical processes in this region. Once close to the Sun, interstellar gas is ionized by photo-ionization and charge-exchange with the solar wind and forms a population of pickup ions. In the outer heliosphere, the pickup ions become the dominant internal pressure force in the solar wind, and a fraction of them is accelerated to form the Anomalous Cosmic Ray component. Superimposed on the interstellar pickup ions are pickup ions from other sources, e.g. neutrals released from dust grains and then ionized.**

Interstellar gas provides a sample of the present-day Galaxy to be compared with the Protosolar Cloud (PSC) from which the Solar System formed some 4.6 Gyr ago. Interstellar gas thus provides essential information about the nucleosynthetic evolution of the Galaxy and the Universe. The influence of infall of extra-Galactic matter on the chemical evolution of the Galaxy during the last 5 Gyr and the origin of this infall are discussed.

5.1 Introduction

The heliopause, i.e. the outer boundary of the heliosphere, separates two plasmas of entirely different origin and history: (a) the plasma in the local Interstellar

[1]in *The Physics of the Heliospheric Boundaries*, V. Izmodenov and R. Kallenbach (eds.), ISSI Scientific Report No. 5, pp. 137 - 181, ESA-ESTEC, Paris 2006

Cloud (LIC), a sample of galactic material, and (b) the solar wind, carrying material that is ultimately derived from the Protosolar Cloud (PSC), a sample of galactic material that existed 4.6×10^9 years ago.

The heliopause is not impenetrable. Comets coming from the distant Oort cloud ignore it. Planets, particularly those farthest away from the Sun, will find themselves outside the heliosphere at times of increased galactic pressure. Galactic cosmic ray particles are able to diffuse against the out-streaming solar wind plasma and, depending on their momentum, advance deep into the heliosphere.

Aside from the electrons, ions and fields making up the plasma, the LIC contains grains and neutral gas, cf. Figure 5.1. Both of these components can pass through the heliopause, but the effectiveness of their passage and the depth to which they can advance into the heliosphere depends on their specific properties. Dust particles are sorted out progressively according to their mass/charge ratio when advancing towards the Sun. In the case of the neutral gas, atomic properties determine the probability of crossing the heliospheric interaction region, and they determine the depth of penetration into the heliosphere.

The first theoretical studies of the entry and passage of the neutral interstellar gas appeared in the late 1960s (cf. Blum and Fahr 1970). It was shown that significant fractions of the interstellar atomic hydrogen and helium reach interplanetary space where they could be investigated by appropriate methods.

Bertaux and Blamont (1971) and Thomas and Krassa (1971) achieved the first mapping of interstellar atomic hydrogen that had proceeded to inside the orbit of Jupiter, using two instruments on the OGO-5 spacecraft. One of these maps is shown in Figure 5.2. Both instruments measured the resonant scattering of the solar Lyman-α emission. By comparing Lyman-α maps obtained during three periods separated by a few months, the authors where able to distinguish the emission coming from the geocorona and the emission from beyond. The resulting distribution of atomic hydrogen in the inner heliosphere was compatible with the distribution expected for interstellar atoms that approached the Solar System with a speed of the order of 20 km/s.

When approaching the Sun, the interstellar gas is gradually ionized by solar EUV and/or charge exchange with solar wind protons and alpha particles, and very close to the Sun also by solar wind electrons. The interstellar ions formed in these processes are picked up by the solar wind and carried away from the Sun. $^4He^+$, the most abundant interstellar pickup ion species at 1 AU, was discovered by Möbius et al. (1985) with the Suleica instrument on the AMPTE spacecraft (see Figure 5.3).

During the solar minimum in the early 1970's a new component of the cosmic radiation was discovered that reinforced the importance of interstellar gas in the heliosphere. As discussed in Section 5, Hovestadt et al. (1973), Garcia-Munoz et al. (1973) and McDonald et al. (1974) observed that cosmic rays of order 10^7 eV in energy were enhanced in N and O relative to C, and in He relative to H. This so-called Anomalous Cosmic Ray component, or the ACR, was subsequently attributed by Fisk et al. (1974) to interstellar gas that is ionized and accelerated in the heliosphere. The discovery of the ACR and their explanation had a profound influence on our understanding of the heliosphere. Prior to their discovery, the heliosphere was considered to be relatively passive, an inconvenience to our understanding of

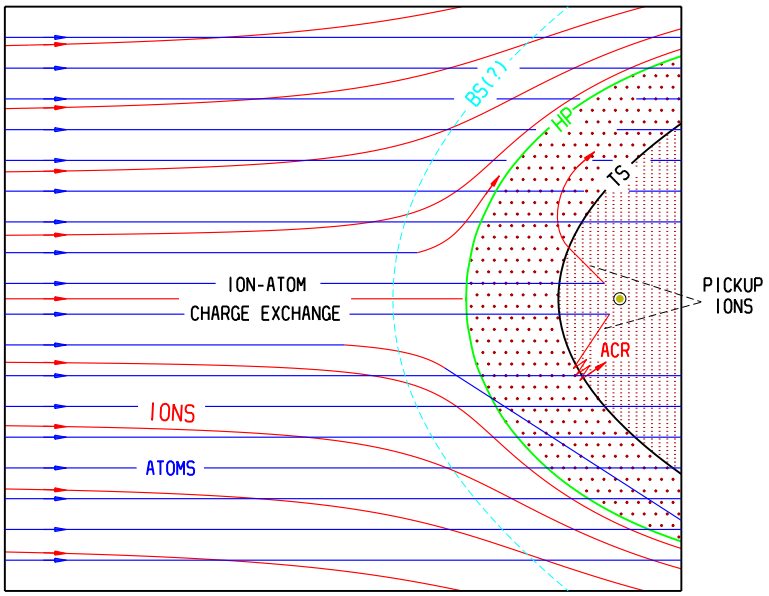

Figure 5.1: Schematic representation of the interaction of the solar wind with the interstellar gas. Shown are the three main regimes: (1) the supersonic solar wind between Sun and termination shock (TS), (2) the heliosheath between TS and heliopause (HP) and (3) the interstellar medium beyond the HP. The interstellar ions are directed around the heliosphere. The flow lines of these ions (red) are shown for potential flow without Bow Shock (BS) as calculated by Parker (1963). Model results by Baranov and Malama (1996) and data of Gloeckler et al. (1997) indicate that a weak BS exists. The kink in the flow lines at the BS is not of great importance for the flow of the atoms (blue), the main subject of this paper. The charge exchange between ions and atoms (shown in the picture at three points, blue to red and red to blue) causes "filtering", i.e. the thinning-out of the flow of some neutrals, primarily hydrogen, directed towards the inner heliosphere. When travelling through the heliosphere some atoms are ionized, picked up, and convected radially outwards by the solar wind until they cross the TS and enter the heliosheath. They are energized and a small percentage of ions is accelerated to high energies somewhere between the TS and the HP resulting in the Anomalous Cosmic Rays (ACR). In addition to the interstellar atoms, interstellar grains with low charge to mass ratio also enter the heliosphere.

galactic cosmic rays, whose intensities are modulated by passage through the heliosphere. The ACR, however, demonstrated that the heliosphere was in fact a powerful accelerator. As is discussed in Section 5, interstellar gas picked up by the solar wind following its ionization acquires energies of order 10^3 eV per nucleon, and thus had to be accelerated by more than four orders of magnitude in energy in the heliosphere.

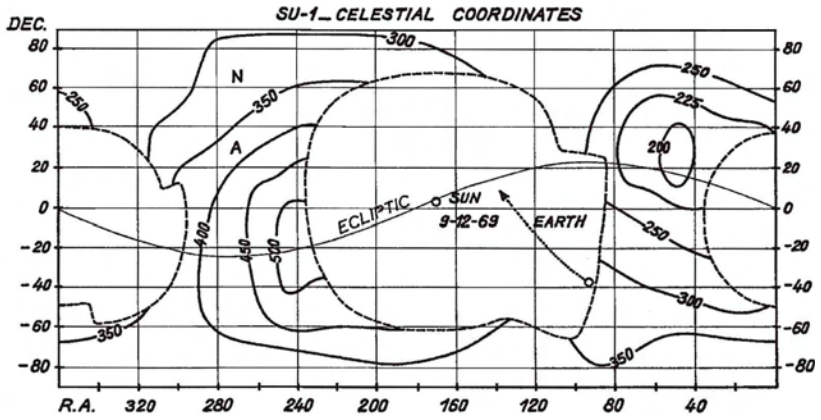

Figure 5.2: Contour map of the Lyman-α intensity in celestial coordinates observed with the OGO-5 photometer for the period 12-14 September 1969. The dashed line is the limit of the area covered on the sky during the observation period, after removal of geocoronal measurements (from Bertaux and Blamont 1971). For the discussion and interpretation of this map see also Lallement (2001).

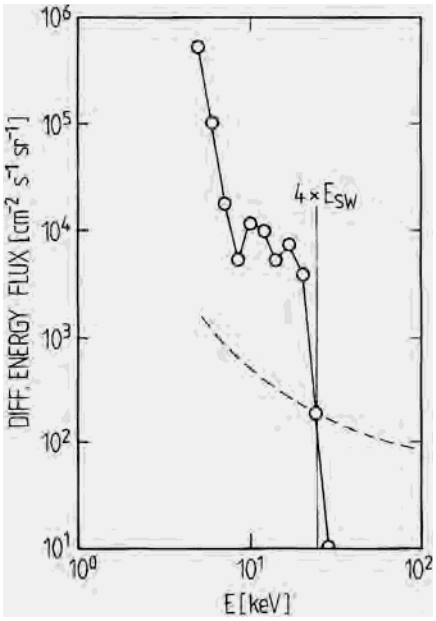

Figure 5.3: First detection of interstellar pickup ions in 1984. The differential energy flux spectrum for M/Q = 4 (He^+) shows the expected cutoff at about twice the solar wind speed. The sharp rise in the spectrum below 8 keV is attributed to heavy solar wind ions with M/Q = 4, such as Si^{7+}. The dashed line represents the 1 count level (after Möbius et al., 1985, with copyright permission from Nature).

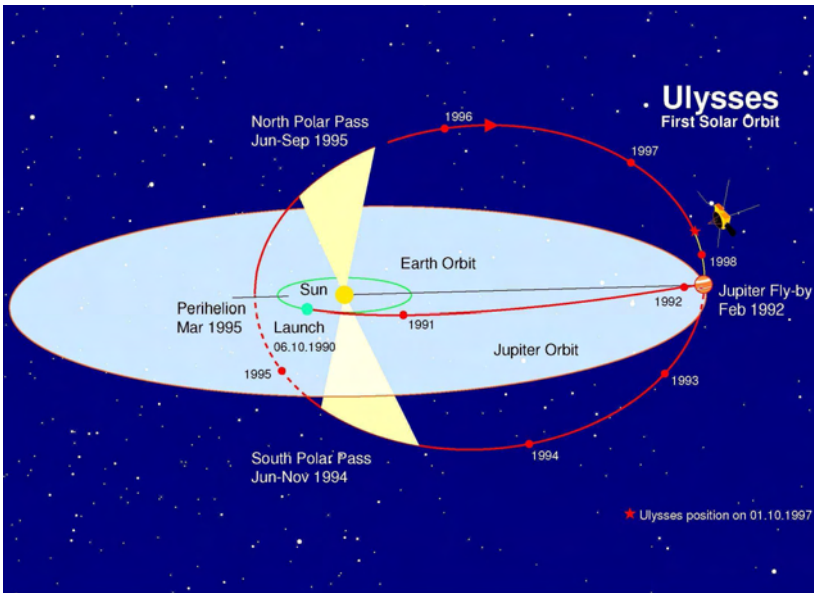

Figure 5.4: Trajectory of the ESA/NASA Ulysses spacecraft. Shown is the path from launch to Jupiter and the first solar polar orbit 1992-1998. Ulysses has completed its second solar polar orbit in 2004, and is approved to continue through 2008. (http://helio.estec.esa.nl/ulysses/).

A new epoch of heliospheric research has been brought about by the Ulysses mission, which was a highly successful joint venture by ESA and NASA. The orbit of this spacecraft with an aphelion at 5.4 AU and a heliospheric inclination of ∼80 degrees (Figure 5.4) has enabled a truly three-dimensional investigation of the heliosphere and of the matter and fields that populate it. This was achieved by a set of instruments on board Ulysses that was as unique for investigating interstellar gas and grains as was the out-of-ecliptic trajectory of the spacecraft (see *Astron. Astrophys. Suppl. Ser.* **92**, 1992) .

Thus, the first in-situ detection of the neutral interstellar gas was achieved by the novel GAS-instrument. From a 3-D mapping of atomic helium (Figure 5.5), Witte et al. (1993) could precisely determine the speed and the arrival direction of the interstellar gas flow. Using another new instrument, SWICS, Gloeckler et al. (1993) measured for the first time interstellar pickup hydrogen, and Geiss et al. (1994a) the heavier pickup ions of nitrogen, oxygen and neon from which the interstellar abundances of these species were determined. Finally, with the dust experiment, Grün and collaborators (Baguhl et al., 1996) achieved the first detection and identification of interstellar grains inside the heliosphere. Last but not least, the cosmic ray experiments on Ulysses allowed a direct three-dimensional investigation of galactic cosmic rays, ACRs and particles accelerated to high energies near the Sun ("flare particles") or the CIR (Corotationg Interaction Region) particles accelerated in the inner heliosphere that Simnett et al. (1995) unexpectedly observed at high heliospheric latitude.

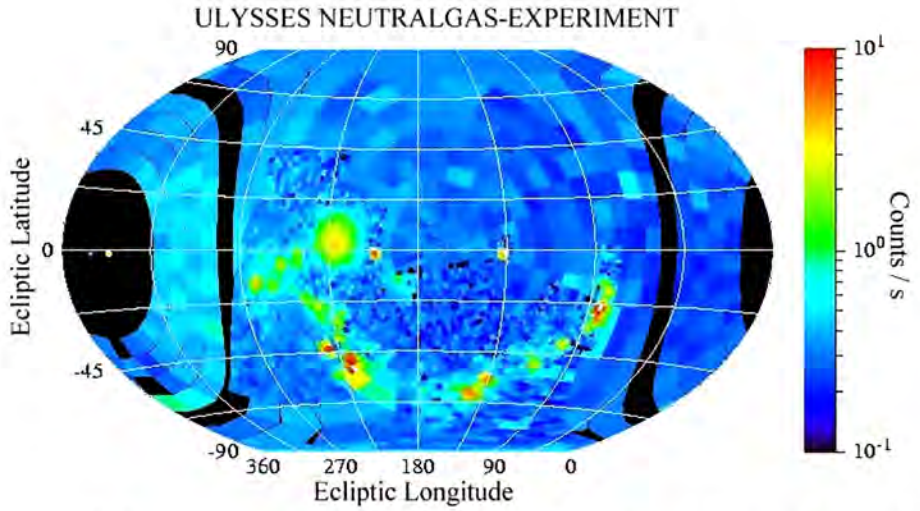

Figure 5.5: A map recorded by the GAS experiment onboard Ulysses. Interstellar helium atoms correspond to the bright spot at (220°, +3°). The bright stars of the Milky Way are seen as a half ring in the Southern Hemisphere. The neutrals coming from the Jupiter direction produce a spot at (136°, −2°). (From Witte et al., 1993.)

5.2 The flow of the neutral interstellar gas through the heliosphere

The LIC is a diffuse interstellar cloud. The gas is made up of neutral atoms, atomic ions and electrons. Molecules are rare. In a reference system moving with the Sun, the interstellar gas in the LIC approaches the Solar System with a speed of $\sim$ 26 km/s. It is assumed that the neutral gas and the plasma move with the same speed and that ions and atoms have the same temperature. Physical properties of the gas, as determined by remote observations and in situ measurements are summarized in Table 5.1. Velocities and temperatures are given for the LIC and also just inside the Termination Shock (TS). These values were derived by Witte (2004), from the distribution of the interstellar helium inside the heliosphere and

Table 5.1: Physical Parameters of the neutral gas in the Local Interstellar Cloud (LIC). Also given are the velocity and the temperature of neutral hydrogen (H^0) just inside the Termination Shock (TS)

	Velocity (km/s)	Temperature (K)	β (degree)	λ (degree)	H^0 (cm^{-3})	He^0 (cm^{-3})
LIC	26.24 ± 0.45	6306 ± 390	74.68 ± 0.56	-5.31 ± 0.28	0.18	0.0148 ± 0.002
TS	22 ± 1	$11,000 \pm 1000$				

by Lallement (1999), Costa et al. (1999) and Lallement et al. (2004) from Lyman-α observations outside and inside the heliosphere. The flow direction (β and λ) is from Witte (2004), and the densities of neutral H and He in the LIC are those derived by Gloeckler and Geiss (2001) and recently updated by Gloeckler (2005).

In the LIC, ionization and recombination are slow, except for resonant charge exchange processes. Exchange between H and H^+ is so fast that the mean free path of an H atom is smaller than the dimensions of the heliosphere (cf. Izmodenov, 2000). Therefore, when the plasma is diverted around the heliosphere, the drag exerted on the neutral hydrogen component through charge exchange becomes significant, which has important consequences for heliospheric physics:

1. The bulk speed of the atomic hydrogen is reduced by ~ 4 km/s (Table 5.1). This is confirmed by the measured difference in the speed of H and He inside the heliosphere.

2. The momentum transfer in the forward direction between the neutral and ionized gas causes a piling up of H in front of (on the LIC side of) the heliopause, producing the "hydrogen wall" as described by Lallement (2001).

3. The loss of momentum flux of the neutral gas in the forward direction increases the pressure exerted on the heliosphere by the interstellar plasma. This has to be taken into account in calculating the position of the termination shock from the balance between external and internal pressure (Gloeckler et al., 1997).

4. The temperature of atomic hydrogen is increased by the passage through the heliospheric interaction region (cf. Table 5.1).

5. Charge exchange reactions in front of the heliopause cause a reduction in the neutral flux directed towards the inner heliosphere. Ripken and Fahr (1983) calculated the strength of this filtering effect as a function of the degree of ionization. Filtering depends on the charge exchange cross sections of atoms with H^+ and of ions with H. Thus, the loss through filtering is most severe for atomic hydrogen, followed by oxygen and nitrogen (Geiss et al., 1994a; Izmodenov et al., 1999a). Filtering is lowest for He, Ne and Ar. Some additional ionization is caused by electron impact in the Heliosheath. This effect is strongest for oxygen (Izmodenov et al., 1999b).

The transmission factor η through the heliospheric interaction region is defined as the ratio of the neutral flux passing through the termination shock in the subsolar region to the interstellar flux approaching the heliosphere. The combined effects of filtering by charge exchange and ionization in the heliosheath are taken into account in calculating the transmission factor η (see Section 5.6).

When approaching the Sun, the trajectories of interstellar atoms are bent by solar gravity. This becomes important when the speed of the interstellar atoms is equal to the escape speed at the heliocentric distance

$$R_\gamma = 2\,(1-\mu)\,\gamma M_0/V_0^2, \tag{5.1}$$

with γ the gravitational constant, M_0 the solar mass, and V_0 the speed of the interstellar atom at the termination shock. $\mu = a_{\rm rad}/a_{\rm grav}$ is the ratio of the

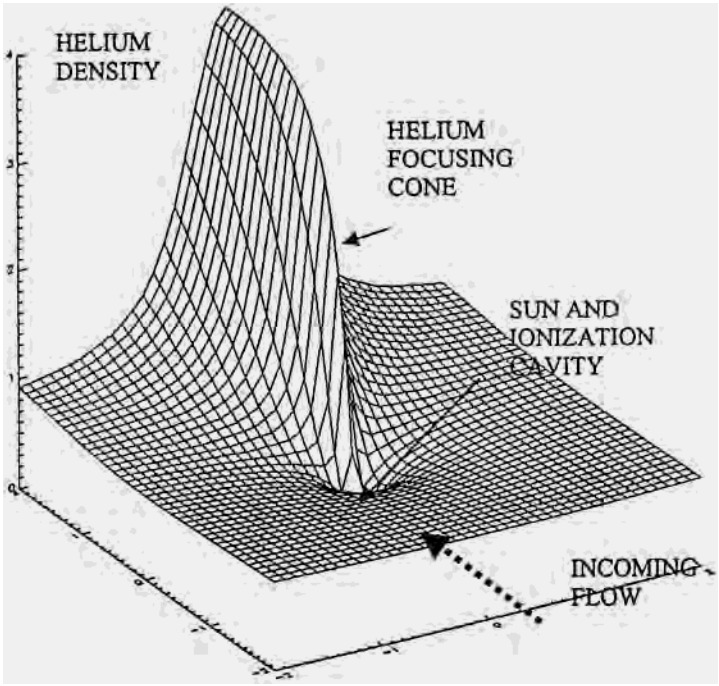

Figure 5.6: Density of interstellar neutral helium as predicted by model calculations, after Lallement (2001). The X and Y axes are Cartesian coordinates in astronomical units in a plane containing the Sun and the interstellar wind vector. Since helium has the longest lifetime of all interstellar atoms, it shows a pronounced focusing cone in the downwind direction.

acceleration caused by solar radiation to the gravitational acceleration. For $\mu = 0$ and $V_0 = 26$ km/s, $R_\gamma = 2.6$ AU is obtained. $a_{\rm rad}$ is particularly strong for atomic H, due to resonant scattering of the intense solar Lyman-α flux. Because this flux depends on solar activity, $\mu_{\rm H}$ is variable, $\mu_{\rm H} = 1$ being a typical value (Bertaux et al., 1985). $a_{\rm rad}$ is much smaller for other interstellar atomic species found in the inner heliosphere, so that μ is practically negligible.

Due to the deflection by solar gravity, a detector will receive interstellar atoms with identical μ and V_0 from two different directions, those coming directly with only moderate deflection and those that had first swung around the Sun before having been detected. The GAS experiment on Ulysses has indeed simultaneously observed the particles on direct and on indirect orbits. Since the intensity ratio of the two depends very strongly on the loss rate by ionization, this rate can be determined from such observations (Witte et al., 1993; 1996; Witte, 2004).

It was recognized early on (Blum and Fahr, 1970) that the Sun's gravitational field should focus the neutral interstellar wind on the downwind side of the Sun (Figure 5.6). The existence of this focussing effect has been verified for helium as shown in Figure 5.7. The position and width of the focussing cone provide independent checks on the inflow direction of interstellar gas, on the temperature

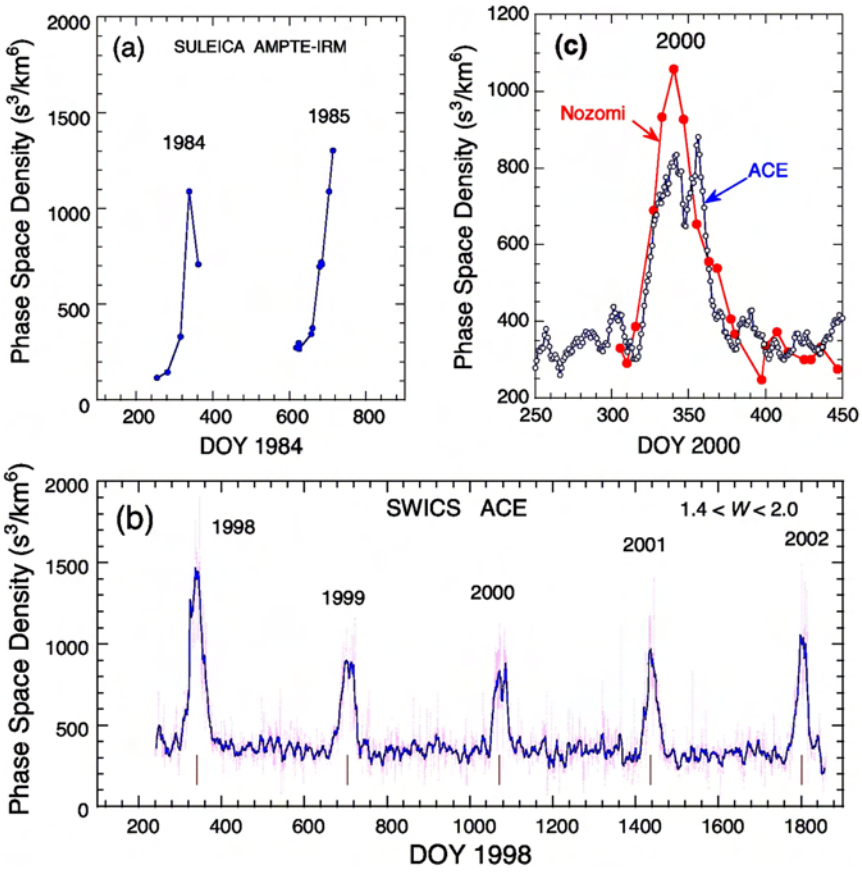

Figure 5.7: Traversals of the gravitational focusing cone of interstellar helium at and near 1 AU for 1984, 1985, and 1998 - 2002, as observed with pickup ions. Shown is the phase space density of He^+ pickup ions obtained with three different instruments. The observations with AMPTE SULEICA (a) were made from Earth orbit, and with ACE SWICS (b, c) from L1. The AMPTE observations were limited by the orbit, telemetry coverage and instrument sensitivity to high solar wind speeds only, thus not allowing any averaging over consecutive days. The cone position in longitude, $\lambda = 74.6°$ corresponds to DOY 339.75 (Earth crossing of the cone center). (c): Observations of the 2000 cone with ACE and NOZOMI. These observations are contiguous and have been averaged over 9 and 15 days, respectively. NOZOMI is on an interplanetary trajectory just outside 1 AU. (See text for further explanation).

of neutral helium, and on the ionization rate of helium atoms inside the heliosphere (Gloeckler and Geiss, 2001a; Gloeckler et al., 2004). The position of the focusing cone of suprathermal particles gives an indication of transport along the field lines of the heliospheric magnetic field $\mathbf{B}_{\mathrm{HMF}}$.

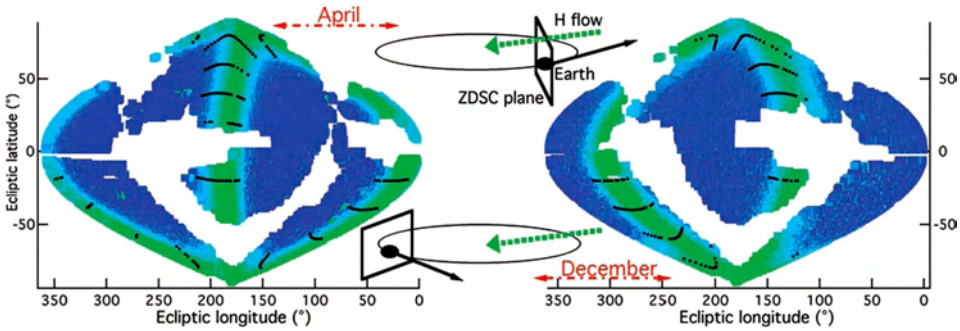

Figure 5.8: Two examples of absorption cell transmission maps recorded by SOHO/SWAN (on 25 April 1996 and 29 December 1996) at Lagrangian point L1 near Earth. These maps are in ecliptic coordinates. Blank areas correspond to the absence of measurements or to contaminated data. Maximum absorption directions (green areas) form a pattern close to a great circle. This ZDSC (zero-Doppler shift circle) is in a plane that is perpendicular to the interstellar gas velocity in the observer frame, i.e. the difference between the H flow motion (green dashed vector) and the Earth velocity (black vector). The data used for the present analysis (black dots) are series of secants of the ZDSC (Lallement et al., 2005).

Indication of a transport effect of interstellar protons in the interstellar magnetic field $\mathbf{B}_{\rm ISM}$ has recently been found by Lallement et al. (2005). Interstellar neutral hydrogen atoms inside the heliosphere propagate in a different direction from the interstellar neutral helium atoms, the difference amounting to about 4° (Figure 5.8). This shift appears to be an effect of the interstellar magnetic field: a high percentage of the primary hydrogen atoms of interstellar origin are ionized outside the heliopause, where the interstellar magnetic field $\mathbf{B}_{\rm ISM}$ dominates. If the orientation of the interstellar magnetic field $\mathbf{B}_{\rm ISM}$ (Figure 5.9) is neither perpendicular nor parallel to the interstellar neutral gas flow, the protons (i.e. the ionized primary hydrogen atoms) are deflected with respect to the primary interstellar neutral gas flow. Once neutralized again by charge exchange, the so-called secondary interstellar neutral hydrogen atoms propagate in a different direction in the heliosphere from the primary interstellar hydrogen atoms. Such a shift in propagation direction of interstellar hydrogen inside the heliosphere has been detected by remote sensing using the SOHO/SWAN instrument (Figure 5.8). In-situ detection of interstellar neutral hydrogen atoms near Earth's orbit is impossible because at heliocentric distances smaller than about 7.5 AU virtually all interstellar hydrogen is ionized by solar ultraviolet radiation.

Other than neutral interstellar hydrogen, a high percentage of neutral interstellar helium and – somewhat less – neon reaches 1 AU without charge exchange. Since atoms pass through the magnetosphere without much interference, neutral interstellar helium and neon can be detected by spacecraft in low Earth orbit, before they enter the atmosphere (see Geiss, 1972). A Swiss-Russian team (Salerno et al., 2001; Busemann et al., 2006) succeeded in capturing interstellar helium and

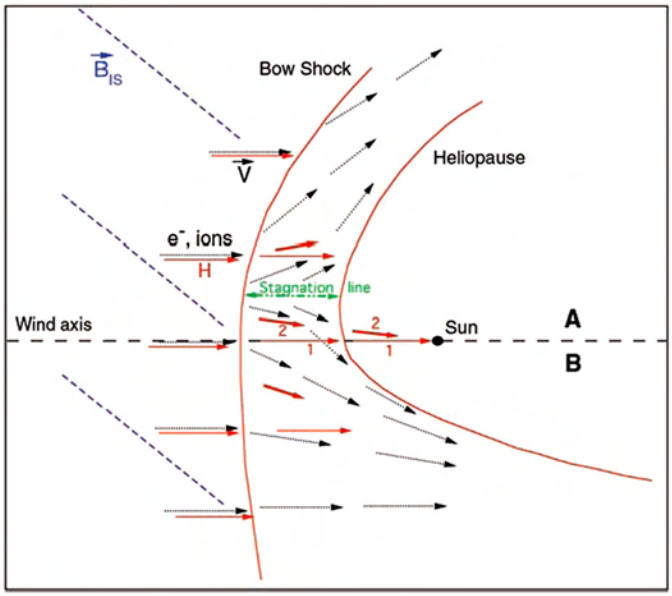

Figure 5.9: Possible scheme for the heliosphere (Lallement et al., 2005). Neutrals (red arrows) and plasma (electrons and ions, black arrows) are shown in the plane which contains the interstellar magnetic field $\mathbf{B}_{\rm ISM}$ and the interstellar neutral gas flow vector. The secondary flow of H atoms (marked as 2) arriving at Earth is created outside the heliopause in a region between the line that points from the Sun to the undeflected interstellar neutral flow (marked as 1) and the shifted stagnation line. The secondary flow to Earth is deflected into the direction between the interstellar magnetic field direction and the primary flow direction (Lallement et al., 2005).

investigating the isotopes with their COLISA instrument onboard the MIR space station (Figure 5.10 and Section 5.6).

The lifetime of helium in the atmosphere is relatively short, so that gain and loss (by escape) are approximately in equilibrium. Whereas virtually all ^{4}He stems from α-decay of uranium and thorium in the Earth, ^{3}He comes from four sources (estimates from Bühler et al., 1976): Outgassing of originally accreted helium, (25%), solar wind (30%), interstellar gas (30%), and spallation in the atmosphere by cosmic rays ($\sim$ 5%).

During their lifetime, the Sun and planets have passed through very different interstellar environments, including times of sufficient density to overwhelm the solar wind down to 1 AU and even less (Talbot and Newman, 1977). The total interstellar gas flux that Earth or Mars may have encountered over their lifetimes is constrained by the neon in the atmospheres of these planets (Geiss and Bochsler, 1982).

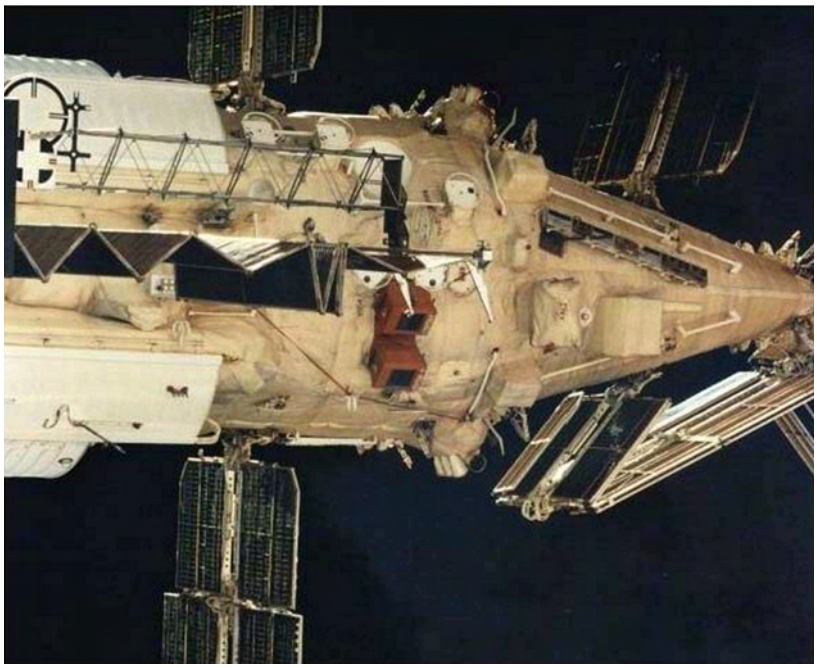

Figure 5.10: The MIR space station in low Earth orbit. Interstellar helium was collected in foils exposed by the COLISA experiment (reddish). After the cosmonauts had brought the foils back to Earth, the interstellar ^{4}He and ^{3}He collected in them were measured in the laboratory (Salerno et al., 2001; Busemann et al., 2006).

5.3 Sources of heliospheric ions

The heliosphere is populated by ions of various sources. Of prime importance are the solar wind ions carrying most of the mass and momentum of the expanding plasma. Second in abundance are the pickup ions of interstellar origin. Thirdly, there are neutral gas sources inside the heliosphere from which solar EUV and charge exchanges produce pickup ions. At low solar latitude, where asteroids and their debris are concentrated, there must be various sources, but they have not been explored. However, even away from the ecliptic plane, there is a distributed source, the "Inner Source", that provides pickup ions over a large range of heliospheric longitudes and latitudes. Table 5.2 shows the great differences in source strengths of various ion sources. These differences are of course a primary reason why many interstellar ions can be identified and quantitatively studied without much interference from other sources.

At times, comets shed appreciable amounts of pickup ions into the heliosphere. The in-situ detection of ions in the distant tail of comet Hyakutake is an example (Gloeckler et al., 2000). For the heliosphere as a whole, the cometary C^+ may be relatively significant because neutral C is very low in the interstellar gas (Table 5.3

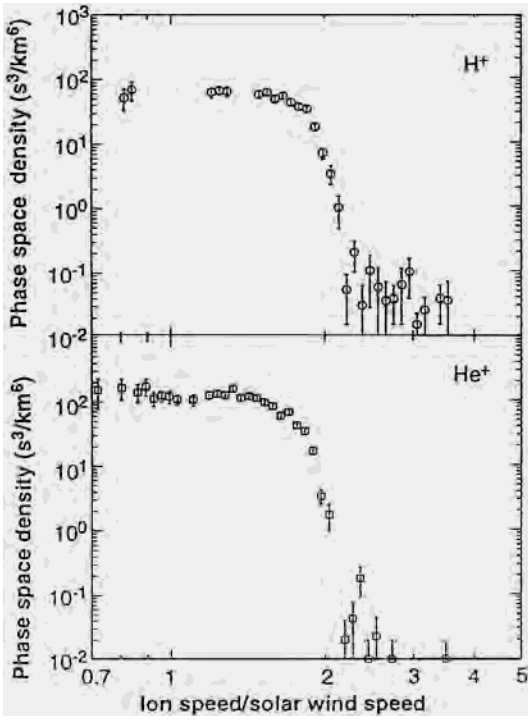

Figure 5.11: First measurement of H^+ pickup ions of interstellar origin with the time-of-flight mass spectrometer SWICS onboard Ulysses (Gloeckler et al. 1993). Shown are phase space density versus $W = v/v_{\rm SW}$ plots of H^+ and He^+ obtained in November/December 1991 at a heliocentric radial distance of 4.82 AU. The velocity distribution for both ions shows the characteristic cutoff at $W = 2$. The H^+ data near $W = 1$ are not shown, because solar wind protons dominate at these velocities. He^+ is absent in the solar wind, (i.e. there is no peak at $W = 1$). (Reprinted with permission from Gloeckler et al., *Science* **261**, 70, Fig. 2, ©1993 American Association for the Advancement of Science.)

and Gloeckler et al., 2000b). Small comets might even contribute appreciably to the inner source C^+ "background." Since, however, the size distribution of comets is poorly known, this contribution cannot be estimated at the present time.

5.3.1 Interstellar pickup ions

Most of the interstellar gas entering the heliosphere leaves it again in neutral form. The relatively small portion that is ionized has, however, great significance, because it is the source of interstellar pickup ions and of Anomalous Cosmic Rays in the heliosphere. The total production rate P inside the termination shock of an interstellar pickup ion species is

$$P = \sigma_{\rm Sun} f_n, \tag{5.2}$$

Table 5.2: Estimates by Geiss et al. (1996) and Geiss et al. (2002) of total production, in tons per second, of O ions from major sources in the heliosphere (1 ton = 1000 kg).

	O [tons/s]
Solar wind ($O^{6+,7+,8+}$)	2×10^4
Interstellar gas (O^+ pickup ions)	2×10^3
Inner source (O^+)	2
Halley, outbound at 0.9 AU (O^+)	15
Io-torus, fast atoms (O^+)[a]	< 0.3
Mars, total O^+ release[b]	10^{-5}

[a] Cheng (1996); [b] Carlsson et al. (2006)

Table 5.3: Sources of Heliospheric Ions away from the Ecliptic Plane.

Source	Main Charge	Velocity Distribution at 1–5 AU	C/O	N/O	Ne/O
Solar wind (SW)	multiple	very narrow	∼solar	∼solar	∼solar
Interstellar gas	single	broad	very low	∼solar	∼solar
Inner source (SW-grain interaction)	single	narrow	∼solar	∼solar	∼solar
Interstellar grains	single	intermediate	>∼solar	unknown	very low

where $\sigma_{\rm Sun}$ is the cross section for ion production by solar photons and charge exchange with solar wind ions, and f_n is the flux of neutral species at the termination shock. Evaluation of the cross section gives (Geiss et al., 1995; Geiss et al., 1996)

$$\sigma_{\rm Sun} = 4\pi R_{\rm ion} \left(R_{\rm sh} - \kappa R_{\rm ion} \right), \tag{5.3}$$

where $R_{\rm sh}$ is the distance to the termination shock, $R_{\rm ion} = \beta_{\rm E} R_{\rm E}^2 / V_0$ is a characteristic ionization distance and $\beta_{\rm E}$ is the ionization rate at $R_{\rm E}$ (1 AU). κ is a slowly varying function of $R_{\rm ion}$ which is obtained numerically (Geiss et al., 1996). In Table 5.2 the production rates P for interstellar O^+ are compared to those of oxygen ions from other heliospheric sources. The values given for $P(O^+)$ are derived from pickup ion measurements (Gloeckler and Geiss, 2001).

For discussing pickup ion results, it is customary to use the ratio $W = v/v_{\rm SW}$, where v is the velocity of an incoming ion and $v_{\rm SW}$ the solar wind velocity measured at that time. W is thus a normalized velocity in the reference frame of the spacecraft.

For identifying the sources of individual pickup ion species, three criteria are available (Table 5.4):

1. The charge states: Solar wind ions of heavy elements have high charge states resulting from the coronal temperature of $\sim 10^6$ K. On the other hand, the

Table 5.4: Densities of atoms at the termination shock and of atoms and ions in the Local Interstellar Cloud (LIC, from Gloeckler, 2005)

	Termination Shock (cm^{-3})	Filtration Factor[a]	Neutral Fraction[b]	Local Interstellar Cloud (cm^{-3})				LIC/PSC Ratio[c]
				atoms	ions	grains	total	
H	0.1025±0.010	0.55±0.06	0.806±0.014	0.186	0.045	0	0.231	1
He	0.0143±0.0014	0.94±0.02	0.659±0.026	0.0152	0.0079	0	0.0231	1
N	$(5.47\pm1.37)\times10^{-6}$	0.76±0.08	0.675±0.006	7.20×10^{-6}	3.5×10^{-6}	2.0×10^{-6}	1.27×10^{-5}	0.76±0.20
O	$(4.82\pm0.53)\times10^{-5}$	0.70±0.11	0.831±0.012	6.88×10^{-5}	1.4×10^{-5}	4×10^{-5}	1.23×10^{-4}	1.06±0.30
Ne	$(5.82\pm1.16)\times10^{-6}$	0.88±0.04	0.206±0.025	6.61×10^{-6}	2.5×10^{-5}	0	3.20×10^{-5}	1.15±0.40

[a] From Cummings et al. (2002); [b] Results of model No. 25 of Slavin and Frisch (2002);
[c] Local Interstellar Cloud (LIC) to Protosolar Cloud (PSC) ratios.
PSC abundances: H and He from Bahcall et al. (1995); Ne from Grevesse and Sauval (1998);
for N and O see Table 5.6

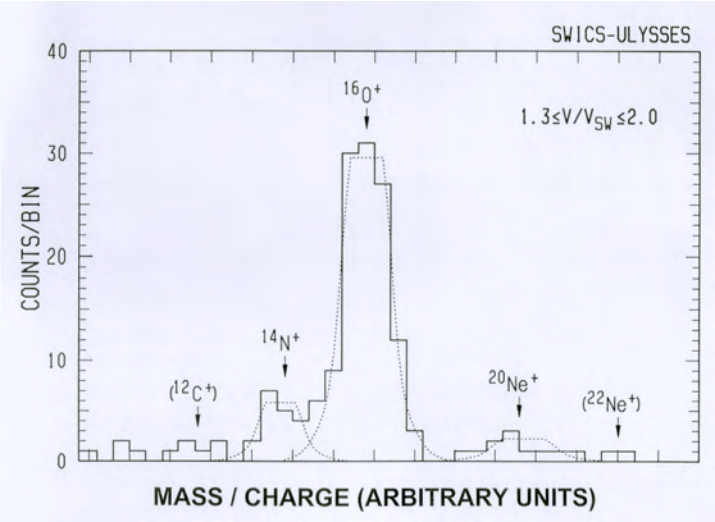

Figure 5.12: Mass/charge of interstellar pickup ions from nitrogen to neon obtained in 1992 at a heliocentric radial distance > 5 AU with the time-of-flight mass spectrometer SWICS on Ulysses (Geiss et al., 1994a). The positions of the ions indicated by arrows and the relative widths of the peaks (dotted lines) were directly determined by laboratory calibration (Ipavich et al., 1982). Only ions with normalized speed $W = v/v_{\rm SW}$ between 1.3 and 2 were included in the spectrum. In this velocity range and at 5 AU the background as well as interferences from solar wind ions or inner source ions are virtually absent in the region of the nitrogen, oxygen and neon peaks. The low abundance of C^+ (only an upper limit is obtained from this spectrum) confirms that the gas in the Local Interstellar Cloud (LIC) is very much depleted in neutral atomic carbon.

solar EUV spectrum and the charge exchange cross sections with solar wind particles are such that most of the pickup ions are observed with one charge only.

2. The spatial distribution in the heliosphere: Ions produced from the interstellar gas have a very characteristic distribution in space, which is governed by the ionization rate and the direction of the solar apex (cf. Figures 5.6 and 5.7).

3. The velocity distribution: Pickup ions are produced by solar EUV or charge exchange from slowly moving neutrals ($W \ll 1$). The newly formed ions are picked up by the electromagnetic field of the solar wind. Subsequent pitch-angle scattering and adiabatic cooling produce a velocity distribution that ranges from $W \approx 0$ to $W \approx 2$ (cf. Figure 5.11). Applying the three criteria, mass spectra of interstellar pickup ions are obtained with minimal interference from solar wind ions or ions from other sources (Figure 5.12).

5.3.2 Inner source pickup ions

The interstellar gas is not the only source of pickup ions in the heliosphere. Solar wind ions are implanted into interplanetary grains, and then released as neutral atoms or molecules, become ionized and form what is known as inner source pickup ions. Away from the ecliptic plane, this is the most important pickup ion source next to the interstellar gas (Table 5.2). Since the inner source is located near the Sun (10–50 solar radii), the pickup ions produced from it are adiabatically cooled on their way out to the spacecraft, and therefore can be readily distinguished from the interstellar ions. This is shown in Figure 5.13. The flat portions of the spectrum ($W \sim 1.3$ to $W \sim 1.8$) is dominated by interstellar ions. The peaks around $W = 1$ are due to inner source pickup ions produced close to the Sun and adiabatically cooled on the way out to the spacecraft.

5.4 The propagation of pickup ions

Pickup ions in the solar wind provide important information on the propagation of very low-rigidity particles. Indeed, prior to the observations of pickup ions, the only information on the behaviour of low rigidity particles came from observations of solar flare electrons. In Palmer (1982) an analysis of many solar flares revealed that the mean free path for lower rigidity particles was of the order a sizeable fraction of 1 AU, much larger than some applications of quasi-linear scattering theory predicted. However, Bieber et al. (1994) pointed out that the lowest rigidity particles in the Palmer (1982) analysis were all solar flare electrons, and suggested that ions might be scattered more extensively, and be closer to these earlier theoretical predictions. Pickup ions have rigidities of < 2.5 MV, and are comparable to the rigidities of low energy solar flare electrons. The propagation properties of pickup ions thus provide an important test of scattering theories.

Interstellar pickup ions have a well-defined source, and initial anisotropies in the solar wind. The spatial distribution of interstellar neutral H, for example, peaks at ∼3-4 AU from the Sun. Inward from this distance the neutrals are heavily ionized by charge-exchange with the solar wind. A steep positive radial gradient is thus expected in the resulting pickup H^+ in the inner heliosphere. Immediately following ionization, the ions gyrate about the magnetic field in the solar wind, at a fixed pitch angle, i.e. an effective ring-distribution, and propagate along the magnetic field. Thus, in the inner heliosphere, where the magnetic field lies predominantly in the radial direction, the pickup ions are initially highly anisotropic, driven by the positive radial gradient, and propagating inward in the frame of the solar wind. The extent to which this anisotropy is preserved is thus an excellent measure of the scattering of the low-rigidity pickup ions. There is a possibility that these ions could excite waves and thus generate their own scattering and decay of the anisotropy (e.g., Lee and Ip, 1987). Thus, any residual anisotropy that remains provides a safe upper limit to the scattering by ambient turbulence in the solar wind.

Shown in Figure 5.14 from Gloeckler et al. (1995) are the observed distribution functions for solar wind and interstellar pickup H^+ as seen from Ulysses in the high speed solar wind streams at high latitudes, near solar minimum. The steadiness of

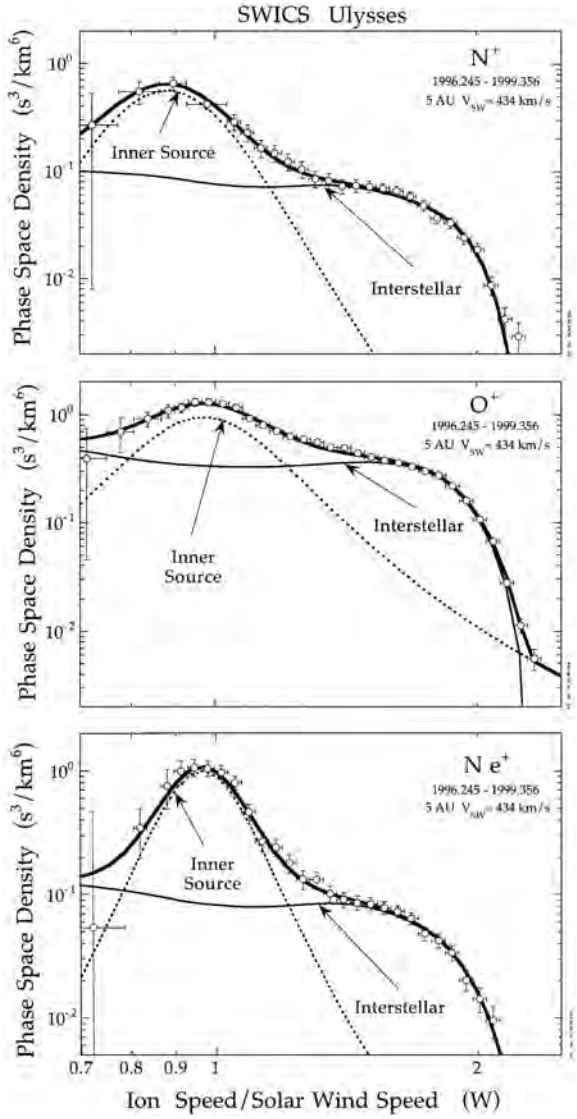

Figure 5.13: Phase space density as a function of W, the normalized speed of the N^+, O^+ and Ne^+ ions measured with SWICS on Ulysses (Gloeckler and Geiss, 2001a). During the measurement period (40 months) Ulysses was in the slow solar wind (average speed: 434 km/s) near 5 AU. The flat portion of the spectrum ($W \sim 1.3$ to ~ 1.8) is dominated by interstellar ions. The peaks around $W = 1$ are due to inner source pickup ions produced close to the Sun and adiabatically cooled on the way out to the spacecraft. Model curves for the interstellar and the inner source ions are fitted to the data, allowing one to derive the loss rates for the interstellar N, O and Ne and their densities at the termination shock.

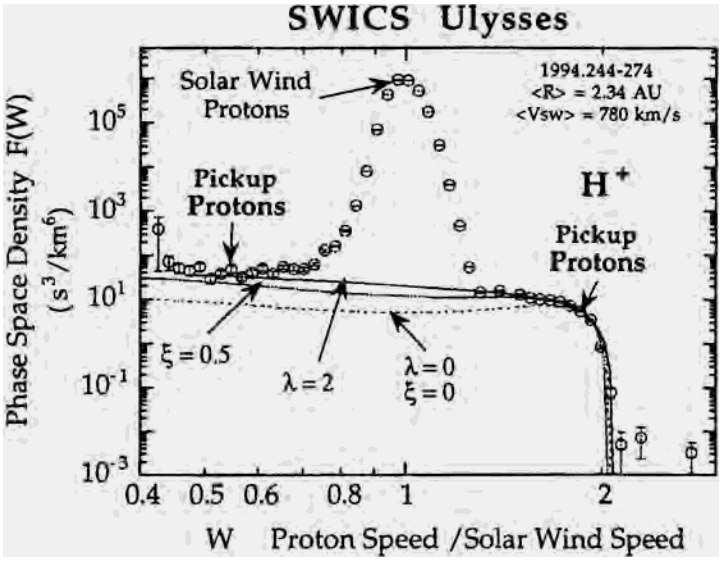

Figure 5.14: Phase space density of protons as a function of W, the normalized speed, measured in 1994 with SWICS on Ulysses in the high-speed solar wind. The pickup protons of interstellar origin are clearly distinguished from the solar wind protons by their difference in velocity distributions. λ is the scattering mean free path (measured in AU) and ξ is the anisotropy predicted for the position of the spacecraft. Whereas the model with $\xi = 0$ and $\lambda = 0$ does not fit the data point, the model with a high anisotropy ($\xi = 0.5$) and a long scattering mean free path ($\lambda = 2$ AU) fits best.

the high-speed streams permits clear observations of pickup H^+ at speeds below the solar wind speed, and thus propagating inward in the frame of the solar wind. The curve marked $\xi = 0$ is what is expected if the distribution function is isotropic. Clearly there is an excess corresponding to a large anisotropy, $\xi = 0.5$, which requires a mean free path of order 1 AU. Thus, both ions and electrons of low rigidity have large mean free paths, which remains somewhat of a challenge for scattering theory to explain.

Inner source pickup ions present even a greater challenge. These particles are injected into the solar wind at a few tens of solar radii, again propagating inward in the frame of the solar wind (Gloeckler et al., 2001). At these radial distances the solar wind is undergoing considerable expansion. The decrease in the magnetic field strength in the frame of the solar wind adiabatically cools the pickup ions, reducing their energies to close to those of the solar wind. The observations, and detailed modelling by Schwadron et al. (2000) show that the mean free path for scattering, however, is long, comparable to the mean free path inferred from interstellar pickup ions. The inner source pickup ions are lower in rigidity than interstellar pickup ions, due to the cooling, and thus the evidence for a long mean free path is extended to even lower rigidities.

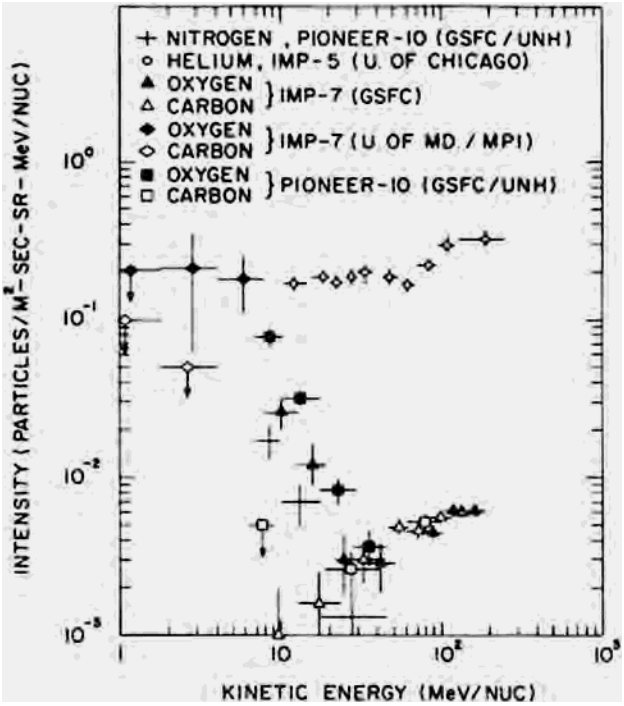

Figure 5.15: The observed spectra of low-energy oxygen, nitrogen, and carbon during quiet times in 1972-1973. The data are taken from McDonald et al. (1974), Hovestadt et al. (1973), and Garcia-Munoz et al. (1973).

5.5 Anomalous Cosmic Rays

One of the most important consequences of interstellar gas inside the heliosphere is the creation of the so-called Anomalous Cosmic Ray (ACR) component. In the early 1970's a new component of galactic cosmic rays was observed that had an unusual, indeed anomalous composition. As shown in Figure 5.15, at energies ~ 10 MeV/nucleon, Hovestadt et al. (1973) and McDonald et al. (1974) observed that O and N were substantially enhanced relative to C; Garcia-Munoz et al. (1973) observed that He was enhanced relative to H. The new component was dubbed the Anomalous Cosmic Ray (ACR) component, a name that has persisted since.

Shortly after the discovery of ACRs the explanation for their origin was provided by Fisk et al. (1974), who noted that the composition of He, N, and O was what would be expected for interstellar neutral gas that was swept into the heliosphere by the motion of the Solar System relative to the local interstellar medium. Interstellar neutral H had been observed in the heliosphere in Lyman-α backscatter, and the expectation was that He, N, and O, all of which have first ionization potentials as high as or higher than H, would also be primarily neutral in the interstellar medium, and present along with interstellar neutral H. Fisk et al. (1974) noted that the interstellar neutral gas would be ionized by photo-ionization by the Sun

and charge-exchanged with the solar wind, and then picked-up by the solar wind flow and convected back out of the Solar System. Fisk et al. (1974) argued that the new pickup ions would be accelerated as they are convected outward, and could achieve energies of ~ 10 MeV/nucleon where they are observed as ACRs.

This theory could account for the observed composition of ACRs, and also their spectral shapes, which had the puzzling feature of a very steep slope at the higher energies. Galactic cosmic rays are known to suffer substantial adiabatic deceleration in the expanding solar wind, at lower energies losing ~ 200 MeV/nucleon of their original energy (Goldstein et al., 1970). Spectra with steep slopes thus suffer considerable reductions in intensity, since the particles observed originated at much higher energies, where few particles are present. However, if ACRs originate as interstellar neutral gas they should be primarily singly charged; the particles enter the heliosphere neutral, and have time to be ionised only once (see discussion below concerning multiple charge-states). Galactic cosmic rays in contrast are fully stripped, and thus an ACR O-ion has 8 times the rigidity of a galactic cosmic ray O-ion at a comparable energy. The scattering of lower rigidity particles is more extensive than at high rigidity, or equivalently lower rigidity particles have a much longer dwell time in the heliosphere and suffer substantially more adiabatic deceleration. The inherently higher rigidity of ACRs, due to their single charge, permits them to escape substantial cooling, and allows the steep spectral shapes to persist. Thus, confirming the predicted single charge of ACRs provided a definitive test of their origin as interstellar neutral gas. Instrumentation in the 1970's and even the 1980's could not determine the charge state of energetic particles directly. Since the charge state determines the rigidity of the ACRs, and thus their transport and modulation by the solar wind, the charge state could be inferred from studies of the temporal and spatial behaviour of the ACRs. McKibben (1977), Klecker et al. (1980), and Cummings et al. (1984) performed such studies and the inference was, as expected, that the ACRs are of low charge, if not singly charged. It remained, however, for the SAMPEX mission in the early 1990's to settle the issue definitively. SAMPEX is in a relatively low Earth orbit, and can use the magnetic field of the Earth as a screening mechanism to filter out higher charge-state particles. This technique was used with Skylab and Spacelab instruments, which showed results consistent with ACRs having low charge states. Then with the advanced instruments on SAMPEX, Klecker et al. (1995) placed firm upper limits on the charge states. Most were singly charged. The SAMPEX observations confirmed the principal prediction of the theory for the origin of the ACRs – they are interstellar neutral gas ionized and accelerated in the solar wind. Interesting enough there are some higher charge states as well, which has led to some important limits on the dwell time (Mewaldt et al., 1996) and location of the acceleration of the anomalous particles. As has been modelled in detail by Jokipii (1996), the presence of multiple charged ACRs, and the energies they obtain, is consistent with acceleration at the termination shock of the solar wind, where the supersonic solar wind flow becomes subsonic.

Since the initial observations of ACRs in the early 1970's, far more detailed compositional measurements have been made, in particular from the SIS and CRIS instruments on the Advanced Composition Explorer (ACE) mission, as is shown in Figure 5.16 from Leske et al. (2000). The panel on the left shows the dominant

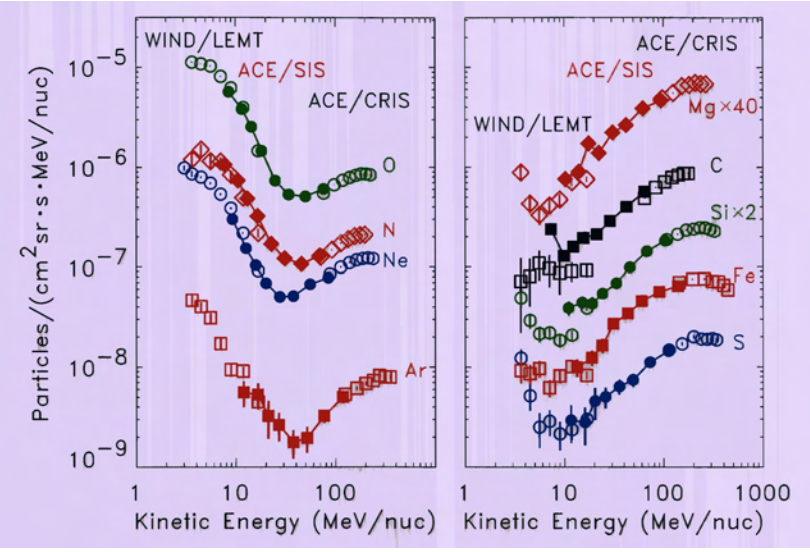

Figure 5.16: Elemental spectra using data from the SIS (filled symbols) and CRIS instruments (high energy open symbols) on the Advanced Composition Explorer mission, and from the LEMT instrument (low energy open symbols) on WIND (from Leske et al. 2000).

heavy ACR species, O, N, Ne, and Ar, exactly as would be expected from the interstellar neutral gas. ACR H should also be present in the heliosphere, and has in fact been detected from Voyager (Cummings and Stone, 1996; Cummings et al., 1999). Since ACR H has the same rigidity, at a given energy, as galactic cosmic ray H, it suffers too much modulation in the solar wind to be seen at the orbit of ACE at 1 AU. In the right panel of Figure 5.16 is the evidence for some minor species in the ACRs. The spectra above $\sim$ 10 Mev/nucleon are due to galactic cosmic rays. However, there is evidence for some small turn-ups in the spectra below $\sim$ 10 MeV/nucleon in Mg, C, Si, Fe, and S. It should be emphasized that these additional ACR components are of very low intensity and do not affect the basic interpretation that ACRs are dominated by interstellar neutral gas that is ionized and accelerated in the solar wind. They are, however, interesting and potentially consistent with other sources of pickup ions in the solar wind, besides interstellar gas, as we discuss below.

It has also been possible from ACE to measure the isotopic composition of ACRs. ACR ^{18}O/^{16}O and ^{22}Ne/^{20}Ne ratios are consistent with those found in Solar System material, cf. Table 5.6. The ^{22}Ne/^{20}Ne ratio is a factor of order 5 below that of galactic cosmic rays (e.g. Connell and Simpson, 1993; Lukasiak et al., 1994). This shows again that galactic cosmic rays and ACRs are not accelerated from the same sample. ACR ^{15}N and ^{21}Ne are below detectability, which places an upper limit on the ^{15}N/^{14}N and ^{21}Ne/^{20}Ne ratios in the LIC.

5.5.1 The acceleration of Anomalous Cosmic Rays

The origin of the ACRs as interstellar neutral gas is well established. What is less well established is how they are accelerated in the solar wind. Immediately following their ionization, the interstellar ions are forced to gyrate about the magnetic field in the solar wind, thereby acquiring energies of the order the solar wind flow energy $\sim$ 1 keV/nucleon. The ACRs are observed at energies of $>$ 10 MeV/nucleon. There is thus an order of magnitude 4 acceleration in the solar wind.

For many years, almost since the beginning of the study of ACRs, the prevailing theory for their acceleration has been diffusive shock acceleration at the termination shock of the solar wind, as suggested by, for example Pesses et al. (1981). The supersonic solar-wind flow ends at the so-called termination shock, which surrounds the Solar System; the solar wind is subsonic in the heliosheath beyond the termination shock. Energetic particles making multiple crossings of a shock can in principle gain significant energy, and thus this large all-encompassing termination shock provides a natural acceleration site for the ACRs.

There was thus the full expectation that when Voyager 1 crossed the termination shock in December 2004, at 94 AU from the Sun (Burlaga et al., 2005; Decker et al., 2005a; Gurnett and Kurth, 2005; Stone et al., 2005), the ACRs would peak in intensity; their spectra, which show evidence of modulation by the solar wind, would unfold and reveal a spectral characteristic of diffusive shock acceleration. One of the great surprises, then, and significant discoveries of the Voyager mission was that no evidence for the acceleration of ACRs at the termination shock was found (Stone et al., 2005; Decker et al., 2005a). The spectra of the ACRs were essentially unchanged, continuing to show evidence of modulation, and indicating that their acceleration must be occurring elsewhere. These observations have forced reconsideration of how ACRs are accelerated, which is currently an ongoing research activity.

What are accelerated at the termination shock are low-energy ions, with less than about 3 MeV/nucleon (Decker et al., 2005a). The intensity of these particles increases abruptly at the shock. Their composition is also that of the interstellar pickup ions in that they are depleted in carbon. The accelerated particles have a surprisingly constant spectrum, with a spectral index of -1.5 when expressed as differential intensity, or -5 when expressed as a distribution function (Decker et al., 2005b). Indeed, throughout the downstream heliosheath, the spectral index of the accelerated particles is unchanged, one of the more constant quantities ever observed in the heliosphere.

In the inner heliosphere, the spectral shape is also observed to have a spectral index of -5, as can be seen in Figure 5.17 from Fisk and Gloeckler (2006). These observations are averaged over periods when the solar wind is quiet, i.e. in the absence of nearby shocks. The spectra are observed in the frame of the spacecraft. When the spectra are transformed back to the solar wind frame, the spectral index is -5. Fisk and Gloeckler (2006) argue that the suprathermal tail in Figure 5.17 results from particles undergoing a stochastic acceleration in compressional turbulence, in which the particles are accelerated by and do an equal amount of work on the turbulence. In these circumstances the suprathermal tail is formed by a cascade in energy. Fisk and Gloeckler show that the spectral index must be -5 by

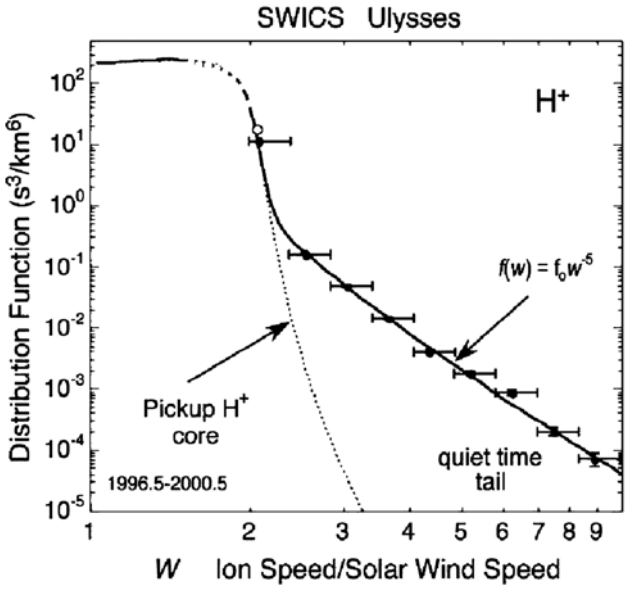

Figure 5.17: Distribution function of protons versus W (proton speed/solar wind speed), showing the suprathermal tail portion of the velocity distribution, as measured by the SWICS instrument on Ulysses from mid-1996 to mid-2000 (after Fisk and Gloeckler, 2006). Ulysses was in the slow solar wind at a mean distance of 4.82 AU from the Sun and a mean heliographic latitude of 7.4°. Data represented by the filled circles are selected for quiet times (see text) where any contributions from shocks were excluded. Unfilled circles represent the high-resolution velocity distribution for the entire time period showing the core pickup H^+ below $W = 2$. The dotted curve is the model pickup proton distribution computed by using standard interstellar parameters (Gloeckler and Geiss, 2004). The solid curve is the sum of the pickup ion core distributions and a suprathermal tail of the form $f(w) = f_0 w^{-5}$ (where w is the proton speed/solar wind speed in the solar wind frame), transformed to the spacecraft frame of reference.

an argument analogous to the determination of the spectral index in the inertial range of a turbulent cascade (Kolomogorov, 1941).

The following picture then emerges for acceleration in the heliosphere. Suprathermal tails are formed in the solar wind by a cascade in energy and convected into the outer heliosphere. The spectral index is -5, and the tails extend upward in energy until the particles can no longer experience the stochastic acceleration, which occurs presumably when the gyro-radii of the particles exceeds the scale size of the turbulence. These suprathermal tails are then convected into the termination shock. Fisk et al. (2006) have pointed out that a spectral index of -5 can be preserved in crossing the termination shock. With this spectral index the pressure in the suprathermal particles will increase across the shock in proportion to the pressure increase of the core pickup ions, and thus the pressure in the accelerated particles will behave according to the Rankine-Hugoniot relationship. It is neces-

sary to assume in this argument that diffusive acceleration does not apply at the termination shock, a situation that may be justified since these low-energy particles cannot propagate easily upstream in the essentially azimuthal magnetic field of the outer heliosphere.

Voyager 1 also observed strong anisotropic beams upstream from the termination shock, presumably from particles leaking upstream from a termination shock with a distorted shape. Gloeckler and Fisk (2006) have shown that the observed beams are consistent with a downstream spectrum with spectral index of -5, and upstream spectra that are distorted by velocity dispersion. The beams originate from a wide range of heliographic longitudes on the termination shock, and so the arguments of Gloeckler and Fisk (2006) demonstrate that the downstream spectrum of -5 occurs over this same broad longitudinal range. Thus, Voyager 1 saw representative conditions when it crossed the termination shock.

Voyager 1 also observed strong compressional turbulence in the heliosheath (Burlaga et al., 2005), and thus the conditions exist for stochastic acceleration, similar to but more enhanced than what is observed in the inner heliosphere by Fisk and Gloeckler (2006). It is reasonable to assume that this process is the likely acceleration mechanism for the ACRs. The pickup ions are accelerated in the suprathermal solar wind by stochastic acceleration in compressional turbulence, which forms a power law spectrum with spectral index of -5, when expressed as a distribution function. The particles are further accelerated at the termination shock, by processes that preserve the spectral index. Some of the particles leak upstream to form the observed anisotropic beams. The remaining particles are convected into the heliosheath where they experience an enhanced stochastic acceleration in the pronounced compressional turbulence that is present. Again the spectral index is -5, but now extends to much higher energies as the particles are convected further into the heliosheath. Eventually the particles reach sufficiently high energies that they are mobile in the solar wind, and diffuse inwards to be observed as modulated ACRs.

The picture of continuous acceleration of the pickup ions to form the ACRs will become clearer as Voyager 1 penetrates deeper into the heliosheath, and Voyager 2 first reaches and crosses the termination shock, and performs its exploration of the heliosheath, but at different latitudes from Voyager 1. Voyager 2 also has the advantage over Voyager 1 that it includes a working solar wind plasma detector that can directly measure the flow properties of the solar wind. Furthermore, there is now considerable theoretical work underway to produce models and make predictions that can be tested against these observations.

5.5.2 Minor components of Anomalous Cosmic Rays

As is indicated in Figure 5.16, also present in ACRs are small amounts of other elements such as Mg, C, Si, Fe, and S (minor ACRs). If these particles are accelerated at the termination shock and in the heliosheath, and propagate back into the inner heliosphere to be seen at Earth, they should also be of relatively high rigidity, i.e. as with the dominant interstellar ions, they need to be primarily singly-charged. It is unlikely that they originate as interstellar neutral gas; particularly elements such as C are readily ionized and should not be neutral in the interstellar

medium. A more likely source is the inner source of pickup ions, described in Sections 5.2 and 5.3, where solar wind ions become embedded in grains in the very inner heliosphere, are released as neutral particles and form an additional pickup ion source (Geiss et al., 1995; Schwadron et al., 2000). The composition of the inner source resembles the composition of the solar wind, and thus includes Mg, C, Si, Fe, and S (Gloeckler et al., 2000). The inner source ions will also be singly-charged since they are released from the grains as neutrals, and ionized only once.

If inner source pickup ions are accelerated at the termination shock, they will likely require pre-acceleration as they are convected outwards with the solar wind. As discussed in Section 5.3, most of the inner source pickup ions are created at a few tens of solar radii, where the solar wind is expanding rapidly. The result is substantial adiabatic cooling, such that the speeds of the inner source pick up ions are reduced to close to the solar wind thermal speeds. It is interesting to note that the distribution functions of the inner source, which are peaked at speeds moving slower than the mean speed of the solar wind, in the frame of the termination shock, are ideal for injecting these ions into a shock-drift injection mechanism, such as has been proposed by Lee et al. (1996) and Zank et al. (1996). More likely it will be necessary to raise the energies of the inner source pickup ions, perhaps by the statistical acceleration mechanism that appears to create the tails on the distributions of interstellar pickup ions. A significant fraction of these inner source pickup ions would then arrive at the termination shock with suprathermal tails similar to those of interstellar pickup ions and then be accelerated at the termination shock and in the inner heliosheath in the same manner as interstellar pickup ions. It is also likely that pickup ions produced at heliocentric distances extending to tens of AUs by the same mechanism as inner source pickup ions or by sputtering from grains, contribute to the minor ACRs.

5.6 Abundances of elements and isotopes in the Local Interstellar Cloud

The elemental abundances in the interstellar gas were adopted from Gloeckler (2005). They are presented in Table 5.4. The neutral densities at the Termination Shock (column 2) are derived from pickup ion measurements. The atomic densities in column 5 are obtained from the data in column 2, after correcting for the filtering effect in the heliospheric interaction region, using the filtration factors given in column 3. The ion densities given in column 4 are calculated with the ionization fraction in the LIC given in column 4. The densities in grains are estimates. The protosolar abundances used are the averages of the values given by Holweger (2001) and Asplund et al. (2005) for oxygen and the values given by Grevesse and Sauval (1998) for the other elements.

Isotopic abundances are of particular importance for understanding the nuclear galactic evolution (see Section 5.7). In Figure 5.18 the mass spectrum and the phase space density of the helium isotopes are shown.

Isotopic abundances in the LIC are given in Table 5.5. The D/H ratio comes from an analysis of H and D absorption lines from nearby stars by Linsky and Wood (1998). The ^{3}He/^{4}He ratio in the LIC has been deduced using pickup ion

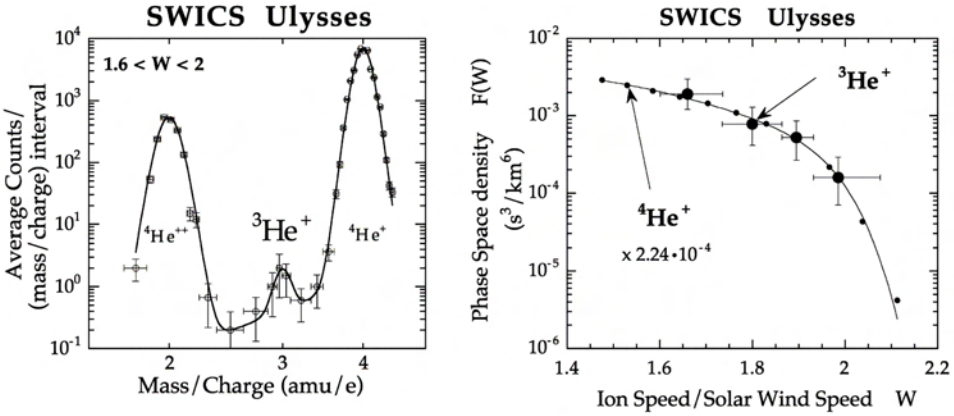

Figure 5.18: First detection of interstellar ^{3}He inside the heliosphere. Shown on the left is a mass per charge spectrum of the triple coincidence counts of ions with relative velocity W between $1.6 < W < 2$. The right hand side shows the velocity distribution functions of $^3He^+$ and $^4He^+$, with $^3He^+$ corrected for a 10% background. The two distribution functions match if the phase space density of $^4He^+$ is multiplied by 2.24×10^{-4}. Thus the $^3He^+/^4He^+$ ratio is 2.24×10^{-4} (after Gloeckler and Geiss, 1996, with copyright permission from Nature).

measurements by Gloeckler and Geiss (1996, 1998) and foil collection techniques by Salerno et al. (2001) and Busemann et al. (2006). The isotopes of nitrogen were investigated by Leske et al. (1996), and the results for the oxygen and neon isotopes are from Leske (2000). For ^{15}N and ^{18}O, only upper limits are available so far. Nevertheless, these limits are very valuable, because the abundances of these isotopes are much higher in the galactic cosmic rays. This underlines the difference in origin: in the galactic cosmic rays, rare isotopes are strongly augmented by spallation processes in the Galaxy, while the ACRs with their local origin and the corresponding short lifetime did not receive any noticeable addition of spallation products.

5.7 Nucleosynthesis and galactic evolution

Our concept of nucleosynthesis, as well as what we know about the origin of the elements and their isotopes, is largely based on abundance measurements in the Solar System. We know, with high precision in most cases, the relative abundance of nearly 300 nuclear species in the protosolar cloud. This cloud represents a sample of galactic matter frozen-in (in terms of nuclear evolution) 4.6 billion years ago. In meteorites, we also have measurements of isotopic ratios in relatively well-preserved stellar grains. Such grains were embedded into asteroids, the parent bodies of meteorites, at the time of Solar System formation. These isotope data represent very specific information about the composition released from certain stellar sources, such as AGB stars or supernovae. Finally, we have a large body

Table 5.5: Isotopic abundances in the Local Interstellar Cloud (LIC).

Isotope Ratio	Method	LIC Abundance	Ref.	LIC Abundance to Protosolar Abundance
D/H	Lyman-α	$(1.7\pm0.2) \times 10^{-4}$	^{a}	0.85±0.2
^{3}He/^{4}He	Pickup Ions	$(2.2\pm0.7)\times10^{-4}$	^{b}	
^{3}He/^{4}He	Pickup Ions	$(2.48\pm0.6)\times10^{-4}$	^{c}	1.2±0.2
^{3}He/^{4}He	Foil collection	$(1.71^{+0.50}_{-0.42})\times10^{-4}$	^{d}	
^{3}He/^{4}He	Foil collection	$(1.62\pm0.29)\times10^{-4}$	^{e}	
^{15}N/^{14}N	ACR	< 0.023	^{f}	< 6
^{18}O/^{16}O	ACR	< 0.0032	^{g}	< 1.6
^{22}Ne/^{20}Ne	ACR	$0.08^{+0.030}_{-0.026}$	^{g}	1.1±0.4

^{a} Linsky (1998); Linsky et al. (2006), see text; ^{b} Gloeckler and Geiss (1996); ^{c} Gloeckler and Geiss (1998); ^{d} Salerno et al. (2001); ^{e} Busemann et al. (2006); ^{f} Leske et al. (1996); ^{g} Leske (2000)

of spectroscopic data on elemental abundances (and to a lesser extent on isotopic abundances) of a variety of galactic and extra-galactic objects.

Missing until recently, however, was a sample of the present-day Galaxy with reliable observations of a number of important elemental and isotopic abundance ratios, all measured in one and the same galactic sample. Investigation of the interstellar atoms and ions inside the heliosphere, combined with remote spectroscopy in the LIC, is beginning to fill this gap.

The chemical elements and their isotopes are synthesized at three principal sites: the Big Bang, which yielded only light nuclei such as H, He, their isotopes ^{3}He and D, and also ^{7}Li; the stars, which synthesize some additional ^{3}He and ^{4}He and all of the C and the heavier elements; and finally high-energy cosmic rays, which yield very rare nuclei, such as beryllium, ^{6}Li and ^{10}B.

Stars, of course, release the material they synthesize through stellar winds and supernova or nova explosions. Over time, then, the interstellar medium should become more enriched in the heavy elements.

Once several key elemental and isotopic ratios can be measured with sufficient precision, the LIC will become an important source of information for the evolution of the Galaxy. Elemental ratios must, however, be interpreted carefully, because they are affected by filtration in the heliospheric interaction region (see Figure 5.1) and by differences in the degree of ionization in the LIC (Table 5.4). For isotopic ratios, this is generally not an issue since ionization, recombination, and transport should be virtually the same for all isotopes of a given element.

5.7.1 The isotopes of H and He

Among the isotopic ratios in the LIC, only D/H and ^{3}He/^{4}He are now measured with sufficient precision to constrain primordial nucleosythesis and galactic evolution models.

Deuterium (D), the heavy isotope of hydrogen, is the only nucleus that is produced exclusively in the Big Bang. Moreover, the production of deuterium in the Big Bang is strongly dependent on the baryonic matter density in the Universe, and therefore this density can be derived if the primordial D/H ratio is reliably determined.

^{3}He is also in a category of its own. It is produced by three processes: Big Bang nucleosynthesis, D-burning in the early life of stars of all sizes, and incomplete H burning. The last process is important for studying the late galactic evolution. A fraction of ^{3}He in the present-day interstellar gas was produced by incomplete hydrogen burning at intermediate depth in small stars (Iben and Truran, 1978) and released into interstellar space when the star had left the Main Sequence, i.e. $\sim 10^{10}$ years after its birth. Therefore, the importance of this mode of ^{3}He production increased in the later stages of the life of the Galaxy.

^{1}H and ^{4}He represent more than 99.9% of the total baryonic mass coming out of the Big Bang. D and ^{3}He are rare and their yields depend inversely on the baryonic density. This is analogous to chemical reactions, where the yields of intermediate products decrease with increasing supply of reacting partners. Since the early 1970s, deuterium abundance measurements in the solar wind (estimated from measurements of the ^{3}He abundance in the present-day solar wind), meteorites, Jupiter and the galactic interstellar gas were used to extrapolate to the primordial abundance of deuterium. Values of D/H in the range $(3-5)\times10^{-5}$ were obtained from which a universal baryonic density of $(3-6)\times10^{-28}$ kg/m^3 was calculated, corresponding to about 0.2 atoms per cubic metre. A general consensus has existed on these values since the 1970s (Geiss and Reeves, 1972; Reeves et al., 1973; Walker et al., 1991), although occasionally inaccurate measurements were published creating doubts about the validity of extrapolation of galactic D/H ratios to primordial values.

The observational basis for deriving the universal baryon density was greatly broadened in the 1990s, when both D and ^{3}He were determined by Linsky and Wood (1996) and by Gloeckler and Geiss (1996) in the Local Interstellar Cloud (LIC), and the first reliable D/H values in low-metallicity distant clouds were published by Tytler et al. (1996). The best current D/H, and ^{3}He/H and (D+^{3}He)/H ratios in the LIC, the PSC and the early Universe are shown in Figure 5.19.

The universal densities of baryons as derived from these three abundance ratios are in perfect agreement and presently give a universal baryon/photon ratio of $(5.8\pm0.6)\times10^{-10}$ and a present-day universal density of baryonic matter of $\sigma_{\rm B} = (4.1\pm0.4)\times10^{-31}$ g/cm^3 or about 0.2 atoms per cubic metre. The baryon/photon ratio is one of the fundamental numbers of cosmology. So far, it is known only empirically. Any theory of the earliest phases of the Big Bang will have to predict a value that is compatible with the number derived from deuterium and ^{3}He.

The question of stellar production of ^{3}He was discussed intensely until the mid 1990's. Theoretical estimates predicted a sharp increase of ^{3}He in the Galaxy during the last 5 Gyr. On the other hand, the earliest reports on D/H in very distant clouds (Songaila et al., 1997) suggested a very high primordial D/H ratio above 10^{-4}. Then, in about 1995 experimental and theoretical work solved the problem. In the LIC both D/H (Linsky and Wood, 1996) and ^{3}He/^{4}He (Gloeckler and Geiss, 1996) were measured. Moreover, the theoretical work showed that ^{3}He

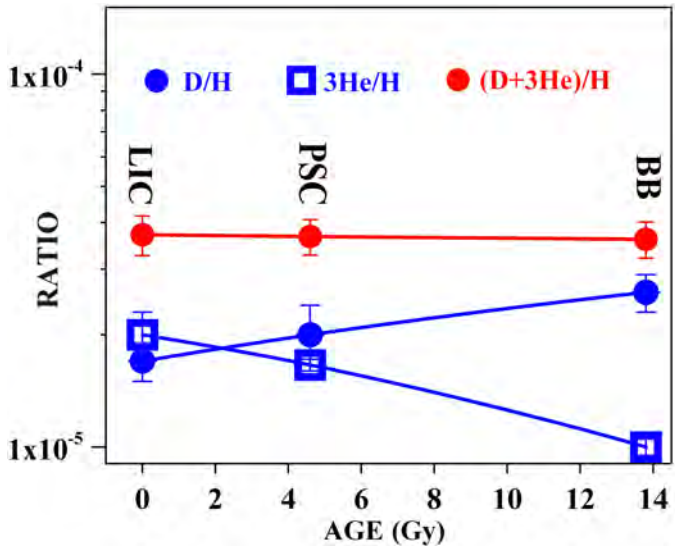

Figure 5.19: Abundances – relative to hydrogen – of deuterium (D) - the light helium isotope (^{3}He) and D + ^{3}He in the Local Interstellar Cloud (LIC), the Protosolar Cloud (PSC) and very distant clouds (or other extremely metal-poor regions) that approximately represent matter released from the Big Bang (BB). The primordial abundance of D is the average recommended by Romano et al. (2006). For ^{3}He/H we took the theoretical value of 1×10^{-5} that corresponds to the measured D/H value (see Geiss and Gloeckler, 2005) which is compatible with the upper limit given by Bania et al. (2002). For the PSC and LIC abundances see Table 5.6. Deuterium is exclusively produced in the Big Bang and converted thereafter into ^{3}He in stars. The net effect of other nuclear processes on the abundance of these two nuclides is relatively small so that throughout galactic history the (D+^{3}He)/H ratio remained nearly constant. (D + ^{3}He)/H in the PSC was directly derived from solar wind data (Geiss and Reeves, 1972; Geiss and Gloeckler, 2003).

from incomplete H burning does not have a large effect on the chemical evolution of the Galaxy, i.e. the main ^{3}He production in the Galaxy is from D burning (Charbonnel, 1998; Tosi, 2000; Bania et al., 2002). The result is that (D + ^{3}He)/H has remained approximately constant (Figure 5.19).

Since the sum of D and ^{3}He is nearly independent of galactic evolution, the primordial baryonic density can be derived from this sum with little, if any, extrapolation. As Figure 5.19 shows, (D+^{3}He)/H in the two galactic samples and in the distant low-metallicity clouds are nearly the same. Thus, at the time of primordial nucleosynthesis, the baryonic densities in the far-away regions of these clouds and in our part of the Universe were the same, which is evidence for a homogenous Universe at the time of primordial nucleosynthesis.

5.7.2 Galactic evolution during the last 5 Gyrs

By comparing elemental and isotopic abundances in the PSC with those in the LIC or in the local interstellar medium (LISM) the chemical evolution during the last 5 Gyr can be investigated in the solar ring, i.e. the region of the Milky Way with a distance from the centre of the order of 8.5 kpc. Such a comparison reveals that the composition of the matter in the solar ring of the Galaxy could not have evolved from matter with PSC composition in a closed system environment. There are three observations in particular that defy a closed system interpretation:

1. The D/H ratio in the solar ring has not decreased as much as would be expected in a closed system Galaxy. The explanation, now generally accepted, is that infall into the Milky Way of moderately processed material has limited the decrease of the D/H ratio in the ISM (Tosi, 1988).

2. Within the limits of uncertainty, the metallicity is the same in the PSC and the present-day ISM in the solar neighbourhood. The apparent lack of growth in metallicity is again best explained by infall into the Galaxy of moderately processed matter. Using a mixing model (see Section 7.3), Geiss et al. (2002) showed that infall of matter with the nucleosynthetic signature of dwarf galaxies, such as the Magellanic Clouds, explains the limited increase in D/H as well as the absence of a significant growth in metallicity during the last 5 Gyr.

3. The relative abundances of the three oxygen isotopes in the PSC and ISM are very different (Wilson and Rood, 1994), and it is difficult to find a chemical evolution model that explains this "^{18}O-puzzle" (Prantzos et al., 1996) and is, at the same time, consistent with other relevant observations. Particularly puzzling is the large difference between the $^{18}O/^{17}O$ ratio in the PSC of 5.34 and that in the interstellar medium of 3.6. Since an average $^{18}O/^{17}O = 3.6 \pm 0.3$ is observed in the ISM between 4 kpc and 12 kpc from the centre of the Galaxy (Kahane, 1995; Prantzos et al., 1996; see Henkel and Mauersberger, 1993) this difference between the PSC and ISM values can hardly be explained by assuming that, relative to its present position, the Sun's birthplace was a few kpc closer to the galactic centre.

Many years ago it was discussed whether the Sun was born in an OB association and incorporated an extra amount of freshly processed material ejected by Massive Stars (e.g. Reeves, 1978; Olive and Schramm, 1982). Later it was considered (e.g. Henkel and Mauersberger, 1993) that this could have led to a general increase of metallicity in the PSC and also to some exceptional isotopic abundances such as a high $^{18}O/^{17}O$ ratio. Since OB associations typically last for 30 Myrs (e.g. Preibisch et al., 2006), this hypothesis is difficult to reconcile with the low abundances in the PSC of extinct radioactive nuclides that are derived from the abundances of their decay products in meteorites. If in the PSC a significant fraction of stable nuclides from massive stars was synthesized in the last OB association, a very high concentration of heavy extinct radioactive nuclides with $T_{1/2} \sim 10^7$ to 10^8 yrs should have been present in the PSC and incorporated into meteorites. However, nuclides such as ^{244}Pu ($T_{1/2} = 82$ Myr), ^{182}Hf ($T_{1/2} = 9$ Myr), ^{146}Sm ($T_{1/2} = 103$

Myr), $^{1}29$I ($T_{1/2}$ = 17 Myr) or ^{107}Pd ($T_{1/2}$ = 6.5 Myr) are found to have only approximately "uniform galactic production" abundances (e.g. Shukoliukov and Begemann, 1996; Lee and Halliday, 1996; Podosek and Nichols, 1997; Wasserburg et al., 2006), implying that no significant excess of ^{18}O and other stable products from Massive Stars could have been synthesized during the 10^7 to 10^8 yrs that preceded the formation of the Solar System.

Here we do not assume a non-typical history of the Sun for explaining differences between the composition of the PSC and the ISM. Instead we seek to find the cause for these differences in processes that affected a large portion of the Galaxy. We assume that at least a significant fraction of the infall into the Milky Way comes from dwarf galaxies, and we argue that infall could very well be changing in intensity and composition on a time scale of $10^9 - 10^{10}$ years. Using the mixing model of Geiss et al. (2002), we infer the intensity and composition of infall that would reproduce the differences between the PSC and LIC or LISM abundances.

Geiss et al. (2002) included in their model the isotopes of hydrogen and helium and the element abundances of nitrogen and oxygen relative to hydrogen. Here we include also the isotopes of oxygen. The three O-isotopes are very important for chemical evolution studies because their nuclear origins are very different. ^{16}O is an alpha-nuclide, i.e. it is an authentic primary product of stellar nucleosynthesis. ^{18}O is considered to be a relatively pure secondary product, and ^{17}O is primary as well as secondary. Whereas ^{16}O and ^{18}O are mainly products of massive stars, most of ^{17}O comes from intermediate mass stars, released during the RGB and AGB phases (e.g. Prantzos et al., 1996; Ventura et al., 2002).

5.7.3 The mixing model

A comparison of abundances in the Protosolar Cloud (PSC), the Local Interstellar Cloud (LIC) and the Large Magellanic Cloud (LMC) led Geiss, Gloeckler and Charbonnel (2002) to propose that external matter falling into the galactic disk during the last 5 Gyr carries the nucleosynthetic signature of dwarf galaxies. They introduced a two component mixing model with "PSC_0" and "excess-infall" as the two components. PSC_0 represents a hypothetical cloud that had PSC composition 4.6 Gyr ago and has since continued to evolve under nucleosynthetic, infall, and galactic-wind conditions that are consistent with the evolution of the matter in the PSC prior to 4.6 Gyr. For the second component, the "excess-infall", they assumed a composition of the type found in dwarf galaxies. Since the Large Magellanic Cloud (LMC) is the best studied, they assumed the "excess-infall" to have an LMC composition. In Figure 5.20 some abundance ratios in the interstellar gas of the Galaxy in the solar neighbourhood and of the LMC are compared with the abundances in the PSC. Remarkable is the very low abundance in the LMC of ^{14}N and ^{18}O, two authentic secondary nuclides. The differences between $(^{18}O/^{17}O)_{PSC}$, $(^{18}O/^{17}O)_{LISM}$ and $(^{18}O/^{17}O)_{LMC}$ are particularly significant and, indeed, the $^{18}O/^{17}O$ values in Figure 5.20 suggest that ISM oxygen can be seen as a mixture of oxygen from PSC and LMC.

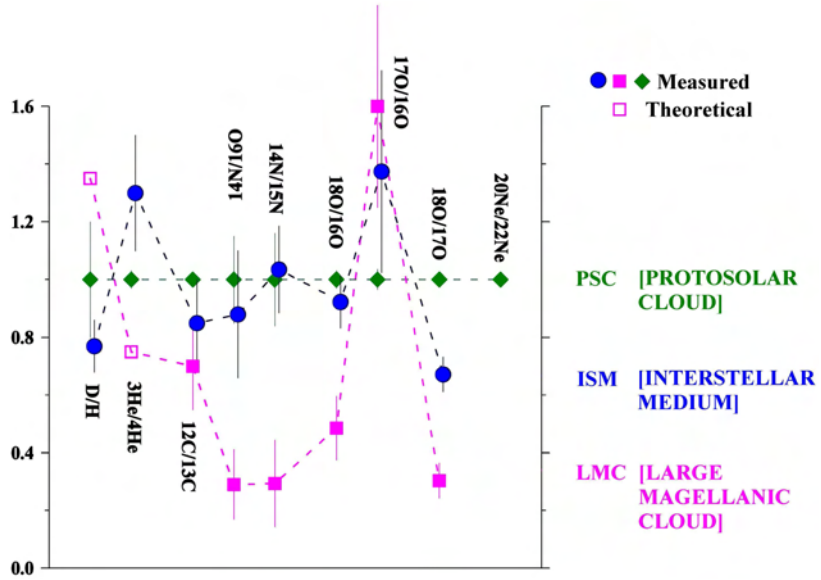

Figure 5.20: Abundance ratios in the local Galactic Interstellar Medium (ISM) and in the Large Magellanic Cloud (LMC), normalized to the protosolar ratios (Chin et al., 1999, and references quoted therein). The large differences, especially the low abundances of the secondary nuclides ^{14}N and ^{18}O reflect differences in the nucleosynthetic origin, allowing study of the chemical and dynamic history of the Galaxy and of the Local Group.

If $Y_1 = (\mathrm{A/H})_{\mathrm{PSC}_0}$ and $Y_2 = (\mathrm{A/H})_{\mathrm{excess-infall}}$ are the abundances – relative to hydrogen – of a nuclide A in the PSC_0 and excess-infall, respectively, we have

$$Y_{\mathrm{LIC}} = (1 - X)Y_1 + XY_2, \tag{5.4}$$

where $Y_{\mathrm{LIC}} = (\mathrm{A/H})_{\mathrm{LIC}}$, and X is the mixing ratio, defined as

$$X = N_2\,(\mathrm{H}) \,/\, [N_1\,(\mathrm{H}) + N_2\,(\mathrm{H})]\,. \tag{5.5}$$

$N_1\,(\mathrm{H})$ and $N_2\,(\mathrm{H})$ are the number of H atoms in PSC_0 and excess-infall matter, respectively.

Völk (1991) pointed out that loss from the Galaxy by galactic winds could have a significant effect on chemical evolution, if the wind is strong enough and if products from Massive Stars are lost preferentially. Indeed, wind-loss could contribute to reducing the increase of metallicity (see also Veilleux et al., 2005). Although we shall deal here quantitatively only with the infall of external matter, we shall formulate the mixing model for a combination of excess-infall and excess-loss by wind. However, to retain the character of a two-component mixing model, we introduce the ratio of the hydrogen number density of the excess-loss produced by the galactic wind to the hydrogen number density of the excess-infall

$$\eta = N_{\mathrm{excess-loss}}\,(\mathrm{H})\,/N_{\mathrm{excess-infall}}\,(\mathrm{H})\,, \tag{5.6}$$

leading to $Y_2 = (\mathrm{A/H})_{\mathrm{excess-infall}} - \eta\,(\mathrm{A/H})_{\mathrm{excess-loss}}$.

Solving Equation (5.4) for X and expressing abundance ratios relative to PSC values by braces { }, the mixing ratio X obtained for the O/H ratio measured in the LIC is given by

$$X\,(\mathrm{O/H}) = \frac{\{\mathrm{O/H}\}_{\mathrm{PSC_0}} - \{\mathrm{O/H}\}_{\mathrm{LIC}}}{\{\mathrm{O/H}\}_{\mathrm{PSC_0}} - \{\mathrm{O/H}\}_{\mathrm{excess-infall}} - \eta\{\mathrm{O/H}\}_{\mathrm{excess-loss}}}. \tag{5.7}$$

The X-values for other nuclides relative to H are obtained in an analogous way.

In the following we consider only the excess-infall case, i.e. we put $\eta = 0$. In the general case of a non-negligible excess-loss, $\{\mathrm{A/H}\}_{\mathrm{excess-infall}}$ must be replaced by $\{\mathrm{A/H}\}_{\mathrm{excess-infall}} - \eta\ \{\mathrm{A/H}\}_{\mathrm{excess-loss}}$ in Equation (5.7) and the following discussion.

Mixing ratios can also be calculated for the ratio of any two nuclides, especially for an abundance ratio of isotopes of a given element. The corresponding equation is obtained by writing Equation (5.4) for the two species and dividing the two resulting equations. For the case of $^{18}\mathrm{O}/^{17}\mathrm{O}$ one obtains

$$\{^{18}\mathrm{O}/^{17}\mathrm{O}\} = \frac{(1-X)\,\{^{18}\mathrm{O/H}\}_{\mathrm{PSC_0}} + X\{^{18}\mathrm{O/H}\}_{\mathrm{excess-infall}}}{(1-X)\,\{^{17}\mathrm{O/H}\}_{\mathrm{PSC_0}} + X\{^{17}\mathrm{O/H}\}_{\mathrm{excess-infall}}}. \tag{5.8}$$

The mixing ratio X can be determined from the measured ratio $^{18}\mathrm{O}/^{17}\mathrm{O}$ in the LIC or LISM and the given model parameters contained in the right-hand side of Equation (5.7). This equation is in fact independent of the abundance of hydrogen in the LIC or LISM. In cases where the ratio of the two species is well determined and better known than their abundances relative to hydrogen, Equation (5.7) yields mixing ratios with smaller errors than Equation (5.4).

Here we apply the mixing model to the abundance ratios D/H, ^{3}He/H, O/H and N/H, as did Geiss et al. (2002), but we have included here also ^{16}O/H (virtually identical to O/H), ^{18}O/H and $^{18}\mathrm{O}/^{17}\mathrm{O}$. Since in the LIC the heavier oxygen isotopes are not yet sufficiently well determined, we use average $^{16}\mathrm{O}/^{18}\mathrm{O}$ and $^{18}\mathrm{O}/^{17}\mathrm{O}$ ratios obtained in molecular clouds in the Local Interstellar Medium (LISM) outside the LIC. This seems justified, since the variability of these isotopic ratios is larger than gradients in any direction.

In Table 5.6 we show the PSC, LIC-LISM and LMC abundances used here. The sources of the abundances are given in the table. For the PSC abundances of N and O we took the averages of the values given by Holweger (2001) and by Asplund et al. (2005). We raised the $\{\mathrm{O/H}\}_{\mathrm{LMC}}$ value of 0.3 (de Boer, 1991) used by Geiss et al. (2002) to 0.35, because the value of 0.30 referred to the higher solar oxygen abundance adopted earlier.

The parameters for calculating the mixing ratios X are given in Table 5.7. For deriving $\mathrm{PSC_0}$ abundances we applied the methods of Geiss et al. (2002). However, we adopted $N_{\mathrm{PSC_0}} = 1.4 N_{\mathrm{PSC}}$ for all N and O atoms.

We discuss in this paper two models. In model 1, we use for the excess-infall the LMC abundances (measured for N and the isotopes of O; inferred for D and ^{3}He), see Tables 5.6 and 5.7 (Geiss et al., 2002; Geiss and Gloeckler, 2006). The only difference between models 1 and 2 is that for model 2 we increase the abundance of ^{17}O in the excess-infall (see Table 5.7).

Table 5.6: Abundances in the Protosolar Cloud (PSC), the Local Interstellar Cloud - Local Interstellar Medium (LIC - LISM) and the Large Magellanic Cloud (LMC).

Ratio	Unit	PSC	LIC-LISM	LMC
D/H	10^{-5}	2.0 ± 0.4^{a}	1.7 ± 0.2^{f}	
^{3}He/H	10^{-5}	1.66 ± 0.05^{b}	2.0 ± 0.4^{f}	
O/H	10^{-5}	50.1 ± 8^{cd}	53.2 ± 15^{h}	17.5 ± 7^{am}
N/H	10^{-5}	7.2 ± 1.0^{cde}	5.5 ± 1.5^{h}	0.75 ± 0.25^{a}
^{16}O/^{18}O	1	496±15	540 ± 50^{ij}	$\sim 1000^{ijl}$
^{18}O/^{17}O	1	5.34±0.1	3.6 ± 0.3^{jkl}	1.65 ± 0.3^{il}

[a] Geiss et al. (2002); [b] Mahaffy et al. (1998); [c] Holweger (2001);
[d] Asplund et al. (2005); [e] Owen et al. (2001); [f] from Table 5.5; [h] from Table 5.4;
[i] Chin (1999); [j] Chin et al. (1999); [k] Prantzos et al. (1996);
[l] Heikkilä and Johansson (1999); [m] de Boer (1991), see text

Mixing ratios X for individual species were calculated from Equation (5.6), and for ^{18}O/^{17}O from Equation (5.7). The results are presented in the last column of Table 5.7. In Figure 5.21 the measured LIC or LISM data points are plotted on the respective mixing line at the calculated X-value. These mixing lines are defined by the composition of the two components, PSC_0 and excess-infall.

For ^{17}O we present here the mixing ratio calculated from Equation (5.6) and for ^{18}O/^{17}O the mixing ratio calculated from Eq. (5.7). The $(^{17}O/H)_{LISM}$ and $(^{18}O/H)_{LISM}$ abundance ratios, needed for Equation (5.6) and not for Equation (5.7), are not well known in the samples of the LISM from which we adopted the oxygen isotope measurements. As mentioned above, Equation (5.7) is particularly adequate when the differences of the isotopic ratios in the three samples PSC, LISM, and excess-infall are larger than the uncertainties. This is the case for ^{18}O/^{17}O (see Figure 5.20). For the isotope ^{18}O the ratio ^{18}O/H provides a much better determination of X than the ratio ^{16}O/^{18}O. The reason is that the difference in ^{16}O/^{18}O between the PSC and LISM is small compared to the uncertainties (Figure 5.20).

Model 1 yields mixing ratios in the narrow range $0.32 \leq X \leq 0.49$ for all species except for those involving ^{17}O. ^{17}O/H even yields a negative X value. Its error limits, however, overlap with this range. ^{18}O/^{17}O has a well-defined mixing ratio of $X = 0.69 \pm 0.07$, which is outside the above range. This is not acceptable. This discrepancy led us to introduce Model 2 (see Geiss and Gloeckler, 2006). We retain the idea of the mixing model as expressed in Equations (5.4 - 5.7), and make an adjustment in the composition of only the excess-infall by adding to the LMC-like matter a small amount of matter, Δ, that is released from Intermediate Mass Stars (IMS). Adopting the yields given by Ventura et al. (2002) for these stars, we have calculated the composition of Δ for the metallicity $Z = 0.01$ and the stellar mass range $3.5 - 6M_{\odot}$. We note that the theoretical yields of some of the rare isotopes of the CNO elements are quite uncertain (Romano and Matteucci, 2003), which one has to take into account when quantitatively discussing Model 2 results.

Table 5.7: Abundances used for the Mixing Model (abundances given in braces are relative to PSC).

Ratio	PSC_0	Excess-Infall	LIC-LISM	X
Model 1: $(^{18}O/^{17}O)_{excess-infall} = 1.65$				
{D/H}	0.6^a	1.2^a	0.85±0.15*	0.42±0.25
$\{^3He/H\}$	1.5^a	0.75^a	1.20±0.20*	0.40±0.27
$\{^{14}N/H\}$	1.4	0.1	0.76±0.20*	0.49±0.16
$\{^{16}O/H\}$	1.4	0.35	1.06±0.30*	0.32±0.24
$\{^{18}O/H\}$	1.4	0.17	0.97±0.35**	0.35±0.28
$\{^{17}O/H\}$	1.4	0.56	1.48±0.52**	−0.10±0.62
$\{^{18}O/^{17}O\}$	1.0		0.674±0.056**	0.69±0.07
Model 2: $(^{18}O/^{17}O)_{excess-infall} = 0.80$				
$\{^{17}O/H\}$	1.4	1.16	1.48±0.52**	−0.33±2.16
$\{^{18}O/^{17}O\}$	1.0		0.674±0.056**	0.43±0.07

[a] Estimate, using interpolation based on metallicity (see also Geiss et al., 2002);
* Observed in the LIC; ** Observed in the LISM

Intermediate Mass Stars (IMS) are such specific ^{17}O-producers (see Figure 5.22) that the composition and the mixing ratios of models 1 and 2 remain virtually identical for all the species we are considering, except for values involving ^{17}O: the admixture of 0.5% of IMS-produced matter to the matter with LMC composition raises $\{^{17}O/H\}_{excess-infall}$ from 0.56 in Model 1 to 1.16 in Model 2, and it decreases the $(^{18}O/^{17}O)_{excess-infall}$ ratio from 1.65 to 0.80 (Geiss and Gloeckler, 2006). With the Model 2 parameters listed in Table 5.7, the mixing ratio is still negative. But because of its large error, it is not in contradiction with the other mixing ratios. All other ratios, including $^{18}O/^{17}O$ now yield mixing ratios in the range of $0.32 \leq X \leq 0.49$ (Table 5.7 and Figure 5.21) in satisfactory agreement with prediction and observation. The admixture of 0.5% of IMS-produced matter affects essentially ^{17}O. According to the predictions of Ventura et al. (2002), ^{14}N and also ^{13}C are increased in the excess infall by only 1% or less.

The solution to the ^{18}O puzzle offered by Model 2 is not unique, however. An excess is needed in the infall of matter from Intermediate Mass Stars. If other model parameters such as metallicity or $^{16}O/^{18}O$ are suitably adjusted as well, agreement can be achieved for a smaller ^{17}O-excess.

$^{18}O/^{17}O$ ratios as low as 0.80 are not unrealistic for the oxygen in the excess-infall. Much lower values are theoretically predicted for IMS-released matter (Ventura et al., 2002; Figure 5.22). Moreover, ratios $^{18}O/^{17}O = 1$ are typically observed in the spectra of red giant stars, and they are common in the pre-solar grains of meteorites (see Figure 5.22).

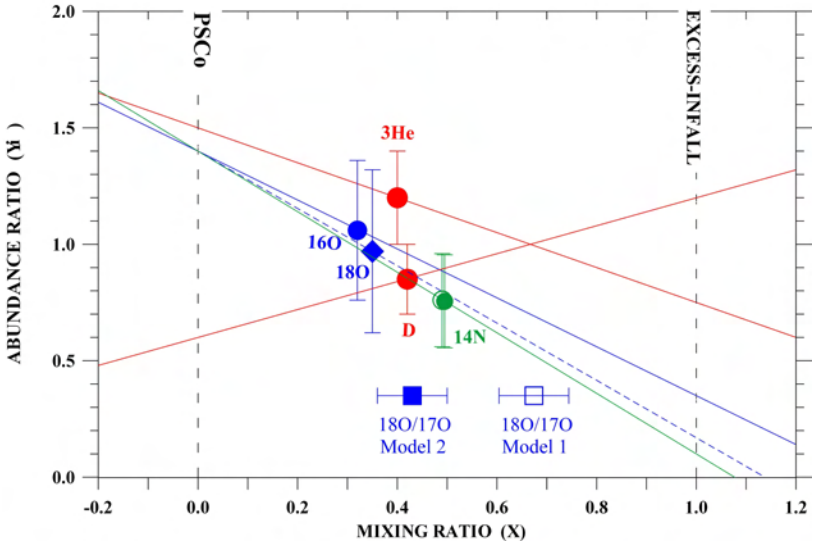

Figure 5.21: Results obtained with the "mixing model" of galactic evolution during the last 5 Gyr. All abundance ratios are normalized to PSC values. The figure shows the mixing lines connecting the values of a given abundance ratio in the defining reservoirs, PSC_0 (at $X = 0$) and "excess-infall" (at $X = 1$), see Equations (5.4 - 5.7) and Table 5.7. The measured abundances, relative to H and normalized to the protosolar ratios, of D, ^{3}He, O and N in the LIC and of the oxygen isotopes in the LISM are plotted versus the respective mixing ratios X (Equation 5.6). Model 2 data points are shown as full symbols and model 1 data points as open symbols. Except for $^{18}O/^{17}O$ the mixing ratios obtained by the two models are nearly identical. Thus all model 1 data points are hidden (the model 1 point of ^{14}N is just barely visible), except for those involving ^{17}O. Model 2 gives mixing ratios X in a narrow range ($0.32 \leq X \leq 0.49$) for all species shown here, implying that galactic matter in the LIC and the local ISM can be represented by a mixture of PSC matter (extrapolated to the present) and an excess-infall with the composition assumed for model 2 (Table 5.7).

Although isotopic abundances of C and N were determined in the LMC (see Figure 5.20), we have not included these nuclides in the results in Table 5.7 and Figure 5.21. The mixing ratios X for the carbon isotopes and for $\{^{15}N/H\}$ agree well enough with the bulk of the X values in Figure 5.21. However, the error limits for the resulting mixing ratios are so large that $\{^{13}C/H\}$ and $\{^{15}N/H\}$ do not really give independent confirmation for infall of matter from dwarf galaxies. Measurements of D and ^{3}He in the LMC, of the oxygen isotopes in dwarf galaxies other than the Magellanic Clouds, and of the $^{22}Ne/^{20}Ne$ ratio in the LIC would test our model.

Figure 5.21 shows that the limited decrease in D/H, the absence of a significant increase in metallicity, and the strong decrease in $^{18}O/^{17}O$ from the PSC to the local ISM during the last 5 Gyrs can be explained by postulating that the infall

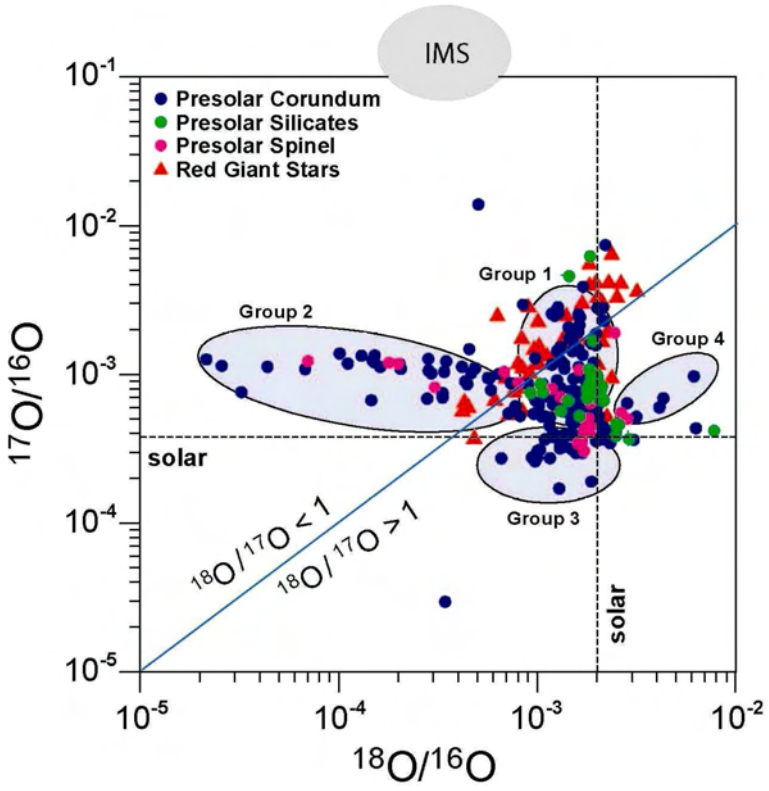

Figure 5.22: The isotopic composition of oxygen measured in presolar grains of meteorites and observed in red giant stars (after Hoppe, 2006). The composition in the protosolar cloud (PSC) is at the crossing point of the two dashed lines. The theoretically expected (Ventura et al., 2002) composition of oxygen released by Intermediate Mass Stars (IMS) lies in the grey region. Oxygen released from Red Giants and AGB stars is expected to have $^{18}O/^{17}O < 1$. Thus the presolar grains of Group 1 and Group 2 are from Intermediate Mass and Low Mass Stars. Oxygen released by Massive Stars should have $^{18}O/^{17}O > 5$. Red Giant observations from Harris and Lambert (1984), Harris et al. (1987), and Smith and Lambert (1990). Presolar grains and meteorites from Nittler et al. (1997), Zinner et al. (2005), and Mostefaoui and Hoppe (2004).

into the Galaxy carries – at least in part – the nucleosynthetic signature of dwarf galaxies. To understand what really happened, we must complete the chemical and isotopic evidence with evidence regarding the geometrical and dynamical evolution of the Local Group, including the effects of Dark Matter.

5.7.4 The ^{18}O puzzle: does ^{17}O provide the answer?

By adding a small percentage of ejecta from intermediate mass stars, we have achieved agreement between the predictions of model 2 and the observations, for

all species including the $^{18}O/^{17}O$ ratio (Geiss and Gloeckler, 2006). The question, however, remains: How could a particular nucleosynthetic component, i.e. the products from intermediate mass stars (IMS), become strongly overabundant in the matter falling into the Galaxy? Here, we do not develop a complete scenario for the cause of the "^{18}O-puzzle". We merely point to some factors that could have contributed:

1. Matter released by SN explosions may have escaped from dwarf galaxies preferentially (D'Ercole and Brighenti, 1999), enriching, over time, the matter released from intermediate mass stars.

2. During starbursts, matter from massive stars could have escaped efficiently from a dwarf galaxy. A few 10^8 years later, when the intermediate mass stars have reached the AGB phase, the starburst activity has weakened, suppressing the escape of nuclides produced from these stars.

3. The approach and eventual accommodation of dwarf galaxy material into the Galaxy is a complex process that probably takes $> 10^9$ years. During approach to the Galaxy, tidal forces could enhance star formation and may even trigger starbursts. The matter from massive stars would be released with higher temperature and further away from the Galactic Centre than the products of intermediate mass stars that are released a few 10^8 years later, and therefore are more likely to arrive at the inner regions of the Milky Way. Moreover gases released from stars far away from the Galactic Centre are more likely to be blown away by galactic winds than products released closer to the Centre.

This whole process is likely to have been repeated several times. The Magellanic Clouds, for example, are presently on an elongated orbit around the Galaxy with an estimated period of 1.5 Gyr (Gardiner et al., 1994), and the Magellanic stream indicates that matter is already added to the Galaxy.

When, finally, the dwarf galaxy interacts materially with the Milky Way, starbursts, fountains and galactic winds may be triggered. The resulting effect on the chemical composition and isotopic abundances is of course difficult to model. However, loosing more products of massive stars from the Galaxy than IMS products is more likely, because of the time delay of several 10^8 years caused by the H-burning time of intermediate mass stars.

In order to get from the oxygen isotope composition in the PSC to the present-day composition in the local ISM, one has either to reduce ^{18}O or to increase ^{17}O. Even if one assumes $\{^{18}O/H\} = 0$ for the excess-infall the effect would be minor as can be seen in Figure 5.21.

Galactic winds will be very effective in large scale-mixing of the ISM, and they will contribute to limiting the growth of metallicity in the Milky Way. However, the very limited decrease in the deuterium abundance can be achieved only if one includes infall of weakly processed or unprocessed matter. The ^{18}O puzzle could be solved by winds only if the winds would favour ejecta from Massive Stars strongly enough over those of Intermediate Mass Stars. Galactic winds by themselves could hardly reduce the N/O ratio. In fact, the case for infall of dwarf galaxy-type matter

would be strengthened if it were confirmed, by reducing the error limits (see Figure 5.20), that N/O is lower in the LIC or LISM than in the PSC.

The evolution of the ISM in some galaxies and dwarf galaxies has been dominated by wind losses, while in other galaxies the winds are weak (Strickland et al., 2000; Silich et al., 2004; Vazquez et al., 2004). For our Galaxy both wind loss and infall may have significantly affected the chemical evolution (Völk, 1991). More refined composition measurements are needed in order to determine the specific contributions of the two competing processes, wind-loss and infall.

Also needed is a better understanding of the origin and dynamical evolution of the Galaxy and the Local Group. If small galaxies were originally more abundant, than presently recognized (e.g. Ostriker and Steinhardt, 2003), the probability increases that dwarfs have in the past fallen into the Galaxy. Recently, a few additional dwarf galaxies near the Milky Way were discovered. Evidence for ongoing infall of matter from small galaxies into the Milky Way is provided by the Magellanic Stream and the Sagittarius dwarf galaxy. Improved knowledge about the distribution of Dark Matter would allow one to better extrapolate into the past, because to this day the distribution of Dark Matter controls the dynamics in the Local Group. The Andromeda galaxy, for example, has two centres, probably resulting from an impact of a small galaxy (Lauer et al., 1993; Gerssen et al., 1995). Perhaps the warp in the galactic rotation curve at $\sim$ 14 kpc (e.g. Honma and Sofue, 1997) is due to Dark Matter that is a remnant from the infall of a small galaxy in the past (de Boer et al., 2005).

Acknowledgements

We thank Monica Tosi, Rudolf Treumann, and Reinald Kallenbach for their critical reading the manuscript and for constructive comments.

Bibliography

Asplund, M., Grevesse, N., Sauval, A.J., Allende Prieto, C., and Blomme, R.: 2005, *Astron. Astrophys.* **431**, 693–705 (Erratum: Astron. Astrophys. **435**, 339–340, 2005).

Baguhl, M., Gruen, E., and Landgraf, M.: 1996, *Space Sciences Series of ISSI*, vol.1, and *Space Sci. Rev.* **78**, 165–172.

Bania, T.M., Rood, R.T., and Balser, D.S.: 2002, *Nature* **415**, 54.

Baranov, V.B. and Malama, Yu.G.: 1996, *Space Sci. Rev.* **78**, 305–316.

Bertaux, J.L. and Blamont, J.E.: 1971, *Astron. Astrophys.* **11**, 200.

Bertaux, J.L., Lallement, R., Kurt, V.G., and Mironova, E.N.: 1985, *Astron. Astrophys.* **150**, 1.

Bieber, J.M., Matthaeus, W.H., and Smith, C.W.: 1994, *Astrophys. J.* **420**, 294.

Blum, P.W. and Fahr, J.H.: 1970, *Astron. Astrophys.* **4**, 280.

Bühler, F., Axford, W.I., Chivers, H.J.A., and Marti, K.: 1976, *J. Geophys. Res.* **81**, 111–115.

Burlaga, L.F., Ness, N.F., Acuña, M.H., Lepping, R.P., Connerney, J.E.P., Stone, E.C., and McDonald, F.B.: 2005, *Science* **309**, 2027.

Decker, R.B., et al.: 2005a, *Science* **309**, 2020.
Decker, R.B., S.M. Krimigis, E.C. Roelof, and M.E. Hill: 2005b, Eos Trans. AGU 86(52), Fall Meeting Suppl, Abstract SH43B-05.
Busemann, H., Bühler, F., Grimberg, A., Heber, V.S., Agafonov, Y.N., Baur, H., Bochsler, P., Eismont, N.A., Wieler, R., and Zastenker, G.N.: 2006, *Astrophys. J.* **639**, 246–258.
Carlsson, E., et al.: 2006, *Icarus* **182**, 320–328.
Charbonnel, C.: 1998, in *Primordial Nuclei and their Galactic Evolution*, N. Prantzos, N. Tosi, R. von Steiger (eds.), SSSI Vol. 4, and *Space Sci. Rev.* **84**, 199–206.
Cheng, A.F.: 1986, *J. Geophys. Res.* **91**, 4524–4530.
Chin, Y.-N.: 1999, in *New Views of the Magellanic Clouds*, IAU Symp. **190**, Y.-H. Shu et al. (eds.) , p. 190.
Chin, Y.-N., Henkel, C., Langer, N., and Mauersberger, R.: 1999, *Astrophys. J.* **512**, L143.
Connell, J.J. and Simpson, J.A.: 1993, *Proc. 23rd Int. Cosmic Ray Conf.* **1**, 559.
Costa J., Lallement, R., Quémerais, E., Bertaux, J.L., Kyrola, E., and Schmidt, W.: 1999, *Astron. Astrophys.* **349**, 660.
Cummings, A.C., Stone, E.C., and Webber, W.R.: 1984, *Astrophys. J.* **287**, L99–L102.
Cummings, A.C. and Stone, E.C.: 1996, *Space Sci. Rev.* **78**, 43–52.
Cummings, A.C., Stone, E.C., and Steenberg, C.D.: 1999, *Proc. 26th Intl. Cosmic Ray Conf.* **7**, 531.
Cummings, A.C., Stone, E.C., and Steenberg, C.D.: 2002, *Astrophys. J.* **578**, 194–210.
de Boer, K.S.: 1991, in R. Haynes and D. Milne (eds.), *The Magellan Clouds*, Dordrecht, Kluwer Acad. Publ.
de Boer, W., Sander, C., Zhukov, V., Gladyshev, A.V., and Kazakov, D.I.: 2005, *Astron. Astrophys.* **444**, 51–67.
Decker, R.B., et al.: 2005a, *Science* **309**, 2020.
Decker, R.B., Krimigis, S.M., Roelof, E.C., and Hill, M.E.: 2005b, Eos Trans. AGU, 86(52), Fall Meeting Suppl., Abstract SH43B-05.
Fisk, L.A.: 1976, *J. Geophys. Res.* **81**, 4641.
Fisk, L.A. and Gloeckler, G.: 2006, *Astrophys. J.* **640**, L79.
Fisk, L.A., Kozlovsky, B., and Ramaty, R.: 1974, *Astrophys. J.* **190**, L35.
Fisk, L.A., Gloeckler, G., and Zurbuchen, T.H.: 2006, *Astrophys. J.*, in press.
Garcia-Munoz, M., Mason, G.M., and Simpson, J.A.: 1973, *Astrophys. J.* **182**, L81–L84.
Gardiner, L.T., Sawa, T., and Fujimoto, M.: 1994, *MNRAS* **266**, 567.
Geiss, J.: 1972, in *Solar Wind*, P.J. Coleman, C.P. Sonett, and J.M. Wilcox (eds.), NASA SP-308, p. 559.
Geiss, J. and Reeves, H.: 1972, *Astron. Astrophys.* **18**, 126.
Geiss, J. and Bochsler, P.: 1982, *Geochim. Cosmochim. Acta* **46**, 529–548.
Geiss, J. and Witte, M.: 1996, *Space Sciences Series of ISSI*, Vol. 1, and *Space Sci. Rev.* **78**, 229–238.
Geiss, J. and Gloeckler, G.: 2003, in *Solar System History from Isoptopic Signatures of Volatile Elements*, R. Kallenbach, T. Encrenaz, J. Geiss, K. Mauersberger, T. Owen, and F. Robert (eds.), SSSI Vol. 16 and *Space Sci. Rev.* **106**,

3–18.
Geiss, J. and Gloeckler, G.: 2005, in *The solar system and beyond: Ten years of ISSI*, J. Geiss and B. Hultqvist (eds.), ISSI Scientific Report SR-003, ESA-ESTEC Publ. Division. Noordwijk, The Netherlands, pp. 53–68.
Geiss, J. and Gloeckler, G.: 2006, *Astron. Astrophys.*, in preparation.
Geiss, J., Gloeckler, G., and Charbonnel, C.: 2003, *Astrophys. J.* **578**, 862.
Geiss, J., Gloeckler, G., Mall, U., von Steiger, R., Galvin, A.B., and Ogilvie, K.W.: 1994a, *Astron. Astrophys.* **282**, 924–933.
Geiss J., Gloeckler, G., and von Steiger, R.: 1994b, *Phil. Trans. R. Soc. Lond.* **A 349**, 213–226.
Geiss, J., Gloeckler, G., Fisk, L.A., and von Steiger, R.: 1995, *J. Geophys. Res.* **100**, 23373–23377.
Geiss, J., Gloeckler, G., and von Steiger, R.: 1996, *Space Sci. Rev.* **78**, 43–52.
Gerssen, J., Kuijken, K., and Merrifield, M.R.: 1995, *MNRAS* **277**, L21–L24.
Gloeckler, G., presented at the LoLaGE ISSI Team Meeting, Spring 2005.
Gloeckler, G. and Geiss, J.: 1996, *Nature* **381**, 210–212.
Gloeckler, G. and Geiss, J.: 1998, *Space Sciences Series of ISSI*, Vol. 4, and *Space Sci. Rev.* **84**, 275–284.
Gloeckler, G. and Geiss, J.: 2000, "Deuterium and Helium-3 in the Protosolar Cloud", in *The Light Elements and Their Evolution*, IUA Symposium **198**, L. da Silva, M. Spite, and J. R. de Medeiros (eds.), 224–233.
Gloeckler, G. and Geiss, J.: 2001a, *Space Sci. Rev.* **97**, 169.
Gloeckler, G. and Geiss, J.: 2001b, in R.F. Wimmer-Schweingruber (ed.), *Solar and Galactic Compositition*, AIP Conf Proc. **598**, 281–289.
Gloeckler, G. and Geiss, J.: 2004, *Adv. Space Res.* **34**, 53.
Gloeckler, G. and Fisk, L.A.: 2006, *Astrophys. J. Lett.*, in press.
Gloeckler, G., Geiss, J., Balsiger, H., Fisk, L.A., Galvin, A., Ipavich, F.M., Ogilvie, K.W., von Steiger, R., and Wilken, B.: 1993, *Science* **261**, 70–73.
Gloeckler, G., Schwadron, N.A., Fisk, L.A., and Geiss, J.: 1995, *Geophys. Res. Lett.* **22**, 2665.
Gloeckler, G., Fisk, L.A., and Geiss, J.: 1997, *Nature* **386**, 374–377.
Gloeckler, G. et al.: 2000a, *Nature* **404**, 576.
Gloeckler, G., Fisk, L.A., Geiss, J., Schwadron, N.A., and Zurbuchen, T.H.: 2000b, *J. Geophys. Res.* **105**, 7459.
Gloeckler, G., Fisk, L.A., Zurbuchen, T.H., and Schwadron, N.A.: 2000c, in R.A. Mewaldt et al. (eds.), *Acceleration and Transport of Energetic Particles Observed in the Heliosphere*, AIP Conf. Proc. **528**, 221.
Gloeckler, G., Geiss, J., Schwadron, N., Fisk, L.A., Zurbuchen, T.H., Ipavich, F.M., von Steiger, R., Balsiger, H., and Wilken, B.: 2000d, *Nature* **404**, 576–578.
Gloeckler, G., Geiss, J., and Fisk, L.A.: 2001, in A. Balogh, R.G. Marsden and E.J. Smith (eds.), *The Heliosphere Near Solar Minimum: The Ulysses Perspective*, Springer-Praxis, Chichester, p. 287.
Gloeckler, G., Möbius, E., Geiss, J., Bzowski, M., Chalov, S., Fahr, H., McMullin, D.R., Noda, H., Oka, M., Rucinski, D., Skoug, R., Terasawa, T., von Steiger, R., Yamazaki, A., and Zurbuchen, T.: 2004, *Astron. Astrophys.* **426**, 845–854.
Goldstein, M.L., Fisk, L.A., and Ramaty, R.: 1970, *Phys. Rev. Lett.* **25**, 832.

Grevesse, N. and Sauval, A.J.: 1998, *Space Sciences Series of ISSI*, Vol. 5; *Space Sci. Rev.* **85**, 161–174.
Gurnett, D.A. and Kurth, W.S.: 2005, *Science* **309**, 2025.
Harris, M.J. and Lambert, D.L.: 1984, *Astrophys. J.* **281**, 739–745, and **285**, 674–682.
Harris, M.J., Lambert, D.L., Hinkle, K.H., Gustafsson, B., and Eriksson, K.: 1987, *Astrophys. J.* **316**, 294–304.
Heikkilä, A. and Johansson, L.E.B.: 1999, in Y.-H. Chu et al. (eds.), *New Views of the Magellanic Clouds*, IAU Symp. **190**, p. 275.
Henkel, C. and Mauersberger, R.: 1993, *Astron. Astrophys.* **274**, 730–742.
Holweger, H.: 2001, in R.F. Wimmer-Schweingruber (ed.), *Solar and Galactic Composition*, AIP Conf. Proc. **598**, 23–40.
Honma, M. and Sofue, Y.: 1997, *Publ. Astron. Soc. Japan* **49**, 453–460.
Hoppe, P., unpublished, 2006.
Hovestadt, D., O. Vollmer, G. Gloeckler, and C.Y. Fan: 1973, *Phys. Rev. Lett.* **31**, 650–653.
Iben, I. and Truran, J.W.: 1996, *Astrophys. J.* **220**, 980–995.
Ipavich, F.M., Masung, L.S., and Gloeckler, G.: 1982, University of Maryland, Technical Report **82**, 172.
Izmodenov, V.V., Geiss, J., Lallement, R., Gloeckler, G., Baranov, V., and Malama, Y.: 1999a, *J. Geophys. Res.* **104**, 4731.
Izmodenov, V.V., Lallement, R., and Geiss, J.: 1999b, *Astron. Astrophys.* **344**, 317.
Izmodenov, V.V.: 2000, *Astrophys. Space Sci.* **274**, 55–69.
Jokipii, J.R.: 1996, *Astrophys. J.* **466**, L47.
Kahane, C.: 1995, in N. Busso et al. (eds.), *Nuclei in the Cosmos III*, AIP Conf. Proc. **327**, p. 19.
Klecker, B., Hovestadt, D., Gloeckler, G., and Fan, C.Y.: 1980, *Geophys. Res. Lett.* **7**, 1033.
Klecker, B., et al.: 1995, *Astrophys. J.* **442**, L69.
Kolomogorov, A.N.: 1941, *Dokl. Akad. Nauk SSSR* **30**, 31.
Lallement, R.: 1999, in *Solar Wind 9*, AIP Conf. Proc. **471**, 205.
Lallement, R.: 2001, in J. Bleeker, J. Geiss, and M.C.E. Huber (eds.), *The Century of Space Science*, Kluwer, Dordrecht, 1191.
Lallement, R., Raymond, C.J., Vallerga, J., Lemoine, M., Dalaudier, F., and Bertaux, J.L.: 2004, *Astrophys. J.* **426**, 875–884.
Lallement, R., Quémerais, E., Bertaux, J.L., Ferron, S., Koutroumpa, D., and Pellinen, R.: 2005, 'Deflection of the interstellar neutral hydrogen flow across the heliospheric interface', *Science* **307**, 1447–1449.
Lauer, T.R. et al.: 1993, *Astron. J.* **106**, 1436.
Lee, D.-C., and Halliday, A.N.: 1996, *Science* **274**, 1876.
Lee, M.A. and Ip, W.-H.: 1987, *J. Geophys. Res.* **92**, 11041.
Lee, M.A., Shapiro, V.I., and Sagdeev, R.Z.: 1996, *J. Geophys. Res.* **101**, 4777.
Leske, R.A., Mewaldt, R.A., Cummings, A.C., Cummings, J.R., Stone, E.C., and von Rosenvinge, T.T.: 1996, *Space Science Series of ISSI*, Vol. 1, and *Space Sci. Rev.* **78**, 149–154.

Leske, R.A.: 2000, in B.L. Dingus, D.B. Kieda, and M.H. Salamon (eds.), *Proc. 26th Int. Cosmic Ray Conf.*, AIP Conf. Proc. **516**, 274–282.
Linsky, J.L. and Wood, B.E.: 1996, *Astrophys. J.* **462**, 254.
Linsky, J.L. and B.E. Wood: 1998, in L. da Silva, M. Spite, and J.R. de Medeiros (eds.), *The Light Elements and Their Evolution*, IUA Symposium **198**, 141–150.
Linsky, J.L. et al.: 2006, *Astrophys. J.*, in press.
Lukasiak, A., Ferrando, P., McDonald, F.B., and Webber, W.R.: 1994, *Astrophys. J.* **426**, 366.
Mahaffy, P.R., Donahue, T.M., Atreya, S.K., Owen, T.C., and Niemann, H.B.: 1998, *Space Science Series of ISSI*, Vol. 4, and *Space Sci. Rev.* **84**, 251–263.
McDonald, F.B., Teegarten, B.J., Trainor, J.H., and Webber, W.R.: 1974, *Astrophys. J.* **187**, L105–L108.
McKibben, R.B.: 1977, *Astrophys. J.* **217**, L113.
Mewaldt, R.A., et al.: 1996, *Astrophys. J.* **466**, L43.
Moebius, E., Hovestadt, D., Klecker, B., Scholer, M., and Gloeckler, G.: 1985, *Nature* **318**, 426.
Mostefaoui, S. and Hoppe, P.: 2004, *Astrophys. J.* **613**, L149.
Nittler, I.R. et al.: 1997, *Astrophys. J.* **483**, 475.
Olive, K. and Schramm, D.: 1982, *Astrophys. J.* **257**, 276.
Ostriker, J.P. and Steinhardt, P.: 2003, *Science* **300**, 1909.
Owen, T., Mahaffy, P.R., Niemann, H.B., Atreya, S., and Wong, M.: 2001, *Astrophys. J.* **553**, L77.
Palmer, I.D.: 1982, *Rev. Geophys. Space Sci.* **20**, 335.
Parker, E.N.: 1963, *Interplanetary Dynamic Processes*, John Wiley and Sons, New York, 1963.
Pesses, M.E., Jokipii, J.R., and Eichler, D.: 1981, *Astrophys. J.* **246**, L85.
Podosek, F.A. and Nichols, R.H.: 1997, in T.J. Bernatovicz and E.K. Zinner (eds.), *Astrophysical Implications of the Laboratory Study of Presolar Materials*, AIP Conf. Proc. **402**, 617.
Prantzos, N., Aubert, O., and Audouze, J.: 1996, *Astron. Astrophys.* **309**, 760.
Preibisch, T., Briceno, C., Zinnecker, H., Walter, F., Mamajek, E., Mathieu, R., and Sherry, B.: 2006, ppt-presentation, www.as.utexas.edu/astronomy/people/scalo/IMFat50.Scalo5.6.ppt
Reeves, H., Audouze, J., Fowler, W.A., and Schramm, D.N.: 1973, *Astrophys. J.* **179**, 909.
Reeves, H.: 1978, in T. Gehrels (ed.), *Protostars and Planets*, The University of Arizona Press, p. 399.
Ripken, H.W. and Fahr, H.J.: 1983, *Astron. Astrophys.* **122**, 181–192.
Romano, D. and Matteucci, F.: 2003, *MNRAS* **342**, 185.
Romano, D., Tosi, M., Chiappini, C., and Matteucci, F.: 2006, *MNRAS* **369**, 295.
Salerno, E., Bühler, F., Bochsler, P., Busemann, H., Eugster, O., Zastenker, G.N., Agafonov, Y.N., and Eismont, N.A.: 2001, in R.F. Wimmer-Schweingruber (ed.), *Solar and Galactic Composition*, AIP Conf Proc. **598**, 275–280.
Schwadron, N.A., Geiss, J., Fisk, L.A., Gloeckler, G., Zurbuchen, T.H., and von Steiger, R.: 2000, *J. Geophys. Res.* **105**, 7465.
Shukoliukov, A. and Begemann, F.: 1996, *Geochim. Cosmochim. Acta* **60**, 2453.

Silich, S., Tenorio-Tagle, G., and Rodriguez-Gonzalez, A.: 2004, *Astrophys. J.* **210**, 226S.
Simnett, G.M., Sayle, K.A., Tappin, S.J., and Roelof, E.C.: 1995, *Space Sci. Rev.* **72**, 327.
Slavin, J.D. and Frisch, P.C.: 2002, *Astrophys. J.* **565**, 364–379.
Smith, V.V. and Lambert, D.L.: 1990, *Astrophys. J.* **361**, L69.
Songaila, A., Wampler, E.J., and Cowie, L.L.: 1997, *Nature* **385**, 137–139.
Stone, E.C., Cummings, A.C., McDonald, F.B., Heikkilä, B.C., Lal, N., and Webber, W.R.: 2005, *Science* **309**, 2017.
Strickland, D.K., Heckman, T.M., Weaver, K.A., and Dahlem, M.: 2000, *Astron. J.* **120**, 2965S
Talbot, R.J. and Newman, M.J.: 1977, *Astrophys. J. Suppl.* **34**, 295–308.
Thomas, G.E. and Krassa, R.F.: 1971, *Astrophys. J.* **134**, 20.
Tosi, M.: 1988, *Astron. Astrophys.* **197**, 47–51.
Tosi, M.: 1998, *Space Science Series of ISSI*, Vol. 4, and *Space Sci. Rev.* **84**, 207–218.
Tosi, M.: 2000, L. da Silva, R. de Medeiros, and M. Spite (eds.), Proc. of IAU Symposium **198**, p. 525.
Tytler, D., Fan, X.M., and Burles, S.: 1996, *Nature* **381**, 207–209.
Veilleux, S., Cecil, G., and Bland-Hawthorn, J.: 2005, *Annual Rev. Astron. Astrophys.* **43**, 769.
Wasserburg, G.J., Busso, M., Gallino, R., and Nollett, K.M.: 2006, *Nuclear Phys. A*, in press.
Wilson, T.L., and Rood, R.: 1994, *Annual Rev. Astron. Astrophys.* **32**,191–226.
Witte, M.: 2004, *Astron. Astrophys.* **426**, 835–844.
Witte, M., Rosenbauer, H., Banaszkievicz, M., and Fahr, H.: 1993, *Adv. Space Res.* **13**, 121–130.
Witte, M., Banaszkiewicz, M., and Rosenbauer, H.: 1996, *Space Science Series of ISSI*, Vol. 1, and *Space Sci. Rev.* **78**, 289–296.
Vazques, G.A., Leitherer, C., Heckman, T.M., Lennon, D.J., de Mello, D.F., Meuer, G.R., and Martin, C.L.: 2004, *Astrophys. J.* **600**, 162.
Ventura, P., D'Antona, F., and Mazzitelli, I.: 2002, *Astron. Astrophys.* **393**, 215.
Völk, H.: 1991, in *The interstellar disk-halo connection in galaxies*, IAU Symp. **144**, pp. 345–353.
Walker, T.B., Steigman, G., Schramm, D.N., Olive, K.A., and Kang, H.-S.: 1991, *Astrophys. J.* **376**, 51.
Zank, G.P., Pauls, H.L., Cairns, I.H., and Webb, G.M.: 1996, *J. Geophys. Res.* **101**, 457.
Zinner, E., Nittler, L.R., Hoppe, P., Gallino, R., Straniero, O., and D'Alexander, C.M.O.: 2005, *Geochim. Cosmochim. Acta* **69**, 4149.

— 6 —

Heliospheric Magnetic Fields and Termination Shock Crossing: Voyager 1

Norman F. Ness[1]
The Catholic University of America
Washington, DC, USA
nfnudel@yahoo.com

Abstract. **After launch in 1977 and 27 years of continuously studying the Heliospheric Magnetic Field(HMF) from 1 to > 98 AU, the dual magnetometers on the Voyager 1 spacecraft detected a single crossing of the Termination Shock (TS) when at 35 degrees north heliographic latitude and 94.0 AU from the Sun. As the innermost boundary of the heliosphere's interaction with the local interstellar medium, the TS was found to be a quasi-perpendicular MHD shock with a sudden jump in average field magnitude by a factor of ≈ 3, from 0.04 nano-Tesla (nT) to 0.13 nT. This chapter discusses the observed characteristics of the HMF, both pre- and post-TS crossing. The latter data demonstrate the discovery of a new astrophysical plasma regime in the heliosheath, wherein fluctuations, some might consider turbulence, are primarily compressive, isotropic and have a Gaussian distribution of components and magnitude.**

6.1 Introduction

Measurements of the interplanetary magnetic field with the dual magnetometer system (Behannon et al., 1977) on the twin USA Voyager 1 and 2 spacecraft (V1 and V2) began immediately after their launches in 1977. Nearly fulltime daily reception of the telemetry signals and scientific data by the JPL Deep Space Network (DSN) continued until the V1 Neptune encounter in 1989. Thereafter, scheduling conflicts of the DSN capability with other spacecraft missions led to a reduction in coverage of V1 and V2 due to overlapping plane-of-the-sky positions of the Voyagers with other NASA and joint ESA-NASA missions.

Fortunately, V1's priority rank in the DSN list of mission responsibilities has provided fairly good data return each day up to the present moment. Typically data coverage is up to 50% each day although even that fraction is sub-divided so that continuous 12 hours of data is not routinely available.

This chapter presents a brief overview of the observed structure of the Heliospheric Magnetic Field (HMF) from 1 to 96 AU as observed by V1 from 1977 to the

[1]in *The Physics of the Heliospheric Boundaries*, V. Izmodenov and R. Kallenbach (eds.), ISSI Scientific Report No. 5, pp. 183 - 202, ESA-ESTEC, Paris 2006

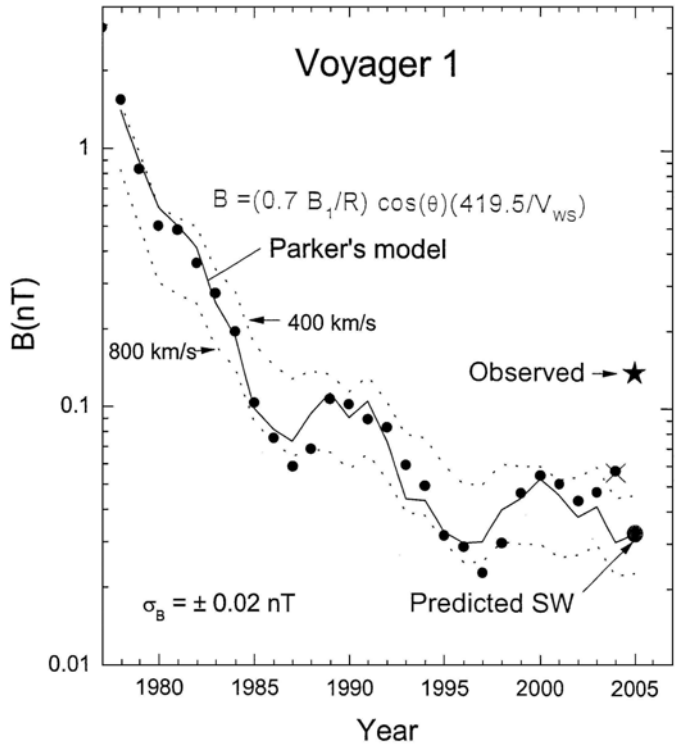

Figure 6.1: Comparison of V1 annual averages of HMF magnitude since launch with the Parker model using measured HMF field at 1 AU and measured or estimated solar wind speed by or at V1. Notable are solar cycle changes with a period of ≈11 years superimposed on the general decrease with distance from Sun in AU.

crossing of the Termination Shock (TS) in late 2004 and subsequent entry into the heliosheath. The actual TS crossing was not observed due to lack of data coverage and most likely occurred partially or perhaps primarily as a result of the inward motion of the TS past V1 (Whang et al., 2004).

That the quasi-perpendicular TS was crossed is not in doubt, however, in spite of the data gap, due to the permanent increase in average field strength by a factor of 3±1, the ratio depending upon scale size chosen. In subsequent data obtained in 2005, two sector boundaries were observed in the subsonic heliosheath. Additionally, significantly different characteristics of the fluctuations of the subsonic heliosheath have been observed, identified and studied, when compared to the characteristics in the supersonic solar wind within the heliosphere, ie., inside the TS.

6.2 Overall global structure of HMF from 1 to 96 AU

Figure 6.1 from Ness et al. (2005b) presents the annual averages of the magni-

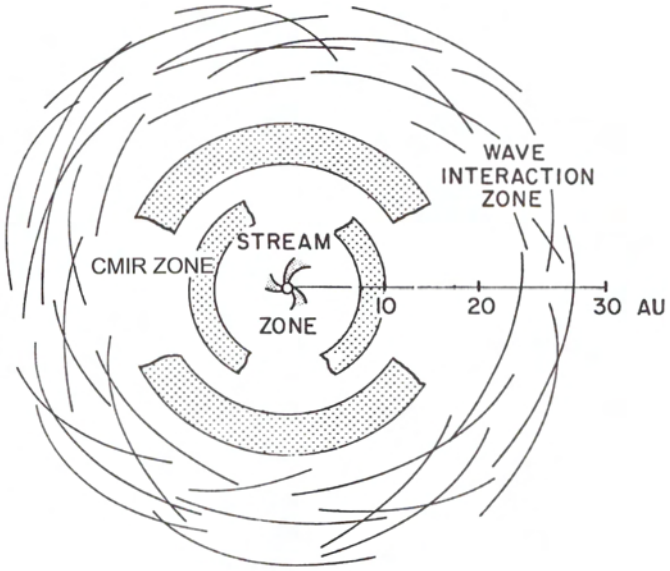

Figure 6.2: Schematic representation of evolution of individual, identifiable corotating high speed solar wind streams changing through interactions to Corotating Merged Interaction Regions (CMIR).

tude of the HMF as measured by V1 since launch. A comparison with the expected field, based upon Parker's theory (Parker, 1963) for an Archimedean field structure, is shown as a solid line. Deviations of the estimated field due to lower or higher average solar wind speeds used are shown as dashed lines and are bounded by 400 km/sec and 800 km/sec.

The HMF estimate is based upon actually measured HMF fields at 1 AU and V1 measured, or estimated, solar wind speeds. The V1 solar wind plasma probe failed shortly after Saturn encounter in 1979. Clearly evident in the V1 observed magnetic field data and model is the 11 year variation associated with the solar magnetic polarity and activity cycles.

From many different spacecraft missions, including V1 and V2, the overall structure of the heliosphere is known to change significantly from close to the Sun to far from it (Burlaga, 1995). Figure 6.1 illustrates the change from the near-solar region, < 10 AU, where individual high-speed solar wind streams can be readily identified and easily followed on successive solar rotations. They are known to be associated with specific long-lived coronal hole regions on the Sun.

As these streams propagate outward from the Sun, they interact and evolve by overtaking each other to create Merged Interaction Regions (MIR). Some MIRs are observed to co-rotate with the Sun, recurring every $27 - 29$ days and have been denoted as CMIR's (Burlaga et al., 1997). Depending upon their 3-dimensional structure, certain CMIRs at $> 30 - 40$ AU are more appropriately described as Global MIRs or GMIRs at great distances.

Another aspect of the heliosphere at greater distances, > 30 AU, is the increasingly important role played by pick-up ions in the solar wind plasma-magnetic field dynamics. These ions originate as a result of the interaction of the solar wind ions with neutral atoms entering the heliosphere from the Local Inter-Stellar Medium (LISM), into which the heliosphere is moving.

A very important feature of the average direction of the HMF is the polarity of the field, either pointing towards (−) or away (+) from the Sun along the spiral arms of the Parker field for extended periods of time, typically several to many days. The pattern of the + and − sectors is roughly repetitive with a period of $27 - 29$ days, indicating that the origin of the changes in polarity is due to the rotation of the Sun.

This alternating uni-polar sector structure was discovered by Explorer 18 in 1963 (see review by Ness, 1987). It has been extensively studied since then by many missions including the USA Pioneer 11 and the ESA-NASA Ulysses spacecraft. P11's trajectory crossed the Solar System from Jupiter encounter in 1975 to Saturn encounter in 1979. P11 thus moved well out of the ecliptic to moderate heliographic latitudes. Observations by P11 (Smith et al., 1986) detailed the 3-dimenisonal characteristics of the theoretically studied Heliospheric Current Sheet (Schulz, 1973) as the boundary of the uni-polar regions which had been named as sectors.

V1 has tracked and mapped this HCS in its long-lived trajectory (Ness and Burlaga, 2001). A sample of the nature of the 3-dimensional variations in the HCS position is illustrated in Figure 6.3. This shows the positions of V1 and V2 in a meridian plane projection relative to the superimposed location of the changing HCS during the indicated year. In 1997, V1 and V2 were located in oppositely directed uni-polar HMF regions associated with the opposite poles of the solar field and well removed at higher latitudes than the HCS excursions.

Each was overtaken subsequently in $1998 - 1999$ by the HCS extending to higher heliographic latitudes during the solar cycle. Thus each spacecraft began to measure the alternate polarities of the HMF as the HCS crossed over them.

6.3 HMF and cosmic ray variations and pre-cursor TS particle events

Throughout the Voyager missions, especially at planetary encounters, variations in observed energetic particles over a wide range of energies and of different species and charge states have been correlated with fluctuations of the HMF. These studies have been conducted on short time and spatial scales.

The period $1990 - 1996$ is shown in Figure 6.4 to illustrate the manner of how the stronger HMF during days $260 - 280$, 1991 of a GMIR sweep out the cosmic ray particles with energies > 70 Mev/nucleon. Another aspect of these data is that as V1 continued to move away from the Sun, the intensity of the cosmic rays steadily increased as long as the HMF magnitude remained fairly steady.

Studies of the time correlated variations of the intensity of these cosmic rays with the magnitude of the HMF has revealed a straight-forward mathematical relationship between the decrease and recovery of the cosmic ray intensity.

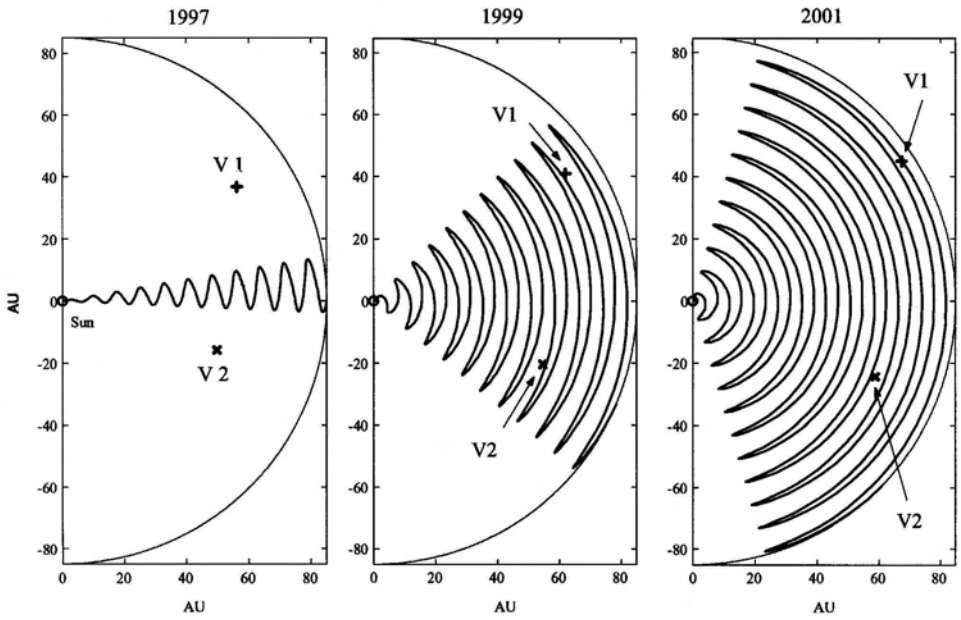

Figure 6.3: Meridian plane projection of positions of V1 and V2 from 1997 to 2001 as solar cycle variations in tilt of Heliospheric Current Sheet (HCS) leads to overtaking of each spacecraft as the HCS co-rotates with the Sun.

A simple empirical relationship has been derived, shown in Figure 6.5, and is illustrated for data from 1991 comparing the observed and predicted CR intensity using the HMF magnitude. Results for different years have shown a nearly constant set of the two parameters: the rates of the decrease (D) and increases (C) of cosmic ray flux. Close inspection of Figure 6.5 shows the surprisingly good agreement between observations and predictions based upon the decreases and increases of the HMF.

When V1 was near 85 AU, Krimigis et al. (2003) reported that the Termination Shock had been crossed twice: once in mid-2002 and again in early 2003. The basis for this interpretation was two-fold. There was a period in which sudden increases of lower energy charged particles were observed. Also, the deduced solar wind speed, obtained from estimates of the Compton-Getting factor and observed anisotropies, changed from supersonic to subsonic and back to supersonic. This was interpreted to mean a temporary entry of V1 into the heliosheath.

However, the higher energy cosmic ray particles, i.e. > 70 MeV, showed no such correlated temporal behaviour. For the same $2002 - 2003$ event, McDonald et al. (2003) interpreted these particle flux variations differently. They did not support the thesis that the TS had been crossed. Rather, their interpretation was that the observed particle events were pre-cursors to any TS crossing, and named the Krimigis et al. Heliosheath Immersion event as Termination Shock Precursor event # 1, TSP-1. This interpretation meant that V1 was approaching the TS and that the observed particle enhancements had simply been due to parti-

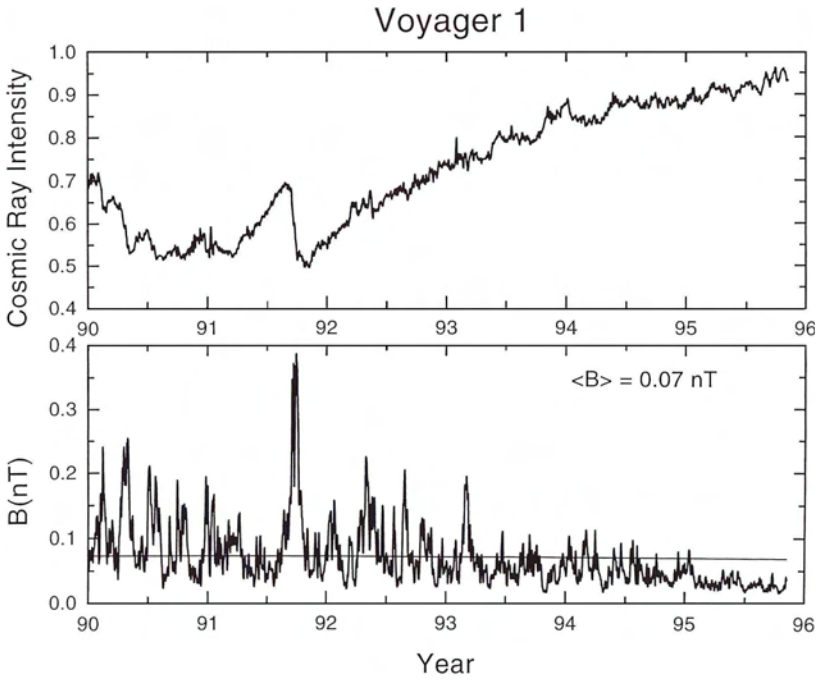

Figure 6.4: Relationship of cosmic rays > 70 MeV/nucleon with HMF magnitude. Note sudden decrease in 1991 associated with strong HMF pulse of limited duration. Five day running averages are used for both parameters.

cles injected/accelerated by the TS at some greater distance and which had then propagated along the spiral HMF field lines.

Burlaga et al. (2003) carefully studied the HMF during these purported TS crossing events and concluded that the HMF variations were not consistent with the two alleged TS crossings. The HMF averaged magnitude did not change as was to be expected. The HMF showed no increased average following the 1^{st} alleged crossing but did increase at the 2^{nd} alleged crossing. This is exactly the opposite of what is to be expected from MHD theory.

In a further study of the HMF and its fluctuations during the event, its short term fluctuations and the cosmic ray variations, Ness et al. (2005) showed that the 2^{nd} alleged TS crossing event was most likely that associated with a travelling HMF shock preceeding a modest GMIR. Figure 6.6 summarizes the HMF and cosmic ray data for 2002-2003 and identifies the alleged TS crossings as TS-1? and TS-2? A measure of the field fluctuations is also shown (SD is defined in Figure 6.8).

Zhang (2005) analyzed the Krimigis et al. (2003) data and showed that there may have been an error in estimating the solar wind speeds in the Compton-Getting computations of Krimigis et al. (2003). This was due to the failure to correctly consider the effects of the instrument background and the correct orientation of the HMF. Subsequently there were additional observations of similar pre-cursor

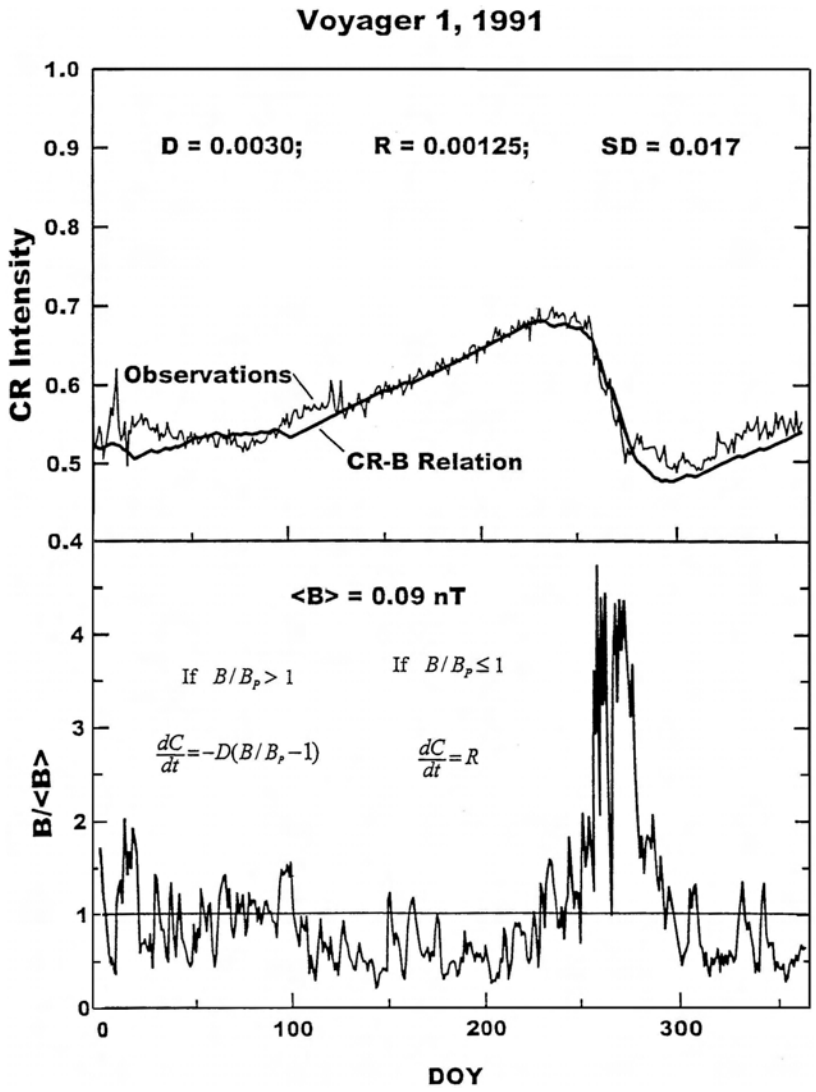

Figure 6.5: Expanded time scale plots of the 1991 event of daily averages of cosmic rays and HMF magnitude illustrating the correlated and simple relationship of increasing fields with decreasing flux and vice versa.

particle events, TSP-2 and TSP-3, by V1 before the actual TS crossing in Burlaga et al. (2005), Decker et al. (2005) and Stone et al. (2005).

6.4 V1 termination shock crossing

At the end of 2004, V1 crossed or was crossed by the Termination Shock. HMF hourly averaged magnitude observations from a $\approx$5 month period in $2004 - 2005$

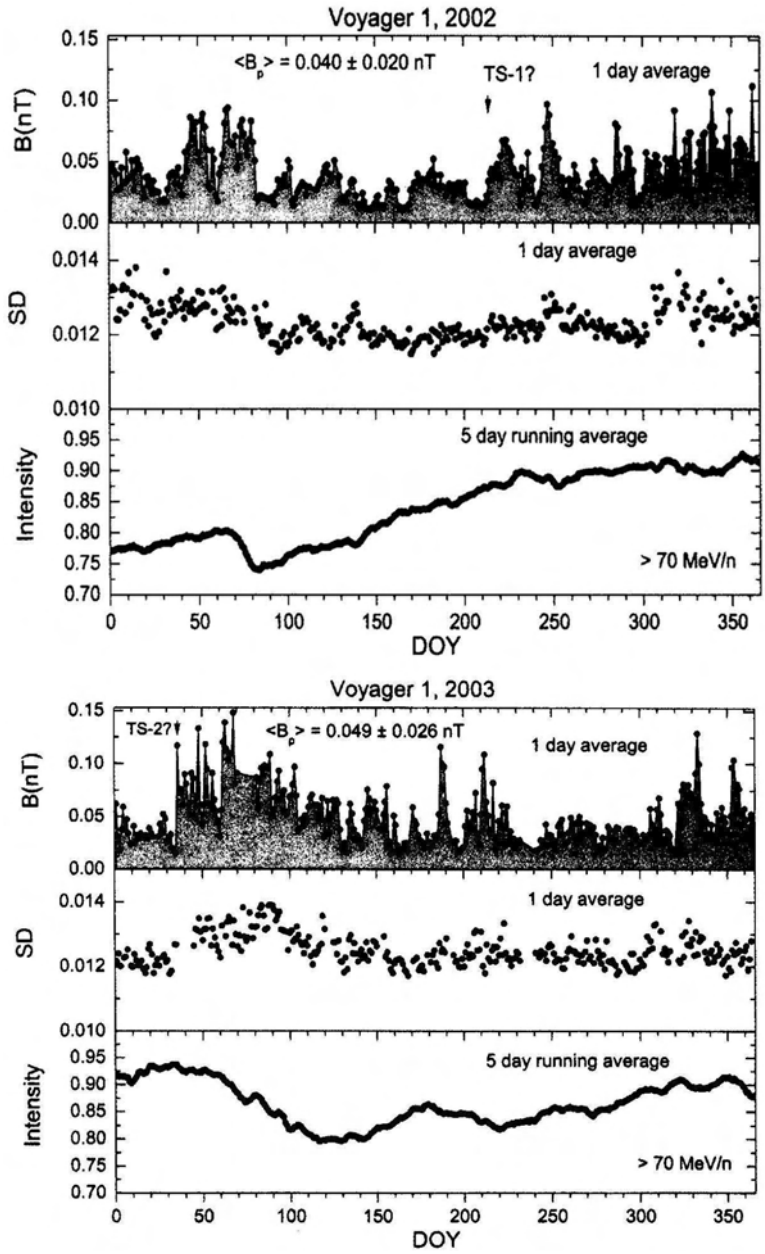

Figure 6.6: Observations of cosmic rays (> 70 MeV/nucleon) and HMF field magnitude and fluctuations (SD) in $2002 - 2003$. Daily and running 5 day averages are shown for each parameter. (See Figure 6.8 for quantitative definition of SD parameter).

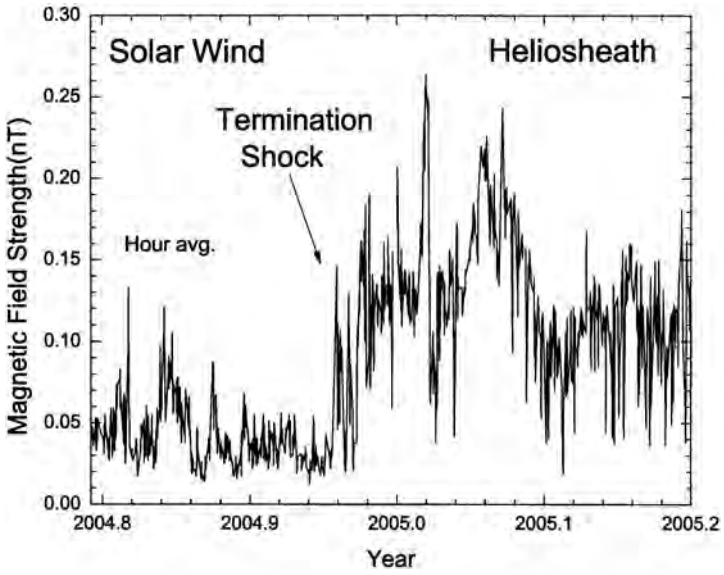

Figure 6.7: Hourly averages of HMF during period in 2004−2005 when Termination Shock crossing occurred. Average HMF magnitude jumps by factor of 2−4 from 15 to 17 December, 2004. Data gap on 16 December precludes study of microstructure of shock interface.

are shown in Figure 6.7. The increase in the averaged HMF ranges between $2-4$, depending upon the time scale chosen. This large jump is characteristic of a classic perpendicular or quasi-perpendicular MHD shock. These are seen near all the Solar System's planets associated with the solar wind interactions with either the planetary magnetic fields or their atmospheres and/or ionospheres. These are also seen on occasions in the heliosphere, i.e. propagating shocks associated with solar disturbances such as coronal mass ejections.

Figure 6.8 presents a much finer time scale coverage of the TS crossing event during an 18 day interval in 2004 using 48 second averaged magnitudes and standard deviations over 16 minute periods of the Pythagorean mean of the 1.92 second sampled vector HMF fluctuations. This figure also illustrates the discontinuous coverage of the V1 telemetry signal by the JPL-DSN.

The TS crossing is identified by the large increase, ≈ 3, in the averaged HMF magnitude occurring between data from DOY 350 and $352-353$. 16 December (plus or minus small fractions of adjacent days) is chosen as the time of the TS crossing. There is also a significant change in the daily average of the SD parameter, defined quantitatively in the figure, indicating a substantial increase in the total energy in fluctuations of the HMF (up to 0.26 Hz, the Nyquist frequency for the detailed 1.92 second vector sampled data).

Burlaga et al. (2005) and Burlaga et al. (2006) studied the characteristics of the HMF fluctuations in the heliosheath and found a notable distinguishing difference in their statistical properties. Figure 6.9 shows that the hourly averages of the

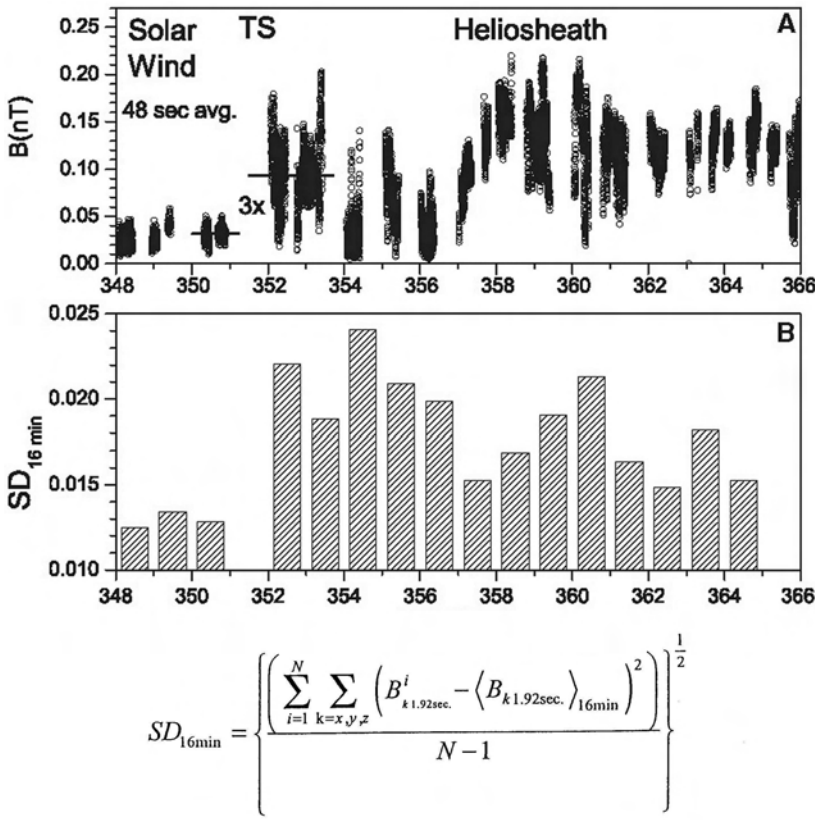

Figure 6.8: Forty eight seconds averaged HMF magnitude and associated daily averaged standard deviation of Pythagorean mean over 16 minutes of detailed 1.92 second vector sampled HMF during TS Crossing. Data gaps readily evident.

HMF magnitude have a Gaussian distribution in the subsonic heliosheath. This is in sharp contrast to the supersonic solar wind where the HMF has consistently shown a log-normal distribution, illustrated by data from 2003 in Figure 6.9.

Continued HMF observations in 2005 are summarized in Figure 6.10 presenting the daily averages of the vector HMF in the magnitude, heliographic latitude and longitude format. An important feature of this data is the extremely long duration of the 1st uni-polar sector to be observed in the heliosheath. The sector polarity remained constant for ≈125 days. It has been suggested that the obvious reason for this is because the heliosheath solar wind speed is so much reduced after passage through the TS (Jokipii, 2005).

Figure 6.10 also includes a plot of the 6 hour averaged flux of cosmic ray ions with energies > 0.5 MeV/nucleon. There are several short term temporal peaks in the flux prior to and at the TS crossing. These pulses are followed by a slow and very steady increase beyond. Especially interesting is the fact that the level of flux fluctuations decreases significantly after the TS crossing. This suggests that V1

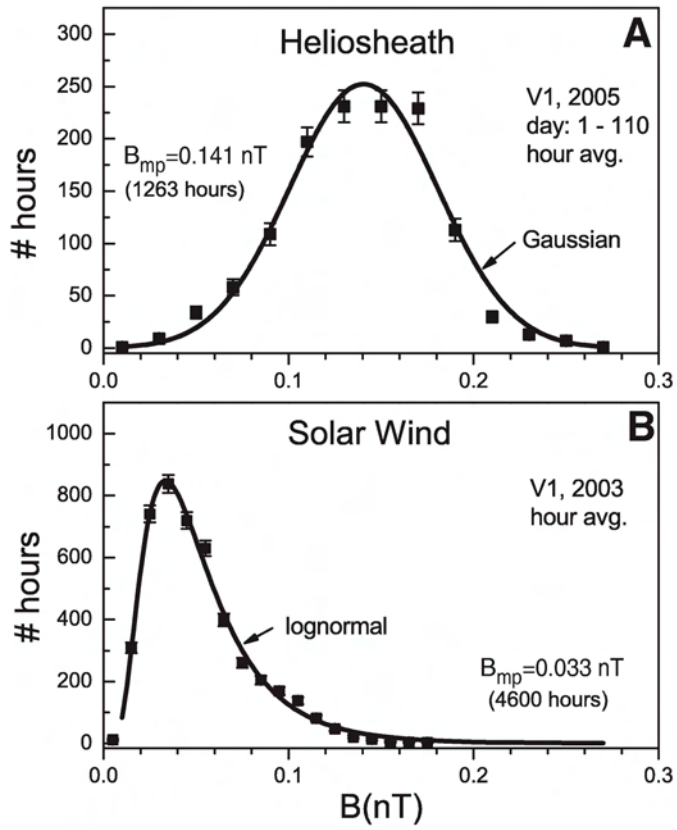

Figure 6.9: Statistical distribution of hourly averaged HMF magnitude for supersonic solar wind in 2003 compared to subsonic solar wind heliosheath in 2005. Striking difference is noted with log-normal distribution for former period but Gaussian for latter.

has entered a plasma-field-particle region beyond the TS in which the acceleration of such CR particles is continuously and uniformly occurring.

An interesting single pulse of a very strong HMF is identified in Figure 6.10 at point A in early 2005, shortly after the TS crossing. An expanded time scale of 48 second averaged vector data surrounding this pulse is shown in Figure 6.11 in heliographic coordinates. A new result in the observations of the HMF is well-illustrated here. The direction of the HMF remains constant throughout the pulse, from DOY 8.8 to DOY 9.2. Beyond that interval, the HMF becomes sufficiently weak that the intrinsic spacecraft and instrument noise, ± 0.02 nT, and intrinsic ambient field fluctuations preclude accurate and precise determination of HMF directions.

In order to examine more comprehensively the more detailed characteristics of the HMF fluctuations in the heliosheath, 48 second averaged data from DOY $50 - 70$ 2005 was examined for its statistical properties. The results for the magni-

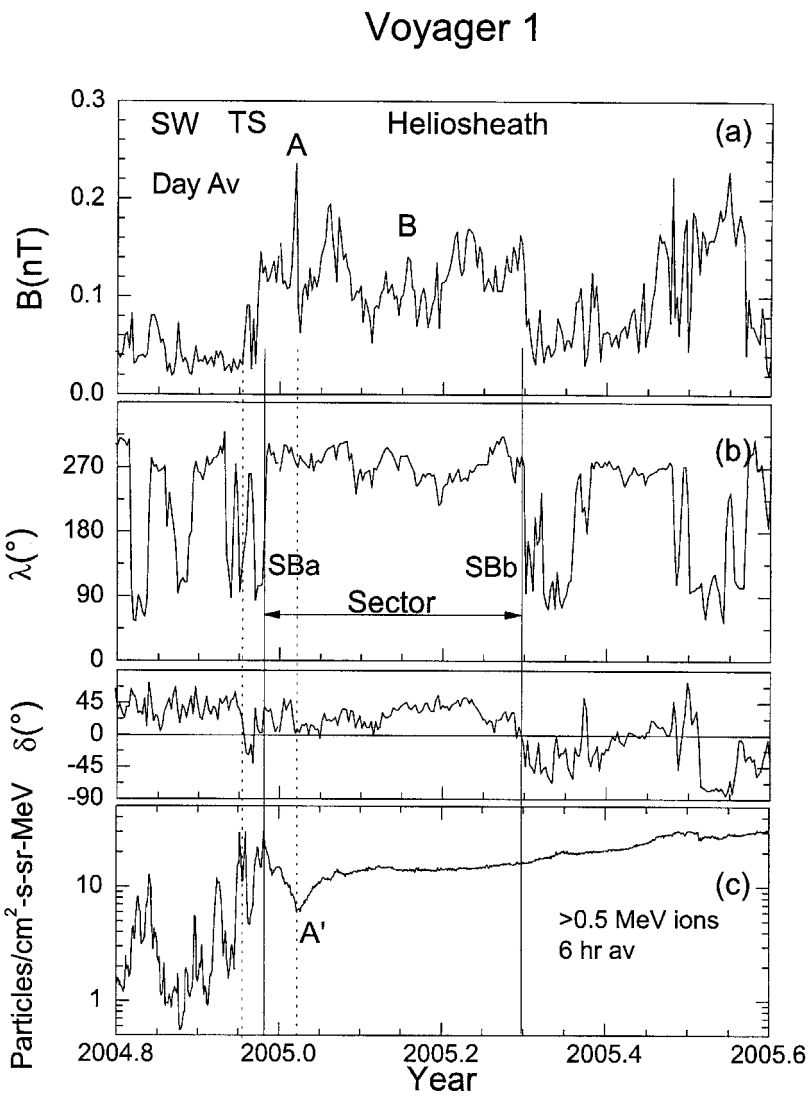

Figure 6.10: Interval of HMF vector observations in 2004−2005, including TS crossing in heliographic coordinates in format of magnitude-latitude-longitude. First heliosheath sector ever observed is noted by its boundaries. Plot of simultaneous energetic particle flux shows sharp change in intensity and level as well as character of fluctuations at TS crossing.

tude and individual three orthogonal R, T and N components are shown in Figure 6.12. The distributions of these four parameters again show well defined Gaussian characteristics with nearly identical widths for the component fluctuations. Thus, Figures 6.11 and 6.12 lead to the surprising and unpredicted conclusion that he-

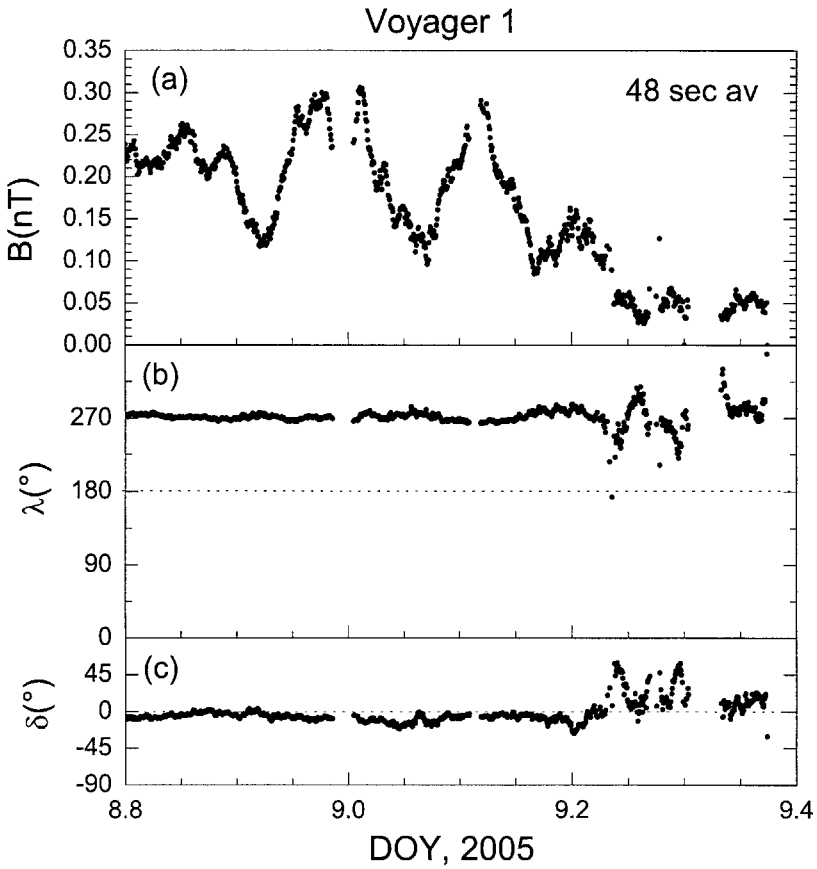

Figure 6.11: Expanded time scale presentation of 48-seconds averaged HMF data of peak magnitude pulse identified as A in Figure 6.10.

liosheath HMF fluctuations are primarily compressible and also isotropic, at least in this sample of data.

6.5 HMF micro-structure

Certain micro-structural features of the heliosheath field have been identified which are reminiscent of characteristics of the supersonic solar wind throughout the heliosphere. The 1st of these is illustrated with 48 second averages in Figure 6.13 by a relatively short-lived dip in the field magnitude, while the direction is essentially invariant. This feature is similar to a microstructure which had been identified and elaborated upon in earlier studies of MHD discontinuities often observed in the solar wind plasma near 1 AU. They were referred to as "magnetic holes" (Turner et al., 1977) and studies have shown that they are observed to occur at a rate of $\approx$1.5 each day.

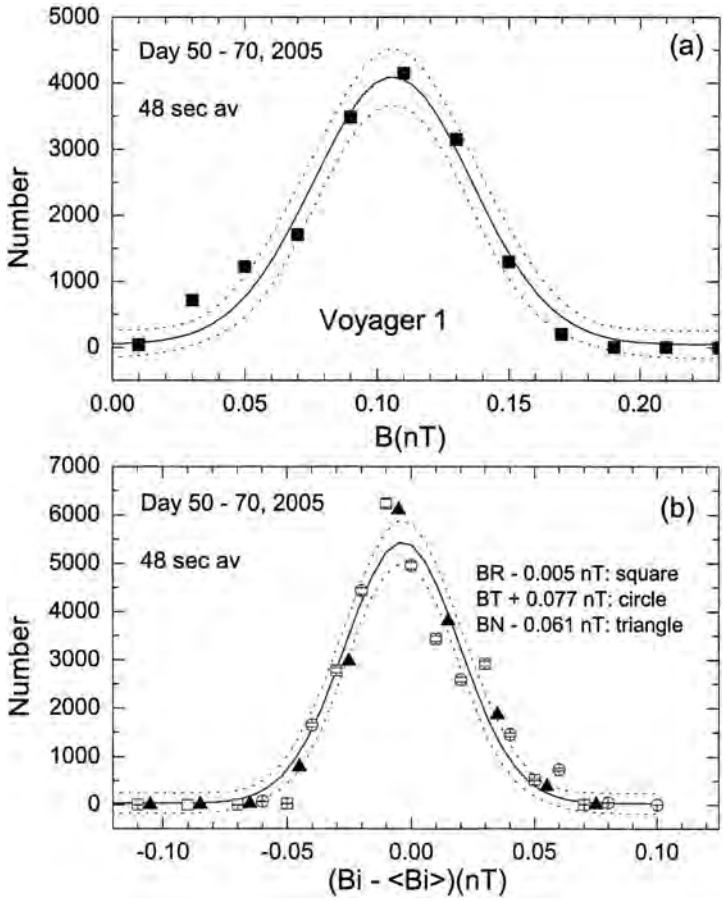

Figure 6.12: Statistical properties of HMF in 20 day interval in heliospheric sector. Plots of magnitude and each of three orthgonal components shows Gaussian distributions of 48 seconds averages for all four measures and identical widths for R, T, and N components.

The long time duration of this "hole," ≈150 minutes, by comparison with those in the supersonic solar wind, a few minutes, is consistent with a contribution from time dilation caused by the sub-sonic solar wind speed in the heliosheath. But it is probably due to the physical fact that the scale size of such micro-structures is determined more by the gyro-radius of the pick-up protons in the heliosheath, ≈12000 km for an HMF field of 0.10 nT.

A fine time scale view of a text-book example of a sinusoidal fluctuation of the HMF magnitude, while the direction remains unchanged, is shown in Figure 6.14, which presents 48 second averages during a fortunately continuous data interval > 12 hours. The constancy of the vector direction while the magnitude varies by a factor of ≈5 is impressive support for the initial conclusion from studies of the

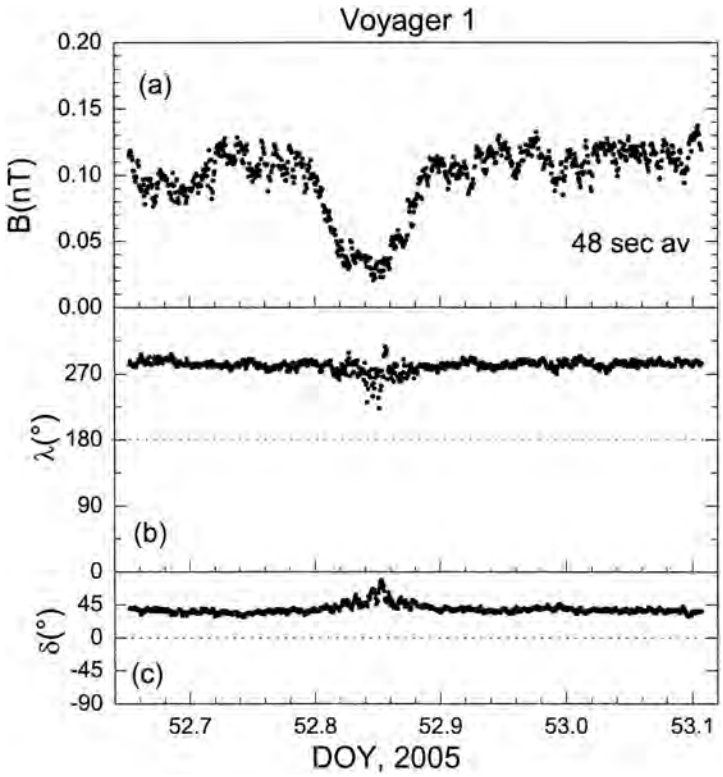

Figure 6.13: Magnetic hole observed in 48 second averaged vector data with large variation in magnitude, but essentially no change in direction, except immediately adjacent to HMF minimum.

V1 HMF statistical data that the fluctuations of the HMF in the heliosheath are mainly compressive.

Another micro-structural feature in the heliosheath and an important one are sector boundaries. The two observed by V1, SBa and SBb, are both identified as such in Figure 6.10. The trailing boundary, SBb, in Figure 6.15 is an extremely thin one and fortuitous data coverage permits identification and study of its details. The boundary SBb appears to be a paradigm for a classical D-Sheet, across which there may be merging or re-connection. The leading sector boundary, SBa, is rather more extended and complex, which merits further study. It is compromised by the several data gaps which exist in the changing polarity of the field from one uni-polar sector to the other.

Initial studies of the Power Spectral Density (PSD) of the HMF magnitude and individual component fluctuations before and after the TS crossing have shown a characteristic decrease with increasing frequency. The PSD is found to decrease at nearly a uniform $-5/3$ exponent for frequencies greater than the proton cyclotron frequency, which ranges between 0.003 to 0.0025 HZ for the intervals studied.

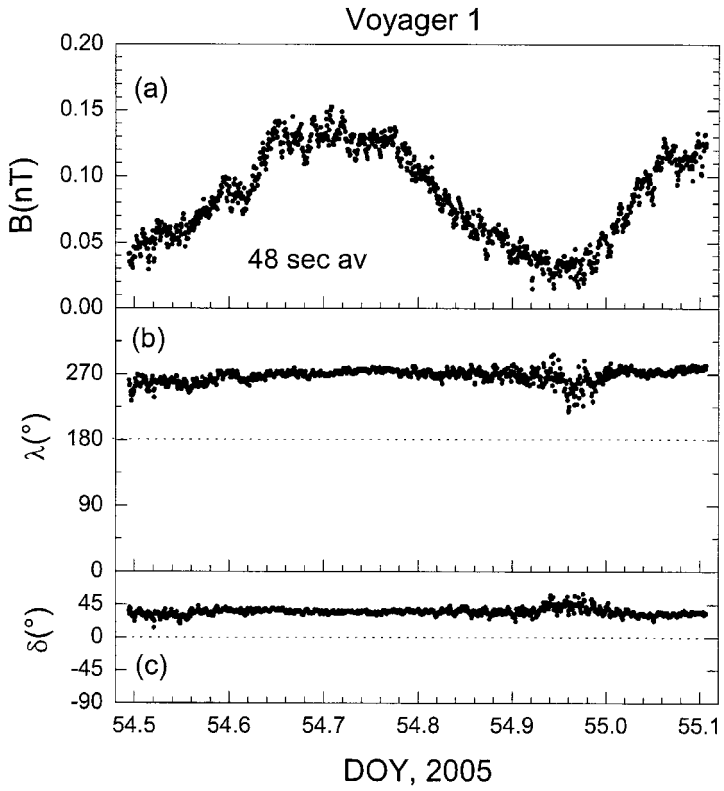

Figure 6.14: Sinusoidal HMF magnitude variation with no change of direction in 48 seconds averaged vector V1 data.

There is no evident peak or even increased band of energy near these frequencies either before or after the TS crossing. But there is a slight difference in the amount of energy at lower frequencies. A decreased energy by up to a factor of 10 pre-TS crossing is noted when compared to intervals post TS crossing. This means that HMF fluctuations and turbulence increase in the heliosheath at the lowest frequencies.

6.6 Summary

The Termination Shock was observed in late 2004 when V1 was at 94 AU and 35 degrees north heliographic latitude. The TS is inferred to have the characteristics of a quasi-perpendicular MHD shock with a sudden and large jump in field magnitude by a factor of ≈3 and an insignificant change in direction. This is as to be expected for the location of V1 relative to the stagnation point of flow of the Local Interstellar Medium as the heliosphere interacts with it.

Fluctuations of the sub-sonic HMF are found to be compressible and isotropic and well described as Gaussian. Structural features such sector boundaries, micro-

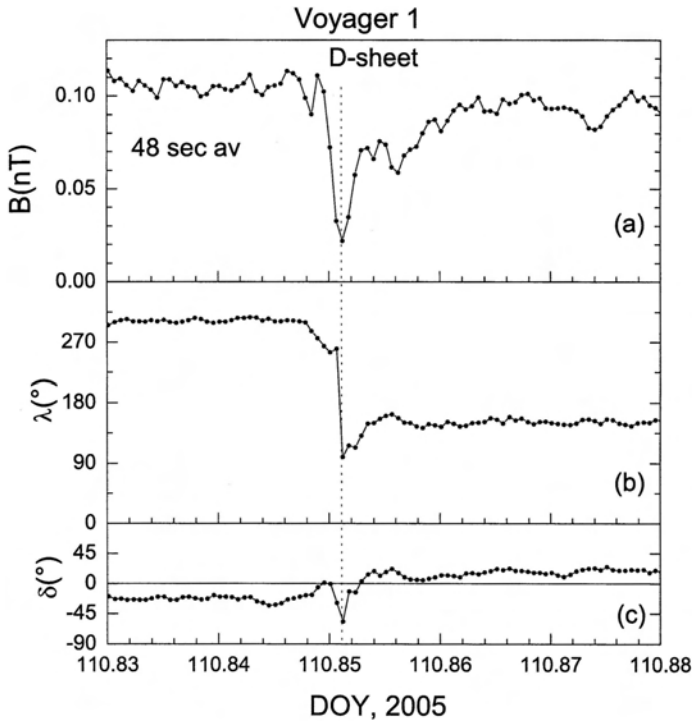

Figure 6.15: 48 second averaged vector data for trailing sector boundary, SBb. Appears to be paradigm classic D-sheet structure across which merging and reconnection may be occurring as HMF on either side change polarity.

structural D-sheets and magnetic holes are observed which are reminiscent of those seen in the supersonic solar wind inside the TS. They have quantitative physical properties appropriate for a pickup ion dominated, weakly magnetized solar originating plasma. The heliosheath is thus identified to have a new set of parameters and, no doubt, processes. It is therefore an example of an astrophysical plasma regime not previously studied in-situ and which has also not been studied theoretically to any degree.

It is to be noted, as shown in Figure 6.16, that the cosmic ray flux and HMF magnitude in the heliosheath are no longer correlated in the same way as in the heliosphere. Although the HMF magnitude increases and decreases substantially, there are no, as yet, readily identifiable corresponding changes in the flux of particles with > 70 MeV/nucleon.

Moreover, their flux continues to steadily increase deeper into the heliosheath suggesting that the acceleration source(s) of these particles is more uniformly distributed thought the heliosheath and is also well beyond V1, which in mid-2005 was at $\approx$96.5 AU. These data and this observation may also lead to the rejection of the thesis that the TS is a global source for anomalous cosmic rays. Additional future observations and studies are needed to fully understand the origin of the heliosheath's unique characteristics.

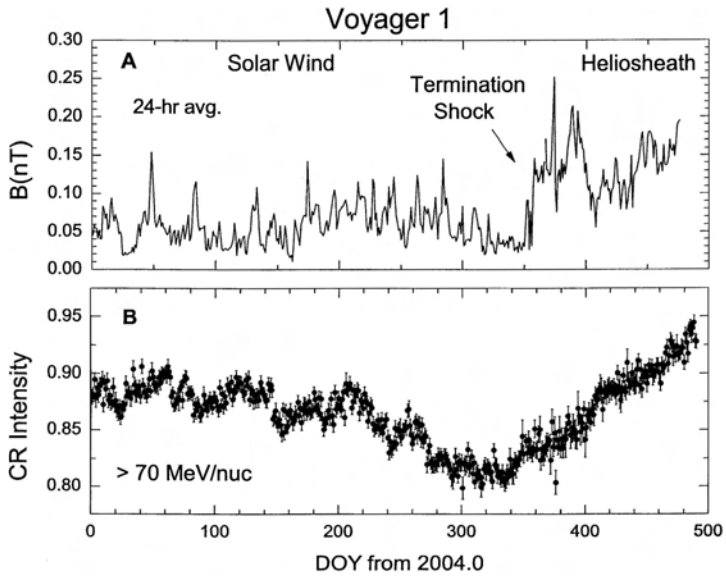

Figure 6.16: Comparison plots of cosmic ray intensity and HMF magnitude over an extended time interval in 2004 – 2005, spanning the TS crossing. Illustrates clear change in character and correlations of fluctuations before the crossing and uniform and steady increase of higher flux post crossing.

Note added in proof

Since this manuscript was submitted, additional reports by Burlaga et al. (2006a, b, c, d) on new studies of the magnetic field data have been published or are in press.

Acknowledgements

I am indebted to my colleagues on the Voyager Magnetometer experiment, Drs. Leonard F. Burlaga and Mario H. Acuña at the NASA-GSFC, for their significant contributions to the overview summary presented here of the important and significant 1st magnetic field observations of the heliosphere's closest major boundary, the Termination Shock. The author also appreciates use of data from the Cosmic Ray Science (CRS) instrument/experiment of Drs. Stone and McDonald on V1. N.F. Ness is supported, in part, by NASA-GSFC Grant NNG04GB71G to the Catholic University of America (CUA).

Bibliography

Behannon, K.W., Acuña, M.H., Burlaga, L.F., Lepping, R.P., Ness, N.F., and Neubauer, F.M.: 1977, 'Magnetic field experiment for Voyagers 1 and 2', *Space Sci. Rev.* **21**, 235–257.

Burlaga, L.F.: 1995, *Interplanetary Magnetohydrodynamics*, Oxford Univ. Press, New York.

Burlaga, L.F., Ness, N.F., and Belcher, J.W.: 1997, 'Radial evolution of corotating merged interaction regions and flows between ≈14 AU and ≈43 AU', *J. Geophys. Res.* **102**, 4661–4672.

Burlaga, L.F., Ness, N.F., Stone, E.C., McDonald, F.B., Acuña, M.H., Lepping, R.P., and Connerney, J.E.P.: 2003, 'Search for the heliosheath with Voyager 1 magnetic field measurements', *Geophys. Res. Lett.* **30**, 2072–2075, DOI 10.1029/2003GL018291.

Burlaga, L.F., Ness, N.F., Acuña, M.H., Lepping, R.P., Connerney, J.E.P., Stone, E.C., and McDonald, F.B.: 2005, *Science* **308**, 2027–2029.

Burlaga, L.F. , Ness, N.F., and Acuña, M.H.: 2006a, 'Magnetic fields in the heliosheath: Voyager 1 Observations', *Astrophys. J.* **642**, 584–592.

Burlaga, L.F., Vinas, A.F., Ness, N.F., and Acuña, M.H.: 2006b, 'Tsallis statistics of the magnetic field in the heliosheath', *Astrophys. J.* **644** L83–L86.

Burlaga, L.F., Ness, N.F., and Acuña, M.H.: 2006c, 'Trains of magnetic holes and magnetic humps in the heliosheath', *J. Geophys. Res.*, in press.

Burlaga, L.F., Ness, N.F., and Acuna, M.H.: 2006d, 'Multifractal structure of the magnetic field in the heliosheath', *Geophys. Res. Lett.*, in press.

Decker, R.B., Krimigis, S.M., Roelof, E.C., Hill, M.E., Armstrong, T.P., Gloeckler, G., Hamilton, D.C., and Lanzerotti, L.J.: 2005, 'Voyager 1 in the foreshock, termination shock, and heliosheath', *Science* **309**, 2020–2024.

Jokipii, J.R.: 2005, 'The magnetic field structure in the heliosheath', *Astrophys. J.* **631**, L163–L165.

Krimigis, S.M., Decker, R.B., Hill, M.E., Armstrong, T.P., Gloeckler, G., Hamilton, D.C., Lanzerotti, L.J., and Roelof, E.C.: 2003, 'Voyager 1 exited the solar wind at a distance of ≈85 AU from the Sun', *Nature* **426**, 45–48.

McDonald, F.B., Stone, E.C., Cummings, A.C., Heikkila, B., Lal, N., and Webber, W.R.: 2003, 'Enhancements of energetic particles near the heliospheric termination shock', *Nature* **426**, 48–51.

Ness, N.F.: 1987, 'Studies of the interplanetary magnetic field: IMP's to Voyager', in R. Ramaty, T.L. Cline, and J.F. Ormes (eds.), *Essays in Space Science*, NASA Conf. Publ. **2464**, 99–121.

Ness, N.F., and Burlaga, L.F.: 2001, 'Spacecraft studies of the interplanetary magnetic field', *J. Geophys. Res.* **106**, 15,803–15,818.

Ness, N.F., Burlaga, L.F., Acuña, M.H., Stone, E.C., and McDonald, F.B.: 2005, Search for the heliospheric termination shock (TS) and heliosheath (HS)', in G. Li, G.P. Zank, and C.T. Russell (eds.), *Physics of Collisionless Shocks*, AIP Conf. Proc. **781**, 267–272.

Parker, E.N.: 1963, *Interplanetary Dynamical Processes*, Interscience Publishers, New York.

Schulz, M.: 1973, 'Interplanetary sector structure and the heliomagnetic equator', *Astrophys. Space Sci.* **24**, 371–383.

Smith, E.J., Slavin, J.A., and Thomas, B.T.: 1986, 'The heliospheric current sheet – 3-dimensional structure and solar cycle changes', in R.G. Marsden (ed.), *The Sun and the Heliosphere in Three Dimensions*, D. Reidel Publishing Co., pp. 267–274.

Stone, E.C., Cummings, A.C., McDonald, F.B., Heikkila, B.C., Lal, N., and Webber, W.R.: 2005, 'Voyager 1 explores the termination shock region and the heliosheath beyond', *Science* **309**, 2017–2020.

Turner, J.M., Burlaga, L.F., Ness, N.F., and Lemaire, J.F.: 1977, 'Magnetic holes in the solar wind', *J. Geophys. Res.* **82**, 1921–1924.

Whang, Y.C., Burlaga, L.F., Wang, Y.M., and Sheeley, N.R.: 2004, 'The termination shock near 35° latitude', *Geophys. Res. Lett.* **31**, L03805.

Zhang, M.: 2005, 'The Compton-getting effect of energetic particles with an anisotropic pitch-angle distribution: an application to Voyager 1 results at ≈85 AU', *Astrophys. J.* **624**, 1038–1048.

— 7 —

Turbulence and Ion Acceleration in the Outer Heliosphere

Reinald Kallenbach[1]
International Space Science Institute, Bern, Switzerland

Andrzej Czechowski
Space Research Centre, Polish Academy of Sciences, Warsaw, Poland

Martin Hilchenbach
Max-Planck-Institut für Sonnensystemforschung, Katlenburg-Lindau, Germany

Peter Wurz
Physikalisches Institut, University of Bern, Switzerland

Abstract. **The transport parameters of suprathermal and energetic particles in the heliosphere are intimately linked to the properties of the plasma turbulence in the supersonic solar wind flow and in the subsonic heliosheath plasma flow beyond the termination shock. Based on observations with the magnetometers on board the Helios, ACE, Ulysses, and Voyager spacecraft, and on theoretical calculations, the quantitative evolution of transport parameters of suprathermal particles over heliocentric distances is estimated. From these transport parameters, the stochastic acceleration efficiencies and spatial pressure profiles of suprathermal ions in the solar wind termination region are derived. The scattering mean free path in the heliosheath plasma also yields the injection threshold speed and characteristic time-scales for first-order Fermi acceleration of ions at the termination shock. The theoretical results are compared to observations of suprathermal ions, i.e. the termination shock energetic particles (TSPs) and the Anomalous Cosmic Rays (ACRs), with the Voyager spacecraft in the outer heliosphere, and with data on energetic neutral atoms (ENAs) detected with the CELIAS/HSTOF sensor onboard SOHO and with the ASPERA-3 sensor onboard Mars Express.**

7.1 Introduction

The transport of suprathermal charged particles in the magnetized solar wind plasma is qualitatively described by convection, drift, adiabatic deceleration in the expanding solar wind, and by diffusion. The process of diffusion is subdivided into

[1]in *The Physics of the Heliospheric Boundaries*, V. Izmodenov and R. Kallenbach (eds.), ISSI Scientific Report No. 5, pp. 203 - 243, ESA-ESTEC, Paris 2006

spatial diffusion and diffusion in momentum space. The basis for a quantitative description of the transport is given by the Parker equation, which may be written in the form

$$\frac{\partial f}{\partial t}+(\mathbf{V}+\mathbf{V}_{\mathrm{D}})\cdot\nabla f=\nabla\cdot(\mathcal{K}\nabla f)+\frac{v}{3}\frac{\partial f}{\partial v}\nabla\cdot\mathbf{V}+\frac{1}{v^2}\frac{\partial}{\partial v}\left(v^2D_{vv}\frac{\partial f}{\partial v}\right)+Q-S \quad (7.1)$$

or in other variations. The velocity $\mathbf{V}$ is the convection velocity of the bulk plasma in some reference frame such as the spacecraft frame, the tensor $\mathcal{K}$ describes the spatial diffusion, the parameter D_{vv} the diffusion of a nearly isotropic charged particle distribution in velocity space, and Q and S are source and sink terms such as the creation of ions in the plasma by ionization of neutrals or the reverse process, respectively. The term $(\nabla\cdot\mathbf{V})\,v\partial_v f/3$ describes the adiabatic deceleration (acceleration) in an expanding (converging) plasma flow. The velocity $\mathbf{V}_{\mathrm{D}}$ describes the drift of the suprathermal particles such as magnetic-field gradient or curvature drift. Parker's equation has been developed for theories on cosmic ray transport. It applies for a minority population of particles which are not "members" of the thermal distribution of the bulk plasma. The equation also applies to some extent to particles which are only slightly suprathermal, although the approach breaks down at some lowest energy. Equation (7.1) is usually written in the solar wind rest frame in order to have a nearly isotropic particle distribution in the bulk plasma frame even for the lowest-energy suprathermal particles such as pick-up ions.

The transport parameters $\mathcal{K}$ and D_{vv} of suprathermal ions are usually described in the frame of the quasi-linear theory (QLT), a theory based on the original work by Jokipii (1966). A recent study by Bamert et al. (2004) suggests that the parallel mean free path described by the QLT, $\lambda_{\parallel}=3v^2/\left[8\pi\Omega_{\mathrm{p}}^2\tilde{P}\,(k)\right]$, describes fairly well the propagation of energetic protons with speed v and angular gyro-frequency Ω_{p} in the solar wind plasma, if only the Alfvénic fluctuations in slab geometry enter the power spectral density $\tilde{P}\,(k)=\delta\tilde{B}^2/B_0^2$ at the resonant wave number $k\approx\Omega_{\mathrm{p}}/v$.

If this result holds for the solar wind termination region, the evolution of the Alfvénic fluctuations with heliocentric distance gives an estimate of the injection threshold for suprathermal ions into first-order Fermi acceleration at the termination shock and for the confinement and build-up of pressure of suprathermal (energetic) particles in the turbulent heliosheath plasma flow. Some uncertainty enters the estimate because it is not entirely clear what happens to the Alfvénic turbulence at the quasi-perpendicular termination shock itself. However, Voyager 1 (Acuña et al., 2006) magnetic field data give some constraints on the order of magnitude of Alfvénic fluctuations in the heliosheath.

This tutorial will be organized as follows: In Section 7.2 we will review the properties of solar wind turbulence and its evolution over heliocentric distance. In Section 7.3, we calculate the injection threshold for first-order Fermi acceleration at the solar wind termination shock as a function of the shock normal angle and as a function of heliolongitude and heliolatitude. In Section 7.4 we will derive the transport parameters $\mathcal{K}$ and D_{vv} and discuss the evolution of suprathermal tails in the ion distributions over heliocentric distance. Section 7.5 discusses the dynamical role of energetic particles near the termination shock. In Section 7.6 numerical simulations of the termination shock reformation and of the microscopic structure are summarized. Section 7.7 contains the conclusions. Appendix 7.A presents a

compact mathematical derivation of the relation of the transport parameters $\mathcal{K}$ and D_{vv} to the power spectral densities of compressive and non-compressive MHD solar wind turbulence, while Appendix 7.B summarizes in detail the mathematical model of magnetohydrodynamic (MHD) turbulence in the supersonic solar wind plasma, which is briefly wrapped up in the following Section.

7.2 Evolution of solar wind turbulence

Present models consider the Alfvén radius – the distance from the Sun, where the bulk solar wind reaches the Alfvén speed – as the "birth place" of Alfvénic solar wind turbulence. This view has been initiated by models that dealt with purely non-compressive fluctuations that propagate in a proton-dominated solar wind with the Alfvén speed $v_{\rm A} = B_0/\sqrt{\mu_0 n_{\rm p} m_{\rm p}}$, where B_0 is the ambient interplanetary magnetic field strength, $n_{\rm p}$ is the proton density and $m_{\rm p}$ the proton mass. Once the solar wind has reached the Alfvén speed, the Alfvénic fluctuations cannot return any more to the solar source, and, therefore, the properties of the Alfvénic turbulence in a homogeneous solar wind are determined by the boundary conditions at the Alfvén radius. This situation may approximately be realized in the polar coronal hole regions (vertical axis in Figure 7.1). There, quasi-stationary fast solar wind streams with non-compressional (Alfvénic) fluctuations dominate.

However, there are many more sources of solar wind turbulence outside the Alfvén radius, in particular close to the ecliptic plane (horizontal axis in Figure 7.1). Coronal mass ejections and stream interactions between slow and fast solar wind streams drive compressional fluctuations through interplanetary shocks and global structures such as Co-rotating Interaction Regions (CIRs) and (Global) Merged Interaction Regions (GMIRs).

Furthermore, any anisotropy in particle distributions at speed v, $f(v,\mu) - f(v,-\mu)$, leads to growth of Alfvén waves by the resonance condition $\Omega + k_\parallel v\mu - \omega$, where μ is the pitch-angle cosine and $k_\parallel$ can have both signs describing Alfvén waves travelling parallel and antiparallel along the ambient magnetic field B_0. Any spatial pressure gradient of a particle distribution leads to an anisotropy. The contribution of Solar Energetic Particles (SEPs) to the Alfvén wave driving in the inner heliosphere is not yet evaluated sufficiently in the literature.

An example of SEP-driven interplanetary Alfvén waves is shown in Figure 7.2. In panel (B) the increase of Alfvénic wave power above the ambient level of solar wind turbulence due to energetic protons is shown (Bamert et al., 2004). The amplified waves have indeed been identified as being Alfvénic. Panel (C) shows the increase in the power of magnetic fluctuations at an interplanetary quasi-parallel shock, which matches fairly well the model by Vainio and Schlickeiser (1999). The interplanetary shocks driven by coronal mass ejections (CMEs) are presumably strongest close to the Sun at about $4-6$ solar radii so that most of SEP-driven turbulence may be generated there. This location of maximum shock strength, however, is still outside the Alfvén radius.

The Alfvénic turbulence in the solar wind is anisotropic (Figure 7.3). There are more anti-sunward than sunward propagating waves. This may be a natural consequence of the fact that outward propagating waves have a higher escape prob-

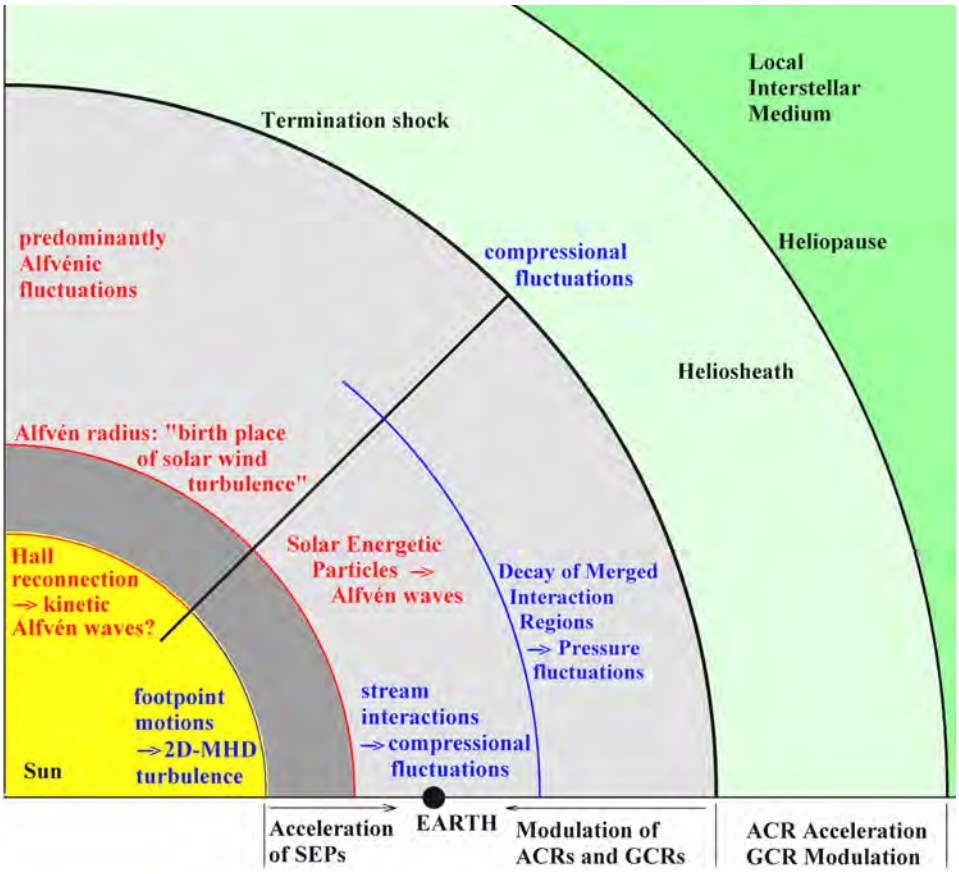

Figure 7.1: Schematic overview of the heliosphere showing some of the most important processes of solar wind turbulence generation.

ability from the region inside the Alfvén radius. On the other hand, SEP-driven Alfvén waves also preferentially propagate anti-sunward.

The generation and amplification of turbulence at a quasi-perpendicular shock such as the solar wind termination shock and near stream interfaces of co-rotating interaction regions (CIRs) has not yet been studied theoretically in detail. However, the data shown in Figure 7.3 suggest that stream interactions decrease the anisotropy, which may be an indicator for the generation of isotropic compressional fluctuations. As outlined by Ness (2006, this volume), the inner heliosheath i.e. the turbulence region downstream of the solar wind termination shock, is indeed a region of strongly compressional turbulence.

In contrast, the polar coronal hole (fast) solar wind is a region with nearly incompressional fluctuations. Horbury and Balogh (2001) have studied the radial evolution of the solar wind turbulence in Ulysses magnetometer data (Figure 7.4). It appears that the turbulence in the inertial range scales with r^{-3}, where r is the heliocentric distance. This scaling corresponds to the so-called WKB-scaling,

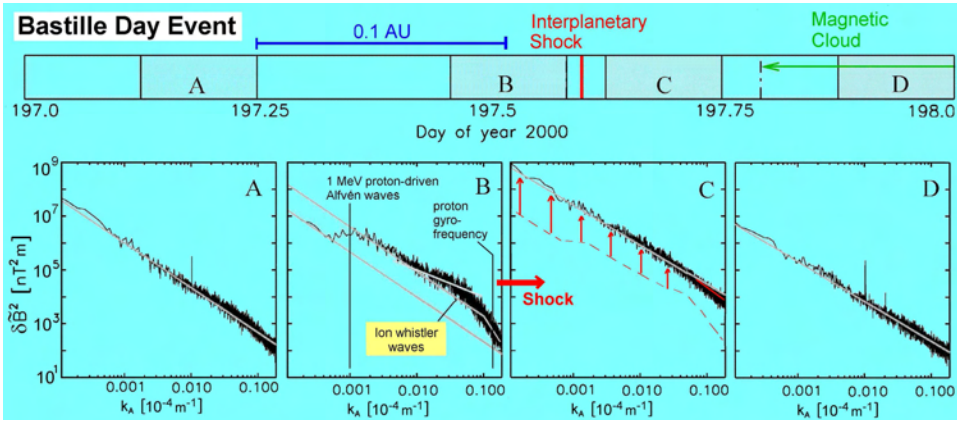

Figure 7.2: Overview of power spectral densities of magnetic field fluctuations near the strongest interplanetary shock during the Bastille Day event (Kallenbach and Bamert, ACE news #91).

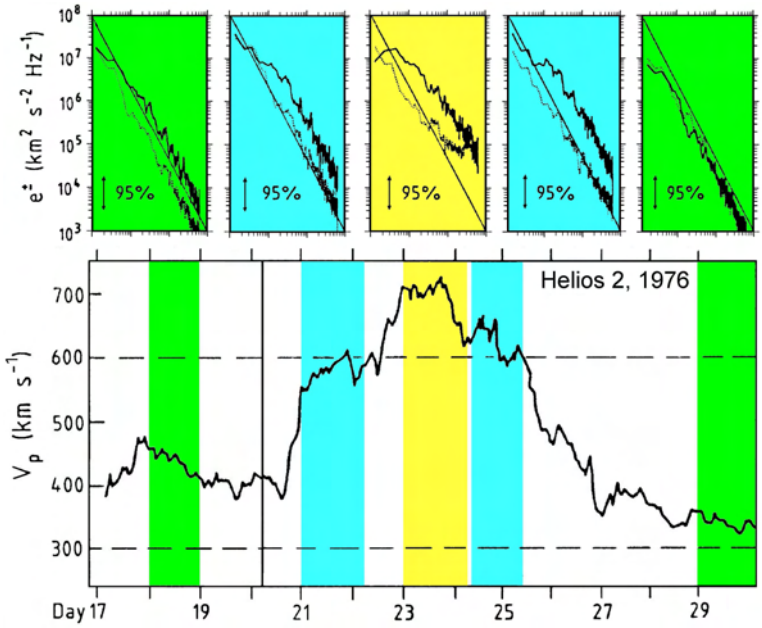

Figure 7.3: Turbulence properties of the solar wind at 1 AU (Tu et al., 1990).

which applies if there are no sources of turbulence, in particular no sources for compressional fluctuations.

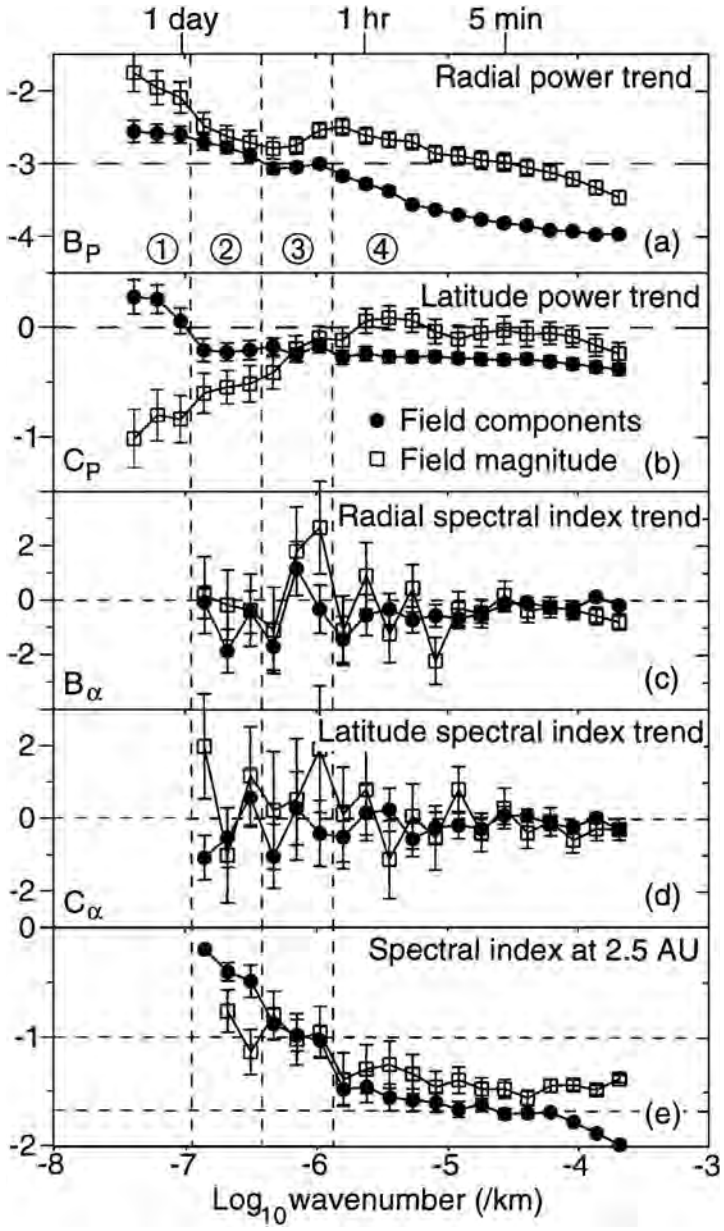

Figure 7.4: Evolution of solar wind turbulence properties between 1.4 and 4.1 AU in polar coronal hole streamers (Horbury and Balogh, 2001). The power of solar wind turbulence follows the law $\log_{10} P = A_{\rm P} + B_{\rm P} \log_{10} r + C_{\rm P} \sin\theta$, where r is the heliocentric distance and θ the heliolongitude. The power spectral index α of the turbulence follows the law $\alpha = A_\alpha + B_\alpha \log_{10} r + C_\alpha \sin\theta$.

A detailed mathematical model of solar wind MHD turbulence is summarized in the Appendix (Section 7.B). The resulting equations of evolution with heliocentric distance are (Equation 7.70):

$$\begin{aligned}\left(\frac{\partial}{\partial t}+\nabla\cdot\frac{\mathbf{U}}{2}+\mathbf{U}\cdot\nabla-\Gamma\frac{U}{r}\right)E_b &= -\frac{E_b^{3/2}}{l_\mathrm{c}}+S\ ;\\ \left(\mathbf{U}\cdot\nabla+\Gamma\frac{U}{r}\right)l_\mathrm{c} &= \frac{E_b^{1/2}}{2}-\frac{l_\mathrm{c}S}{2E_b}\ .\end{aligned}\tag{7.2}$$

Here, $\mathbf{U}$ is the solar wind bulk velocity, and the magnetic energy is defined as $E_b = b^2/(2\mu_0\rho)$, where $\mathbf{b}$ is the amplitude of the magnetic field fluctuations. For slab and 2D-MHD turbulence, the mixing parameter Γ describes the coupling of magnetic and velocity fluctuations. As is derived in the Appendix (Section 7.B), we have $\Gamma = -\sigma_\mathrm{D}\cos^2\Psi$, where $\sigma_\mathrm{D} = (r_\mathrm{A}-1)/(r_\mathrm{A}+1)$ with the Alfvén ratio $r_\mathrm{A} = E_v/E_b$. The Alfvén ratio gives the ratio between the power per unit mass in the kinetic fluctuations $E_v = v^2/2$ and the magnetic fluctuations E_b. In general, i.e. for $\sigma_\mathrm{D} \neq 0$, the coupling between magnetic and kinetic fluctuations depends on the angle Ψ between the plasma flow and the ambient magnetic field.

In the solar wind, we have $\Gamma > 0$ ($\sigma_\mathrm{D} < 0$) or $r_\mathrm{A} = E_v/E_b < 1$, respectively. For purely Alfvénic fluctuations, we have $\sigma_\mathrm{D} = 0$ and, thus, $\Gamma = 0$. This means that Alfvénic fluctuations with $E_v - E_b = 0$ convect unchanged at any angle Ψ in the solar wind plasma as long as the expansion can be neglected. Even at $\Psi = 90°$ magnetic and kinetic fluctuations do not couple.

Without dissipation, sources, or mixing, i.e. $l_\mathrm{c} = \infty$, $S = 0$, and $\Gamma = 0$, Equation (7.2) fulfils the familiar WKB solution

$$U\frac{\partial E_b}{\partial r}+\frac{U}{r}E_b = 0 \quad\Rightarrow\quad \frac{E_b}{E_{\mathrm{b}0}} = \frac{r_0}{r} \quad\Rightarrow\quad \frac{b^2}{b_0^2} = \left(\frac{r_0}{r}\right)^3 \text{ if } \frac{\rho}{\rho_0} = \left(\frac{r_0}{r}\right)^2.\tag{7.3}$$

For $\Psi \approx 0$ and $\sigma_\mathrm{D} \approx -1$, i.e. for a solar wind flow parallel to the ambient magnetic field dominated by magnetic fluctuations, we have $\Gamma \approx 1$. In that case it follows that $b/b_0 \propto r_0/r$ as was suggested by Jokipii and Kota (1989) for the polar magnetic field. Such a field with strong magnetic fluctuations enhances cosmic ray transport across the ambient magnetic field. Further out at the Ulysses orbit, where the interplanetary (heliospheric) magnetic field is rather perpendicular, the fluctuations in the coronal hole regions rather follow the WKB solution (Figure 7.4).

For a general $\Gamma \neq 1$, i.e. for a stronger coupling between kinetic and magnetic fluctuations and/or non-Alfvénic fluctuations, and including sources of the form $S = C_\mathrm{S}UE_b/r$, the solution of Equation (7.2) is

$$\begin{aligned}\frac{E_b}{E_{\mathrm{b}0}} &= \frac{(r_0/r)^{1-\Gamma-C_\mathrm{S}}}{1+A^{-1}C^{-1}\left[(r/r_0)^A-1\right]} \ \propto\ r^{-(3+\Gamma)/2} \ \text{ for } \ r\to\infty;\\ \frac{l_\mathrm{c}}{l_{\mathrm{c};0}} &= \left\{1+A^{-1}C^{-1}\left[(r/r_0)^A-1\right]\right\}^{1/2}\left(\frac{r_0}{r}\right)^{\Gamma+C_\mathrm{S}/2} \ \to\ r^{(1-\Gamma)/4}\ ;\\ A &= \frac{1+3\Gamma+2C_\mathrm{S}}{2}\ ; \quad C = \frac{l_{\mathrm{c};0}U}{r_0E_{\mathrm{b};0}^{1/2}}\ .\end{aligned}\tag{7.4}$$

All acceleration and modulation processes of Solar Energetic Particles (SEPs), Galactic Cosmic Rays (GCRs), and Anomalous Cosmic Rays (ACRs) involve turbulence in the solar wind and in its source regions. Therefore, the above described evolution of solar wind turbulence, which determines the evolution of transport parameters over heliocentric distance, is essential to understand the behaviour of all suprathermal tails and energetic particle populations, such as ACRs, GCRs, and SEPs, in the heliosphere.

In the next section, the evolution of the parallel mean free path over the heliocentric distance is evaluated in order to estimate the injection threshold for suprathermal ions in the solar wind into the first-order Fermi acceleration process at the solar wind termination shock.

7.3 Injection threshold at the termination shock

Transport parameters of energetic ions are usually described in the frame of the quasi-linear theory (QLT), a theory based on the original work by Jokipii (1966). A recent study by Bamert et al. (2004) suggests that the parallel mean free path derived from the QLT,

$$\lambda_{\parallel} = \frac{3}{16} r_{\mathrm{g}}^2 P^{-1}\left(r_{\mathrm{g}}^{-1}\right) = \frac{3\,(s-1)}{16} r_{\mathrm{g}} \left(\frac{2\pi r_{\mathrm{g}}}{l_{\mathrm{c;A}}}\right)^{1-s} \zeta_{\mathrm{A}}^{-1}, \quad \zeta_{\mathrm{A}} = \frac{\langle \delta B_{\mathrm{A}}^2 \rangle}{B_0^2} \propto E_b, \tag{7.5}$$

describes fairly well the propagation of energetic protons with speed v and angular gyro-frequency Ω_{p} in the solar wind plasma, if only the Alfvénic fluctuations in slab geometry enter the power spectral density $P\left(k_r\right) = \delta\tilde{B}^2\left(k_r\right)/B_0^2$ at the resonant wavenumber $k_r \approx \Omega_{\mathrm{p}}/v = r_{\mathrm{g}}^{-1}$. We assume that the power spectral density of the Alfvénic fluctuations follow a power law, e.g. a Kolmogorov law with spectral index $s = 5/3$, and that there are as many forward as backward travelling waves. The parameter ζ_{A} describes the square of the total Alfvénic fluctuation amplitude in relation to the square of the ambient magnetic field amplitude B_0 and is proportional to the power per unit mass in the magnetic fluctuations E_b used in Equation (7.2). The correlation length or outer scale $l_{\mathrm{c;A}}$ of the Alfvénic fluctuations can be interpreted as the maximum wavelength of the turbulence, structures larger than $l_{\mathrm{c;A}}$ are ordered, while structures smaller than $l_{\mathrm{c;A}}$ are chaotic or turbulent. Near Earth, the Alfvénic correlation length is about $l_{\mathrm{c;A}} \approx 0.03\mathrm{AU}$ (Goldstein et al., 1995).

The above expression for $\lambda_{\parallel}$ is derived in Appendix 7.A.3. In the literature, however, one often finds the pre-factor $3/(8\pi)$ instead of $3/16$.

7.3.1 Evolution of turbulence with heliocentric distance

The parallel mean free path is the basic transport parameter for charged-particle transport in the supersonic solar wind. It is also one reference for charged particle transport in the heliosheath and, therefore, can be used to estimate the injection threshold speed for ions to be diffusively accelerated at the termination shock. Diffusive acceleration at the termination shock occurs when the diffusion speed in the heliosheath overcomes the steady-state convection speed of suprathermal ions.

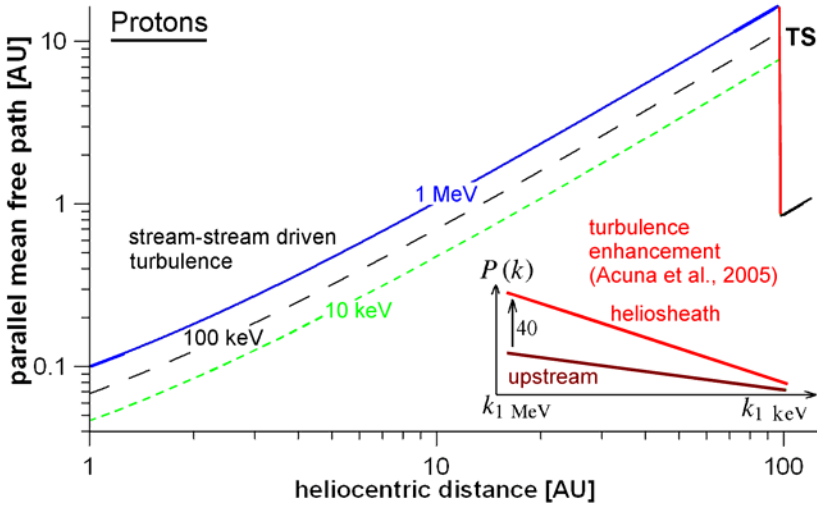

Figure 7.5: Evolution of the parallel mean free path of protons with heliospheric distance in the ecliptic plane. The inset qualitatively represents the increase in turbulent power observed by the Voyager 1 magnetometer (see Acuña et al., 2006, for the precise data).

And this diffusion speed is related to the parallel mean free path. Therefore, the calculation of the evolution of the turbulent power with heliocentric distance is the basis to evaluate the transport parameters in the solar wind termination region.

The parallel mean free paths for different proton energies at 1 AU are taken from the observations by Bamert et al. (2004) of the upstream region of the Bastille Day shock (see Figure 7.5 for the values). The evolution of the Alfvénic component of solar wind turbulence is calculated according to Equation (7.4). This equation is equivalent to the model of Zank et al. (1996a). As in their work, we assume a constant mixing ratio $\Gamma = 0.2$ between magnetic field and velocity fluctuations in the solar wind. The parameter Γ is then defined as $\Gamma = \langle -\sigma_D \cos^2 \Psi \rangle$ (see Eq. 7.65), where σ_D is the Alfvénicity and the brackets mean the average over the heliocentric distance. The assumption of constant Γ allows for an analytical solution of the problem. Note, that the pick-up ion driven magnetohydrodynamic (MHD) turbulence is not important for the mean free paths of the higher-energetic particles because these waves are at higher frequencies. However, these MHD-waves partly heat the solar wind and actually mainly heat the pick-up ions themselves (Isenberg et al., 2003; Chalov et al., 2006).

Some uncertainty enters the estimate of turbulent power in the heliosheath because it is not entirely clear what happens to the Alfvénic turbulence at the quasi-perpendicular termination shock itself. Voyager 1 magnetic field data give some constraints on the order of magnitude of Alfvénic fluctuations in the heliosheath as shown in Figure 7.5. The estimate of the downstream parallel mean free path is not obvious, however, as it is not clear whether the amplification of Alfvénic turbulent power corresponds to the factor 40 observed by Voyager 1 for the total amplification

of magnetic turbulent power. However, the gradients of the energetic particle flux at different energies in the heliosheath suggest approximate agreement with the assumption that the Alfvénic turbulent power also increases by a factor close to 40 at the termination shock. Figure 7.6 shows the Voyager data and the derivation of a mean free path by applying Equation (7.31) to the downstream region. The question of why the flux of energetic particles still increases in the heliosheath has been interpreted in different ways. As depicted in Figure 7.7, McComas and Schwadron (2006) suggest that the most efficient acceleration of Anomalous cosmic rays (ACRs) and Termination Shock Energetic Particles (TSPs) mainly takes place at the "flanks" of the heliosphere because the magnetic field lines connecting to the termination shock are longest and most time is available to accelerate ions to high energies. As the termination shock is typically closest to the Sun at the nose (apex), the connecting lines are longest for the regions at heliolongitudes 90° away from the nose, as should become clear from the geometry in Figure 7.7 (*left*). In the nose region, where Voyager 1 has crossed the termination shock, the flux tubes connecting to the shock become longer and longer while travelling into the heliosheath. This explains the increasing flux of TSPs/ACRs. McComas and Schwadron (2006) also assume that the injection threshold into first-order Fermi acceleration is lower at the "flanks" because the termination shock is less perpendicular. These ideas have in fact already been formulated by Chalov (1993; 2000; 2005), Chalov and Fahr (1996; 2000), and Chalov et al. (1997). We will get to the variation of the injection threshold with heliolongitude in the next Section.

Alternatively, the TSP/ACR flux could increase while penetrating the downstream region of the termination shock because of stochastic acceleration in the compressional fluctuations of the heliosheath plasma. Decker et al. (2005) originally suggested that the suprathermal ions behave like an ideal gas which gets compressed during the transition from the upstream solar wind to the heliosheath, and that first-order Fermi acceleration plays a minor role. We will get to this hypothesis in Section 7.4.

7.3.2 The injection threshold as a function of the shock normal angle

According to Giacalone and Jokipii (1999), the threshold for injection of suprathermal ions into the first-order Fermi acceleration process at a shock with upstream solar wind speed V_1 in the shock frame is

$$v_{\mathrm{inj}} \;=\; 3V_1 \left[1 + \frac{\left(\kappa_{\mathrm{A}}/\kappa_{\parallel}\right)^2 \sin^2\Psi + \left(1 - \kappa_{\perp}/\kappa_{\parallel}\right)^2 \sin^2\Psi \cos^2\Psi}{\left[\left(\kappa_{\perp}/\kappa_{\parallel}\right)\sin^2\Psi + \cos^2\Psi\right]^2} \right]^{1/2} \quad ; \tag{7.6}$$

Here, $\kappa_{\parallel}$ and $\kappa_{\perp}$ are the spatial diffusion parameters parallel and perpendicular to the magnetic field, and κ_{A} is the antisymmetric component of the diffusion tensor. See Appendix 7.A.4 for a derivation of Equation (7.6) and for the expressions for $\kappa_{\perp}$ and κ_{A} for the case in which the gyroradius r_{g} of the ion at speed v is small compared to the parallel mean free path $\lambda_{\parallel}$.

Figure 7.8 shows the injection threshold (Equation 7.6) for protons as a function

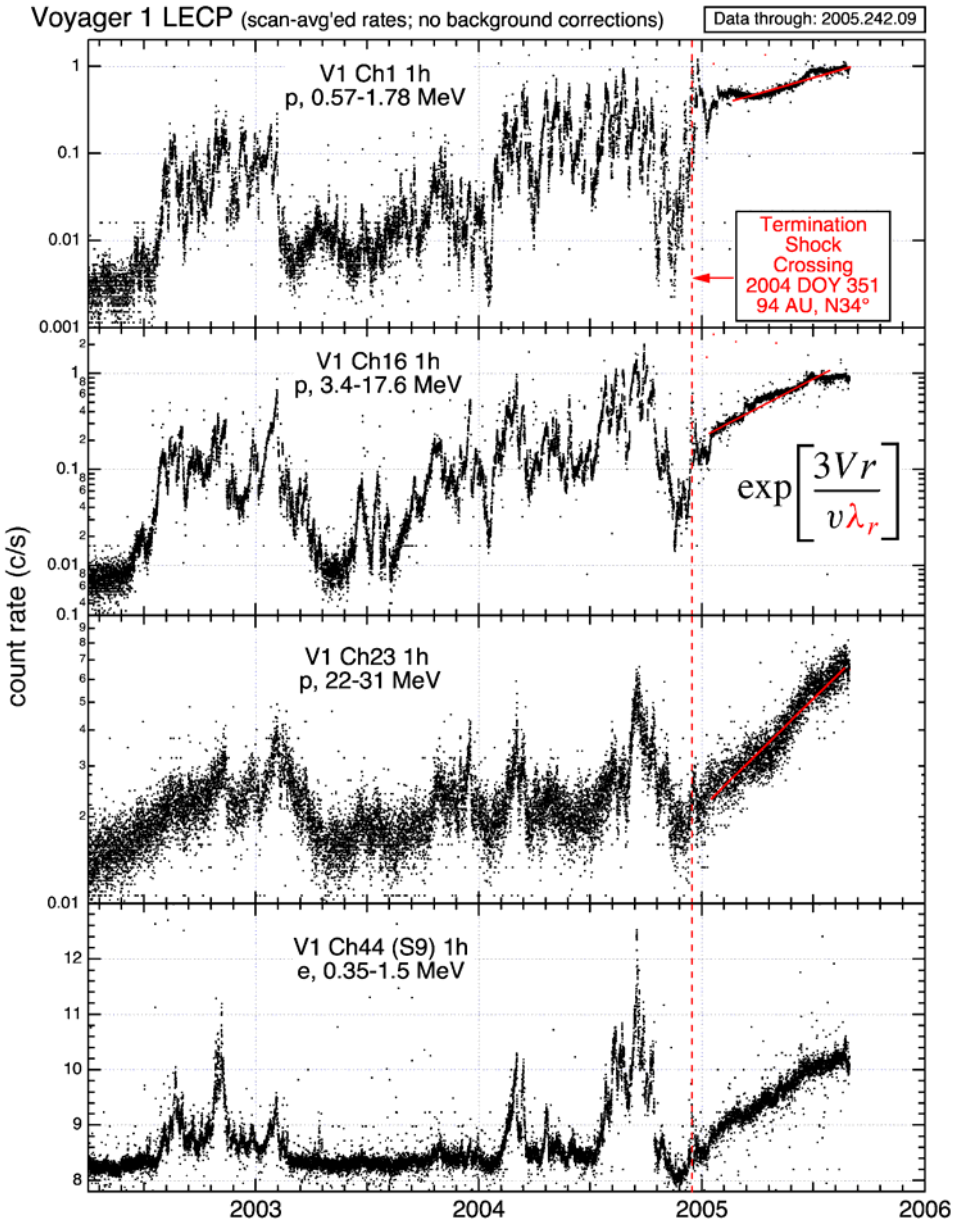

Figure 7.6: Spatial variation of energetic particle flux near the solar wind termination shock. The gradients of the downstream flux can be translated to a parallel mean free path of 0.2 AU for 1 MeV protons, if the magnetic field deviates on average by about 6° from the shock surface as measured by Burlaga et al. (2005) with the magnetometer onboard Voyager 1. For a strict Parker magnetic field angle of $\Psi \approx 89.3°$ and a totally spherical termination shock, the radial mean free path $\lambda_r \approx \lambda_\parallel \cos^2\Psi + \lambda_\perp \sin^2\Psi$ would yield $\lambda_\parallel \approx 15$ AU for 1 MeV protons. However, this seems unrealistic, so that $\lambda_\parallel \approx 0.2$ AU can be taken as a baseline value. http://sd-www.jhuapl.edu/VOYAGER/images/vgr_qlp/v1_lecp/

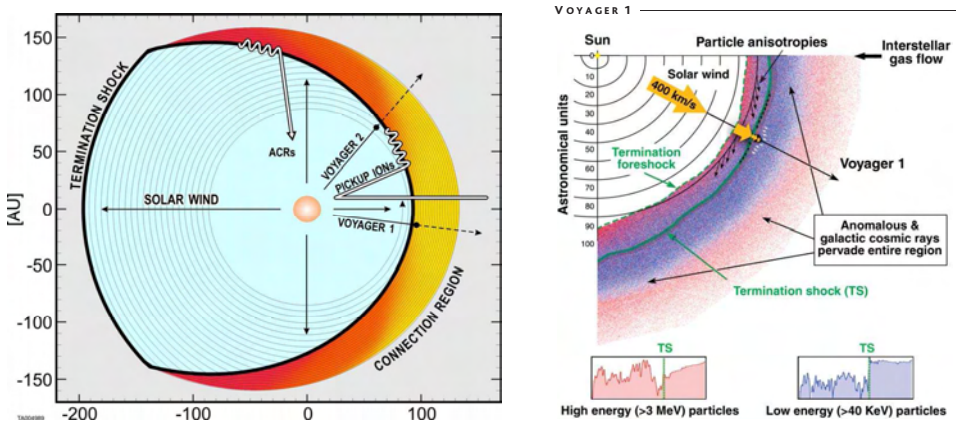

Figure 7.7: *Left:* Schematic geometry of the *termination shock* and the heliospheric magnetic field (McComas and Schwadron, 2006). *Right:* Description of the solar wind termination region by Decker et al. (2005).

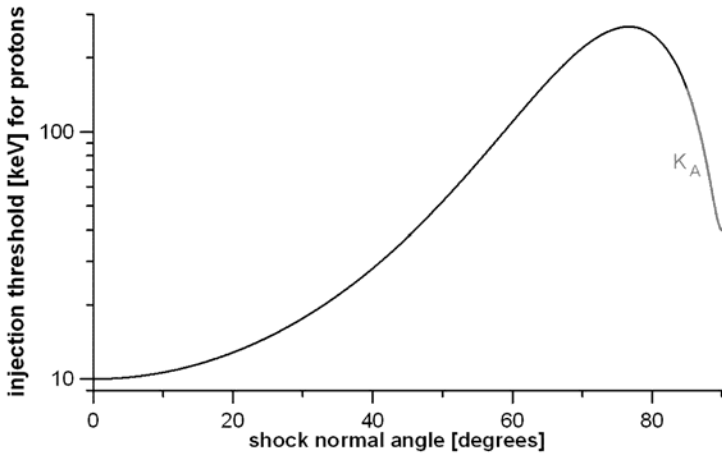

Figure 7.8: Injection threshold into first-order Fermi acceleration of protons at the solar wind termination shock as a function of the shock normal angle.

of the shock normal angle Ψ, based on the turbulence levels that determine the parallel mean free paths in Figure 7.5. The limiting cases are angles between the ambient magnetic field $\mathbf{B}_0$ and the shock normal angle of $\Psi = 90°$ and $\Psi = 0°$. This yields injection threshold speeds $v_{\rm inj}\,(\Psi = 90°) = 3V_1\lambda_\parallel/r_{\rm g}$ and $v_{\rm inj}\,(\Psi = 0°) = 3V_1$. The decrease of the injection threshold at $\Psi = 90°$ with respect to $\Psi \approx 80°$ comes from the dominance of the term with $\kappa_{\rm A}$. The return of the ions from the downstream plasma at $\Psi \approx 90°$ is a combination of gyration and perpendicular scattering, which is more efficient than the perpendicular scattering at $\Psi \approx 80°$. It is interesting that the termination shock with $\Psi \approx 90°$ is particularly well suited for injection because the process of pre-acceleration during multiple reflections also works best at $\Psi \approx 90°$ (le Roux et al., 2000), in particular if the scale size of the shock ramp is of the order of the electron inertial length (see Section 7.6).

The expressions in Equation (7.6) correspond to the classical hard-sphere scattering theory, which is only valid if the gyro-radius of the ions, $r_{\rm g}$, is larger than the correlation length of the turbulence (Giacalone and Jokipii, 1999). This is not the case in the supersonic upstream solar wind, but may be the case in the downstream thermalized heliosheath plasma (Burlaga et al., 2005). The correlation length may be of the order of the gyro-radius of the bulk protons, which is shorter than the gyro-radius of suprathermal and energetic particles.

7.4 Evolution of suprathermal tails

We solve the Parker equation (7.1) by neglecting spatial diffusion and drift. We assume spherical symmetry and constant solar wind speed. We consider momentum diffusion in compressional turbulence regions which are larger than the mean free path for pitch-angle scattering and neglect momentum diffusion in Alfvénic turbulence (see Section 7.A). For the momentum diffusion parameter we assume that it scales as $D_{vv} \propto r^{-1}v^2$. Any scaling law of D_{vv} close to r^{-1} may be approximated over some range of heliocentric distance by r^{-1}. Observations point towards $D_{vv} \propto r^{-0.7}v^2$ (see Chalov, this volume, and references therein), but the case $D_{vv} \propto r^{-1}v^2$ can be solved analytically because all terms in the Parker equation (7.1) get the same power in r. This leads to an ordinary differential equation in v. We first solve the homogeneous part of the Parker equation (7.A), i.e. with $Q = 0$ and $S = 0$, and then add a source $Q_{\rm PUI}\,(\mathbf{r}, v)$ of freshly ionized pick-up ions. The Parker equation is rewritten in speed units $u = v/V_{\rm SW}$ and radius $\rho = r/1{\rm AU}$. In these normalized units the momentum diffusion parameter has the form $D_2\rho^{-1}u^2$, where D_2 is dimensionless.

We obtain a homogeneous solution $f_{\rm hom}$:

$$-\frac{\partial f}{\partial \rho} + \frac{1}{\rho}\frac{2u}{3}\frac{\partial f}{\partial u} + \frac{D_2}{\rho}\frac{1}{u^2}\frac{\partial}{\partial u}\left[u^4\frac{\partial f}{\partial u}\right] = 0 \quad \Rightarrow \quad f_{\rm hom}\,(u,\rho) = f_0\rho^{-\beta}u^{-\alpha}$$
$$\text{with} \quad \beta = \frac{2}{3}\alpha - \alpha\,(\alpha-3)\,D_2 \quad \text{or} \quad \alpha \approx 3 + \frac{2}{3D_2} - \frac{3\beta}{2+9D_2}, \tag{7.7}$$

where the approximation for α applies as long as $3\beta/\,(2+9D_2) \ll 3 + 2/\,(3D_2)$.

The pre-factor f_0 is determined from the local source of freshly ionized interstellar hydrogen atoms. This source scales as ρ^{-2} outside the ionization cavity

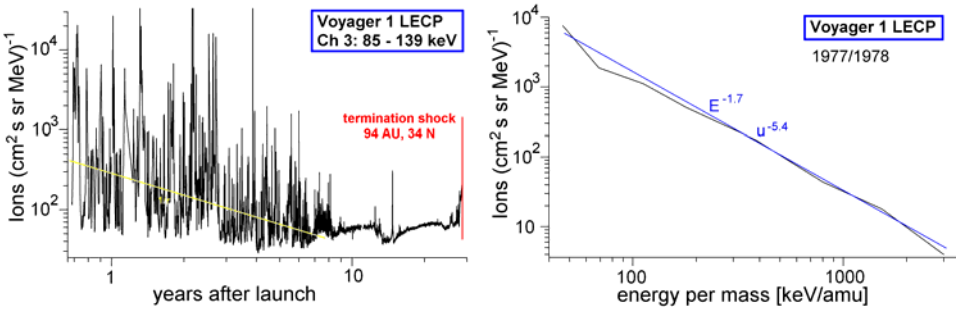

Figure 7.9: Evolution of the flux of suprathermal ions with heliocentric distance ρ from uncalibrated data of the Low Energy Charged Particle (LECP) instrument from the project homepage at Caltech. Voyager 1 moves in average about 3 AU per year. Despite the large variations due to events such co-rotating and merged interaction regions, the mean scaling may be close to ρ^{-1} as denoted by the yellow line. A spectral index $\alpha = 5.4$ of the phase space density seems to be fairly typical.

around the Sun extending out to about 7.5 AU. For interstellar helium atoms, the ρ^{-2} scaling is valid further inwards, in particular in the upwind direction of the interstellar medium, i.e. $Q(u, \rho) = \rho^{-2} q(u)$ for $\rho > 1$. The inhomogeneous solution $f_{\rm inhom}$ then scales as ρ^{-1} i.e. $\beta = 1$.

Trusting the simplified model typical values of D_2 can be derived from the observed spectral index of suprathermal tails. They are in the range $\alpha \approx 5...6$ (Gloeckler, 2003). For a momentum diffusion parameter $D_2 \approx 0.2$ (and $\beta = 1$) the spectral index is $\alpha \approx 5.4$. Note that α cannot be smaller than 5. This is the limit, when stochastic acceleration becomes the dominant term in the transport equation, i.e. $D_2 > 1$. In that case, the quasi-linear description breaks down and one gets a cascade in speed represented by a phase space density scaling as v^{-5} (Fisk et al., 2006). Figure 7.9 shows the data of the Voyager 1 LECP instrument which supports the idea that the suprathermal ion flux scales on average inversely with heliocentric distance, and that a spectral index of 5.4 of the phase space density is fairly typical.

Decker et al. (2005) have suggested that first-order Fermi acceleration at the termination shock plays a minor role for ACRs. Instead, stochastic acceleration in the heliosheath could be an important process. As the momentum diffusion parameter is already $D_2 \approx 0.2$ in the region upstream of the termination shock, it could easily be larger than unity in the heliosheath plasma and make stochastic acceleration very efficient.

It is instructive to evaluate the acceleration time scales for first-order Fermi acceleration at the termination shock with stochastic acceleration (second-order Fermi) in the heliosheath. The time scale for first-order Fermi acceleration is (Kallenbach et al., 2005, and references therein):

$$t_{\rm acc} \quad = \quad \frac{3}{V_{\rm up} - V_{\rm ds}} \int_{v_0}^{v_1} \left(\frac{v \Lambda_{\rm r;up}}{3 V_{\rm up}} + \frac{v \Lambda_{\rm r;ds}}{3 V_{\rm ds}} \right) \frac{{\rm d}v}{v} \quad \Rightarrow$$

$$\tau_{\mathrm{acc;F1}} := \frac{\mathrm{d}t_{\mathrm{acc}}}{\mathrm{d}v} v \approx \left(\frac{E}{1\mathrm{MeV}}\right)^{2/3} \cos^2\Psi \left(\frac{A}{Q}\right)^{1/3} \mathrm{yr}\ , \tag{7.8}$$

For this rough estimate, mean free paths of order 0.5 AU for protons with 1 MeV energy have been assumed. Compared to this, the acceleration time scale for stochastic acceleration in compressional fluctuations in the upstream slow solar wind with $D_2 \approx 0.2$ is about 4 years ($\rho \approx 100$). This is derived from Equation (7.7), which is written in units of the solar wind convection time scale near Earth. If the compressional fluctuations are stronger by a factor 40 in the heliosheath compared to the upstream solar wind, the acceleration time scale may be about 0.1 year at any energy and mass-per-charge ratio of the ions. This shows that at the high energies in particular stochastic acceleration may well compete with first-order Fermi acceleration.

Note that only in the slow solar wind is the momentum diffusion parameter as large as $D_2 \approx 0.2$, while the fast solar wind has mainly Alfvénic fluctuations, and D_2 is much smaller. If stochastic acceleration is the main process to energize the ACRs, their source is concentrated around the ecliptic plane.

7.5 The dynamical role of energetic particles near the termination shock

Energetic particles near the termination shock can influence the structure of the shock and in a self-consistent manner their own intensity. The mean free path of energetic particles is usually much larger than the scale size of the shock ramp and their energy is much higher than the electric cross-shock potential. Therefore, they move rather freely over the shock layer, i.e. they penetrate from the downstream region far into the upstream region before they are scattered and convected back over the shock into the downstream region. While they are scattered they transfer momentum to the upstream plasma and slow down the upstream plasma if their pressure is comparable to the bulk plasma pressure. A shock precursor is formed and the subshock compression ratio is reduced.

Whenever there is a spatial gradient in energetic particle distributions, there is an anisotropy in the distribution observed in the plasma frame. These anisotropies lead to the generation of plasma waves. These plasma waves cascade and convect over the shock to the downstream region and, consequently, increase the injection threshold for first-order Fermi acceleration and thus limit the energetic particle intensity. These phenomena will be discussed in the next two subsections.

7.5.1 Self-consistent limitation of the TSP flux?

The influence of self-generated upstream waves on the injection threshold for termination shock energetic particles (TSPs) is described in Kallenbach et al. (2005). The termination shock may on average mostly have shock normal angles of $\Psi \approx 80^\circ \pm 5^\circ$. In that range of angles Ψ, if $\cos^2\Psi > r_{\mathrm{g}}^2/\lambda_{\parallel}^2$, the term $\cos^2\Psi$ in

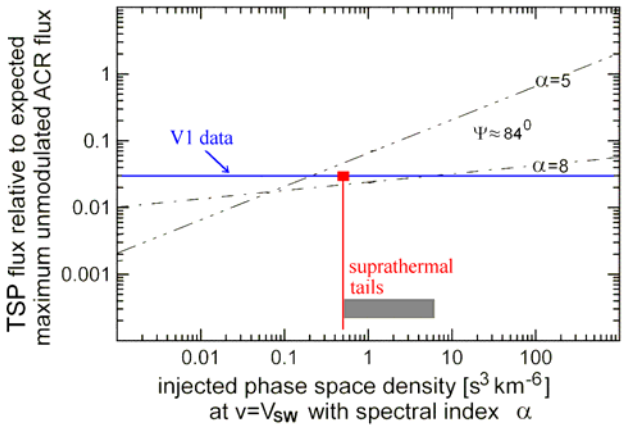

Figure 7.10: The flux of particles accelerated by the first-order Fermi process does not increase proportionally with the flux of injected suprathermal tails because the higher flux of energetic protons generates waves, which in turn increase the injection threshold for first-order Fermi acceleration. The red line denotes the minimum pre-factor $f_0\rho_{\rm TS}^{-1}$ of the proton phase space density injected at the termination shock, where it is assumed that the proton suprathermal tails observed by Gloeckler (2003) scale in the heliosphere as $f_0\rho^{-1}u^{-\alpha}$. The spectral index of the phase space densities α of the suprathermal tails is typically between 5 and 8. The TSP flux is normalized to the typical unmodulated flux of the ACRs. The proton TSP phase space density at 1 MeV (*blue line*) observed by Stone et al. (2005) is 10^{-5} s^3 km^{-6}.

the denominator of the expression for the injection threshold (Eq. 7.6) eventually dominates, so that the injection condition becomes

$$v_{\rm inj} = 3V_1 r_{\rm g}/\left(\lambda_\parallel \cos^2\Psi\right) \ . \tag{7.9}$$

This is the injection threshold condition used in Kallenbach et al. (2005). If $\cos^2\Psi < r_{\rm g}^2/\lambda_\parallel^2$, this evaluation has to be modified. For an ideal stationary spherical termination shock and a heliospheric magnetic field in the form of a Parker spiral, the self-limitation of energetic particle intensity would occur because upstream energetic protons drive turbulent waves. The amplification of the power spectral density of Alfvénic turbulence is of order $G_{\rm A}(k) = 1500\cos\Psi\,(k/k_{1\,\rm MeV})^{\gamma_{\rm sh}-13/3}$ (Kallenbach et al., 2005), where $\gamma_{\rm sh}$ is the spectral index of first-order Fermi accelerated particles, $\gamma_{\rm sh} = 3\xi_{\rm sh}/(\xi_{\rm sh}-1)$ with $\xi_{\rm sh} = V_{\rm up}/V_{\rm ds} = n_{\rm ds}/n_{\rm up}$ the shock compression ratio. The wave number $k_{1\,\rm MeV}$ is approximately the wave number of Alfvén waves which resonate with protons at 1 MeV energy. The amplified Alfvén waves are transmitted through the termination shock and, thus, decrease the parallel mean free path, $\lambda_\parallel$, in the heliosheath. This increases the injection threshold and consequently decreases the energetic particle flux – a self-limiting process. This self-limitation becomes evident in Figure 7.10. It seems that it may be hard to reach the ACR flux levels by first-order Fermi acceleration at a homogeneous termination shock. Even at high injection phase space density (ordinate in Figure 7.10) the TSP flux does not reach the unmodulated ACR flux (unity on

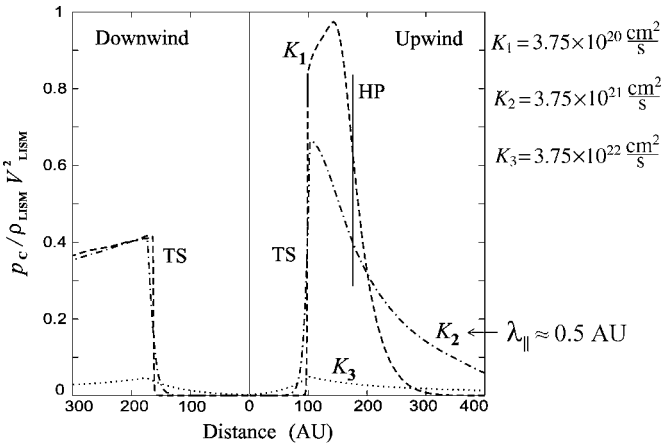

Figure 7.11: Pressure build-up of energetic particles in the heliosheath (Alexashov et al., 2004).

the abscissa of Figure 7.10) originally expected to be observed at the termination shock. The observed level of TSP flux at the termination shock (Stone et al., 2005) in fact matches the model shown in Figure 7.10 (line for 1 MeV particles). Perhaps, additional stochastic acceleration in the heliosheath is necessary to reach the unmodulated ACR level (Kallenbach et al., 2005).

Another possibility is that there are areas of *injection* at *low turbulence* levels and other areas of *acceleration* at *high turbulence* levels causing short acceleration time scales. In this way, the unmodulated ACR flux may be reachable by the first-order Fermi process at the termination shock.

7.5.2 ACR pressure build-up in the heliosheath

Figure 7.11 shows the pressure build-up of TSPs and ACRs in the heliosheath according to numerical simulations by Alexashov et al. (2004). The parameter with index 2 corresponds to the evolution of the mean path over the heliocentric distance displayed in Figure 7.5. The parallel mean free path is in that case very roughly about $\lambda_r \approx \lambda_{\parallel} \approx 0.5$ AU for protons at 1 MeV energy in the heliosheath. This in fact matches the observed gradients of the TSP/ACR flux in the heliosheath after Voyager 1 had crossed the solar wind termination shock (Stone et al., 2005). For this parameter set, the TSP/ACR pressure builds up to a significant fraction of the dynamical pressure of the neutral gas component of the Local Interstellar Medium (LISM).

7.5.3 Comparison to data

In order to compare the model results to real data one must know the solar wind parameters and the flux and spectra of suprathermal ions in the outer heliosphere for regions both upstream and downstream of the termination shock, i.e. in the heliosheath.

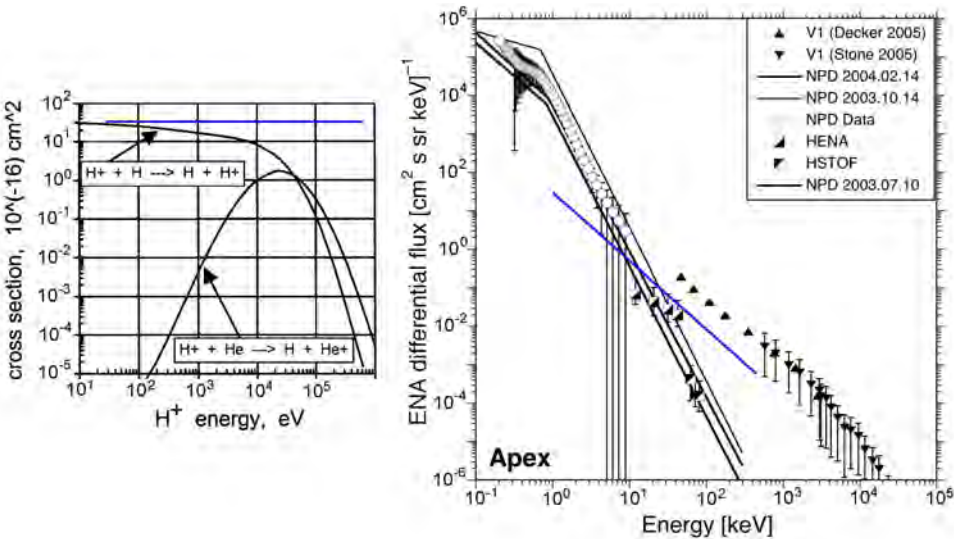

Figure 7.12: Voyager 1 in-situ ion flux data (Stone et al., 2005) from the heliosheath plasma and "remote-sensing" energetic neutral atom data from CELIAS/HSTOF (see also Czechowski et al., this volume), HENA IMAGE data (E. Roelof, private communication), and Mars Aspera-3 data (NPD, Galli et al., 2006). The blue line indicates the model proton spectra in the heliosheath for the injection of the minimum flux of suprathermal tails in the slow solar wind $f = f_0 \rho^{-1} u^{-5}$, $f_0\,(u = 1) \approx 50$ s^3 (Gloeckler, 2003), and an enhancement of their flux by about a factor 10 at the termination shock. That HSTOF data are below the blue line is due to the fact that the charge exchange cross section decreases at higher energies, as is illustrated in the left panel (Gruntman et al., 2001).

Until December 2004, only energetic neutral atom (ENA) observations for H and He by CELIAS/HSTOF were available to analyze suprathermal ion flux data in the heliosheath. The flux of ENAs near Earth's orbit created from the suprathermal ion tails anywhere in the heliosphere is modelled in detail by Gruntman et al. (2001), Czechowski et al. (this volume), and Kallenbach et al. (2005). Since the crossing of the termination shock by Voyager 1 (Stone et al., 2005) in December 2004, there are in-situ measurements of suprathermal ion distributions in the heliosheath plasma. Figure 7.12 demonstrates that estimates of the suprathermal ion flux in the heliosheath from CELIAS/HSTOF data are in agreement with the in-situ measurements. Some new data have been contributed by the Neutral Particle Detector (NPD) onboard Mars Express. At low energies (< 10 keV), the phase space densities of hydrogen atoms are definitely higher than the values derived from pre-acceleration in the supersonic solar wind and acceleration at the termination shock. This indicates that further stochastic acceleration of low-energy protons takes place in the heliosheath. In fact, this stochastic acceleration appears to be very efficient. The high levels of compressional fluctuations observed in the heliosheath (Ness et al., this volume) support this view.

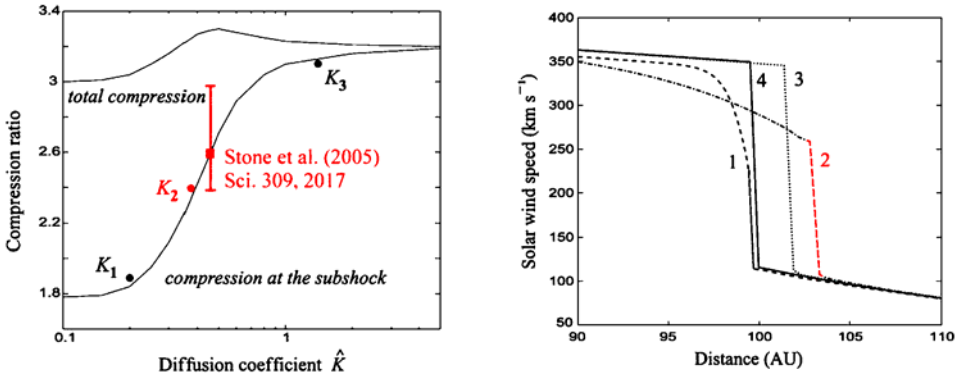

Figure 7.13: *Left:* Reduction of the solar wind termination shock compression ratio. *Right:* Shape of the precursor to be compared to the data in Figure 7.14 (Alexashov et al., 2004).

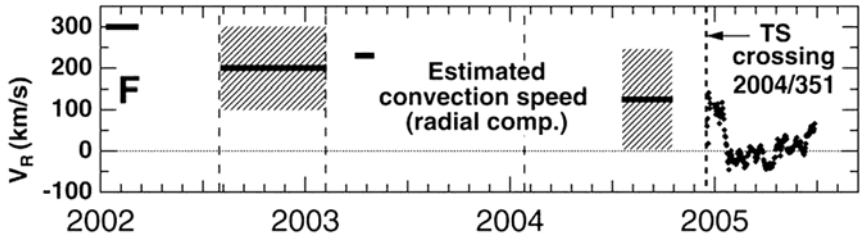

Figure 7.14: Observed slow-down of the solar wind upstream of the termination shock (Decker et al., 2005).

The data seem to support the idea that the solar wind termination shock is a cosmic-ray-mediated shock. Figure 7.13 shows the modelled reduction in the compression ratio of the solar wind termination subshock, in particular for the parallel mean free path denoted by Index 2 that corresponds to the model of the evolution of solar wind turbulence and the observed increase in turbulence at the shock (Figure 7.5). Figure 7.14 shows the slow-down of the solar wind observed by Voyager 1. The error bars are large because the plasma instrument onboard Voyager 1 is not operating anymore, so that the solar wind velocity has to be derived from anisotropies in the energetic particle flux measured by LECP. Although the uncertainties are large, the solar wind seems to be slowed down much below the speed of about 250–300 km/s, which corresponds to the maximum slow-down due to the mass loading of interstellar pick-up protons in the outer heliosphere. Therefore, it seems likely that the solar wind termination shock is cosmic-ray-mediated by the TSP/ACR population. However, as is visible from Figure 7.6, the energetic particle pressure gradient in the upstream solar wind plasma is not in the form of a smooth precursor, but rather spiky and intermittent.

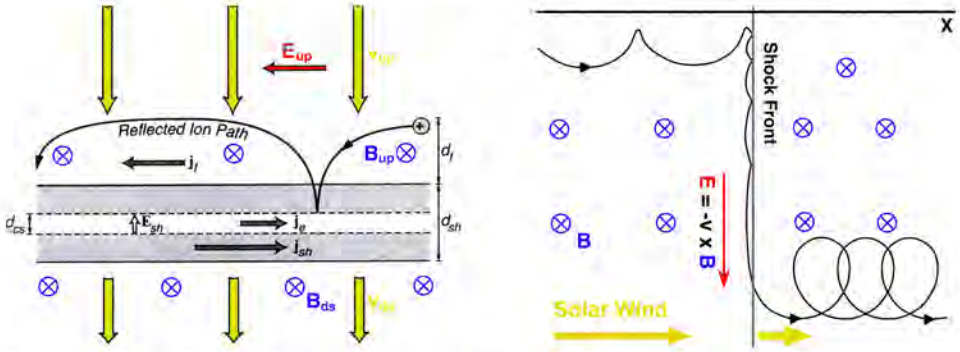

Figure 7.15: *Left:* Simplified structure of a perpendicular shock: Protons penetrate into the downstream plasma with the scale size of their gyroradius, while electrons are 'stopped' within an electron gyroradius. This charge separation causes a cross-shock electric field $E_{\rm sh}$ over the ramp scale size of order $d_{\rm cs}$. The cross-shock potential $e\phi = eE_{\rm sh}d_{\rm cs}$ is of the order of the upstream proton energy, i.e. the kinetic bulk plasma energy. The jump in the tangential component of the magnetic field $[B_{\rm t}] = B_{\rm ds} - B_{\rm up} > 0$ causes a current $j_{\rm sh} = [B_{\rm t}] \,/\, (\mu_0 d_{\rm cs})$, according to $\mu_0 \mathbf{j} = \nabla \times \mathbf{B}$. The shock current $j_{\rm sh}$ increases the downstream magnetic field, and consequently is responsible for a downstream 'overshoot' of the magnetic field. This overshoot is increased by an $\mathbf{E}_{\rm sh} \times \mathbf{B}$ drift current $\mathbf{j}_{\rm e}$ of the electrons in the cross-shock potential. The effect of reflected ions is particularly strong for the termination shock because a large fraction of pick-up ions with their shell-like velocity distribution (Geiss et al., this volume) is reflected in the cross-shock electric field and the pick-up ion pressure near the termination shock is comparable to the bulk plasma pressure. The reflected ions form an upstream current $\mathbf{j}_{\rm f}$ that causes a 'foot' in the upstream magnetic field (adapted from Baumjohann and Treumann, 1996, p. 183). *Right:* The specularly reflected ions are also accelerated in the upstream convective electric field $\mathbf{E}_{\rm up}$ until they have sufficient energy to cross the shock potential $\phi = E_{\rm sh}d_{\rm cs}$. These ions, accelerated by 'shock surfing' may surpass the injection threshold for first-order Fermi acceleration (from Möbius and Kallenbach, 2005).

7.6 The injection problem: shock surfing vs. stochastic acceleration

Besides the scale length of the ACR pressure, the scale length of the termination shock ramp is an important characteristic size that has an influence on suprathermal particle populations. If the scale size of the shock ramp of a quasi-perpendicular shock, $d_{\rm cs}$, is of the order of the electron inertial length, $d_{\rm cs} \approx L_{\rm e} = c/\omega_{\rm pe}$, the pick-up ions may undergo acceleration in the convective electric field $\mathbf{E}_{\rm up}$ (Figure 7.15) of the shock front during multiple reflections at the electric cross-shock potential $\phi = E_{\rm sh}d_{\rm cs}$ (le Roux et al., 2000). This kind of acceleration is most efficient when the pickup ions are trapped at the shock between the electrostatic cross-shock potential $\phi = E_{\rm sh}d_{\rm cs}$ and the upstream Lorentz force (shock surfing; Sagdeev, 1966; Zank et al., 1996b; Lee et al., 1996). Trapping occurs if (1) the particles' incident normal velocity v_x satisfies the condition

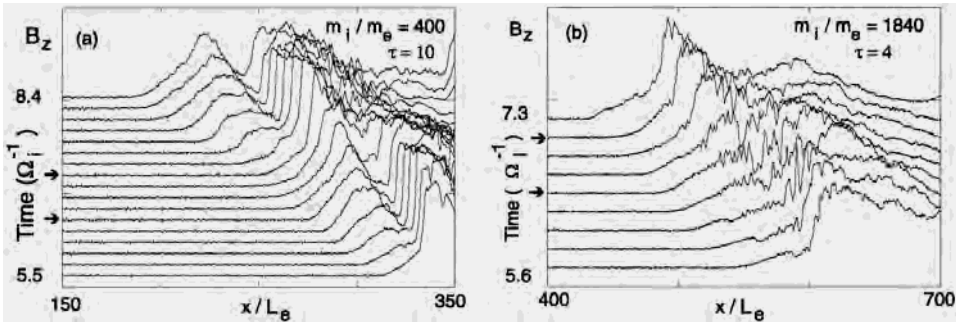

Figure 7.16: Reformation of a quasi-perpendicular shock (Scholer et al., 2003). Present computer resources prohibit a simulation with a realistic mass ratio $m_\mathrm{i}/m_\mathrm{e}$ and at the same time a value of $\tau = (\omega_\mathrm{pe}/\Omega_\mathrm{ce})^2$ appropriate for the solar wind. However, from independent variations of both parameters, the structure of the termination shock has been inferred, assuming a shock normal angle to the downstream magnetic field of $\theta_{B\mathrm{n}} = 87°$.

$(m/2)v_x^2 \ll e\phi$, where m is the particles' mass, and e the electron charge, and (2) the Lorentz force is smaller than the force exerted by the electrostatic potential $e\phi$, i.e., $ev_yB < e\phi/d_\mathrm{cs}$, where B is the magnetic field magnitude in the shock ramp. Thus, the maximum energy a particle can reach by shock surfing is inversely proportional to the square of the cross-shock potential length scale d_cs. Assuming that the cross-shock potential is of the order of the upstream bulk energy per charge, and that d_cs is of the order of the electron inertial length L_e, the maximum pickup ion energy is close to about 1 MeV/amu for ions of any atomic mass A or atomic charge Q. This is sufficient to overcome the injection threshold for first-order Fermi acceleration (Figure 7.8).

However, the typical shock ramp scale size may be much larger, of the order of the ion (proton) inertial length $L_\mathrm{p} = L_\mathrm{e}\sqrt{m_\mathrm{p}/m_\mathrm{e}}$ or of the order of the gyroradius (Larmor radius). The latter scale size would be plausible from Figure 7.15. The shock ramp can be as short as the electron inertial length, if the shock wave is similar to a damped solitary magnetosonic wave (Tidman and Krall, 1971).

Scholer et al. (2003) have performed one-dimensional (1-D) full particle simulations of almost perpendicular supercritical collisionless shocks. The ratio of electron plasma frequency ω_pe to gyrofrequency Ω_ce, the ion-to-electron mass ratio, and the ion and electron β (β = plasma to magnetic field pressure) have been varied. Due to the accumulation of specularly reflected ions upstream of the shock, ramp shocks can reform on time scales of the gyroperiod in the ramp magnetic field (Figure 7.16).

Figure 7.17 demonstrates the process by which reformation occurs. It shows a $v_{\mathrm{i}x}x$ phase space plot for $\beta_\mathrm{i} = 0.1$ at a specific time and the respective magnetic field profile. The large velocity difference between the cold incoming solar wind distribution and the cold specularly reflected ions results in a large-scale vortex between the ramp and the position upstream where the reflected ions are turned around perpendicular to the shock normal and to the magnetic field, and accumu-

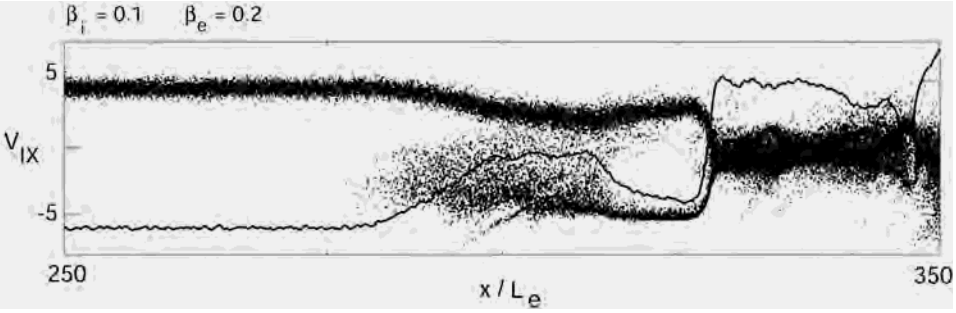

Figure 7.17: $v_{ix} - x$ phase space plot and superimposed magnetic field profile at a specific time (Scholer et al., 2003).

late. Since B/n is essentially constant in a compressible plasma, this results in an upstream magnetic field hump. The solar wind is slowed down, and the solar wind density increases, causing a further magnetic field increase. Eventually the hump takes over the role of the reformed shock. This behaviour of the ion phase space density is typical for all reformation cycles.

Self-reformation is not only a low $\omega_{\rm pe}/\Omega_{\rm ce}$ process, but occurs also in $(\omega_{\rm pe}/\Omega_{\rm ce})^2 \gg 1$, low-$\beta$ simulations. Self-reformation also occurs in low ion β runs with an ion to electron mass ratio $m_{\rm i}/m_{\rm e} = 1840$, so that it may actually occur at the solar wind termination shock. However, in the realistic mass ratio runs, an electromagnetic instability is excited in the foot of the shock, and the shock profile is considerably changed compared to lower mass ratio runs. Linear analysis based on three-fluid theory with incident ions, reflected ions, and electrons (Matsukiyo and Scholer, 2003) indicates that the instability is a modified two-stream instability between the decelerated solar wind electrons and the solar wind ions on the whistler mode branch. If the waves generated by this instability are sufficiently strong to trap pick-up ions, it may be the instability that causes the self-reformation.

In the reforming shock, part of the potential drop occurs at times across the foot, and part of the potential ($\sim 40\%$) occurs over a few ($\sim 4L_{\rm e}$) electron inertial lengths in the steepened-up ramp. Self-reformation is a low ion β process and disappears for a Mach 4.5 shock at/or above an ion $\beta_{\rm i} \sim 0.4$. The ion thermal velocity has to be an order of magnitude smaller than the shock velocity in order for reformation to occur. Scholer et al. (2003) conclude that according to these simulations only part of the potential drop occurs for relatively short times over a few electron inertial lengths $L_{\rm e}$, and that, therefore, coherent shock surfing is not an efficient acceleration mechanism for pickup ions at the low $\beta_{\rm i}$ heliospheric termination shock.

Nonetheless, the electric shock potential may have important consequences for Anomalous Cosmic Ray and Termination Shock Energetic Particles (ACRs and TSPs). Possibly, these abundances can be explained by the following scenario: (1) TSPs are ions that are multiply reflected at the shock potential and injected into first-order Fermi acceleration, which has an injection threshold much lower than often assumed (Figure 7.8). The TSPs do not undergo mass-per-charge (A/Q) fractionation because shock surfing is a process independent of A/Q. (2) ACRs

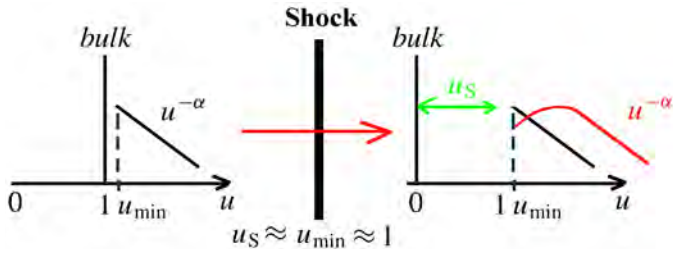

Figure 7.18: Schematic showing the characteristics of the transmission of power-law suprathermal tails through a shock potential.

are suprathermal ions directly transmitted through the electric potential of the termination shock, but not returned to the shock for first-order Fermi acceleration. These ions undergo stochastic acceleration in the heliosheath. The transmission through the termination shock potential prefers high A/Q species in concordance with ACR abundances. (3) A fraction of the reflected ions are thermalized into the bulk plasma of the heliosheath. Low A/Q species are preferentially thermalized. This scenario would match observations. For instance, the H/He ratio is about 10 for TSPs and about 5 for ACRs (Stone et al., 2005).

This 'transmission' scenario is quite simple, but can be explained in some more detail as follows: Three populations approach the termination shock from the upstream solar wind: (1) the bulk solar wind ions idealized as a pencil beam $f_{\rm bulk} \propto \delta(u-1, \mu-1)$, (2) the freshly ionized pick-up ions in a shell distribution $q(u) \propto \delta(u-1)$, and (3) the suprathermal tails $f_{\rm ST} \propto u^{-\alpha}$ for $u > u_{\rm min}$. The suprathermal tails at the termination shock presumably reach down to almost $u_{\rm min} \approx 1$ ($u = v/V_{\rm up}$ with $V_{\rm up}$ the upstream solar wind speed) because the speeds of the waves causing these tails are much smaller than the speed $U_{\rm up} = 1$ of the supersonic bulk solar wind. Population (2) is presumably negligible at the termination shock (Kallenbach et al., 2005). In a very idealized picture, the cross-shock potential is characterized by $u_{\rm S} = V_{\rm S}/V_{\rm up} \approx 1$, which stops the bulk protons to zero speed and conserves the number of suprathermal ions at $u > u_{\rm min}$. Of course, in reality $u_{\rm S}$ is less than unity because the downstream plasma does not have zero speed.

We define a normalized transmission function $T_{{\rm S};\mathcal{R}}$ for the suprathermal tails, which yields the downstream distribution function when multiplied with the upstream distribution function. The upstream distribution function is assumed to be a power-law above the minimum speed $u_{\rm min}$ with the same spectral index α as upstream. The data of Figure 7.5 suggest that this is a valid approach. Therefore, the normalized transmission function $T_{{\rm S};\mathcal{R}}$ for the suprathermal tails at speeds $u > u_{\rm min}$ is (see Figure 7.18 for an illustration):

$$\int_{u_{\rm min}}^{\infty} u^{-\alpha+2} {\rm d}u \;=\; T_{{\rm n};\mathcal{R}} \int_{\frac{u_{\rm S}}{\sqrt{\mathcal{R}}}}^{\infty} \left(1 - \frac{u_{\rm S}^2}{\mathcal{R}u^2}\right) u^{-\alpha+2} {\rm d}u$$

$$\Rightarrow\; T_{{\rm n};\mathcal{R}} = \frac{\alpha-1}{2} \left(\frac{u_{\rm S}}{\sqrt{\mathcal{R}} u_{\rm min}}\right)^{\alpha-3} \quad ; \qquad T_{{\rm S};\mathcal{R}} = T_{{\rm n};\mathcal{R}} \left(1 - \frac{u_{\rm S}^2}{\mathcal{R}u^2}\right). \qquad (7.10)$$

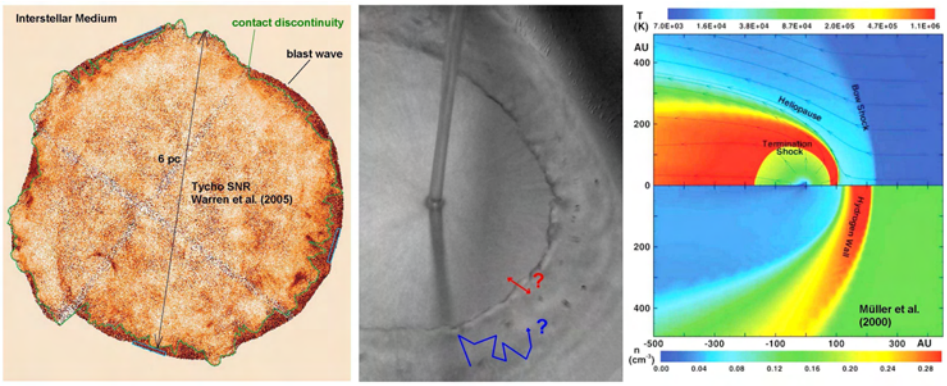

Figure 7.19: Comparison of the Tycho supernova bubble with the heliosphere.

The normalizing factor $T_{\mathrm{n};\mathcal{R}}$ indicates the increase in the phase space density at high speeds downstream, and hence yields the availability of suprathermal ions in the heliosheath for further stochastic acceleration. If further stochastic acceleration occurs by compressional fluctuations, no more A/Q fractionation occurs, and the ACR abundances are given by the transmission factor $T_{\mathrm{n};\mathcal{R}}$. For the typical tails with $\alpha \approx 5$, the fractionation pattern is mass-proportional for singly charged pick-up ions. For larger α, the fractionation is stronger.

7.7 Conclusions

Turbulence and ion acceleration are intimately linked processes of the outer heliosphere. The analysis of this article supports the idea that stochastic acceleration in compressional fluctuations in the heliosheath is a process that can compete with first-order Fermi acceleration at the solar wind termination shock. A viable explanation for the composition of Termination Shock Energetic Particles (TSPs) and Anomalous Cosmic Rays (ACRs) is that TSPs are particles which are reflected as slightly suprathermal ions at the electric cross-shock potential of the solar wind termination shock (TS) and subsequently accelerated by the first-order Fermi process, while ACRs are particles transmitted as slightly suprathermal ions through the electric cross-shock potential of the TS and subsequently stochastically accelerated in the compressional fluctuations of the heliosheath. Probably, the two processes of first-order Fermi acceleration and second-order Fermi acceleration are intertwined. Particles that are stochastically accelerated in the heliosheath may eventually reach an energy which gives them a sufficiently large mean free path to cross the TS again to participate in first-order Fermi acceleration.

Lessons may be learned from the heliosphere for galactic acceleration processes. Second-order Fermi acceleration may also be responsible for the energization of the Galactic Cosmic Rays (GCRs). Warren et al. (2005) have observed that the turbulence region downstream of the blast wave of the Tycho supernova is thinner than magnetohydrodynamic models predict (Figure 7.19). This may be analogous with the reduced size of the heliosheath due to the ACR pressure there. As the

sum of the ACR pressure and the heliosheath bulk pressure balances the pressure of the interstellar medium, the heliosheath bulk pressure is reduced in the presence of the ACRs and the size of the heliosheath is consequently reduced.

This has been taken as an argument for the presence of GCRs in the region between the blast wave and the contact discontinuity of the bubble of the Tycho supernova. In fact, it has been taken as evidence that a supernova shock wave accelerates the GCRs. This result may have to be verified. It may actually be the turbulence downstream of the supernova shock that accelerates the GCRs.

Appendix

7.A Diffusion of charged particles

Diffusion parameters are usually derived in the literature with significant mathematical effort. In principle, they easily trace back to the Vlasov-Maxwell equation. The Vlasov-Maxwell equation states that the total variation of the distribution function of a suprathermal particle species s is extremal, which leads to

$$(\partial_t + \mathbf{v}\cdot\nabla)\, f_s + \nabla_{\mathbf{v}} f_s \cdot \dot{\mathbf{v}} = 0 \ . \tag{7.11}$$

Usually the distinction is made between diffusion in non-compressional and diffusion in compressional fluctuations. In the first case the plasma is treated as a plasma with uniform bulk speed containing Alfvénic magnetic field fluctuations with wave amplitudes $\delta\mathbf{B}$ and $\delta\mathbf{E}$ perpendicular to the ambient magnetic field, $\delta\mathbf{E} \perp \mathbf{B}_0$, $\delta\mathbf{B} \perp \mathbf{B}_0$, and $\delta\mathbf{E} \perp \delta\mathbf{B}$. In the second case, as a consequence of compression, there are fluctuations $\delta\mathbf{U} \parallel \mathbf{B}_0$. It is convenient to choose a coordinate system in which the mean plasma velocity is zero, $\langle\mathbf{U}\rangle = 0$. The particle velocity can then be split into two parts $\mathbf{v} = \mathbf{v}' + \delta\mathbf{U}$, where it is convenient to drop the prime for the particle velocity in the plasma frame. The Vlasov-Maxwell equation then reads

$$(\partial_t + \mathbf{v}\cdot\nabla + \delta\mathbf{U}\cdot\nabla)\, f_s + \nabla_{\mathbf{v}} f_s \cdot \left(\dot{\mathbf{v}} + \delta\dot{\mathbf{U}}\right) = 0 \ . \tag{7.12}$$

7.A.1 Diffusion in non-compressional magnetic field fluctuations in slab geometry

We assume a homogeneous plasma with $\mathbf{E}_0 = 0$, $\delta\mathbf{U} = 0$, and an ambient magnetic field $\mathbf{B}_0$. To the equilibrium distribution of the suprathermal species s with charge-to-mass ratio $\eta_s := q_s/m_s$, determined by

$$\partial_t f_s + (\mathbf{v}\cdot\nabla)\, f_s + \eta_s\,(\mathbf{v}\times\mathbf{B}_0)\cdot\nabla_{\mathbf{v}} f_s = 0 \ , \tag{7.13}$$

we add small fluctuating fields $\delta\mathbf{E}$ and $\delta\mathbf{B}$, and a small deviation δf_s of the distribution function. Adding these terms to the above equation yields to first order:

$$\begin{aligned}
\partial_t \delta f_s + (\mathbf{v}\cdot\nabla)\,\delta f_s + \eta_s\,(\delta\mathbf{E} + \mathbf{v}\times\delta\mathbf{B})\cdot\nabla_{\mathbf{v}} f_s + \eta_s\,(\mathbf{v}\times\mathbf{B}_0)\cdot\nabla_{\mathbf{v}}\delta f_s = 0 \\
\Rightarrow (-i\omega + i\mathbf{v}\cdot\mathbf{k})\,\delta f_s + \eta_s\,(\delta\mathbf{E} + \mathbf{v}\times\delta\mathbf{B})\cdot\nabla_{\mathbf{v}} f_s = 0 \\
\Rightarrow \delta f_s = \eta_s \frac{\delta\mathbf{E} + \mathbf{v}\times\delta\mathbf{B}}{i\,(\omega - \mathbf{v}\cdot\mathbf{k})}\cdot\nabla_{\mathbf{v}} f_s \Rightarrow \nabla_{\mathbf{v}}\delta f_s = \eta_s \nabla_{\mathbf{v}}\left[\frac{\delta\mathbf{E} + \mathbf{v}\times\delta\mathbf{B}}{i\,(\omega - \mathbf{v}\cdot\mathbf{k})}\cdot\nabla_{\mathbf{v}} f_s\right].
\end{aligned} \tag{7.14}$$

The last term of the first line is zero because $\nabla_{\mathbf{v}} \perp \mathbf{v}$. Adding $\nabla_{\mathbf{v}}\delta f_s$ to ∇f_s in the above first-order Vlasov-Maxwell equation and averaging over the fluctuation scales, one identifies the second-order macroscopic term

$$\eta_s \left\langle \left| (\delta\mathbf{E} + \mathbf{v}\times\delta\mathbf{B})\cdot\nabla_{\mathbf{v}}\delta f_s \right| \right\rangle = \eta_s^2 \left\langle \left| (\delta\mathbf{E} + \mathbf{v}\times\delta\mathbf{B})\cdot\nabla_{\mathbf{v}}\left[\frac{\delta\mathbf{E} + \mathbf{v}\times\delta\mathbf{B}}{(\mathbf{v}\cdot\mathbf{k} - \omega)}\cdot\nabla_{\mathbf{v}} f_s\right] \right| \right\rangle . \tag{7.15}$$

We transform the above term in such a way that it describes a diffusion equation. With $\mathbf{a} := \eta_s^2 (\delta\mathbf{E} + \mathbf{v} \times \delta\mathbf{B})$, $\mathbf{b} := \nabla_{\mathbf{v}} (\mathbf{c} \cdot \mathbf{d})$, $\mathbf{c} := (\delta\mathbf{E} + \mathbf{v} \times \delta\mathbf{B}) (\mathbf{k} \cdot \mathbf{v} - \omega)^{-1}$, and $\mathbf{d} := \nabla_{\mathbf{v}} f_s$ we obtain

$$\begin{aligned}\langle \mathbf{a} \cdot \mathbf{b} \rangle &= \left\langle \sum_{i=1}^{3} a_i b_i \right\rangle = \left\langle \sum_{i,j} a_i \frac{\partial (c_j d_j)}{\partial v_i} \right\rangle = \left\langle \sum_{i,j} \frac{\partial (a_i c_j d_j)}{\partial v_i} - \sum_{i,j} c_j d_j \frac{\partial a_i}{\partial v_i} \right\rangle \\ &= \left\langle \nabla_{\mathbf{v}} \cdot \tilde{D} \nabla_{\mathbf{v}} f_s \right\rangle ; \; \tilde{D} = \eta_s^2 \left\langle \left| \frac{(\delta\mathbf{E} + \mathbf{v} \times \delta\mathbf{B}) \otimes (\delta\mathbf{E} + \mathbf{v} \times \delta\mathbf{B})}{(\mathbf{k} \cdot \mathbf{v} - \omega)} \right| \right\rangle . \quad (7.16)\end{aligned}$$

The last step follows because $\nabla_{\mathbf{v}} \cdot \mathbf{a} = 0$ as the fields do not depend on the velocity $\mathbf{v}$. Also, we have taken the term $\nabla_{\mathbf{v}} f_s$ out of the averaging parenthesis because this is the mean distribution function describing the evolution on space and time scales larger than the fluctuation scales. The tensor $\tilde{D}$ is the general form of a diffusion tensor, with which the stochastic motion of the charged minority particles in the plasma is described. Two parameters are relevant: (1) the power, which is in the plasma waves, and (2) the resonance condition that is applied to describe the wave-particle interaction between ions of species s and the waves.

We evaluate the direct product $\tilde{A} = (\delta\mathbf{E} + \mathbf{v} \times \delta\mathbf{B}) \otimes (\delta\mathbf{E} + \mathbf{v} \times \delta\mathbf{B})$ for 'slab' geometry turbulence which propagates gyrotropically parallel to the ambient magnetic field, $\mathbf{k} \parallel \mathbf{B}_0$. As $\nabla \cdot \mathbf{B} = 0$ we have $\delta\mathbf{B} \perp \mathbf{B}_0$. Furthermore, for MHD-modes, we have $\nabla \times \delta\mathbf{E} = -\delta\dot{\mathbf{B}}$ or in Fourier components $\delta\mathbf{E} = -\hat{\mathbf{k}} \times \delta\mathbf{B}\omega/k = -\hat{\mathbf{k}} \times \delta\mathbf{B} V_{\rm ph}$. This means that the electric fluctuation amplitude is $\delta\mathbf{E} = -\mathbf{V}_{\rm ph} \times \delta\mathbf{B}$, i.e. the negative cross product of the phase velocity with the magnetic fluctuation amplitude. In other words, the electric field amplitude is zero in the wave frame. We take $\delta\mathbf{B} = \delta B \mathbf{e}_x$ and define $v'_\parallel = v_\parallel - V_{\rm ph}$. This yields

$$\begin{aligned}(\mathbf{v} - \mathbf{V}_{\rm ph}) \times \delta\mathbf{B} &= v'_\parallel \delta B \mathbf{e}_y - v_\perp \delta B \sin\phi \mathbf{e}_z \\ &= \delta B \Big[v'_\parallel \sin\phi (\mathbf{e}_r \sin\theta + \mathbf{e}_\theta \cos\theta) + v'_\parallel \mathbf{e}_\phi \cos\phi - v_\perp \sin\phi (\mathbf{e}_r \cos\theta - \mathbf{e}_\theta \sin\theta) \Big] \\ &= \delta B \Big[\mathbf{e}_r \sin\phi \left(v'_\parallel \sin\theta - v_\perp \cos\theta \right) + \mathbf{e}_\theta \sin\phi \left(v'_\parallel \cos\theta + v_\perp \sin\theta \right) + \mathbf{e}_\phi v'_\parallel \cos\phi \Big]. \quad (7.17)\end{aligned}$$

The angle θ is the pitch angle, and the angle ϕ is the generally time-varying angle between the magnetic fluctuation amplitude $\delta B \mathbf{e}_x$ and the perpendicular velocity vector $\mathbf{v}_\perp$. We will see that we can drop the term $\mathbf{e}_\phi v'_\parallel \delta B \cos\phi$ because we derive the result for a gyrotropic situation. Because of

$$\begin{aligned} v'_\parallel \sin\theta - v_\perp \cos\theta &= -V_{\rm ph} \sin\theta = -V_{\rm ph} \sqrt{1 - \mu^2} \; , \\ v'_\parallel \cos\theta + v_\perp \sin\theta &= v - \mu V_{\rm ph} \quad , \; \mu = \cos\theta \; , \end{aligned} \quad (7.18)$$

and averaging over $\sin^2\phi$, we get

$$\begin{aligned}\tilde{A} &= \frac{\delta B^2}{2} \begin{pmatrix} -V_{\rm ph}\sqrt{1-\mu^2} \\ v - \mu V_{\rm ph} \\ 0 \end{pmatrix} \otimes \begin{pmatrix} -V_{\rm ph}\sqrt{1-\mu^2} \\ v - \mu V_{\rm ph} \\ 0 \end{pmatrix} \\ &= \frac{\delta B^2}{2} \begin{pmatrix} V_{\rm ph}^2 (1-\mu^2) & V_{\rm ph}\sqrt{1-\mu^2}(\mu V_{\rm ph} - v) & \ldots \\ V_{\rm ph}\sqrt{1-\mu^2}(\mu V_{\rm ph} - v) & (v - \mu V_{\rm ph})^2 & \ldots \\ \ldots & \ldots & \ldots \end{pmatrix}. \quad (7.19)\end{aligned}$$

If this tensor $\tilde{A}$ is multiplied with the velocity gradient of a gyrotropic distribution $\nabla_{\mathbf{v}} f = (\partial_v f, \partial_\theta f/v, 0)$, then we get a vector $\mathbf{A}$:

$$\mathbf{A} = \frac{\delta B^2}{2} \begin{pmatrix} V_{\rm ph}^2 \left(1-\mu^2\right) \partial f/\partial v - V_{\rm ph}\sqrt{1-\mu^2}\left(1-\mu V_{\rm ph}/v\right) \partial f/\partial\theta \\ -V_{\rm ph}\sqrt{1-\mu^2}\left(v-\mu V_{\rm ph}\right) \partial f/\partial v + v\left(1-\mu V_{\rm ph}/v\right) \partial f/\partial\theta \\ 0 \end{pmatrix}. \quad (7.20)$$

This vector's divergence in spherical coordinates divided by $\mathcal{R} = (\mathbf{k}\cdot\mathbf{v} - \omega)$ is

$$\begin{aligned} \frac{1}{v^2}\frac{\partial}{\partial v}\left(v^2 A_r\right) + \frac{1}{v\sin\theta}\frac{\partial}{\partial\theta}\left(\sin\theta A_\theta\right) = {} & \frac{1}{v^2}\frac{\partial}{\partial v}\left[v^2 V_{\rm ph}^2\left(1-\mu^2\right)\frac{\delta B^2}{2\mathcal{R}}\frac{\partial f}{\partial v}\right] \\ & + \frac{1}{v^2\partial v}\left[v^2\frac{\delta B^2}{2\mathcal{R}}V_{\rm ph}\left(1-\mu^2\right)\left(1-\frac{\mu V_{\rm ph}}{v}\right)\frac{\partial f}{\partial\mu}\right] \\ & + \frac{1}{v}\frac{\partial}{\partial\mu}\left[\frac{\delta B^2}{2\mathcal{R}}V_{\rm ph}\left(1-\mu^2\right)\left(1-\frac{\mu V_{\rm ph}}{v}\right)\frac{\partial f}{\partial v}\right] \\ & + \frac{\partial}{\partial\mu}\left[\frac{\delta B^2}{2\mathcal{R}}\left(1-\mu^2\right)\left(1-\frac{\mu V_{\rm ph}}{v}\right)^2\frac{\partial f}{\partial\mu}\right]. \quad (7.21) \end{aligned}$$

Now we have to take the average of these expressions, which is equivalent to the integration of $\delta\tilde{B}^2(k)/\mathcal{R}$ over $\mathrm{d}k$. For a slab geometry $\mathbf{k}$-space is only one-dimensional. Only the gyro-resonant interaction is taken into account, so that the integration is equivalent to a multiplication with $k_r^\pm = (\omega \pm \Omega)/(v\mu)$ of the value of the function at $k_r^\pm$. Equation (7.15) can now be written as

$$\begin{aligned} \frac{\partial f_s}{\partial t} &= \frac{\partial}{\partial\mu}\left(D_{\mu\mu}\frac{\partial f}{\partial\mu}\right) + \frac{\partial}{\partial\mu}\left(D_{\mu v}\frac{\partial f}{\partial v}\right) + \frac{1}{v^2}\frac{\partial}{\partial v}\left(v^2 D_{v\mu}\frac{\partial f}{\partial\mu}\right) + \frac{1}{v^2}\frac{\partial}{\partial v}\left(v^2 D_{vv}\frac{\partial f}{\partial v}\right) \\ D_{\mu\mu} &= \sum_\pm \frac{\Omega^2}{2}\left(1-\frac{\mu V_{\rm ph}}{v}\right)^2 \frac{\left(1-\mu^2\right)}{v\mu - V_{\rm ph}}\frac{\delta\tilde{B}^2\left(k_r^\pm\right)}{B_0^2} \\ D_{\mu v} &= D_{v\mu} = \sum_\pm \frac{\Omega^2}{2}\frac{V_{\rm ph}}{v\mu - V_{\rm ph}}\left(1-\frac{\mu V_{\rm ph}}{v}\right)\left(1-\mu^2\right)\frac{\delta\tilde{B}^2\left(k_r^\pm\right)}{B_0^2} \\ D_{vv} &= \sum_\pm \frac{\Omega^2}{2}\frac{V_{\rm ph}^2}{v\mu - V_{\rm ph}}\left(1-\mu^2\right)\frac{\delta\tilde{B}^2\left(k_r^\pm\right)}{B_0^2}\ . \end{aligned} \quad (7.22)$$

These are the most often used diffusion parameters which are found in the most recent literature (Isenberg et al. , 2003). While they give a useful description of pitch-angle scattering or parallel mean free paths, respectively, in the supersonic solar wind plasma, they do not necessarily reflect the proper description of momentum diffusion and perpendicular diffusion.

7.A.2 Momentum diffusion in compressional fluctuations

We go back to Equation (7.12), but add compressional fluctuations $\delta\mathbf{U} \parallel \mathbf{B}_0$:

$$\left(\partial_t + \mathbf{v}\cdot\nabla + \delta\mathbf{U}\cdot\nabla\right) f_s + \nabla_{\mathbf{v}} f_s \cdot \left(\dot{\mathbf{v}} + \delta\dot{\mathbf{U}}\right) = 0\ . \quad (7.23)$$

The compressional fluctuations have much larger temporal and spatial scale than the magnetic fluctuations in a slab geometry. The term $\dot{\mathbf{v}}$ leads to the diffusion parameters treated above. The term $\delta\dot{\mathbf{U}}$, however, yields additional momentum diffusion in analogy with $\tilde{D}$ in Equation (7.16):

$$\tilde{D} = \left\langle \frac{\delta\dot{\mathbf{U}} \otimes \delta\dot{\mathbf{U}}}{[\mathbf{k}\cdot(\mathbf{v}+\delta\mathbf{U})-\omega]} \right\rangle \approx \left\langle \frac{\delta\dot{\mathbf{U}} \otimes \delta\dot{\mathbf{U}}}{\mathbf{k}\cdot\delta\mathbf{U}} \right\rangle \quad \text{if} \quad \lambda_{\parallel} \ll L_{\rm cor} \ . \tag{7.24}$$

The latter approximation is a substantial shortcut for all the mathematics formulated in Bykov and Toptygin (1993) for the case that the mean free path for pitch-angle scattering is small compared to the correlation length of the large-scale compressional fluctuations, $\lambda_{\parallel} \ll L_{\rm cor}$. It takes $\langle \mathbf{k}\cdot\mathbf{v}\rangle = \langle kv\mu\rangle$ as a small number because the pitch angle cosine μ changes rapidly over the trajectory of a charged particle. The interaction between waves and charged particles is dominated by $kv\mu - \omega \approx 0$. This leaves the above term. We further evaluate

$$\delta\dot{\mathbf{U}} \otimes \delta\dot{\mathbf{U}} \approx [\partial_t + (\delta\mathbf{U}+\mathbf{v})\cdot\nabla]\,\delta\mathbf{U} \otimes [\partial_t + (\delta\mathbf{U}+\mathbf{v})\cdot\nabla]\,\delta\mathbf{U} \ . \tag{7.25}$$

We neglect $\delta\mathbf{U}\cdot\nabla$ and ∂_t with respect to $\mathbf{v}\cdot\nabla$. Then we express $\delta\mathbf{U} = \mathbf{e}_z\delta U = \delta U\,(\mathbf{e}_r\cos\theta - \mathbf{e}_\theta\sin\theta)$ in spherical coordinates. The ∇-operator only acts along the direction of the ambient magnetic field $\mathbf{B}_0$, i.e. along the z-axis on $\delta\mathbf{U}$. Therefore, $\mathbf{v}\cdot\nabla = v\mu\partial_z$. The tensor $\tilde{A}$ in analogy with Equation (7.19) is

$$\begin{aligned}
\tilde{A} &= v^2\mu^2\,(\partial_z U)^2 \begin{pmatrix} \mu \\ -\sqrt{1-\mu^2} \\ 0 \end{pmatrix} \otimes \begin{pmatrix} \mu \\ -\sqrt{1-\mu^2} \\ 0 \end{pmatrix} \\
&= v^2\mu^2\,(\partial_z U)^2 \begin{pmatrix} \mu^2 & -\mu\sqrt{1-\mu^2} & ... \\ -\mu\sqrt{1-\mu^2} & 1-\mu^2 & ... \\ ... & ... & ... \end{pmatrix} .
\end{aligned} \tag{7.26}$$

The vector $\mathbf{A}$ in analogy with Equation (7.20) is

$$\mathbf{A} = \mu^2 v^2\,(\partial_z U)^2 \begin{pmatrix} \mu^2\partial f/\partial v + \mu\left(1-\mu^2\right) v^{-1}\partial f/\partial\mu \\ -\mu\sqrt{1-\mu^2}\partial f/\partial v - \left(1-\mu^2\right)^{3/2}\partial f/\partial\mu \\ 0 \end{pmatrix} . \tag{7.27}$$

The diffusion parameters in analogy with Equation (7.22) are

$$\begin{aligned}
D_{\mu\mu} &= \left\langle \mu^2\left(1-\mu^2\right)^2 (\partial_z U)^2\,(\mathbf{k}\cdot\delta\mathbf{U})^{-1} \right\rangle \\
D_{\mu v} &= D_{v\mu} = v\left\langle \mu^3\left(1-\mu^2\right)(\partial_z U)^2\,(\mathbf{k}\cdot\delta\mathbf{U})^{-1} \right\rangle \\
D_{vv} &= v^2\left\langle \mu^4\,(\partial_z U)^2\,(\mathbf{k}\cdot\delta\mathbf{U})^{-1} \right\rangle \propto v^2\left\langle \delta U^2 \right\rangle^{1/2} L_{\rm cor}^{-1} \ .
\end{aligned} \tag{7.28}$$

These momentum and spatial diffusion parameters correspond to those derived in more detail in Le Roux et al. (2005).

7.A.3 Spatial diffusion

The spatial diffusion along the ambient magnetic field is caused by *pitch-angle scattering* (parameter $D_{\mu\mu}$ in Equation 7.22). If there is a spatial gradient in the density of suprathermal ions along the ambient magnetic field, more ions are scattered in the direction of decreasing density rather than in the opposite direction. The spatial diffusion coefficient is calculated as

$$\frac{v\lambda_\parallel}{3} = \kappa_\parallel = v^2 \int_0^1 \frac{\mu \mathrm{d}\mu}{2} \int_0^\mu \frac{1-\mu'^2}{D_{\mu'\mu'}} \mathrm{d}\mu' \ . \tag{7.29}$$

It is plausible that the parallel mean free path $\lambda_\parallel$ scales inversely with the rate of *pitch-angle scattering*. Large $D_{\mu\mu}$ means a large frequency of direction changes of order π. The ion rapidly changes direction from "backward" to "forward" motion and does not get very far. At low scattering frequency, however, the ions move far along the magnetic field without distortion of their trajectory.

The double integral is explained as follows: $D^{-1}_{\mu'\mu'} = \tau_{\mu'}$ is the temporal expectation value for scattering in the pitch angle at pitch-angle cosine $\mu' = \cos\Psi'$ and has the dimension time / $\cos^2\Psi$. The increase in the quadratic parallel velocity through a change $\mathrm{d}\mu'$ is $v'^2 = v^2\left(1-\mu'^2\right)\mathrm{d}\mu'$. The quadratic distance per time that an ion moves while scattering from $\mu = 0$ to $\mu \neq 0$ is given by the inner integral over $v'^2\tau_{\mu'}\mathrm{d}\mu'$. The statistics representing the fact that scattering not only occurs from smaller to larger μ, but also vice versa, is given by averaging over the half-sphere $0 < \mu < 1$.

In Equation (7.22) the coefficient $D_{\mu\mu}$ has been given as a function of the power spectral density of the magnetic fluctuations:

$$D_{\mu\mu} = \sum_\pm \frac{\Omega^2}{2}\left(1 - \frac{\mu V_{\mathrm{ph}}}{v}\right)^2 \frac{\left(1-\mu^2\right)}{v\mu - V_{\mathrm{ph}}} \frac{\delta\tilde{B}^2\left(k_r^\pm\right)}{B_0^2} \ . \tag{7.30}$$

Therefore, the parallel mean free path is

$$\lambda_\parallel^\pm = \frac{3v^2}{16\Omega^2} P^{-1}\left(k_r^\pm\right) \quad \text{mit} \quad P\left(k_r^\pm\right) = \frac{\delta\tilde{B}^2\left(k_r^\pm\right)}{B_0^2} \ . \tag{7.31}$$

In the literature one usually finds the version with the factor $3/(8\pi)$ instead of $3/16$. Figure 7.20 shows experimentally determined parallel mean free paths, which approximately match QLT. These mean free paths have been determined from a fit to measured turbulence levels upstream of an interplanetary shock and from the spatial gradients of suprathermal particle populations. The turbulence level varies because the energetic protons generate waves near the shock.

7.A.4 Derivation of the injection threshold

The derivation of Equation (7.6) is based on estimates for the streaming flux

$$\mathbf{S} = \tilde{\kappa}\nabla f - \mathbf{V}\frac{v}{3}\frac{\partial f}{\partial v} \ ; \ \nabla\cdot\mathbf{S} = \nabla\cdot(\tilde{\kappa}\nabla f) - \frac{v}{3}\frac{\partial f}{\partial v}\nabla\cdot\mathbf{V} \ . \tag{7.32}$$

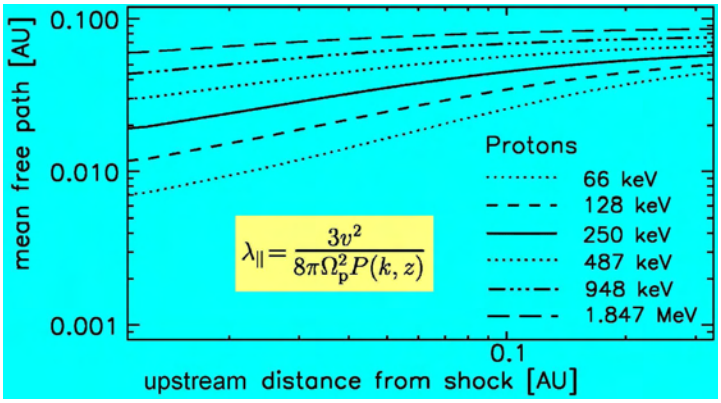

Figure 7.20: Experimentally determined mean free paths *upstream* of the strongest interplanetary shock of the Bastille Day event (Bamert et al., 2004).

The first term in the streaming flux is the anisotropic "diffusion speed" $\tilde{\kappa}\nabla f$ with

$$\tilde{\kappa} = \begin{pmatrix} \kappa_\parallel & 0 & 0 \\ 0 & \kappa_\perp & \kappa_A \\ 0 & -\kappa_A & \kappa_\perp \end{pmatrix} ;$$

$$\kappa_\parallel = \frac{1}{3} v \lambda_\parallel ; \quad \frac{\kappa_\perp}{\kappa_\parallel} = \frac{r_g^2}{\lambda_\parallel^2} \frac{1}{1 + \left(r_g/\lambda_\parallel\right)^2} \approx \frac{r_g^2}{\lambda_\parallel^2} ; \quad \frac{\kappa_A}{\kappa_\parallel} = \frac{r_g}{\lambda_\parallel} \frac{1}{1 + \left(r_g/\lambda_\parallel\right)^2} \approx \frac{r_g}{\lambda_\parallel} . \quad (7.33)$$

The parameter $\kappa_\perp$ may become plausible with the following considerations: If we assume turbulence with correlation length $l_{c;A} \approx r_g$ and $\zeta_A = \langle \delta B_A^2 \rangle / B_0^2 \approx 1$, then the parallel mean free path $\lambda_\parallel$ is of the order of the gyroradius r_g and parallel and perpendicular gyrations have about the same amplitude. The latter means $\lambda_\parallel \approx \lambda_\perp$, i.e. $\kappa_\parallel \approx \kappa_\perp$.

For decreasing turbulence amplitude, the parallel mean free path increases while the particle has difficulties in moving across the ambient magnetic field. For small ζ_A we have $\lambda_\parallel \gg r_g \gg \lambda_\perp$ with $\lambda_\perp \lambda_\parallel \approx r_g^2$. The parameter κ_A describes a superposition of gyration and scattering.

The term $(v/3)(\partial f/\partial v)\nabla \cdot \mathbf{V}$ can be understood as an expansion in orders of the speed $|\mathbf{V}|$ of the convective derivative of the distribution function $f(\mathbf{v} + \mathbf{V})$ in a medium streaming with velocity $\mathbf{V}$:

$$\langle (\mathbf{v} + \mathbf{V}) \cdot \nabla f(\mathbf{v} + \mathbf{V}) \rangle \approx \mathbf{V} \cdot \nabla f(\mathbf{v}) + \left\langle \mathbf{v} \cdot \nabla \left[\frac{\partial f(\mathbf{v})}{\partial \mathbf{v}} \cdot \mathbf{V} \right] \right\rangle . \quad (7.34)$$

The brackets mean directional averaging for nearly isotropic distributions. Taking the direction of the streaming velocity $\mathbf{V}$ as the projection axis, the two scalar products lead to a term μ^2, and averaging gives a factor of $1/3$.

The spatial diffusion speed $\tilde{\kappa}\nabla f$ increases with speed. At some injection threshold speed v_{inj} the downstream diffusion speed will balance the upstream convection speed. This means that the majority of particles are not just convected through the shock, but undergo diffusion, i.e. scattering back and forth across the shock.

The diffusion speed along the shock normal has to be evaluated for a planar shock. The diffusion tensor $\tilde{\kappa}$ refers to the reference system fixed to the ambient magnetic field. The transformation on the shock normal is performed by a rotation by the shock normal angle Ψ with respect to the magnetic field.

$$\begin{pmatrix} \cos\Psi & -\sin\Psi & 0 \\ \sin\Psi & \cos\Psi & 0 \\ 0 & 0 & 1 \end{pmatrix} \begin{pmatrix} \kappa_\parallel & 0 & 0 \\ 0 & \kappa_\perp & \kappa_\mathrm{A} \\ 0 & -\kappa_\mathrm{A} & \kappa_\perp \end{pmatrix} \begin{pmatrix} \cos\Psi & \sin\Psi & 0 \\ -\sin\Psi & \cos\Psi & 0 \\ 0 & 0 & 1 \end{pmatrix} = \begin{pmatrix} \kappa_\parallel \cos^2\Psi + \kappa_\perp \sin^2\Psi & \left(\kappa_\parallel - \kappa_\perp\right)\sin\Psi\cos\Psi & -\kappa_\mathrm{A}\sin\Psi \\ \left(\kappa_\parallel - \kappa_\perp\right)\sin\Psi\cos\Psi & \kappa_\parallel \sin^2\Psi + \kappa_\perp\cos^2\Psi & \kappa_\mathrm{A}\cos\Psi \\ \kappa_\mathrm{A}\sin\Psi & -\kappa_\mathrm{A}\cos\Psi & \kappa_\perp \end{pmatrix} . \quad (7.35)$$

The small-scale downstream gradient scale size of the distribution function f points normal to the shock surface $\nabla f = f\left(r_\mathrm{G}^{-1}, 0, 0\right)$. This gradient "picks out" the first row of the matrix in Equation (7.35).

The most fundamental approach for solving the Parker equation (7.1) is to assume infinitely large upstream and downstream plasma regions. If one takes x as the parameter along the shock normal, the Parker equation becomes

$$V\frac{\partial f}{\partial x} + \frac{\partial}{\partial x}\left[V\frac{v}{3}\frac{\partial f}{\partial v} + \left(\tilde{\kappa}\cdot\nabla f\right)_x\right] = 0 \; . \quad (7.36)$$

Integrating this equation over x yields

$$V_1 f\left(0,v\right) = \left(V_2 - V_1\right)\frac{v}{3}\frac{\partial f}{\partial v}\left(0,v\right) \;\Rightarrow\; f\left(0,v\right) = f_0 v^{-\gamma},\; \gamma = \frac{3V_1}{V_1 - V_2} \; , \quad (7.37)$$

with 1 denoting the upstream region and 2 the downstream region. This is the standard distribution of first-order Fermi accelerated ions. It is based on the assumptions, that far away from the shock the distribution f has no gradient, that far upstream the distribution function vanishes, $f\left(-\infty,v\right) = 0$, and that the downstream distribution function is constant ($r_\mathrm{G} \to \infty$), i.e. describing a particle distribution flushed away in diffusive equilibrium, and that the variation of the second term is dominated by the jump in speed from V_1 to V_2 at the shock.

However, it is necessary to add sources to the above equation in order to have any particles. These could be far upstream, $f\left(-\infty,v\right)$, and convected to the shock, or be near the shock, $f_\mathrm{S}\left(v\right)$:

$$f\left(0,v\right) = \gamma\; v^{-\gamma} \int_{v_\mathrm{inj}}^{v} \left(v'\right)^\gamma \left[f\left(-\infty,v'\right) + f_\mathrm{S}\left(v'\right)\right]\frac{\mathrm{d}v'}{v'} \; . \quad (7.38)$$

Upstream from the shock ($x < 0$) the spatial distribution is given by

$$f\left(x,v\right) = f\left(-\infty,v\right) + \left[f\left(0,v\right) - f\left(-\infty,v\right)\right]\exp\left(\int_0^x \frac{V_1 \mathrm{d}x'}{\kappa_1\left(x',v,A/Q\right)}\right) . \quad (7.39)$$

Here, it is assumed that a single parameter κ_1 describes diffusion along the shock normal upstream from the shock. The diffusion parameter depends in general on speed, through the level of turbulence at the location x, and on speed v.

In Equation (7.38), the injection speed $v_{\rm inj}$ is introduced. For $v > v_{\rm inj}$, the downstream diffusion speed is equal to the upstream convection speed V_1, i.e. all particles convected into the shock are scattered back:

$$\left(\tilde{\kappa}\cdot\nabla f\right)_x = V_1 f \quad\rightarrow\quad \frac{\kappa_\parallel}{r_{\rm G}}\left(\cos^2\theta + \kappa_\perp \sin^2\theta/\kappa_\parallel\right) = V_1 \ . \tag{7.40}$$

In this way, the downstream gradient scale $r_{\rm G}$ adjusts to balance a stationary situation at the shock. At high speeds the spatial diffusion parameter becomes large ($\kappa \rightarrow \infty$) and thus the gradient scale is large $r_{\rm G} \rightarrow \infty$. The lower the speed, the smaller is κ, but $r_{\rm G}$ cannot be smaller than the gyroradius $r_{\rm g}$ or some other characteristic value. For $v = v_{\rm inj}$ the gradient scale $r_{\rm G}$ reaches its smallest value; for $v < v_{\rm inj}$ the diffusive acceleration no longer operates with full efficiency.

The diffusive streaming anisotropy is (Giacalone and Jokipii, 1999):

$$\delta := \frac{|3\tilde{\kappa}\cdot\nabla f|}{vf} = \frac{3V_1}{v}\left[1 + \frac{\left(\kappa_{\rm A}/\kappa_\parallel\right)^2 \sin^2\Psi + \left(1-\kappa_\perp/\kappa_\parallel\right)^2 \sin^2\Psi\cos^2\Psi}{\left[\left(\kappa_\perp/\kappa_\parallel\right)\sin^2\Psi + \cos^2\Psi\right]^2}\right]^{1/2} . \tag{7.41}$$

If this anisotropy is small, then the Parker equation (7.1) can be applied and diffusive first-order Fermi acceleration operates as derived. It can be argued here whether the upstream or the downstream diffusion parameters must be entered to ensure that δ be small. As the downstream parameters of $\tilde{\kappa}_2$ are larger than those of $\tilde{\kappa}_1$, we tend to use $\tilde{\kappa}_2$ as a more stringent constraint.

7.B MHD-description of solar wind turbulence

The following derivation of the magnetohydrodynamic (MHD) model of plasma turbulence follows closely the work by Zhou and Matthaeus (1990). The properties of the plasma are described by the proton mass density $\rho\left(\mathbf{X},t\right)$, the plasma velocity $\mathbf{V}\left(\mathbf{X},t\right)$, and the magnetic field $\mathbf{B}\left(\mathbf{X},t\right)$. We distinguish large scales $\mathbf{X}$ and fluctuation scales $\mathbf{x}$ and assume incompressibility. We have the mass continuity equation, the induction equation with diffusive term $\mathbf{D}'$, vanishing divergence of the magnetic field $\mathbf{B}$, and an equation of motion:

$$\begin{aligned} \dot{\rho} \;&=\; -\nabla\cdot\left(\rho\mathbf{V}\right), \quad \dot{\mathbf{B}} = \nabla\times\left(\mathbf{V}\times\mathbf{B}\right) + \mathbf{D}', \quad \nabla\cdot\mathbf{V} = 0, \quad \nabla\cdot\mathbf{B} = 0, \\ &\rho\left[\dot{\mathbf{V}} + \left(\mathbf{V}\cdot\nabla\right)\mathbf{V}\right] = -\nabla p + \mathbf{J}\times\mathbf{B} + \mathbf{D}, \end{aligned} \tag{7.42}$$

where p is the mechanical plasma pressure, and $\mathbf{J} = \mu_0\nabla\times\mathbf{B}$ is the electric current density. Alternative forms of the equation of motion and the equation of induction without the dissipation terms are

$$\begin{aligned} \mathcal{D}\mathbf{V} - \left(\mu_0\rho\right)^{-1}\left(\mathbf{B}\cdot\nabla\right)\mathbf{B} \;&=\; -\rho^{-1}\nabla p^{\rm T} \quad , \quad p^{\rm T} = p + \mu_0^{-1}B^2 \ , \\ \mathcal{D}\mathbf{B} - \left(\mathbf{B}\cdot\nabla\right)\mathbf{V} \;&=\; -\left(\nabla\cdot\mathbf{V}\right)\mathbf{B} \ , \quad \mathcal{D} := \partial_t + \mathbf{V}\cdot\nabla \ . \end{aligned} \tag{7.43}$$

We decompose the plasma properties into a mean part, typically varying on a spatial scale that corresponds to the heliocentric radial coordinate R, and a turbulent inertial part, typically ranging in spatial scale over more than three decades from a correlation scale $L_{\rm c} \ll R$ down to the thermal ion gyroscale:

$$\mathbf{V} = \mathbf{U} + \mathbf{v}, \ \mathbf{B} = \mathbf{B}_0 + \mathbf{b}, \ \rho = \rho_0 + \delta\rho, \ p^{\rm T} = p_0^{\rm T} + \delta p^{\rm T}, \ \mathcal{D} := \partial_t + \mathbf{U}\cdot\nabla. \tag{7.44}$$

It is assumed that the fluctuating part of the turbulence part is incompressible, i.e. $\delta\rho = 0$, an assumption which is not necessarily true but is made in many models on solar wind MHD-turbulence. The average $\langle ... \rangle$ of a turbulent component vanishes, while the average of the product of two turbulent components does not vanish in general. Averaging of the equations of motion and induction yields

$$\begin{aligned} \mathcal{D}\mathbf{U} + \langle (\mathbf{v}\cdot\nabla)\,\mathbf{v}\rangle - (\mu_0\rho)^{-1}\left[(\mathbf{B}_0\cdot\nabla)\,\mathbf{B}_0 + \langle(\mathbf{b}\cdot\nabla)\,\mathbf{b}\rangle\right] &= -\rho_0^{-1}\nabla p_0^{\mathrm{T}}, \\ \mathcal{D}\mathbf{B}_0 + \langle (\mathbf{v}\cdot\nabla)\,\mathbf{b}\rangle - \left[(\mathbf{B}_0\cdot\nabla)\,\mathbf{U} + \langle(\mathbf{b}\cdot\nabla)\,\mathbf{v}\rangle\right] & \\ - \left[(\nabla\cdot\mathbf{U})\,\mathbf{B}_0 + \langle(\nabla\cdot\mathbf{v})\,\mathbf{b}\rangle\right] &= 0. \end{aligned} \tag{7.45}$$

The difference between Equations (7.43) and (7.45) yields

$$\begin{aligned} \mathcal{D}\mathbf{v} + (\mathbf{v}\cdot\nabla)\,\mathbf{U} - (\mu_0\rho)^{-1}\left[(\mathbf{B}_0\cdot\nabla)\,\mathbf{b} + (\mathbf{b}\cdot\nabla)\,\mathbf{B}_0\right] &= -\rho^{-1}\nabla\delta p^{\mathrm{T}} + \mathbf{N}^v; \\ \mathcal{D}\mathbf{b} + (\mathbf{v}\cdot\nabla)\,\mathbf{B}_0 - (\mathbf{B}_0\cdot\nabla)\,\mathbf{v} - (\mathbf{b}\cdot\nabla)\,\mathbf{U} &= -(\nabla\cdot\mathbf{U})\,\mathbf{b} - (\nabla\cdot\mathbf{v})\,\mathbf{B}_0 + \mathbf{N}^b; \\ \mathbf{N}^v &= -\left[(\mathbf{v}\cdot\nabla)\,\mathbf{v} - \langle(\mathbf{v}\cdot\nabla)\,\mathbf{v}\rangle\right] + (\mu_0\rho)^{-1}\left[(\mathbf{b}\cdot\nabla)\,\mathbf{b} - \langle(\mathbf{b}\cdot\nabla)\,\mathbf{b}\rangle\right]; \\ \mathbf{N}^b &= -\left[(\mathbf{v}\cdot\nabla)\,\mathbf{b} - \langle(\mathbf{v}\cdot\nabla)\,\mathbf{b}\rangle\right] + \left[(\mathbf{b}\cdot\nabla)\,\mathbf{v} - \langle(\mathbf{b}\cdot\nabla)\,\mathbf{v}\rangle\right]. \end{aligned} \tag{7.46}$$

We have neglected non-averaged products of "small" variables $\mathbf{v}$ and $\mathbf{b}$. In a similar fashion one obtains

$$\nabla\cdot\rho\mathbf{v} = 0\ . \tag{7.47}$$

7.B.1 Description of MHD turbulence by Elsässer variables

Using the Elsässer variables

$$\mathbf{z}^{\pm} = \mathbf{v} \pm \frac{1}{\sqrt{\mu_0\rho}}\mathbf{b} \tag{7.48}$$

Equations (7.46) become

$$\begin{aligned} \frac{\partial\mathbf{z}^{\pm}}{\partial t} + (\mathbf{U}\mp\mathbf{V}_{\mathrm{A}})\cdot\nabla\mathbf{z}^{\pm} + \frac{1}{2}\left(\mathbf{z}^{\pm}-\mathbf{z}^{\mp}\right)\nabla\cdot\left(\frac{\mathbf{U}}{2}\pm\mathbf{V}_{\mathrm{A}}\right) & \\ +\mathbf{z}^{\mp}\cdot\left(\nabla\mathbf{U}\pm\frac{1}{\sqrt{\mu_0\rho}}\nabla\mathbf{B}_0\right) = -\frac{1}{\rho}\nabla p + \mathbf{N}_0^{\pm}\ ; & \\ \mathbf{N}_0^{\pm} = \mathbf{N}^v \pm \frac{1}{\sqrt{\mu_0\rho}}\mathbf{N}^b\ . \end{aligned} \tag{7.49}$$

In N_b the term $(\nabla\cdot\mathbf{v})\,\mathbf{b} - \langle(\nabla\cdot\mathbf{v})\,\mathbf{b}\rangle$ has been set to zero because the turbulence is assumed to be incompressible, i.e. $(\nabla\cdot\mathbf{v}) = 0$.

The above equation is derived in the following way:

$$\begin{aligned} \frac{\partial\mathbf{v}}{\partial t} \pm \frac{1}{\sqrt{\mu_0\rho}}\frac{\partial\mathbf{b}}{\partial t} &= \frac{\partial\mathbf{z}^{\pm}}{\partial t}\ ; \\ (\mathbf{U}\cdot\nabla)\,\mathbf{v} \pm \frac{1}{\sqrt{\mu_0\rho}}(\mathbf{U}\cdot\nabla)\,\mathbf{b} &= (\mathbf{U}\cdot\nabla)\,\mathbf{z}^{\pm} \mp \mathbf{b}\,(\mathbf{U}\cdot\nabla)\,\frac{1}{\sqrt{\mu_0\rho}}\ ; \\ (\mathbf{v}\cdot\nabla)\,\mathbf{U} \pm \frac{1}{\sqrt{\mu_0\rho}}(-\mathbf{b}\cdot\nabla)\,\mathbf{U} &= \left(\mathbf{z}^{\mp}\cdot\nabla\right)\mathbf{U}\ ; \end{aligned}$$

$$
\begin{aligned}
-\frac{(\mathbf{B}_0\cdot\nabla)}{\mu_0\rho}\mathbf{b}\pm\frac{1}{\sqrt{\mu_0\rho}}\left(-\mathbf{B}_0\cdot\nabla\right)\mathbf{v} &= \mp\left(\mathbf{V}_\mathrm{A}\cdot\nabla\right)\mathbf{z}^\pm+\mathbf{b}\left(\mathbf{V}_\mathrm{A}\cdot\nabla\right)\frac{1}{\sqrt{\mu_0\rho}}\ ;\\
\left(\mathbf{b}\cdot\nabla\right)\mathbf{B}_0\pm\frac{1}{\sqrt{\mu_0\rho}}\left(\mathbf{v}\cdot\nabla\right)\mathbf{B}_0 &= \pm\frac{1}{\sqrt{\mu_0\rho}}\left(\mathbf{z}^\mp\cdot\nabla\right)\mathbf{B}_0\ . \qquad (7.50)
\end{aligned}
$$

The first line is valid because $\dot\rho = 0$ ($\delta\rho = 0$ or $\rho = \langle\rho\rangle$). The last term of the fourth line yields

$$
\mathbf{b}\left(\mathbf{V}_\mathrm{A}\cdot\nabla\right)\frac{1}{\sqrt{\mu_0\rho}}=\frac{\mathbf{b}}{\sqrt{\mu_0\rho}}\left(\mathbf{B}_0\cdot\nabla\right)\frac{1}{\sqrt{\mu_0\rho}}=\frac{1}{2}\left(\mathbf{z}^\pm-\mathbf{z}^\mp\right)\left(\pm\nabla\cdot\mathbf{V}_\mathrm{A}\right) \qquad (7.51)
$$

because $\nabla\cdot\mathbf{B}_0 = 0$.

The last term of the fourth line and the term $\pm\left(\nabla\cdot\mathbf{U}\right)\mathbf{b}/\sqrt{\mu_0\rho}$ remaining from the second equation in (7.46) are added:

$$
\begin{aligned}
\mp\mathbf{b}\left(\mathbf{U}\cdot\nabla\right)\frac{1}{\sqrt{\mu_0\rho}}\pm\frac{\mathbf{b}\left(\nabla\cdot\mathbf{U}\right)}{\sqrt{\mu_0\rho}} &= \frac{1}{2}\left(\mathbf{z}^\pm-\mathbf{z}^\mp\right)\left(\nabla\cdot\frac{\mathbf{U}}{2}\right)\\
\text{because of}\quad \frac{\mathbf{U}}{\rho}\cdot\nabla\rho=-\nabla\cdot\mathbf{U}\quad\text{i.e.}\quad \nabla\cdot(\rho\mathbf{U}) &= 0\ . \qquad (7.52)
\end{aligned}
$$

7.B.2 Assumptions for the solar wind turbulence

We now mainly follow the work by Zank et al. (1996a). With $V_\mathrm{A} \ll U$, the equations reduce to

$$
\begin{aligned}
\frac{\partial\mathbf{z}^\pm}{\partial t}+\mathbf{U}\cdot\nabla\mathbf{z}^\pm+\frac{1}{2}\mathbf{z}^\pm\nabla\cdot\frac{\mathbf{U}}{2}+\mathbf{z}^\mp\cdot\mathcal{M} &= N\mathbf{L}^\pm+\mathbf{S}^\pm\\
\mathcal{M} &= \left[\nabla\otimes\mathbf{U}-\frac{1}{2}\tilde{1}\nabla\cdot\frac{\mathbf{U}}{2}\right]\ . \qquad (7.53)
\end{aligned}
$$

The dissipation and source terms on the r.h.s of the first line are somewhat rewritten and will be evaluated later.

In order to obtain an equation for the evolution of turbulent power, one needs to multiply the above equation by $\mathbf{z}^\pm$ and to average over small scale fluctuations. The tensor $\mathcal{M}$ is then a contraction tensor for the Elsässer variables $\mathbf{z}^\pm\mathcal{M}\mathbf{z}^\mp$. However, the heliosphere will usually be described in heliocentric coordinates, while the Elsässer variables refer to a coordinate system that is fixed to the heliospheric magnetic field, which in the most simple approach is described by a Parker spiral with Parker angle Ψ of the magnetic field with respect to the radial direction of the heliosphere. Therefore the contraction $\mathcal{M}$ needs to include the coordinate transformation from heliocentric coordinates to the coordinate system aligned to the large-scale heliospheric magnetic field. This is done by a rotation

$$
\mathcal{O}=\begin{pmatrix}\cos\Psi & 0 & \sin\Psi\\ 0 & 1 & 0\\ -\sin\Psi & 0 & \cos\Psi\end{pmatrix} \qquad (7.54)
$$

We can reduce the mathematical effort by constraining ourselves to certain symmetries of turbulence. Three types of turbulence are most often discussed in the

literature: (1) isotropic turbulence, (2) turbulence in slab geometry with the fluctuation amplitudes $\mathbf{v}$ and $\mathbf{b}$ perpendicular to the ambient magnetic field $\mathbf{B}_0$ and the wave vector $\mathbf{k}$ parallel to $\mathbf{B}_0$, and (3) the so-called 2D-MHD turbulence (Bieber et al. (1996) with $\mathbf{k} \perp \mathbf{B}_0$ and $\mathbf{v}$ and $\mathbf{b}$ mutually perpendicular to both $\mathbf{k}$ and $\mathbf{B}_0$ but isotropic distribution of the wave vectors in the plane orthogonal to $\mathbf{B}_0$. This enables us to introduce projection matrices $\mathcal{P}_{\rm S}$ and $\mathcal{P}_{\rm 2D}$ for symmetric and slab/2D turbulence, respectively, in the frame aligned with $\mathbf{B}_0$:

$$\mathcal{P}_{\rm S} = \frac{1}{3}\begin{pmatrix} 1 & 0 & 0 \\ 0 & 1 & 0 \\ 0 & 0 & 1 \end{pmatrix} \; ; \; \mathcal{P}_{\rm 2D} = \frac{1}{2}\begin{pmatrix} 0 & 0 & 0 \\ 0 & 1 & 0 \\ 0 & 0 & 1 \end{pmatrix} \; . \tag{7.55}$$

The action of the contraction tensor $\mathcal{M}_{\rm B}$ and the projection tensor $\mathcal{P}_{\rm 2D;B}$ needs to be transformed from the coordinate system aligned to $\mathbf{B}_0$ to the heliocentric coordinate system, where the contraction tensor is denoted by $\mathcal{M}_{\rm H}$ and the projection tensor $\mathcal{P}_{\rm 2D;H}$:

$$\begin{aligned} \mathbf{z}_{\rm B}^{\pm;{\rm T}}\mathcal{P}_{\rm 2D;B}^{\rm T}\mathcal{M}_{\rm B}\mathbf{z}_{B}^{\mp} &= \mathbf{z}_{\rm B}^{\pm;{\rm T}}\mathcal{O}^{\rm T}\mathcal{O}\mathcal{P}_{\rm 2D;B}^{\rm T}\mathcal{O}^{\rm T}\mathcal{O}\mathcal{M}_{\rm B}\mathcal{O}^{\rm T}\mathcal{O}\mathbf{z}_{\rm B}^{\mp} = \mathbf{z}_{\rm H}^{\pm;{\rm T}}\mathcal{P}_{\rm 2D;H}^{\rm T}\mathcal{M}_{\rm H}\mathbf{z}_{\rm H}^{\pm;{\rm T}} \\ \mathbf{z}_{\rm H}^{\pm;{\rm T}} = \mathbf{z}_{\rm B}^{\pm;{\rm T}}\mathcal{O}^{\rm T} \quad &; \quad \mathcal{P}_{\rm 2D;H}^{\rm T} = \mathcal{O}\mathcal{P}_{\rm 2D;B}^{\rm T}\mathcal{O}^{\rm T} \; ; \; \mathcal{M}_{\rm H} = \mathcal{O}\mathcal{M}_{\rm B}\mathcal{O}^{\rm T} \; ; \\ \mathcal{P}_{\rm 2D;H}^{\rm T} &= \begin{pmatrix} \sin^2\Psi & 0 & \sin\Psi\cos\Psi \\ 0 & 1 & 0 \\ \sin\Psi\cos\Psi & 0 & \cos^2\Psi \end{pmatrix} \; . \end{aligned} \tag{7.56}$$

The superscript T denotes a transposed tensor. The subscripts H and B at the Elsässer variables denote the heliocentric coordinate system and that aligned with the ambient magnetic field $\mathbf{B}_0$, respectively. We derive the tensor $\mathcal{M}_{\rm H}$ (Equation 7.53) in heliocentric coordinates:

$$\begin{aligned} \nabla \cdot \mathbf{U} &= \frac{1}{r^2}\frac{\partial}{\partial r}\left(r^2 U\right) + \frac{1}{r}\frac{\partial U}{\partial \theta} + \frac{1}{r\sin\theta}\frac{\partial U}{\partial \Psi} \quad \text{and} \\ \nabla \otimes \mathbf{U} &= \begin{pmatrix} \partial_r U & 0 & 0 \\ r^{-1}\partial_\theta U & 0 & 0 \\ \left(r\sin\theta\right)^{-1}\partial_\Psi U & 0 & 0 \end{pmatrix} \quad \text{if} \quad \mathbf{U} = U\mathbf{e}_r \quad \Rightarrow \\ \mathcal{M} &= \begin{pmatrix} 1 & 0 & 0 \\ 0 & -1 & 0 \\ 0 & 0 & -1 \end{pmatrix}\frac{U}{2r} + \begin{pmatrix} -1 & 0 & 0 \\ 0 & 1 & 0 \\ 0 & 0 & 1 \end{pmatrix}\frac{1}{2}\frac{\partial U}{\partial r} \\ &\quad + \begin{pmatrix} 0 & 0 & 0 \\ 1 & 0 & 0 \\ 0 & 0 & 0 \end{pmatrix}\frac{1}{r}\frac{\partial U}{\partial \theta} + \begin{pmatrix} 0 & 0 & 0 \\ 0 & 0 & 0 \\ 1 & 0 & 0 \end{pmatrix}\frac{1}{r\sin\theta}\frac{\partial U}{\partial \Psi} \; . \end{aligned} \tag{7.57}$$

After multiplying the contraction term by $\mathbf{z}^{\pm}$ and averaging over the short fluctuation scales, we obtain

$$\left(\frac{1}{3}\frac{U}{2r} - \frac{1}{3}\frac{1}{2}\frac{\partial U}{\partial r}\right)\left\langle \mathbf{z}^{-} \cdot \mathbf{z}^{+} \right\rangle =: M_{\rm S}\left\langle \mathbf{z}^{-} \cdot \mathbf{z}^{+} \right\rangle \tag{7.58}$$

in the case of isotropic turbulence and

$$\left[\frac{\cos^2\Psi}{2}\left(\frac{U}{r} - \frac{\partial U}{\partial r}\right) + \frac{1}{2}\frac{\partial U}{\partial \theta} + \frac{1}{2\sin\theta}\frac{\partial U}{\partial \Psi}\right]\left\langle \mathbf{z}^{-} \cdot \mathbf{z}^{+} \right\rangle =: M_{\rm 2D}\left\langle \mathbf{z}^{-} \cdot \mathbf{z}^{+} \right\rangle \tag{7.59}$$

for the 2D and the slab case, if $\langle z_i^{\pm} z_j^{\mp} \rangle = 0$ for $i \neq j$ Zank et al. (1996a).

By multiplying Equations (7.53) for the evolution of $\mathbf{z}^+$ and $\mathbf{z}^-$ by $\mathbf{z}^+$ and $\mathbf{z}^-$, respectively, we obtain two equations

$$\frac{1}{2}\mathcal{D}'\left\langle \left(\mathbf{z}^{\pm}\right)^2 \right\rangle + M_{\mathrm{S/2D}} \left\langle \mathbf{z}^- \cdot \mathbf{z}^+ \right\rangle = S^{\pm} + D^{\pm}, \quad \mathcal{D}' = \left(\frac{\partial}{\partial t} + \nabla \cdot \frac{\mathbf{U}}{2} + \mathbf{U} \cdot \nabla \right), \tag{7.60}$$

where S and D denote source and dissipation terms and $\mathcal{D}'$ is a differential operator. Multiplying Equation (7.53) for $\mathbf{z}^+$ by $\mathbf{z}^-$ and that for $\mathbf{z}^-$ by $\mathbf{z}^+$ and adding the resulting equations yields

$$\mathcal{D}' \left\langle \mathbf{z}^- \cdot \mathbf{z}^+ \right\rangle + M_{\mathrm{S/2D}} \left[\left\langle \left(\mathbf{z}^+\right)^2 \right\rangle + \left\langle \left(\mathbf{z}^-\right)^2 \right\rangle \right] = S_m + D_m. \tag{7.61}$$

The Elsässer variables $\mathbf{z}^{\pm}$ are related to kinetic and magnetic energy E_v and E_b and to the cross helicity H^{C} through

$$\begin{aligned} E = E_v + E_b &= \frac{1}{4}\left[\left\langle \left(\mathbf{z}^+\right)^2 \right\rangle + \left\langle \left(\mathbf{z}^-\right)^2 \right\rangle \right]; \; E^{\mathrm{R}} = E_v - E_b = \frac{1}{2}\left\langle \mathbf{z}^- \cdot \mathbf{z}^+ \right\rangle; \\ H^{\mathrm{C}} = E^+ - E_- &= \frac{1}{4}\left[\left\langle \left(\mathbf{z}^+\right)^2 \right\rangle - \left\langle \left(\mathbf{z}^-\right)^2 \right\rangle \right]. \end{aligned} \tag{7.62}$$

Therefore, Equations (7.60) and (7.61) represent

$$\begin{aligned} \mathrm{D}'\left(E_v + E_b\right) + 2M_{\mathrm{S/2D}}\left(E_v - E_b\right) &= \frac{1}{2}\left(S^+ + S^- + D^+ + D^-\right), \\ \mathcal{D}'\left(E_v - E_b\right) + 2M_{\mathrm{S/2D}}\left(E_v + E_b\right) &= \frac{1}{2}\left(S_1 + D_1\right), \end{aligned} \tag{7.63}$$

where the difference of these two equations describes the evolution of E_b and the sum the evolution of E_v. In the case of constant Alfvén ratio $r_{\mathrm{A}} = E_v/E_b$, the first equation can be written as

$$\mathcal{D}' E_b + 2M\sigma_{\mathrm{D}} E_b = S' + D' \qquad \text{with} \qquad \sigma_{\mathrm{D}} = \left(r_{\mathrm{A}} - 1\right) / \left(r_{\mathrm{A}} + 1\right) \; . \tag{7.64}$$

We introduce the parameter $\Gamma_{\mathrm{iso}} = 2M_{\mathrm{iso}}\sigma_{\mathrm{D}}$ for the contraction term of isotropic turbulence (7.58) and $\Gamma_{\mathrm{2D}} = 2M_{\mathrm{S/2D}}\sigma_{\mathrm{D}}$ for slab/2D turbulence (7.59):

$$\Gamma_{\mathrm{iso}} = -\frac{1}{3}\sigma_{\mathrm{D}} > 0 \;\; \text{and} \;\; \Gamma_{\mathrm{2D}} = -\sigma_{\mathrm{D}} \cos^2 \Psi > 0 \; , \tag{7.65}$$

where Ψ is the angle between the magnetic field and the plasma flow.

With the parameter Γ, Equation (7.64) takes the form

$$\mathcal{D}'' E_b = S' + D' \; ; \; \mathcal{D}'' = \left(\frac{\partial}{\partial t} + \nabla \cdot \frac{\mathbf{U}}{2} + \mathbf{U} \cdot \nabla \right) - \Gamma \frac{U}{r} \tag{7.66}$$

for a stationary flow.

7.B.3 Dissipation

Now we need to incorporate the source and dissipation terms. Rather than going through a detailed treatment of the dissipation terms, we use the dimension and scale invariance arguments of von Karman and Howarth (1938, see also Matthaeus et al., 1996):

$$\frac{\partial v^2}{\partial t} = -\alpha \frac{v^3}{l_\mathrm{c}} + S \ , \quad \frac{\partial l_\mathrm{c}}{\partial t} = \beta v \ , \quad v^2 l_\mathrm{c}^{\alpha/\beta} = \text{const.} \ , \tag{7.67}$$

where S is the source term. The dissipation is assumed to depend on a typical length scale l_c (correlation length) of the turbulence and on the third power of the speed. If α and β are dimensionless parameters, the above equations have terms of equal dimensions. As is easily verified, the solutions of the above equations are

$$\begin{aligned} v\,(t) &= v_0 \left[1 + A\,(t - t_0)\right]^{-\alpha/(\alpha+2\beta)} \ , \\ l_\mathrm{c}\,(t) &= l_{\mathrm{c};0} \left[1 + A\,(t - t_0)\right]^{2\beta/(\alpha+2\beta)} \ , \quad A^{-1} = \frac{2}{\alpha + 2\beta} \frac{l_{\mathrm{c};0}}{v_0} \ . \end{aligned} \tag{7.68}$$

For $t \gg A^{-1}$, these solutions are power laws. The typical behaviour of a fluctuating variable is that $v^2\,(t) \to t$, and thus $\alpha = 2\beta$. As the scales for l_c and v can be changed independently, we should have $A^{-1} = l_{\mathrm{c};0}/v_0$, and thus $\alpha + 2\beta = 2$. This yields $\alpha = 1$ and $\beta = 1/2$.

We transfer the above principle to the case of expanding hydromagnetic systems by postulating that

$$\begin{aligned} \mathcal{D}'\left(E_b l_\mathrm{c}^2\right) = 0 \quad \Rightarrow \quad & l_\mathrm{c}^2 \mathcal{D}' E_b + 2 l_\mathrm{c} E_b \left(\partial_t + \mathbf{U} \cdot \nabla\right) l_\mathrm{c} = 0 \quad \Rightarrow \\ & -\frac{E_b^{3/2}}{l_\mathrm{c}} + S + 2 l_\mathrm{c} E_b \left(\frac{\partial}{\partial t} + \mathbf{U} \cdot \nabla + \Gamma \frac{U}{r}\right) l_\mathrm{c} = 0 \quad \Rightarrow \\ & \left(\frac{\partial}{\partial t} + \mathbf{U} \cdot \nabla + \Gamma \frac{U}{r}\right) l_\mathrm{c} = \frac{E_b^{1/2}}{2 l_\mathrm{c}} - \frac{S l_\mathrm{c}}{2 E_b} \ . \end{aligned} \tag{7.69}$$

The second line follows because the term $\nabla \cdot \mathbf{U}/2$ is only applied once as a scalar, while for the other differential operator the product rule has to be used. The third line follows from Equation (7.66).

For a stationary situation, we have the set of equations:

$$\begin{aligned} \left(\frac{\partial}{\partial t} + \nabla \cdot \frac{\mathbf{U}}{2} + \mathbf{U} \cdot \nabla - \Gamma \frac{U}{r}\right) E_b &= -\frac{E_b^{3/2}}{l_\mathrm{c}} + S \ ; \\ \left(\mathbf{U} \cdot \nabla + \Gamma \frac{U}{r}\right) l_\mathrm{c} &= \frac{E_b^{1/2}}{2} - \frac{l_\mathrm{c} S}{2 E_b} \ . \end{aligned} \tag{7.70}$$

Bibliography

Acuña *et al.*: 2006, Proc. 5th IGPP Conf. *The Physics of the Inner Heliosheath: Voyager Observations, Theory, and Future Prospects*, Waikiki Beach, Hawaii, 3–9 March 2006, in press.

Alexashov, D.B., Chalov, S.V., Myasnikov, A.V., Izmodenov, V.V., and Kallenbach, R.: 2004, 'The dynamical role of anomalous cosmic rays in the outer heliosphere', *Astron. Astrophys.* **420**, 729–736.

Bamert, K., Kallenbach, R., Ness, N.F., Smith, C.W., Terasawa, T., Hilchenbach, M., Wimmer-Schweingruber, R.F., and Klecker, B.: 2004, 'Hydromagnetic wave excitation upstream of an interplanetary traveling shock', *Astrophys. J.* **601**, L99–L102.

Baumjohann, W., and Treumann, R.A.: 1996, *Basic Space Plasma Physics*, Imperial College Press, London.

Bieber, J.W., Wanner, W., and Matthaeus, W.H.: 1996, 'Dominant two-dimensional solar wind turbulence with implications for cosmic ray transport', *J. Geophys. Res.* **101**, 2'511–2'522.

Burlaga, L.F., Ness, N.F., Acuña, M.H., Lepping, R.P., Connerney, J.E.P., Stone, E.C., and McDonald, F.B.: 2005, 'Crossing the termination shock into the heliosheath: magnetic fields', *Science* **309**, 2027–2029.

Bykov, A.M., and Toptygin, I.N.: 1993, *Phys.-Uspekhi* **36**, 1020.

Chalov, S.V.: 1993, 'Longitudinal distribution of anomalous hydrogen near the solar wind termination shock', *Planet. Space Sci.* **41**, 133.

Chalov, S.V.: 2000, 'Acceleration of pick-up ions at the solar wind termination shock', *Astrophys. Space Sci.* **274**, 25.

Chalov, S.V.: 2005, 'Acceleration of interplanetary pick-up ions and anomalous cosmic rays', *Adv. Space Res.* **35**, 2106.

Chalov, S.V., and Fahr, H.J.: 1996, 'Reflection of pre-accelerated pick-up ions at the solar wind termination shock: the seed for Anomalous Cosmic Rays', *Solar Phys.* **168**, 389.

Chalov, S.V., and Fahr, H.J.: 2000, 'Pick-up ion acceleration at the termination shock and the post-shock pick-up ion energy distribution', *Astron. Astrophys.* **360**, 381.

Chalov, S.V., Fahr, H.J., and Izmodenov, V.: 1997, *Astron. Astrophys.* **320**, 659.

Chalov, S.V., Alexashov, D.B., and Fahr, H.J.: 2006, 'Interstellar pickup protons and solar wind heating in the outer heliosphere', *Astron. Lett.* **32**, 206–213.

Decker, R.B., Krimigis, S.M., Roelof, E.C., Hill, M.E., Armstrong, T.P., Gloeckler, G., Hamilton, D.C., and Lanzerotti, L.J.: 2005, 'Voyager 1 in the foreshock, termination shock, and heliosheath', *Science* **309**, 2020–2024.

Fisk, L.A.: turbulent cascade.

Galli, *et al.*: 2006, 'Direct measurements of energetic neutral hydrogen in the interplanetary medium', *Astrophys. J.* **644**, 1317–1325.

Giacalone, J. and Jokipii, J.R.: 1999, 'The transport of cosmic rays across a turbulent magnetic field', *Astrophys. J.* **520**, 204–214.

Gloeckler, G.: 2003, 'Ubiquitous suprathermal tails on the solar wind and pickup ion distributions', *Solar Wind 10*, AIP Conf. Proc. **679**, pp. 583–588.

Gruntman, M., Roelof, E.C., Mitchell, D.G., Fahr, H.J., Funsten, H.O., and McComas, D.J.: 2001, 'Energetic neutral atom imaging of the heliospheric boundary region', *J. Geophys. Res.* **106**, 15'767–15'782.

Horbury, T.S. and Balogh, A.: 2001, 'Evolution of magnetic field fluctuations in high-speed solar wind streams: Ulysses and Helios observations', *J. Geophys. Res.* **106**, 15'929–15'940.

Isenberg, P.A., Smith, C.W., and Matthaeus, W.H.: 2003, 'Turbulent heating of the distant solar wind by interstellar pickup protons', *Astrophys. J.* **592**, 564–573.

Jokipii, J.R.: 1966, 'Cosmic-ray propagation. I. Charged particles in a random magnetic field', *Astrophys. J.* **146**, 480–487.

Jokipii, J.R., and Kota, J.: 1989, 'The polar heliospheric magnetic field', *Geophys. Res. Lett.* **16**, 1–4.

Kallenbach, R., Hilchenbach, M., Chalov, S.V., Le Roux, J.A., and Bamert, K.: 2005, 'On the injection problem at the solar wind termination shock', *Astron. Astrophys.* **439**, 1–22.

Lee, M.A., Shapiro, V.D., and Sagdeev, R.Z.: 1996, 'Pickup ion energization by shock surfing', *J. Geophys. Res.* **101**, 4'777.

le Roux, J.A., Fichtner, H., and Zank, G.P., 'Self-consistent acceleration of multiply reflected pickup ions at a quasi-perpendicular solar wind termination shock: a fluid approach', *J. Geophys. Res.* **105**, 12'557–12'578.

Matsukiyo, S., and Scholer, M.: 2003, 'Modified two-stream instability in the foot of high Mach number quasi-perpendicular shocks', *J. Geophys. Res.* **108**, SMP 19-1, CiteID 1459, DOI 10.1029/2003JA010080.

Matthaeus, W.H., Zank, G.P., and Oughton, S.: 1996, 'Phenomenology of hydromagnetic turbulence in a uniformely expanding medium', *J. Plasma Physics* **56**, 659–675.

McComas, D.J., and Schwadron, N.A.: 2006, 'An explanation of the Voyager paradox: Particle acceleration at a blunt termination shock', *Geophys. Res. Lett.* **33**, CiteID L04102.

Möbius, E., and Kallenbach, R.: 2005, 'Acceleration in the heliosphere', in J. Geiss and B. Hultqvist (eds.), *The solar system and beyond: ten years of ISSI.* ISSI scientific report, SR-003 Bern, Switzerland: The International Space Science Institute, p. 165.

Ness, N.F.: 2006, 'Heliospheric magnetic fields and termination shock crossing: Voyager 1', this volume.

Sagdeev, R.Z.: 1966, 'Cooperative phenomena and shock waves in collisionless plasmas', *in* M.A. Leotovich (ed.), *Reviews of Plasma Physics*, vol. 4, Consultants Bur., New York, p. 23.

Scholer, M., Shinohara, I., and Matsukiyo, S.: 2003, 'Quasi-perpendicular shocks: Length scale of the cross-shock potential, shock reformation, and implication for shock surfing', *J. Geophys. Res.* **108**, 1014, doi:10.1029/2002JA009515.

Stone, E.C., Cummings, A.C., McDonald, F.B., Heikkila, B.C., Lal, N., and Webber, W.R.: 2005, 'Voyager 1 explores the termination shock region and the heliosheath beyond', *Science* **309**, 2017–2020.

Tidman, D.A., and Krall, N.A.: 1971, 'Shock waves in collisionless Plasmas', in S.C. Brown (ed.), Series in Plasma Physics, Wiley, New York, pp. 29–38.

Tu, C.-Y., Marsch, E., and Rosenbauer, H.: 1990, 'The dependence of MHD turbulence spectra on the inner solar wind stream structure near solar minimum', *Geophys. Res. Lett.* **17**, 283–286.

Vainio, R. and Schlickeiser, R.: 1999, 'Self-consistent Alfvén-wave transmission and test-particle acceleration at parallel shocks', *Astron. Astrophys.* **343**, 303–311.

Vasyliunas, V.M., and Siscoe, G.L.: 'On the flux and the energy spectrum of interstellar ions in the solar system' *J. Geophys. Res.* **81**, 1247–1252.

von Karman, T., and Howarth, L.: 1938, 'On the statistical theory of isotropic turbulence', *Proc. R. Soc. London* **164**, 192.

Warren, J.S., Hughes, J.P., Badenes, C., Ghavamian, P., McKee, C.F., Moffett, D., Plucinsky, P.P., Rakowski, C., Reynoso, E., and Slane, P.: 2005, 'Cosmic-ray acceleration at the forward shock in Tycho's supernova remnant: evidence from Chandra X-ray observations', *Astrophys. J.* **634**, 376–389.

Wu, C.S., and Davidson, R.C.: 1972, 'Electromagnetic instabilities produced by neutral-particle ionization in interplanetary space', *J. Geophys. Res.* **77**, 5399–5406.

Zank, G.P., Matthaeus, W.H., and Smith, C.W.: 1996a, 'Evolution of turbulent magnetic fluctuation power with heliospheric distance', *J. Geophys. Res.* **101**, 17'093–17'107.

Zank, G.P., Pauls, H.L., Cairns, I.H., and Webb, G.M.: 1996b, 'Interstellar pickup ions and quasi-perpendicular shocks: Implications for the termination shock', *J. Geophys. Res.* **101**, 457.

Zhou, Y., and Matthaeus, W.H.: 1990, 'Transport and turbulence modeling of solar wind fluctuations', *J. Geophys. Res.* **95**, 10'291–10'311.

— 8 —

Interstellar Pickup Ions and Injection Problem for Anomalous Cosmic Rays: Theoretical Aspect

Sergey Chalov[1]
Institute for Problems in Mechanics
Moscow, Russia

Abstract. **The physical properties of pickup ions originating in the solar wind due to ionization of interstellar atoms penetrating the heliosphere are considered here. The equation for the anisotropic velocity distribution function of the ions is derived and some particular solutions illustrating their transport in the heliosphere are presented. Special attention is concentrated on stochastic acceleration of pickup ions in the solar wind and shock-drift acceleration at the termination shock. The injection problem for anomalous cosmic rays at the termination shock is discussed.**

8.1 Introduction

The local interstellar medium (LISM) surrounding the Solar System is a partly ionized medium consisting mainly of neutral components. It has become evident in recent years that the interstellar atoms have a pronounced effect on the global structure of the extensive region separating the supersonic solar wind and LISM and on the physical processes operating in the heliosphere. Apart from the fact that the position and shape of the heliospheric termination shock and heliopause are significantly determined by the action of the atoms, they give rise to a peculiar hot population of pickup ions in the solar wind.

Due to large mean free paths, which are comparable with the dimensions of the heliosphere, interstellar atoms can penetrate close to the Sun. In the heliosphere some portion of the atoms is ionized through charge exchange with protons or through the processes of photoionization and electron impact ionization. According to current knowledge, the speed of the interstellar wind relative to the Sun is about 26 km/s. The speeds of interstellar atoms in the heliosphere can deviate from this value due to the thermal velocity spread, due to acceleration by solar gravity (near the Sun), or due to the charge exchange process in the disturbed interstellar

[1]in *The Physics of the Heliospheric Boundaries*, V. Izmodenov and R. Kallenbach (eds.), ISSI Scientific Report No. 5, pp. 245 - 282, ESA-ESTEC, Paris 2006

medium between the heliopause and bow shock. But in any case, this speed is much smaller compared with the solar wind speed ranging from 350 km/s up to 750 km/s depending on heliolatitude or solar activity. Therefore, we can conclude that the speed of newly created ions in the solar wind frame approximately equals the local solar wind speed V_{SW}. The ions are then picked up by the solar wind electric and magnetic fields, so that they have a ring velocity distribution in the solar wind frame: the pickup ions gyrate around magnetic field lines and stream along the lines with a speed $V_{SW}|\cos\xi|$, where ξ is the initial pitch angle. The angle ξ is determined by the local configuration of the interplanetary magnetic field $\mathbf{B}$: $\cos\xi = -\mathbf{B}\cdot\mathbf{V}_{SW}/(BV_{SW})$. Thus the initial streaming velocity of newly created pickup ions is parallel or antiparallel to $\mathbf{B}$ depending on the polarity of the solar magnetic field, but in any case it is directed towards the Sun in the solar wind rest frame. This ring velocity distribution of pickup ions is highly unstable, as was shown by Wu and Davidson (1972), and for rather short times (as compared with the solar wind convection time) evolves to a nearly isotropic distribution, while free kinetic energy of the initial distribution is realized in the form of Alfvén waves.

Direct observations of pickup helium (Möbius et al., 1985) and pickup hydrogen (Gloeckler et al., 1993) made it apparent that the velocity distributions of pickup ions differ in significant ways from the velocity distributions of primary solar wind ions. In consequence of their specific features the pickup ions have been proposed by Fisk et al. (1974) as a seed population for anomalous cosmic rays (ACRs). Originally, it was believed that stochastic acceleration by solar wind turbulence is the principal acceleration mechanism producing ACRs (e.g., Fisk, 1976). Later Pesses et al. (1981) proposed an alternative model in which the anomalous components are originated at the solar wind termination shock through the diffusive acceleration process. At present, this idea of ACR origin is commonly accepted.

8.2 Anisotropic transport of pickup ions in the solar wind

The general kinetic equation for the velocity distribution function of charged particles $f(t, \mathbf{x}, \mathbf{v}')$ can be written as

$$\frac{\partial f}{\partial t} + \mathbf{v}'\cdot\frac{\partial f}{\partial \mathbf{x}} + \frac{\mathbf{F}'}{m}\cdot\frac{\partial f}{\partial \mathbf{v}'} = \hat{S}f + Q\,. \tag{8.1}$$

In Equation (8.1) $\mathbf{v}'$ and $\mathbf{x}$ are the velocity vector and vector in configuration space in the inertial frame, m is the mass of a particle, $\mathbf{F}'$ is the external large-scale electromagnetic force, $\hat{S}f$ is the scattering operator applied to the function f describing the effect of stochastic wave-particle interactions, and Q is the source term.

8.2.1 Kinetic equation for the velocity distribution function

As regards pickup ions, we would point to the next two facts. The gyroradius and gyroperiod of pickup ions are generally much smaller than other spatial and time scales, respectively. Thus their velocity distribution can be considered

as gyrotropic. Furthermore, the velocity distribution is highly anisotropic in the inertial frame since the thermal velocities of pickup ions are comparable with the solar wind speed, while in the solar wind rest frame the anisotropy is much smaller. Therefore it is more convenient to consider the distribution function in the moving frame. According to Skilling (1971) and Isenberg (1997) the transport equation describing the phase-space evolution of the gyrotropic velocity distribution function $f(t, \mathbf{x}, v, \mu)$ of pickup ions in a background plasma moving at a velocity $\mathbf{U}(t, \mathbf{x})$ can be written in the following form (see Appendix A):

$$\frac{\partial f}{\partial t} + (U_i + v\mu b_i)\frac{\partial f}{\partial x_i} + \left[\frac{1-3\mu^2}{2} b_i b_j \frac{\partial U_j}{\partial x_i} - \frac{1-\mu^2}{2}\frac{\partial U_i}{\partial x_i} - \right.$$
$$- \frac{\mu b_i}{v}\left(\frac{\partial U_i}{\partial t} + U_j \frac{\partial U_i}{\partial x_j}\right)\left] v\frac{\partial f}{\partial v} + \frac{1-\mu^2}{2}\left[v\frac{\partial b_i}{\partial x_i} + \mu\frac{\partial U_i}{\partial x_i} - \right.\right.$$
$$\left.\left. -3\mu b_i b_j \frac{\partial U_j}{\partial x_i} - \frac{2b_i}{v}\left(\frac{\partial U_i}{\partial t} + U_j\frac{\partial U_i}{\partial x_j}\right)\right]\frac{\partial f}{\partial \mu} = \hat{S}f + Q(t, \mathbf{x}, v, \mu)\,, \tag{8.2}$$

where v and $\mu = \cos\xi$ are the speed and cosine of the particle pitch angle ξ in the solar wind rest frame, $\mathbf{b}$ is the unit vector of the large-scale magnetic field.

The general form of the scattering operator is (see, e.g., Schlickeiser, 1989)

$$\begin{aligned}\hat{S}f &= \frac{\partial}{\partial\mu}\left(D_{\mu\mu}\frac{\partial f}{\partial\mu}\right) + \frac{\partial}{\partial\mu}\left(D_{\mu v}\frac{\partial f}{\partial v}\right) + \frac{1}{v^2}\frac{\partial}{\partial v}\left(v^2 D_{\mu v}\frac{\partial f}{\partial\mu}\right) \\ &+ \frac{1}{v^2}\frac{\partial}{\partial v}\left(v^2 D_{vv}\frac{\partial f}{\partial v}\right)\,.\end{aligned} \tag{8.3}$$

Operator $\hat{S}$ describes the pitch-angle scattering and energy diffusion of charged particles. The Fokker-Planck diffusion coefficients $D_{\mu\mu}$, $D_{\mu v}$, and D_{vv} in Equation (8.3) can be calculated in the frame of the quasi-linear theory of resonant wave-particle interactions.

We will consider further a spherically symmetric solar wind with the spatially independent radial speed V_{SW}. The large-scale interplanetary magnetic field is generally well described by the Parker model (Parker, 1963):

$$B_r = B_{r\mathrm{E}}\left(\frac{r_\mathrm{E}}{r}\right)^2\,, \qquad B_\vartheta = 0\,, \qquad B_\varphi = -B_{r\mathrm{E}}\frac{r_\mathrm{E}^2\Omega}{rV_\mathrm{SW}}\sin\vartheta\,, \tag{8.4}$$

where the radial component of the magnetic field $B_{r\mathrm{E}}$ does not depend on heliolatitude [see, e.g., Ulysses data in Balogh et al., 1995; Smith and Balogh, 1995), $\Omega = 2.7\times10^{-6}$ s^{-1}, $r_\mathrm{E} = 1$ AU, and ϑ is the polar angle (colatitude) in the heliocentric spherical coordinate system (r, ϑ, φ). If we introduce the variable $\chi = \cos\psi$, where $\psi(r, \vartheta)$ is the angle between the vectors $\mathbf{V}_\mathrm{SW}$ and $\mathbf{B}$, we obtain:

$$b_r = \chi, \qquad b_\varphi = -\mathrm{sign}(\chi)\left(1-\chi^2\right)^{1/2}\,. \tag{8.5}$$

Then in the case of the outward pointing magnetic field

$$\chi(r, \vartheta) = \left[1 + \left(\Omega r/V_\mathrm{SW}\right)^2\sin^2\vartheta\right]^{-1/2}\,. \tag{8.6}$$

The general transport equation (8.2) then becomes

$$\frac{\partial f}{\partial t} + (V_{\mathrm{SW}} + v\mu\chi)\frac{\partial f}{\partial r} - \frac{v\mu\left(1-\chi^2\right)^{1/2}}{r\sin\theta}\frac{\partial f}{\partial \varphi} + \\ + \left[\frac{1-3\mu^2}{2}\frac{1-\chi^2}{r} - \frac{1-\mu^2}{r}\right] V_{\mathrm{SW}} v\frac{\partial f}{\partial v} + \\ + \frac{1-\mu^2}{2}\left[\frac{v}{r^2}\frac{\mathrm{d}}{\mathrm{d}r}\left(r^2\chi\right) + \frac{2V_{\mathrm{SW}}}{r}\mu - 3\mu V_{\mathrm{SW}}\frac{1-\chi^2}{r}\right]\frac{\partial f}{\partial \mu} = \\ = \hat{S}f + Q\left(t, r, \vartheta, \varphi, v, \mu\right) . \tag{8.7}$$

The second and third terms on the left-hand side of Equation (8.7) describe the convective motion of particles with the solar wind and their streaming along the magnetic field lines due to anisotropy of the pitch-angle distribution. The forth term corresponds to adiabatic cooling in the expanding solar wind, and the last term to adiabatic focusing in the nonuniform magnetic field.

8.2.2 Fokker-Planck diffusion coefficients

In collisionless plasma the interaction of charged particles with electromagnetic waves is determined by the resonance condition

$$\omega - k_{\parallel} v_{\parallel} = n\Omega_{\mathrm{g}} , \tag{8.8}$$

where ω is the wave frequency, $k_{\parallel}$ is the projection of the wave number vector $\mathbf{k}$ on $\mathbf{B}$, $v_{\parallel}$ is the velocity of a particle along the magnetic field, and Ω_{g} is the gyrofrequency. In the frame of the quasi-linear theory, the Fokker-Planck diffusion coefficients are derived by expanding the collisionless Vlasov equation for the phase space density of particles to second order in perturbated quantities and ensemble averaging over the statistical properties of the electromagnetic waves [e.g., Kennel and Engelmann, 1996). Due to their particular importance in space plasma we will consider here only Alfvén waves propagating along the magnetic field (the slab component of solar wind turbulence). In fact, it follows from observations (Matthaeus et al., 1990; Bieber et al., 1996) that magnetic fluctuations in the solar wind can be considered as composed of a combination of a dominant two-dimensional component (wave vectors are perpendicular to the mean magnetic field) and a minor slab component. However, the two-dimensional component cannot be involved in resonant wave-particle interactions. More general expressions for coefficients $D_{\mu\mu}$, $D_{\mu v}$, and D_{vv} in the case of turbulence consisting of nondispersive and nondissipative parallel and antiparallel propagating Alfvén waves have been obtained by Schlickeiser (1989), and in a modified form taking into account dissipation of waves near the ion cyclotron frequency by Chalov and Fahr (1998).

When the dissipative range has an exponential form (e.g., Schlickeiser et al., 1991), the differential intensities of parallel and antiparallel propagating Alfvén waves can be written as

$$I_{\pm}(k) = I_{0\pm} k^{-q} \exp(-k l_{\mathrm{d}}) \qquad k > k_{\min}, \tag{8.9}$$

where k is the wave number, $l_{\rm d}$ is the dissipative scale, q is the spectral index ($= 5/3$), and $k_{\rm min}$ corresponds to the largest scale of energy-containing fluctuations. The mean square amplitude of the fluctuations is given by

$$\left\langle \delta B^2 \right\rangle = \int_{k_{\rm min}}^{\infty} \left(I_+ + I_- \right) dk \,. \tag{8.10}$$

If left- and right-handed, circularly polarized waves are identical in intensities, the Fokker-Planck coefficients are (Schlickeiser, 1989; Chalov and Fahr, 1998)

$$\begin{aligned} D_{\mu\mu} &= D_0 \left(1-\mu^2\right) \left\{ \left(1-\mu v_{\rm A}/v\right)^2 \mid 1-\mu v/v_{\rm A} \mid^{q-1} \exp\left[-\frac{L}{\mid 1-\mu v/v_{\rm A} \mid} \right] \right. \\ &\left. + \epsilon \left(1+\mu v_{\rm A}/v\right)^2 \mid 1+\mu v/v_{\rm A} \mid^{q-1} \exp\left[-\frac{L}{\mid 1+\mu v/v_{\rm A} \mid} \right] \right\} , \end{aligned} \tag{8.11}$$

$$\begin{aligned} D_{\mu v} &= v_{\rm A} D_0 \left(1-\mu^2\right) \left\{ \left(1-\mu v_{\rm A}/v\right) \mid 1-\mu v/v_{\rm A} \mid^{q-1} \exp\left[-\frac{L}{\mid 1-\mu v/v_{\rm A} \mid} \right] \right. \\ &\left. - \epsilon \left(1+\mu v_{\rm A}/v\right) \mid 1+\mu v/v_{\rm A} \mid^{q-1} \exp\left[-\frac{L}{\mid 1+\mu v/v_{\rm A} \mid} \right] \right\} , \end{aligned} \tag{8.12}$$

$$\begin{aligned} D_{vv} &= v_{\rm A}^2 D_0 \left(1-\mu^2\right) \left\{ \mid 1-\mu v/v_{\rm A} \mid^{q-1} \exp\left[-\frac{L}{\mid 1-\mu v/v_{\rm A} \mid} \right] \right. \\ &\left. + \epsilon \mid 1+\mu v/v_{\rm A} \mid^{q-1} \exp\left[-\frac{L}{\mid 1+\mu v/v_{\rm A} \mid} \right] \right\} , \end{aligned} \tag{8.13}$$

where

$$D_0 = \frac{\pi}{2} \Omega_{\rm g} \left(\frac{v_{\rm A} k_{\rm min}}{\Omega_{\rm g}} \right)^{q-1} \frac{1}{(1+\epsilon) E_q \left(l_{\rm d} k_{\rm min} \right)} \frac{\left\langle \delta B^2 \right\rangle}{B^2} , \tag{8.14}$$

$v_{\rm A}$ is the Alfvén speed, $L = \Omega_{\rm g} l_{\rm d}/v_{\rm A}$, $\epsilon = I_0^-/I_0^+$, and $E_q(z)$ is the exponential integral

$$E_q(z) = \int_1^{\infty} y^{-q} \exp(-zy)\, dy \,. \tag{8.15}$$

The parameter ϵ is related to the normalized cross-helicity of Alfvénic turbulence as $\sigma_{\rm c} = (1-\epsilon)/(1+\epsilon)$. It follows from Helios and Voyager data that $\epsilon \leq 1$ for solar distances of between 0.3 AU up to 20 AU (Roberts et al., 1987).

Furthermore, the mean-square amplitude of Alfvénic fluctuations decreases with increasing of the heliocentric distance, so we adopt here that

$$\left\langle \delta B^2 \right\rangle = \left\langle \delta B_{\rm E}^2 \right\rangle \left(r_{\rm E}/r \right)^{\alpha} \,. \tag{8.16}$$

It follows from the WKB theory for the transport of nondissipative Alfvén waves in the solar wind without any spatially distributed sources that $\alpha = 3$ (Hollweg, 1974).

8.2.3 Cold model of the interstellar atom distribution in the heliosphere

The source term in Equation (8.7) describes the production of pickup ions due to ionization of interstellar atoms. It therefore essentially depends on the spatial distribution of the atoms in the heliosphere.

The properties of interstellar atoms penetrating the heliosphere suffer essential modification in the heliospheric interface (see Chapter 4). In general, multidimensional numerical models are needed to describe precisely the parameters of the atoms. For some purposes, however, it is sufficient to use simple analytical models. The simplest of them is the so-called cold model in the frame of which interstellar atoms are considered as a flow of neutral particles with zero temperature. Up to the moment of ionization, atoms follow planar hyperbolic orbits under the action of gravitation attraction and the repulsion by solar radiation pressure. The spatial distribution of the atoms in the heliosphere is axisymmetric and the axis of symmetry is determined by the velocity vector of the interstellar flow $\mathbf{V}_\infty$. In the frame of the cold model, the number density $n(\mathbf{r})$ of interstellar atoms in the heliocentric system of coordinates is given by (Fahr, 1968; Blum and Fahr, 1970; Axford, 1972)

$$\begin{aligned}\frac{n(\mathbf{r})}{n_\infty} &= \frac{\left[(r\sin\phi)^2 + 4r\,(1+\cos\phi)\,/C\right]^{-1/2}}{r\sin\phi}\left\{p_1^2\exp\left[-\frac{r_\mathrm{E}^2 P_\mathrm{loss}\,(r_\mathrm{E})\,(\pi-\phi)}{V_\infty p_1}\right]\right. \\ &+ \left. p_2^2\exp\left[-\frac{r_\mathrm{E}^2 P_\mathrm{loss}\,(r_\mathrm{E})\,(\pi+\mathrm{sign}(C)\phi)}{V_\infty p_2}\right]\right\}, \end{aligned} \tag{8.17}$$

where n_∞ is the number density of atoms of given species in the interstellar medium, $P_\mathrm{loss}\,(r_\mathrm{E})$ is the ionization rate at 1 AU, ϕ is the angle between vectors $\mathbf{r}$ and $\mathbf{V}_\infty$ ($\phi \geq 0$), p_1 and p_2 are the impact parameters identifying a direct and indirect orbit which pass through the point given by $\mathbf{r}$:

$$p_{1,2} = \left|\left[\left(\frac{1}{2}\,r\sin\phi\right)^2 + \frac{r}{C}\,(1+\cos\phi)\right]^{1/2} \pm \frac{1}{2}\,r\sin\phi\right|. \tag{8.18}$$

In Equations (8.17) and (8.18) $C = V_\infty^2/\,(1-\eta)\,GM_\odot$, where G is the gravitational constant, $M_\odot$ is the mass of the Sun, and η is the ratio of the radiation pressure and gravitational attraction (see Appendix B). The exponential terms in Equation (8.17) show the presence of the ionization cavity in a vicinity of the Sun with the characteristic size $\lambda = r_\mathrm{E}^2 P_\mathrm{loss}\,(r_\mathrm{E})\,/V_\infty$. Note that the sizes of ionization cavities around stars are essentially smaller in the case when a star moves relative to the surrounding medium as compared with the case when the relative motion is absent.

The most important ionizing processes in the heliosphere are photoionization and charge exchange with solar wind protons. Accordingly, it was assumed in Equation (8.17) that the ionization rate changes as r^{-2}. We note here that P_loss is the ionization rate averaged over several years (over the time of passage of atoms

though the heliosphere). It differs from the production rate of pickup ions $P_{\rm prod}$, which is local in time.

In the following subsections we consider two interesting numerical solutions of Equation (8.7) which show the anisotropic properties of pickup ions.

8.2.4 Point source of pickup protons

In this subsection, for the purposes of illustration we consider the time evolution of the velocity distribution of pickup protons injected at $t = 0$ on a spherical shell with radius $r_{\rm E}$ (Chalov and Fahr, 1998). The injection efficiency does not depend on longitude (angle φ), so the velocity distribution function does not depend on φ either. In addition, we shall restrict our consideration to the ecliptic plane ($\vartheta = 90°$).

For this type of injection, the source term in Equation (8.7) has the following form:

$$Q\left(t, r, v, \mu\right) = Q_0 \delta(t) \delta\left(r - r_{\rm E}\right) \delta\left(v - V_{\rm SW}\right) \delta\left(\mu - \mu_0\left(\pi/2\right)\right) , \tag{8.19}$$

where $\delta(x)$ is the Dirac delta function and $\mu_0\left(\vartheta\right) = -\chi\left(r_{\rm E}, \vartheta\right)$ (see Equation (8.6)). The sign "-" in the expression for μ_0 shows that the particles are injected in the sunward hemisphere (see Introduction).

In the numerical calculations we use the following values for the basic parameters: $V_{\rm SW} = 450$ km s^{-1}, $n_{\rm eE} = 7$ cm^{-3}, $B_{r\rm E} = 3.5$ nT, $k_{\rm min} = 10^{-11}$ cm^{-1}, $v_{\rm A}/\Omega_{\rm g} = 2.3 \times 10^7 \left(n_{\rm e}/1{\rm cm}^{-3}\right)^{-1/2}$ cm, and the electron number density decreases with the distance as $n_{\rm e} = n_{\rm eE}\left(r_{\rm E}/r\right)^2$. For simplicity, we assume here that $\epsilon = 1$ and $l_{\rm d} = 0$ cm.

Figure 8.1 shows the spatial distributions of pickup protons at subsequent times $\tau = 1$, 2, 3, 4, 5, where the dimensionless time $\tau = V_{\rm SW} t/r_{\rm E}$ (i.e. the solar wind passage time over 1 AU) is introduced. Consequently a solar wind parcel, started at $\tau = 0$ from $r = 1$ AU, reaches at times $\tau = 1$, 2,... solar distances of $r = 2$,3,... AU. The number density N of particles in Figure 8.1 is given by

$$N(t, r) = C_N \int_0^\infty \int_{-1}^{+1} v^2 f \, dv d\mu \, , \tag{8.20}$$

where the constant C_N is defined with the normalization

$$\int_0^\infty r^2 N \, dr = 1 \, . \tag{8.21}$$

The solid and dashed curves correspond to different levels of Alfvénic turbulence $\zeta_{\rm AE} = \left\langle \delta B_{\rm E}^2 \right\rangle / B_{\rm E}^2$ at 1 AU: $\zeta_{\rm AE} = 0.004$ (solid curves) and $\zeta_{\rm AE} = 0.02$ (dashed curves). Figure 8.1 demonstrates the spatial broadening of the distributions of pickup protons which were initially injected according to a spatial $\delta-$function. The broadening can be explained by spatial diffusion of the particles along the magnetic field lines. The diffusion is more efficient at low levels of Alfvénic turbulence since the pitch-angle scattering rate decreases and, therefore, pitch-angle anisotropy increases when $\zeta_{\rm A}$ decreases (compare solid and dashed curves). The pitch-angle anisotropy is also reflected by the fact that the average speed of the

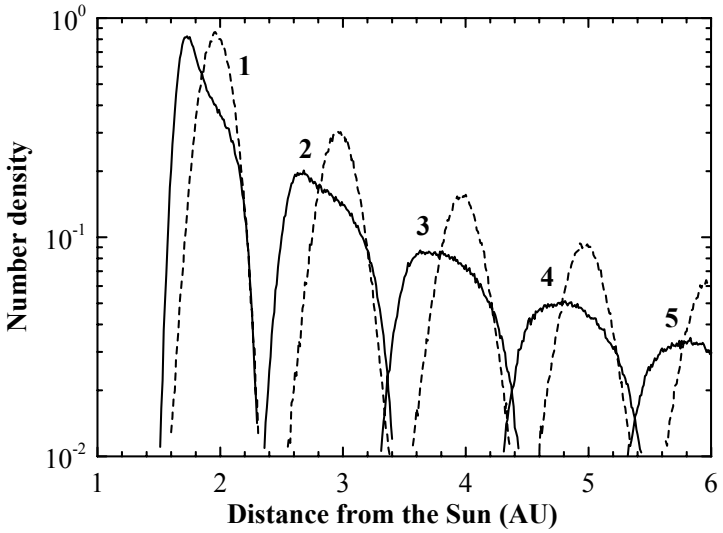

Figure 8.1: Spatial distributions of pickup protons injected at $\tau = 0$ and $r = r_{\rm E}$. The numbers denote the subsequent moments: $\tau = 1$, 2, 3, 4, 5. The solid lines correspond to $\zeta_{\rm AE} = 0.004$, dashed to $\zeta_{\rm AE} = 0.02$.

pickup proton bulk is smaller than the solar wind speed. This is clearly seen in Figure 8.1. The maxima of the spatial distributions at low $\zeta_{\rm A}$ (solid curves) are systematically shifted towards the Sun with respect to the isochronical solar wind bulk.

To reveal the degree of the velocity anisotropy at $\zeta_{\rm AE} = 0.004$ Figure 8.2 shows pitch-angle averaged velocity distributions at times τ =1 and 5. The velocity distribution functions f_v, $f_v^{(+)}$, and $f_v^{(-)}$ are given by the formulae

$$f_v(t,r,v) = C_f \int_{-1}^{+1} f\, d\mu\,, \quad f_v^{(+)}(t,r,v) = C_f^{'} \int_{0}^{+1} f\, d\mu\,,$$
$$f_v^{(-)}(t,r,v) = C_f^{'} \int_{-1}^{0} f\, d\mu\,, \tag{8.22}$$

where the following normalization is used:

$$\int_0^\infty f_v\, d\,(v/V_{\rm SW}) = 1\,, \qquad f_v = f_v^{(+)} + f_v^{(-)}\,. \tag{8.23}$$

The dashed curves labelled by $(-)$ represent particles with $\mu < 0$ and the solid ones labelled by $(+)$ represent particles with $\mu > 0$. At $\tau = 1$ the bulk of pickup protons have negative pitch angles, that is they move inwards as judged by the solar wind reference frame. Measurements of pitch-angle anisotropy of pickup ions at spacecraft are presented, e.g., by Gloeckler et al. (1995) and Möbius et al. (1998). At large times ($\tau = 5$) the distribution is almost isotropic as a result of pitch-angle scattering.

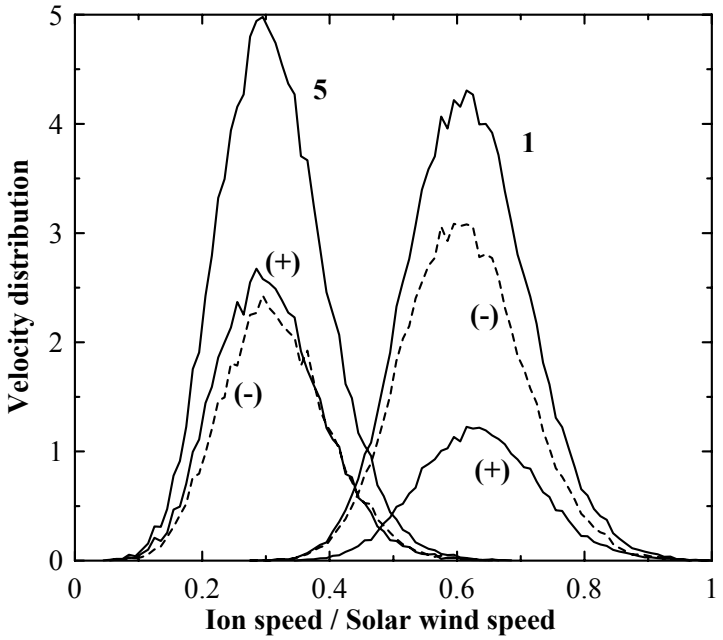

Figure 8.2: Velocity distributions of pickup protons at $\tau = 1$ and 5 ($\zeta_{\rm AE} = 0.004$). The dashed curves labelled by $(-)$ represent particles with $\mu < 0$ and the solid curves labelled by $(+)$ represent particles with $\mu > 0$.

One can identify considerable adiabatic cooling of pickup protons (decrease of the thickness of the distribution) when they move outwards from the Sun. Another interesting feature is a shift between maxima of the $(+)$ and $(-)$ curves at $\tau = 1$, denoting that particles with negative pitch angles suffer more efficient cooling than particles with positive ones. An explanation of this effect has been given by Fisk et al. (1997): particles propagating inwards in the frame of the solar wind have a longer than average dwell time in the inner heliosphere and as a result they suffer substantial adiabatic cooling.

8.2.5 Interplanetary helium focusing cone

Interstellar helium atoms penetrating the heliosphere suffer mainly gravitational attraction from the Sun, since the gravitational force for helium atoms is essentially larger than the radiation pressure. As a result of the focusing effect of gravity, a region of enhanced helium atom number density is formed on the downwind side relative to the Sun (see Chapter 5). In Equation (8.18), therefore, we should put $\eta = 0$. This equation gives the spatial distribution of the atoms rather precisely, however, for positions far enough away from the downwind focusing cone only. It is not correct near the cone since it gives an infinitely large density of particles at its axis. This effect is connected with the fact that the thermal velocities of atoms were not taken into account. Feldman et al. (1972) proposed a modified

cold model for helium atoms in the heliosphere which takes into account thermal spreading of trajectories near the axis of the cone. In the frame of the modified model the number density is given as before by Equation (8.18) at $\phi > \phi_c$, where ϕ_c is the half angle of the focussing cone:

$$\phi_c = \frac{2}{3}\left(\frac{2k_B T_\infty}{\pi m V_\infty^2}\right)^{1/2} . \tag{8.24}$$

Here T_∞ is the temperature of helium in the LISM, m is the mass of the helium atom, and k_B is the Boltzmann constant. For angles $\phi \le \phi_c$ Feldman et al. (1972) obtained, assuming the Maxwellian velocity distribution function atoms in the LISM (see Appendix C),

$$\frac{n(r,\phi)}{n_\infty} = \left(\frac{\pi G M_\odot m}{r k_B T_\infty}\right)^{1/2} \exp\left[-\frac{\pi r_E^2 P_{\rm loss}(r_E)}{(2GM_\odot r)^{1/2}}\right]\left(1 - D\phi^2\right) , \tag{8.25}$$

where

$$D = \frac{2\pi m V_\infty^2}{27 k_B T_\infty} . \tag{8.26}$$

Since the production rate of pickup ions is proportional to the number density of atoms, the He^+ cone should exist along with the neutral helium cone. One could expect then that the geometrical shapes of the both structures coincide. However, as was noted by Möbius et al. (1995) the anisotropic velocity distribution of pickup ions can result in some broadening of the pickup ion cone (due to spatial diffusion) and a relative shift in the positions of the cones. A detailed study of these effects has been carried out by Chalov and Fahr (1999) on the basis of Equation (8.7). At an initial moment in the solar wind reference frame the motion of pickup ions originating in the region of the neutral helium cone is the sum of gyration and streaming along a magnetic field line towards the Sun. Interaction of the pickup ions with solar wind turbulence results in pitch-angle scattering. However, in the case of weak scattering, their velocity distribution is anisotropic and the bulk of the ions move towards the Sun. This effect leads to a systematic shift (in the ecliptic plane) of the pickup ion cone relative to the LISM velocity vector in the direction of motion of the Earth around the Sun (see Figure 8.3). The angle of the shift depends on the level of solar wind turbulence (or on the mean free path). At sufficiently high levels of turbulence when the velocity distribution function is almost isotropic, the shift is absent.

Here we will present the results of numerical solutions of Equation (8.7) in the ecliptic plane corresponding to the above-mentioned problem. Using Equations (8.18) or (8.25) the production rate of He^+ pickup ions is given by

$$q(r,\phi) = n(r,\phi) P_{\rm prod}(r_E)\left(r_E/r\right)^2 . \tag{8.27}$$

Then if we ignore small peculiar velocities of atoms as compared with the solar wind speed, the source term in Eq. (8.7) for the velocity distribution function of pickup ions can be written as

$$Q(r,\phi,v,\mu) = \frac{q(r,\phi)}{2\pi V_{SW}^2}\,\delta(v - V_{SW})\,\delta(\mu - \mu_0(r,\pi/2)) , \tag{8.28}$$

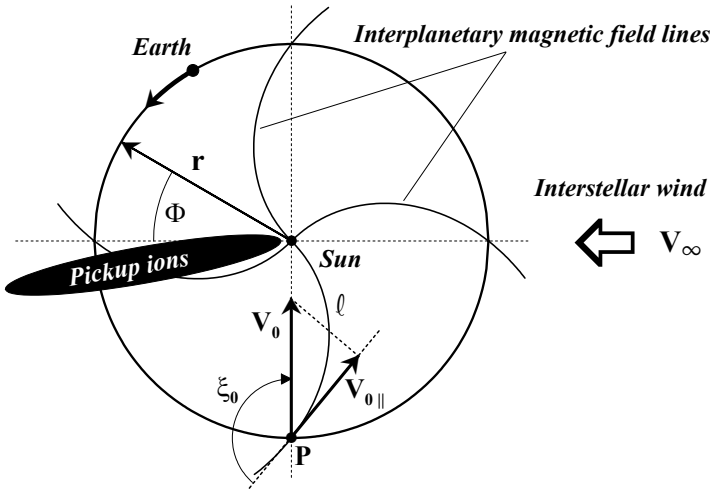

Figure 8.3: Schematic representation of the He^+ pickup cone in the ecliptic plane. Kinematics of newly created pickup ions is also shown. The initial velocity $\mathbf{V_0}$ of a pickup ion in the solar wind rest frame is directed towards the Sun. The motion of the pickup ion is combination of cyclotron rotation around a magnetic field line l and motion along this line with velocity $\mathbf{V_{0||}}$. As a result, pickup ions, on average, move in the same angular direction as the Earth moves around the Sun.

where the initial pitch angle cosine $\mu_0 = \cos\xi_0 = -\chi(r,\vartheta)$ (see Equation 8.6). Thus, seen from the solar wind reference frame, injection, as it was in the previous subsection, always occurs into the sunward half of the velocity space, i.e. with negative pitch-angle cosine μ_0.

We restrict our considerations to the solar wind parameters corresponding to the period of crossing of the focusing helium cone by the ACE spacecraft in 1998: $V_{\rm SW} = 430$ km s^{-1}, $n_{\rm eE} = 4.9$ cm^{-3}, $B_{r\rm E} = 6.9$ nT, $P_{\rm loss} = 1.2 \times 10^{-7}$ s^{-1}, $P_{\rm prod} = 1.3{\times}10^{-7}$ s^{-1} (Gloeckler et al., 2004). The more recent values for the LISM parameters we take from Möbius et al. (2004): $V_\infty = 25.3$ km s^{-1}, $n_\infty\,(He) = 0.015$ cm^{-3}, $T_\infty = 7000$ K. As in the previous subsection, we assume that $k_{\rm min} = 10^{-11}$ cm^{-1}, $l_{\rm d} = 3 \times 10^7$ cm. The values of $\zeta_{\rm AE}$ and ϵ were determined from the best agreement between theoretical and observed spectra of He^+ during the passage of the helium cone (Chalov and Fahr, 2006): $\zeta_{\rm AE} = 0.007$, $\epsilon = 0.1$.

Let us introduce the normalized number densities of He^+:

$$n^*_{\rm PUI} = \frac{n_{\rm PUI}}{n_\infty\,({\rm He})}\,, \qquad n^{*(+)}_{\rm PUI} = \frac{n^{(+)}_{\rm PUI}}{n_\infty\,({\rm He})}\,, \qquad n^{*(-)}_{\rm PUI} = \frac{n^{(-)}_{\rm PUI}}{n_\infty\,({\rm He})}\,, \tag{8.29}$$

where

$$n_{\rm PUI} = \int_0^\infty \int_{-1}^{+1} 2\pi v^2 f\, dv d\mu\,, \qquad n^{(+)}_{\rm PUI} = \int_0^\infty \int_0^{+1} 2\pi v^2 f\, dv d\mu\,,$$
$$n^{(-)}_{\rm PUI} = \int_0^\infty \int_{-1}^{0} 2\pi v^2 f\, dv d\mu\,. \tag{8.30}$$

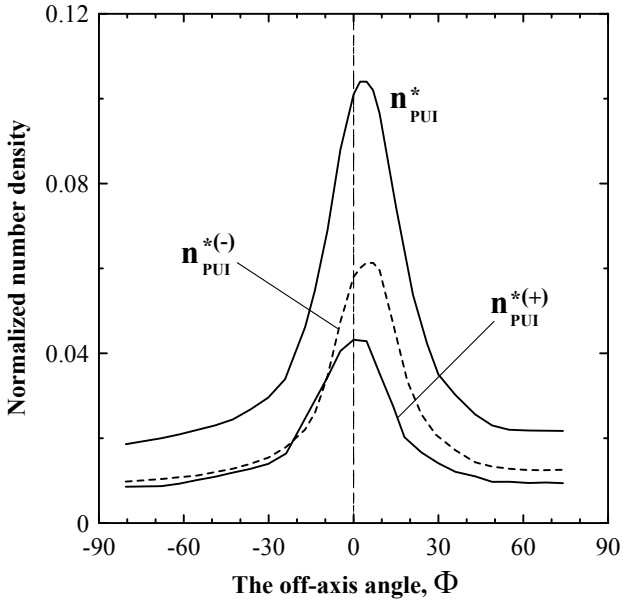

Figure 8.4: Spatial distribution of pickup helium in the focusing cone. $n^*_{\rm PUI}$ is the total number density, $n^{*(+)}_{\rm PUI}$ and $n^{*(-)}_{\rm PUI}$ are the number densities of pickup ions with $\mu > 0$ and $\mu < 0$, respectively.

Figure 8.4 shows $n^*_{\rm PUI}$, $n^{*(+)}_{\rm PUI}$, and $n^{*(-)}_{\rm PUI}$ as functions of the off-axis angle Φ. This angle differs from ϕ, which is by definition not negative ($0 \le \phi \le \pi$), while Φ is positive ($0 < \Phi < \pi$) if it is counted from $\mathbf{V}_\infty$ in the direction of the Earth's motion and negative $-\pi \le \Phi < 0$ in the opposite case (see Figure 8.3). One can clearly see the expected shift in $n_{\rm PUI}$ (about 5° under such level of turbulence) with respect to the interstellar helium flow direction. The shift is connected with anisotropy of the velocity distribution, which is evident if we compare $n^{(+)}_{\rm PUI}$ with $n^{(-)}_{\rm PUI}$. Note that the distribution with $\mu > 0$ behaves as isotropic (no shift!). This result can explain measurements of He^+ ions in the focusing cone by the ACE spacecraft (Gloeckler et al., 2004), which do not show evidences of any differences between positions of maxima in the distributions of neutral and singly charged helium. The SWICS instrument onboard ACE detects particles moving mainly in the anti-sunward direction, i.e. particles with $\mu > 0$.

8.3 Stochastic acceleration of pickup ions in the supersonic solar wind

The velocity distribution function of pickup ions is anisotropic in the case of weak pitch-angle scattering, i.e. when the level of solar wind turbulence is low. However, under disturbed solar wind conditions the velocity distribution is close

to isotropic and it is possible to obtain a transport equation for the pitch-angle averaged distribution

$$F(t,\mathbf{r},v)=\frac{1}{2}\int_{-1}^{+1} f(t,\mathbf{r},v,\mu)\,d\mu\,, \tag{8.31}$$

which includes the effects of spatial and energy diffusion (see, e.g., Jokipii, 1966). In its most common use, ignoring spatial diffusion which is generally unimportant for pickup ions, this equation can be written in the form:

$$\frac{\partial F}{\partial t}+\mathbf{V}_{\rm SW}\frac{\partial F}{\partial \mathbf{r}}=\frac{1}{v^2}\frac{\partial}{\partial v}\left(v^2 D\frac{\partial F}{\partial v}\right)+\frac{v}{3}\frac{\partial F}{\partial v}{\rm div}\mathbf{V}_{\rm SW}+Q(t,\mathbf{r},v)\,, \tag{8.32}$$

where in the case of Alfvénic turbulence (e.g. Schlickeiser, 1989)

$$D_{\rm A}(\mathbf{r},v)=\frac{1}{2}\int_{-1}^{+1}\left(D_{vv}-\frac{D_{\mu v}^2}{D_{\mu\mu}}\right)\,d\mu\,. \tag{8.33}$$

The spatial evolution of the velocity distribution function of pickup ions in the outer heliosphere governed by Equation (8.32) was the subject of extensive research (Fisk, 1976; Isenberg, 1987; Bogdan et al., 1991; Chalov et al., 1995, 1997; Fichtner et al., 1996; le Roux and Ptuskin, 1998; Chalov and Fahr, 1996; Chalov, 2000; Fichtner, 2001).

8.3.1 Simplest analytical model for the velocity distribution of pickup ions

In the case of vanishing energy diffusion ($D=0$ in Equation 8.32), when only convection and adiabatic cooling are taken into account, a simple but very important analytical solution for the velocity distribution function was obtained by Vasyliunas and Siscoe (1976). Let us assume a steady spherically expanding solar wind with $V_{\rm SW}=const$. Then the source term is

$$Q(r,\theta,v)=\frac{\delta\left(v-V_{\rm SW}\right)}{4\pi V_{\rm SW}^2}\,n(r,\theta)P\left(r_{\rm E}\right)\left(r_{\rm E}/r\right)^2\,. \tag{8.34}$$

In Equation (8.34) $n(r,\theta)$ is given by Equation (8.17) and instead of the angle ϕ, which is appropriate for description of the helium cone, we introduce the angle θ between the upwind direction and vector $\mathbf{r}$ ($\theta=\pi-\phi$). Here we assume that $P_{\rm loss}=P_{\rm prod}=P$. According to Vasyliunas and Siscoe (1976) the isotropic velocity distribution function at $\eta=1$ is given by

$$F(r,\theta,v)=\frac{3}{8\pi}\frac{n_\infty V_\infty}{V_{\rm SW}^4}\left(\frac{V_{\rm SW}}{v}\right)^{3/4}\frac{\lambda}{r}\,\exp\left[-\frac{\lambda}{r}\,\frac{\theta}{\sin\theta}\left(\frac{V_{\rm SW}}{v}\right)^{3/2}\right]\,. \tag{8.35}$$

This expression is valid at $v\le V_{\rm SW}$, while at $v>V_{\rm SW}$ $F(r,\theta,v)=0$.

Figure 8.5 shows the velocity distribution functions at 1 AU and $\theta=0^\circ$ for different values of the ionization cavity size $\lambda=r_{\rm E}^2P\left(r_{\rm E}\right)/V_\infty$ (see Section 8.2.3). The distributions are essentially dependent on this parameter (or on the ionization

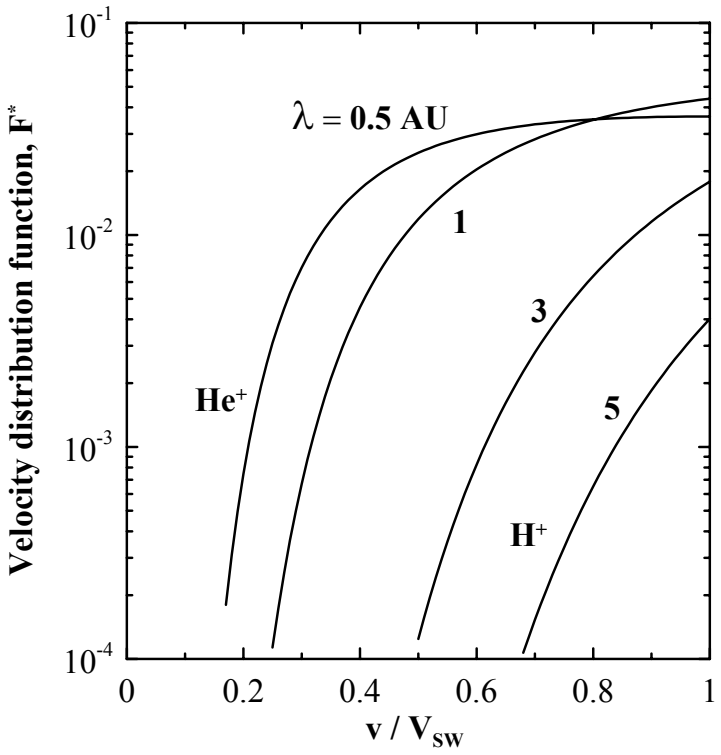

Figure 8.5: Velocity distributions of pickup ions at 1 AU and $\theta = 0°$ for different values of the characteristic ionization cavity size, λ. He^+ and H^+ show approximately the velocity distributions of pickup helium and hydrogen.

rate). The ionization rate is different for different neutral species. For instance, since this value for interstellar helium is mach smaller than for hydrogen, helium atoms can penetrate closer to the Sun and produce there a more abundant population of pickup ions (of course taking into account their relative abundances in the LISM). These solutions clearly demonstrate efficient cooling of pickup ions in the expanding solar wind (remembering that all of them are injected at $v = V_{\rm SW}$). On the other hand, we do not see particles with speeds larger than the solar wind speed. It is the natural consequence of ignoring energy diffusion, which in most physically acceptable cases inevitably leads to acceleration of ions above the injection speed as we will show in the next subsection.

8.3.2 Illustration of the stochastic acceleration process

As an example we consider a simplified version of Equation (8.32) which contains only the time derivative and velocity diffusion term:

$$\frac{\partial F}{\partial t} = \frac{1}{v^2}\frac{\partial}{\partial v}\left(v^2 D \frac{\partial F}{\partial v}\right) . \tag{8.36}$$

Upon integrating Equation (8.36) with respect to $2\pi E v^2 dv$, where $E = mv^2/2$ is the kinetic energy, we obtain

$$\frac{\partial w}{\partial t} = 4\pi m \int_0^\infty F(t,v) \frac{\partial}{\partial v} \left(v^3 D\right)\, dv\,. \tag{8.37}$$

In Equation (8.37) w is the energy density of ions:

$$w(t) = 4\pi \int_0^\infty E v^2 F(t,v)\, dv\,. \tag{8.38}$$

The derivative $\partial \left(v^3 D\right)/\partial v$ is positive since the diffusion coefficient D is usually a growing function of v. The statement concerning the derivative is valid even if D decreases with increasing of v, but not faster than v^{-3}. This argument clearly shows that the energy density of particles, the velocity distribution function of which is governed by Equation (8.36), increases with time.

A further illustration of the stochastic (or second-order Fermi) acceleration can be given, e.g., at $D = const$ (Toptygin, 1983). Let us assume that at $t = 0$ some portion of particles is injected at a speed v_0, i.e., $F(0,v) = F_0 v_0 \delta\,(v - v_0)$. Then the solution of Equation (8.36) under such an initial condition is

$$F(t,v) = \frac{F_0 v_0^2}{(4\pi D t)^{1/2}\, v} \left\{ \exp\left[-\frac{(v - v_0)^2}{4Dt} \right] - \exp\left[-\frac{(v + v_0)^2}{4Dt} \right] \right\}. \tag{8.39}$$

Fig. 8.6 shows the time evolution of the normalized velocity distribution function $v^2 F / v_0^2 F_0$. The distributions are presented for different values of the dimensionless time $\tau = Dt/v_0^2$: 0.01, 0.1, 1.0, and 10. Besides broadening of the distributions due to velocity diffusion, a time shift in their maxima towards high speeds is clearly seen. The shift (or stochastic acceleration) is the general property of high-speed particles in turbulent plasma.

8.3.3 Stochastic acceleration of pickup ions in the outer heliosphere by Alfvénic turbulence and large-scale magnetosonic oscillations

A large body of observations of pickup ions by the Solar Wind Ion Composition Spectrometer (SWICS) on the Ulysses and ACE spacecraft has revealed the ubiquitous presence of pronounced suprathermal tails on the pickup ion distributions (Gloeckler et al., 1994; Gloeckler et al., 2000; Fisk et al., 2000; Gloeckler, 2003). Observational data for the pickup ion distributions in the distant solar wind are scarce. Evidence of acceleration of pickup ions at $\sim$ 70 AU from the Low Energy Charged Particle (LECP) instrument on the Voyager spacecraft has been presented by Krimigis et al. (2000). Beginning in mid-2002, Voyager 1 (LECP) detected a set of events with enhanced fluxes of energetic charged particles (Krimigis et al., 2003; McDonald et al., 2003), which likely are pickup ions accelerated at the termination shock of the solar wind and reached the spacecraft along magnetic field lines connected with the shock front (Jokipii et al., 2004). The enhanced fluxes of energetic particles and ACRs were observed for a long time after crossing the termination shock on 16 December 2004, although any evidence of ACR acceleration at the

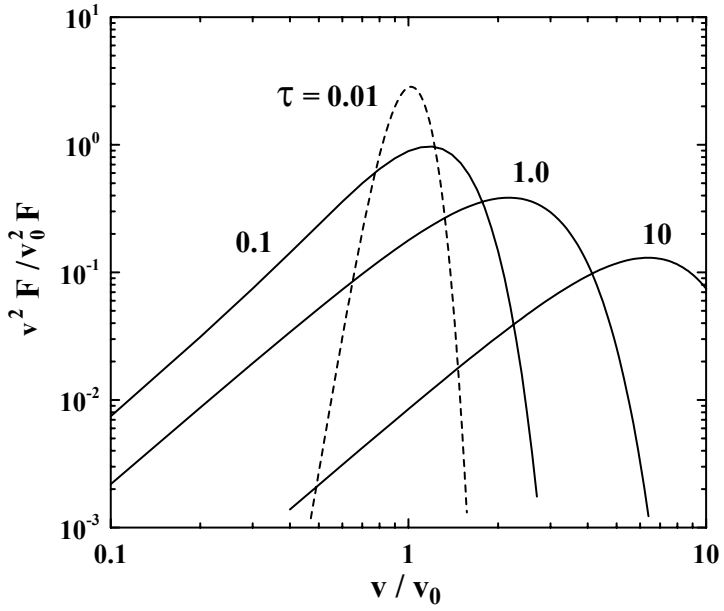

Figure 8.6: Time evolution of the velocity distribution of particles injected initially with $v = v_0$.

place where Voyager 1 crossed the shock was absent (Decker et al., 2005; Stone et al., 2005).

The acceleration mechanism of pickup ions in the outer heliosphere is of obvious interest since it can be considered as a pre-energization mechanism for subsequent acceleration of the pickup ions up to ACR energies at the termination shock. It is apparent that the level of Alfvénic fluctuations decreases as the distance from the Sun increases, and therefore it is not likely that stochastic acceleration by this type of turbulence can produce pronounced high velocity tails in the vicinity of the termination shock. It should be mentioned that Alfvénic turbulence can be generated in the distant solar wind by different kinds of instabilities (Zank et al., 1996a), e.g. by instability of the ring velocity distribution of freshly created pickup ions. However, even in this case the wave intensity is too low to accelerate particles to high speeds, as was shown by Chalov et al. (2004) in the frame of a self-consistent model taking into account reabsorption of self-generated turbulent energy by pickup protons. Thus, some additional energy reservoir is required to provide an energy input to pickup ions in the outer heliosphere. We show below that large-scale magnetosonic oscillations in the solar wind can serve as such a reservoir.

In the following we will assume that Alfvénic turbulence has the same power law spectrum as in previous sections and is composed of dispersionless, unpolarized waves with equal intensities in the forward and backward directions of propagation. Under the given assumptions the velocity diffusion coefficient D_{A} derived

from the quasi-linear theory of the cyclotron resonant wave-particle interaction (see Equation 8.33) can be written as (Isenberg, 1987; Chalov et al., 1997)

$$D_{\rm A} = \frac{\pi^2(q-1)}{q(q+2)} \left(\frac{Ze\,BL_{\rm A}}{2\pi mcv} \right)^{2-q} \frac{v_{\rm A}^2 v}{L_{\rm A}} \frac{\langle \delta B_{\rm A}^2 \rangle}{B^2}\,, \tag{8.40}$$

As before, q is the spectral index of turbulence (the value $q = 5/3$ is adopted here), $v_{\rm A}$ is the Alfvénic speed, Ze and m are the ion charge and mass, B is the magnitude of the interplanetary magnetic field, $L_{\rm A}$ is the correlation length of Alfvénic turbulence, and $\langle \delta B_{\rm A}^2 \rangle$ is the mean-square amplitude of magnetic fluctuations. The spatial distributions of the large-scale magnetic field and mean-square amplitude of Alfvénic fluctuations are given by Equations (8.4) and (8.16), respectively. For the spatial behaviour of the correlation length, we assume that

$$L_{\rm A} = L_{\rm AE} \left(\frac{r}{r_{\rm E}} \right)^{\delta}\,. \tag{8.41}$$

The spatial evolution of the correlation length and mean-square amplitude of Alfvénic fluctuations in the outer heliosphere are presently not well understood. Zank et al. (1996a) and le Roux et al. (1999) proposed a model of the radial evolution of the energy density in magnetic fluctuations and their correlation length taking into account (a) the generation of waves by stream-stream interactions and by pickup ions, and (b) the damping of waves due to turbulent dissipation and stochastic acceleration of pickup ions. Here, however, we assume for simplicity that $\alpha = 3$ (Hollweg, 1974) and $\delta = 1$ (Jokipii, 1973) can be used in Equations (8.4) and (8.16) according to the WKB theory.

In addition to Alfvénic fluctuations with $L_{\rm AE} \sim 0.01$ AU, large-scale oscillations in the magnitudes of the solar wind velocity and magnetic field with spatial scales of up to several AU are observed. As a rule these oscillations are connected with corotating interaction regions and merged interaction regions, and contain the structures of large-scale interplanetary shock waves (see, e.g., Gazis et al., 1999). It has been demonstrated by Toptygin (1983) that acceleration of particles by this type of fluctuations is equivalent to the second-order Fermi acceleration, because in a first order of view, the acceleration at shock fronts (or compression waves) is compensated by the deceleration in the following rarefaction waves. The corresponding energy diffusion coefficient can be written in the form:

$$D_{\rm m}(v) = \frac{v^2}{9} \int_0^{\infty} \langle \nabla \cdot \delta \mathbf{V}_{\rm SW,m}(\mathbf{r},t)\; \nabla \cdot \delta \mathbf{V}_{\rm SW,m}(\mathbf{r}, t-\tau) \rangle\, d\tau \tag{8.42}$$

under the two following assumptions: (1) the mean free path of particles with respect to scattering by short-wavelength Alfvénic fluctuations, $\Lambda_{\parallel}$, is much less than the correlation length of large-scale fluctuations, $L_{\rm m}$, i.e. $\Lambda_{\parallel} \ll L_{\rm m}$, and (2) the time of diffusive propagation of particles over the distance $L_{\rm m}$, $\tau_{\rm dif} \cong L_{\rm m}^2/K_{\parallel}$, is much larger than $\tau_{\rm conv} \cong L_{\rm m}/V_{\rm SW}$, the convective time for the passage of the distance $L_{\rm m}$, i.e.

$$\tau_{\rm dif}/\tau_{\rm conv} = 3V_{\rm SW}L_{\rm m}/v\Lambda_{\parallel} \gg 1, \tag{8.43}$$

where $K_{\parallel} = v\Lambda_{\parallel}/3$ is the spatial diffusion coefficient corresponding to short-wavelength Alfvénic turbulence. In Equation (8.42) $\delta \mathbf{U}_{\rm SW,m}$ is the large-scale

fluctuation of the solar wind velocity and brackets $\langle ... \rangle$ denote a large-scale correlation average. It can be shown then that

$$D_{\rm m} = \frac{\langle \delta V^2_{\rm SW,m} \rangle^{1/2} v^2}{9 L_{\rm m}} \,. \tag{8.44}$$

In what follows we will assume that

$$\langle \delta V^2_{\rm SW,m} \rangle = \langle \delta V^2_{\rm SW,m} \rangle_{\rm E} \left(\frac{r_{\rm E}}{r} \right)^{2\beta} \,. \tag{8.45}$$

With regard to the correlation length of large-scale fluctuations, it seems to be reasonable to assume that $L_{\rm m}$ is the mean distance between large-scale interplanetary shock waves. From observations by the Pioneer and Voyager spacecraft and from numerical simulations of the evolution of recurrent solar wind structures in the distant heliosphere (Whang and Burlaga, 1988; Whang and Burlaga, 1990; Richardson et al., 2001) one can obtain that $L_{\rm m} = 3$ AU and $\beta = 0.7$.

We will consider the combined effects of small-scale Alfvénic and large-scale magnetosonic fluctuations on the formation of pickup ion spectra in the outer heliosphere, so that in Equation (8.32) $D = D_{\rm A} + D_{\rm m}$ (Chalov et al., 1997; Chalov, 2000; Chalov et al., 2003). One can see from Equations (8.40) and (8.44) that $D_{\rm A}$ and $D_{\rm m}$ are the increasing functions of v and, therefore, according to the results of Section 8.3.2, their functional form inevitably results in acceleration of pickup ions.

The source term Q is given by Equation (8.34). Let us consider pickup protons in the ecliptic plane in the upwind direction (i.e. $\theta = 0°$). We then can adopt in Equations (8.17) and (8.34): $\eta = 1$, $P\,(r_{\rm E}) = 6 \times 10^{-7}$ s^{-1}, $n_\infty(H) = 0.1$ cm^{-3}, $V_\infty = 20$ km s^{-1}. The last two values are at the termination shock since the cold model (Equation 8.17) does not take into account filtration of interstellar hydrogen in the interface region. Furthermore, we assume that $V_{\rm SW} = 430$ km s^{-1}, $n_{\rm eE} = 6.5$ cm^{-3}, and $v_{\rm AE} = 50$ km s^{-1}.

The magnitudes of the Alfvénic and magnetosonic fluctuations at the Earth's orbit are described by $\zeta_{\rm AE} = \langle \delta B^2_{\rm AE} \rangle / B^2_{\rm E})$ and $\zeta_{\rm mE} = \langle \delta V^2_{\rm SW,mE} \rangle^{1/2} / V_{\rm SW,E})$, respectively.

Figure 8.7 shows calculated differential fluxes (in the solar wind rest frame) of pickup protons accelerated in the combined small-scale and large-scale turbulent field at $\zeta_{\rm AE} = 0.05$ (solid lines), $\zeta_{\rm AE} = 0.1$ (dashed lines), and $\zeta_{\rm mE} = 0$, 0.3, and 0.5 (curves 1, 2, and 3, respectively). The fluxes are in front of the termination shock located at 90 AU in the upwind direction. It is evident from Figure 8.7 that for reasonable values of the slab component of Alfvénic turbulence at the Earth's orbit, acceleration by this kind of turbulence alone can not produce extended suprathermal tails in the pickup ion distributions near the termination shock. The inclusion of Alfvénic turbulence generated by pickup protons due to anisotropy of their initial ring distribution does not change this conclusion (Chalov et al., 2004). On the other hand, acceleration of pickup ions by large-scale turbulence is essentially more efficient in the outer heliosphere and it can result in the formation of suprathermal tails as can be seen in Figure 8.7.

We did not consider here acceleration of charged particles by short-wavelength compressible (magnetosonic) turbulence (e.g., Fisk, 1976; Toptygin, 1983). This

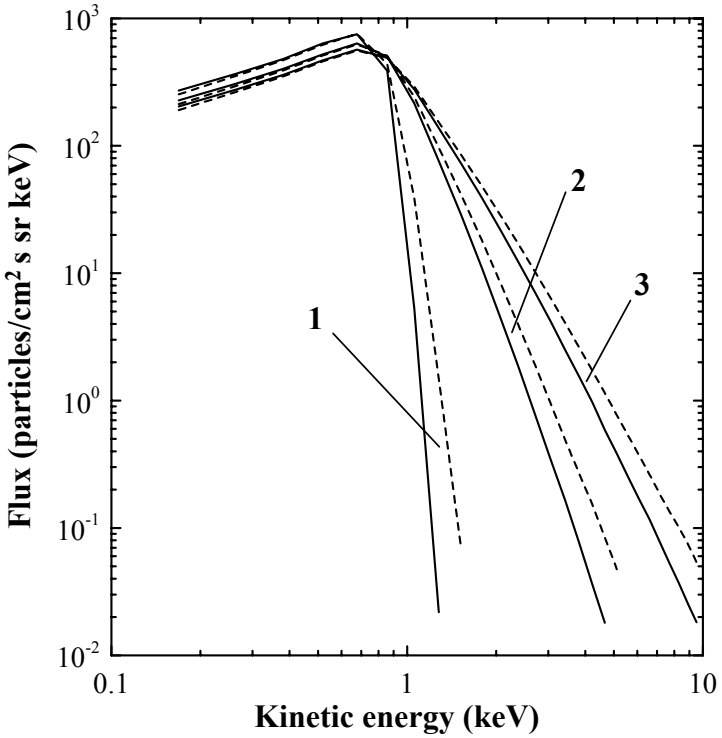

Figure 8.7: Fluxes of pickup protons in the solar wind rest frame in front of the termination shock for different levels of Alfvénic and large-scale magnetosonic turbulence. Solid and dashed lines correspond to $\zeta_{\rm AE} = 0.05$ and $\zeta_{\rm AE} = 0.1$, while curves 1, 2, and 3 correspond to $\zeta_{\rm mE} = 0$, 0.3, and 0.5, respectively.

type of acceleration was considered for a long time as being of minor importance since amplitudes of the fluctuations are essentially smaller as compared with incompressible fluctuations (Smith, 1974) due to damping connected with interactions between magnetosonic waves and solar wind protons and electrons (Barnes, 1966, 1968a,b, 1969). However, recently Fisk and Gloeckler (2006) proposed that the short-wavelength compressible turbulence can be responsible for the formation of universal high-energy tails in pickup ion spectra in the quiet-time solar wind, if a back reaction of pickup ions on the turbulence is taken into account.

8.4 Pickup ions and origin of anomalous cosmic rays

It is accepted at present that the solar wind termination shock is a specific structure in the heliosphere where anomalous cosmic rays are produced. There are strong theoretical grounds presented by Jokipii (1992), which reveal that only diffusive acceleration of pickup ions at the quasi-perpendicular termination shock

has a high enough acceleration rate to produce ACRs with the energies of up to several hundred MeV measured by spacecraft and the acceleration is determined primarily by diffusion normal to the ambient magnetic field. According to this consideration, charged particles can be involved in the diffusive acceleration process only if their initial speeds are sufficiently large. While the initial estimations by Jokipii (1992) are based on a specific model of solar wind turbulence, which possibly is not correct in the outer heliosphere. The existence of the minimum energy threshold is nevertheless confirmed by other findings.

8.4.1 Energy threshold for diffusive acceleration at the termination shock

The general form of the condition that the the diffusive approximation is valid in some vicinity of a shock has been written by Giacalone and Jokipii (1999), Giacalone and Ellison (2000) as

$$\frac{v}{V_{\rm sh}} \gg 3 \left[1 + \frac{\left(K_{\rm A}/K_{\parallel}\right)^2 \sin^2\Psi + \left(1 - K_{\perp}/K_{\parallel}\right)^2 \sin^2\Psi \cos^2\Psi}{\left(\left(K_{\perp}/K_{\parallel}\right)\sin^2\Psi + \cos^2\Psi\right)^2} \right]^{1/2} , \quad (8.46)$$

where v is the speed of a particle in the upstream plasma frame, $V_{\rm sh}$ is the shock speed relative to upstream plasma, $K_{\parallel}$, $K_{\perp}$, and $K_{\rm A}$ are the parallel, perpendicular, and antisymmetric components of the diffusion tensor, respectively, and Ψ is the upstream shock-normal angle.

For a perpendicular shock one can obtain from Equation (8.46) in the frame of the hard-sphere scattering theory:

$$\frac{v}{V_{\rm sh}} \gg 3 \left[1 + \left(\Lambda_{\parallel}/r_{\rm g}\right)^2 \right]^{1/2} . \quad (8.47)$$

Here $\Lambda_{\parallel}$ is the parallel mean free path and $r_{\rm g}$ is the gyroradius. The components of the diffusion tensor in the frame of this theory are given by (e.g., Toptygin, 1983)

$$K_{\parallel} = \frac{1}{3} v \Lambda_{\parallel} , \quad K_{\perp} = \frac{K_{\parallel} \left(r_{\rm g}/\Lambda_{\parallel}\right)^2}{1 + \left(r_{\rm g}/\Lambda_{\parallel}\right)^2} , \quad K_{\rm A} = \frac{K_{\parallel} r_{\rm g}/\Lambda_{\parallel}}{1 + \left(r_{\rm g}/\Lambda_{\parallel}\right)^2} . \quad (8.48)$$

The condition (8.47) is very close to that given by Jokipii (1987, 1992) in the case when $\Lambda_{\parallel} \gg r_{\rm g}$. Equations (8.46) and (8.47) give a lower energy limit for particles to be involved in the process of the diffusive acceleration at the shock. According to the latter equation the minimum energy ranges from $\simeq 100$ keV to 1 MeV (Zank et al., 1996b; Chalov et al., 2003), depending on the value of the mean free path. It should be noted, however, that the hard-sphere scattering theory is valid in the case when $r_{\rm g} > L_{\rm c}$, where $L_{\rm c}$ is the correlation length of turbulence. As regards pickup ions, the opposite condition, $r_{\rm g} \ll L_{\rm c}$, is more appropriate. Giacalone and Ellison (2000) and Giacalone (2003) considered the case when the ratio $K_{\perp}/K_{\parallel}$ is constant, while $K_{\parallel}$ and $K_{\rm A}$ are given by Equations (8.48). For this case, condition (8.46) becomes

$$\frac{v}{V_{\rm sh}} \gg 3 \left[1 + \left(\frac{K_{\parallel}}{K_{\perp}}\right)^2 \left(\frac{r_{\rm g}/\Lambda_{\parallel}}{1 + \left(r_{\rm g}/\Lambda_{\parallel}\right)^2} \right)^2 \right]^{1/2} . \quad (8.49)$$

The authors point out that the injection threshold for the diffusive acceleration given by Equation (8.49) can be much lower than that given by Equation (8.46). For quasi-perpendicular shocks ($\sin\Psi \sim \cos\Psi$) in the case where $K_{\parallel} \gg K_{\perp}, K_{\rm A}$ Equation (8.46) gives

$$v/V_{\rm sh} \gg 3/\cos\Psi\,. \tag{8.50}$$

It is evident from inequalities (8.47), (8.49), and (8.50) that pickup ions can not be involved in the diffusive acceleration without pre-energization somewhere in the heliosphere since their initial energies are only about several keV/nuc. The stochastic acceleration of pickup ions discussed above can be considered as a mechanism for such pre-energization.

Interaction of pickup ions with solar wind turbulence results in energy diffusion and acceleration of some fraction of the particles to high energies (see Fig. 8.7). Thus one can expect that pickup ions arriving at the termination shock have pronounced high energy tails. Particles from the tails can experience further acceleration at the shock. It is important to emphasize that it is not necessary for particles to have energies larger than the diffusive shock acceleration threshold for this to happen. Really, in the frame of the diffusive theory high energies are required for particles to consecutive crossing of the shock front due to their scattering from magnetic fluctuations. However, a single interaction of a pickup ion with the termination shock can lead to reflection of the particle from the shock front due to its experiencing abrupt changes in both the strength and direction of the magnetic field. The reflection condition can be written as (Decker, 1988)

$$v > V_{\rm sh}\sec\Psi/\sqrt{b}\,, \tag{8.51}$$

where b is the jump in magnetic field strength across the shock. Thus the reflection process operates for high speed particles, different from a simple reflection by the electric cross-shock potential. The minimum speed given by Equation (8.51), however, can be considerably smaller than the diffusive shock acceleration threshold for quasi-perpendicular shocks. During the first reflection, the mean kinetic energy of pickup ions increases by approximately a factor of 10 (Chalov and Fahr, 1996; Chalov et al., 1997) due to their drifting motion along the shock front in the direction of the induced electric field. Reflected particles upstream of the shock have a highly anisotropic velocity distribution. Interaction of the particles with upstream turbulence causes diffusion in pitch-angle space and, as a result of that, these particles can again return to the shock and thus suffer second or higher order consecutive encounters.

8.4.2 Shock-drift acceleration of pickup ions

On arrival at the termination shock, energetic particles from the tails of the velocity distributions can experience multiple reflections at the shock front due to abrupt changes of the magnetic field and gain energy from the shock-drift acceleration process. To describe the interaction of a particle with the shock front we use the adiabatic theory ignoring scattering of the particle during its encounter with the front, which is considered as a discontinuity. This assumption is a fairly

good approximation for quasi-perpendicular shocks in the case when $r_g/\Lambda_\parallel \ll 1$ (week scattering). However, upstream and downstream of the shock wave pickup ions can experience pitch-angle scattering, which provides a way for reflected and transmitted particles to return to the shock.

Since in the solar wind rest frame the gyroradius of a typical pickup ion is much larger than that of a solar wind proton, and since the thickness of the shock front can be expected to be of the order of a few gyroradii of solar wind protons, for the passage of pre-accelerated pickup ions one can therefore approximate the shock by a discontinuity, neglecting the magnetic field overshoot and cross-shock potential in the transition region of the collisionsless shock. In this case the reflection conditions at the shock front can be derived from the conservation of the energy for a particle in the de Hoffmann-Teller frame (HT-frame) and from the assumption that the magnetic moment of this particle is the same before and after the encounter with the shock front, i.e. it behaves as an adiabatic invariant. The last assumption is likely to be true for nearly perpendicular shocks but numerical investigations have even shown that this assumption is fairly good also for quasi-perpendicular cases (Terasawa, 1979).

The pitch-angle cosines in the upstream plasma frame corresponding to the loss cone in the HT-frame can be written in the form (Decker, 1988):

$$\mu_\pm = \varepsilon_1 b^{-1} \pm \left[(1-b^{-1})(1-b^{-1}\varepsilon_1^2)\right]^{1/2}, \tag{8.52}$$

where

$$\varepsilon_i = (V_{\mathrm{SW},i}/v_i)\sec\Psi_i \cos\delta_i\,, \qquad b = B_2/B_1\,. \tag{8.53}$$

Here Ψ_i and δ_i are the angles between the shock normal $\mathbf{n}$ and the magnetic field vector $\mathbf{B}_i$ on the one hand, and the shock normal and the solar wind velocity vector $\mathbf{V}_{\mathrm{SW},i}$, on the other; v_i is the speed of pickup ions in the solar wind frame (i = 1, 2 corresponds to the upstream and downstream parts of the flow, respectively). We shall adopt in the following that $\Psi_1 + \delta_1 = \pi/2$, thus excluding the polar regions, i.e. the magnetic field lines are perpendicular to the solar wind velocity.

Following Decker (1988) one can conclude that:

(1) A particle with the pitch cosine μ_1 and speed v_1 in the upstream flow frame is reflected at the shock if

$$-\varepsilon_1 < \mu_1 \le \mu_+ \qquad (\varepsilon_1 < 1)\,, \tag{8.54}$$

$$\mu_- < \mu_1 \le \mu_+ \qquad (1 \le \varepsilon_1 < b^{1/2})\,. \tag{8.55}$$

In the nonrelativistic case the kinetic energy and the pitch angle of the particle after reflection are given by

$$E_1^{\mathrm{R}} = E_1\left[1 + 4\varepsilon_1\left(\varepsilon_1 + \mu_1\right)\right], \tag{8.56}$$

$$\mu_1^{\mathrm{R}} = -(2\varepsilon_1 + \mu_1)\left[1 + 4\varepsilon_1(\varepsilon_1 + \mu_1)\right]^{-1/2}. \tag{8.57}$$

(2) A particle is transmitted downstream if

$$\mu_+ < \mu_1 \le 1 \qquad (\varepsilon_1 < 1)\,, \tag{8.58}$$

$$-1 \le \mu_1 \le \mu_- \text{ and } \mu_+ < \mu_1 \le 1 \quad (1 \le \varepsilon_1 < b^{1/2}), \tag{8.59}$$

$$-1 \le \mu_1 \le 1 \qquad (\varepsilon_1 \ge b^{1/2}). \tag{8.60}$$

In this case

$$\begin{aligned} E_2^{\rm D} &= E_1\Big\{1 + 2\varepsilon_1\Big[\left(1 + b^2/\sigma^2\right)\varepsilon_1/2 + \mu_1 \\ &\quad - (b/\sigma)\left[\left(\varepsilon_1 + \mu_1\right)^2 - (b-1)\left(1-\mu_1^2\right)\right]^{1/2}\Big]\Big\}, \end{aligned} \tag{8.61}$$

$$\begin{aligned} \mu_2^{\rm D} &= \left\{\left[\left(\varepsilon_1 + \mu_1\right)^2 - (b-1)\left(1-\mu_1^2\right)\right]^{1/2} - b\varepsilon_1/\sigma\right\} \times \\ &\quad \times\left\{\left[b\varepsilon_1/\sigma - \left[\left(\varepsilon_1 + \mu_1\right)^2 - (b-1)\left(1-\mu_1^2\right)\right]^{1/2}\right]^2 \right. \\ &\quad \left. + b\left(1-\mu_1^2\right)\right\}^{-1/2}, \end{aligned} \tag{8.62}$$

where $\sigma = \mathbf{V}_{\rm SW,1}\mathbf{n}/\mathbf{V}_{\rm SW,2}\mathbf{n}$ is the compression ratio at the shock.

(3) A particle is transmitted upstream if

$$-1 \le \mu_2 < -\varepsilon_2 \qquad (\varepsilon_2 < 1). \tag{8.63}$$

In this case

$$\begin{aligned} E_1^{\rm U} &= E_2\Big\{1 + 2\varepsilon_2\Big[\left(1 + \sigma^2/b^2\right)\varepsilon_2/2 - \mu_2 - \\ &\quad (\sigma/b)\left[\left(\varepsilon_2 + \mu_2\right)^2 + \left(1 - b^{-1}\right)\left(1-\mu_2^2\right)\right]^{1/2}\Big]\Big\}, \end{aligned} \tag{8.64}$$

$$\begin{aligned} \mu_1^{\rm U} &= \left\{-\left[\left(\varepsilon_2 + \mu_2\right)^2 + \left(1 - b^{-1}\right)\left(1-\mu_2^2\right)\right]^{1/2} + \sigma\varepsilon_2/b\right\} \\ &\quad \times\left\{\left[\sigma\varepsilon_2/b + \left[\left(\varepsilon_2 + \mu_2\right)^2 + \left(1 - b^{-1}\right)\left(1-\mu_2^2\right)\right]^{1/2}\right]^2 \right. \\ &\quad \left. + b^{-1}\left(1-\mu_2^2\right)\right\}^{-1/2}. \end{aligned} \tag{8.65}$$

(4) An upstream particle does not interact with the shock if

$$-1 \le \mu_1 \le -\varepsilon_1 \qquad (\varepsilon_1 < 1). \tag{8.66}$$

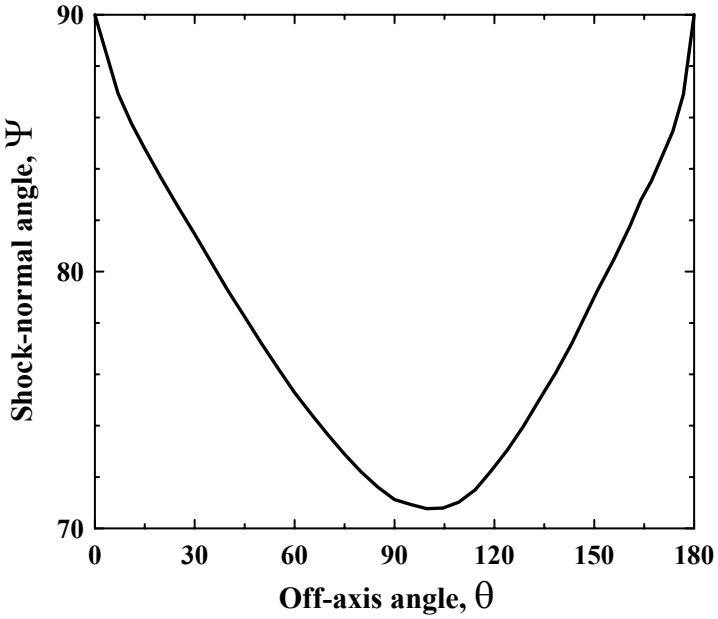

Figure 8.8: The shock normal angle, Ψ, as a function of the off-axis angle, θ.

(5) A downstream particle does not interact with the shock if

$$-\varepsilon_2 \leq \mu_2 \leq 1\,. \tag{8.67}$$

Thus, if the velocity distribution of pickup ions on their arrival at the termination shock is known, Equations (8.54)-(8.67) allow one to calculate the velocity distributions (upstream and downstream) after their interaction with the shock. As we have mentioned above, upstream and downstream of the shock pickup ions can experience pitch-angle scattering which provides a way for reflected and transmitted particles to return to the shock. To describe this process, we solve a kinetic transport equation for the anisotropic velocity distribution function of pickup ions near the termination shock taking into account pitch-angle and energy diffusion (see Chalov and Fahr, 2000).

We use here a one-dimensional planar approximation for the plasma flow close to the termination shock. When the x-axis is directed perpendicular to the shock front from the upstream to the downstream part of the flow, then the transport equation (8.7) for the evolution of the velocity distribution function $f = f(t, x, v, \mu)$ of pickup ions can be written in the form:

$$\frac{\partial f}{\partial t} + (V_{\mathrm{SW},x} + v\mu\chi)\,\frac{\partial f}{\partial x} = \hat{S}f\,, \tag{8.68}$$

where the scattering operator $\hat{S}f$ is given by Equation (8.3).

One can see that the reflection conditions depend essentially on the geometry of the interplanetary magnetic field near the termination shock. If the termination

shock had a spherically symmetric shape and the centre of the sphere was at the Sun position, then the interplanetary magnetic field would be nearly perpendicular to the shock-normal for the largest part of the shock surface, as is usually assumed in the literature. However, the real termination shock has an upwind-downwind asymmetry due to the interaction of the solar wind with the moving interstellar medium. Figure 8.8 shows the shock-normal angle as a function of the angle counted from the direction of the Sun's motion relative to the LISM. This dependence was obtained from numerical calculations in the frame of the self-consistent two-dimensional model by Baranov and Malama (1993) for typical parameters of the solar wind and LISM. It is evident that the shock-normal angle, Ψ, depends significantly on the off-axis angle (angle between the solar radian and the interstellar wind axis). While the nose and tail parts of the termination shock it is almost perpendicular, the shock-normal angle can be as small as 70° at the flanks of the shock. It can then be estimated from Equation (8.51) that the minimum reflection velocity at the flanks is only two times larger than $V_{\rm sh}$. We can conclude, therefore, that pickup ions can experience the shock-drift acceleration at the termination shock even in the case where their speeds are only several times larger than the solar wind speed, and the efficiency of the acceleration depends strongly on where at the shock surface it takes place.

We should emphasize, however, that while the interplanetary magnetic field has the Parker structure on average in the outer heliosphere, measurements from spacecraft show that the distributions of the angle between the magnetic field and the solar wind flow direction are rather broad, with a half width of about 25° (Smith, 1993). It means that even at the nose part of the termination shock the shock-normal angle can be smaller than 90° for some time periods.

Figure 8.9 shows calculated fluxes (in the solar wind rest frame) of pickup protons downstream of the termination shock at different values of the shock-normal angle: $\Psi = 70°, 80°$, and 85° (see also Chalov and Fahr, 2000; Chalov, 2005). In order to calculate these fluxes, the stochastic acceleration in the supersonic solar wind has been taken into account with $\zeta_{\rm mE} = 0.5$, $\zeta_{\rm AE} = 0.05$ (solid lines) and $\zeta_{\rm mE} = 0.5$, $\zeta_{\rm AE} = 0.1$ (dashed line). The heavy solid line is the ACR hydrogen spectrum at the termination shock estimated by Cummings and Stone (1996).

It can be seen from Figure 8.9 that the downstream fluxes consist of two parts. The low energy parts are formed by ions which were directly transmitted through the shock front and did not suffer multiple reflections. The high energy parts of the fluxes are formed by ions which did suffer multiple reflections at the shock. It should be mentioned that the planar shock approximation which we use here to describe the interaction of the pickup ions with the shock front is valid for particles with low and intermediate energies only, so we restricted our consideration to energies < 10 MeV. Furthermore, at high energies the cross-field diffusion, which was ignored in the present model, can be of considerable importance in the acceleration mechanism.

The second interesting feature which can be seen in Figure 8.9 is the strong dependence of the downstream fluxes on the shock-normal angle. In the case of small Ψ the termination shock produces much higher fluxes of accelerated ions in the energy range from several tens of keV to about 10 MeV than in the case of large Ψ. This fact can be explained by increasing the reflection efficiency when the

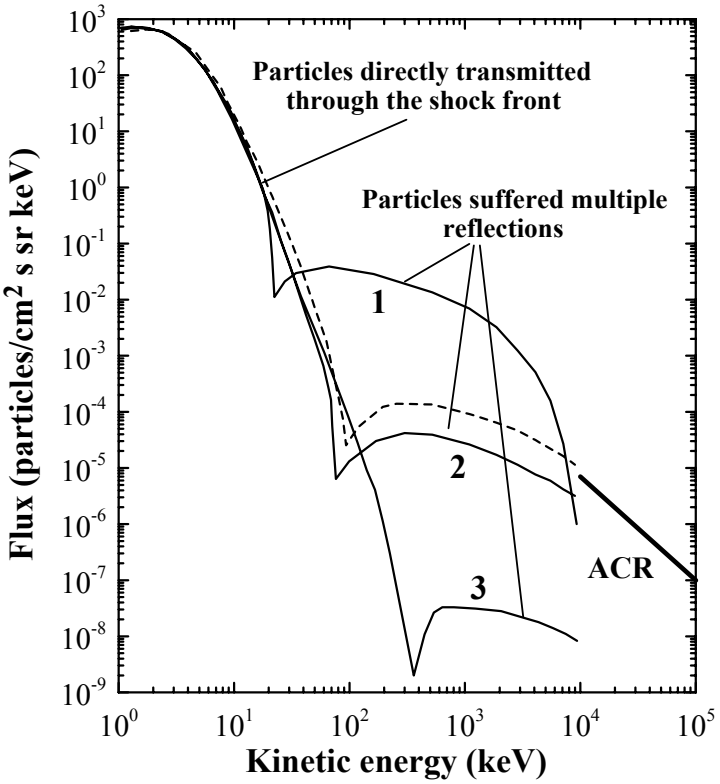

Figure 8.9: Downstream fluxes of pickup protons in the solar wind rest frame for different values of the shock-normal angle at $\zeta_{\rm mE} = 0.5$, $\zeta_{\rm AE} = 0.05$ (solid lines) and $\zeta_{\rm mE} = 0.5$, $\zeta_{\rm AE} = 0.1$ (dashed line). 1–$\Psi = 70°$, 2–$\Psi = 80°$, 3–$\Psi = 85°$. The heavy solid line is the estimated ACR hydrogen spectrum at the termination shock according to Cummings and Stone (1996).

shock-normal angle decreases. However, though the reflection efficiency decreases when Ψ increases, the maximum energy that particles can reach due to reflections increases with Ψ. The dependence of the fluxes on the shock-normal angle will result in their dependence on the off-axis angle measured from the direction to the inflowing LISM. Note, however, that the off-axis gradients will be partially smoothed out at high energies due to the diffusion of particles along the magnetic field lines downstream of the termination shock.

8.5 Concluding remarks

Since the speed of pickup ions in the rest frame of the termination shock varies approximately from 0 to $2V_{\rm sh}$, some portion of the ions will approach the shock front with a relatively low speed. These low speed ions can experience specular reflection by the electrostatic shock potential barrier and gain some energy in the

motional electric field. Zank et al. (1996b) and Lee et al. (1996) have shown that pickup ions trapped in the vicinity of the shock front by the electrostatic cross shock potential and Lorentz force can, under certain conditions, reach sufficiently high energies to be involved in the diffusive acceleration process. The advantage of this shock surfing mechanism lies in the fact that it operates without any pre-acceleration in the supersonic solar wind. However, the efficiency of this mechanism depends essentially on the fine shock structure. Namely, the maximum energy gain varies in inverse proportion to the square of the cross-shock potential length scale: $E_{\max} \sim L_{\rm s}^{-2}$. Zank et al. (1996b) assume that $L_{\rm s} \approx L_{\rm ramp}$, where $L_{\rm ramp}$ is the thickness of the shock ramp. $L_{\rm ramp}$ ranges from the electron inertial length $\lambda_{\rm e} = c/\omega_{\rm e}$ to the ion inertial length $\lambda_{\rm i} = c/\omega_{\rm i}$, where $\omega_{\rm e}$ and $\omega_{\rm i}$ are the electron and ion plasma frequencies, respectively. Acceleration by shock surfing is very efficient in the case where $L_{\rm ramp} \approx \lambda_{\rm e}$ and negligible at $L_{\rm ramp} \sim \lambda_{\rm i}$. At present there is not a reasonable theory describing the fine structure of supercritical collisionless shocks.

Balikhin et al. (1995) presented measurements of the shock parameters including the ramp thickness corresponding to 11 crossings of the Earth's bow shock. In all cases $\lambda_{\rm e} \ll L_{\rm ramp} \ll \lambda_{\rm i}$ or $L_{\rm ramp} \sim \lambda_{\rm i}$. In addition, it has been shown by Scudder (1995) and Scholer et al. (2003) that the cross-shock potential length scale can be much larger than the ramp thickness. Taken together these studies impose strong restrictions on the efficiency of the shock surfing process at the termination shock.

Of interest is a possible dependence of the efficiency of the shock surfing acceleration on the shock-normal angle. It is known that in the frame of a two-fluid model the thickness of a fast magnetosonic shock wave is of the order of $\lambda_{\rm e}$ when $\Psi > \Psi_{\rm c}$. As Ψ decreases from $\Psi_{\rm c}$, the thickness increases considerably from $\sim \lambda_{\rm e}$ to $\sim \lambda_{\rm i}$. In low β plasma (β = plasma to magnetic field pressure) the critical angle is defined by

$$\Psi_{\rm c} = \arctan\left(m_{\rm i}/m_{\rm e}\right)^{1/2} , \tag{8.69}$$

and it decreases when finite β effects are taken into account (see, e.g., Ohsawa, 1986 and references therein). One can therefore expect that the ramp thickness at perpendicular shocks is smaller than at quasi-perpendicular shocks. This expectation is confirmed by the fact that the shock with the smallest measured ramp scale ($2\lambda_{\rm e}$) was almost perpendicular (Newbury and Russell, 1996), while the shock with the largest ramp scale ($0.5\lambda_{\rm i}$) of 11 shocks analyzed by Balikhin et al. (1995) was quasi-perpendicular with $\Psi = 64^\circ$.

From the above reasoning and taking into account the results presented in Figures 8.8 and 8.9, we can propose the following schematic picture for the injection mechanism at the termination shock: at the nose and tail parts of the shock, where it is almost perpendicular, the shock surfing mechanism operates, while at the flanks of the shock the prevailing acceleration mechanism is the shock-drift acceleration based on multiple reflections of pickup ions from the magnetic field jump. However, this picture of the acceleration mechanisms can be changed to some extent if fluctuations of the magnetic field direction in the outer heliosphere are taken into account. Due to the fluctuations, the shock-normal angles near the nose and tail parts of the termination shock can be smaller than 90° for some

time intervals, with the result that reflections of pickup ions and the shock-drift acceleration can take place even there.

Acknowledgements

This work was supported by INTAS cooperation project 2001-0270, RFBR grants 03-02-04020, 04-01-00594, 04-02-16559, and the International Space Science Institute in Bern.

Appendix

8.A Averaging of the kinetic equation for the velocity distribution function of pickup ions over gyrophase

Equation (8.1) is written in the inertial frame. It is convenient to use this frame if the velocities of energetic particles are much larger than the bulk velocity of background plasma, since velocity anisotropy in this case is low. If, however, the thermal velocities of energetic particles and bulk velocity of background plasma are comparable, as with pickup ions, transformation of the velocity space from the inertial frame to a local co-moving frame is desirable. We therefore define the velocity variable $\mathbf{v}$ measured in the reference frame moving with velocity $\mathbf{U}(t,\mathbf{x})$ by $\mathbf{v}' = \mathbf{U} + \mathbf{v}$. Transforming Equation (8.1) into the variables $(t,\mathbf{x},\mathbf{v})$ yields

$$\frac{\partial f}{\partial t} + (U_i + v_i)\frac{\partial f}{\partial x_i} + \left[\Omega_{\mathrm{g}}\left(\mathbf{v}\times\mathbf{b}\right)_i - \frac{\partial U_i}{\partial t} - (U_j + v_j)\frac{\partial U_i}{\partial x_j}\right]\frac{\partial f}{\partial v_i} = \mathcal{R}\,, \quad (8.70)$$

where Ω_{g} is the gyrofrequency, $\mathbf{b}$ is the unit vector of the large-scale magnetic field, $\mathcal{R}$ denotes the right-hand side of Equation (8.1), and summations are implied where repeated subscripts appear.

If the large-scale magnetic field is sufficiently strong, transport of energetic particles is essentially affected by the action of the Lorentz force. It is convenient in this case to consider the motion of a particle as consisting of gyration around a field line and streaming along the line and to introduce new velocity variables v, μ, φ instead of Cartesian coordinates v_i, where v is the magnitude of the velocity, μ is the cosine of the pitch-angle ξ, and φ is the gyrophase angle. We assume in the following that the gyroperiod of energetic particles is much smaller than other timescales and their gyroradius is much smaller than other spatial scales. In this case the term with Ω_{g} is dominant in Equation (8.70). One can easily show then that the velocity distribution function f does not depend on φ, or in other words this term equals zero if $\partial f/\partial\varphi = 0$.

Therefore, in addition to the Cartesian coordinate system $(\mathbf{e}_1,\mathbf{e}_2,\mathbf{e}_3)$ we introduce a new orthogonal coordinate system $(\mathbf{i}_1,\mathbf{i}_2,\mathbf{i}_3)$ related to the large-scale magnetic field orientation by (see Fig. 8.10)

$$\mathbf{i}_3 = \mathbf{b}\,, \qquad \mathbf{i}_1 = \frac{\mathbf{b}\times\mathbf{e}_3}{|\mathbf{b}\times\mathbf{e}_3|}\,, \qquad \mathbf{i}_2 = \mathbf{i}_1\times\mathbf{i}_3 = \frac{(\mathbf{b}\times\mathbf{e}_3)\times\mathbf{b}}{|\mathbf{b}\times\mathbf{e}_3|}\,. \quad (8.71)$$

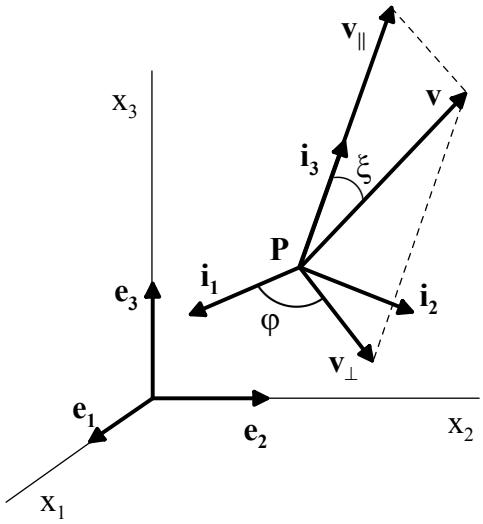

Figure 8.10: Velocity of pickup ions in the inertial and moving coordinate systems.

The following relations between v_i and v, μ are valid

$$v = \left(\sum_{i=1}^{3} v_i^2 \right)^{1/2} , \qquad \mu = v_i b_i \left(\mathbf{x} \right) / v \, . \tag{8.72}$$

The velocity vector $\mathbf{v}$ can be written in the two velocity coordinate systems as

$$\mathbf{v} = v_i \mathbf{e}_i = v_\perp \cos\varphi \, \mathbf{i}_1 + v_\perp \sin\varphi \, \mathbf{i}_2 + v_\parallel \mathbf{i}_3 =$$
$$v\mu \mathbf{b} + \frac{v\sqrt{1-\mu^2}}{|\mathbf{b} \times \mathbf{e}_3|} \left\{ (\mathbf{b} \times \mathbf{e}_3) \cos\varphi + [(\mathbf{b} \times \mathbf{e}_3) \times \mathbf{b}] \sin\varphi \right\} , \tag{8.73}$$

where

$$v_\parallel = v\mu \, , \qquad v_\perp = v\sqrt{1-\mu^2} \, . \tag{8.74}$$

The spatial and velocity derivatives are given by

$$\frac{\partial f}{\partial x_i} \to \frac{\partial f}{\partial x_i} + \frac{\partial \mu}{\partial x_i} \frac{\partial f}{\partial \mu} = \frac{\partial f}{\partial x_i} + \frac{v_j}{v} \frac{\partial b_j}{\partial x_i} \frac{\partial f}{\partial \mu} \, , \tag{8.75}$$

and

$$\frac{\partial f}{\partial v_i} = \frac{\partial v}{\partial v_i} \frac{\partial f}{\partial v} + \frac{\partial \mu}{\partial v_i} \frac{\partial f}{\partial \mu} = \frac{v_i}{v} \frac{\partial f}{\partial v} + \left(\frac{b_i}{v} - \mu \frac{v_i}{v^2} \right) \frac{\partial f}{\partial \mu} \, . \tag{8.76}$$

Let us insert (8.75) into Equation (8.70) and average this equation over gyrophase φ taking into account that f does not depend on φ. We will then have

$$\frac{\partial f}{\partial t} + \left(U_i + \langle v_i \rangle \right) \frac{\partial f}{\partial x_i} + \left(U_i \langle v_j \rangle + \langle v_i v_j \rangle \right) \frac{1}{v} \frac{\partial b_j}{\partial x_i} \frac{\partial f}{\partial \mu} -$$
$$- \left(\frac{\partial U_i}{\partial t} + U_j \frac{\partial U_i}{\partial x_j} \right) \left\langle \frac{\partial f}{\partial v_i} \right\rangle - \frac{\partial U_i}{\partial x_j} \left\langle v_j \frac{\partial f}{\partial v_i} \right\rangle = \langle \mathcal{R} \rangle \, . \tag{8.77}$$

From Equation (8.73) one can obtain averaged velocities

$$\langle v_i \rangle = v\mu b_i \,, \qquad \langle v_i v_j \rangle = \frac{1-\mu^2}{2} v^2 \delta_{ij} + \frac{3\mu^2-1}{2} v^2 b_i b_j \,, \tag{8.78}$$

while averaged velocity derivatives can be obtained from Equation (8.77):

$$\left\langle \frac{\partial f}{\partial v_i} \right\rangle = \left(\mu \frac{\partial f}{\partial v} + \frac{1-\mu^2}{v} \frac{\partial f}{\partial \mu} \right) b_i \,, \tag{8.79}$$

$$\left\langle v_j \frac{\partial f}{\partial v_i} \right\rangle = \left(\frac{1-\mu^2}{2} \delta_{ij} + \frac{3\mu^2-1}{2} b_i b_j \right) v \frac{\partial f}{\partial v} + \\ + \frac{1-\mu^2}{2} \left(3\mu b_i b_j - \mu \delta_{ij} \right) \frac{\partial f}{\partial \mu} \,. \tag{8.80}$$

Inserting Equations (8.78)-(8.80) into Equation (8.77) and taking into account that $b_i b_i = 1$ or $b_i \partial b_i / \partial x_j = 0$, we will obtain Equation (8.2). In this equation we omit average $\langle ... \rangle$ in the right-hand side.

8.B Distribution of interstellar atoms in the heliosphere in the limit of low temperatures

Let us consider the spatial distribution of particles (interstellar atoms) in the vicinity of a point force field source (the Sun). If the flow of the particles is uniform at large distances, their spatial distribution is axisymmetric. We assume that the central force is spherically symmetric and is a combination of gravitational attraction and repulsion by the radiation pressure. Here we neglect chaotic (thermal) velocities of particles, so all the particles have the same velocity $\mathbf{V}_\infty$ at infinity.

When a particle moves under the action of the central force field, their angular momentum $\mathbf{l}$ is conserved:

$$\mathbf{l} = \mathbf{r} \times \mathbf{V} = const \,. \tag{8.81}$$

Since $\mathbf{l} \perp \mathbf{r}$, the position vector $\mathbf{r}$ of the particle always lies in the same plane. The trajectory of the particle in the plane is hyperbolic with the central body as focus. Conservation of $\mathbf{l}$ and the total energy allows one to determine trajectories and velocities of particles in any such plane. We will follow further the approach presented by *Axford* [1972]. Taking polar coordinates (r, Θ), where $0 \le \Theta < 2\pi$, we can write the trajectory of a particle as

$$\frac{A}{r} = 1 + B \sin\left(\Theta + \alpha\right) \,, \tag{8.82}$$

where

$$A = \frac{l^2}{V_\infty^2} C \,, \quad B = \left(1 + AC\right)^{1/2} \,, \quad C = \frac{V_\infty^2}{\left(1-\eta\right) G M_\odot} \,, \quad \sin\alpha = -\frac{1}{B} \,,$$

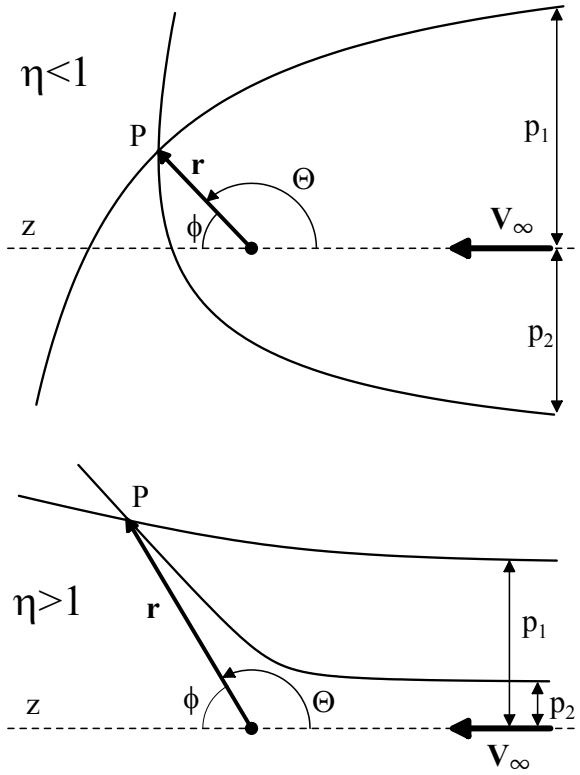

Figure 8.11: Trajectories of interstellar atoms in the heliosphere in the cases when $\eta < 1$ (upper) and $\eta > 1$ (bottom).

G is the gravitational constant, $M_\odot$ is the mass of the Sun, η is the ratio of the radiation pressure and gravitational attraction, l is the angular momentum of the particle about the Sun, and the direction $\Theta = 0$ is antiparallel to $\mathbf{V}_\infty$.

Any point in the plane (r, Θ) is a point of intersection of two trajectories (direct and indirect) with angular momenta given by

$$l_{1,2} = V_\infty \left[\frac{1}{2} r \sin\Theta \pm \sqrt{\left(\frac{1}{2} r \sin\Theta \right)^2 + \frac{r}{C} (1 - \cos\Theta)} \right] . \tag{8.83}$$

Direct and indirect trajectories are shown schematically in Figure 8.11 for two cases when the combined force is attraction ($\eta < 1$) and repulsion ($\eta > 1$). Instead of the angular momenta l, the impact parameters p are presented in the figure (see below). The velocity components in the r and Θ directions are

$$V_r = \pm \left[\left(1 + \frac{2}{Cr} \right) V_\infty^2 - \frac{l^2}{r^2} \right]^{1/2} , \quad V_\Theta = \frac{l}{r} . \tag{8.84}$$

The number density n of interstellar atoms in the vicinity of the Sun can be calculated from the equation of continuity. The velocity vector in this equation is given by Equations (8.84).

$$\operatorname{div}(n\mathbf{V}) = -P_{\rm loss} n\,, \tag{8.85}$$

where $P_{\rm loss}$ is the loss rate of interstellar atoms due to ionization processes. One way to solve Equation (8.85) is to introduce a local orthogonal coordinate system $\left(x^1, x^2, x^3\right)$ such that the axis x^1 is directed along a trajectory given by Equation (8.82) and x^3 is the azimuthal coordinate relative to the axis of symmetry $\Theta = 0$. In the frame of this local coordinate system Equation (8.85) can be written as

$$\frac{1}{\sqrt{g_{11} g_{22} g_{33}}}\,\frac{\partial}{\partial x^1}\left(nV\sqrt{g_{22} g_{33}}\right) = -P_{\rm loss} n\,, \tag{8.86}$$

where g_{ik} are components of metric tensor which determines an line element ds by

$$ds^2 = \sum_{i=1}^{3}\sum_{k=1}^{3} g_{ik}\left(x^1, x^2, x^3\right) dx^i dx^k\,. \tag{8.87}$$

In the case of orthogonal coordinate systems $g_{ik} = 0$ if $i \neq k$.

Integration of Equation (8.86) gives

$$\int_{-\infty}^{x^1} d\left[\ln\left(nV\sqrt{g_{22} g_{33}}\right)\right] = -\int_{-\infty}^{x^1} \frac{P_{\rm loss}}{V}\,\sqrt{g_{11}}\,dx^1\,. \tag{8.88}$$

Equation (8.87) allows one to determine the metric tensor components. If dx^1 is the value of the displacement along a trajectory then

$$g_{11} = 1\,, \quad dx^1 = Vr\,d\Theta/V_\Theta\,. \tag{8.89}$$

Taking $x^2 = l/V_\infty$ and assuming that x^3 is the azimuthal angle, one can obtain

$$g_{22} = \frac{r^2\sin^2\Theta + 4r\left(1-\cos\Theta\right)/C}{1 + 2/rC}\,\frac{V_\infty^2}{l^2}\,, \quad g_{33} = r^2\sin^2\Theta\,. \tag{8.90}$$

Then assuming that $P_{\rm loss} = P_{\rm loss}\left(r_{\rm E}\right) r_{\rm E}^2/r^2$, the spatial distribution of interstellar atoms can be easily obtained from Equation (8.88). It is convenient to introduce the off-axis angle ϕ ($\phi = |\pi - \Theta|$, $0 \leq \phi \leq \pi$) instead of Θ and the impact parameters $p_{1,2}$ (see Equation 8.18) instead of the angular momenta. The final solution of Equation (8.86) is given by Equation (8.17), where n_∞ is the number density of atoms at large distances from the Sun.

8.C Modified cold model for interstellar helium

For interstellar helium atoms the radiation pressure is considerably smaller than the gravitational attraction, that is $\eta = 0$ and, hence, $C = V_\infty^2/GM_\odot$. Then in the frame of the cold model the number density of atoms given by Equation (8.17) increases without limit when $\phi \to 0$. This uncertainty can be removed if the

thermal velocities of atoms are taken into account. The simplest analytical model for the interstellar atom distribution in the heliosphere, which incorporates their thermal velocities was proposed by Feldman et al. (1972). The model gives an appropriate expression for the number density of helium near the semi-axis $\eta = 0$ at $mV_\infty^2/2k_\mathrm{B}T_\infty \gg 1$, where T_∞ is the temperature of atoms of mass m in the interstellar medium and k_B is the Boltzmann constant. The analytical expression at $\phi = 0$ can be obtained by integrating $n\,(r, \phi)$ weighted by an isotropic Maxwellian velocity distribution function $F\left(\mathbf{V}_\infty^{'}\right)$ over $\mathbf{V}_\infty^{'}$, where

$$F\left(\mathbf{V}_\infty^{'}\right) = \left(\frac{m}{2\pi k_\mathrm{B}T_\infty}\right)^{3/2} \exp\left[-\frac{m}{2k_\mathrm{B}T_\infty}\left(\mathbf{V}_\infty^{'} - \mathbf{V}_\infty\right)^2\right]. \tag{8.91}$$

At $\phi \ll 1$ (here ϕ is the angle between the bulk flow velocity vector $\mathbf{V}_\infty$ and $\mathbf{V}_\infty^{'}$) the Maxwellian distribution can be written as

$$F\left(\mathbf{V}_\infty^{'}\right) = \left(\frac{m}{2\pi k_\mathrm{B}T_\infty}\right)^{3/2} \exp\left[-\frac{m}{2k_\mathrm{B}T_\infty}\left(V_\infty^{'} - V_\infty\right)^2\right] \times \\ \times \exp\left[-\frac{m}{2k_\mathrm{B}T_\infty} V_\infty^{'} V_\infty \phi^2\right]. \tag{8.92}$$

Then the number density of helium atoms in the frame of the modified cold model at $\phi = 0$ is

$$\begin{aligned} n^\mathrm{M}(r, 0) &= \int n\,(r, \phi \to 0)\, F\left(\mathbf{V}_\infty^{'}\right) d\mathbf{V}_\infty^{'} \\ &= 2\pi \int_0^\infty \int_0^\pi n\,(r, \phi \to 0)\, F\left(\mathbf{V}_\infty^{'}\right) V_\infty^2 \sin\phi\, dV_\infty^{'} d\phi\,, \end{aligned} \tag{8.93}$$

where axisymmetry of the velocity distribution relative to the vector $\mathbf{V}_\infty$ is taken into account. The function $n\,(r, \phi \to 0)$ can easily be found from Equation (8.17):

$$\frac{n\,(r, \phi \to 0)}{n_\infty} = \frac{1}{\phi}\left(\frac{2}{Cr}\right)^{1/2} \exp\left[-\frac{\pi r_\mathrm{E}^2 P_\mathrm{loss}\,(r_\mathrm{E})}{\sqrt{2r/C}\, V_\infty}\right]. \tag{8.94}$$

In order to evaluate the integrals in Equation (8.93) exactly we extend the limits of integration for ϕ to $+\infty$ since $mV_\infty^{'}V_\infty/2k_\mathrm{B}T_\infty \gg 1$ and the exponential will cut off the integral. The result for the modified number density at $\phi = 0$ is

$$\frac{n^\mathrm{M}(r, 0)}{n_\infty} = \left(\frac{\pi G M_\odot m}{r k_\mathrm{B} T_\infty}\right)^{1/2} \exp\left[-\frac{\pi r_\mathrm{E}^2 P_\mathrm{loss}\,(r_\mathrm{E})}{\sqrt{2r/C}\, V_\infty}\right]. \tag{8.95}$$

Off-axis values of n^M are constructed using the parabolic-interpolation formula

$$n^\mathrm{M}(r, \phi) = n^\mathrm{M}(r, 0)\left(1 - D\phi^2\right). \tag{8.96}$$

The value of D is determined by the imposed constraints

$$n^\mathrm{M}(r, \phi_\mathrm{c}) = n\,(r, \phi_\mathrm{c})\,, \quad \frac{\partial n^\mathrm{M}(r, \phi_\mathrm{c})}{\partial \phi} = \frac{\partial n\,(r, \phi_\mathrm{c})}{\partial \phi} \tag{8.97}$$

at some angle ϕ_c. The values of D and ϕ_c obtained from Equations (8.97) are given by Equations (8.24) and (8.26). Thus at $\phi > \phi_\mathrm{c}$ the number density is given by Equation (8.17) (cold model), and at $\phi \le \phi_\mathrm{c}$ by Equation (8.25) (modified cold model). In the latter equation, the index "M" is omitted.

Bibliography

Axford, W.I., The interaction of the solar wind with the interstellar medium, in C.P. Sonnett, P.J. Coleman, Jr., and J.M. Wilcox (eds.), The solar wind, NASA SP-308, 609, 1972.

Balikhin, M., Krasnosselskikh, V., and Gedalin, M., The scales in quasiperpendicular shocks, *Adv. Space Res.* **15**, 247–260, 1995.

Balogh, A., Smith, E.J., Tsurutani, B.T., Southwood, D.J., Forsyth, R.J., and Horbury, T.S., The heliospheric magnetic field over the sourth polar region of the Sun, *Science* **268**, 1007–1010, 1995.

Baranov, V.B. and Malama, Y.G., The model of the solar wind interaction with the local interstellar medium: Numerical solution of self-consistent problem, *J. Geophys. Res.* **98**, 15157–15163, 1993.

Barnes, A., Collisionless damping of hydromagnetic waves, *Phys. Fluids* **9**, 1483, 1966.

Barnes, A., Quasi-linear theory of hydromagnetic waves in collisionless plasma, *Phys. Fluids* **11**, 2644, 1968a.

Barnes, A., Collisionless heating of the solar wind plasma, 1. Theory of the heating of collisionless plasma by hydromagnetic waves, *Astrophys. J.* **154**, 751, 1968b.

Barnes, A., Collisionless heating of the solar wind plasma, 2. Application of the theory of plasma heating by hydromagnetic waves, *Astrophys. J.* **155**, 311, 1969.

Bieber, J.W., Wanner, W., Matthaeus, W.H., Dominant two-dimensional solar wind turbulence with implications for cosmic ray transport, *J. Geophys. Res.* **101**, 2511–2522, 1996.

Blum, P.W. and Fahr, H.J., Interaction between interstellar hydrogen and the solar wind, *Astron. Astrophys.* **4**, 280, 1970.

Bogdan, T.J., Lee, M.A., and Schneider, P., Coupled quasi-linear wave damping and stochastic acceleration of pick-up ions in the solar wind, *J. Geophys. Res.* **96**, 161–178, 1991.

Chalov, S.V., Acceleration of pick-up ions at the solar wind termination shock, *Astrophys. Space Sci.* **274**, 25–33, 2000.

Chalov, S.V., Acceleration of interplanetary pick-up ions and anomalous cosmic rays, *Adv. Space Res.* **35**, 2106–2114, 2005.

Chalov, S.V. and Fahr, H.J., Reflection of pre-accelerated pick-up ions at the solar wind termination shock, *Solar Phys.* **168**, 389–411, 1996.

Chalov, S.V. and Fahr, H.J., Phase space diffusion and anisotropic pick-up ion distributions in the solar wind: an injection study, *Astron. Astrophys.* **335**, 746–756, 1998.

Chalov, S.V. and Fahr, H.J., Signatures of the interplanetary helium cone reflected by pick-up ions, *Solar Phys.* **187**, 123–144, 1999.

Chalov, S.V. and Fahr, H.J., Pick-up ion acceleration at the termination shock and the post-shock pick-up ion energy distribution, *Astron. Astrophys.* **360**, 381–390, 2000.

Chalov, S.V. and Fahr, H.J., Interstellar helium pick-up ions in the region of the solar gravitational focusing cone, *Astron. Lett.* **32**, 2006.

Chalov, S.V., Fahr, H.J., and Izmodenov, V., Spectra of energized pick-up ions upstream of the heliospheric termination shock. I. The role of Alfvénic turbulences,

Astron. Astrophys. **304**, 609–616, 1995.

Chalov, S.V., Fahr, H.J., and Izmodenov, V., Spectra of energized pick-up ions upstream of the two-dimensional heliospheric termination shock. II. Acceleration by Alfvénic and by large-scale solar wind turbulence, *Astron. Astrophys.* **320**, 659–671, 1997.

Chalov, S.V., Fahr, H.J., and Izmodenov, V., Evolution of pickup proton spectra in the inner heliosheath and their diagnostics by energetic neutral atoms, *J. Geophys. Res.* **108**, 1266, 2003.

Chalov, S.V., Alexashov, D.B., and Fahr, H.J., Reabsorption of self-generated turbulent energy by pick-up protons in the outer heliosphere, *Astron. Astrophys.* **416**, L31–L34, 2004.

Cummings, A.C. and Stone, E.C. Composition of anomalous cosmic rays and implications for the heliosphere, *Space Sci. Rev.* **78**, 117–128, 1996.

Decker, R.B., Computer modeling of test particle acceleration at oblique shocks, *Space Sci. Rev.* **48**, 195–262, 1988.

Decker, R.B., Krimigis, S.M., Roelof, E.C., et al., Voyager 1 in the foreshock, termination shock, and heliosheath, *Science* **309**, 2020–2024, 2005.

Fahr, H.J., On the influence of neutral interstellar matter on the upper atmosphere, *Astrophys. Space Sci.* **2**, 474–495, 1968.

Feldman, W.C., Lange, J.J., and Scherb, F., Interstellar helium in interplanetary space, in C.P. Sonnett, P.J. Coleman, Jr., and J.M. Wilcox (eds.), The solar wind, NASA SP-308, 684, 1972.

Fichtner, H., Anomalous cosmic rays: Messengers from the outer heliosphere, *Space Sci. Rev.* **95**, 639–754, 2001.

Fichtner, H., le Roux, J.A., Mall, U., and Rucinsci, D., On the transport of pick-up ions in the heliosphere, *Astron. Astrophys.* **314**, 650–662, 1996.

Fisk, L.A., The acceleration of energetic particles in the interplanetary medium by transit time damping, *J. Geophys. Res.* **81**, 4633–4645, 1976.

Fisk, L.A. and Gloeckler, G., The common spectrum for accelerated ions in the quiet-time solar wind, *Astrophys. J. 640*, L79–L82, 2006.

Fisk, L.A., Kozlovsky, B., Ramaty, R., An interpretation of the observed oxygen and nitrogen enhancements in low-energy cosmic rays, *Astrophys. J. 190*, L35–L37, 1974.

Fisk, L.A., Schwadron, N.A., Gloeckler, G., Implications of fluctuations in the distribution functions of interstellar pickup ions for the scattering of low rigidity particles, *Geophys. Res. Lett.* **24**, 93–96, 1997.

Fisk, L.A., Gloeckler, G., Zurbuchen, T.H., and Schwadron, N.A., Ubiquitous statistical acceleration in the solar wind, In Acceleration and Transport of Energetic Particles Observed in the Heliosphere, ACE-2000 Symposium, eds. R.A. Mewaldt, J.R. Jokipii, M.A. Lee, E. Möbius, and T.H. Zurbuchen (AIP), 229–233, 2000.

Gazis, P.R., McDonald, F.B., Burger, R.A., et al. Corotating interaction regions in the outer heliosphere, *Space Sci. Rev. 89*, 269–305, 1999.

Giacalone, J., The physics of particle acceleration by collisionless shocks, *Planetary Space Sci.* **51**, 659–664, 2003.

Giacalone, J. and Jokipii, J.R., The transport of cosmic rays across a turbulent magnetic field, *Astrophys. J.* **520**, 204–214, 1999.

Giacalone, J. and Ellison, D.C., Three-dimensional numerical simulations of particle injections and accelerations at quasi-perpendicular shocks, *J. Geophys. Res.* **105**, 12541–12556, 2000.

Gloeckler, G., Ubiquitous suprathermal tails on the solar wind and pickup ion distributions, Proc. Solar Wind 10 Conf. AIP. 679, 583–588, 2003.

Gloeckler, G., Geiss, J., Balsiger, H., Fisk, L.A., Galvin, A.B., Ipavich, F.M., Ogilvie, K.W., von Steiger, R., Wilken, B., Detection of interstellar pick-up hydrogen in the solar system, *Science* **261**, 70–73, 1993.

Gloeckler, G., Geiss, J., Roelof, E.C., Fisk, L.A., Ipavich, F.M., Ogilvie, K.W., Lanzerotti, L.J., von Steiger, R., and Wilken, B., Acceleration of interstellar pickup ions in the disturbed solar wind observed on Ulysses, *J. Geophys. Res.* **99**, 17637–17643, 1994.

Gloeckler, G., Schwadron, N.A., Fisk, L.A., and Geiss, J., Weak pitch angle scattering of few MV rigidity ions from measurements of anisotropies in the distribution function of interstellar pickup H^+, *Geophys. Res. Lett.* **22**, 2665–2668, 1995.

Gloeckler, G., Fisk, L.A., Zurbuchen, T.H., and Schwadron, N.A., Sources, injection and acceleration of the heliospheric ion population, In Acceleration and Transport of Energetic Particles Observed in the Heliosphere, ACE-2000 Symposium, eds. R.A. Mewaldt, J.R. Jokipii, M.A. Lee, E. Möbius, and T.H. Zurbuchen (AIP), 221–228, 2000.

Gloeckler, G., Möbius, E., Geiss, J., et al., Observations of the helium focusing cone with pickup ions, *Astron. Astrophys.* **426**, 845–854, 2004.

Hollweg, J.V., Transverse Alfvén waves in the solar wind: arbitrary $\mathbf{k}$, $\mathbf{v_0}$, $\mathbf{B_0}$, and $|\delta\mathbf{B}|$, *J. Geophys. Res.* **79**, 1539–1541, 1974.

Isenberg, P.A., Evolution of interstellar pickup ions in the solar wind, *J. Geophys. Res.* **92**, 1067–1073, 1987.

Isenberg, P.A., A hemispherical model of anisotropic interstellar pickup ions, *J. Geophys. Res.* **102**, 4719–4724, 1997.

Jokipii, J.R., Cosmic-ray transport propagation. I. Charged particles in a random magnetic field, *Astrophys. J.* **146**, 480–487, 1966.

Jokipii, J.R., Radial variation of magnetic fluctuations and the cosmoc-ray diffusion tensor in the solar wind, *Astrophys. J.* **182**, 585–600, 1973.

Jokipii, J.R., Rate of energy gain and maximum energy in diffusive shock acceleration, *Astrophys. J.* **313**, 842–846, 1987.

Jokipii, J.R., Constraints on the acceleration of the anomalous cosmic rays, *Astrophys. J.* **393**, L41–L43, 1992.

Jokipii, J.R., Giacalone, J., and Kota, J., Transverse streaming anisotropies of charged particles accelerated at the solar wind termination shock, *Astrophys. J.* **611**, L141–L144, 2004.

Kennel, C.F. and Engelmann, F., Velocity space diffusion from weak plasma turbulence in a magnetic field, *Phys. Fluids* **9**, 2377–2388, 1966.

Krimigis, S.M., Decker, R.B., Hamilton, D.C., Gloeckler, G. Observations of pickup ions in the outer heliosphere by Voyagers 1 and 2. In Acceleration and Transport of Energetic Particles Observed in the Heliosphere, ACE-2000 Symposium, eds. R.A. Mewaldt, J.R. Jokipii, M.A. Lee, E. Möbius, and T.H. Zurbuchen (AIP), 333–336, 2000.

Krimigis, S.M., Decker, R.B., Hill, M.E., et al., Voyagers 1 exited the solar wind at distance of ∼85 AU from the Sun, *Nature* **426**, 45–48, 2003.

le Roux, J.A. and Ptuskin, V.S., Self-consistent stochastic preacceleration of interstellar pick-up ions in the solar wind including effects of wave coupling and damping, *J. Geophys. Res.* **103**, 4799–4808, 1998.

le Roux, J.A., Zank, G.P., and Ptuskin, V.S., An evaluation of perpendicular diffusion models regarding cosmic ray modulation on the basis of a hydrodynamic description for solar wind turbulence, *J. Geophys. Res.* **104**, 24845–24862, 1999.

Lee, M.A., Shapiro, V.D., and Sagdeev, R.Z., Pickup ion energization by shock surfing, *J. Geophys. Res.* **101**, 4777–4789, 1996.

Matthaeus, W.H., Goldstein, M.L., Roberts, D.A., Evidance for the presence of quasi-two-dimensional nearly incompressible fluctuations in the solar wind, *J. Geophys. Res.* **95**, 20673, 1990.

McDonald, F.B., Stone, E.C., Cummings, A.C., et al., Enhancements of energetic particles near the heliospheric termination shock, *Nature* **426**, 48–51, 2003.

Möbius, E., Hovestadt, D., Klecker, B., Scholer, M., Gloeckler, G., Ipavich, F.M. Direct observations of He^+ pickup ions of interstellar origin in the solar wind, *Nature* **318**, 426–429, 1985.

Möbius, E., Rucinski, D., Hovestadt, D., Klecker, B., The helium parameters of the very local interstellar medium as derived from the distributions of He^+ pickup ions in the solar wind, *Astron. Astrophys.* **304**, 505–519, 1995.

Möbius, E., Rucinski, D., Lee, M.A., and Isenberg, P.A., Decreases in the antisunward flux of interstellar pickup He^+ associated with radial interplanetary magnetic field, *J. Geophys. Res.* **103**, 257–265, 1998.

Möbius, E., Bzowski, M., Chalov, S., et al., Synopsis of the interstellar He parameters from combined neutral gas, pickup ion and UV scattering observations and related consequences, *Astron. Astrophys.* **426**, 897–907, 2004.

Newbury, J.A. and Russell, C.T., Observations of a very thin collisionless shocks, *Geophys. Res. Lett.* **23**, 781–784, 1996.

Ohsawa, Y., Resonant ion acceleration by oblique magnetosonic shock wave in a collisionless plasma, *Phys. Fluids* **29**, 773–781, 1986.

Parker, E.N., Interplanetary dynamical processes, Interscience Publishers, New York, 1963.

Pesses, M.E., Jokipii, J.R., Eichler, D., Cosmic-ray drift, shock wave acceleration, and the anomalous component of cosmic rays, *Astrophys. J.* **246**, L85–L88, 1981.

Richardson, J.D., Wang, C., and Paularena, K.I., The solar wind in the outer heliosphere, *Adv. Space Res.* **27**, 471–479, 2001.

Roberts, D.A., Goldstein, M.L., Klein, L.W., Matthaeus, W.H., Origin and evolution of fluctuations in the solar wind: Helios observations and Helios-Voyager comparisons, *J. Geophys. Res.* **92**, 12023–12035, 1987.

Schlickeiser, R., Cosmic-ray transport and acceleration. I. Derivation of the kinetic equation and application to cosmic rays in static cold media, *Astrophys. J.* **336**, 243–263, 1989.

Schlickeiser, R., Dung, R., Jaekel, U., Interplanetary transport of solar cosmic rays and dissipation of Alfvén waves, *Astron. Astrophys.* **242**, L5, 1991.

Scholer, M., Shinohara, I., and Matsukiyo, S. Quasi-perpendicular shocks: Length scale of the cross-shock potential, shock reformation, and implication for shock

surfing, *J. Geophys. Res.* **108**, 1014, 2003.
Skilling, J., Cosmic rays in the Galaxy: convection or diffusion? *Astrophys. J.* **170**, 265–273, 1971.
Scudder, J.D., A review of the physics of electron heating at collisionless shocks, *Adv. Space Res.* **15**, 181–223, 1995.
Smith, E.J., Radial gradients in the interplanetary magnetic field between 1.0 and 4.3 AU: Pioneer 10, in C.T. Russell (ed.), Solar wind three, University of California Press, Los Angeles, 257, 1974.
Smith, E.J., Magnetic fields throughout the heliosphere, *Adv. Space Res.* **13**, 5, 1993.
Smith, E.J. and Balogh, A., Ulysses observations of the radial magnetic field, *Geophys. Res. Lett.* **22**, 3317–3320, 1995.
Stone, E.C., Cummings, A.C., McDonald, F.B., et al., Voyager 1 explores the termination shock region and the heliosheath beyond, *Science* **309**, 2017–2020, 2005.
Terasawa, T., Energy spectrum and pitch angle distribution of particles reflected by MHD shock waves of fast mode, *Planetary Space Sci.* **27**, 193, 1979.
Toptygin, I.N., Cosmic rays in interplanetary magnetic fields, Reidel, Dordrecht, 1983.
Vasyliunas, V.M. and Siscoe, G.L., On the flux and the energy spectrum of interstellar ions in the solar system, *J. Geophys. Res.* **81**, 1247–1252, 1976.
Whang, Y.G. and Burlaga, L.F., Evolution of recurrent solar wind structures between 14 AU and the termination shock, *J. Geophys. Res.* **93**, 5446–5460, 1988.
Whang, Y.G. and Burlaga, L.F., Radial evolution of interaction regions, in Physics of the Outer Heliosphere, eds. S. Grzeldzielski, D.E. Page, pp. 245–248, Pergamon, New York, 1990.
Wu, C.S. and Davidson, R.C., Electromagnetic instabilities produced by neutral-particle ionization in interplanetary space, *J. Geophys. Res.* **77**, 5399, 1972.
Zank, G.P., Matthaeus, W.H., and Smith, C.W., Evolution of turbulent magnetic fluctuation power with heliospheric distance, *J. Geophys. Res.* **101**, 17093–17107, 1996a.
Zank, G.P., Pauls, H.L., Cairns, I.H., and Webb, G.M., Interstellar pickup ions and quasi-perpendicular shocks: Implications for the termination shock and interplanetary shocks, *J. Geophys. Res.* **101**, 457–477, 1996b.

— 9 —

The Interplanetary Lyman-α Background

Eric Quémerais[1]
Service d'Aéronomie, CNRS, Verrières le Buisson, France

Abstract. **This chapter describes the problem of the Lyman-α background in the interplanetary medium. The interplanetary background is due to the scattering of solar Lyman-α photons by the hydrogen atoms present in the interplanetary medium. It was discovered at the end of the 1960's. This phenomenon results in the UV glow seen in all directions of space and which can be used to characterize the hydrogen distribution.**

We will present here the basic equations used to compute this Lyman-α emission. We will also discuss the radiative transfer equation and its application to this problem. We will compare results from radiative transfer computations and simplified approaches such as the optically thin approximation often used in other works. This will be done for both photometric and spectrometric studies.

The last section will detail some results obtained concerning the interplanetary hydrogen distribution from the study of interplanetary Lyman-α data obtained both in the inner and the outer heliosphere.

9.1 Introduction

The existence of the interplanetary Lyman-α background has been known for more than thirty years (Thomas and Krassa, 1971; Bertaux and Blamont, 1971). This emission is due to the presence of hydrogen atoms in the interplanetary medium which resonantly backscatter the solar H Lyman α photons emitted by the Sun. This phenomenon has been studied with many space instruments because it is a source of information on the interplanetary medium, the local interstellar medium, the solar wind, the heliospheric interface and activity distribution on the solar disk. Lists of previous space experiments studying the interplanetary UV background can be found in Ajello et al. (1987) and Quémerais et al. (1994). A review of interplanetary Lyman-α background studies can be found in Bertaux et al. (1996).

We can divide the study of the Lyman-α background into two main categories, photometric and spectroscopic, with different methods and applications.

In the inner heliosphere, full sky photometric observations allow one to derive latitudinal variations of the solar wind mass flux distribution from remote sensing, a method that is complementary to the in-situ measurements of Ulysses (Bertaux

[1]in *The Physics of the Heliospheric Boundaries*, V. Izmodenov and R. Kallenbach (eds.), ISSI Scientific Report No. 5, pp. 283 - 310, ESA-ESTEC, Paris 2006

et al., 1996). The SWAN instrument on the SOHO spacecraft, which was launched in December 1995, has been applying this technique quite successfully (Bertaux et al., 1997; Kyrölä et al., 1998).

Photometric observations also have an application in the outer heliosphere, say outside 40 AU. There, the hydrogen distribution is not affected by solar EUV photo-ionization or charge exchange with solar wind protons as is the case in the inner heliosphere. The H atoms are mainly influenced by the interface structure between the expanding solar wind and the ionized component of the interstellar medium. This interface is the object of much speculation concerning its nature, stability and actual position, as seen in various chapters of this book.

The neutral H atoms are coupled to the plasma components of the solar wind and of the interstellar medium through charge exchange processes. As a result, the outer heliosphere hydrogen distribution is substantially different from the case of the hot model where the H atom distribution is a simple Gaussian distribution with constant number density far away from the Sun (Thomas, 1978). One striking feature of the outer hydrogen atom distribution obtained by theoretical models including the effects of the heliospheric interface is the so-called hydrogen wall. This wall is due to a pile-up of neutral H atoms in the region where the interstellar plasma is strongly heated and decelerated. Charge exchange between slowed down interstellar protons and neutral hydrogen atoms leads to a new neutral hydrogen component. It is characterized by a large temperature and a small bulk velocity in the solar frame (Baranov and Malama, 1993; Zank et al., 1996; Baranov et al., 1998). Since 1993, a series of observations have been performed by the UV spectrometers onboard the Voyager 1 and Voyager 2 spacecraft to try to observe the signature of the hydrogen wall in the Lyman-α pattern (Quémerais et al., 1995). Hall et al. (1993) reported that the Lyman-α intensity measured away from the Sun was falling off with distance less quickly than expected from a standard hot model. This result suggested that there was a positive gradient of neutral hydrogen at large distance from the Sun and it could be explained by the existence of an interface region. However, the actual gradient observed by Hall et al. (1993) was not confirmed by later dedicated observations (Quémerais et al., 1995).

Spectroscopic study of the interplanetary background is possible too. The Goddard High Resolution Spectrometer on the Hubble Space Telescope has been used to measure the interplanetary Lyman-α line profile (Clarke et al., 1995). More recently (2001), the STIS instrument which replaced the GHRS onboard HST was also used and gave excellent data. Using hydrogen absorption cell measurements made by the SWAN instrument on SOHO, Quémerais et al. (1999) have developed a technique to derive interplanetary Lyman-α line shifts by accumulating one year of data. The same data will also be used to measure line widths.

In what follows we show how to compute the interplanetary UV background given a model of the hydrogen distribution in the interplanetary medium (density, velocity, temperature). In previous published works, radiative transfer effects have not often been considered very precisely. The main reason is that in the inner heliosphere, the interplanetary medium is supposed to be optically thin at Lyman-α. In such a case, one needs only to integrate the first scattering order over the line of sight to compute the scattered intensity. Unfortunately, this is not quite correct as shown by Keller et al. (1981) and confirmed by Hall et al. (1992) and Quémerais

and Bertaux (1993). Although the neutral hydrogen number density in the vicinity of the Sun is small enough to have an optically thin medium, the number density increases with distance from the Sun. At 10 AU from the Sun, the medium is not optically thin anymore and second, or larger, scattering order photons have to be considered. Moreover, a fraction of the photons which are scattered at a larger distance can come back towards the Sun and contribute to the inner heliosphere emission pattern. This phenomenon was clearly obtained by Keller et al. (1981), Hall (1992) and Quémerais and Bertaux (1993), who used different computation schemes.

Finally, after discussing various representations of the Lyman-α scattering process and frequency redistribution function, we will show how to compute the actual line profile based on a study of the Angle Dependent Partial Frequency Redistribution (A.D.P.F.R.) function, which was extensively described by Mihalas (1978). This computation uses actual non-Maxwellian distribution functions of the hydrogen atoms in the inner heliosphere.

The last part of this chapter will focus on some of the results that have been obtained from the study of the interplanetary Lyman-α background concerning the heliospheric interface. The main results are the deceleration and heating of hydrogen flow, compared to the helium flow which reflects the condition in the interstellar medium. More recently, the apparent deflection of 4° between the two neutral flows suggests that the geometry of the whole heliospheric region might be more complicated than previously assumed.

We will complete this chapter with a list of open questions on this subject which will have to be addressed to get a clear understanding of this global study.

9.2 Computation of the Lyman-α background

9.2.1 Some definitions

We assume that the Sun is a point source. The emission profile has a known shape, given as a parameter of the model. We also assume that the source is isotropic.

The frequency of the Lyman-α transition is denoted ν_0, the corresponding wavelength is λ_0 and is equal to 1215.67 Å.

In what follows we will use the variable x which is the normalized frequency

$$x = \frac{(\nu - \nu_0)\ c}{\nu_0 \sqrt{\frac{2kT_g}{m}}} = \frac{\nu - \nu_0}{\Delta\nu_d} \approx \frac{\lambda_0 - \lambda}{\Delta\lambda_d} \tag{9.1}$$

k is the Boltzmann constant, c the speed of light in vacuum and m the hydrogen atom mass. The Doppler width $\Delta\nu_d$ is proportional to the thermal velocity of the gas at temperature T_g.

$$\Delta\nu_d = \nu_0 \frac{v_{th}}{c} = \frac{\nu_0}{c}\sqrt{\frac{2kT_g}{m}} \tag{9.2}$$

For atomic hydrogen gas at 8000 K, the thermal speed v_{th} is equal to 11.5 km/s, and the Doppler width is equal to 0.05 Å.

We denote as $\mathcal{F}_\nu(\boldsymbol{r})\, d\nu\, dS\, dt$ the number of photons emitted by the Sun for a frequency between ν and $\nu + d\nu$ that cross a surface dS at distance r from the Sun in a time interval of dt. The solar profile can be represented by its spectral shape and its value at line centre.

$$\mathcal{F}_\nu(\boldsymbol{r}) = \mathcal{F}_o(\boldsymbol{r})\ s(x) \tag{9.3}$$

If N_0 is the number of photons isotropically emitted by the Sun per second in the frequency interval (ν_1, ν_2), we have the following expression

$$N_0 = 4\pi r^2 \int_{\nu_1}^{\nu_2} \mathcal{F}_\nu(r)\ d\nu = 4\pi r^2\ \Delta\nu_d\ \mathcal{F}_o(r) \int_{x_1}^{x_2} s(x)\ dx \tag{9.4}$$

This shows that the illuminating flux is proportional to the square of the inverse of the distance to the Sun. It is then defined by its value at line centre at a given distance from the Sun and its spectral shape. In what follows, the term white source will be used for a source with a flux independent of frequency ($s(x)$ is constant). The term Doppler source is used when $s(x)$ is proportional to a Gaussian function.

The illuminating flux is often defined by its value at 1 AU. In the literature, the values are given per wavelength unit instead of per frequency unit.

The solar illuminating flux at H Lyman α can be expressed by $\mathcal{F}_\lambda(1\text{AU}) = \mu \times 3.32\ 10^{11}$ photons s^{-1} cm^{-2} Å^{-1}. Here the term μ is the ratio of the radiation pressure force over solar gravitational pull. A value of μ equal to 1 means that the effects of radiation pressure and solar attraction balance and the paths of H atoms in the interplanetary medium are straight lines.

9.2.2 Absorption profiles

Considering n_ν photons with the same direction $\boldsymbol{\Omega}$, frequency ν within $d\nu$ and going through a medium with local density $N(\boldsymbol{r})$, the absorption probability after crossing a distance ds is proportional to the density multiplied by ds.

The absorbed fraction dn_ν/n_ν is given by

$$\frac{dn_\nu}{n_\nu} = -\sigma_\nu\ N(\boldsymbol{r})\ ds = -\sigma_0\ a_{\boldsymbol{r}}\,(\nu)\ N(\boldsymbol{r})\ ds \tag{9.5}$$

σ_ν is the absorption cross-section at frequency ν. This term has the dimension of a surface. This function can be represented by its value at line centre multiplied by its spectral shape $a_{\boldsymbol{r}}\,(\nu)$.

The shape of the absorption profile depends on the local velocity distribution. To compute the absorption profile, we assume that a photon is absorbed by an atom only if the photon frequency is exactly equal to the Lyman-α transition frequency ν_0 in the atom rest frame. So if the photon travels following a direction $\boldsymbol{\Omega}$ at frequency ν, only an atom with velocity v can absorb it, with $\boldsymbol{v}$ satisfying

$$\nu = \nu_0 \left(1 + \frac{\boldsymbol{v}\cdot\boldsymbol{\Omega}}{c}\right) = \nu_0 \left(1 + \frac{\overline{v}}{c}\right) \tag{9.6}$$

where $\overline{v}$ is the projection of the atom velocity on the direction of propagation of the photon.

The local velocity distribution is defined by a function $f(\boldsymbol{r}, \boldsymbol{v})$

$$N(\boldsymbol{r}) = \int_{\mathcal{V}} f(\boldsymbol{r}, \boldsymbol{v})\ d^3\boldsymbol{v}, \tag{9.7}$$

where $\mathcal{V}$ denotes a summation on the velocity space. The projection of this distribution on direction $\boldsymbol{\Omega}$ is noted $f_p(\boldsymbol{r}, \overline{v})$. So the absorbed fraction at frequency ν is proportional to $f_p(\boldsymbol{r}, \overline{v})$ where the projected velocity satisfies Equation (9.6).

Thus the absorption profile has the following shape,

$$\sigma(\nu) = \kappa_0\ f_p\left(\boldsymbol{r}, \frac{\nu - \nu_0}{\nu_0}\ c\right) \tag{9.8}$$

The cross section at line centre is $\sigma_0 = \kappa_0\ f_p(\boldsymbol{r}, 0)$.

In the case of a Boltzmann distribution at temperature T_g, the absorption profile is given by

$$\sigma(\nu) = \sigma_0\ a(x) = \sigma_0\ e^{-x^2} = \sigma_0\ e^{-\left(\frac{\nu-\nu_0}{\Delta\nu_d}\right)^2} \tag{9.9}$$

where x is the normalized frequency and $\Delta\nu_d = \frac{\nu_0}{c}\sqrt{\frac{2kT_g}{m}}$ the Doppler width.

A more detailed representation must include the natural width of the H Lyman α transition. This comes from the fact that the lifetime of the electron on the excited level of the transition is not zero. Thus collisions can modify the velocity of the scattering atom. It has been shown (Mihalas 1978, page 276) that the absorption cross section becomes a Lorentzian distribution if the Doppler width can be neglected before the natural width. This gives

$$\sigma(\nu) = \sigma_0\ \left(\frac{1}{1 + \left(\frac{\nu-\nu_0}{\Delta\nu_n}\right)^2}\right) \tag{9.10}$$

To obtain the actual absorption profile, we must convolve this Lorentzian profile with the local velocity distribution. Considering a local distribution of hydrogen atoms proportional to $f_p(\boldsymbol{r}, \overline{v})$, hydrogen atoms can asorb any photon with frequency ν with different probabilities. In the rest frame of an atom, the photon frequency is ν' such as

$$\nu' = \nu\left(1 - \frac{\overline{v}}{c}\right) \approx \nu - \nu_0\frac{\overline{v}}{c} \tag{9.11}$$

where $\overline{v}$ is the projection of the atom velocity on the direction of propagation of the photon. The approximation is valid for non-relativistic velocities. Following this, the probability that the atom will absorb the photon of frequency ν is proportional to

$$\frac{1}{1 + \left(\frac{\nu'-\nu_0}{\Delta\nu_n}\right)^2} = \frac{1}{1 + \left(\frac{\nu-\nu_0(1+\overline{v}/c)}{\Delta\nu_n}\right)^2} \tag{9.12}$$

Taking into account the local distribution, and integrating over the velocity space, we find that a photon of frequency ν has a total probability of being absorbed proportional to

$$C(\nu) = \int_{-\infty}^{+\infty} \frac{1}{1 + \left(\frac{\nu-\nu_0(1+\overline{v}/c)}{\Delta\nu_n}\right)^2}\ f_p(\boldsymbol{r}, \overline{v})\ d\overline{v} \tag{9.13}$$

If the gas follows a Maxwell-Boltzmann distribution, the function f_p is a Gaussian and using $a = \Delta\nu_n/\Delta\nu_d$, which is the ratio of the natural width over the Doppler width at temperature $T_{\rm g}$ and setting $y = (\overline{v}\sqrt{m})/\sqrt{2kT_{\rm g}}$,we find

$$C(\nu) = \sqrt{\frac{2kT_{\rm g}}{m}} \int_{-\infty}^{+\infty} \frac{a^2}{a^2 + (x-y)^2}\ e^{-y^2}\ dy \tag{9.14}$$

This can be rearranged into the classical expression

$$\sigma(\nu) = \sigma_0\ H(a,x) = \sigma_0\ \frac{a}{\pi} \int_{-\infty}^{+\infty} \frac{e^{-y^2}}{a^2 + (x-y)^2}\ dy \tag{9.15}$$

The function H is called the *Voigt function*. Ivanov (1973, page 27) has shown that the limit $a \to 0$ yields a gaussian profile. The Voigt function has been studied by Mitchell & Zemansky (1934) and Thomas (1963).

For the Lyman-α transition, we have

$$\Delta\nu_n = \frac{1}{4\pi\ \tau} = \frac{A}{4\pi} = 4.986\ 10^7\ {\rm s}^{-1} \tag{9.16}$$

The value of A, the transition probability, which is the inverse of τ the electron lifetime in the excited state, is given by Morton (1991), $A = 6.265\ 10^8\ {\rm s}^{-1}$. The value of a for a hydrogen gas at 8000 K.

$$a = \frac{\Delta\nu_n}{\Delta\nu_d} = \frac{\Delta\nu_n}{\nu_0}\ c\ \sqrt{\frac{m}{2kT_{\rm g}}} = 5.27\ 10^{-4} \tag{9.17}$$

This value suggests that the use of a Gaussian absorption profile will give good results in our study.

The value of the cross section at line centre is obtained by integration over frequency. The total cross section of the Lyman-α transition (in CGS units) is given by (Mihalas 1978 page 81).

$$\sigma_{tot} = \int_0^\infty \sigma(\nu)\ d\nu = \frac{\pi\ e^2}{m_e\ c}\ f \tag{9.18}$$

This classical expression is obtained from the harmonic oscillator theory. The oscillator strength f is equal to 0.416. In the international system of units (MKSA), this relation becomes

$$\int_0^\infty \sigma(\nu)\ d\nu = \frac{1}{4\pi\ \epsilon_o}\ \frac{\pi\ q^2}{m_e\ c}\ f \tag{9.19}$$

where ϵ_o is defined as

$$\epsilon_o = \frac{1}{\mu_o\ c^2} = \frac{10^7}{4\pi\ c^2} \tag{9.20}$$

The cross section at line centre for a gas at temperature $T_{\rm g}$ is then obtained from

$$\sigma_0 = \sigma(\nu_0) = \frac{\sigma_{tot}}{\sqrt{\pi}\ \Delta\nu_d} = \sigma_{tot}\ \lambda_0\ \sqrt{\frac{m_H}{2\pi kT_{\rm g}}} \tag{9.21}$$

The following numerical values are found

$$\sigma_{tot} = 1.11\ 10^{-2} \quad \mathrm{cm}^2\ \mathrm{s}^{-1}$$

$$\sigma_0 = 5.96\ 10^{-12}\ \times\ \frac{1}{\sqrt{T_\mathrm{g}}} \quad \mathrm{cm}^2$$

Integrating over wavelength instead of frequency gives the relation

$$\sigma_\lambda = \int_0^\infty \sigma(\lambda)\ d\lambda = \sigma_{tot}\ \frac{\lambda_0}{\nu_0} = 5.47\ 10^{-15} \quad \mathrm{cm}^2\ \text{Å}$$

In the interplanetary medium, all absorptions of Lyman-α photons by H atoms are followed by the emission of new photons. The scattering profile expresses the relation between the absorbed profile and the emitted profile.

9.2.3 Scattering phase function

The scattering phase function expresses the relation between the direction of propagation of the photon before and after scattering. If we call ω the angle between the two directions, the phase function $\phi(\omega)$ gives the probability of having a scattering at angle ω. An isotropic scattering has a constant phase function equal to $1/4\pi$.

Brandt & Chamberlain (1959) have given the expression of the scattering phase function at Lyman-α , normalized over 4π steradian:

$$\phi(\omega) = \frac{11/12 + (1/4)\ \cos^2\omega}{4\pi} \tag{9.22}$$

More recently, Brasken and Kyrölä (1998) made a new computation, based on the general theory of resonance scattering. Their result is numerically very similar to the previous expression which we will use.

9.2.4 Frequency redistribution

The frequency redistribution function expresses the change in frequency of the photon during the scattering process. First, we must note that in the interplanetary medium the time between two collisions is of the order of 10^{10} seconds, which is much larger than the lifetime of the electron in the excited state. In that case, the velocity of the scattering atom does not change.

In the rest frame of the atom, we denote x and x' as the frequency of the photon before and after scattering, respectively. Let us define a referential $(O, \boldsymbol{\imath}, \boldsymbol{\jmath}, \boldsymbol{k})$, where $\boldsymbol{\imath}$ is the direction of propagation of the incoming photon. The velocity of the scattering atom is $\boldsymbol{v} = v_i\ \boldsymbol{\imath} + v_j\ \boldsymbol{\jmath} + v_k\ \boldsymbol{k}$. The direction of propagation of the scattered photon is equal to $\boldsymbol{d} = \cos\omega\ \boldsymbol{\imath} + \sin\omega\ \boldsymbol{\imath'}$, where $\boldsymbol{\imath'}$, is perpendicular to $\boldsymbol{i}$ and belongs to the plane defined by vectors $\boldsymbol{j}$ and $\boldsymbol{k}$.

Neglecting the natural width of the Lyman-α transition, we use the fact that the frequency of the photons in the atom rest frame is equal to the frequency of the Lyman-α transition. We find the following relation where v_{th} is the local thermal velocity

$$x = \frac{\boldsymbol{v} \cdot \boldsymbol{\imath}}{v_{th}} = \frac{v_i}{v_{th}} \tag{9.23}$$

For the outgoing photon,

$$x' = \frac{\boldsymbol{v} \cdot \boldsymbol{d}}{v_{th}} = \frac{v_i}{v_{th}} \cos\omega + \frac{\boldsymbol{v} \cdot \boldsymbol{\imath'}}{v_{th}} \sin\omega = x \cos\omega + \left(\frac{\boldsymbol{v} \cdot \boldsymbol{\imath'}}{v_{th}}\right) \sin\omega \tag{9.24}$$

Let us denote y as the projection of the velocity of the atom on the plane $(O, \boldsymbol{\jmath}, \boldsymbol{k})$ normalized to the local thermal velocity. This becomes,

$$x' = x \cos\omega + y \sin\omega \tag{9.25}$$

The variables x and ω being fixed, we can determine the distribution of y denoted by $g(y)$. Let us assume that the local distribution is a Maxwell-Boltzmann distribution. In that case, the normalized distribution function $g(y)$ is

$$g(y) = \frac{e^{-y^2}}{\sqrt{\pi}} \tag{9.26}$$

From the relation between x' and y for a given x and ω, we find

$$g(y)\, dy = a_1(x'/x, \omega)\, dx'$$

which leads to the conditional distribution of x' for a given x and ω

$$a_1(x'/x, \omega) = \frac{1}{\sin\omega\, \sqrt{\pi}}\, e^{-\left(\frac{x' - x \cos\omega}{\sin\omega}\right)^2} \tag{9.27}$$

This formula corresponds to the expression of the *Angle Dependent Partial Frequency Redistribution*. Note that this is independent of the shape of the absorption cross section, but has been obtained assuming a local Maxwell-Boltzmann distribution for the hydrogen atoms.

Mihalas (1978) has shown that an equivalent relation is obtained when the natural width effect is accounted for. In that case, the Gaussian function in $g(y)$ is replaced by a Voigt function.

Often used assumptions

The previous relation allows us to introduce two types of assumption often used when computing scatter profiles.

The first one is called *coherent scattering*, when the frequency of the photon is conserved during the scattering process. This is true only if the atom has a zero velocity in the local frame, which is unrealistic. It also happens if ω is equal to 0. Let us note also that $\omega = \pi$ corresponds to $x' = -x$ which is also called coherent scattering.

The opposite assumption is called *Complete Frequency Redistribution* and postulates that there is no correlation between the two frequencies x and x'. This applies if the time between two collisions is short before the Lyman-α transition

de-excitation time, which is not the case in the interplanetary medium. This applies also if $\omega = \pi/2$ which means that for perpendicular scattering, the scattered profile is proportional to the local velocity distribution.

Finally, the exact relation is a combination between the two extreme cases of coherent scattering and Complete Frequency Redistribution.

Using (9.27), we can compute the spectral shape of a scattered profile, given the absorption profile and the scattering phase function. For instance, let us take a white source (constant illuminating flux) with a constant scattering function; in that case we have

$$a(x') = \int_{-\infty}^{+\infty} dx\ \frac{e^{-x^2}}{\sqrt{\pi}} \int_0^{\pi} d\omega\ \frac{\sin\omega}{2}\ a_1(x'/x, \omega) = \frac{e^{-x'^2}}{\sqrt{\pi}} \tag{9.28}$$

This demonstrates that, in the case of isotropic scattering and a white source, the scattered profile is proportional to a Gaussian profile with a Doppler width defined by the temperature of the scattering gas. This result is the same as the one obtained assuming Complete Frequency Redistribution.

As mentioned by Thomas (1963), the exact scattering phase function gives more weight to coherent scattering.

Early works on the geocorona (Thomas 1963, Bertaux 1974) often used the hypothesis of Complete Frequency Redistribution, which simplifies the computation of the scattered profile.

9.2.5 Optical thickness

The optical thickness τ_ν for a photon at frequency ν between two points defined by vectors $\boldsymbol{r}$ and $\boldsymbol{r'}$ is defined by the following relation, where z is a dimensionless variable:

$$\tau_\nu(\boldsymbol{r}, \boldsymbol{r'}) = \int_0^1 \sigma(\nu)\ N(\boldsymbol{r} + z\,(\boldsymbol{r'} - \boldsymbol{r}))\ \|\boldsymbol{r'} - \boldsymbol{r}\|\ dz = \tau_0(\boldsymbol{r}, \boldsymbol{r'})\ a(x) \tag{9.29}$$

τ_0 is the optical thickness at line centre. Following (9.5), the absorbed fraction of photons along a length ds is equal to $d\tau_\nu = \sigma(\nu)\ N\ ds$.

If at $\boldsymbol{r}$, n photons at frequency ν are going towards $\boldsymbol{r'}$, $n\ e^{-\tau_\nu}$ représents those that reach $\boldsymbol{r'}$. This quantity is defined by the optical thickness at line centre and the absorption profile.

9.3 Radiative transfer equation at Lyman-α

9.3.1 General formalism

Let us set

$$dn = I(\boldsymbol{r}, \boldsymbol{\Omega}, \nu)\ d\nu\ d\Omega\ dS\ dt$$

The intensity $I(\boldsymbol{r}, \boldsymbol{\Omega}, \nu)$ is defined in units of photons per second per surface unit per frequency unit and per unit of solid angle (i.e. s^{-1} cm^{-2} Hz^{-1} ster^{-1})). It measures the number of photons dn with a frequency within ν and $\nu + d\nu$ that cross within a period of time dt a perpendicular surface dS following a direction of propagation $\boldsymbol{\Omega}$ within a solid angle $d\Omega$.

The intensity is the solution of the transfer equation which expresses the elementary variation of the number of photons on their trajectory due to source and loss terms. Following Chandrasekhar (1952), we write

$$\boldsymbol{\Omega} \cdot \boldsymbol{\nabla} I(\boldsymbol{r}, \boldsymbol{\Omega}, \nu) = -\sigma(\nu)\ N(\boldsymbol{r})\ I(\boldsymbol{r}, \boldsymbol{\Omega}, \nu) + N(\boldsymbol{r})\ j(\boldsymbol{r}, \boldsymbol{\Omega}, \nu) \tag{9.30}$$

The loss term due to absorption is given by $\sigma(\nu)\ N\ I$, with the local density equal to N and the absorption cross section equal to $\sigma(\nu)$.

The local source term is equal to the product of the local density of scattering atoms multiplied by the atomic emission coefficient $j(\boldsymbol{r}, \boldsymbol{\Omega}, \nu)$ which measures the number of photons emitted by a hydrogen atom per second per frequency unit and per solid angle.

The formal solution of (9.30) is obtained classically as

$$I(\boldsymbol{r}, \boldsymbol{\Omega}, \nu) = \int_0^\infty N(\boldsymbol{r} + s\boldsymbol{\Omega})\ j(\boldsymbol{r} + s\boldsymbol{\Omega}, \boldsymbol{\Omega}, \nu)\ e^{-\tau_\nu(\boldsymbol{r}, \boldsymbol{r}+s\boldsymbol{\Omega})}\ ds \tag{9.31}$$

The quantity τ_ν is computed following (9.29). For an observer at position $\boldsymbol{r}$ looking in direction $\boldsymbol{\Omega}$, the integration over s is performed from 0 to ∞. Let us note here that the line of sight $\boldsymbol{\Omega}$ is in the opposite direction to the direction of travel of the photons. In what follows, the direction refers to the line of sight and not the direction of travel of the photons. In that case, one must replace $j(\boldsymbol{r}, \boldsymbol{\Omega}, \nu)$ by $j(\boldsymbol{r}, -\boldsymbol{\Omega}, \nu)$.

By integration over frequency, we find

$$I(\boldsymbol{r}, \boldsymbol{\Omega}) = \int_0^\infty ds\ N(\boldsymbol{r} + s\boldsymbol{\Omega}) \left(\int_0^\infty j(\boldsymbol{r} + s\boldsymbol{\Omega}, -\boldsymbol{\Omega}, \nu)\ e^{-\tau_\nu(\boldsymbol{r}, \boldsymbol{r}+s\boldsymbol{\Omega})}\ d\nu \right) \tag{9.32}$$

The emissivity $\varepsilon(\boldsymbol{r})$ is defined as the total number emitted locally per unit of time and per unit of volume. It relates to the atomic emission coefficient by

$$\varepsilon(\boldsymbol{r}) = \int_{4\pi} d\Omega \int_0^\infty d\nu\ N(\boldsymbol{r})\ j(\boldsymbol{r}, \boldsymbol{\Omega}, \nu) \tag{9.33}$$

It is possible to split the emissivity into two terms $\varepsilon = \varepsilon_0 + \varepsilon_m$. The first term is due only to the scattering of photons from the source (the Sun). The second term sums the photons coming from all direction of space and which have been scattered more than once.

Considering the source profile introduced in the previous section, the primary emissivity is given by

$$\varepsilon_0(\boldsymbol{r}) = \int_0^\infty \mathcal{F}_\nu(\boldsymbol{r})\ \sigma(\nu)\ e^{-\tau_\nu(0, \boldsymbol{r})}\ N(\boldsymbol{r})\ d\nu \tag{9.34}$$

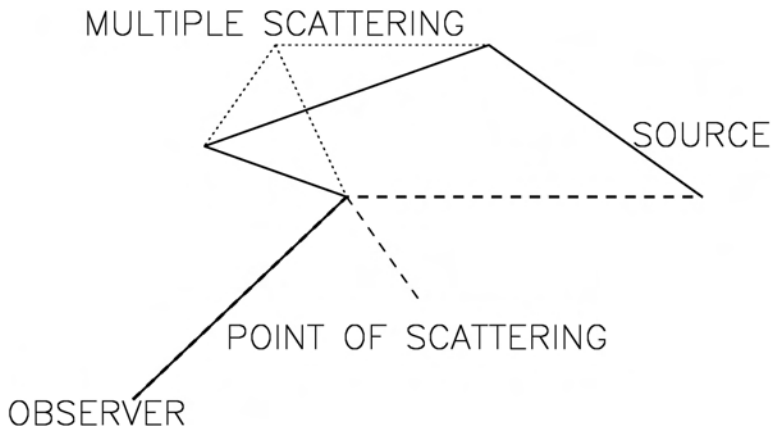

Figure 9.1: Sketch showing the difference between single and multiple scattering. Photons can leave the source and reach the observer with different trajectories. The simplest and most direct way involves only one scattering (dashed line). This corresponds to a majority of the photons in the case of the interplanetary Lyman-α background. However, a non-negligible number of photons are scattered more than once, as shown in the sketch (solid line).

$\tau_\nu(0, \boldsymbol{r})$ is the optical thickness at frequency ν between the Sun and the local point.

The second term ε_m is due to the absorption of photons which have already been scattered at least once before. This means that they come from all directions of the sky. This becomes

$$\varepsilon_m(\boldsymbol{r}) = \int_{4\pi} d\Omega \int_0^\infty d\nu \; \sigma(\nu) \; N(\boldsymbol{r}) \; I(\boldsymbol{r}, \boldsymbol{\Omega}, \nu) \tag{9.35}$$

where the 4π notation denotes integration over all spatial directions.

9.3.2 Optically thin approximation

Many authors simplify the computation of the intensity by using the optically thin approximation. This assumes that the optical thickness is small enough that only first order scattering is taken into account. The photons are scattered only once ($\varepsilon_m = 0$). The emissivity given by (9.34) becomes proportional to the local density multiplied by the excitation rate. It is easy to include the complete scattering phase function.

Equation (9.32) becomes

$$I(\boldsymbol{r}, \boldsymbol{\Omega}) = \int_0^\infty \phi(\omega_0) \; \varepsilon(\boldsymbol{r} + s\boldsymbol{\Omega}) \; ds = \int_0^\infty g_0(r) \; \phi(\omega_0) \; N(\boldsymbol{r} + s\boldsymbol{\Omega}) \; ds \tag{9.36}$$

where ω_0 is the angle between the travel direction of the photons before and after scattering and $g_0(r)$ is the excitation rate due to the source.

One has to be very cautious when using the optically thin approximation. For instance, in the interplanetary medium, the hydrogen density close to the orbit

of the Sun is very small and the medium is optically thin. Yet we cannot apply the optically thin approximation because integration over the line of sight includes areas of the heliosphere which are not optically thin.

9.3.3 Solution for complete frequency redistribution

Isothermal gas at constant bulk velocity

In the case of complete frequency redistribution, most of the equations take a simpler form. We also assume that the scattering is isotropic. With these assumptions, the atomic emission coefficient is proportional to a spectral shape function $a(x)$. Its integral over frequency is equal to the emissivity, and we find then that

$$N(\boldsymbol{r})\ j(\boldsymbol{r},\boldsymbol{\Omega},\nu) = \frac{1}{4\pi}\ \frac{1}{\Delta\nu_d}\ \varepsilon(\boldsymbol{r})\ \frac{a(x)}{\int_{-\infty}^{+\infty} a(y)\ dy} \tag{9.37}$$

where the normalized function $a(x)/\int_{-\infty}^{+\infty} a(y)\ dy$ gives the spectral dependence of the emission profile. If we assume that the local distribution is a Maxwell-Boltzmann distribution and we neglect the natural width, this becomes

$$N(\boldsymbol{r})\ j(\boldsymbol{r},\boldsymbol{\Omega},\nu) = \frac{1}{4\pi}\ \frac{1}{\Delta\nu_d}\ \varepsilon(\boldsymbol{r})\ \frac{e^{-x^2}}{\sqrt{\pi}} \tag{9.38}$$

If we choose to represent the source profile by $s(x)$ as in (9.4), Equation (9.34) becomes

$$\varepsilon_0(\boldsymbol{r}) = \mathcal{F}_0\ \frac{r_0^2}{r^2}\ \sigma_0\ N(\boldsymbol{r})\ \Delta\nu_d \int_{-\infty}^{+\infty} s(x)\ a(x)\ e^{-\tau_0(0,\boldsymbol{r})\ a(x)} dx \tag{9.39}$$

The excitation rate at Lyman-α measures the number of photons per second which can excite the Lyman-α transition for one H atom. This rate varies like the solar flux with distance to the Sun, so using a reference value g_0 at $\boldsymbol{r}_0$,

$$g_0 = \mathcal{F}_0\ \sigma_0\ \Delta\nu_d\ \left(\int_{-\infty}^{+\infty} s(x)\ a(y)\ dy\right) \tag{9.40}$$

In the simpler case of the white source, where $s(x) = 1$,

$$g_0 = \mathcal{F}_0\ \sigma_0\ \Delta\nu_d\ \left(\int_{-\infty}^{+\infty} a(y)\ dy\right) \tag{9.41}$$

If the spectral shape is represented by a Gaussian function (Maxwell-Boltzmann)

$$g_0 = \mathcal{F}_0\ \sigma_0\ \Delta\nu_d\ \sqrt{\pi} = \mathcal{F}_0\ \frac{1}{4\pi\ \epsilon_o}\ \frac{\pi\ q^2}{m_e\ c}\ f \tag{9.42}$$

For an illuminating flux at 1 AU, $\mathcal{F}_0 = \mu \times 3.3\ 10^{11}$ phot s^{-1} cm^{-2} Å^{-1}, the corresponding excitation rate is $\mu \times 1.8\ 10^{-3}$ s^{-1}.

Using all previous assumptions, Equation (9.39) becomes

$$\varepsilon_0(\boldsymbol{r}) = g_0\ \frac{r_0^2}{r^2}\ N(\boldsymbol{r})\ \int_{-\infty}^{+\infty} \frac{e^{-x^2}}{\sqrt{\pi}} e^{-\tau_0(0,\boldsymbol{r})\ e^{-x^2}} dx \tag{9.43}$$

$$\varepsilon_0(\boldsymbol{r}) = g_0 \, \frac{r_0^2}{r^2} \, N(\boldsymbol{r}) \, T(\tau_0(0, \boldsymbol{r})) \tag{9.44}$$

Here, we introduce the Holstein transmission function as

$$T(\tau) = \int_{-\infty}^{+\infty} \frac{e^{-x^2}}{\sqrt{\pi}} e^{-\tau \, e^{-x^2}} \, dx \tag{9.45}$$

It measures the extinction integrated over frequency when the optical thickness at line centre is equal to τ, the source term is constant and the spectral shape of absorption is proportional to e^{-x^2}.

The second Holstein transmission function $G(\tau)$ is defined by (Holstein, 1948):

$$G(\tau) = \int_{-\infty}^{+\infty} \frac{e^{-2x^2}}{\sqrt{\pi}} e^{-\tau \, e^{-x^2}} \, dx \tag{9.46}$$

It measures the extinction integrated over frequency when both the source and the absorption profile are proportional to e^{-x^2}. This applies to second order scattering in the case of Complete Frequency Redistribution.

Using the Holstein transmission, we can write

$$I(\boldsymbol{r}, \boldsymbol{\Omega}) = \frac{1}{4\pi} \int_0^{+\infty} \varepsilon(\boldsymbol{r} + s\boldsymbol{\Omega}) \, T(\tau_0(\boldsymbol{r} + s\boldsymbol{\Omega}, \boldsymbol{r})) \, ds \tag{9.47}$$

Finally, we can remove the intensity term by combining the previous equations. We then find the following relation for the emissivity

$$\varepsilon(\boldsymbol{r}) = \varepsilon_0(\boldsymbol{r}) + N(\boldsymbol{r}) \, \sigma_0 \int_{4\pi} \frac{d\Omega}{4\pi} \int_0^{+\infty} \varepsilon(\boldsymbol{r} + s\boldsymbol{\Omega}) \, G(\tau_0(\boldsymbol{r} + s\boldsymbol{\Omega}, \boldsymbol{r})) \, ds \tag{9.48}$$

This formalism was developed and applied to the study of the geocorona by Thomas (1963), Bertaux (1974) and Anderson & Hord (1977). Meier (1991) is a review paper on these types of studies.

9.4 Computation methods

The aim of this section is to describe a few numerical methods used to solve the transfer equation at Lyman-α in the interplanetary medium. The first models were developed to compute the Lyman-α emission in the geocorona in the Earth geocorona; see Thomas (1963), Bertaux (1974) and Anderson & Hord (1977). This method could easily be implemented in the case of the interplanetary medium.

Firstly we would like to point out that the geometry of the problem is not well adapted to a plane parallel study. Most of the models use a cylindrical symmetry around the interstellar wind axis. Secondly, the optical thickness at line centre is at most equal to a few units. This means that assumptions made for problems with very large optical thickness values do not apply here.

9.4.1 Iterative method

This method has been applied in the frame of the Complete Frequency Redistribution assumption with an isotropic scattering by Bertaux (1974) and Quémerais and Bertaux (1993). A similar work was published by Hall (1992). It is based on a discretization of Equation (9.48). If we represent the continuous emissivity function by a vector $\boldsymbol{\epsilon}$ giving its value at a finite set of points (computation grid), we can write that

$$\boldsymbol{\epsilon} = \boldsymbol{\epsilon}_0 + (A) \cdot \boldsymbol{\epsilon} \tag{9.49}$$

The coefficients a_{ij} of the matrix (A) are given by Equation (9.48); see Quémerais and Bertaux (1993) for a detailed presentation. If we note $(1) = (\delta_{ij})$ the unity matrix for the dimension of matrix (A) and that $((1) - (A))$ can be inverted, we can write

$$\boldsymbol{\epsilon} = ((1) - (A))^{-1} \cdot \boldsymbol{\epsilon}_0 = \left(\sum_{i=0}^{\infty} (A)^i \right) \cdot \boldsymbol{\epsilon}_0 \tag{9.50}$$

Instead of simply inverting matrix $((1) - (A))$, it is much more efficient to introduce a series of vectors $(\boldsymbol{\epsilon_n})$ which satisfy

$$\boldsymbol{\epsilon}_{n+1} = \boldsymbol{\epsilon}_0 + (A) \cdot \boldsymbol{\epsilon}_n = \left(\sum_{i=0}^{n} (A)^i \right) \cdot \boldsymbol{\epsilon}_0 \tag{9.51}$$

The limit of this series of vectors is the solution of Equation (9.49). Each term $\boldsymbol{\epsilon_n}$ represents the emissivity due to photons scattered up to n times. The emissivity due to photons scattered exactly n times is equal to $(\boldsymbol{\epsilon_n} - \boldsymbol{\epsilon_{n-1}})$.

The main limitation of this method is due to the time needed to compute the influence matrix (A). This limits the size and resolution of the computation grid. Also, because Complete Frequency Redistribution is assumed, it is not possible to compute exact line profiles. A generalization of the method with exact scattering functions could be implemented, but would require long computation times.

9.4.2 Monte Carlo methods

Monte Carlo solutions of this problem were developed to allow for a more exact description of the scattering process, including the phase function effect, coupled with non-Maxwellian local distribution functions of the hydrogen atoms. This applies also to multi-component atom distributions with very distinct populations as described in Chapter 7.

The first detailed analysis was published by Keller et al. (1981). It was followed by works by Gangopadhay and Judge (1989) and Quémerais and Bertaux (1993). Recent improvements using non-Maxwellian hydrogen distributions and Angle Dependent Partial Frequency Redistribution – see Equation (9.27) – were published by Quémerais (2000) and Quémerais and Izmodenov (2002).

To compute the intensity in the interplanetary medium, two approaches were used. The first one, used by Keller et al. (1981) and Gangopadhay and Judge (1989), simulates detectors at the position of observation. As the model follows

photons in the interplanetary medium, the chance that they can hit the virtual detectors is computed after each scattering. This method requires little computer memory, but long simulations are needed to get good statistics. Also, changing the position of the virtual detectors requires one to run the computation again. A second approach was used by Quémerais and Bertaux (1993) and in the following works of this group. In that case, each scattering is counted as the model follows photons on their path through the heliosphere. At the end of the computation, the number of scatterings in each cell of the computation grid is used to compute the local emissivity. This quantity can also be computed as a function of frequency and direction, thus allowing for line profile computations. Intensities are computed by integration of the following equation

$$I(\boldsymbol{r}, \boldsymbol{U}, \nu) = \int_0^\infty \varepsilon(\boldsymbol{r} + s\boldsymbol{U}, -\boldsymbol{U}, \nu)\ e^{-\tau_\nu(s)}\ ds \tag{9.52}$$

where $\boldsymbol{U}$ defines the line of sight and $\varepsilon(\boldsymbol{r}, \boldsymbol{U}, \nu)$ measures the total volume emissivity as a function of direction and frequency.

This second approach gives very good results when it is necessary to compute the intensity for many lines of sight and observer positions. On the other hand, it requires a lot of computer memory to store all the necessary information during the running of the Monte Carlo model.

9.4.3 Comparison with optically thin computations

Neglecting multiple scattering effects when computing Lyman-α intensities in the interplanetary medium makes the problem much simpler. However, most of the authors using various approximations have not quantified the bias induced by this simplification.

Keller et al. (1981) were the first authors who carefully computed the effects of multiple scattering for an observer at various distances from the Sun and looking radially away from the Sun. Their computations were based on a Monte-Carlo approach and used the assumption of Complete Frequency Redistribution. Their conclusions were very important for the study of the interplanetary Lyman-α background. Indeed, they showed that even at 1 AU from the Sun, where the H number density is very small, the optically thin approach does not apply. In the downwind cavity, they found an intensity ratio for multiple scattering over the optically thin assumption equal to 1.35. These results were later confirmed independently by Hall (1992) and Quémerais and Bertaux (1993).

Following this result, various approaches have been adopted. The first one includes a correction to the optically thin computation derived from a comparison with a radiative transfer computation. This was done by Ajello et al. (1987) and Pryor et al. (1992). Usually this correction is computed for one set of parameters defining the hydrogen distribution, assuming that the ratio of intensity from radiative transfer to intensity from optically thin approximation will not change too much with different hydrogen distributions.

The second approach used by Scherer and Fahr (1996) or Scherer et al. (1999) computes only the first scattering term. These authors then claim that all higher orders of scattering are negligible, which is contradicted by the results of Keller et

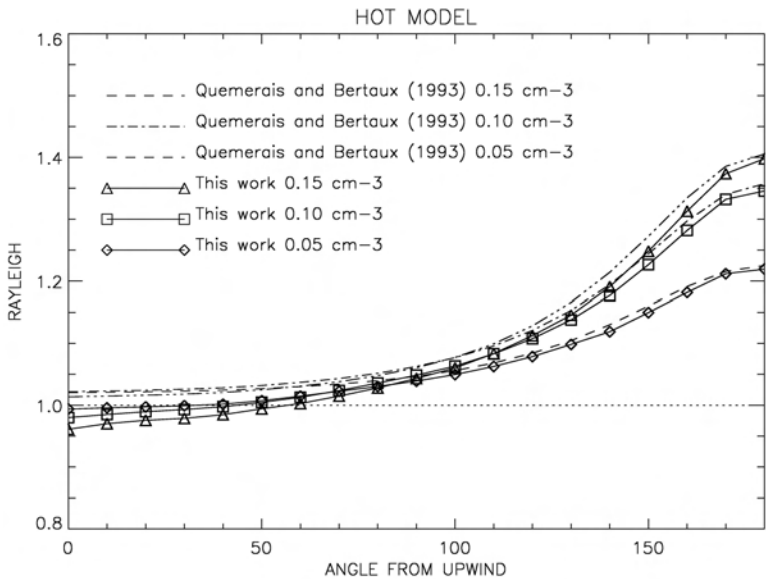

Figure 9.2: Figure taken from Quémerais (2000) (denoted by 'this work' in figure) which compares ADPFR results of multiple scattering computations for different hot models with the corresponding optically thin results. Multiple scattering results in CFR are from Quémerais and Bertaux (1993). For a hot model, CFR and ADPFR intensities are very similar. Multiple scattering results show a large discrepancy compared with optically thin values for lines of sight in the downwind direction, as shown originally by Keller et al. (1981).

al. (1981), Hall (1992) and Quémerais and Bertaux (1993) which were obtained independently and the results of Quémerais (2000) in the case of Angle Dependent Partial Frequency Redistribution. Our explanation for this discrepancy is the following. Scherer et al. (1996) have computed the emissivity change at 1 AU created by photons which undergo two scatterings (secondary term). They have found that these photons change the total emissivity by a few percent. Quémerais (2000) estimated that the change at 1 AU was less than 2% . However, intensities are not emissivities, but rather emissivities integrated over the line of sight. Because of the relatively small optical thickness of the medium, the integration must be performed on tens of AU. At 5 AU from the Sun, the secondary emissivity is already 25% of the primary term. It is 75% at 10 AU from the Sun. The optical thickness at Lyman-α between 1 AU and 10 AU is smaller than one which means that the emissivity term at 10 AU contributes to the intensity seen at 1 AU. In that case, even at 1 AU from the Sun multiple scattering terms must be included when computing intensities. Numerical values used here have been published by Quémerais (2000); see this work for more details. Figure (9.2) extracted from this work shows some results.

Finally, Bertaux et al. (1985) have introduced a third approach, which is based on the following method. The total intensity can be divided between first order

scattering photons and higher orders. It is rather easy to compute the first term which includes extinction between the Sun, the scattering point and the observer. However by neglecting extinction between the Sun and the scattering point, one will somewhat overestimate the first term thus compensating for the lack of the second term. The main problem with this assumption is that it is not based on any actual computation. To fill this gap, Quémerais (2000) has published correction tables computed for a few sets of parameter models. This correction is still not completely satisfactory because multiple scattering effects are non-linear and cannot be linearly compensated for. When possible, one should always try to compute the full multiple scattering solution to the problem.

9.5 Diagnostics of the heliospheric interface

In this section, we will review the past and present observations of the Lyman-α background which have been used to constrain the heliopsheric interface. Most of these studies are still on-going and many aspects are not completely understood, leaving open questions which we will summarize at the end.

This presentation is not a comprehensive review of all existing UV background data – see Ajello et al. (1987) or Quémerais et al. (1994) for lists of existing data sets – but rather a sample of the most important observations linked to the heliospheric interface and which cover both total intensity measurements and line profile measurements.

9.5.1 Backscattered intensity in the outer heliosphere

Various spacecraft have measured the variations of the Lyman-α background as they were going away from the Sun. The data from the UV photometers on the Pioneer spacecraft were studied by Wu et al (1988) and Gangopadhyay and Judge (1989). The data from the UV spectrometers of the Voyager 1 and Voyager 2 spacecraft were studied by Hall et al. (1993) and Quémerais et al. (1995). A study covering the latest available Voyager 1 UVS data can be found in Quémerais et al. (2003). The most recent Voyager 1/UVS measurements of the interplanetary background were made in 2005 more than 90 AU from the Sun. The Voyager 2/UVS data ends in 1998.

Early models of the hydrogen atom distribution in the outer heliosphere, like the hot model, were very simple because they didn't include the effects of the heliospheric interface due to the coupling of the interstellar plasma and hydrogen atoms. In that case, because the Sun was too far away to have any influence on the hydrogen atoms, the distribution beyond 20 AU from the Sun in the upwind direction was close to a constant number density and a Maxwellian distribution with the parameters of the interstellar gas. The extension of the ionization cavity in the downwind direction changed the distribution further away from the Sun in that direction. When more accurate models of the outer heliosphere hydrogen population were published, they clearly showed a strong departure from that simple image. The model of Baranov and Malama (1993) predicted the existence of a hydrogen wall in the upwind direction (see Chapter 7), due to the pile-up of slowed down

hydrogen atoms created by charge exchange in the nose region of the heliospheric interface.

This pile-up was expected only in the nose region of the interface, i.e. in the upwind direction. The two Voyager spacecraft were roughly going towards the upwind direction whereas the Pioneer spacecraft were mostly going downwind. Because the downwind region is also much more affected by variations in the solar parameters with the solar cycle, the Pioneer data set is much more difficult to use to study the heliospheric interface. In what follows, we will focus on the Voyager/UVS data as the spacecraft move in the upwind direction.

Variation with solar distance

The first comprehensive study of the variation of the Voyager UVS upwind intensity with solar distance was made by Hall et al. (1993). These authors used a power law description of the intensities to measure how fast they decrease with heliocentric distance. For a constant density value, this power law coefficient is expected to vary between -1 and -2. In the optically thin case, the emissivity (volume emission) is proportional to the density (constant) and the solar flux ($1/r^2$). Its integral (intensity) is proportional to $1/r$. As optical thickness increases with heliocentric distance, extinction on the line of sight changes the power law coefficient. A limit value equal to -2 for a uniform density distribution was found by Hall (1992). Extinction on the line of sight reduces the length of integration, and then the intensity tends to be proportional to the density multiplied by the illuminating flux.

The values reported by Hall et al. (1993) were obtained between 15 and 40 AU. The Pioneer data show a radial coefficient of -1.07 ± 0.1, which is not a surprising value for data obtained in the downwind part of the heliosphere. On the other hand, Voyager data showed a power law coefficent equal to 0.75 ± 0.05. This value, larger than -1, could not be made to agree with a constant density in the upwind direction. The most likely explanation was that the hydrogen number density was increasing with heliocentric distance thus forewarning of the existence of the hydrogen wall, predicted theoretically by Baranov and Malama (1993).

Later studies (see Quémerais et al., 2003, Figure 9.3) have confirmed the qualitative result obtained by Hall et al. (1993). However, the numerical values derived by Hall et al. (1993) were not correct. Because the intensities were recorded over long periods of time, it is necessary to correct the data for variations in the solar Lyman-α illuminating flux. The correction used by Hall et al. (1993) was based on older solar flux measurements. UARS solar data have lead to new estimates of the solar Lyman-α flux variations during the solar cycle (Pryor et al., 1992; Tobiska et al., 1997). Based on this new correction, Quémerais et al. (2003) have found a power law decrease for the Voyager 1/UVS data between 50 and 65 AU equal to -1.58 ± 0.02. More striking, after 1998 or 70 AU from the Sun, the intensity variation flattens very much with a power law coefficient equal to -0.22 ± 0.07. Although, the result found by Hall et al. (1993) is quantitatively exact, the flattening found in their data around 35 AU is not compatible with later measurements, which show a flattening only around 70 AU from the Sun. A recent analysis of the Voyager 1/UVS background measurements between 2003 and 2005 gives a power

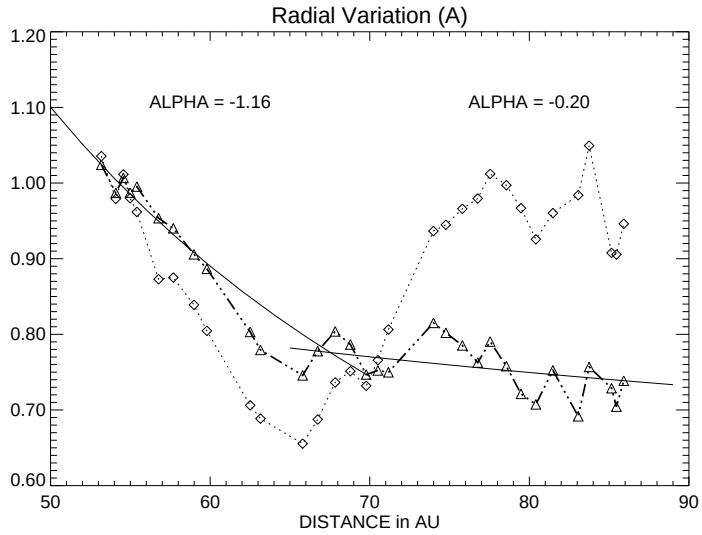

Figure 9.3: Figure taken from Quémerais et al. (2003) showing the radial variation in upwind intensity recorded by UVS on Voyager 1. The intensity measurements are normalized to the value at 55 AU. The slope clearly changes after 70 AU. This suggests that the hydrogen number density is not constant at large distances from the Sun, hinting of the existence of the hydrogen wall. The diamonds joined by the dotted line show the raw data. The triangles show the data corrected for solar Lyman-α flux variations.

law coefficient equal to -0.20 ± 0.1, which implies that the background intensity is decreasing much more slowly than any model predicts (Quémerais, 2006).

At the present time, we don't have a model that fits the Voyager 1/UVS Lyman-α background data completely. The very steep flattening beyond 70 AU might be due in part to an incomplete correction of the solar Lyman-α variation. However, these data strongly suggest that the hydrogen number density in the upwind direction increases with heliocentric distance and that the increase is more pronounced beyond 70 AU.

Scans across the sky

To alleviate the problems linked with the corrections of solar Lyman-α variations and instrument sensitivity changes, heliospheric scans were performed by the Voyager 1 and 2 UVS (Quémerais et al., 1995). These scans were made along great circles going from the upwind to downwind directions in a short period of time. The idea was to try to determine the ratio between the upwind to downwind intensities and to see if any excess could be detected in the upwind direction. Quémerais et al. (1995) reported an excess of intensity close to the upwind direction. However this excess was offset in the direction of the galactic plane, suggesting that part of it might be due to emission from the HII regions close to that plane. The pat-

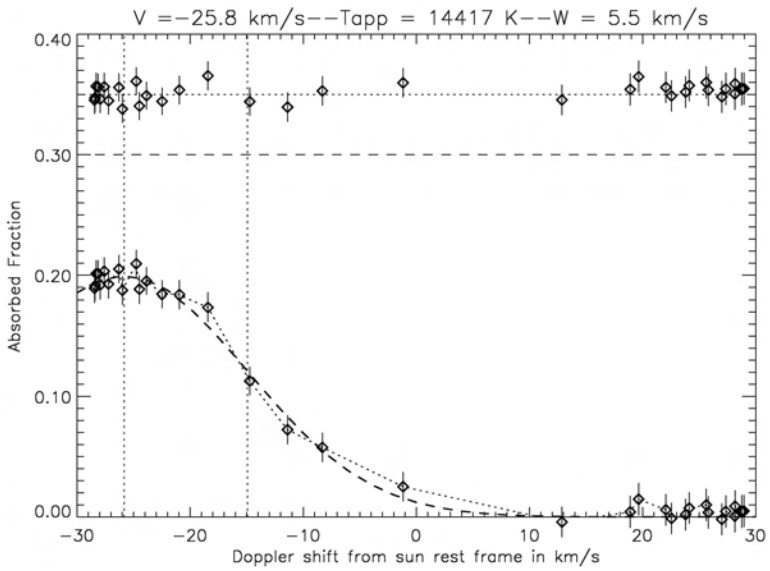

Figure 9.4: Upwind line profile reconstructed by Quémerais et al. (1999) using the SWAN H absorption cell data. These data were obtained in 1996. The abscissae is the Doppler shift in the solar rest frame. The apparent shift of the line in the solar rest frame is -25.8 km/s. When getting closer to the Sun, hydrogen atoms feel the opposing effects of the gravitational attraction of the Sun and the repulsion by the solar radiation pressure. Faster atoms also have less chance to be ionized. This results in a net apparent acceleration of the hydrogen population close to the Sun.

tern observed during the first scans in 1993 and 1994 was repeated throughout the whole study, which ended in 2003 when Voyager 1 stopped performing platform scans. As in the case of the radial intensity decrease with heliocentric distance, those scans were showing that the hydrogen number density was not constant in the outer heliosphere and was increasing in the upwind direction. However, no model could fit the observed intensity distribution completely (Quémerais et al., 1996; Quémerais et al., 2003). New models including non axi-symmetric representations of the heliospheric interface and its effects on the hydrogen distribution in the outer heliosphere will have to be tested to try to fit the data more accurately.

9.5.2 Line shape in the inner heliosphere

Line profiles of the interplanetary background can provide strong constraints on the hydrogen distribution and the changes induced when the hydrogen atoms cross the heliospheric interface. Because the medium is collisionless, those effects are propagated to the inner heliosphere. Effects of the heliospheric interface on the interplanetary Lyman-α line profiles deduced from multi-population models (see Chapter 4) were discussed by Quémerais and Izmodenov (2002). To get a correct measurement of the interplanetary line profile, a minimum resolution $R = \lambda/\Delta\lambda$ of $10^4 - 10^5$ is necessary. In space, such a resolution is only available from spectra

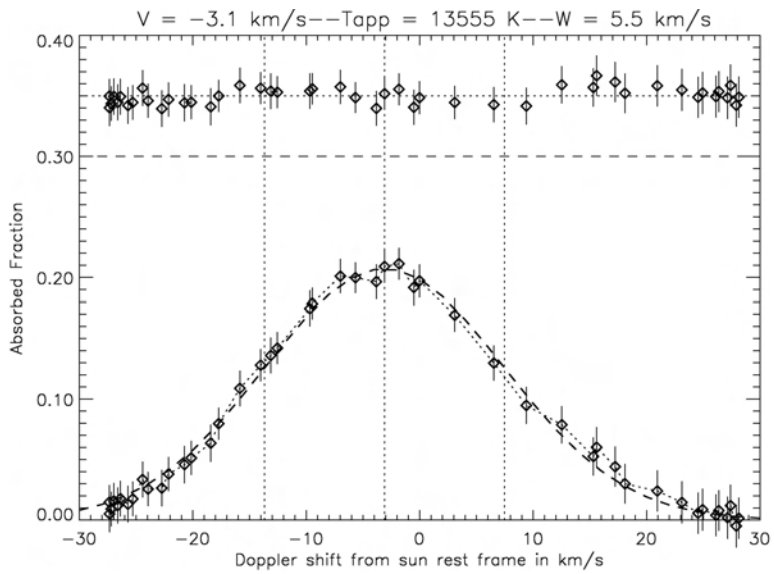

Figure 9.5: Crosswind line profile reconstructed by Quémerais et al. (1999) using the SWAN H cell data. The abscissae is the Doppler shift in the solar rest frame. These data were obtained in 1996. Crosswind spectra have close to zero Doppler shift in the solar rest frame because the line of sight is almost perpendicular to the relative motion between the H atoms and the observer (here the SOHO spacecraft).

measured by the Hubble Space Telescope (Clarke et al., 1995). Alternatively, it is possible to study the line profile with a hydrogen cell. The SWAN instrument onboard SOHO (Bertaux et al., 1995) is the latest instrument to use this technique.

SWAN hydrogen cell data and HST line profiles

A hydrogen cell contains diatomic hydrogen which can be dissociated into monoatomic hydrogen when a current passes through a filament contained in the cell. The cell is put in the light path before the detector. A fraction of the Lyman-α photons going through the cell can be absorbed if their frequency corresponds to the Lyman-α transition in the reference frame of the cell. The cell is then used as a negative filter. Consecutive measurements are made when the cell is active and non-active. The ratio of thoses measurements gives the fraction of Lyman-α photons which can be absorbed by the H atoms in the cell. This fraction is characteristic of the line profile of the measured profile.

Using previous measurements made by the Prognoz 5/6 spacecraft, Lallement et al. (1993) showed that the H cell measurements were compatible with a hydrogen bulk velocity of 22 km/s at large distance from the Sun. Compared to the helium velocity of 26 km/s assumed to be the same as the relative motion between the Sun and the surrounding interstellar medium, the hydrogen flow displayed an apparent deceleration of 4 km/s. This deceleration could be due to the crossing of the heliospheric interface as computed by Baranov and Malama (1993). Exten-

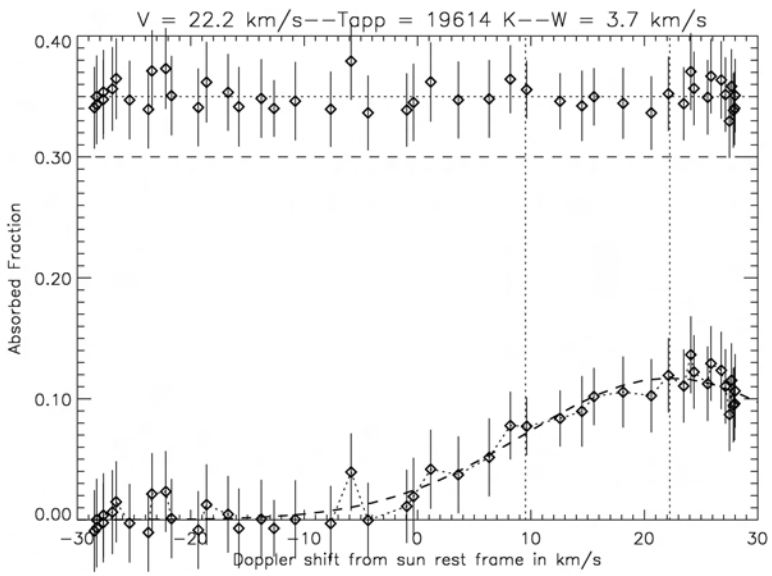

Figure 9.6: Downwind line profile reconstructed by Quémerais et al. (1999) using the SWAN H cell data. The abscissae is the Doppler shift in the solar rest frame. These data were obtained in 1996. Conditions in the downwind direction are more difficult to interpret due to the complex trajectories of the atoms in the downwind region.

sive measurements by the H cell of the SWAN instrument in 1996 and 1997 have confirmed this deceleration. Costa et al. (1999) also reported that the hydrogen flow had a temperature close to 11000 K, thus showing a strong heating over the 6000 K found for the interstellar medium or for the helium flow (Witte, 2004).

Observations of the interplanetary Lyman-α line profile have been made by the GHRS spectrometer and later the STIS spetrometer on the Hubble Space Telescope (Clarke et al., 1995). Those observations are difficult because the Earth geocorona emission at Lyman-α seen from the HST orbit is very bright and tends to cover the interplanetary Lyman-α line. The best measurements were made when the Doppler shift between the Earth emission and the interplanetary line was largest. Results for the interplanetary lineshifts are compatible with the H flow deceleration effect reported by Lallement et al. (1993). A work in progress is comparing the line profile measured by STIS in 2001 in the upwind direction with the SWAN H cell data obtained in the same period. This work is finding very similar results for the two instruments.

Ben Jaffel et al. (2000) re-analysed the early GHRS/HST spectra and noticed a small bump at shorter wave lengths than the interplanetary Lyman-α line. They attributed this to a first-order Fermi acceleration of Lyman-α photons at the interface region. This conclusion seems unlikely due to the very small optical thickness of the interface region at Lyman-α (of the order of $\tau = 1$). Furthermore, upwind observations obtained with STIS in 2001 do not show this small bump on the blue

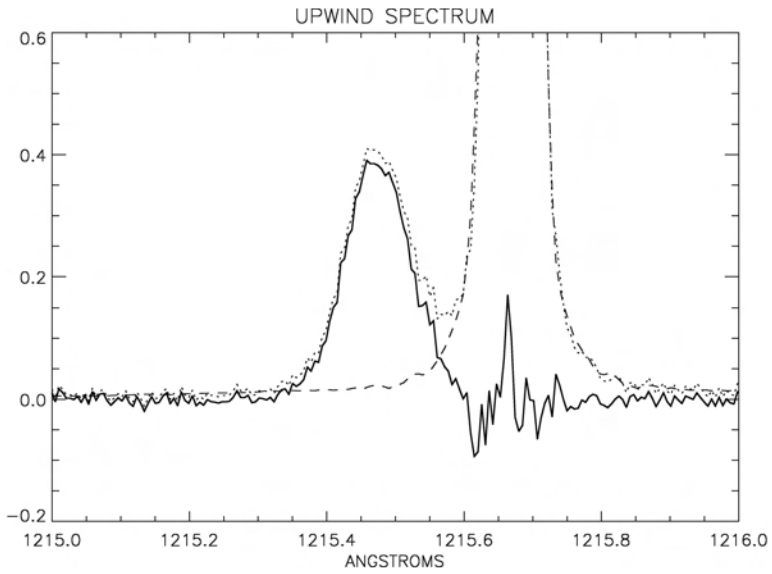

Figure 9.7: HST upwind line profile (Clarke et al., private communication) recorded by STIS/HST in March 2001. The dotted line shows the Earth coronal emission at Lyman-α which is Doppler shifted from the interplanetary line profile due to the relative motion of the Earth on that date. The interplanetary line gives an apparent velocity of 21 km/s in the solar rest frame. This apparent velocity is a value averaged over the different atoms contributing to the intensity on the line of sight. The relatively small Doppler shift is representative of solar maximum conditions when the radiation pressure counteracts the gravitational pull, thus slowing down the H atoms close to the Sun. Figure (9.4) is representative of conditions of solar minimum when the radiation pressure from the Sun is smaller.

wing of the Lyman-α line. Most likely, the previously observed feature was due to an emission from the Earth's atmosphere (telluric D Lyman-α).

9.5.3 Apparent direction of the hydrogen flow

The SWAN H cell data have been used by Lallement et al. (2005) to derive accurately the direction of the interstellar hydrogen flow relative to the Solar System. The values found with two independent analyses $(\lambda, \beta) = (252.2° \pm 0.5°, 9.0° \pm 0.5°)$ are significantly different from those found for the interstellar helium flow, i.e. $(\lambda, \beta) = (254.7° \pm 0.4°, 5.2° \pm 0.2°)$ (Witte, 2004).

The most likely explanation for this deflection presented by the authors is a distortion of the heliosphere under the action of an ambient interstellar magnetic field. In that case, the helium flow vector, unaffected by the heliospheric interface, and the hydrogen flow vector constrain the direction of the magnetic field in a plane containing these two vectors. This analysis will need to be tested against actual model computations to be completely demonstrated. Such a distortion might also be linked to the unexpected pattern of the Lyman-α excess detected by Quémerais

et al. (1995) in the upwind direction from the Voyager/UVS outer heliosphere scans.

9.6 Open questions and future developments

Study of the Lyman-α background started more than 35 years ago. In the course of this study, it has been realized that the interplanetary UV background data could be used to study the limits of the heliosphere and help constrain the structure of the boundary between the expanding solar wind and the neighbouring interstellar medium.

There are still a number of key questions that will have to be addressed in the coming years.

First, we need to derive as accurately as possible the actual variation of the intensity with heliocentric distance in the upwind direction. It was shown unambiguously that the coefficient α of the power law $I(r) \propto r^{\alpha}$ is larger than -1 . However, there is still some uncertainty about the actual value of this coefficient due to the fact that the data need to be corrected for solar Lyman-α flux variations with the 11-year solar cycle.

Also, scans along great circles performed in the outer heliosphere have shown that the observed upwind excess of Lyman-α background was slightly offset ($\approx 20°$) from the upwind direction. Is this due to a secondary emission from outside the heliopshere ? Is this due to an asymmetry in the hydrogen distribution caused by a tilted heliospheric boundary ? If this tilt is due to the local interstellar magnetic field, is the excess upwind emission compatible with the deflection measured between the hydrogen and helium flow vectors ? These questions will only be answered when a complete model of the hydrogen distribution in the upwind outer heliosphere is available.

The wealth of interplanetary background data in the inner heliosphere also raises a lot of answered questions.

First, as shown in Chapter 4, charge exchange of interstellar hydrogen atoms with heated and decelerated solar protons in the heliosheath produces a hot component of neutral hydrogen atoms which can reach deep inside the heliosphere. This component has not been observed yet because it is Doppler shifted outside the solar illuminating line. However, for some observation positions, it might be observed in absorption using a hydrogen absorption cell. This will have to be confirmed using the SWAN H cell data. At least an upper limit to the intensity should be derived, even without positive detection.

Computing the interplanetary Lyman-α line profile also requires taking into account effects of the radiation pressure, photo-ionization by solar EUV photons and ionization by charge exchange with solar wind protons. Those three effects strongly vary with the 11-year solar cycle and are the main cause of changes in the interplanetary line profile as seen from Earth orbit. At the present time, there is no model of the hydrogen distribution in the inner heliosphere which takes all of these variations into account. Yet, such models will be necessary to study possible changes of line shape caused by changes at the heliospheric interface. One clear

application of such models is the study of the deflection between the hydrogen and helium flows and its possible variation with solar cycle.

Bibliography

Ajello, J.M., Stewart, A.I., Thomas, G.E., and Graps, A.: 1987, 'Solar cycle study of interplanetary Lyman-α variations: $Pioneer - Venus$ orbiter sky background results', *Astrophys. J.* **317**, 964.

Anderson, D.E., and Hord, C.W.: 1977, 'Multidimensional radiative transfer: Applications to planetary coronae', *Planet. Space Sci.* **25**, 563.

Baranov, V.B., and Malama, Y.G.: 1993, 'Model of the solar wind interaction with the local interstellar medium – numerical solution of self-consistent problem', *J. Geophys. Res.* **98**, 15'157.

Baranov, V.B., Izmodenov, V.V., and Malama, Y.G.: 1998, 'On the distribution function of H atoms in the problem of the solar wind interaction with the local interstellar medium', *J. Geophys. Res.* **103**, 9575–9586.

Ben-Jaffel, L., Puyoo, O., and Ratkiewicz, R.: 2000, 'Far-ultraviolet echoes from the frontier between the solar wind and the Local Interstellar Cloud', *Astrophys. J.* **533**, 924–930.

Bertaux, J.L., and Blamont, J.E.: 1971, 'Evidence for an extra-terrestrial Lyman-α emission, the interstellar wind', *Astron. Astrophys.* **11**, 200.

Bertaux, J.L.: 1974, L'hydrogène atomique dans l'exosphère terrestre: mesures d'intensité et de largeur de raie de l'émission Lyman-α à bord du satellite OGO 5 et interprétation, Thèse d'état, Université Paris 6.

Bertaux, J.L., Lallement, R., Kurt, V.G., and Mironova, E.N.: 1985, 'Characteristics of the local interstellar hydrogen determined from *Prognoz* 5 and 6 interplanetary Lyman-α line profiles measurements with a hydrogen absorption cell', *Astron. Astrophys.* **150**, 82.

Bertaux, J.L., *et al.*: 1995, 'SWAN: A study of solar wind anisotropies on SOHO with Lyman-α sky mapping', *Solar Physics* **162**, 403.

Bertaux, J.L., Lallement, R., and Quémerais, E.: 1996, 'UV studies and the solar wind', *Space Sci. Rev.* **78**, 317.

Bertaux, J.L., *et al.*: 1997, 'First results from SWAN Lyman-α solar wind mapper on SOHO', *Solar Physics* **175**, 737.

Brandt, J.C., and Chamberlain, J.W.: 1959, 'Interplanetary gas. I. Hydrogen radiation in the night sky', *Astrophys. J.* **130**, 670.

Brasken, M., and Kyrölä, E.: 1998, 'Resonance scattering of Lyman-α from interstellar hydrogen', *Astron. Astrophys.* **332**, 732.

Chandrasekhar, S.: 1952, *Radiative Transfer*, Dover, New York.

Clarke, J.T., Lallement, R., Bertaux, J.-L., and Quémerais, E.: 1995, 'HST/GHRS observations of the interplanetary medium downwind and in the inner solar system', *Astrophys. J.* **448**, 893.

Costa Costa, J., Lallement, R., Quémerais, E., Bertaux, J.-L., Kyrölä, E., and Schmidt, W.: 1999, 'Heliospheric interstellar H temperature from SOHO/SWAN H cell data', *Astron. Astrophys.* **349**, 660.

Gangopadhyay, P., and Judge, D.L.: 1989, 'The heliospheric neutral hydrogen density profile in the presence of a solar wind shock', *Astrophys. J.* **336**, 999–1011.

Hall, D.T.: 1992, Ultraviolet resonance radiation and the structure of the heliosphere, Ph. D. thesis, University of Arizona.

Hall, D.T., Shemansky, D.E., Judge, D.L., Gangopadhyay, P., and Gruntman, M.A.: 1993, *J. Geophys. Res.* **98**, 15'185.

Holstein, T.: 1947, 'Imprisonment of resonance radiation in gases', *Phys. Rev.* **72**, 1212.

Ivanov, V.V.: 1973, 'Transfer of radiation in spectral lines', N.B.S. special publication 385.

Keller, H.U., Richter, K., and Thomas, G.E.: 1981, 'Multiple scattering of solar resonance radiation in the nearby interstellar medium. II', *Astron. Astrophys.* **102**, 415.

Kyrölä, E., Summanen, T., Schmidt, W., Mäkinen, T., Bertaux, J.-L., Lallement, R., Quémerais, E., and Costa, J.: 1998, 'Preliminary retrieval of solar wind latitude distribution from solar wind anisotropies/SOHO observations', *J. Geophys. Res.* **103**, 14'523.

Lallement, R., Bertaux, J.-L., and Clarke, J.T.: 1993, 'Deceleration of interstellar hydrogen at the heliospheric interface', *Science* **260**, 1095–1098.

Lallement, R., Quémerais, E., Bertaux, J.-L., Ferron, S., Koutroumpa, D., and Pellinen, R.: 2005, 'Deflection of the interstellar neutral hydrogen flow across the heliospheric interface', *Science* **307**, 1447–1449.

Meier, R.R.: 1991, 'Ultraviolet spectroscopy and remote sensing of the upper atmosphere', *Space Sci. Rev.* **58**, 1.

Mihalas, D.: 1978, *Stellar atmospheres*, Freeman and Co Publisher.

Mitchell, A.C.G., and Zemansky, M.W.: 1934, *Resonance Radiation and Excited Atoms*, 3^{rd} edition 1971, Cambridge University Press.

Morton, X.: 1991, 'Atomic data for resonance absorption lines. I – wavelengths longward of the Lyman limit', *Astrophys. J. Supp. Ser.* **77**, 119.

Pryor, W.R., *et al.*: 1992, 'The Galileo and Pioneer Venus ultraviolet spectrometer experiments – Solar Lyman-α latitude variation at solar maximum from interplanetary Lyman-α observations', *Astrophys. J.* **394**, 363.

Quémerais, E., and Bertaux, J.L.: 1993, 'Radiative transfer in the interplanetary medium at Lyman-α, *Astron. Astrophys.* **277**, 283.

Quémerais, E., Bertaux, J.L., Sandel, B.R., and Lallement, R.: 1994, 'A new measurement of the interplanetary hydrogen density with ALAE/ATLAS 1', *Astron. Astrophys.* **290**, 941.

Quémerais, E., Sandel, B.R., Lallement, R., and Bertaux, J.L.: 1995, 'A new source of Lyman-α emission detected by Voyager UVS: heliospheric or galactic origin?', *Astron. Astrophys.* **299**, 249.

Quémerais, E., Malama, Y.G., Sandel, W.R., Lallement, R., Bertaux, J.-L., and Baranov, V.B.: 1996, 'Outer heliosphere Lyman-α background derived from two-shock model hydrogen distributions: application to the Voyager UVS data', *Astron. Astrophys.* **308**, 279–289.

Quémerais, E., Bertaux, J.-L., Lallement, R., Berthé, M., Kyrölä, E., and Schmidt, W.: 1999, 'Interplanetary Lyman-α line profiles derived from SWAN/SOHO hy-

drogen cell measurements: full-sky velocity field', *J. Geophys. Res.* **104**, 12'585.
Quémerais, E.: 2000, 'Angle dependent partial frequency redistribution in the interplanetary medium at Lyman-α', *Astron. Astrophys.* **358**, 353–367.
Quémerais, E., and Izmodenov, V.: 2002, 'Effects of the heliospheric interface on the interplanetary Lyman-α glow seen at 1 AU from the Sun', *Astron. Astrophys.* **396**, 269–281.
Quémerais, E., Bertaux, J.-L., Lallement, R., Sandel, B.R., and Izmodenov, V.: 2003, 'Voyager 1/UVS Lyman-α glow data from 1993 to 2003: hydrogen distribution in the upwind outer heliosphere', *J. Geophys. Res.* **108**, LIS 4-1.
Quémerais, E.: 2006, 'Interplanetary Lyman-α background and the heliospheric interface', Proceedings of the IGPP Annual International Astrophysics Conference, Hawaii, 2006.
Scherer, H., and Fahr, H.J.: 1996, 'H Lyman-α transport in the heliosphere based on an expansion into scattering hierarchies', *Astron. Astrophys.* **309**, 957.
Scherer, H., Bzowski, M., and Rucinski, D.: 1999, 'Improved analysis of interplanetary HST-Lyman-α spectra using time-dependent modelings', *Astron. Astrophys.* **342**, 601.
Thomas, G.E.: 1963, 'Lyman-α scattering in the Earth's hydrogen geocorona', *J. Geophys. Res.* **68**, 2639.
Thomas, G.E., and Krassa, R.F.: 1971, 'OGO-5 measurements of the Lyman-α sky background', *Astron. Astrophys.* **11**, 218.
Thomas, G.E.: 1978, 'The interstellar wind and its influence on the interplanetary environment', Ann. Rev. Earth Planet. Sci. **6**, 173.
Tobiska, W.K., Pryor, W.R., Ajello, J.M.: 1997, 'Solar hydrogen Lyman-α variation during solar cycles 21 and 22', *Geophys. Res. Lett.* **24**, 1123.
Witte, M.: 2004, 'Kinetic parameters of interstellar neutral helium; review of results obtained during one solar cycle with the Ulysses/GAS-instrument', *Astron. Astrophys.* **426**, 835–844.
Wu, F.M., Gangopadhyay, P., Ogawa, H.S., and Judge, D.L.: 1988, 'The hydrogen density of the local interstellar medium and an upper limit to the galactic glow determined from Pioneer 10 ultraviolet photometer observations', *Astrophys. J.* **331**, 1004–1012.
Zank, G.P., Pauls, H.L., Williams, L.L., and Hall, D.T.: 1996, 'Interaction of the solar wind with the local interstellar medium: a multifluid approach', *J. Geophys. Res.* **101**, 21'639–21'656.

— 10 —

Diagnostics of the Heliospheric Interface: High Energy ENAs

Andrzej Czechowski[1]
Space Research Centre, Polish Academy of Sciences
Warsaw, Poland

Martin Hilchenbach
Max-Planck-Institut für Sonnensystemforschung
Katlenburg-Lindau, Germany

Reinald Kallenbach
International Space Science Institute
Bern, Switzerland

Abstract. **Energetic neutral atoms (ENAs) detected near Earth's orbit in the energy range from a few to a few hundred keV/nucleon carry information about the ion acceleration and transport mechanisms in the distant heliosphere, processes that are sensitive to the magnetic field structure, turbulence, and the plasma flow pattern. We summarize here the ENA observations of the CELIAS/HSTOF sensor onboard SOHO in the energy range 58 – 88 keV/nucleon and compare them to models of the structure of the heliosphere and of the transport of energetic ion populations in the distant heliosphere.**

10.1 Introduction

The low energy (less than few keV/nucleon) ENAs are derived from the thermal and the pick-up ions and therefore reflect the properties of the bulk plasma. The more energetic ENAs considered in this chapter (few to few hundred keV/nucleon) originate from the ions accelerated to higher energies, either by the shock waves or by plasma turbulence. As a result, they carry information about the ion acceleration and transport mechanisms in the distant heliosphere, processes that are sensitive to the magnetic field structure, turbulence and the plasma flow pattern.

The upper limit of few hundred keV/n is due to the ENA production mechanism. In the heliosheath it is dominated by the electron capture by singly charged parent ions from low energy neutral H and He atoms of interstellar origin. The probability of picking up an electron decreases rapidly with energy (Figure 10.1) so that the flux of the ENAs above some 200 keV/nucleon would be difficult to measure. The

[1]in *The Physics of the Heliospheric Boundaries*, V. Izmodenov and R. Kallenbach (eds.), ISSI Scientific Report No. 5, pp. 311 - 334, ESA-ESTEC, Paris 2006

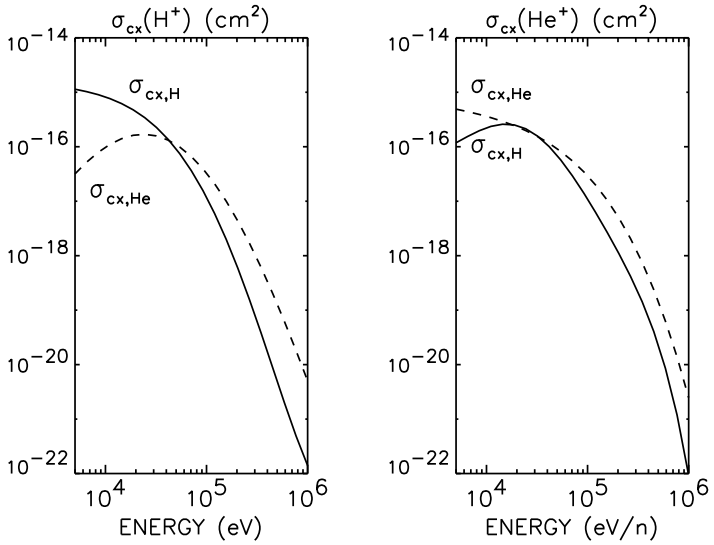

Figure 10.1: Charge exchange cross sections for protons and He^+ with H and He atoms (Barnett et al. 1990).

time needed for neutralization of an H^+ or He^+ ion in the heliosheath (taking $n_{\rm H}$=0.07 cm^{-3} and $n_{\rm He}$=0.015 cm^{-3} for the densities of H and He components of the neutral gas) is of the order of 10 years at 40 keV/n and 90 years at 120 keV/n.

While the low energy ENAs of heliospheric origin have not been detected up to now, there are observations of ENAs of higher energy (55–88 keV for hydrogen, 28–58 keV/nucleon for helium) by the CELIAS/HSTOF instrument onboard SOHO (Hilchenbach et al., 1998; Hilchenbach et al., 2001). These observations commenced in 1996 and continue today. The most important boost for the observations in this energy range comes, however, from the Voyager 1 LECP data obtained after crossing of the termination shock in December 2004 (Decker et al., 2005). Since the energy range covered by LECP starts at 40 keV, it is now possible to compare the ENA measurements with the in-situ measurements of the parent ion energy spectrum.

The plan of this chapter is as follows. We start by listing the sources of the high energy ENAs that can contribute to observations from the inner Solar System. The main source of interest to us, the energetic ions in the heliosheath, is discussed in the next section. We review available models of the energetic ion distribution beyond the termination shock and what they imply for the observations of the ENAs. We also consider in detail those elements that are still missing and must be included to obtain a realistic description. The ENA signal from the heliosheath may be obscured by the ENAs coming from other sources. Therefore we estimate the contributions to the ENA flux coming from the regions other than the heliosheath: the interstellar medium and the part of the heliosphere upstream from the termination shock. The next section presents the observations by CELIAS/HSTOF on SOHO, which are at present the only successful observations of the heliospheric

ENAs. We discuss two proposed interpretations of these observations: the ENAs of ACR origin coming from the heliosheath, and the ENAs from the ions accelerated at the transient shocks in the inner heliosphere. We also describe an attempt to use these data to derive the parent ion spectrum at the termination shock and (assuming that the ENAs are of ACR origin) estimate the shock compression ratio, and discuss how the results of this approach compare with the Voyager 1 data from beyond the shock. The last section summarizes our conclusions.

10.2 Sources of the high energy ENAs

Since we are interested in the use of ENAs for imaging the heliospheric interface (Gruntman, 1992; Hsieh et al., 1992; Gruntman et al., 2001; Roelof, 2001), it is enough to consider only the observations along the lines of sight away from the Sun. The flux $J_{\rm ENA}(E, \mathbf{n})$ of the ENAs of energy E arriving from direction $\mathbf{n}$ at the observation point can be expressed in terms of the parent ion flux $J_{\rm ion}(E, \mathbf{n}, s)$ along the line of sight

$$J_{\rm ENA}(E, \mathbf{n}) = \int_0^\infty {\rm d}s \frac{J_{\rm ion}(E, \mathbf{n}, s)}{\lambda_{\rm ion}(E, s)} \exp\left[- \int_0^s {\rm d}s' 1/\lambda_{\rm ENA}(E, s') \right] \qquad (10.1)$$

where s is the distance along the line of sight, $\lambda_{\rm ion}$ and $\lambda_{\rm ENA}$ are the mean free paths for neutralization of the parent ion and for ionization of the ENA, respectively, and the exponent represents the losses of the ENAs on the way from the source to the observer. For the ENAs in the energy range considered in this chapter the losses are small. The mean free path $\lambda_{\rm ion}$ can be expressed as $1/(\sigma_{\rm cx,H} n_{\rm H} + \sigma_{\rm cx,He} n_{\rm He})$, where $\sigma_{\rm cx,H}$, $\sigma_{\rm cx,He}$ are the cross sections for the electron capture by the ions from H or He neutral atoms.

Possible sources of the ENAs in the few keV - few hundred keV energy range are (Hsieh et al., 1992):

1. Ions accelerated in the distant heliosphere, particularly at the termination shock. These include in particular the termination shock particles (TSP) discovered downstream from the shock by Voyager 1 and the low energy part of the anomalous cosmic ray (ACR) ions. The ENAs from this source (TSP/ACR ENAs) are produced downstream from the termination shock (in the heliosheath).

2. Ions accelerated in the inner heliosphere. These include the ions accelerated by the turbulence and transient shock waves in the bulk solar wind upstream of the termination shock (pre-acceleration). One example is the ions accelerated at the shock waves connected with the co-rotating interaction regions (CIR). Since these ions are convected outwards by the plasma flow, the ENAs are generated both in the inner and in the outer heliosphere.

3. Energetic ions associated with solar events. This is a strong, but transient source of the ENAs.

4. The low energy part of the spectrum of the galactic cosmic rays (GCR). The resulting ENAs (GCR ENAs) come from outside the heliosphere.

10.3 Energetic ions beyond the termination shock

Before the crossing of the termination shock by Voyager 1, the observations of the anomalous cosmic ray ions were necessarily restricted to high energy particles (above ∼1-10 MeV/n) since only those were able to penetrate far enough upstream of the termination shock. This naturally applied also to the theoretical studies of cosmic ray transport, which concentrated on modulation of the high energy ACR spectra in the inner heliosphere. The region downstream from the shock was not essential for these studies. Theoretical investigations of the ACR distribution in the distant heliosphere (Czechowski et al., 1995; 2001a; 2004a; 2005a,b) and of the pre-accelerated pick-up ions (Chalov et al., 2003) were motivated by the possibility of remote observations of the low-energy part (up to few 100 keV/n) of the ACR spectrum by means of the ENAs, and by the ENA observations by HSTOF (Hilchenbach et al., 1998; 2001).

10.3.1 Energetic ions transport processes in the heliosheath

Let us list the most important processes that would determine the distribution of the energetic ions in the distant heliosphere (Figure 10.2):

1. Convection with the plasma flow, which transports the particles downstream from the termination shock, ultimately into the heliotail region.

2. Losses due to neutralization by electron capture from the hydrogen and helium atoms.

3. Diffusion in space, caused predominantly by scattering off magnetic field irregularities. It can be viewed as a combination of a random walk along the magnetic field lines (parallel diffusion) and a motion perpendicular to the magnetic field, characterized by a much smaller step size.

4. Drift motion, caused by the nonuniformity of the magnetic field. The drift would be particularly effective for particles encountering a current sheet: a narrow boundary surface at which the magnetic field changes sharply.

5. Adiabatic acceleration or decelaration caused by compression or expansion of plasma, respectively.

6. Acceleration by scattering off converging plasma flows at shock waves, in particular at the termination shock.

7. Acceleration due to interactions with wave turbulence.

8. Escape from the heliosphere into the interstellar space. Since the ions tend to be tied to the field lines of the magnetic field of solar origin, the escape process must be sensitive to the detailed structure of the region near the heliopause.

All of these effects are included in the transport equation. Assuming that the velocity distribution of the ions is approximately isotropic, the transport equation for the pitch-angle-averaged particle distribution $f(\mathbf{x}, p, t)$ is (Parker, 1965)

$$\partial_t f = \nabla \cdot \kappa \cdot \nabla f - (\mathbf{V} + \mathbf{V_D}) \cdot \nabla f + \frac{1}{3} \frac{\partial f}{\partial \ln p} \nabla \cdot \mathbf{V} - \beta f \tag{10.2}$$

where:

$\mathbf{V} = \mathbf{V}(\mathbf{x}, t)$ is the velocity of the plasma flow,

$\mathbf{V_D} = \mathbf{V_D}(\mathbf{x}, t)$ the drift velocity,

$\kappa = \kappa(\mathbf{x}, t)$ the particle diffusion tensor,

p the absolute value of the particle momentum,

$\beta = \beta(\mathbf{x}, t)$ the loss rate.

We have omitted the term describing the acceleration effects due to turbulence which is described in Chapter 6.

The diffusion tensor κ can be written as $\kappa_{ij} = \kappa_\parallel b_i b_j + \kappa_\perp(\delta_{ij} - b_i b_j)$ where $b_i = \mathbf{B}_i/|\mathbf{B}|$ is the local direction of the magnetic field, and $\kappa_\parallel$, $\kappa_\perp$ are the parallel and perpendicular diffusion coefficients, which in turn are defined in terms of the mean free paths $\lambda_\parallel$, $\lambda_\perp$ as $\kappa_\parallel = (1/3)\lambda_\parallel v$, $\kappa_\perp = (1/3)\lambda_\perp v$, where v is the particle speed. Typically, $\kappa_\perp/\kappa_\parallel \sim 10^{-2}$ is assumed.

Taking a definite model of the heliosphere and assuming that the energetic ion spectrum at the termination shock is known, one can calculate the ion distribution downstream of the termination shock by solving numerically the transport equation in this region. This requires that initial and boundary conditions are set. The boundary conditions in space (taking the Sun as the origin of coordinates) can be chosen as follows:

$f(\mathbf{x}, p, t)|_{\text{shock}}$ is given,

$f(\mathbf{x}, p, t)|_{|\mathbf{x}|\to\infty} = 0$

A difficulty occurs with the boundary conditions in p which should be specified at the ends of the momentum interval chosen for calculations. At large p, one can specify that $f(\mathbf{x}, p, t)|_{p\to\infty} = 0$ but at the lower bound $p_{\min}$ setting the boundary condition for f requires that the solution for f (or its derivative $\partial f/\partial p$) at $p = p_{\min}$ is known. In most of the calculations discussed here (Czechowski et al., 2001a) the boundary conditions in p were set by assuming (position and time-independent) values of the slope of the ion energy spectrum (or, equivalently, $\partial \log f/\partial \log p$) at $p_{\min}$ and $p_{\max}$. It was found that, except for the values of p close to $p_{\min}$ and $p_{\max}$, the solution was only weakly dependent on the assumed values.

We shall now summarize the results for the ion distributions in the outer heliosphere and the associated production of the ENAs obtained by solving the transport equation in some models of the heliosphere. It must be stressed that all of the models considered up to now were highly simplified.

10.3.2 The models

For reasons of simplicity, most of the simulations of the ion distributions in the heliosheath up to now were restricted to the two-dimensional case: that is, the heliosphere and the ion distribution were assumed to be symmetric with respect to rotations around the Sun's trajectory relative to the interstellar medium. Within

this approximation, there are two options for treatment of the heliospheric magnetic field, which determines diffusion and drift terms:

1. Disregard it completely, neglecting the spatial diffusion and drifts. Neglecting diffusion is likely to be a good approximation for ions of sufficiently low energy, for which the diffusion coefficients are expected to be small.

2. Assume that the magnetic field downstream of the termination shock can, in some "lowest order" approximation, be treated as isotropically disordered, leading to a scalar diffusion model. In this case, the diffusion tensor is proportional to the unit matrix: $\kappa_{ij} = \kappa\delta_{ij}$ with scalar diffusion coefficient κ.

Since we are considering the ions of relatively low energy, for which the components of the diffusion tensor are smaller than for the high energy particles, it is possible that the spatial diffusion effects are unimportant, or only moderately important, compared to the convection and loss terms. Validity of this conjecture depends on the values of the diffusion parameters for the energetic ions in the outer heliosphere, which are unknown. Calculations based on extrapolating the diffusion coefficients from the models used in the inner heliosphere (Czechowski et al., 2001a) suggest that the "no diffusion" approximation may be applicable below a few 10 keV/n, although it would be invalidated if large ion density gradients are present. Also, it is possible that the diffusion effects at low energy may be treated approximately, with the "no-diffusion" model taken as a lowest order.

The scalar diffusion model could be partially justified by observing that there must be extended regions of disordered magnetic field in the outer heliosphere, caused by the solar magnetic field reversals during solar maximum periods (see, e.g., Nerney et al., 1995).

Two recent studies go beyond this approximation. They are both based on the axisymmetric model of the heliospheric flow, but the diffusion tensor is not taken to be axisymmetric, but determined from the three-dimensional model of the heliospheric magnetic field. The magnetic field is obtained in the "kinetic" approximation (Nerney et al., 1991; 1993) in which the effect of the magnetic field on the heliospheric plasma flow is neglected. Scherer and Ferreira (2005) have solved Equation (10.2) numerically, but the energy range they covered was above the range considered in this chapter. In the approach of Czechowski et al. (2005b) only the parallel diffusion along the magnetic field lines is considered, and the diffusion process is described by the approximate one-dimensional Green's function. The results shown in Figure 10.3 were obtained by this method.

10.3.3 Results from the scalar diffusion model

Consider first the results obtained in the scalar diffusion model (Figure 10.2, Czechowski et al., 2001a). The model of the heliosphere was based on the time-independent 5-component axisymmetric gas-dynamical solution (Fahr et al., 2000). The simulations were restricted to the region downstream of the termination shock. The ion spectrum at the shock was prescribed as a boundary condition. The case illustrated in Figure 10.2 corresponds to assuming that the ion spectrum at the shock has a power-law form $CE^{-\delta}$ with C and δ varying over the shock surface:

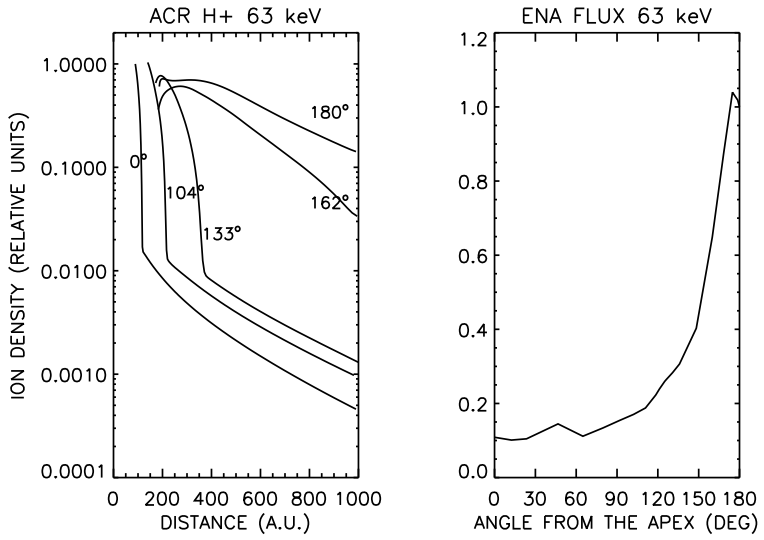

Figure 10.2: Distribution of the ACR protons at 63 keV outside the termination shock and the angular dependence of the corresponding energetic hydrogen flux, calculated in a scalar diffusion model. The ACR distribution is presented as a function of the heliocentric distance for five directions: Θ=0^o, 104^o, 133^o, 162^o, 180^o, where Θ is counted from the nose direction. The curves start at the termination shock, where the ACR density was set as a boundary condition. Note that the dip at Θ $\sim$162^o in the ACR density near the shock (following from the assumed boundary conditions) is filled within $\sim$50-100 AU by spatial diffusion. Sharp slope changes indicate the position of the heliopause (the cosmic ray diffusion coefficient in the interstellar medium was taken to be much larger than inside the heliopause). The energetic hydrogen flux has a sharp peak from the heliotail (Θ=180^o) direction.

in particular, δ is determined by the local shock compression ratio r according to $\delta = (3/2)r/(r-1)$, the formula valid for diffusive shock acceleration mechanism. The region outside the heliopause was formally included in the calculations. The diffusion coefficient outside the heliopause was taken to be much larger (typically by a factor of 100) than inside. In effect, the heliopause was approximately a free escape boundary.

In the forward heliosphere, the calculated ion density decreases rapidly towards the heliopause. This falloff is caused most of all by the escape of particles across the heliopause, which in the forward region is close to the termination shock (30-50 AU). In the heliotail region the distance to the heliopause is larger (of the order of 200 AU from the axis of the heliotail) and the falloff of the ion distribution is to a large part due to the loss of the ions by neutralization (the same mechanism that produces the ENAs). As a result the ENA flux from the heliotail direction is higher than from other directions. Interestingly, such a peak was observed in the HSTOF energetic hydrogen data (Hilchenbach et al., 1998; 2001), although the tail/apex ENA flux ratio was less than that obtained in the model. The presence of the ENA

intensity peak from the heliotail direction is the main result of the scalar diffusion models.

In the case illustrated in Figure 10.2, the ion density at the termination shock in the heliotail region was assumed to be smaller (approximately by a factor of 5) than in the forward region. Nevertheless, the dip in the ion distribution was filled by spatial diffusion within 50-100 AU downstream from the shock.

10.3.4 No-diffusion model: effect on the ENA peak from the heliotail

The no-diffusion approximation is very simple in application, and may be a good approximation in favourable cases (low ion energy and low spatial gradients in the ion density distribution).

Neglecting spatial diffusion leads to two potentially important changes in the ion transport processes beyond the termination shock. If the drift term is also neglected, then:

1. there is no possibility of ions escaping across the heliopause.

2. there is no exchange of ions between different plasma flow lines.

As a result, the ion distribution in the forward (LISM apex) part of the heliopause will not "feel" the proximity of the outer heliospheric boundary and so will not decrease towards the heliopause as fast as in the scalar diffusion model. Thus the ENA flux from the apex direction will be increased. Also, the ion distribution in most of the heliotail will be fed by the flow lines emerging from the rear part of the termination shock. If this region of the shock is less efficient in producing energetic ions, the ion distribution in the heliotail will be suppressed. These two effects can remove the ENA intensity peak from the heliotail direction. Including diffusion tends to restore the peak.

In the class of models considered in the earlier work by Czechowski et al. (1995; 2001a) the scalar diffusion and no-diffusion models led to similar results and were in agreement below ∼40 keV. In these models the boundary condition for the energetic ion density at the termination shock was assumed to have only a limited (less than one order of magnitude) spatial variation over the termination shock surface. On the other hand, if the energetic ion flux at the shock would vary strongly over the shock surface, the results of "no-diffusion" and scalar diffusion models should be qualitatively different.

Large spatial variation of the ion flux at the termination shock could occur as follows. Suppose that above some energy E_0 the ion spectrum at the termination shock is given by a simple power law $(E/E_0)^{-\delta}$ where δ is determined by the local shock strength r ($\delta = (3/2)r/(r-1)$ is the formula resulting from diffusive shock acceleration mechanism). Then, when E/E_0 is large enough, even moderate variation of δ over the shock surface would lead to a large change in the ion density. If the termination shock in the heliotail sector is weaker than in the frontal region, the accelerated ion flux at the shock would be much lower in the heliotail region than in the forward region. This is what indeed occurred in some calculations

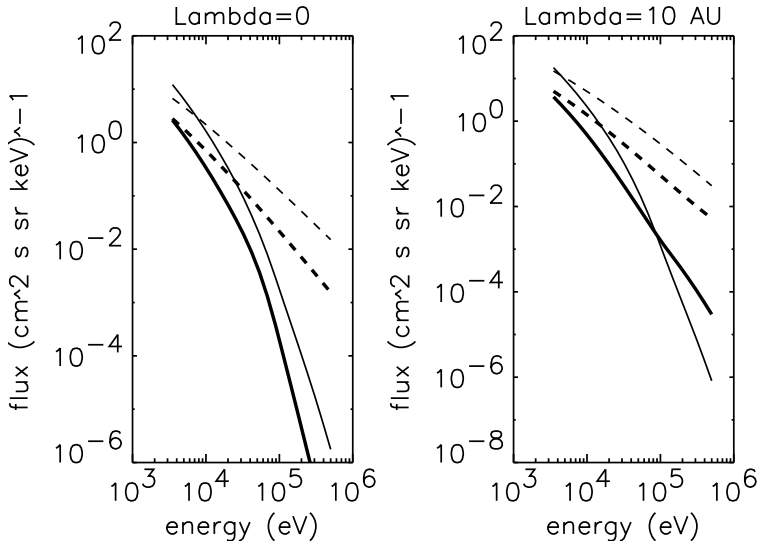

Figure 10.3: Effect of spatial diffusion of the parent ions on the ENA spectrum. The figure on the left shows calculated energy spectra for the energetic hydrogen atoms arriving from the apex (thin solid line) and from the heliotail (thick solid line) directions in the approximation neglecting spatial diffusion of the parent ions. In the figure on the right, parallel diffusion is included, with the mean free path equal to 10 AU. The proton spectra assumed at the termination shock are shown by the thin dashed line (apex) and the thick dashed line (heliotail), respectively.

(Czechowski et al., 2004b) based on the model of the heliosphere developed by Scherer and Fahr (Scherer and Fahr, 2003a,b,c; Fahr and Scherer, 2004).

Figure 10.3 shows the energy spectra of the ENAs from the apex and from the heliotail directions calculated for such a case. When spatial diffusion is neglected, the ENA flux from the apex direction is higher than from the heliotail. When diffusion is included, the ion density in the heliotail downstream from the shock increases and so does the ENA flux from the heliotail direction. Above some minimum energy, where the diffusion coefficient becomes large enough, the ENA peak from the heliotail is restored (Czechowski et al., 2005b).

10.3.5 Time-dependent models

We now present briefly the results of the simulations of the ion distributions in the heliosheath that include the effect of time variation caused by the solar cycle (Czechowski et al., 2004; 2005b). They are based on the time-dependent model of the heliosphere of Scherer and Fahr (Scherer and Fahr, 2003a,b,c; Fahr and Scherer, 2004). The ion distributions are obtained in the no-diffusion approximation.

Although these are preliminary results (large spatial gradients imply that the diffusion should be included) we note them here because they illustrate a second possible signature of the heliosheath ENAs: the weak dependence on time. The

calculated ion distributions are strongly dependent on time, but in the ENA fluxes this dependence is much reduced. This is to be expected on general grounds. Conversion of the ions to the ENAs is slow: the characteristic time for neutralization by charge-exchange for an ion of few 10 - few 100 keV/n energy is comparable to or longer that the period of the solar cycle. Time dependence of the parent ion distribution occurring on a shorter time scale will therefore be smoothed out in the ENA flux, particularly from the region of the heliotail.

10.3.6 Discussion

To conclude, the available results from numerical simulations are not yet sufficient to make definite predictions about the ENA signal from the outer heliosphere. The suggestions from the simplified models are: the maximum of the ENA flux is from the heliotail direction, at least when diffusion effects are large; there is weak time-dependence of the ENA flux, caused by the large effective size of the ENA source region. There is a need for more realistic models that would combine improved descriptions of the heliosphere (fully three-dimensional and time-dependent) and of the energetic ion transport in the heliosheath.

The major elements missing from the available simulations of the energetic ion transport in the outer heliosphere are:

1. a full account of the heliospheric magnetic field structure beyond the termination shock, including time dependence and the current sheets, and

2. a realistic description of the heliospheric plasma flow, in particular of its three-dimensional structure and time dependence.

Heliospheric magnetic field and the current sheet

Every 11 years the Sun's magnetic field goes through a reversal process near solar maximum. During this period the magnetic field near the Sun has a complicated form, with regions of opposite polarity intermingled in both nothern and southern hemispheres, as opposed to approximately unipolar fields during solar minimum (Nerney et al., 1995). These regions of disordered magnetic field extending to high latitudes form "shells" carried outwards with the solar wind (Figure 10.4) and piling up at the heliopause. As a result, the magnetic field near the heliopause is likely to be disordered.

This picture of the heliospheric magnetic field has implications both for the spatial diffusion of ions (dominated by the motion parallel to the magnetic field lines) and for the drift motion. The drift effect is particularly important near the heliospheric current sheet: a thin ($\sim 10^5$ km) surface in the heliospheric plasma separating the magnetic field regions of different polarity. In the heliosheath, the heliospheric current sheet has a complicated, time-dependent shape and can extend to high heliolatitudes. A charged particle that encounters the magnetic current sheet will start drifting rapidly along its surface.

For the ion distribution calculations it is important also to include the possibility of ion transport across the heliopause. The scalar diffusion models most probably overestimate the transport rate of the ions towards and across the heliopause. On

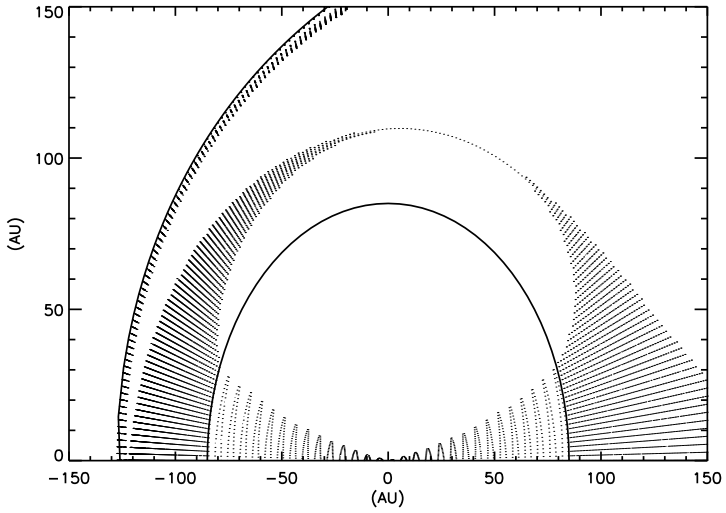

Figure 10.4: A view of the heliospheric current sheet in a time-dependent model of the heliospheric magnetic field. The figure shows the northern part of the model heliosphere cut by the meridional plane, defined to include the solar rotation axis (vertical) and the Sun's trajectory through the interstellar medium (horizontal), which are assumed to be perpendicular to each other (the solar equator plane is perpendicular to the figure). The outlines of the termination shock and of the heliopause are shown. The Sun is at the point $y = z = 0$ and its velocity relative to the interstellar medium is directed along the negative z axis. The heliospheric current sheet is indicated by dots. Within the termination shock, the heliospheric current sheet is a wavy surface (with the wavelength equal to the solar wind speed multiplied by the solar rotation period), confined (at the selected moment of time) to the vicinity of the solar equator. Downstream from the termination shock, the sheet is more tightly folded, because of slower plasma speed. A shell of disordered field, filled by the folded plasma sheet, is shown between the termination shock and the heliopause. Note also a disordered field region near the heliopause.

the other hand, in a simplified model that includes the heliospheric magnetic field only of the unipolar type (for example, with flat current sheet), the escape across the heliopause would have to occur via slow transverse diffusion. The role of the layer of disordered magnetic field near the heliopause, with the associated current sheets, has not yet been investigated.

Fast and slow solar wind

The solar wind is known to have two components: the "fast" and the "slow" solar wind. Except for the period of time close to the solar maximum, the "slow" solar wind is confined to the vicinity of the solar equator and the "fast" solar wind flows out from the polar coronal holes. It was suggested that the boundary between

the slow and fast solar wind regions may correspond to the termination shock being oblique rather than perpendicular, which may result in easier injection of the ions into the acceleration process. Downstream from the shock, the fast solar wind is likely to form two channels of faster flowing plasma separated from the slow wind regions. The magnetic field must reflect this structure, with implications for spatial diffusion and drifts.

Asymmetric termination shock

Because of the motion of the Sun through the interstellar medium and the solar wind asymmetry, the termination shock is expected to be nonspherical in shape, with the parameters (like shock strength) varying over the shock surface. This must affect the distribution of the shock accelerated ions, which may become strongly dependent on the position at the shock. One possibility is the existence of favoured locations where the injection of the ions into the acceleration process is easier due to shock geometry (Schwadron and McComas, 2003).

10.3.7 ENA from the regions other than the heliosheath

The ENA observations would be useful for diagnostics of the outer heliosphere only provided the ENA signal from the outer heliosphere would not be obscured by the ENAs from the other sources. It is therefore important to estimate the contribution to the flux of the ENAs from regions other than the heliospheric interface: the interstellar medium (GCR ENAs) and the inner Solar System.

ENAs from GCR

The ENA flux from the galactic cosmic rays can be estimated as follows. Assume that the GCR ion flux intensity in the interstellar medium is constant in space. From Equation (10.1) it follows that

$$J_{\rm ENA}(E) = \int_0^\infty {\rm d}s \frac{J_{\rm GCR}(E)}{\lambda_{\rm GCR}(E)} \exp[-s/\lambda_{\rm ENA}(E)] = \frac{\lambda_{\rm ENA}(E)}{\lambda_{\rm GCR}(E)} J_{\rm GCR}(E) \quad (10.3)$$

where the mean free paths are defined as in Equation (10.1). Assuming that $\lambda_{\rm GCR}$ and $\lambda_{\rm ENA}$ are of the same order, we obtain an order-of-magnitude estimation $J_{\rm ENA}(E) \sim J_{\rm GCR}(E)$. The estimations of the GCR proton flux at low energy give $\sim$30 (m^2 s sr MeV)$^{-1}$ at $\sim$ 100 keV (Ip and Axford, 1985; Webber, 1998) which is small in comparison to the ENA flux measured by HSTOF.

ENAs from the inner heliosphere

The ENA flux arriving at the observation point in the inner heliosphere consists of atoms coming from a wide range of distances. The ion spectra measured in the inner Solar System (where, e.g., Ulysses data are available) are therefore insufficient to estimate the total ENA flux from the inner heliosphere. More complete information could be derived by analyzing Voyager/LECP data along the spacecraft trajectories. Up to now, this has been done only for a few points (Giacalone et al.,

1997; Krimigis et al., 2003). Estimates of the ENA flux from the inner heliosphere must rely, therefore, on extrapolations of the data and on theoretical models.

Hsieh et al. (1992) used simple models of the accelerated ion distributions for solar mass ejections and for co-rotating interaction regions to calculate the expected ENA fluxes and compare them with the ENAs coming from the ACR ions. The result was that the ENA flux from solar events is (at 1 AU) stronger than the ACR ENA signal, but since it is a transient effect the ACR ENAs should nevertheless be observable. The ENA production from the co-rotating interaction regions (CIR) was also considered by Kota et al. (2001) and found to be about one order of magnitude below the HSTOF data. Similarly, the ENA flux from the pick-up protons in the inner heliosphere accelerated by turbulence according to the theoretical model developed by Chalov and Fahr (Chalov et al. 1995, Fahr and Lay 2000) was found to be lower than the ENA flux from the outer heliosphere (Czechowski et al., 2001b).

These results are, however, model dependent and the possibility of a high contribution to the ENA flux from the inner heliosphere cannot be excluded at present.

Helium cone and the CIR ENA peak

Hsieh and Kota (Kota et al., 2001) are the authors of an interesting interpretation of the ENA intensity peak from the ISM anti-apex direction, which is a possible alternative to the ACR ENA model. According to this idea the peak arises because of the "helium cone". The helium cone forms because the interstellar helium atoms passing near the Sun have their trajectories bent by the solar gravity: as a result, a region of enhanced helium density emerges behind the Sun, in the LISM anti-apex direction. The production of the ENAs is enhanced in this region, because of the larger probability of picking up an electron from the helium atom.

For the case of HSTOF, the CIR ENA interpretation predicts that due to parallax effects the ENA peak should be slightly shifted with respect to the LISM anti-apex direction. The maximum intensity should be observed not on DOY 195, when the instrument line of sight points in the ISM anti-apex direction, but a few days later (Figure 10.5). The HSTOF data for the years 1996 and 1997 are consistent with such a shift. The exact amount of the shift depends on the model of the helium cone, but the direction of the shift is a definite prediction.

10.3.8 Voyager 1 post-shock data and the implications for ENAs

The above discussion shows that our understanding of the inner heliospheric sources of the ENAs is incomplete. This complicates the problem of separation of the parts of the observed ENA signal coming from the outer and from the inner heliosphere, since we cannot rely on a reliable estimation of the inner heliospheric ENA flux. Another approach would be to estimate the probable ENA flux level from the outer heliosphere and, if possible, identify the signatures of the ENAs from this source.

The main source of uncertainty in estimating the ENA flux from the outer heliospheric sources was, until recently, the lack of information about the flux

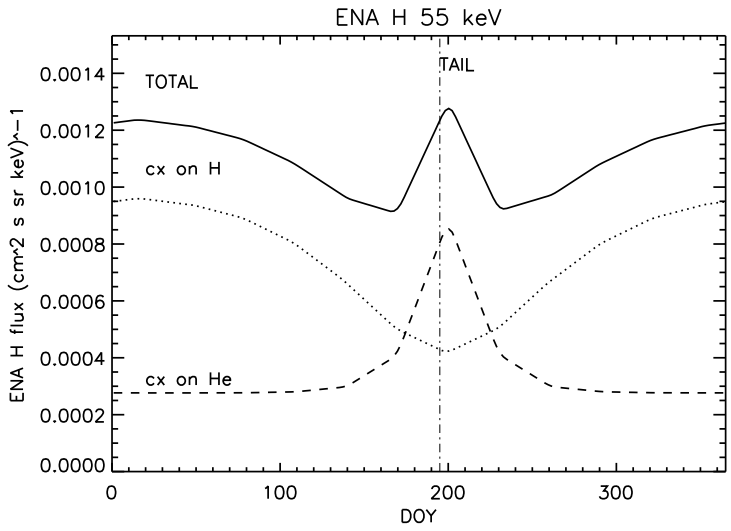

Figure 10.5: CIR ENA H flux as seen by HSTOF calculated in a simplified model. The H and He spatial distributions are taken from Thomas (1978) and the energetic proton spectra from Decker et al. (1995). The contributions from charge-exchange of energetic protons with the background H and He atoms are shown. Note the shift in the ENA peak intensity from the heliotail direction.

intensity of the parent ions near the termination shock. The reason was that the ions in the energy range of few 10 to few 100 keV/n cannot penetrate upstream of the shock, where the measurements were possible. The uncertainty in the flux intensity of these ions was large, more than one order of magnitude for the case of the ACR ions. This was caused by the need to extrapolate the ACR energy spectrum down from the high energy region ($\sim$100 MeV), where the measured flux intensity could be taken as an estimate of the flux at the shock. This uncertainty has now been removed after the crossing of the termination shock by Voyager 1.

Voyager 1 crossed the termination shock in mid-December 2004 entering the heliosheath. A clear sign of the heliosheath was the increase in the magnetic field by a factor of $\sim$3, suggesting a similar value for the shock compression ratio (Burlaga et al., 2005). This confirmation was lacking (Burlaga et al., 2003) for previous events involving an ion intensity rise (Krimigis et al., 2003; McDonald et al., 2003). For our purposes, the most relevant observations were those of the energetic ions, which were performed by two experiments: the Low-Energy Charged Particles (LECP) covering the range 40 keV to 30 MeV (Decker et al., 2005) and the Cosmic Ray System, with the low energy part (Low Energy Telescope System, LETS) covering the energies from 150 keV/n to 30 MeV/n and the high energy part (High Energy Telescope System, HETS) from 3 to 100 MeV/n (Stone et al., 2005). The results have shown a significant increase in the ion fluxes at lower energies (40 to 350 keV). However, the shapes of the energy spectra beyond the shock were different from expectations. The high energy ACR fluxes beyond the shock continue to increase

with distance and the spectra still show modulation (Stone et al., 2005; Decker et al., 2005). This was taken as an indication that the main source of high energy particles is in another part of the shock (Stone et al., 2005). On the other hand, the spectrum of the less energetic ions has a power law form, with a roll-off at few MeV/nucleon, much below the ACR roll-off energy. These ions are now regarded as a separate population: the termination shock particles (TSP) (Stone et al., 2005).

In the HSTOF energy range, the Voyager LECP measurements provide only the total flux of the ions of $Z \geq 1$. The proton and helium fluxes can be found using the estimated fractions of the protons and helium ions (Decker et al., 2005). Assuming the thickness of the heliosheath to be ~40 AU, the corresponding ENA fluxes are of the same order as the results from HSTOF (apex direction). We must remember, however, that the Voyager data only represent the situation at the time and the position of the measurement.

10.4 Observations of the high energy ENAs: HSTOF on SOHO

At the present time the only instrument that detected the ENAs of the heliospheric origin is HSTOF onboard SOHO.

10.4.1 The instrument

HSTOF is one of two sections of the Suprathermal Time-of-Flight instrument (STOF) of CELIAS onboard SOHO. A detailed description of the instrument is given by Hovestadt et al. (1995).

SOHO is positioned at the Lagrange point L1 between the Earth and the Sun. The HSTOF has its line of sight set at 37° west of the Sun-SOHO line and scans the ecliptic with a field of view ±2° in and ±17° off the ecliptic as SOHO orbits the Sun. Figure 10.6 shows the viewing geometry of HSTOF in the ecliptic plane.

The scheme of the instrument is shown in Figure 10.7. HSTOF identifies the mass and energy of each incident energetic particle by its speed measured by a time-of-flight (TOF) unit and the residual energy deposited in a pixellated solid-state detector (PSSD). In front of the TOF unit is a flat-field electrostatic energy/charge (E/Q) filter that cuts off ions of $E/Q < 80$ keV/e.

Between the E/Q filter and the TOF unit is a layered foil of Si-Lexan-C (of thicknesses 28, 31, and 5 nm, respectively), supported by a Ni grid with 82% transmission. The foil suppresses the incident photons, most importantly the H Lyman-α, by 10^{-3}. It also provides the secondary electrons, produced by the passage of an incident particle, to generate the start pulse for TOF analysis. The particle passes through the TOF unit and reaches the PSSD, which has an energy resolution of about 12 keV. HSTOF has an energy threshold of 55 keV for protons (established by the layered foil, the Al window of the PSSD, and the electronic threshold) and an energy ceiling of 80 MeV for heavy ions. The stop signals for TOF are generated by secondary electrons emitted from the front Al window of the PSSD upon particle impact. The secondary electrons from the rear of the foil and the front of the PSSD are accelerated and deflected by an electrostatic mirror

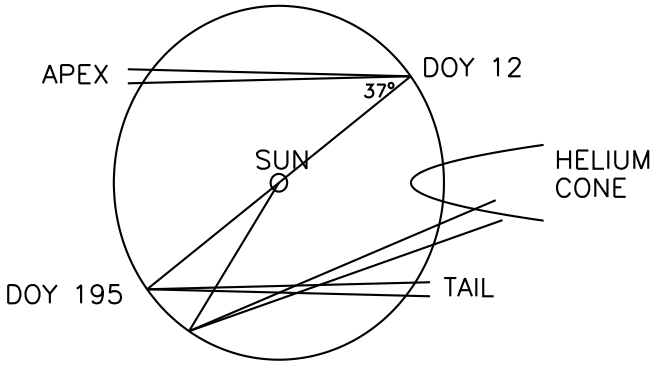

Figure 10.6: The orbit and some HSTOF viewing directions.

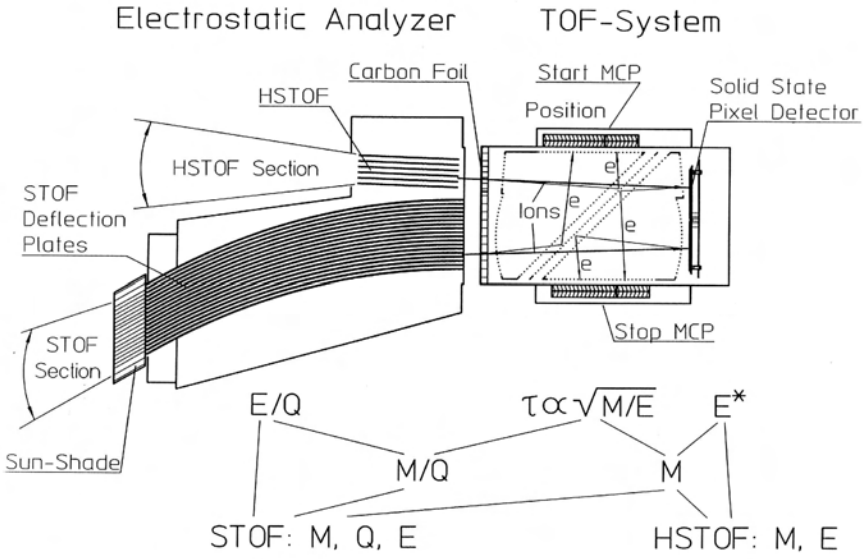

Figure 10.7: Schematic of the STOF instrument including the HSTOF part.

onto the respective microchannel plates (MCPs). The particles are detected as triple coincidence events: start and stop of the TOF and the energy signal from the PSSD. The detection efficiency depends on the energetic particle energy loss and scattering in the foil and PSSD Al window and dead layer. The efficiency of the TOF unit is 0.05 at 55 keV and 0.03 at 500 keV. The total geometrical factor of HSTOF for an isotropic flux is 0.22 cm^2 sr.

HSTOF's E/Q filter consists of a stack of six parallel plates, each 0.45 cm apart. Serration on the plates suppresses scattered particles from entering the TOF unit. The voltages of +1.26 kV and -1.26 kV applied to the adjacent plates determine the E/Q cutoff of the filter. The ability of the HSTOF flat-plate filter to effectively suppress ions <89 keV/e is indicated by the ion transmission based on preflight calibration. The actual cutoff (ion transmission <1%) should be closer to 100 keV/e. Since neutral particles incident within the FOV of ($\pm 2°$,$\pm 17°$) pass the HSTOF E/Q filter unimpeded, it is safe to take 80 keV/e as the cutoff for separating energetic hydrogen atoms (EHAs) from protons.

It follows that the ENA measurements by HSTOF are restricted to an energy range from 55 to about 80 keV (hydrogen).

10.4.2 ENA observations: results

The results of the observations of the energetic hydrogen atoms by HSTOF are presented in Figure 10.8. The differential ENA hydrogen flux for the energy range 55-88 keV is shown as a function of time (or, equivalently, of the spacecraft position during each year: the upper horizontal scale) for the years 1996 to 2003. Besides the hydrogen, the energetic helium atom flux was also detected (see Czechowski et al., 2004a). The energy spectra of the observed ENAs were also derived (Hilchenbach et al. 2001; Czechowski et al., 2004a; 2005a).

The first two years of observations are clearly the most successful in terms of the number of data points. This is due to low solar activity during that period: observations of the ENAs by HSTOF are only possible during "quiet time" periods, when the ion fluxes are low. The data for first two years show the peaks in the ENA flux intensity when the viewing direction includes the heliotail. The peak maxima are only slightly shifted from the LISM anti-apex direction.

The data for the corresponding part of 1998 are lacking, because there was a loss of contact with SOHO. In subsequent years, the data are scanty because of increasing solar activity. It is therefore not clear whether the peak from the heliotail direction was present in these years.

In 2003 the number of data points is higher. However, during this year the orientation of SOHO was changed. From July 2003 neither the heliotail nor the apex directions are accessible to HSTOF. The lack of the peak near DOY 200 therefore has nothing to do with the existence of the peak in the ENA flux from the heliotail direction.

10.4.3 Interpretations of the HSTOF data

Two possible interpretations of the ENA peak from the heliotail direction were proposed:

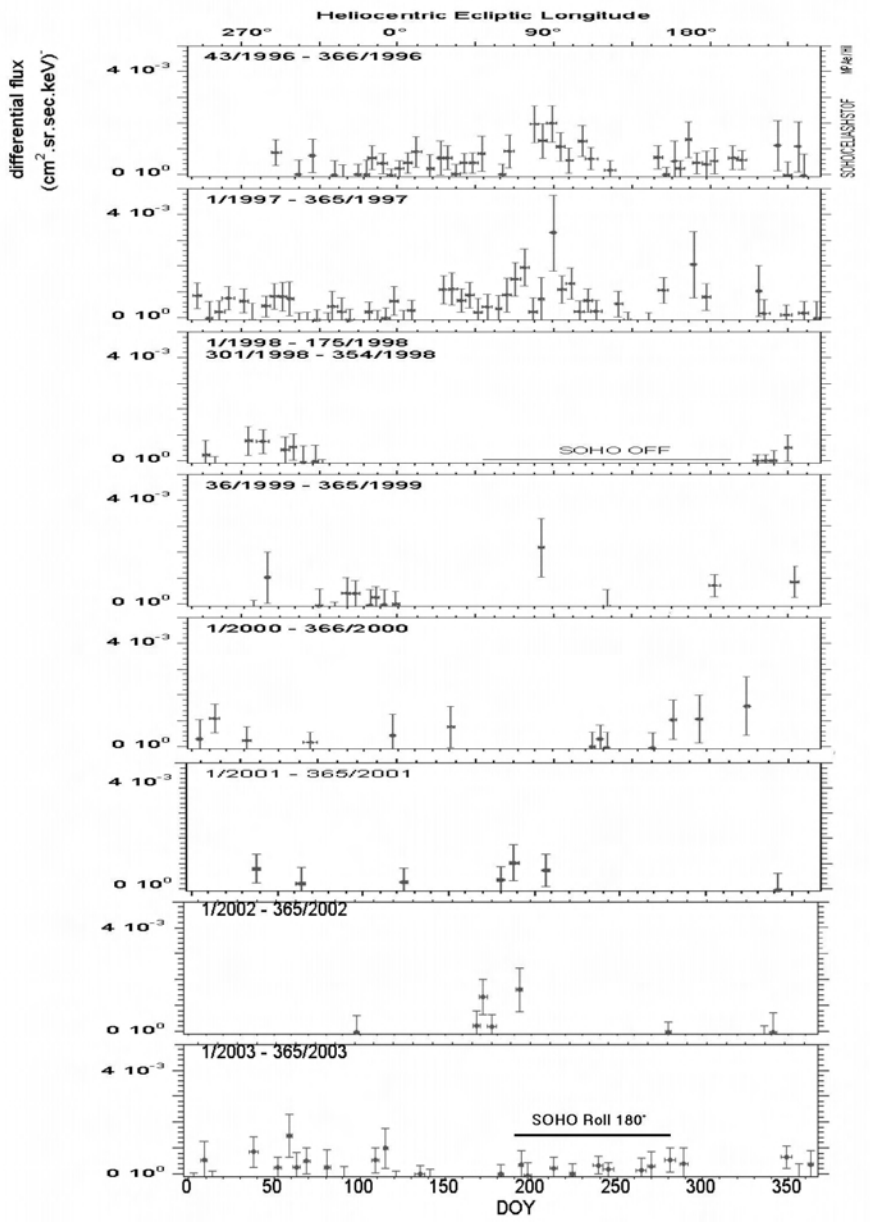

Figure 10.8: Energetic hydrogen flux in the 55-88 keV range measured by HSTOF during the period 1996-2003.

1. The TSP/ACR ENA interpretation (Hilchenbach et al., 1998; Czechowski et al., 2001a): the observed ENAs come from the region beyond the termination shock and are converted from the ions accelerated at the termination shock (TSP or ACR ions). It is also possible that the parent ions are pre-accelerated

pick-up ions, convected downstream from the termination shock (Chalov and Fahr, 1995; Czechowski et al., 2001b). The peak from the heliotail direction is explained by enhanced ion density and the large effective size of the ENA production region in the heliotail, as suggested by model simulations (see previous Section). The important check for this interpretation follows from the Voyager 1 LECP data from beyond the shock: the measured ENA intensity is consistent with the ion fluxes near the shock.

2. The CIR ENA interpretation (Kota et al., 2001): the ENAs come from the inner heliosphere, and the parent ions are accelerated at the transient shock waves associated with the co-rotating interaction regions (CIR). The peak from the heliotail direction is then explained as due to the "helium cone". The advantage of this interpretation is that the shift in the ENA intensity peak from the LISM anti-apex direction can be explained by the effect of parallax. In the ACR ENA case, this shift may be explained as due to deviation of the heliotail from the LISM anti-apex direction caused by the interstellar magnetic field (Ratkiewicz et al., 1998; Izmodenov et al., 2005).

The ACR ENA interpretation was the basis for the attempt to use the HSTOF ENA data to obtain information about the ACR spectrum at the termination shock and the termination shock strength (Czechowski et al. 2005a, 2001c).

10.4.4 Termination shock strength from ACR ENA data

The conversion of an ion into an ENA occurs approximately with no change in the particle momentum. The ENA energy spectrum is, nevetheless, different from that of the parent ions, since the probability of conversion (a product of particle speed, charge-exchange cross section and the number density of the atoms providing the electrons) is itself energy-dependent. In addition, the observed ENA spectrum comes from different points along the line of sight, for which may the parent ion spectra neutral gas density values may be different. Determination of the ion energy spectrum from the ENAs is, therefore, not straightforward and in general can only be done in the context of detailed models.

Interestingly, there is one special situation for which the unknown factors cancel and the ENA energy spectrum is simply related to that of the parent ions (Czechowski et al., 2001c; 2005a). Consider the distribution of the ions downstream from the termination shock in the heliotail direction under the following assumptions:

1. no time dependence,
2. no acceleration downstream from the termination shock,
3. flow speed V =constant and directed along the line of sight,
4. H, He densities uniform,
5. losses of ions from the line of sight occur predominantly by neutralization, and spatial diffusion can be neglected.

It is possible that the picture of the heliotail following from these assumptions can be taken as a reasonable first-order approximation (however, some time-dependent simulations do not agree with them). Neglecting spatial diffusion may be possible in a limited energy range.

The ion distribution down the heliotail is then shaped by two effects: convection with the plasma flow at the velocity V and the loss of ions due to neutralization by charge-exchange with the neutral gas (loss rate β_{cx}). From the transport equation it then follows that the ion flux intensity $J_{\rm ion}(s,E)$ at a distance s from the termination shock can be written in terms of the ion spectrum at the termination shock $J_{\rm ion}(E)|_{\rm shock}$

$$J_{\rm ion}(s,E) = J_{\rm ion}(E)|_{\rm shock} \exp[-s\beta_{cx}(E)/V] \tag{10.4}$$

Inserting this into the Equation (10.1), one obtains for the ENA flux

$$\begin{aligned} J_{\rm ENA}(E) &= \int_0^\infty {\rm d}s \frac{\beta_{\rm cx}(E)}{u} J_{\rm ion}(E)|_{\rm shock} \exp\left[-s\frac{\beta_{\rm cx}(E)}{V}\right] \\ &= \frac{V}{u} J_{\rm ion}(E)|_{\rm shock} \end{aligned} \tag{10.5}$$

where u = particle speed. Since $u \sim E^{1/2}$, this means that the ENA spectrum is steeper than the parent ion spectrum at the shock by a factor $E^{-1/2}$.

This result can in principle be used to deduce the parent ion spectrum from the ENA data alone (Czechowski et al., 2001c). For the HSTOF data this is difficult due to the large uncertainties and narrow energy range. One can, however, use it as a means to estimate the order of magnitude of the parent ion flux from the flux of the ENAs in the HSTOF energy interval, accepting the errors caused by the necessary simplifications.

The latter method was used for the ENA data from HSTOF in order to derive the slope of the ACR spectrum at the termination shock (Czechowski et al., 2005a). This was done as follows. Assuming that the ENAs observed by HSTOF are of ACR origin, Equation (10.5) was used to estimate the ACR flux intensity level at the termination shock in the HSTOF ENA energy range (55-88 keV for protons). This was combined with the high energy ACR data from Voyagers (Cummings et al., 2002), which, although obtained upstream from the shock, at the high energy end ($\sim$140 MeV for protons) can be assumed to be close to the actual ACR flux at the termination shock. The slope of the ACR energy spectrum at the termination shock was obtained by interpolating between these two points.

Note that the large span in energy between the HSTOF and the high energy Voyager data reduces the effect of any error in the estimation of the ACR flux at low energy from Equation (10.5) on the resulting value of the slope of the ACR spectrum. In the simplest version, the spectrum was assumed to be a simple power law $J \sim E^{-\delta}$. The error ΔJ in the ACR flux at low energy corresponds then to the error in δ

$$\Delta\delta = log\frac{J_1 + \Delta J}{J_1 - \Delta J} / log\frac{E_2}{E_1} \tag{10.6}$$

where we use subscripts 1 and 2 to denote the values corresponding to the low and high energy values, respectively. If the uncertainty in determination of the low

energy ACR flux is one order of magnitude, this produces an error of $\pm 1/3$ in δ, because E_2/E_1 is of the order 10^3.

Despite all of the uncertainty involved, this approach led to one result that seemed encouraging: the slope of the ACR proton spectrum came out the same as for the ACR He^+ spectrum. This is what should be expected if the ACR spectra at the termination shock would be determined by the diffusive shock acceleration mechanism, with $\delta = (3/2)r/(r-1)$ where r is the shock compression ratio. The slope of the ACR spectrum could then be used to derive the shock compression ratio r. The result $r \approx 2.9$ corresponds to a weak shock, which is consistent with numerical simulations of the heliosphere, and with recent observations in situ by Voyager 1 (Burlaga, 2005).

Voyager observations refer to another part of the heliosphere (forward rather than the heliotail). Nevertheless, the comparison with Voyager 1 post-shock data is intriguing. The ACR spectrum assumed by Czechowski et al. (2005a) is certainly different from the ion spectrum measured by Voyager 1: in particular, the assumption of a simple power law behaviour between the HSTOF energy region and the ACR roll-off energy is not confirmed. The measured spectrum is steeper at low energy (with the power index apparently not in agreement with the value expected from shock acceleration: Decker et al. 2005) and does not match as assumed with the ACR high energy part. The measured proton and He ions intensities at 100 keV/n are close to those deduced from the HSTOF data (Czechowski et al., 2005a).

10.5 Conclusions

Observations of the high energy (few 10-few 100 keV) ENAs offer a possibility of remote imaging of the outer heliosphere. In contrast to the ENAs of lower energy ($\sim$1 keV) these observations reflect the structure not only of the bulk plasma flow, but also of the accelerated ion population. The additional advantage is the overlap in energy between the high-energy ENAs (observations by HSTOF on SOHO) and the energetic ions measurements by LECP on Voyager 1, which is now beyond the termination shock, in the region that is expected to be the important source of the ENAs.

While the low energy ENAs are the target for forthcoming missions, the high energy ENAs are already detected by HSTOF on SOHO. These observations suggest that the TSP/ACR ENA interpretation is probable. If so, they give us a glimpse of the distant heliosphere, including the regions which (like the heliotail) are not to be reached soon by any planned spacecraft.

The present understanding of the energetic ion distribution in the outer heliosphere, based on simplified models, is incomplete. Improved models must include the full time-dependent structure of the heliospheric magnetic field. These models must also account for the Voyager 1 data, suggesting that the region of the termination shock passed by the spacecraft is away from the region where the ion acceleration occurs.

Interpreting the energetic ENA data will have to be based on the definite models of the heliosphere. That is, it is unlikely that the picture of the outer heliosphere could be derived straight from the ENA data. Instead, it will be necessary to

compare the observations with the results of model simulations and search for the model that fits best. We have, however, presented one example that avoids this restriction, that of using the ENA data from HSTOF to derive information about the spectrum of accelerated ions at the termination shock. This approach relied on the assumption that the observed ENAs are of ACR origin, which must now, however, be reconsidered in view of the Voyager 1 post-shock observations.

The results from HSTOF high energy ENA observations are interesting and tantalizing and strongly suggest the need for a new instrument capable of covering this energy range (Hsieh et al., 2004).

Bibliography

Barnett, C.F., Hunter, H.T., Kirkpatrick, M.I., Alvarez, I., and Phaneuf, R.A., Atomic Data for Fusion. Collisions of H, H2, He and Li Atoms and Ions with Atoms and Molecules, Oak Ridge Natl. Lab. Report, ORNL-6086-VI, Oak Ridge, Tenn., 1990.

Burlaga, L.F., Ness, N.F, Stone, E.C., McDonald, F.B., Acuna, M.H., Lepping R.P. & Connerney, J.E.P., *Geophys. Res. Lett.* **30**, No. 20, 2072, 9-1, 2003.

Burlaga, L.F., Ness, N.F, Acuna, M.H., Lepping R.P., Connerney, J.E.P., Stone, E.C., & McDonald, F.B., *Science* **309**, 2027, 2005.

Chalov, S.V., Fahr, H.J., & Izmodenov, V., *Astron. Astrophys.* **304**, 609, 1995.

Chalov, S.V., Fahr, H.J., & Izmodenov, V., *Journ. Geophys. Res* **108**, SSH 11-1, 2003.

Cummings, A.C., Stone, E.C. & Steenberg, C.D., *Astrophys. J.* **578**, 194, 2002.

Czechowski, A., Fichtner, H., Grzedzielski, S., Hilchenbach, M., Hsieh, K.C. Jokipii, J.R., Kausch, T., Kota, J., & Shaw, A., *Astron. Astrophys.* **368**, 622, 2001a.

Czechowski, A., Fahr, H.J., Lay, G., & Hilchenbach, M., *Astron. Astrophys.* **379**, 601, 2001b.

Czechowski, A., Hilchenbach, M. & Hsieh, K.C., in: Proceedings of the 27th International Cosmic Ray Conference, Hamburg, August 2001, vol.10, p.4227, 2001c.

Czechowski, A., Hsieh, K.C, Hilchenbach, M., Kota, J., & Shaw, A.W., *Adv. Space Res.* **34**, 104, 2004a.

Czechowski, A., Scherer, K., Fahr, H.J., Hilchenbach, M., Hsieh, K.C, presented at 35th COSPAR Assembly, Paris 18-25 July 2004, 2004b.

Czechowski, A., Hilchenbach, M., Hsieh, K.C, *Astron. Astrophys.* **431**, 1061, 2005a.

Czechowski, A., Hilchenbach, M., Scherer, K., Pick-up and low energy ACR ions in a time-dependent heliosphere, presented at EGU General Assembly, Vienna 24-29 April, 2005b.

Czechowski, A., Grzedzielski, S., & Mostafa, I., *Astron. Astrophys.* **297**, 892, 1995.

Decker, R.B., S.M. Krimigis, R.L. McNutt, M. Kane, *Proc. of 24th ICRC*, Vol 4, p. 421-424, 1995.

Decker, R.B., S.M. Krimigis, E.C. Roelof, M.E. Hill, T.P. Armstrong, G. Gloeckler, D.C. Hamilton, L.J. Lanzerotti Voyager 1 in the Foreshock, Termination Shock and Heliosheath, *Science* **309**, 2020, 2005.

Fahr, H.J., Kausch, T., & Scherer, H., *Astron. Astrophys.* **357**, 268, 2000.

Fahr, H.J., & Lay, G., *Astron. Astrophys.* **356**, 327, 2000.
Fahr, H.J.& Scherer, K., *ASTRA* **1**, 3-15, 2004.
Giacalone, J., Jokipii, J.R., Decker, R.B., Krimigis, S.M., Scholer, M., & Kucharek, S.M., *Astrophys. J.* **486**, 471, 1997.
Gruntman, M.A., *Planet. Space Sci.* **40**, 439, 1992.
Gruntman, M., Roelof, E.C., Mitchell, D.G., Fahr, H.J., Funsten, H.O., McComas, D.J., *Journ. Geophys. Res* **106**, 15767, 2001.
Hilchenbach, M., Hsieh, K.C., Hovestadt, D., Klecker, B., Grünwaldt, H., et al., *Astrophys. J.* **503**, 916, 1998.
Hilchenbach, M., Hsieh, K.C., Hovestadt, D., Kallenbach, R., Czechowski, A., Möbius, E., & Bochsler, P., in: The Outer Heliosphere: The New Frontiers, COSPAR Colloquium Series, Vol. 11, p. 273, 2001.
Hilchenbach, M., Czechowski, A., Scherer, K., Solar Wind 11, Proceedings of the Solar Wind 11 Conference, (submitted), 2005.
Hovestadt, D.,Hilchenbach, M., Bürgi, A., Klecker, B., Laeverenz, P., Scholer, M., Grünwaldt, H., Axford, W.I., Livi, S., Marsch. E., et al., *Solar Phys.* **162**, 441-481, 1995.
Hsieh, K.C., Shih, K.L, Jokipii, J.R. & S. Grzedzielski, *Astrophys. J.* **393**, 756, 1992.
Hsieh, K.C., Zurbuchen, T.H., Orr, J., Gloeckler, G. & Hilchenbach, M., *Adv. Space Res.* **34**, 213, 2004.
Ip, W.-H., Axford, W.I., Estimates of galactic cosmic ray spectra at low energies, *Astron. Astrophys.* **149**, 7–10, 1985.
Izmodenov, V., Alexashov, D., Myasnikov, A., *Astron. Astrophys.* **437**, L35–L38, 2005.
Kota, J., K.C. Hsieh, A. Czechowski, J.R. Jokipii, & M. Hilchenbach, *Journ. Geophys. Res.* **106**, 24907, 2001.
Krimigis, S.M., R.B. Decker, M.E. Hill, T.P. Armstrong, G. Gloeckler, D.C. Hamilton, L.J. Lanzerotti, & E.C. Roelof, *Nature* **426**, 45, 2003.
McDonald, F.B., E.C. Stone, A.C. Cummings, B. Heikkila, N. Lal, & Webber, W.R., *Nature* **426**, 48, 2003.
Nerney, S., Suess, S.T., & Schmahl, E.J., *Astron. Astrophys.* **250**, 556, 1991.
Nerney, S., Suess, S.T., & Schmahl, E.J., *Journ. Geophys. Res.* **98**, 15169, 1993.
Nerney, S., Suess, S.T., & Schmahl, E.J., *Journ. Geophys. Res.* **100**, 3463, 1995.
Parker, E.N., The passage of energetic charged particles through interplanetary space, *Planet. Space Sci.* **13**, 9, 1965.
Ratkiewicz, R., Barnes, A., Molvik, G.A., Spreiter, J.R., Stahara, S.S., Vinokur, M., Venkateswaran, S., *Astron. Astrophys.* **335**, 363–369, 1998.
Roelof, E.C., in: The Outer Heliosphere: The New Frontiers, COSPAR Colloquium Series, Vol. 11, p. 291, 2001.
Scherer, K., & Fahr, H.J., *Geophys. Res. Lett.* **30**, 17-1, 2003a.
Scherer, K., & Fahr, H.J., *Astron. Astrophys.* **404**, L47-L50, 2003b.
Scherer, K., & Fahr, H.J., *Ann. Geophys.* **21**, 1303-1313, 2003c.
Scherer, K., & Ferreira, S.E.S., *Astra* **1**, 17-27, 2005.
Schwadron, N.A., & McComas, D.J., *Geophys. Res. Lett.* **30**, 1587, 2003.
Stone, E.C., A.C. Cummings, F.B. McDonald, B. Heikilla, N. Lal, & W.R. Webber, *Science*, **309**, 2017, 2005.

Thomas, G.E., *Ann. Rev. Earth. Planet. Sci.* **6**, 173–204, 1978.
Webber, W.R., *Astrophys. J.* **506**, 329–334, 1998.

— 11 —

Lyman-α Absorption towards Nearby Stars as a Diagnostic of the Heliospheric Interface

Brian Wood[1]
JILA, University of Colorado
Boulder, USA

11.1 Introduction

The heliosphere's bow shock is where the interstellar wind first encounters the obstacle presented by the solar wind. Models of the heliospheric interaction suggest that the plasma component of the interstellar medium (ISM) should be heated, decelerated, and compressed after crossing the bow shock, and will then be deflected around the heliopause. Through charge exchange processes, the neutral hydrogen atoms in the ISM are also involved in the heliospheric interaction [e.g. Baranov and Malama, 1993, 1995; Zank et al., 1996].

The ISM neutrals are not entirely coupled to the protons, since the mean free path for charge exchange interactions involving neutral H is comparable to the size of the heliosphere. Nevertheless, heliospheric models including neutrals predict that interstellar neutral hydrogen atoms crossing the bow shock should be heated, decelerated, and compressed to an extent similar to that of the protons, even though unlike the protons many neutrals are able to penetrate the heliopause. This region of heated, compressed ISM neutrals in between the bow shock and heliopause has been called the "hydrogen wall" [Baranov et al., 1991]. The UV spectrometers that have operated on the Hubble Space Telescope (HST) have actually been able to detect absorption from the hydrogen wall in spectra of the Lyman-α (Lyα) line of neutral hydrogen (H I), thereby providing a unique diagnostic for material in the outer heliosphere.

11.2 The Lyα diagnostic

The bottom panel of Figure 11.1 shows a Lyα spectrum of the very nearby star α Cen B, taken by the Goddard High Resolution Spectrograph (GHRS) instrument on board HST [Linsky and Wood, 1996]. The upper solid line is an estimate of the intrinsic Lyα emission line profile from the star. Intervening H I gas absorbs much

[1]in *The Physics of the Heliospheric Boundaries*, V. Izmodenov and R. Kallenbach (eds.), ISSI Scientific Report No. 5, pp. 335 - 354, ESA-ESTEC, Paris 2006

of this Lyα emission, resulting in the very broad absorption line centered at about 1215.61 Å in the figure. Much narrower and weaker absorption is also seen from neutral deuterium (D I) at 1215.27 Å.

Most of the intervening H I and D I in between us and the star is interstellar gas. At a distance of 1.34 pc (1 parsec=3.086×10^{18} cm), α Cen is the closest star system to us, so the ISM absorption seen towards α Cen should be as low or lower than will be seen towards any other star. Nevertheless, the H I column density towards even this nearest star system is $N_H = 4 \times 10^{17}$ cm^{-2}, easily high enough to yield a very broad and highly saturated Lyα absorption line. For comparison, the weaker D I line in the α Cen B spectrum in Figure 11.1 suggests a column density of $N_D = 6 \times 10^{12}$ cm^{-2}.

However, analysis of the α Cen data reveals that the ISM cannot account for all of the observed H I absorption. In particular, when the H I absorption line is forced to have a temperature consistent with the temperature suggested by the width of the D I Lyα absorption, the ISM H I absorption ends up too narrow to fit the data. Figure 11.1 therefore illustrates a more complex interpretation of the Lyα data involving absorption from both the heliosphere and the analogous "astrosphere" surrounding the star, in addition to the ISM absorption. The middle panels of Figure 11.1 show first the initial Lyα profile emitted by α Cen B, and then the absorption that occurs as the Lyα photons journey towards Earth, illustrating absorption first by the stellar astrosphere, then by the ISM, and finally by the heliosphere.

The astrospheric and heliospheric absorption results in excess H I absorption on both sides of the line. The redshifted excess absorption (i.e. the excess on the high wavelength or "red" side of the line) is from the heliospheric hydrogen wall, while the blueshifted excess (i.e. the excess on the low wavelength or "blue" side of the line) is from an analogous hydrogen wall surrounding α Cen. The appearance of heliospheric and astrospheric absorption on opposite sides of the ISM absorption is consistent with expectations from hydrodynamic models of the heliosphere and astrospheres, which will be discussed in more detail below.

The column densities of the heliospheric and astrospheric hydrogen are at least 1000 times lower than the ISM column density quoted above, so it is fair to wonder how heliospheric and astrospheric Lyα absorption could possibly avoid complete obscuration by the ISM absorption. Part of the answer lies in the high temperature of the hydrogen walls, which leads to broader absorption profiles. Also, ISM neutrals crossing the bow shock are decelerated and deflected away from the heliopause. From our position inside the heliosphere this means that the heliospheric absorption will be redshifted relative to the ISM absorption, while from our position outside α Cen's astrosphere the analogous astrospheric absorption will be blueshifted. Thus, though it remains highly blended with the ISM absorption, the heliospheric and astrospheric absorption are broad enough and shifted away from the ISM absorption enough to be detectable.

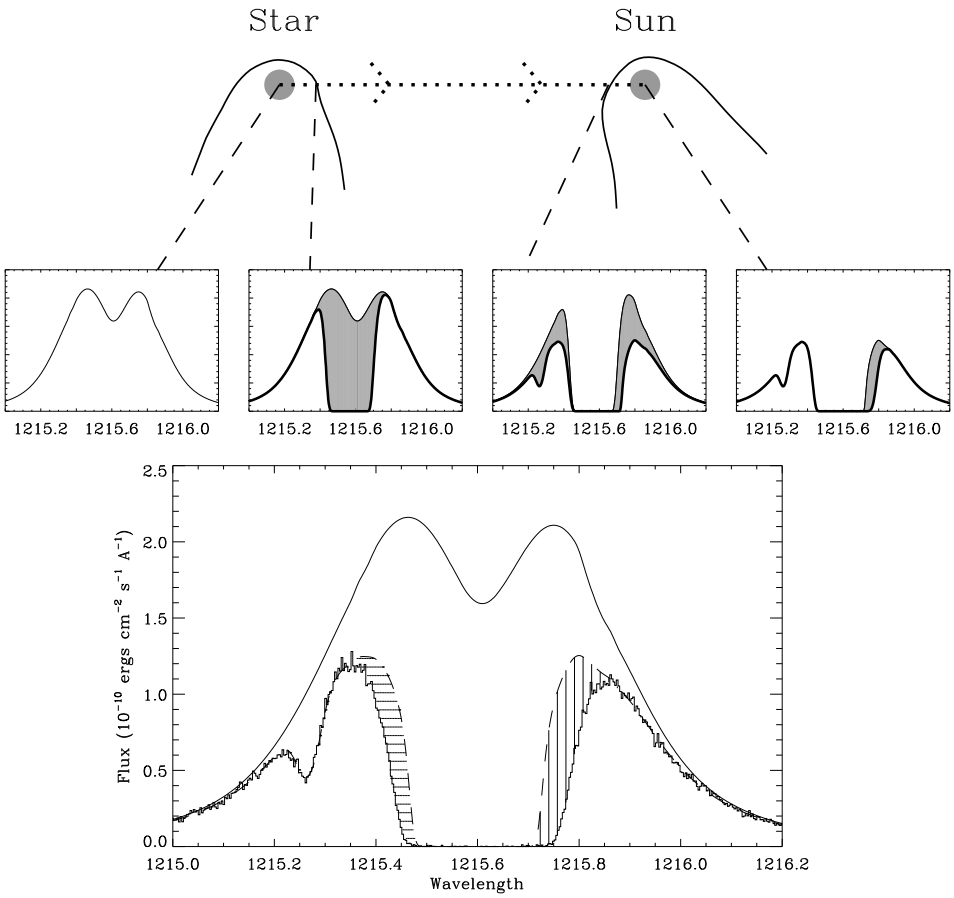

Figure 11.1: Schematic diagram showing how a stellar Lyα profile changes as the Lyα photons travel from the star towards an observer at Earth. The middle panels show the profile after absorption from the stellar astrosphere, the ISM, and finally the heliosphere. The lower panel shows an actual observed Lyα profile of α Cen B. The upper solid line is the assumed stellar emission profile and the dashed line is the ISM absorption alone. The excess absorption is due to heliospheric H I (vertical lines) and astrospheric H I (horizontal lines).

Table 11.1: HST detections of heliospheric and astrospheric Lyα absorption

Star	Spect. Type	Dist. (pc)	Gal. Coord. l (deg)	b (deg)	Hel. Det.?	Ast. Det.?	Ref.
Proxima Cen	M5.5 V	1.30	313.9	-1.9	Yes	No	1
α Cen A	G2 V	1.35	315.7	-0.7	Yes	Yes	2
α Cen B	K0 V	1.35	315.7	-0.7	Yes	Yes	2
Sirius	A1 V	2.64	227.2	-8.9	Yes	No	3
ϵ Eri	K1 V	3.22	195.8	-48.1	No	Yes	4
61 Cyg A	K5 V	3.48	82.3	-5.8	No	Yes	5
ϵ Ind	K5 V	3.63	336.2	-48.0	No	Yes	6
EV Lac	M3.5 V	5.05	100.6	-13.1	No	Yes	7
70 Oph A	K0 V	5.09	29.9	11.4	Yes	Yes	7
36 Oph A	K1 V	5.99	358.3	6.9	Yes	Yes	8
ξ Boo A	G8 V	6.70	23.1	61.4	Yes	Yes	7
61 Vir	G5 V	8.53	311.9	44.1	Yes	Yes?	7
δ Eri	K0 IV	9.04	198.1	-46.0	No	Yes	7
HD 165185	G5 V	17.4	356.0	-7.3	Yes	No	7
HD 128987	G6 V	23.6	337.5	39.2	No	Yes	7
λ And	G8 IV-III+M V	25.8	109.9	-14.5	No	Yes?	6
HZ 43	DA	32.0	54.1	84.2	Yes?	No	9
DK UMa	G4 III-IV	32.4	142.6	38.9	No	Yes?	7

References — (1) Wood et al. [2001]. (2) Linsky and Wood [1996]. (3) Izmodenov et al. [1999]. (4) Dring et al. [1997]. (5) Wood and Linsky [1998]. (6) Wood et al. [1996]. (7) Wood et al. [2005b]. (8) Wood et al. [2000a]. (9) Kruk et al. [2002].

11.3 Searching for heliospheric Lyα absorption

The first detection of heliospheric Lyα absorption was the α Cen detection shown in Figure 11.1 [Linsky and Wood, 1996], but there have been many more detections since then, both from GHRS data and with spectra from the Space Telescope Imaging Spectrograph (STIS) instrument, which replaced GHRS on HST in 1997. Table 11.1 lists the stellar lines of sight observed by HST that have provided detections of heliospheric and/or astrospheric absorption, where the sixth and seventh columns indicate which are the heliospheric and which are the astrospheric detections. Marginal detections are indicated by question marks. The spectral types and distances of the observed stars are listed, and the fourth and fifth columns provide Galactic longitudes (l) and latitudes (b) of the observed stars. In addition to the detections listed in Table 11.1, Lemoine et al. [2002] and Vidal-Madjar and Ferlet [2002] find evidence for weak heliospheric absorption for the similar Capella and G191-B2B lines of sight, but the arguments for these detections are far more subtle.

Table 11.1 indicates that heliospheric absorption has been observed for eight independent sight lines, if the very similar Alpha/Proxima Cen lines of sight are counted as one detection. The heliospheric absorption is not detected for all lines of

sight, though. A full list of HST Lyα analyses is provided by Wood et al. [2005b], which indicates that most observations do *not* lead to heliospheric detections. Why do some observations show the heliospheric signal and others do not?

There are really only two factors that determine whether a line of sight will have detectable heliospheric Lyα absorption: the ISM H I column density along the line of sight, and the direction of the line of sight relative to the orientation of the heliosphere. The line-of-sight orientation is most simply described by the angle, θ, between the line of sight and the upwind direction of the ISM flow seen by the Sun, which has Galactic coordinates of $l = 6.1°$, $b = 16.4°$ [Lallement et al., 1995]. The ISM column densities, $\log N(\mathrm{H\ I})$, are plotted versus θ for all HST-observed lines of sight in Figure 11.2, using different symbols to indicate which lines of sight have detectable heliospheric absorption and which do not [Wood et al., 2005b]. The detections are nicely separated from the nondetections in this parameter space. The lines of sight that yield detections tend to have low $N(\mathrm{H\ I})$ values, which is expected since high ISM column densities will lead to broad ISM absorption that can hide the heliospheric signal. It is also clearly easier to detect heliospheric absorption in upwind directions ($\theta < 90°$) than in downwind directions ($\theta > 90°$). This is also consistent with expectations, since it is in upwind directions that the heliospheric H I suffers the strongest deceleration at the bow shock [e.g. Baranov and Malama, 1993, 1995; Zank et al., 1996], which means that the heliospheric absorption in these directions will be shifted away from the ISM absorption to the greatest extent.

For upwind directions, heliospheric absorption is only detected when $\log N(\mathrm{H\ I}) < 18.2$, but in downwind directions a detection requires $\log N(\mathrm{H\ I}) < 17.8$. There simply are not many lines of sight that will have interstellar column densities of $\log N(\mathrm{H\ I}) < 17.8$. Thus, the downwind detection of heliospheric absorption towards Sirius may forever remain unique [Izmodenov et al., 1999].

Because interstellar H I is capable of penetrating the heliopause, the charge exchange heated neutral hydrogen detected in the Lyα spectra permeates the entire heliosphere. However, the significantly higher densities in the hydrogen wall mean that for all but the most downwind lines of sight the heliospheric H I column density will be dominated by the hydrogen wall. Thus, the heliospheric Lyα absorption detections amount to a detection of the hydrogen wall, thereby confirming an important prediction of heliospheric models that include neutrals. This makes heliospheric Lyα absorption one of the few diagnostics of the heliospheric interaction that truly probes its outermost regions between the heliopause and bow shock. Spacecraft have never travelled that far out, and most remote observational diagnostics are also limited to studying heliospheric processes inside the heliopause. The sensitivity of the Lyα absorption to the heliosphere's largest size scales is perhaps the primary source of its appeal.

11.4 Comparison with models

Models of the heliosphere and astrospheres have been crucial in providing support for the heliospheric/astrospheric interpretation of the excess Lyα absorption observed for the stars in Table 11.1. The first direct comparison between the data

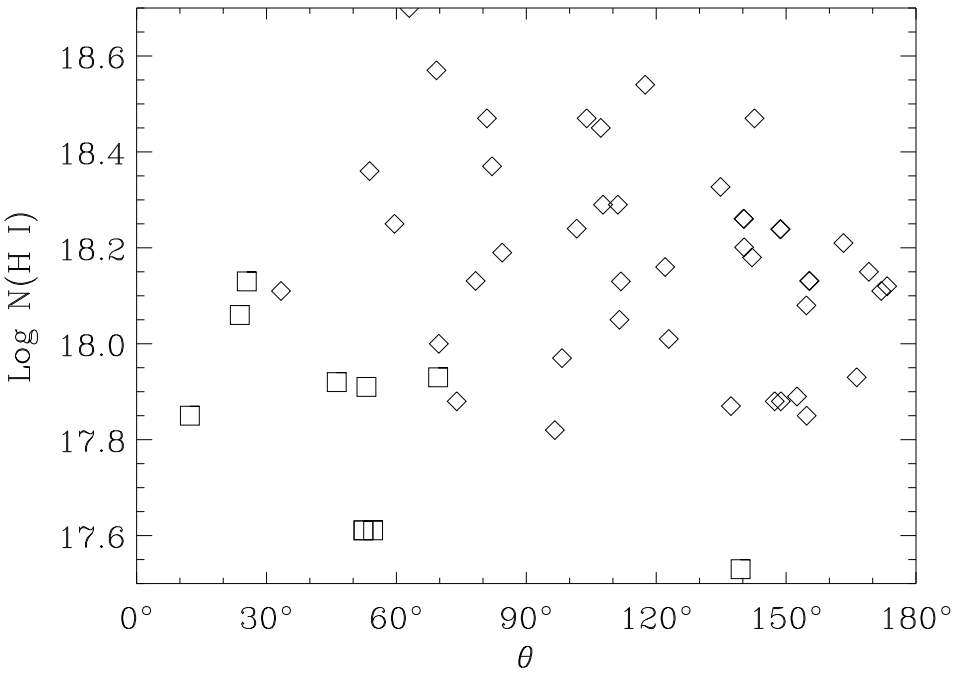

Figure 11.2: The ISM H I column densities measured for all HST-observed lines of sight are plotted versus the angle of the lines of sight relative to the upwind direction of the ISM flow seen by the Sun. The boxes and diamonds indicate lines of sight that yield detections and nondetections of heliospheric absorption, respectively. From Wood et al. [2005b].

and model predictions was by Gayley et al. [1997], who showed that heliospheric models could indeed reproduce the red-side excess absorption seen towards α Cen (see Figure 11.1), but that astrospheric absorption is required to explain the blue-side excess. The primary reason that heliospheric and astrospheric absorption are shifted away from the ISM absorption, but in opposite directions, is that ISM neutrals are decelerated and deflected as they cross the bow shock. In the case of the heliosphere, the absorption from these neutrals is seen as a redshift from our perspective inside the heliosphere, whereas from our perspective outside the astrospheres the resulting astrospheric absorption is instead blueshifted.

The exact amount of absorption that a heliospheric model predicts depends on the precise parameters that are assumed for the surrounding ISM in the model. Thus, the heliospheric Lyα absorption is potentially a diagnostic for properties of the circumsolar ISM. Much of the work on reproducing the observed Lyα absorption has focused on exploring the potential of the absorption as an ISM diagnostic, but with limited success. As will be described below, one problem is that results are highly model dependent, with different methods for computing neutral H velocity distributions in the heliosphere yielding different predictions for the Lyα absorp-

Table 11.2: Parameters for models in Figure 11.3

Model	$n(H\ I)$ (cm^{-3})	$n(H^+)$ (cm^{-3})	Line Style in Fig. 11.3
1	0.10	0.10	solid
2	0.15	0.05	dotted
3	0.15	0.10	dashed
4	0.20	0.05	dot-dash
5	0.20	0.10	dot-dot-dot-dash
6	0.20	0.20	long dash

tion. Another problem is that some models suggest that the Lyα absorption may not be as sensitive a diagnostic of ISM properties as one might have hoped.

The first column of Figure 11.3 shows six Lyα spectra with estimated ISM absorption. These particular stars were chosen for sampling different lines of sight through the heliosphere. The stars and their heliospheric orientation angles are: 36 Oph ($\theta = 12°$), α Cen ($\theta = 52°$), 31 Com($\theta = 73°$), β Cas ($\theta = 112°$), Sirius ($\theta = 139°$), and ϵ Eri ($\theta = 148°$). Three of these stars (36 Oph, α Cen, and Sirius) have detected heliospheric absorption. The other three do not, but those data can still be used to provide upper limits for how much heliospheric absorption is present in those directions.

Figure 11.3 compares the Lyα spectra of the six stars with heliospheric absorption predicted six models of the heliosphere, which are listed in Table 11.4 along with the ISM neutral hydrogen and proton densities assumed for the models [Izmodenov et al., 2002]. The fundamental difficulty with modeling neutrals in the heliosphere is that the charge exchange processes that allow them to take part in the heliospheric interaction drive the neutrals out of thermal and ionization equilibrium, meaning that simple fluid approximations do not work well and complex multi-fluid or kinetic codes are therefore required to reproduce the neutral velocity distributions [Alexashov & Izmodenov, 2005]. The models in Figure 11.3 are computed using a Monte Carlo code developed by Baranov and Malama [1993, 1995], which provides a full kinetic treatment of the neutral hydrogen. The middle column of Figure 11.3 shows the predicted absorption from the hydrogen wall region in between the bow shock and heliopause for the six models, and the third column shows the additional absorption predicted from the heliosheath region in between the termination shock and heliopause.

Absorption from the hydrogen wall dominates for the upwind lines of sight (36 Oph, α Cen, and 31 Com), where the only model that predicts a significant contribution from the heliosheath is Model 4, which does not fit the data as well. Heliosheath absorption becomes more prominent in downwind directions. For β Cas and ϵ Eri, the models seem to predict too much absorption from the heliosheath, but for Sirius the models suggest that this amount of heliosheath absorption is actually necessary to explain the amount of observed absorption. This difference in the fits to the Sirius and β Cas/ϵ Eri sight lines makes it difficult to say which of the six models fits the data best. In upwind directions there is a different problem.

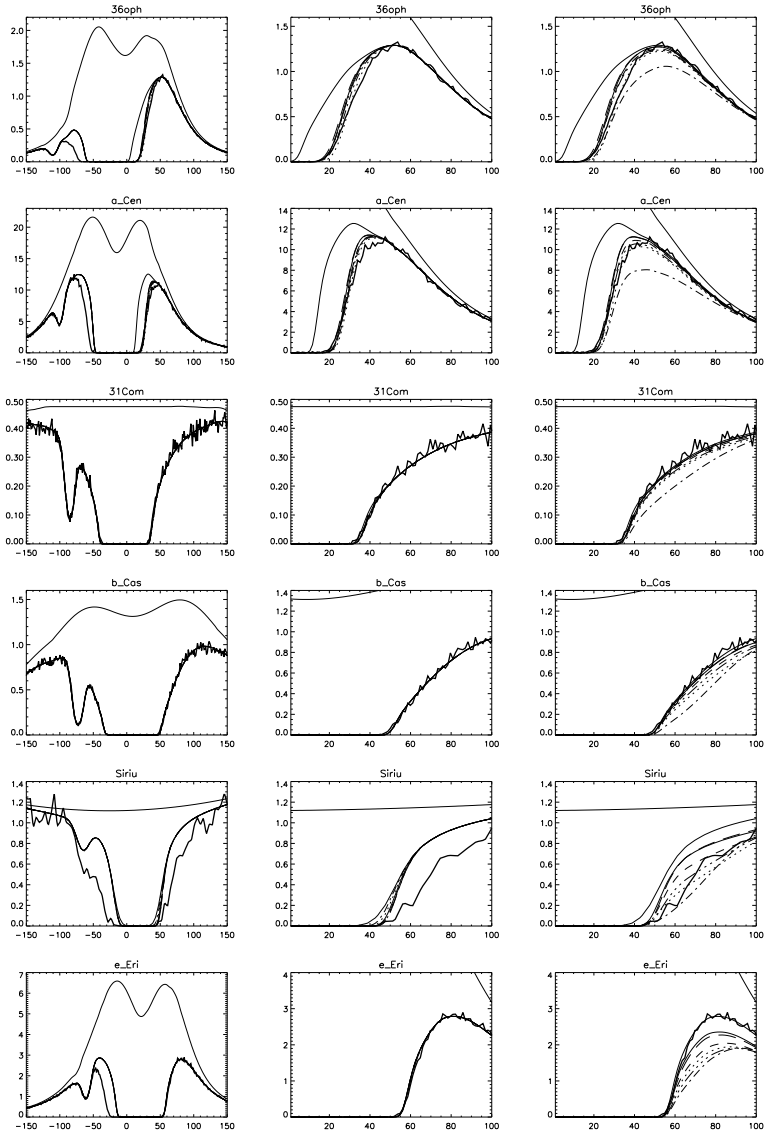

Figure 11.3: Left column: HST Lyα spectra of six stars: 36 Oph, α Cen, 31 Com, β Cas, Sirius, and ϵ Eri. Each plot shows the observed profile (thick solid line) plotted on a heliocentric velocity scale (in km s^{-1}) with a flux scale of 10^{-11} ergs cm^{-2} s^{-1} Å^{-1}. The assumed stellar line profile and ISM absorption are shown as thin solid lines. Middle column: Reproduction of left column, zoomed in on the red side of absorption line, combined with predicted hydrogen wall plus ISM absorption from six heliospheric models. See Table 11.4 for model parameters and their correspondence with line styles. Right column: Same as the middle column, but heliosheath absorption is added to the predicted absorption. From Izmodenov et al. [2002].

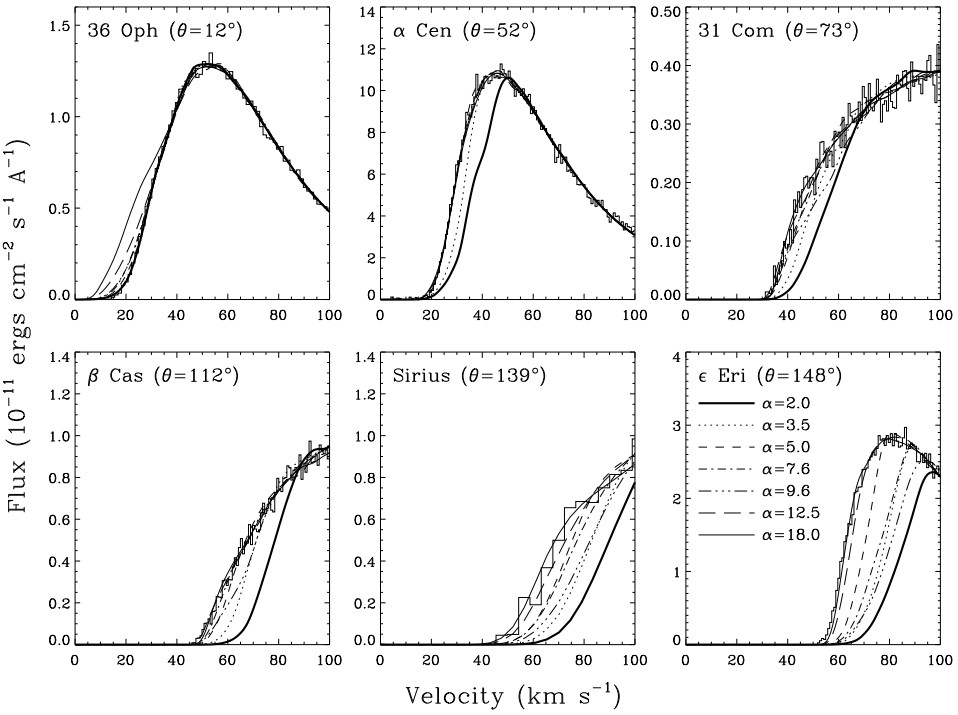

Figure 11.4: Comparison of the Lyα absorption predicted by various heliospheric models with the data, for the same six lines of sight as in Figure 11.3, but using a different heliospheric modeling code. The parameter varied in these models is α (see bottom right panel), the ratio of total ISM pressure to the proton pressure. Values of $\alpha > 2$ are meant to mimic the effects of substantial magnetic and/or cosmic ray pressure in the ISM. From Wood et al. [2000b].

There is surprisingly little difference in the predicted amount of absorption, despite significant differences in assumed ISM densities (see Table 11.4). The hydrogen wall absorption predicted by the models is apparently not very sensitive at all to the ISM parameter variations.

Some of the discrepancies with the data seen for the β Cas and ϵ Eri lines of sight could in principle be reduced by suitable alterations to the assumed stellar Lyα profile (see first column of Figure 11.3), but in general the β Cas and ϵ Eri lines of sight suggest that the models may predict too much heliosheath absorption in downwind directions. This problem is even more apparent for the hybrid kinetic models of Müller et al. [2000], which uses a fluid code to model the protons in the heliosphere, but uses a kinetic treatment of the neutral hydrogen. Figure 11.4 shows a comparison between predictions of these models with the same six lines of sight from Figure 11.3, where the predicted ISM-plus-heliospheric absorption is shown after attempts have already been made to improve the data/model agreement by altering the assumed stellar Lyα profile [Wood et al., 2000b].

The ISM parameter being varied for the seven models in Figure 11.4 is α, the ratio of the total ISM pressure to the proton pressure, where assumptions of $\alpha > 2$ are meant to approximate the effects of substantial magnetic field and/or cosmic ray pressure in the ISM. None of the models fit all of the lines of sight well. The models that agree best with the downwind ϵ Eri line of sight assume values of α that are probably unreasonably high, and these models also underpredict the amount of absorption upwind towards 36 Oph. The models with lower, more probable values of α predict too much heliospheric absorption in downwind directions, somewhat analogous to what is found in Figure 11.3 for the models computed using the Baranov and Malama [1993, 1995] code.

Several possible explanations have been proposed to explain the difficulties that kinetic codes seem to have in reproducing the heliospheric absorption in downwind directions. Perhaps collisions with neutrals not involving charge exchange, which are not considered in the models, become important in the heliotail region [Wood et al., 2000b]. Another possibility is that perhaps protons in the heliosphere should actually be treated as multiple fluids due to the incomplete assimilation of pickup ions into the solar wind plasma interior to the termination shock. Izmodenov et al. [2002] propose that the current single-fluid treatment of the protons could lead to inaccurate velocity distribution functions in the heliotail, resulting in the overpredictions of H I absorption. Hopefully, further modifications of the kinetic codes will improve their ability to reproduce the heliospheric Lyα absorption in the future.

Although the kinetic models are not entirely successful in fitting the Lyα data, Wood et al. [2000b] find that a four-fluid code of the type described by Zank et al. [1996] can fit the data, including the downwind directions. The four-fluid code assumes that the H I velocity distributions can be represented by the sum of three Maxwellian H fluids, one for each distinct region where charge exchange takes place (between the heliopause and bow shock, between the termination shock and heliopause, and inside the termination shock), plus one fluid for the H^+. This is also the code that Gayley et al. [1997] used in the first data/model comparison for the heliospheric absorption. The apparent greater success of the four-fluid code compared to the kinetic codes is surprising since unlike the four-fluid code the kinetic models make no *a priori* assumptions at all about the shape of the velocity distributions. Nevertheless, Figure 11.5 shows the predictions of a four-fluid code, which fit the data reasonably well, though similar to the kinetic models the four-fluid also predicts a little too much absorption towards ϵ Eri. The input ISM parameters for this model are: $V = 26$ km s^{-1}, $n(H^+) = 0.1$ cm^{-3}, $n(H\ I) = 0.14$ cm^{-3}, and $T = 8000$ K. The assumed solar wind parameters at 1 AU are: $V = 400$ km s^{-1}, $n(H^+) = 5$ cm^{-3}, and $T = 10^5$ K [Wood et al., 2000b].

The models described above are all 2D axisymmetric hydrodynamic models. They do not include a proper MHD treatment of magnetic fields, either the heliospheric magnetic field carried outwards by the solar wind or the poorly known ISM field. (The use of the α parameter mentioned above to mimic the effects of magnetic field pressure is only a crude way to estimate the possible effects of the ISM field.) An MHD treatment of the heliosphere is difficult, both because of the additional complexity of magnetic fields in the modelling and because a proper inclusion of magnetic fields really requires a three-dimensional model rather than an

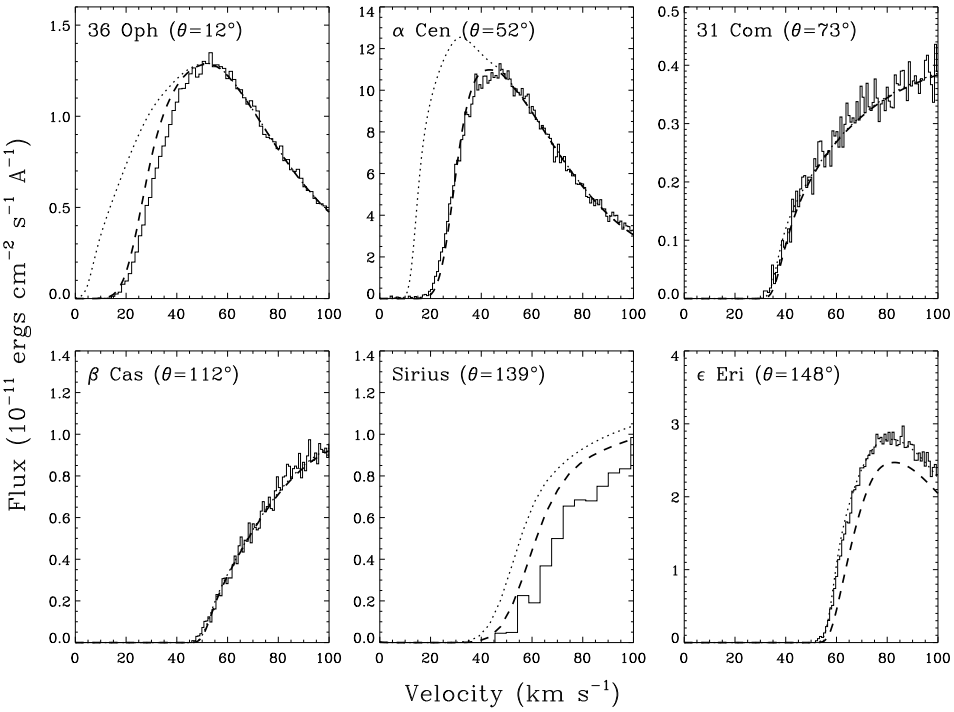

Figure 11.5: Comparison of the H I absorption predicted by a four-fluid heliospheric model and HST observations of the same six lines of sight shown in Figures 11.3 and 11.4. The dotted lines show the ISM absorption alone and the dashed lines show the total Lyα absorption after the model heliospheric absorption is added to the ISM absorption. Reasonably good agreement is observed, although there is a slight underprediction of absorption towards 36 Oph and Sirius, and a slight overprediction towards ϵ Eri. From Wood et al. [2000b].

axisymmetric one. Using a 2D approach, Florinski et al. [2004] find that a strong ISM field oriented parallel to the ISM flow does not yield significantly different predictions for heliospheric Lyα absorption than models without magnetic fields. However, a 3D model is required to include the heliospheric field and to allow ISM field orientations other than parallel to the flow vector.

Dealing with both neutrals and magnetic fields properly in a 3D model is a very formidable problem. Nevertheless, 3D models without neutrals [e.g. Linde et al., 1998] do suggest that MHD effects could in principle lead to changes in the heliospheric structure that could affect the Lyα absorption. One example is the unstable jet sheet predicted by Opher et al. [2003]. Ratkiewicz et al. [1998] find that if the ISM magnetic field is skewed with respect to the ISM flow, the effective nose of the heliosphere could be significantly shifted from the upwind direction. This effect may have been observed by Lallement et al. [2005], and Izmodenov et al. [2005] use models to see what these data imply about the character of the ISM field. Even in the absence of magnetic fields, latitudinal variations in solar wind

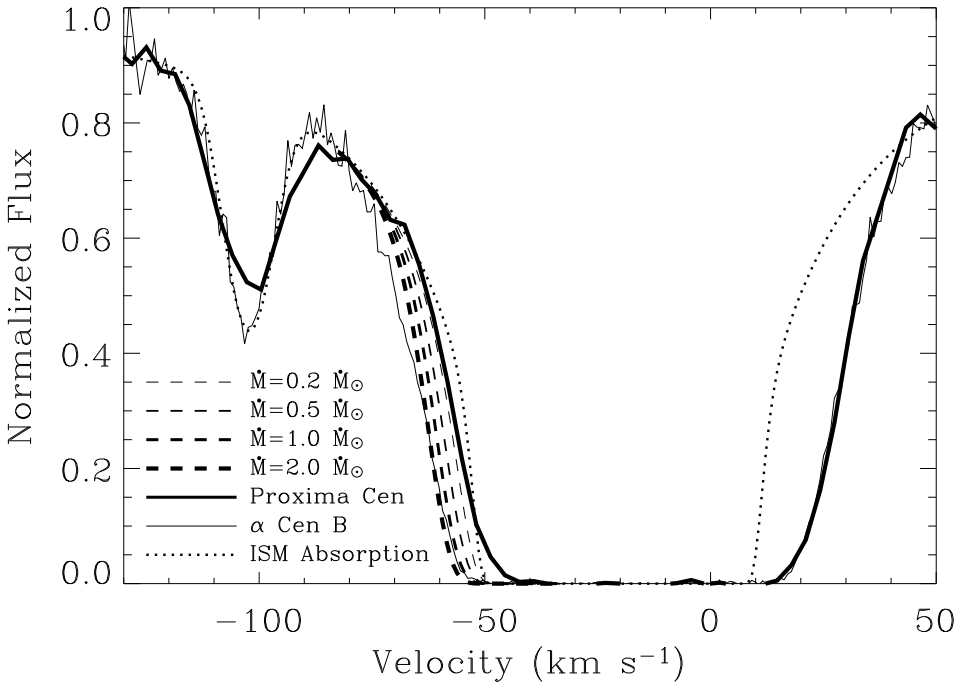

Figure 11.6: The α Cen B spectrum (thin solid line) and inferred ISM absorption (dotted line) from Figure 11.1 are compared with a lower resolution HST spectrum of α Cen's distant companion Proxima Cen (thick solid line). The two spectra agree well on the red side of the H I absorption, but on the blue side the Proxima Cen data do not show the excess Lyα absorption seen toward α Cen (i.e. the astrospheric absorption). The dashed lines show the blue-side excess Lyα absorption predicted by models of the Alpha/Proxima Cen astrospheres, assuming different mass loss rates. From Wood et al. [2001].

properties could also cause asymmetries in the heliosphere [Pauls and Zank, 1997]. However, neutrals must be included properly in the models to indicate whether these effects should have observable consequences for the Lyα absorption.

11.5 The astrospheric absorption

The Lyα absorption diagnostic is completely unique in being the only diagnostic that can be used to study astrospheres around other stars as well as the heliosphere. Comprehensive reviews of work on the astrospheric absorption are provided elsewhere [Wood, 2004; Wood et al., 2005a, b], but it is worth mentioning some of the uses of the astrospheric absorption here as well. After all, the first detections of astrospheres analogous to our heliosphere expand the scope of heliospheric research into a much broader, astrophysical scale.

The strongest evidence that the astrospheric interpretation of the blue-side excess Lyα absorption is correct comes from comparing the α Cen Lyα absorption profile from Figure 11.1 with the Lyα absorption observed for a distant companion of the α Cen binary system, Proxima Cen, which is about 12000 AU from α Cen [Wood et al., 2001]. This comparison is made in Figure 11.6. The absorption profiles agree well on the red side of the absorption line where the heliospheric absorption resides, but the blue-side excess absorption seen towards α Cen is not observed towards Proxima Cen. It is hard to imagine lines of sight so nearly identical in direction and distance having such a large difference in interstellar or heliospheric absorption, so ISM or heliospheric variations are very unlikely explanations for this discrepancy. The astrospheric interpretation provides a much better explanation for α Cen's blue-side excess absorption, since α Cen's astrosphere will not be so large as to encompass Proxima Cen, explaining why this excess is not seen on the blue side of its Lyα line. Apparently, Proxima Cen must have a much smaller astrosphere than α Cen in order to explain why it does not produce any detectable absorption.

The astrospheric detections listed in Table 11.1 represent the first detections of truly solar-like winds from stars like the Sun. The detections are somewhat indirect, since the astrospheric Lyα absorption is mostly from hydrogen wall material that is actually interstellar in nature. Nevertheless, the absorption is still a clear signature of the collision between the stellar wind and the ISM. Furthermore, the amount of absorption will be correlated to the size of the astrosphere, which is in turn related to the mass loss rate of the stellar wind. Thus, the astrospheric absorption has been used to provide the first estimates of mass loss rates for solar-like cool main sequence stars.

Measuring stellar mass loss rates from astrospheric absorption requires the assistance of hydrodynamic models of the astrospheres, using codes such as those described in the previous section developed to model the heliosphere. Extracting mass loss rates from the astrospheric absorption is therefore an important application of heliospheric modeling. Figure 11.7 shows four models of the α Cen astrosphere assuming mass loss rates ranging from $\dot{M} = 0.2 - 2.0\ \dot{M}_{\odot}$, where $\dot{M}_{\odot} = 2 \times 10^{-14}$ $M_{\odot}$ yr^{-1} is the solar mass loss rate [Wood et al., 2001]. These models are computed using the four-fluid code of Zank et al. [1996] described above.

The models are in fact basically extrapolated from the heliospheric model that reproduced the heliospheric Lyα absorption in Figure 11.5. The ISM and stellar wind parameters are kept the same as in this model except for the ISM wind speed, which is changed to the value appropriate for the star; and the stellar wind density, which is changed to experiment with stellar mass loss rates different from that of the Sun. The ISM flow velocity seen by the stars in Table 11.1 can be computed from their known proper motions and radial velocities, and the known local ISM flow vector.

The Lyα absorption predicted by the four models in Figure 11.7 is shown in Figure 11.6. The model with $\dot{M} = 2.0\ \dot{M}_{\odot}$ fits α Cen's blue-side excess absorption best, so that is the estimate for the mass loss rate from the α Cen binary. Such estimates have been made for all the astrospheric detections in Table 11.1 [Wood et al., 2005a].

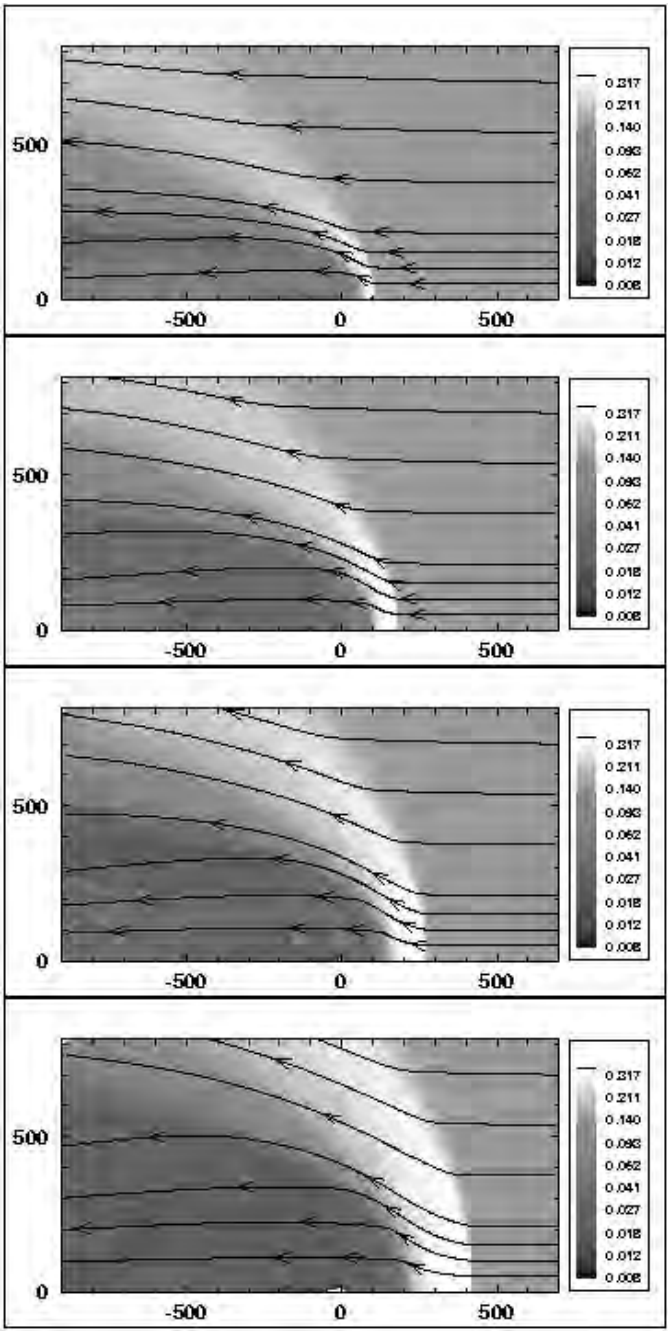

Figure 11.7: Distribution of H I density predicted by hydrodynamic models of the α Cen astrosphere, assuming stellar mass loss rates of (from top to bottom) 0.2 $\dot{M}_\odot$, 0.5 $\dot{M}_\odot$, 1.0 $\dot{M}_\odot$, and 2.0 $\dot{M}_\odot$. The distance scale is in AU. Streamlines show the H I flow pattern. From Wood et al. [2001].

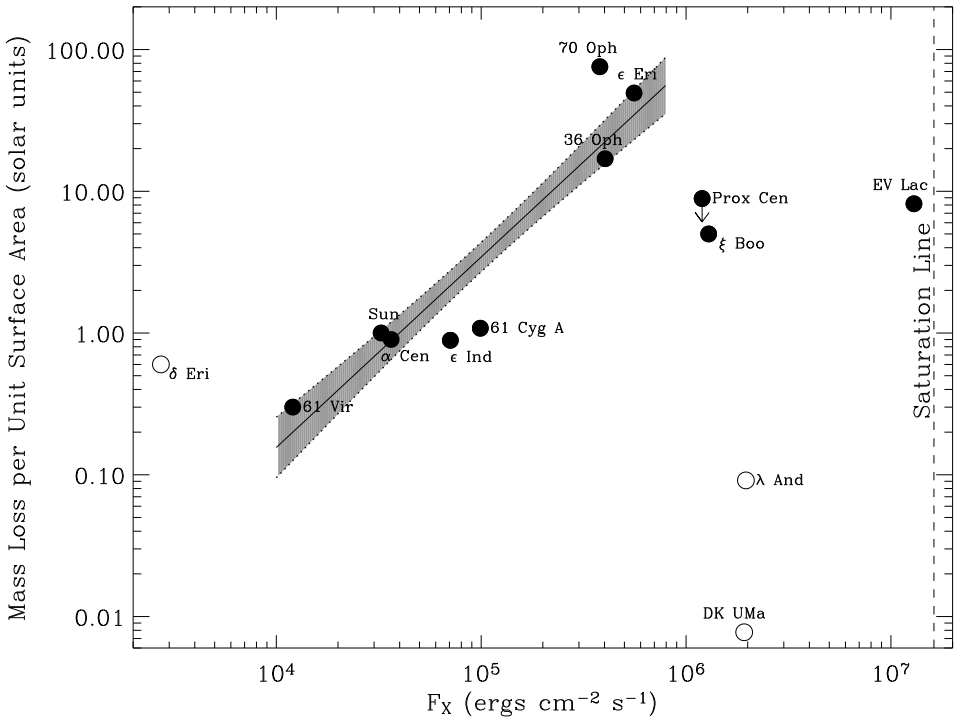

Figure 11.8: (a) Mass loss rates per unit surface area plotted versus stellar X-ray surface fluxes. Filled symbols are for main sequence stars, while open symbols are for evolved stars. A power law has been fitted to the main sequence stars with $\log F_X < 8 \times 10^5$ ergs cm^{-2} s^{-1}. From Wood et al. [2005a].

The mass loss rates (per unit surface area) are plotted versus X-ray surface flux in Figure 11.8 [Wood et al., 2005a]. For solar-like stars, X-ray emission and winds both arise from the hot stellar coronae. Thus, a correlation between X-ray emission and mass loss might be expected. For the main sequence stars, mass loss appears to increase with activity for $\log F_X < 8 \times 10^5$ ergs cm^{-2} s^{-1}. A power law relation has been fitted to those stars, $\dot{M} \propto F_x^{1.34 \pm 0.18}$, which is shown in Figure 11.8. However, this relation does not appear to extend to high activity levels. Additional mass loss measurements would be helpful to better define the mass-loss/activity relation of cool main sequence stars.

The truncation of the mass-loss/activity relation at $\log F_X \approx 8 \times 10^5$ ergs cm^{-2} s^{-1} may be indicative of a fundamental difference in the magnetic field topology of very active stars compared with low activity stars. Perhaps active stars have magnetic field structures that inhibit wind outflows, explaining why they apparently have surprisingly weak winds (see Fig. 11.8). Independent evidence for a different magnetic field structure for active stars is provided by the frequent detections of polar starspots for very active stars [Strassmeier, 2002], in contrast to the solar case where sunspots are always observed only at low latitudes. One could imagine that

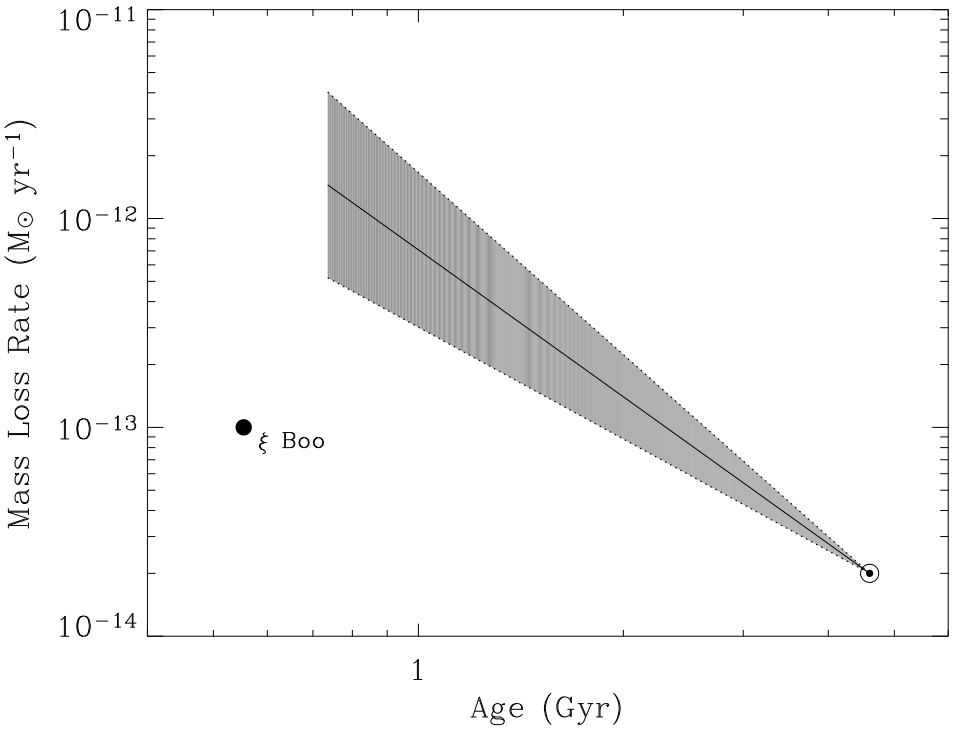

Figure 11.9: The mass loss history of the Sun inferred from the power law relation in Figure 11.8. The truncation of the relation in Figure 11.8 means that the mass-loss/age relation is truncated as well. The low mass loss measurement for ξ Boo suggests that the wind suddenly weakens at $t \approx 0.7$ Gyr as one goes back in time. From Wood et al. [2005a].

polar spots might indicate a magnetic field with a strong dipolar component that could envelope the entire star and inhibit stellar winds.

By far the most solar-like of the stars in the high activity regime in Figure 11.8 is ξ Boo, which is actually a binary star (G8 V+K4 V). The low mass loss rate measured for this active binary therefore provides the strongest evidence for the truncation of the mass-loss/activity relation for solar-like stars. It is therefore worth noting that high latitude starspots have been detected for ξ Boo A [Toner and Gray, 1988], and Petit et al. [2005] have detected magnetic field structures that are significantly different from solar, including a 40 G global dipole field and an 120 G toroidal field component. This is consistent with the interpretation of the truncation of the mass-loss/activity relation as being due to a change in magnetic field topology.

Coronal X-ray flux and stellar age are related by $F_X \propto t^{-1.74\pm0.34}$ for stars with spectral types close to that of the Sun [Ayres, 1997]. Combining this with the mass-loss/activity relation in Figure 11.8 yields $\dot{M} \propto t^{-2.33\pm0.55}$, implying higher mass loss rates for young stars. Figure 11.9 shows what this relation suggests for

the mass loss history of the Sun. The truncation of the power law relation in Figure 11.8 leads to the mass-loss/age relation in Figure 11.9 being truncated as well at about $t = 0.7$ Gyr. Since ξ Boo is the most solar-like star beyond the truncation of the mass-loss/activity relation in Figure 11.8, the location of ξ Boo is shown in Figure 11.9 in order to indicate what the solar wind might have been like at times earlier than $t = 0.7$ Gyr.

The apparently stronger wind of the young Sun may be of great importance for planetary studies, since solar wind erosion may have played an important role in the evolution of planetary atmospheres in our Solar System. Mars is potentially the most interesting case, since it is known that the Martian atmosphere was once much thicker than it is now, which may have allowed water to exist on its surface [Kass and Yung, 1995]. The time when Mars is believed to have lost most of its atmosphere corresponds roughly to the time when Figure 11.9 suggests that the solar wind abruptly strengthens ($t \approx 0.7$ Gyr), and enters the low activity regime where our power law mass-loss/age relation applies. Perhaps this strengthening of the solar wind, which could be due to a change in magnetic field structure, played a role in the dissipation of the Martian atmosphere. However, the loss of Mars's global magnetic field at about this time [Acuña et al., 1999] was surely crucial as well, since the magnetic field would have presumably shielded the Martian atmosphere from solar wind erosion, much as the Earth's magnetosphere does for our atmosphere.

11.6 Summary

This chapter has described how high resolution stellar UV spectra from HST have provided an unexpected observational diagnostic for the heliosphere. The heliospheric Lyα absorption provides a crucial test of models of the large scale structure of our heliosphere. In particular, it confirms the existence of a hydrogen wall in between the bow shock and heliopause, which is responsible for most of the absorption in most directions. The Lyα absorption is in fact the only observational diagnostic available for these outermost regions of the heliosphere. However, the absorption has not yet realized its potential for assessing circumsolar ISM properties, partly due to model dependence and partly due to lack of sensitivity to ISM variations.

Not only can Lyα absorption be used to study the heliosphere, but it can also be used to study analogous astrospheres around other stars. The astrospheric detections represent the first detections of solar-like winds from cool main sequence stars and mass loss measurements have been estimated from these data. These measurements have been correlated with stellar activity and age, allowing an empirical estimate for the solar wind's evolution to be made. Both the heliospheric and astrospheric work could benefit from additional observations. Unfortunately, the apparent demise of HST's Space Telescope Imaging Spectrograph instrument in 2004 August means that high resolution spectroscopy of the Lyα line is no longer possible, so the sample of heliospheric and astrospheric absorption detections in Table 11.1 is unlikely to increase anytime soon.

The use of astrospheric absorption studies to estimate the history of the solar wind represents an excellent example of how solar and stellar research can feed off each other. Our understanding of the solar wind and heliosphere has been used to properly identify the frequently observed blue-side excess Lyα absorption as being astrospheric in nature, and computer codes developed to model the heliosphere have been used to model the observed astrospheres. In doing so, the strength of previously undetectable stellar winds has been measured. However, these stellar measurements also end up telling us something about the solar wind and heliosphere, namely about its long-term time dependence. Thus, we have come full circle, with the application of heliospheric models to astrospheres leading to further knowledge of our heliosphere as well as the astrospheres.

Acknowledgements

The author acknowledges support by NASA through grant NNG05GD69G to the University of Colorado.

Bibliography

Acuña, M.H., Connerney, J.E.P., Ness, N.F., Lin, R.P., Mitchell, D., Carlson, C.W., McFadden, J., Anderson, K.A., Rème, H., Mazelle, C., Vignes, D., Wasilewski, P., and Cloutier, P., Global distribution of crustal magnetism discovered by the Mars Global Surveyor MAG/ER experiment, *Science* **284**, 790-793, 1999.

Alexashov, D., and Izmodenov, V., Kinetic vs. multi-fluid models of H atoms in the heliospheric interface: A comparison, *Astron. Astrophys.* **439**, 1171-1181, 2005.

Ayres, T.R., Evolution of the solar ionizing flux, *J. Geophys. Res.* **102**, 1641-1652, 1997.

Baranov, V.B., Lebedev, M.G., and Malama, Y.G., The influence of the interface between the heliosphere and the local interstellar medium on the penetration of the H atoms to the solar system, *Astrophys. J.* **375**, 347-351, 1991.

Baranov, V.B., and Malama, Y.G., Model of the solar wind interaction with the local interstellar medium — Numerical solution of self-consistent problem, *J. Geophys. Res.* **98**, 15157-15163, 1993.

Baranov, V.B., and Malama, Y.G., Effect of local interstellar medium hydrogen fractional ionization on the distant solar wind and interface region, *J. Geophys. Res.* **100**, 14755-14762, 1995.

Dring, A.R., Linsky, J., Murthy, J., Henry, R.C., Moos, W., Vidal-Madjar, A., Audouze, J., and Landsman, W., Lyman-α absorption and the D/H ratio in the local interstellar medium, *Astrophys. J.* **488**, 760-775, 1997.

Gayley, K.G., Zank, G.P., Pauls, H.L., Frisch, P.C., and Welty, D.E., One- versus two-shock heliosphere: Constraining models with GHRS Lyman-α spectra toward α Centauri, *Astrophys. J.* **487**, 259-270, 1997.

Florinski, V., Pogorelov, N.V., Zank, G.P., Wood, B.E., and Cox, D.P., On the possibility of a strong magnetic field in the local interstellar medium, *Astrophys. J.* **604**, 700-706, 2004.

Izmodenov, V., Alexashov, D., and Myasnikov, A., Direction of the interstellar H atom inflow in the heliosphere: Role of the interstellar magnetic field, *Astron. Astrophys.* **437**, L35-L38, 2005.

Izmodenov, V.V., Lallement, R., and Malama, Y.G., Heliospheric and astrospheric hydrogen absorption towards Sirius: No need for interstellar hot gas, *Astron. Astrophys.* **342**, L13-L16, 1999.

Izmodenov, V.V., Wood, B.E., and Lallement, R., Hydrogen wall and heliosheath Lyman-α absorption toward nearby stars: Possible constraints on the heliospheric interface plasma flow, *J. Geophys. Res.* **107**, 1308-1322, 2002.

Kass, D.M., and Yung, Y.L., Loss of atmosphere from Mars due to solar wind-induced sputtering, *Science* **268**, 697-699, 1995.

Kruk, J.W., Howk, J.C., André, M., Moos, H.W., Oegerle, W.R., Oliveira, C., Sembach, K.R., Chayer, P., Linsky, J.L., Wood, B.E., Ferlet, R., Hébrard, G., Lemoine, M., Vidal-Madjar, A., and Sonneborn, G., Abundances of deuterium, nitrogen, and oxygen toward HZ 43A: Results from the FUSE mission, *Astrophys. J. Supp.* **140**, 19-36, 2002.

Lallement, R., Ferlet, R., Lagrange, A.M., Lemoine, M., and Vidal-Madjar, A. Local cloud structure from HST-GHRS, *Astron. Astrophys.* **304**, 461-474, 1995.

Lallement, R., Quémerais, E., Bertaux, J.L., Ferron, S., Koutroumpa, D., and Pellinen, R., Deflection of the interstellar neutral hydrogen flow across the heliospheric interface, *Science* **307**, 1447-1449, 2005.

Lemoine, M., Vidal-Madjar, A., Hébrard, G., Désert, J.-M., Ferlet, R., Lecavelier des Étangs, A., Howk, J.C., André, M., Blair, W.P., Friedman, S.D., Kruk, J.W., Lacour, S., Moos, H.W., Sembach, K., Chayer, P., Jenkins, E.B., Koester, D., Linsky, J.L., Wood, B.E., Oegerle, W.R., Sonneborn, G., and York, D.G., Deuterium abundance toward G191-B2B: Results from the FUSE mission, *Astrophys. J. Supp.* **140**, 67-80, 2002.

Linde, T., Gombosi, T.I., Roe, P.L., Powell, K.G., and DeZeeuw, D.L., Heliosphere in the magnetized local interstellar medium — Results of a three-dimensional MHD simulation, *J. Geophys. Res.* **103**, 1889-1904, 1998.

Linsky, J.L., and Wood, B.E., The α Centauri line of sight: D/H ratio, physical properties of local interstellar gas, and measurement of heated hydrogen near the heliopause, *Astrophys. J.* **463**, 254-270, 1996.

Müller, H.-R., Zank, G.P., and Lipatov, A.S., Self-consistent hybrid simulations of the interaction of the heliosphere with the local interstellar medium, *J. Geophys. Res.* **105**, 27419-27438, 2000.

Opher, M., Liewer, P.C., Gombosi, T.I., Manchester, W., DeZeeuw, D.L., Sokolov, I., and Toth, G., Probing the edge of the solar system: Formation of an unstable jet sheet, *Astrophys. J.* **591**, L61-L65, 2003.

Pauls, H.L., and Zank, G.P., Interaction of a nonuniform solar wind with the local interstellar medium. 2. A two-fluid model, *J. Geophys. Res.* **102**, 19779-19788, 1997.

Petit, P., Donati, J.-F., Aurière, M., Landstreet, J.D., Lignières, F., Marsden, S., Mouillet, D., Paletou, F., Toqué, N., and Wade, G.A., Large scale magnetic field of the G8 dwarf ξ Bootis A, *Mon. Not. R. Astron. Soc.* **361**, 837-849, 2005.

Ratkiewicz, R., Barnes, A., Molvik, G.A., Spreiter, J.R., Stahara, S.S., Vinokur, M., and Venkateswaran, S., Effect of varying strength and orientation of local

interstellar magnetic field on configuration of exterior heliosphere: 3D MHD simulations, *Astron. Astrophys.* **335**, 363-369, 1998.

Strassmeier, K.G., Doppler images of starspots, *Astronomische Nachrichten* **323**, 309-316, 2002.

Toner, C.G., and Gray, D.F., The starpatch on the G8 dwarf ξ Bootis A, *Astrophys. J.* **334**, 1008-1020, 1988.

Vidal-Madjar, A., and Ferlet, R., Hydrogen column density evaluations toward Capella: Consequences on the interstellar deuterium abundance, *Astrophys. J.* **571**, L169-L172, 2002.

Wood, B.E., Astrospheres and solar-like stellar winds, *Living Rev. Solar Phys.* **1**, URL: http://www.livingreviews.org/lrsp-2004-2, 1995.

Wood, B.E., Alexander, W.R., and Linsky, J.L., The properties of the local interstellar medium and the interaction of the stellar winds of ϵ Indi and λ Andromedae with the interstellar environment, *Astrophys. J.* **470**, 1157-1171, 1996.

Wood, B.E., and Linsky, J.L., The local ISM and its interaction with the winds of nearby late-type stars, *Astrophys. J.* **492**, 788-803, 1998.

Wood, B.E., Linsky, J.L., Müller, H.-R., and Zank, G.P., Observational estimates for the mass-loss rates of α Centauri and Proxima Centauri using Hubble Space Telescope Lyman-α spectra, *Astrophys. J.* **547**, L49-L52, 2001.

Wood, B.E., Linsky, J.L., and Zank, G.P., Heliospheric, astrospheric, and interstellar Lyman-α absorption toward 36 Ophiuchi, *Astrophys. J.* **537**, 304-311, 2000a.

Wood, B.E., Müller, H.-R., and Zank, G.P., Hydrogen Lyman-α absorption predictions by Boltzmann models of the heliosphere, *Astrophys. J.* **542**, 493-503, 2000b.

Wood, B.E., Müller, H.-R., Zank, G.P., Linsky, J.L., and Redfield, S., New mass loss measurements from astrospheric Lyα absorption, *Astrophys. J.* **628**, L143-L146, 2005a.

Wood, B.E., Redfield, S., Linsky, J.L., Müller, H.-R., and Zank, G.P., Stellar Lyα emission lines in the Hubble Space Telescope archive: Intrinsic line fluxes and absorption from the heliosphere and astrospheres, *Astrophys. J. Supp.*, **159**, 118-140, 2005b.

Zank, G.P., Pauls, H.L., Williams, L.L., Hall, D.T., Interaction of the solar wind with the local interstellar medium: A multifluid approach, *J. Geophys. Res.* **101**, 21639-21656, 1996.

— 12 —

The Outer Heliospheric Radio Emission: Observations and Theory

Rudolf A. Treumann[1]
Geophysics Section, Ludwig-Maximilians-University, Munich, Germany
Raymond Pottelette
CETP/CNRS, St. Maur des Fossés, France

Abstract. **This chapter provides a brief review of the observation and interpretation of radio emission from the outer heliosphere in the view of the new knowledge obtained about the outer heliosphere after the Voyager passage of the termination shock. It is discussed whether the termination shock and inner heliosheath could serve as the radiation sources. It is argued that the conditions at both places are not favourable for emitting observable radio waves. Moreover, the observation of electron plasma waves without radiation in the foreshock of the termination shock suggests that the plasma there is unable to excite radiation. It is too cold to excite ion-acoustic waves for scattering Langmuir waves or modulating the plasma, while the mere existence of plasma oscillations identifies the termination shock as a non-perpendicular or at least a non-stationary shock that is supercritical enough to reflect electron beams – and probably also ions beams. In this case it must be a shock that is mediated by the hot pick-up ion component. We therefore confirm the proposal that the radiation can only be produced by interaction between the heliopause plasma and a strong global interplanetary shock wave. We present arguments that put the electron beam primed mechanism of stochastically growing lower-hybrid wave for the production of the observed radiation in question. A possible replacement for this mechanism is the combination of shock acceleration of electrons and reconnection between the spiral interplanetary field and the interstellar field. Electrons accelerated by the purely perpendicular global shock can be released from the shock by reconnection and are injected into the outer heliosheath where in the sufficiently dense plasma they excite sufficiently intense radiation. The low frequency cut-off of the radiation maps the density of the driver piston of the global shock.**

[1]Visiting scientist at the International Space Science Institute, Bern, Switzerland

The Physics of the Solar Wind Termination Region, V. Izmodenov and R. Kallenbach (eds.), ISSI Scientific Report No. 5, pp. 355 - 389, ESA-ESTEC, Paris 2006

12.1 Introduction

The outer heliosphere (a numerical three-component fluid simulation model of which is shown in Figure 12.1) is a huge – on the planetary scale – plasma reservoir [for collections of timely reviews see the two COSPAR Proceedings volumes edited by Grzedzielski & Page, 1990; Scherer et al., 2001] filled with a highly conducting, highly diluted and weakly magnetized plasma that consists of several different particle components [for more details see Axford, 1990; Suess, 1990; Zank, 1999; Wood et al., 2000; Zank and Mueller, 2003; Izmodenov et al., 2003a, b, 2005]. The properties of these components have been described in detail elsewhere in this book. In brief, towards interstellar space the outer heliosphere is bound by the interaction of the solar wind with the interstellar gas which retards the solar wind at the position of the termination shock and confines it inside the heliopause. A presumably highly turbulent region, the inner heliosheath, is caused between the termination shock and the heliopause, while outside the heliosphere the retardation of the interstellar gas may generate an external bow shock in front of the heliosphere and an outer heliosheath between the heliopause and this heliospheric bow shock. The matter in this entire region consists of a mixture of solar wind electrons and protons, a neutral, non-ionized interstellar gas component that penetrates into the heliosphere, interstellar pick-up ions which result from charge exchange interaction between the solar wind and the interstellar gas and become accelerated in the magnetized solar wind stream, and fast neutrals created in the same process from the solar wind protons and which continue to fly in the anti-sunward direction until entering the interstellar space and either undergoing secondary charge exchange or collisional ionization there to contribute to plasma in the outer heliosheath. In Figure 12.2 we show the density and temperature profiles along the Sun-stagnation point line as taken from the simulations in Figure 12.1. We have also included there the plasma frequency $f_{\rm pe}$ and an estimate for the Debye length $\lambda_{\rm D}$. The latter is a function of electron temperature, a very uncertain quantity in the outer heliosphere that does not coincide with the proton temperature given in Figure 12.2 unless some mechanism is responsible for isothermalization. In the absence of collisions, such mechanisms are basically unknown. In the expanding solar wind the electron temperature would decreases about adiabatically until outside the planetary system interstellar pick-up ions are created. However, on the large scale $\sim$ 10 AU collisions come into play again and the electron and ion temperatures may approach each other. In the interstellar pick-up ion region the ion temperature will become dominated by the pick-up component such that for isothermalization the electron temperature may be anywhere between fractions of eV and few keV (the pick-up ion energy), being approximately constant. For simplicity we have taken the electron temperature to be roughly of the order of $T_{\rm e} \sim$ several eV just up to the termination shock.

A mixture of matter like that in the outer heliosphere is subject to different forms of radiation. Here we are basically interested in radiation that is generated in the outer heliosphere at solar radial distances far outside the planetary system. Radiation emitted there is thus independent of the particular conditions prevailing in the vicinity of the different planets. As the emission measure of the outer heliospheric plasma is small (radiation is generated by non-collisional processes)

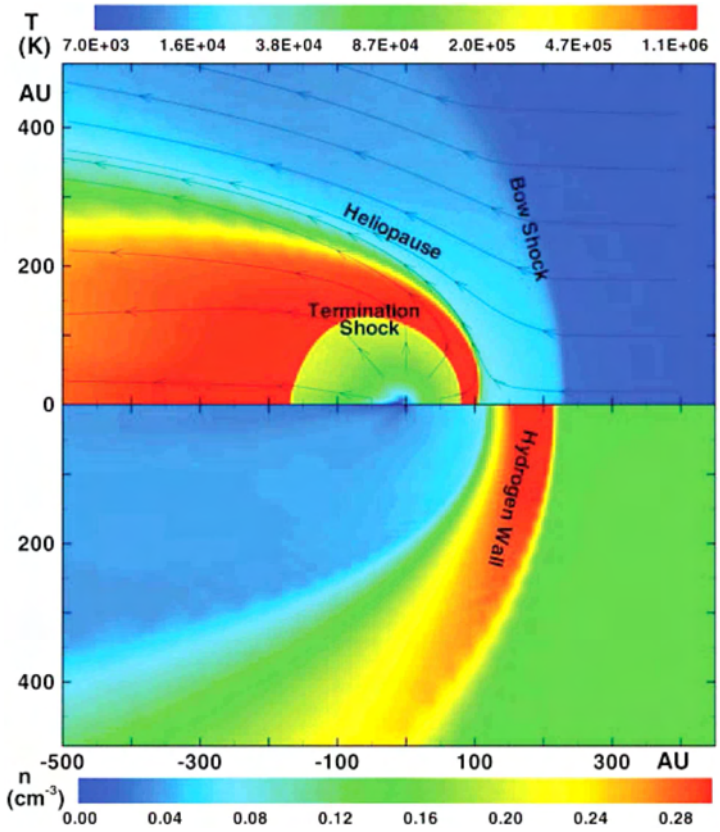

Figure 12.1: Two-dimensional (2-D) steady-state, two-shock heliosphere showing (top) the colour-coded temperature distribution of the solar wind and interstellar plasma and (bottom) the density distribution of neutral hydrogen. The termination shock, heliopause, bow shock and neutral hydrogen wall are identified. The solid lines (top plot) show streamlines. The plasma temperature is plotted logarithmically and the neutral density linearly. Distances along x and y are in AU [from Zank and Mueller, 2003].

the focus is on radio emission [e.g. Cairns et al., 1992]. We note, however, that radio emission is not the only form of radiation the outer heliospheric plasma is able to support. Even though free energy sources for generating radiation in the outer heliosphere are scarce or unknown, X-ray emission from charge transfer with interstellar neutrals has been considered [Cravens, 2000] as a viable radiation from the heliosphere with maximum source strength in the outer heliosphere. In addition, the particle population in the outer heliosphere can scatter short wavelength radiation produced in other places. This is known for solar H Lyman-α radiation, which in recent years has been found to be scattered from the interstellar neutral gas component in the heliosphere. Measurement of the spatial and temporal variation of solar H Lyman-α has allowed detection of the radial gradient of the neutral gas component in the outer heliosphere and inference of global properties

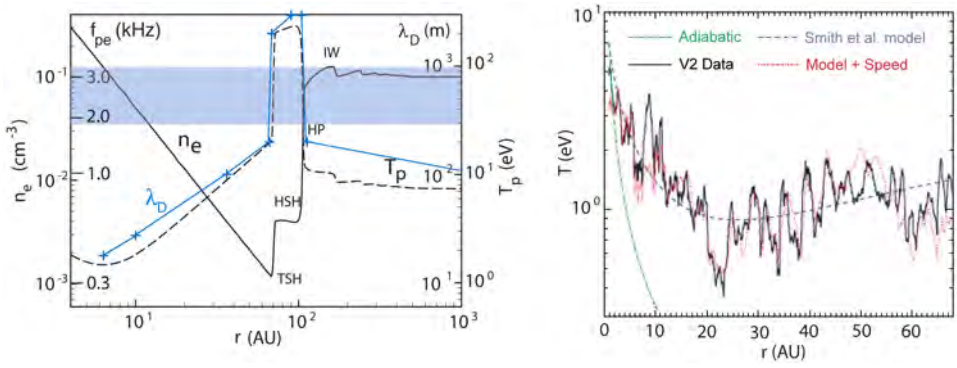

Figure 12.2: *Top*: A 1-D profile of the plasma density $n_{\rm p}(r)$, the corresponding plasma frequency (inner left scale) in kHz, and temperature $T_{\rm p}(r)$ as a function of radial heliocentric distance r along the direction of the Sun-stagnation point [from Zank and Mueller, 2003]. The density profile exhibits the typical radial decrease up to the termination shock, the downstream heliosheath compression, and the increase at the heliopause. The temperature profile shows the temperature control by the anomalous cosmic ray component for $r > 8$ AU, downstream plasma heating in the heliosheath, and the steep temperature drop at the heliopause. This picture is not changed substantially if the LISM is supersonic and a heliospheric bow shock develops at a few Hundred AU. Also shown is the presumable variation of the electron Debye length $\lambda_{\rm D}$ (in m) for the calculated density profile. The shaded area shows the frequency range of heliospheric radio emissions. Clearly, if the emissions are related to the plasma density then they could only come either from the region inside $r < 10$ AU or from the heliopause region near $r \geq 100$ AU. *Bottom*: Actual Voyager 2 measurements of the solar wind ion temperature within the first 70 AU heliocentric distance compared to different model of the relation between the solar wind speed and temperature [from Richardson and Smith, 2003]. The green adiabatic line corresponds to the simulations in the top part. It underestimates the actual temperature. Average measured values do not drop far below 1 eV and though increasing with distance remain close to this value.

of the heliosphere from these measurements [Quémerais et al., 2003; Lallement et al., 2005].

Radio emission from astrophysical objects is usually attributed to the single-particle mechanisms of gyro- or synchrotron emission processes in magnetic fields. Radiation produced by collective processes in high-temperature plasmas like the solar corona [for a collection of reviews see, e.g., Labrum, 1985] assumes much higher radiation intensities (or brightness temperatures). It is usually highly variable in time and space. It is difficult to identify in remote astrophysical objects because of the required long observational times [recent observations have been discussed by Treumann, 2006]. Inside the heliosphere collective plasma radiation processes clearly dominate the gyro-synchrotron emission. In the Solar System, intense radio emissions are generated in numerous regions: the solar corona and solar wind, near interplanetary shock waves and planetary bow shocks, inside the various planetary magnetospheres and the auroral regions of the magnetized planets Earth, Jupiter, Saturn and probably even – though not yet detected – also from Mercury and Nep-

tune, and last but not least also from the outskirts of the heliosphere where the solar wind interacts with the interstellar gas.

In the outer heliosphere the three regions of interest for the emission of radio radiation are the termination shock, the heliopause, and the heliospheric bow shock wave. Recently the termination shock has become subject to in-situ observations when Voyager 1 was crossing it at a distance of ∼94 AU, entering the inner heliosheath [Kerr, 2005; Fisk, 2005; Burlaga et al., 2005; Decker et al., 2005; Gurnett and Kurth, 2005b; Stone et al., 2005]. In contrast to planetary bow shocks, radio emission escaping from the termination shock during the Voyager approach and crossing of the termination shock has not been reported yet even though occasionally Langmuir waves have been detected [Gurnett and Kurth, 2005a] long before the termination shock transition. Observations of this kind render the termination shock on average both a relatively weak shock and at the same time a non-perpendicular shock, as otherwise Langmuir waves which propagate solely along the magnetic field would not be observed at distances of the order of AU in front of the termination shock. Both are different from what had been originally believed, giving support to a modified view on the generation and the global – and even more on the local – properties of the termination shock. On the other hand, radio emission from the turbulent heliosheath medium can hardly be expected. No known mechanism would be able to generate a substantial level of radio waves there. The expected level of radio waves is thus on the level of spontaneous emission and thus low. The only region that remains a candidate for a substantial radio source in the outer heliosphere is the heliopause region. Radio emission from the presumable heliospheric bow shock far outside the heliosphere will hardly pass the broad outer heliosheath region – the ion wall – to penetrate into the heliosphere. Indeed, early on after the first detection of outer heliospheric radio emission – and after the outer planets were convincingly excluded as its source – it had already been suspected that the emissions came from the heliopause [Gurnett et al., 1993]. The reasons for this claim were speculative and based on the observed correlation between solar high-energy particle events and the occurrence of intense outer-heliospheric radio emission.

It should be noted that even though the outer heliosphere is the strongest radio emitter in the Solar System, at least to our current knowledge, the various kinds of radio emissions from the heliospheric plasma are energetically unimportant. This holds also for the strongest emissions emitted from the solar corona and from the auroral regions of the magnetized planets. Observation of radio emission is mainly of diagnostic interest, which in the case of a clear understanding of the emission process provides information about the state of the plasma in the emission region, the plasma parameters, and the free energy sources. The collective processes of emission in collisionless plasma are complex and often non-linear. Even today they are barely understood. Therefore, in most cases very limited information can be extracted from the observation of radio radiation only.

Two basic generation mechanisms are currently believed to be responsible for non-thermal/non-synchrotron radio emission. The first mechanism is the cyclotron maser emission [cf. Treumann, 2006]. It involves the direct generation of the free space X- and O-mode radiation near the non-relativistic electron cyclotron frequency f_{ce} or its harmonics. Its source is a direct (linear) plasma instability that

is driven by semi-relativistic electrons. For emission near the low harmonics of $f_{\rm ce}$ it requires a strong magnetic field and low plasma density such that the electron plasma frequency $f_{\rm pe}$ does not exceed the electron cyclotron frequency, $f_{\rm pe}/f_{\rm ce} < 1$. Under these conditions, the largest growth is obtained at a frequency beneath the non-relativistic electron cyclotron frequency with a frequency gap of the order of $\Delta f \approx f_{\rm ce}/\gamma_{\rm rel}$, where $\gamma_{\rm rel}$ is the relativistic γ-factor (rest energy normalized energy). Emission occurs in narrow lines around the cyclotron harmonics and in weak magnetic fields comes from the Z-mode branch and is thus unable to escape from the plasma unless very high harmonics occur. These, however, have small growth rate. The conditions for the cyclotron maser, at least at first glance, are thus hardly satisfied in the outer heliosphere. It also requires that the electrons have excess energy in their motion perpendicular to the ambient magnetic field.

The second mechanism is known as plasma emission at multiples of f_{pe} by various kinds of collective interactions between electrostatic Langmuir waves leading to escaping free space radiation. In the most familiar and simplest model it involves the generation of free-space radiation near the electron plasma frequency $f_{\rm pe}$ and its low harmonics $2f_{\rm pe}, 3f_{\rm pe}, \ldots$ from interacting Langmuir waves. Here the free energy available is essentially in the motion of the electrons parallel to the magnetic field. This energy is converted by a beam-plasma instability into electrostatic plasma (Langmuir) waves with frequencies $f \sim f_{\rm pe}$. Various linear and nonlinear plasma processes subsequently convert the energy stored in the Langmuir waves into electromagnetic radiation of frequency close to the plasma frequency and its harmonics. This mechanism is believed to be at work in solar type III radio bursts as well as in the electron foreshock of planetary bow shock waves.

There are a few variants of the latter plasma emission mechanism which involve electron currents flowing parallel or perpendicular to the magnetic field, as can be found in boundaries between two plasmas of different magnetization. Typically the termination shock and heliopause are such regions. Parallel currents may excite ion-acoustic or electron-acoustic waves, which under more restricted conditions also may contribute to radiation. Waves generated by perpendicular (and under some conditions also parallel) currents are, however, of much lower frequency, close to the lower-hybrid frequency which in a dense plasma is given by $f_{\rm lh} \sim \sqrt{m_{\rm e}/m_{\rm i}} f_{\rm ce}$. The root of the electron-to-ion mass ratio for protons being involved is $\approx 1/43$. Such low frequencies for becoming involved in radiation require additional means like linear or nonlinear coupling to upper-hybrid or oblique Langmuir waves in order to be transformed into high-frequency free-space radiation modes. In perturbation theory, involving more modes in the interaction usually reduces the volume emissivity. The exception is when the electrostatic modes are concentrated in spatially highly localized wave packets. Mechanisms based on this assumption for generating radiation have been proposed early on, but have so far never been verified from observation. However, such low-frequency waves are very important in a different respect. They can accelerate electrons into beams along the ambient magnetic field. Once this acceleration comes into play, the low frequency electrostatic lower hybrid waves act as a mediator for the generation of high frequency waves, the source of which are the freshly injected electron beams. A mechanism like this one may be responsible for the excitation of radio emission in the outer heliosphere as will be discussed towards the end of this paper.

12.2 Radio observations in the outer heliosphere

The first observations of radio emission from the outer heliosheath [Kurth et al., 1984] date back to 30 August 1983 when the Voyager 1 spacecraft was at a heliocentric distance of 17.9 AU and began to detect an intense radio emission between 1.8-3.6 kHz. Voyager 2 being at 12.7 AU at this time also observed some emission of the same kind. Since Voyager at that time was still deep inside the heliosphere, it could initially not be ruled out that some unusually strong radio emission had been detected from one of the outer planets of the Solar System. It was, however, soon realized [Gurnett and Kurth, 1994] that this could not have been the case, in particular that Jupiter was not the source of the radiation. The observed radiation was correctly attributed to the outskirts of the heliosphere as referred to in the above publication. Early reviews of the emissions from the outer heliosphere can be found in Gurnett [1995] and Gurnett and Kurth [1996]. Receipt of wave information from the Voyagers becomes increasingly sparse, unfortunately, going down to one spectrum per month only [Gurnett and Kurth, 1996]. Also, absolute intensities of the radiation are increasingly difficult to estimate from the University of Iowa wideband receiver with its automatic gain control.

The sequence of radio emissions detected by Voyager 1 during its whole passage outside 12 AU and which can be attributed to the outer heliosphere is shown in the frequency-time spectrograms of the lower panel of Figure 12.3. This spectrogram indicates a number of events, three of which are particularly intense: the first is the event that has been mentioned above, occurring in 1983 to 1984, the second event occurred in 1992 to 1994, and the third event occurred in 2002 to 2003. Several much weaker events can also be identified from the spectrogram. So far no data have been published by the observers for the adjacent years up until this review was written. It has, however, been reported [Gurnett and Kurth, 2005b] that from September 2004 on another radiation event has been detected during the approach of the Voyagers to the termination shock. In the heliosphere the plasma frequency decreases with distance about as $f_{\rm pe} = 25\ {\rm kHz}/r({\rm AU})$, where the heliocentric radial distance r is measured in AU. Hence, at $r = 15$ AU the plasma frequency is roughly $f_{\rm pe} \approx 1.7$ kHz, dropping below 1 kHz at about $r = 25$ AU. It is immediately clear that radio emissions at these frequencies that originate out in the heliosphere are screened by the increase in $f_{\rm pe}$ towards the inner heliosphere and cannot be detected farther inside it. Of course, depending on solar wind conditions, variations in radiation frequency f by up to a factor of two are not excluded. Moreover, in the outer heliosphere the density decreases less strongly because of the increasing contribution of the interstellar pick-up ions that are produced there. The emissions in Figure 12.3 are clearly at higher frequency than plasma frequency and therefore are signatures of free space radiation.

The two dominant radiation events exhibit several distinct properties. They consist of two bands, one at a relatively low frequency $f \geq 2$ kHz, the other one at a higher frequency roughly above 2.5 kHz. The lower frequency band is roughly constant in time, i.e. it does not drift across the spectrum. The higher frequency band instead exhibits a pronounced upward frequency drift, i.e. its central emission frequency increases with time. This was immediately realized when the first detection of outer heliospheric radiation took place, and is also visible in the

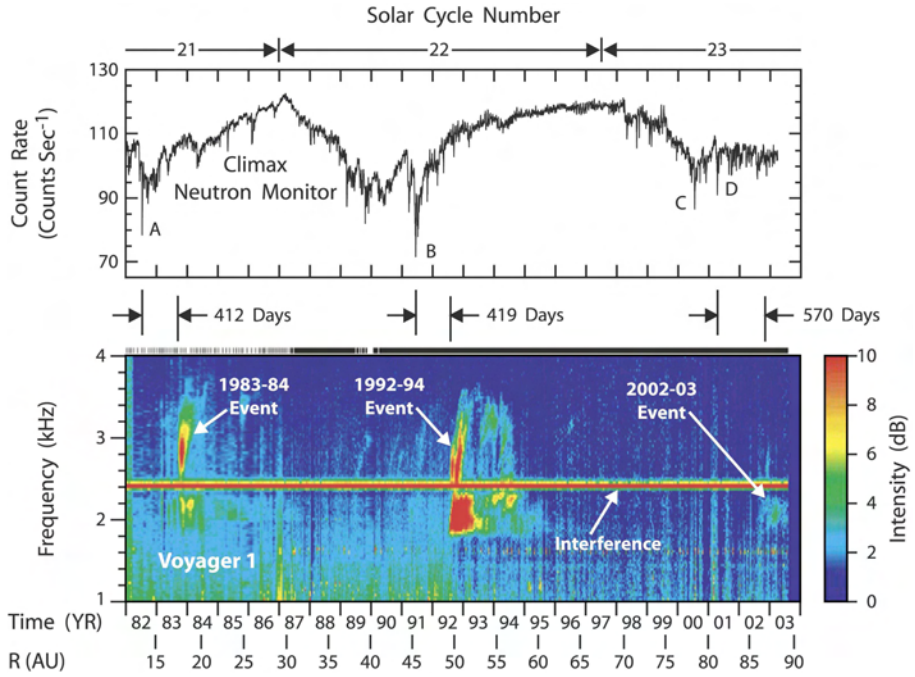

Figure 12.3: Frequency-time spectrogram of electric field intensities (bottom panel) detected by Voyager 1 over a period of twenty-two years. The corresponding cosmic ray counting rate (top panel) detected at Earth from the Climax neutron monitor. The relative electric field intensities (given in dB above a fixed background) are color coded (see scale to the right). The sharp decreases in the cosmic ray intensities labelled A, B, C, and D are Forbush decreases corresponding to the passage of an interplanetary shock and associated plasma disturbances outward though the heliosphere [from Gurnett et al., 2003].

recordings of the much weaker intermediate events in Figure 12.3. This banded structure of the radiation is even more pronounced in Figure 12.4, where the power spectral density as function of frequency is shown for the three dominant events. The 1992-1994 event was by far the most intense of the three, while in bandwidth the two first events were similar. The maximum power spectral density reached in the second event was $\approx 4 \times 10^{-18}$ W/m^{2}Hz, yielding an estimate for the radiated power of $\sim 10^{13}$ W [Gurnett et al., 1993], which identifies the radiation source as the strongest radio emitter in our solar system outside the solar atmosphere.

A very interesting and important observation that had already been made by Gurnett et al. [1993] is shown in the top panel of Figure 12.3. This panel shows the cosmic ray counting rate of the Climax neutron monitor at the Earth, as well as the indications of the solar cycles which passed during the Voyager mission. Decreases in the cosmic ray count rate at the Earth's surface, so-called Forbush decreases seen during magnetic storms [Forbush, 1937], indicate scattering of cosmic rays in the solar wind during strong solar particle events. Gurnett et al. [1993] and Gurnett et al. [2003] realized that just before the detection of outer heliospheric radio

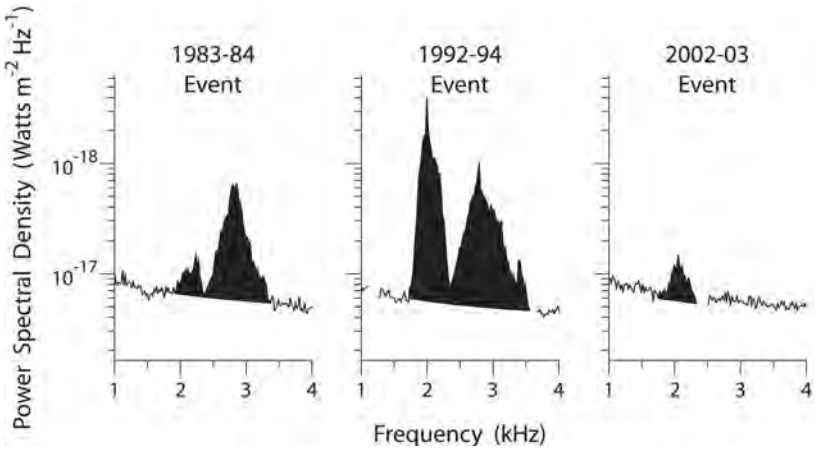

Figure 12.4: Spectra of the three (1983–1984, 1992–1994, and 2002–2003) heliospheric radio events near the times of maximum intensity. The 2002–2003 event was relatively weak, likely due to the low strength of the shock that caused this radio emission [from Gurnett et al., 2003].

emission events, large Forbush decreases occurred. These are indicated in Figure 12.3 by the successive lettering A, B, C, D. Most interestingly, the time delay between the Forbush decreases of 412 days for A, 419 days for B, and 570 days for C almost precisely corresponds to the propagation time of such particle events or the related strong interplanetary shock waves from the Sun to the progressively increasing radial distance of Voyager when accounting for the respective radial shock propagation velocities of 600 to 800 $\mathrm{km\,s^{-1}}$ for the first two events and only 500 $\mathrm{km\,s^{-1}}$ for event C (the so-called 14 July 2000 Bastille Day event), respectively. Gurnett et al. [1993] thus concluded that the trigger for the observed intense radiation must have been causally related to the releases of plasma from the Sun. This causal relationship they could confirm with the more recent observations of the 2002-2003 radiation event.

Also, comparing the shorter and less intense radiation events in Figure 12.3 with the cosmic ray count rates, one finds that almost every one of the weaker events is predated by a weak decrease in the counting rate. This suggests that weaker solar events which are related to weaker shocks cause weaker outer heliospheric radio emissions. Thus the intensity of the radio emission is a function of the strength of the solar event and the strength of the corresponding interplanetary shock. The correct mechanism for the emission and how this relation works is, in fact, not well understood yet. In particular, even though some Forbush events occurred during the early part of solar cycle 23 (cf. Figure 12.3), this time was exceptionally quiet in the radio. The radio emission from the outer heliosphere thus seems to depend not only on the shock and its strength, but also on more general conditions like the general state of the solar activity which was low at this time, on the possible merging of several interplanetary shocks in the form of Co-rotating Interaction Regions, and last not least on the state of the outer heliosphere. The merging of

shocks may increase the shock strength and produce very strong global heliospheric shocks [McDonald and Burlaga, 1994], while a single strong shock like that caused in the Bastille Day event C – which produced a strong Forbush decrease at Earth and an interplanetary shock that was strong enough to even cease the solar wind at 1 AU for short while not detectable at Earth (something that was completely unknown before the occurrence of this event) – did not show any remarkable radio signal even though a shock related to the Bastille Day event strong enough to be detected later on 12 January 2001 was observed at the distant position of Voyager 2 [Wang and Richardson, 2002].

Gurnett et al. [1993] and Gurnett et al. [2003] used their 1993 conjecture that the radiation must have come from the boundary of the heliosphere, the heliopause rather than from the termination shock to find an estimate for the distance of the heliopause. Knowing the speeds of the interplanetary shocks for events A and B and the time delay between the Forbush related decreases and the observed onset of the radio events, they estimated which radial distances had been traversed by the corresponding interplanetary shocks in order to reach the heliopause and to excite radio emission there. The estimates [Gurnett et al., 2003] even take into account the retardation of the shock when passing the heliosheath. The heliopause distance was determined in this way to lie between roughly 150 AU $< r_{\rm hp} <$ 160 AU, with an average value of $r_{\rm hp} = 156$ AU to the nose of the heliopause where direction finding techniques [Gurnett et al., 1993; Kurth and Gurnett, 2003] suggest the initial radiation source to be located from observation of its onset on the two Voyagers. As a byproduct of such a direction finding technique that is based on the measurement of the anisotropy of the radiation, it followed that the emitted radiation cannot be trapped in the heliospheric cavity bouncing back and forth between its boundaries and being amplified in this process as had been suggested [Czechowski and Grzedzielski, 1990]. Such trapping would readily destroy the anisotropy of the radiation, causing almost complete isotropy. Using the above numbers, the estimates of the likely position of the termination shock varied between 101 AU $< r_{\rm ts} <$ 118 AU. Meanwhile, Voyager 1 has passed the termination shock already at a distance of only $r_{\rm ts} = 94$ AU, much closer in the heliosphere suggesting that the heliosphere might be more blunt nosed than originally expected. In any case the promises of the observation of the radio emission from the outer heliosphere have been nicely fulfilled by this passage identifying the radiation as a very good tool for remotely sensing the geometry of the heliosphere and the conditions in the vicinity of its boundary.

12.3 Conditions relevant to radio emission

The sequence of regions which are encountered when moving out radially from the heliosphere into the local interstellar medium are: the termination shock, inner heliosheath, heliopause, outer heliosheath, and heliospheric bow shock. This is exactly the sequence expected to be detected when the two Voyagers will escape from the heliosphere. In this section we briefly compile the expected conditions for radio emission in each of these regions. An important ingredient of the outer heliosphere is that it contains a large fraction, about 10-20%, of freshly generated

pick-up ions, the Anomalous Cosmic Ray (ACR) component that is produced by charge exchange of interstellar neutrals with the solar wind protons. The charge exchange cross section is of the order of $\sigma_{\mathrm{CE}} \sim 10^{-19}\mathrm{m}^2$, and correspondingly the mean free path $\lambda_{\mathrm{CE}} = 1/(n_{\mathrm{SW}}\sigma_{\mathrm{CE}})$ is large, of the order of the radius of the heliosphere. However, as the number of newly created Anomalous Cosmic Ray pick-up ions increases and the solar wind is slowed down, λ_{CE} decreases and the density of the ACR in the outer heliosphere rises until the above value. However, since the ACR couples magnetically to the solar wind and is accelerated to solar wind speed and is thereby heated, it retards the solar wind and accounts for all the thermal energy in the solar wind.

12.3.1 The termination shock

Soon after its first detection it had been speculated [McNutt, 1988; Macek et al., 1991; Cairns et al., 1992] that the termination shock could serve as the ultimate source for the outer heliospheric radiation. The observed radiation power indicated that the termination shock could be an extraordinarily strong shock, in fact the strongest in our entire Solar System. However, such an interpretation has quickly become discredited [Gurnett et al., 1993] as the expected local electron plasma frequency at the termination shock would be far too low in order to come up for the observed frequency of the radiation, unless the emission of high harmonics of f_{pe} would be postulated to occur. In fact, since f_{pe} decreases inversely proportionally to the distance, the local plasma frequency at $r_{\mathrm{ts}} = 94$ AU is about $f_{\mathrm{pe}}(r = 94) \approx 220$ Hz. Since even for a strong shock f_{pe} cannot be higher than a factor of two by compression of the plasma, emission at the harmonic will still be at a frequency below 1 kHz, lower than the observed low frequency cut-off of the radiation. However, emission from shocks is generated mostly in the low density foreshock region where the plasma is not yet compressed, and the frequency of emission is even lower than the above value. It is important to note that in the estimates of Gurnett et al. [1993] still a much larger termination shock distance of 140 AU-180 AU has been assumed. However, reducing the distance to the recently observed crossing distance does not remove the discrepancy between the assumption of termination shock radiation and observation.

Crossings of the termination shock so far occurred only once. Hence, there are no average conditions for the termination shock available yet. However, it seems to be clear that the simple model of a completely stationary standing termination shock is incorrect. This alreay becomes apparent from the above quoted difference between the estimates of the heliopause and termination shock positions from radio observations and the recent actual location of termination shock crossing by Voyager 1 [Fisk, 2005; Stone et al., 2005; Decker et al., 2005; Burlaga et al., 2005] which was much closer to Sun than expected from the models and might be related to variations in solar wind conditions. Actually, strong variations with half year periodicities in solar wind pressure that might shift the position of the termination shock by up to 3–4 AU have been reported [Webber, 2005; Richardson et al., 2005]. Such pressure variations are caused mainly by density spikes in the solar wind that result from merged CMEs and from spikes in velocity. Since the velocity enters the dynamic pressure quadratically and the velocity does not substantially decrease

with distance, the dynamic pressure and hence the position of the termination shock will be controlled mainly by velocity changes. In addition, however, interstellar pick-up ions become increasingly important in the outer heliosphere. Since they are accelerated to solar wind speed at the expense of the bulk motion they do retard the solar wind, contribute to density increases, and control the temperature of the outer solar wind. The interstellar H density is about $n_{\rm H} \sim 0.09$ cm^{-3} at the termination shock yielding a 12-14% contribution of pick-up ion density to solar wind density which is estimated there to be of the order of $n < 6 \times 10^{-4}$ cm^{-3} that maps to a plasma frequency $f_{\rm pe} < 250$ Hz in agreement with the value estimated above. Clearly this excludes the termination shock as a viable source of the observed radiation if the radiation mechanism is related in whatever manner to the plasma frequency – and even more so if it is related to the electron cyclotron frequency like in the maser mechanism. Nevertheless, in preparation for a discussion, albeit brief, of possible and observable radio emissions from the termination shock we list here its relevant in-situ properties.

Upstream [Wang and Richardson, 2003] energetic particle activity simultaneously over a large energy range from the termination shock has been observed by Voyager 1 since mid-2002 [Krimigis et al., 2003], which initially has mistakenly been interpreted as an indication of a back-and-forth crossing of the termination shock. Voyager 1, due to early failure of the plasma instrument, does not provide plasma data. The particles observed have been shock-accelerated but do not show memory of the shock or the magnetic field. This information has, however, been provided by in-situ electrostatic wave observation [Gurnett and Kurth, 2005a]. Electrostatic plasma waves are known to be excited on the Langmuir wave branch by the gentle beam instability in the presence of magnetic-field-aligned electron beams that in the supercritical foreshock are reflected from the shock front into the region upstream of the shock. Energetic electron beams have indeed been inferred in the case of the observations close to the termination shock transition from the energetic electron instrument on Voyager in the energy range 0.35-1.5 MeV [Decker et al., 2005]. The electron fluxes were reported to be highly anisotropic, with large anisotropy along the ambient solar wind magnetic field. Beams of this kind will necessarily cause very narrow-band Langmuir waves. Since Langmuir waves do practically not propagate in a cold electron plasma like that in the outer heliosphere their observation roughly one year ahead of the termination shock transition indicates that the termination shock is by no means a stationary perpendicular shock. On the contrary, it must possess an extended foreshock region that the spacecraft needed about a year to traverse. This is only possible when the termination shock itself is supercritical and bent on a scale such that the angle between the Parker spiral magnetic field and the termination shock normal is small, i.e. the termination shock must occasionally be quasi-parallel. Langmuir waves are most strongly excited along the electron foreshock boundary [Eastwood et al., 2005] which is the solar wind field line that is connected with the quasi-perpendicular region of the termination shock. The observations of Langmuir oscillations shown in Figure 12.5 can thus be interpreted to mean that during the occurrence of the large amplitude spiky plasma waves the Voyager 1 spacecraft has crossed the electron foreshock boundary of the termination shock. Gurnett and Kurth [2005a] therefore assumed that Voyager 1 during these times was magnetically connected to the flanks of the

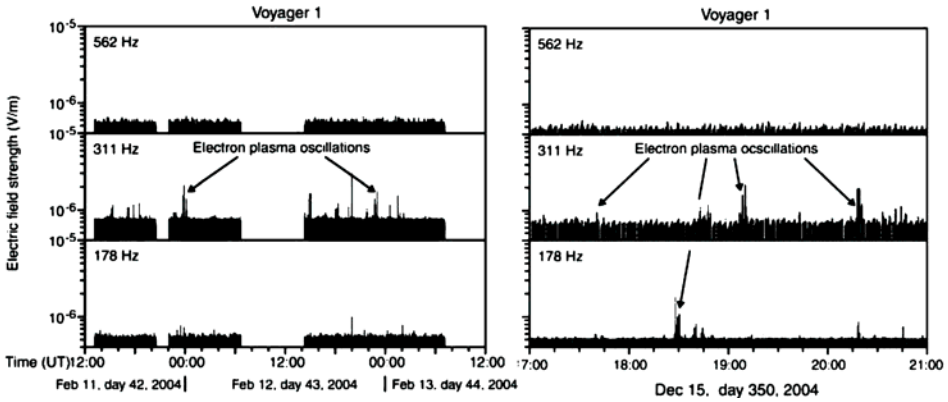

Figure 12.5: *Left*: Voyager 1 electric field intensity at 178, 311, and 562 Hz on 11 to 15 February 2004 at a radial heliocentric distance of 91.0 AU. Short impulsive spikes in the 311 Hz channel indicate Langmuir waves associated with the termination shock. The oscillation frequency of 311 Hz corresponds to an electron density of $n_e = 1.2 \times 10^{-3}$ cm^{-3}. *Right*: Same for 15 December 2004, just before crossing of the termination shock at 94.1 AU. This event is coincident with a highly anisotropic 0.35 to 1.5 MeV electron beam [Decker et al., 2005]. The electric burst duration is less than a few minutes, similar to 11 to 15 February 2004. The oscillation frequency temporarily drops to 178 Hz at 18:30 UT, indicating a decrease in n_e to about 3.9×10^{-4} [from Gurnett and Kurth, 2005a].

termination shock where the termination shock normal is closer to the direction of the interplanetary magnetic field than at the nose of the heliosphere, as shown in Figure 12.6. This might be a viable explanation that only leaves open the question of why the occurrence of the waves is so sporadic once Voyager has entered the magnetically connected region close to the heliosheath. Possibly, the sporadic nature of the oscillations suggests that the termination shock is non-stationary. This interpretation has been adopted by Gurnett and Kurth [2005a] for the 15 December 2004 event where Voyager 1 has been much closer to the termination shock. The termination shock surface in this case performs an oscillation that may have been caused by a surface instability or by shock reformation (see Chapter 6.6, this volume). In any case it seems that the termination shock is by no means stationary on the small scales. In this respect it remains an important and unanswered question why no radio emission has ever been detected during the Voyager approach to the termination shock. Comparing for instance with planetary bow shocks and with the travelling interplanetary shocks, the signature of which are the interplanetary type II radio bursts [Nelson and Melrose, 1985], a very intense radio emission, the absence of any foreshock radiation at the termination shock is surprising (if it is not just so narrow-band that it is hidden in the instrumental gap between the channels of the plasma wave instrument aboard Voyager 1). Langmuir plasma fluctuations excited in the foreshock of the termination shock should in principle couple in order to generate either fundamental or harmonic radio emission, or they could also be scattered off either ion acoustic waves or thermal ions in order to produce radiation. The latter process may occur when hot ions are present as is

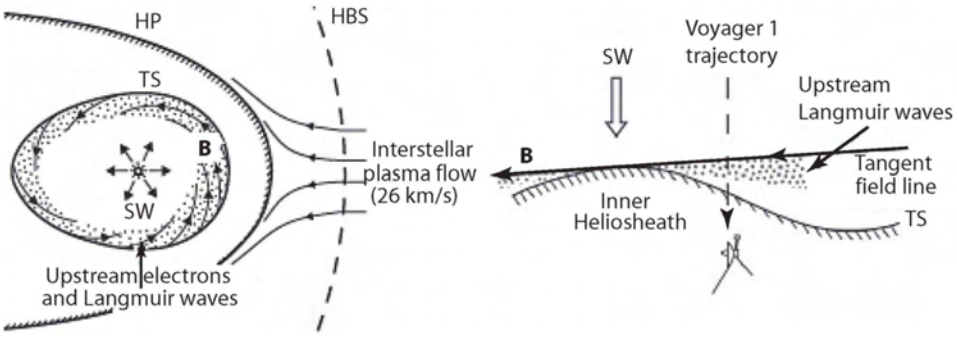

Figure 12.6: *Left*: A possible source region (dotted) of inward streaming (upstream) electron beams released from the highly idealized heliosheath assuming that the electrons come a long way from the quasi-perpendicular regions at the flank of the heliosheath flowing along the interplanetary magnetic field lines that form a Parker spiral. *Right*: The 15 December 2004 event close to the termination shock. In this case an oscillation of the shock front is assumed to have a similar effect on the tangential field line [from Gurnett and Kurth, 2005a].

the case near the termination shock when a hot ring-like distribution of interstellar pick-up ions exists. Now these Langmuir waves have been detected in-situ, the absence of radio radiation is ever more surprising. Such coupling has been known to exist for instance in the Earth's bow shock foreshock, where it appears at the fundamental, the second and even the third harmonic of the plasma frequency. This absence may indicate that the termination shock foreshock region is unable to excite ion acoustic waves because the ambient electrons are too cold. In this case no fundamental emission can be generated for one of its mechanisms requires coupling between ion acoustic and Langmuir waves according to the conservation rules $f = f_{\rm L} + f_{\rm ia}$ and $k = k_{\rm L} - k_{\rm ia} \approx 0$, where the subscripts L, ia indicate Langmuir and ion-acoustic waves, and k is the corresponding wave vector which for radiation is very small. The Langmuir frequency is $f_{\rm pe} \gg f_{\rm ia}$ which formally yields radiation at the fundamental $f \approx f_{\rm pe}$. Of course, such radiation could be hidden in the noise of the 311 Hz channel where it should occur as unstructured continuum. Lack of ion acoustic waves otherwise inhibits backscattering of Langmuir waves. Hence counterstreaming Langmuir waves, required for satisfying the wave number conservation law for the Langmuir-Langmuir process, will be absent. This implies a lack of harmonic radiation at $f = 2f_{\rm pe}$. Radiation at this harmonic should occur in the 562 Hz channel. Moreover, when the plasma is too cold, the ponderomotive force is too weak in order to bring into existence ponderomotive force-driven ion acoustic waves. Hence, Langmuir waves will not self-modulate, and soliton formation and collapse will be suppressed from the very beginning. This inhibits plasmon trapping and thus makes the interaction between trapped Langmuir waves impossible. Finally, in cold plasma no electron acoustic waves can be excited. This eliminates the possibility of interaction between electron acoustic waves and plasmons.

All this can be understood very easily for a cold enough plasma. However, when the plasma is near zero temperature and carries a fast electron beam, as sug-

gested by the observations and the existence of Langmuir waves in the termination shock foreshock, then from plasma theory one expects the Buneman instability to be strongly excited. This instability should generate electron holes, drive local inhomogeneities on the plasma background, and heat the local background electrons until ion acoustic waves come into existence. Possibly the bursty nature of the observed Langmuir oscillations is a signature of the presence of the Buneman instability. It remains a mystery, however, why this instability does not heat the plasma sufficiently for ion acoustic wave excitation to become possible. In any other foreshock region in the Solar System this is a major effect. Finally, over large parts of its surface the termination shock should behave quasi-perpendicularly with strong currents flowing inside the shock front. Again, when the plasma is cold, these currents must excite strong electrostatic instabilities. It remains a mystery as well why, then, the termination shock does not radiate in the same way as any of the fast travelling shocks in the Solar System, and why it does not excite the type II back-bone radiation. At least closer to the termination shock such a radiation should have become observable. Its absence poses a major unresolved problem; its solution may tell us not only about the nature of the termination shock but also more generally about the conditions under which collisionless shocks may radiate at all.

12.3.2 The inner heliosheath

Meanwhile Voyager 1 has entered the heliosheath, the region downstream behind the termination shock. In analogy to planetary magnetosheaths, one does not expect that any kind of electromagnetic radiation would be generated there. None of the planetary magnetosheaths emit radio waves even though they all are highly turbulent. The reason is that in the magnetosheaths no sources for excitation of sufficiently strong Langmuir waves exist, and without their presence in a $\beta \gg 1$ collisionless plasma there is no energy in high frequency waves that could be converted into radiation. The Langmuir wave intensity is on the sporadic thermal fluctuation emission level. In principle this is also expected for the inner heliosheath with a number of important differences with respect to planetary magnetosheaths.

Figure 12.2 contains the relevant information on the heliosheath. The first difference is that planetary magnetosheaths divert the plasma flow around the obstacle. This is not the case for the inner heliosheath, at least not to the extent of the former. As long as magnetic field interaction is not assumed in the heliosheath the plasma is believed to practically freely leave from the heliosphere into the LISM on a scale that is comparable to the collisional mean free path, which is of the order of at least several AU. Moreover, the inner heliosheath contains a substantial number of interstellar pick-up ions produced there by collisional charge exchange with the fast solar wind ions. Like in the termination shock foreshock region, they are accelerated in the global magnetized plasma flow, form ring/shell distributions, retard the heliosheath flow, and contribute to the temperature of the heliosheath. Finally, the inner heliosheath is magnetized, as are planetary magnetosheaths; but the magnetic field in the inner heliosheath has the particular property that in addition to having become turbulent in the course of the formation and reformation of the termination shock, in theory it should on average still follow the Parker

spiral. In the outer heliosheath this is believed to be practically purely azimuthal as long as one does not leave the plane of symmetry. The sector structure of the interplanetary magnetic field then builds up a whole sequence of alternating (turbulent) magnetic sectors which the solar wind traverses when moving outward into the LISM. Since this field is frozen into the retarded solar wind flow, it penetrates the heliopause and outer heliosheath up to the mean free path of the solar wind in the surrounding gas. Here the magnetic flux tubes become mass loaded, which further retards the solar wind flow. Its radial motion comes to rest only at a radial distance where the solar wind diffuses away from the Parker spiral magnetic field, which depends on the mass loading in the ion wall and on the mean free path (or diffusive length). Nevertheless, all of these lengths are short compared to the global scales of the ion wall, even though the heliopause turns out to be a broad plasma transition layer.

The compression of the heliosheath and the slowed down solar wind let the magnetic sectors form a radial succession of undulations of the heliospheric current sheet about the ecliptic. These undulations form a sequence of Harris current sheets. When the width of the current sheets is comparable to the ion inertial length $\lambda_\mathrm{i} = \sqrt{m_\mathrm{i}/m_\mathrm{e}}c/2\pi f_\mathrm{pe}$ (or ion gyroradius), violent intrinsic reconnection sets in inside the heliosheath that is primarily independent of any interstellar or galactic magnetic field. Reconnection generates fast electron beams along the magnetic field. That reconnection can accelerate particles, ions and electrons as well, to high energies is known since the observations made by Øieroset et al. [2002] in the magnetospheric tail and the numerical simulations of reconnection [Drake et al., 2003; Jaroschek et al., 2004] using full particle codes. The electron beams excite Langmuir waves and the plasma enters the conditions when generation of radiation may become possible. However, for agreement with observation of the emitted frequency, the plasma density inside the compressed current sheets should from Figure 12.2 increase by an entire order of magnitude.

In the undisturbed heliosheath this is unrealistic. Assume that the thickness is minimum, i.e. comparable to λ_i. The Harris sheet model then requires pressure equilibrium $\beta = 1$. With B_0 the magnetic field outside the current sheet, and v_c the current velocity, the density in the centre of the current layer is

$$n_\mathrm{e} = \frac{4B_0^2}{\mu_0 m_\mathrm{i} v_\mathrm{c}^2}$$

The recently measured magnetic field strength in the heliosheath is $B_0 \sim 0.15$ nT [Burlaga et al., 2005] yielding compression factors of between 2 and 4. Including a maximum plasma compression factor of 4 at the termination shock one obtains a heliosheath electron density of $n_\mathrm{e} \sim 500/v_\mathrm{c,km}^2$ which requires current speeds of $v_\mathrm{c} > 100$ km/s for an optimum density of $n_\mathrm{e} \sim 5 \times 10^{-2}$ cm^{-3}. Such current velocities are illusionary. Thus, intrinsic reconnection in the heliosheath cannot be responsible for the strong outer heliospheric radio emissions. In the heliosheath the heliospheric current sheet cannot spontaneously thin to become narrow on the scale of λ_i. Electron beams accelerated at the termination shock and possibly entering the heliosheath along the compressed magnetic field lines will be unable to excite the observed frequencies. Any radiation caused by such beams will have frequencies far below the low-frequency cut-off of the radiation events in Figure 12.3.

However, when a strong interplanetary shock driven by a global CIR passes the inner heliosheath it causes an additional compression of the plasma in the inner heliosheath by a maximum factor of 4 in density and magnetic field, reduces the ion inertial length, and permits higher current velocities. In this case the density inside the Harris sheets could under the most favourable conditions locally inside the compressed heliospheric current sheet rise high enough for the plasma frequency to enter the region of interest for emission of radio waves. Reconnection between sector boundaries in the inner heliosheath as a result of such a passage of a strong GMIR could thus be a viable candidate for the observed emissions. The low frequency cut-off of this radiation is then simply related to the piston density that pushed the GMIR. This cut-off is at about 1.6-1.8 kHz. For harmonic radiation, the piston density should thus be of the order of $n_{\mathrm{GMIR}} \approx 10^{-2}$ cm^{-3}, comparable to the density in the compressed Harris sheet segments.

12.3.3 The heliopause-outer heliosheath region

For fundamental emission the required electron densities to explain the radiation range between $0.05 < n_{\mathrm{e}}(\mathrm{cm}^{-3}) < 0.1$. In the case of harmonic radiation these values can be four times less. The heliopause region is the only region where both of these conditions are easily met. It is thus the best and possibly even the only candidate for the generation of outer heliospheric radio radiation. This had been realized early on by Gurnett et al. [1993]. Looking at the density profile (Figure 12.2) across the heliopause from the solar wind into the outer heliosheath one can agree with the fact that the density of the "ion wall" is indeed high enough to account for radiation frequencies of 2-3 kHz. A 3-D view of the heliosphere which shows the extension of the ion wall is given in Figure 12.7. The calculation on which this figure is based does not include any interstellar, nor does it include any heliospheric magnetic fields. These fields are generally assumed to be weak and of little importance for the global processes at the heliopause and in the outer heliosheath. After the crossing of the termination shock by Voyager 1 and its entry into the inner heliosheath, the heliospheric magnetic field is relatively well known and – up to the restrictions made in the previous section – agrees in magnitude fairly well with the predictions of the Parker spiral model. The interstellar magnetic field in the vicinity of the heliosphere, on the other hand, is known only indirectly. Its magnitude is usually taken to be of the order of the interstellar field, which due to screening effects by the LIC is believed to be slightly weaker than the galactic field in the local cloud. An average value is $B = 0.14 \pm 0.2$ nT [Rand and Lyne, 1994], and its direction is inclined with respect to the flow of the interstellar gas pointing towards galactic longitude $\lambda_G = 88^\circ \pm 5^\circ$ [Frisch, 2005]. The precise direction of the field (see Figure 12.8) has been determined only recently [Lallement et al., 2005] from the asymmetry seen in the 4° deflection of interstellar neutral hydrogen flow with respect to the flow of interstellar helium at the heliopause. Since the magnetic field is the crucial ingredient in any of the mechanisms which are believed to be responsible for radiation from the heliopause we need to discuss the various assumptions underlying it.

In addition to being the transition from the compressed though still rather dilute heliosheath to the dense ion wall plasma, the heliopause has a number of other

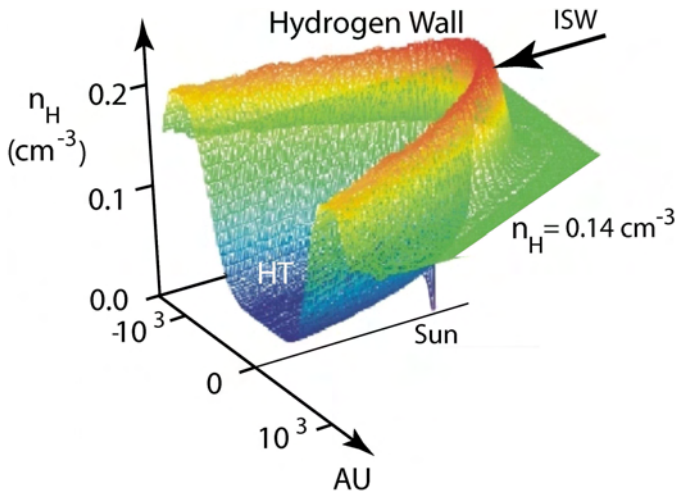

Figure 12.7: Distribution of interstellar atomic hydrogen in and around the heliosphere [after Baranov and Malama, 1993]. ISW is the interstellar wind direction. HT is the heliotail where the interstellar gas density is depleted. The dip in the centre refers to the position of the Sun where no neutrals survive. Lengths are given in AU. The factor of two density enhancement in the upwind direction (hydrogen wall) is due to the effect of the plasma-neutral gas charge-exchange coupling.

interesting properties. Like comet comas or ionospheres it contains a large fraction of interstellar neutral gas that is in motion and on the small scale can pass across the heliopause in an undisturbed way until it undergoes charge exchange with solar wind ions. The fraction of neutral gas that participates in charge exchange close to the heliopause and in the heliosheath is of course small. It is, however, sufficient to pile up as a comparably dense ion wall (or outer heliosheath). On the same scale as charge exchange occurs, the neutrals and ions participate in frictional interaction and thus become retarded. This has been confirmed by various kinds of numerical simulations [Baranov and Malama, 1993; Mueller et al., 2000; Zank and Mueller, 2003; Izmodenov et al., 2003b]. In the presence of a magnetic field, retardation is mediated by the magnetic field. Any slow ($v \sim 26$ km/s) neutral experiencing charge exchange in the outer heliosphere is immediately picked up to become a heated and fast ($v \sim$ solar wind speed) Anomalous Cosmic Ray particle moving outwards and leaves a cold fast neutral that also moves outwards at solar wind speed. While this neutral is free, the ACR particle is frozen into the solar wind magnetic field and, while the newly created neutral passes the heliopause into the ion wall, the ACR ion stops at its contact with the interstellar plasma and interstellar magnetic field in the ion wall. The fast neutral might again experience charge exchange here with ions from the ion wall, creating an ion that is immediately bound to the interstellar magnetic field and adds to the ion wall population, while a slow neutral also remains in place. This new ion wall ion has a large gyro-radius and therefore becomes a member of an anisotropic ion population with perpendicular temperature $T_\perp > T_\parallel$ that can give rise to various kinds of plasma instabilities

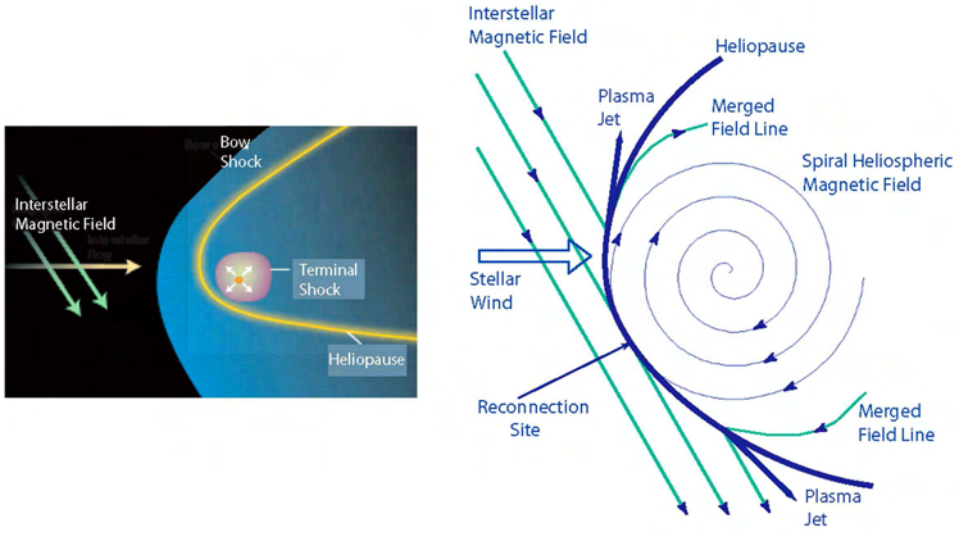

Figure 12.8: *Left*: The direction of the interstellar magnetic field with respect to the heliosphere as inferred from the observation of the asymmetries in the H and He flows inside the heliosphere [after Lallement et al., 2005; Jokipii, 2005]. *Right*: A scenario of reconnection between the projection of the interstellar magnetic field into the ecliptic plane and the heliospheric magnetic field at the heliopause. Shown is the Parker spiral heliosheath magnetic field – for the one polarization only that favours reconnection – on a grossly exaggerated scale, the reconnection between the two fields at the tangential contact point, and the formation of jets along the heliopause. The reconnected heliosheath field becomes highly distorted and turbulent after reconnection. Note that due to changing polarity of the spiral field, reconnection in the regions between the sectors shown here will be different or might even be absent. In any case, the inclination of the interstellar field causes a pronounced asymmetry of the reconnection geometry that will affect the form and dynamics of the heliopause region.

here. Hence, in the presence of an interstellar magnetic field, the ion wall will not only be just as thin as the mean free path is for charge exchange or any other frictional process, it will also host a number of anisotropy driven plasma waves that make it behave as a turbulent medium. Also, there will not be enough outward flowing plasma to be able to blow the interstellar field away from the contact with the heliopause. There is no contribution to the electron population in this process.

Because of these reasons the interstellar field will necessarily get into contact with the magnetized heliospheric plasma. As a consequence, in any mechanism that emits radio waves the presence of the interstellar magnetic field and its interaction with the magnetized heliosheath plasma will be crucial. That the 2-3 kHz radiation from the outer heliosphere is indeed related to the magnetic field and in particular to the direction of the interstellar field close to the heliopause has been demonstrated already by Kurth and Gurnett [2003] and has been discussed in terms of the properties of the interstellar medium by Frisch [2005]. Figure 12.9 shows the

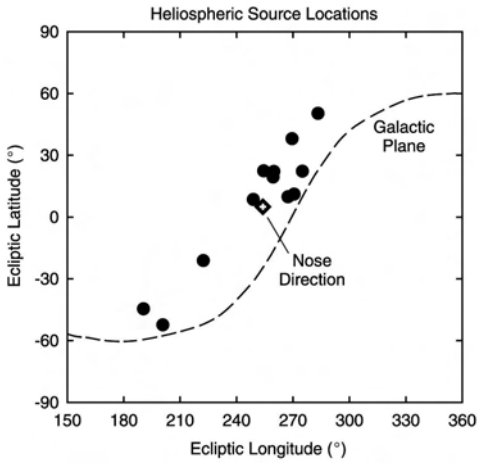

Figure 12.9: Source locations for the two large radiation events of Figure 12.3 as determined from the investigation of the radiation at Voyager 1 and Voyager 2 when taking into account spacecraft maneuvering [from Kurth and Gurnett, 2003]. The distant locations of the radiation sources found under the assumption that they are close to the heliopause are elongated along the galactic plane. This has been taken as a strong hint that the sources are related to the interstellar magnetic field outside but near the heliosphere in the LISM. Note that the positions of the radio sources are all located north of the galactic plane. For an exhausting discussion see the above reference.

relation of the spatial locations of the radiation sources for the different events as determined by [Kurth and Gurnett, 2003]. It is found that they nicely follow the direction of the galactic plane on the sky which is also the average direction of the interstellar magnetic field [Frisch, 2005]. Interestingly, the locations cluster on only one side of the galactic plane. This is an unexplained observation. As Frisch [2005] has shown, the correlation between this location and the direction of the interstellar magnetic field is in fact not as good as shown in Figure 12.9, as the locations cluster much more into nearly one point when taking into account the uncertainties in the magnetic field determination. This does, however, not jeopardarise the connection between radiation and magnetic field. Instead, it suggests that the contact between the heliosheath and interstellar magnetic fields is not a stationary process but undergoes interaction. Figure 12.8 shows one possible interaction between the two fields when the spiral heliosheath magnetic field reconnects with the projection of the interstellar field into the ecliptic. The contact and reconnection site is displaced from the nose of the heliosheath in this case. Here the typical phenomena known from reconnection can occur. Macroscopically, the interconnected fields will relax and accelerate the ion wall plasma into plasma jets, while at the same time generating a motion of the ion wall plasma along the heliopause. This is, however, not a strong effect because the Alfvén velocity in the ion wall is small, of the order of only $v_A \sim 1$ km/s, which is less than the speed of the interstellar gas. However, the gas does not participate in this streaming as it is uncharged, while the ion wall plasma is practically at rest. So the flow is only in the plasma of the ion wall.

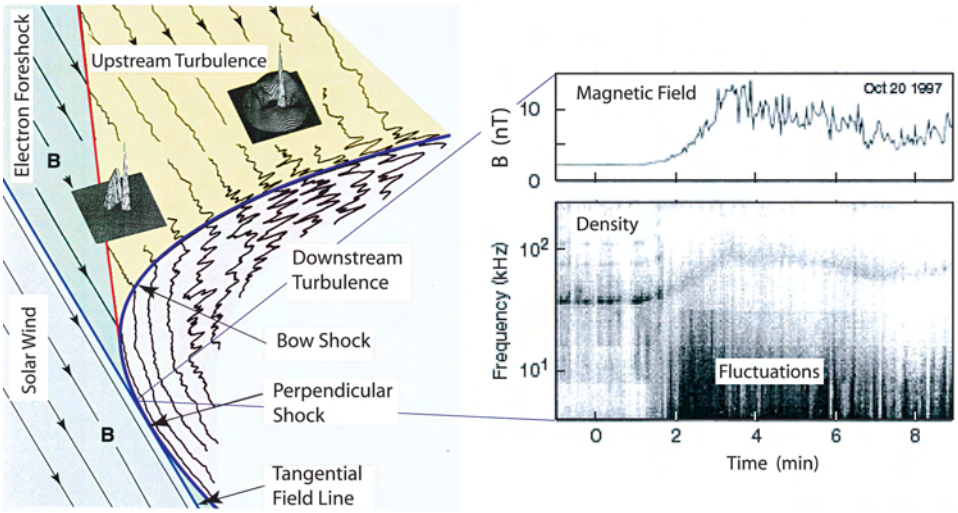

Figure 12.10: *Left*: A typical form for a large scale non-planar supercritical shock wave – like a planetary bow shock or the shock driven by a GMIR. The shock has some quasi-perpendicular and quasi-parallel sections and contains an electron and an ion foreshock. The typical reflected ion distribution functions are indicated as inserts. Diffuse ions that couple to the solar wind are picked up and form the typical ring distributions as seen here. The electron distribution forms a beam along the electron foreshock boundary, but is very sensitive to deformations caused by scattering of electrons off waves once they enter the foreshock itself. This causes an isotropization of the electrons inside the foreshock. This is a reason why the foreshock is not a source of radiation. Radiation is generated only at the electron foreshock boundary and close to the shock ramp where the upstream wave turbulence generated by the ions locally turns the magnetic field into the quasi-perpendicular direction. For the ions the shock remains quasi-parallel, while on the electron scale the shock behaves quasi-perpendicularly and thus locally reflects the electrons. *Right*: Observation of Langmuir fluctuations and the corresponding density profile during a crossing of such a shock (the Earth's bow shock).

For jetting inside the heliosheath the Alfvén speed is much larger by a factor of up to 4 or 5 because of the lower density and the stronger heliosheath magnetic field. It reaches velocities of $v_A \sim 10$ km/s. Reconnection manifests itself as backward convection of the heliosheath plasma in a narrow layer along the heliopause. These macroscopic processes are not so much of interest for the generation of the radiation. They only provide background information for our understanding of the grand scheme in which the radiation may be produced.

12.3.4 The heliospheric bow shock

The final region of interest is the heliospheric bow shock, if it exists at all. Very little is known about the conditions out there. If it is a strong supercritical shock in the weakly magnetized interstellar medium it will have regions which have the properties of a quasi-perpendicular shock and regions having the properties of quasi-

parallel shocks. In these cases it will reflect some incoming electrons that may excite Langmuir waves upstream of the shock and generate radio emissions in a similar way to planetary bow shocks and type II bursts [Nelson and Melrose, 1985]. Such radiation might be the cause of diffuse emission which is observed in remote astrophysical shocks that are generated, for instance, by protostellar jets emanating from massive stars [Reipurt et al., 1998]. However, it is not known whether the heliospheric bow shock is supercritical or subcritial, if it exists at all. Any radiation generated by electron beams in front of it will barely be visible inside the heliosphere because of the barrier that the dense ion wall provides. Thus the most probable place for the generation of the relatively isotropic radio radiation from the outer heliosphere is the heliopause. This has already been correctly concluded early on by Gurnett et al. [1993].

12.4 Radiation from the heliopause

Identifying the heliopause as the most probable source of outer heliospheric radio emission poses a serious problem that is connected with the mechanism that is responsible for the emission. From the rareness and intensity of the emissions and their relation to the most violent Forbush events, Gurnett et al. [1993] and Kurth and Gurnett [2003] proposed that the radiation would be caused when a global CIR interacts with the heliopause plasma. Hence the problem is posed of how such an interaction proceeds and what mechanisms could excite the enormous emissivities in the observed radiation. Since any radiation mechanism must involve electron beams and high frequency electrostatic waves in this weakly magnetized region where maser actions are probably very inefficient, the question can be reduced to that of how high energy electron beams can be generated in this interaction. General conditions for three wave processes in radio emission have recently been discussed by Mitchell et al. [2005].

12.4.1 GMIR shock mediated mechanisms

As we have noted, the coincidence of the Forbush and outer heliospheric radio emission events is a very strong clue about the validity of the proposal [put forward by Gurnett et al., 1993] that the observed intense outer heliospheric radio emissions have in fact been generated by the interaction of a strong GMIR with the heliopause. This may, however, apply only to those strong events that could be observed at large distances from the heliopause and does not exclude the possibility that the heliopause itself is a continuous radio source. In this subsection we will, however, restrict ourselves to CIR shock mediated emissions only.

Conditions for emission in WWI and STI

Since, as noted above, in any of the relevant radiation mechanisms high frequency plasma waves should be involved, conditions are required which allow for the presence of fast electrons with a beam velocity $v_\mathrm{b} > (3-6)v_\mathrm{e}$ exceeding the electron thermal speed v_e in order to overcome Landau damping. Once intense Langmuir waves exist, there are three possible wave-wave interaction (WWI) processes for

the production of transverse waves T (radiation). These are the direct linear decay of the Langmuir wave L $\rightarrow$ T + S into a transverse wave and a sound wave (S), a mechanism that is capable of generating sound waves even in the case when no sound waves are present (as has been suspected for the inner heliosheath above); the subsequent combination L + S $\rightarrow$ T, and the classical coalescence of two Langmuir waves L + L$'$ $\rightarrow$ T$'$. The smallness of the sound wave frequency means that the former two mechanisms generate fundamental radiation at $f \geq f_{\mathrm{pe}}$, while the latter generates harmonic radiation at $f \approx 2f_{\mathrm{pe}}$. It requires, however that counterstreaming Langmuir waves L$'$ have been generated in the above decay process. Scattered L$'$ waves could also be produced by scattering of Langmuir waves L off thermal ions i (STI) according to L + i $\rightarrow$ L$'$ + i$'$. Also the direct process L + i $\rightarrow$ T + i$'$ is possible under similar conditions directly producing fundamental radiation. Of course, STI first requires that a sufficiently high level of Langmuir waves pre-exists.

Since thermal ACR ions are abundant in the outer heliosphere these processes cannot be excluded and could contribute to the radiation. The conversion efficiencies η_{F} and η_{H} for the three wave processes have been given by Robinson et al. [1994] and for STI by Mitchell et al. [2003]. The total emissivities at the fundamental and harmonic consisting of the contributions of the respective processes can be combined from these efficiencies. The conditions for emission due to these processes for type II and also global CIR shocks have been discussed by Mitchell et al. [2005] who confirmed the expected result that STI is completely unimportant in the outer heliosphere. The parameters they used for the electron and ion temperatures, electron density, shock speed, and shock curvature radius, are given in Table 12.1. These parameters are suggested by observation, and the analogy with planetary magnetosheaths, where it had been found that the electron temperature is lower than the proton temperature. As discussed above, in the heliosheath the contribution of the heated ACR component completely determines the proton temperature.

Production of electron beams and radiation

There are several mechanisms that can generate intense electron beams. The first and most simple mechanism that has not yet been exploited in depth is related to the passage of the global CIR shock across the heliopause into the magnetized outer heliosheath. The CIR shock will reflect both electrons and ions in the ion wall back into the upstream region along the inclined interstellar magnetic field, as is well known from planetary bow shocks as shown in Figure 12.11. Both the reflected ions and electrons form a beam that travels upstream and excites various kinds of plasma waves. The ions contribute to low frequency turbulence that causes reformation of the shock and keeps the upstream magnetic field at a small angle with respect to the shock front such that even in the quasi-parallel part of the shock, the latter has a quasi-perpendicular character for electrons and is able to reflect and even weakly accelerate them. The electrons form beams and excite Langmuir waves with the highest Langmuir wave level along the tangent to the shock magnetic field line, i.e. along the boundary of the electron foreshock. Figure 12.12 shows how this knowledge can be translated to a CME shock, and the same picture applies with

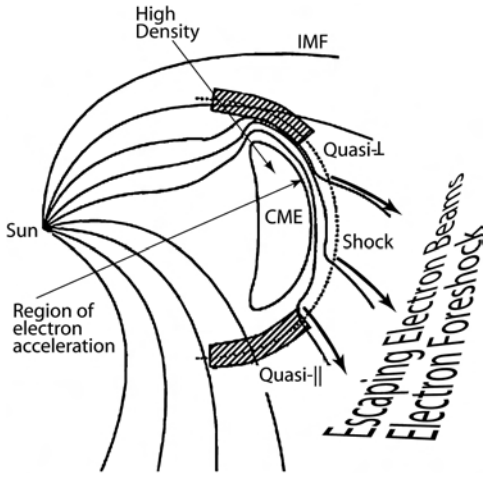

Figure 12.11: Schematic of a shock driven by a solar CME [after Zank et al., 2006]. Shown is the spiral interplanetary field IMF and its distortion by a dense CME piston. Ions and electrons that are reflected from the quasi-perpendicular part of the shock escape upstream along the magnetic field. The ions generate upstream waves and turbulence (not shown in the figure) that is caught up by the shock, participates in shock reformation and locally turns the magnetic field at a tangent to the shock. Thus on the small scale the field is tangent to the CME over large parts of the shock such that the shock behaves perpendicular for the electrons, while for the ions it remains quasi-parallel. Electrons leave as beams along the field after having been reflected by the small scale quasi-perpendicular shock. These beams form an extended electron foreshock where they excite Langmuir waves and generate radiation.

only modest modifications to a GMIR shock. Here the magnetic field oscillations upstream of the GMIR in the quasi-parallel part of the shock are not shown.

By this analogy, radiation from the CIR in the ion wall will follow exactly the same mechanism as type II radiation from travelling interplanetary shocks, for instance by the mechanisms referred to in the previous subsection. This radiation could be both at the harmonic of the local plasma frequency and at the fundamental frequency. The reason why it becomes detectable only when the GMIR shock passes the heliopause is that there the ambient density is high enough to pass the threshold set by the plasma in the piston that drives the CIR. The simulations in Figure 12.1 in fact already included a travelling shock. Its signatures are seen as small wiggles on top of the large ion wall density. Harmonic radiation can in this case easily overcome the barrier, but even the higher frequency part of the fundamental radiation could do so. As already mentioned, the low-frequency cut-off of the observed radiation is a measure of the density behind the travelling GMIR shock.

Another feature that makes us believe that this type II mechanism might be relevant is the observed splitting of the radiation into two bands reported already in the first observations of the outer heliospheric radiation [Kurth et al., 1984]. The gap between the two bands is quite narrow and sharp and has the character of self-absorption. Such splitting is typical for type II bursts and has not yet been

Table 12.1: Parameters in the heliosheath [after Mitchell et al., 2005]

Parameter	100 AU	150 AU
T_e (eV)	3.2	0.8
T_i (eV)	32	0.8
n_e (cm^{-3})	0.02	1.2
U_{sh} (100 km/s)	5.0	6.0
B (nT)	0.1	0.1
$R_{c,sh}(10^7 km)$	3.4	5.0

completely understood. A theory of how such a splitting could occur, based on nonlinear evolution of plasma waves, has been put forward by Treumann and LaBelle [1992], but it remains completely uncertain whether under the conditions in the ion wall at the heliopause the required nonlinear interaction can take place.

Electrons are known to be reflected from perpendicular shocks. In fact, due to upstream wave generation close to the shock front any supercritical shock has perpendicular character on the small electron scale and will thus reflect electrons all over its surface. Electrons reflected from a strong supercritical perpendicular shock might be tied to the shock front and experience shock surfing and acceleration until their gyroradius exceeds the width of the shock ramp. On the width of the shock ramp the ions are unmagnetized and contribute to the shock foot, while the electrons carry the current in the shock ramp. Their flow velocity readily exceeds the electron thermal velocity. This leads to instability and excitation of various large amplitude wave modes. Dominant among these modes are the modified two-stream instability with frequency near the lower-hybrid frequency f_{lh} and the now well confirmed Bernstein-Green-Kruskal (BGK) modes [see, e.g., Davidson, 1973], a kinetic variant of electron-acoustic waves [Dubouloz et al., 1991, 1993] that readily become localized and form electron phase space holes. These modes trap the colder electron component and accelerate the faster electrons into cool beams along the magnetic field by effectively cooling the electron distribution.

The electron beams escaping from the BGK modes excite Langmuir waves, thus setting the conditions for excitation of radiation at the fundamental frequency. This happens when the Langmuir waves interact with the BGK modes. Formally the process can be written as L + BGK → T. In fact, the localized BGK modes comprise a whole spectrum of wavelengths. Hence, the above condition must be understood as a resonance where the Langmuir wave picks out the resonant wave from the BGK spectrum. The radiation frequency is at the fundamental, $f \geq f_{pe}$, for the BGK mode the frequency is $f \ll f_{pe}$. Moreover, since both modes are longitudinal and the typical length of the BGK mode is close to the Debye length, shorter wavelength Langmuir waves can selectively satisfy the momentum relation $k_L - k_{BGK} = k_T \approx 0$. A mechanism like this one may generate the observed radiation under the restrictive conditions in the heliopause ion wall. The trapped electron component may also contribute to either absorbing Langmuir wave energy or generating short wavelength whistler waves. These modes also possess parallel

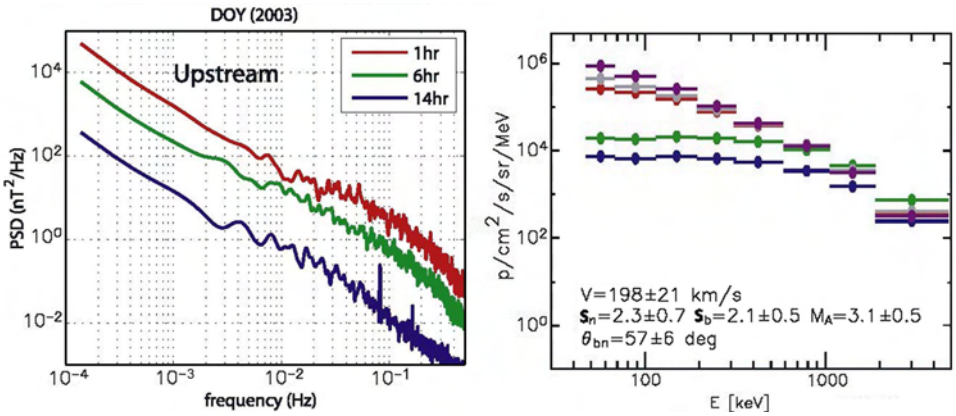

Figure 12.12: *Left*: Turbulent spectra of low frequency waves upstream of a CME shock. *Right*: The energy distribution functions of particles (in this case ions) that have been accelerated in turbulent shock acceleration by the same CME shock. For electrons the mechanism of acceleration might be different. [from Zank et al., 2006].

wave numbers. Whether they interact or not remains, however, unclear. In addition, a third mode that comes into play are ion holes – or ion BGK modes – that are excited by a similar mechanism in a current carrying ion-electron plasma. Such holes are expected in the shock foot. Ion holes provide localized ion-sound like oscillation of the plasma density [Pottelette et al., 2001]. Interaction between Langmuir waves and these oscillations will also contribute to radiation. Finally, direct interaction between ion and electron holes is a process that has not yet been investigated in view of its contribution to radiation.

Lower-hybrid mechanisms

Mechanisms based on the excitation of lower-hybrid waves have also been proposed [Treumann et al., 1998; Cairns and Zank, 2001, 2002; Cairns, 2004a, b; Cairns et al., 2005; Mitchell et al., 2004] starting from different propositions. In the first of these papers it was proposed that the interstellar pick-up ions that are accelerated in the solar wind and heliosheath flows to attain ring distributions of nominal velocity $v_{\rm ring} \approx 50 - 100$ km/s, generate a high level of lower hybrid waves inside the inner heliosheath and heliopause. This occurs over scales of the order of the ACR ion gyroradius and is therefore an effect that should occur all over the region where pick-up ions have been accelerated.

Since electrostatic lower-hybrid waves propagate obliquely with respect to the magnetic field, they possess a parallel electric field component that on the electron scale is stationary. Hence, they are strongly Landau damped, pumping their energy into the acceleration of electrons along the magnetic field. It has been estimated [see Zank, 1999] that the beam electron speed would be of the order of

$$\frac{v_{\rm e,max}}{v_{\rm ring}} \approx \sqrt{\frac{m_{\rm i}}{m_{\rm e}}}$$

corresponding to a beam energy of the order of $\sim$ 10 eV which from Table 12.1 exceeds the electron temperature by a factor of between 3 and 10, depending on the position in the inner or outer heliosheath. Such beam electron energies are sufficiently high to excite Langmuir waves and to give rise to radiation in the various modes we have discussed in the section on WWI. The location of the radiation source is determined by the available beam density. This was found to be large enough for detectable radiation at frequencies of 1.8-3 kHz only in the heliopause ramp (Figure 12.10) where the relative beam density is high enough and at the same time the background density is so large that the frequency fits into the allotted range in figure 12.3. However, a mechanism like this one predicts that in the inner heliosheath radiation should be generated that would become observable already at the termination shock. Since this has not been the case yet the radiation generated under normal conditions must be weak.

Mitchell et al. [2004] have used the above idea to propose that a combination of the propagation of a Global Interaction Region with the above mechanism of production of electron beams by lower hybrid waves could be responsible for the generation of radiation. This theory restricts itself to the consideration of secondary charge exchange beyond the heliopause, formation of ring distributions and acceleration of electron beams there. As these authors say, the heliopause would then be "primed" with a suprathermal electron distribution having a beam number density

$$\frac{n_\mathrm{b}}{n_\mathrm{e}} \approx 0.4\sqrt{\frac{m_\mathrm{i}}{m_\mathrm{e}}} \approx 10^{-5}$$

This primed medium does not yet radiate. However, when a Global Interaction Region shock passes the heliopause, the electrons become accelerated additionally, electron beams are formed in the electron foreshock, and the subsequently excited Langmuir waves give rise to radiation by the conventional mechanism discussed above. In addition to this kind of theory the above authors make use of a stochastic growth theory [Robinson et al., 1994] which takes into account that the waves grow best when the electron beams pass across decreases in plasma density. If these are distributed stochastically in the medium one can average over the volume and determine the average spatial growth rate and quasilinear wave saturation. This theory allows one to determine the expected radio fluxes and bandwidths Δf for fundamental (F) and harmonic (H) emission. With Δv_b the velocity spread of the electron beam, the bandwidths found are

$$\frac{\Delta f^\mathrm{F}}{f_\mathrm{pe}} \approx 3\left(\frac{v_\mathrm{e}}{v_\mathrm{b}}\right)^2 \frac{\Delta v_\mathrm{b}}{v_\mathrm{b}}, \qquad \frac{\Delta f^\mathrm{H}}{f_\mathrm{pe}} \approx 12\left(\frac{v_\mathrm{e}}{v_\mathrm{b}}\right)^2 \frac{\Delta v_\mathrm{b}}{v_\mathrm{b}}$$

Because $v_\mathrm{e} < 3v_\mathrm{b}$ and $\Delta v_\mathrm{b} \sim 0.1 v_\mathrm{b}$, these bandwidths are small, namely 3% and 12% of the plasma frequency for F and H, respectively. These values are clearly less than is observed (see Figures 12.4 and 12.5). This difference might vindicate the model underlying the assumed emission process.

On the other hand, the flux density in the fundamental radio emission found is 2×10^{-17} W/m^{2}Hz, a value that agrees quite nicely with the observed fluxes [Gurnett et al., 1993]. The harmonic emission is much less intense, however. Mitchell et al. [2004] have shown that the observed and theoretical flux values are far (13

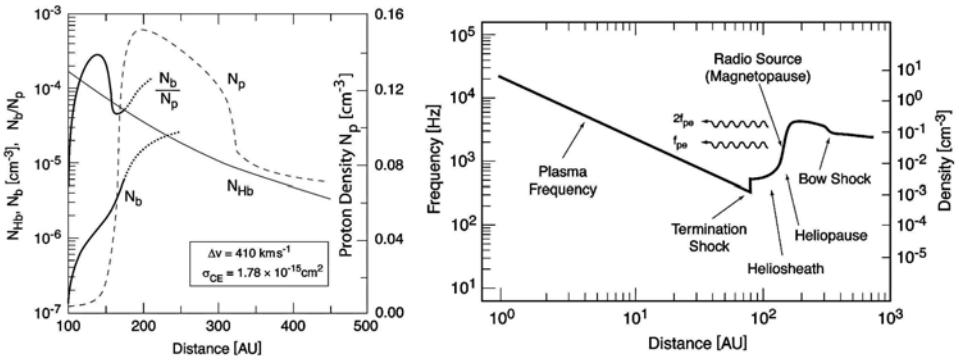

Figure 12.13: *Left*: Conditions near the heliopause and outer heliosheath as derived from an (unmagnetized) PIC simulation of the interaction between the interstellar gas and solar wind. Formation of a ring beam of density N_b is included. The relative beam density is a maximum close to the heliopause. Such ring beam distributions give rise to excitation of lower-hybrid waves which accelerate electrons along the magnetic field. *Right*: A figure similar to that given by Gurnett et al. [1993] but including the ring beam effect in the generation of radiation positioning the radiation source at the heliopause [after Treumann et al., 1998].

orders of magnitude!) above thermal fluctuation level. They also estimated that the instrumental limitations of the Voyager plasma wave receiver restrict any detection of radiation to electromagnetic flux values $> 10^{-18}$ W/m^{2}Hz, which also nicely explains why weaker radiation from, say, the heliosheath or termination shock could not have been detected by Voyager. Hence, these arguments seem to nicely support the stochastic growth model of "primed" emission in the heliopause region.

However, on closer examination the agreement between the observed and the theoretical intensities does not as strongly support the underlying theory. Any mechanism that generates radiation of intensity just above instrument detectability would do. Moreover, as a general rule, emitted intensities agree with observed radiation intensities only in or close to thermodynamic equilibrium. For non-equilibrium processes, there are always too many imponderables that cannot be accounted for. For the application of equilibrium thermodynamics, the radiation source should be optically thick to radiation. This is barely the case, however. Thus the above good agreement of the intensities is a weak argument only for the validity of the stochastic growth model of the combination of three-wave processes involved, and the disagreement in the bandwidths must be given more weight in the judgement.

We may therefore conclude that we are probably still far away from having a realistic theory for the generation of the outer heliospheric radiation. The most certain statement we can make is that the correlation between the radiation and the Forbush decreases, the estimates of the distance to the heliopause, and the requirement of sufficiently high electron densities force us to believe that the radiation is generated in the heliopause whenever a GMIR interacts with the ion wall. This conclusion has already been put forward by Gurnett et al. [1993]. It is nearly as old as the first detection of the outer heliospheric radiation.

12.4.2 Radiation in reconnection

Radiation from reconnection has been reported so far only from the observation of solar radio emission during solar flares [for reviews see Aschwanden, 2002; Aschwanden and Treumann, 1997]. It is thus not clear whether reconnection indeed causes radiation. Observations in-situ of the geomagnetic tail [Øieroset et al., 2002] have, however, demonstrated that reconnection is capable of accelerating electrons and protons to high energies. For electrons this has been confirmed by numerical PIC simulations of reconnection [Drake et al., 2003; Jaroschek et al., 2004]. The accelerated electrons form an extended high-energy power-law tail on the distribution function. Since reconnection occurs in localized places, velocity dispersion effects will readily turn the accelerated particle distributions at larger distances from the reconnection site into fast travelling beams of the kind we are familiar with from type III bursts.

Figure 12.8 (right) shows a possible scenario for reconnection at the heliopause. Due to the inclination of the interstellar magnetic field with respect to the heliosphere the site of reconnection is somewhat displaced from the nose of the heliosphere. Moreover, this site will change periodically with the change in polarity of the interplanetary field which comes into contact with the heliopause.

When reconnection takes place, fast electron beams with speeds much higher than the Alfvén speed have been observed both in space and in simulations to escape from the reconnection site to both sides along the magnetic field, very similar to the case of supercritical-shock reflected electrons, even though the mechanism is completely different from shock acceleration. Such beam are capable of generating waves and radiation. Radiation can be observed and is therefore a signature of ongoing reconnection, whereas the bulk plasma jetting of velocity $v_{flux} \sim 0.2 v_A$ that is usually taken as reconnection signature will, however, remain completely unobservable since the Alfvén speed is small in the neighbourhood of the heliopause, only of the order of 1 km/s.

Radiation from reconnection, however weak, should be a signature even though the radiation itself will not be produced right inside the reconnection site. Its exciter is the electron beam that is leaving from there, causing the radiation source to be displaced. Such radiation maps the local density along the magnetic field line along that the electron beams are released in a similar way as type III bursts map the solar wind density when emanating from the solar corona. At the heliopause electron beams are injected into the inner heliosheath mapping the plasma density of the inner heliosheath and causing radiation at about constant frequency, lower than the frequency in the ion wall. On the other hand, electron beams released into the outer heliosheath, i.e. into the ion wall, climb up the density gradient and will thus cause radiation at a gradually increasing frequency, possibly high enough for being observed from remote.

These conclusions are in agreement with the observation of two outer heliospheric radiation bands. The lower frequency band results from electron beams injected upstream into the heliosheath and is at constant frequency. The higher frequency band has been found to slowly increase in frequency with time. It results from the electron beams injected into the heliopause. The observations have been interpreted as the progression of the GMIR shock into the ion wall by Gurnett et

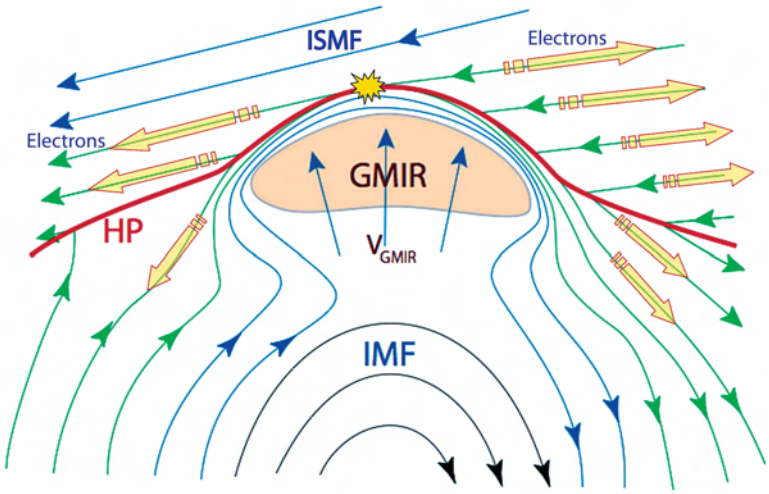

Figure 12.14: Interaction of a GMIR shock with the interstellar gas when the shock passes the heliopause and enters the outer heliosheath, i.e. the ion wall. In this figure the negligible effect of the termination shock is suppressed. The GMIR shock is 100% perpendicular as shown in the figure. There are no escaping magnetic field lines as in the case of Figure 12.11. The GMIR shock carries a layer of energetic reflected electrons in front of it that cannot escape into the upstream medium. However, when the compressed field contacts the interstellar field, reconnection occurs (indicated by the star; reconnected field lines are in green). (Note the asymmetry caused in the heliopause geometry.) The electrons (open arrows) are set free by reconnection and leave the shock as energetic beams in the heliosphere and outer heliosheath. Here they immediately become involved into the radiation process. Of course earlier they have already generated BGK modes in front of the shock and could probably radiate at the fundamental frequency. But in this case the radiation is invisible as the piston height screens it from the heliosphere. When the electron beams after reconnection run up the density gradient in the heliopause the emission frequency exceeds the piston threshold and the radiation is no longer screened from the heliosphere.

al. [1993] and by us. However, the interpretation of the radiation as resulting from reconnection provides another explanation that cannot easily be denied. In particular, it gives a natural explanation for the occurrence of the observed frequency gap, since the electron beams form by velocity dispersion only at a distance from the injection site before radiation can be generated. The width of the frequency gap, of the order of 100 Hz in this case, depends on the density difference between the reconnection and radiation sites. This density difference is about $\Delta n_e = 0.01\text{cm}^{-3}$ for the 2 kHz emission frequency.

Unfortunately, even though such a picture looks promising, the absence of continuous radiation from the heliopause implies that during reconnection the emissivity remains low, so low in fact that it does not overcome the threshold of the Voyager wave instrumentation. Therefore, in order to save the reconnection model and to account for the correlation between radiation and Forbush effects one must combine it with the passage of a strong GMIR piston-driven shock wave. The GMIR

pushes ahead the interplanetary spiral magnetic field much more strongly and in a slightly different way than is shown schematically in Figure 12.11. Close to the heliopause this picture must be modified in order to account for the purely tangential set of the last field lines in the outermost heliosphere.

Firstly, the GMIR shock is different from other shocks because inside the heliosphere it will be purely perpendicular over most of its length. Before reconnection there are no field lines that escape from the shock as it still is true for the case in Figure 12.11. Secondly, the GMIR compresses and pushes the spiral interplanetary field lines ahead out into the interstellar field, as shown schematically in Figure 12.14 for the transition of the GMIR from the heliosphere into the heliopause and outer heliosheath.

This will have two consequences. Firstly, because of the faster plasma inflow the GMIR causes stronger and faster reconnection than in the absence of the GMIR. The budget of energy transfer from the magnetic field to particle acceleration and heating will be enhanced.

Secondly, however, the electrons that are skimming the GMIR shock front and have been shock accelerated in the perpendicular shock will be released by the reconnection process along the newly merged field lines in the two directions parallel to the interstellar field and backwards along the spiral interplanetary part of the field into the heliosphere. Both energetic electron beams will excite plasma waves and produce radiation. But probably only the electron beams that are injected into the interstellar gas and move up the compressed heliopause density gradient will be able to generate radiation at high enough frequency to become visible at Voyager.

The exciter of the radiation is hence not merely the fast electron component generated in the continuous reconnection process at the heliopause. Rather it is the pre-accelerated fast electron population that is injected from the GMIR shock wave into the reconnection. As earlier, the low frequency cut-off of the radiation is the density of the piston that drives the GMIR shock. However, reconnection is required in order to allow the energetic electrons to escape from the GMIR shock and travel along the interconnected field lines. Only then can visible radiation be generated.

This scenario might explain why the occasions of radiation will be rare and must necessarily be related to a strong driver that produces a global shock wave. The details of this process will not be given here; it is not very different from what is already known about shock generation of radiation in dense plasma. We have pointed out these similarities above: the backbone radiation, the frequency drift, and in particular the observed band splitting. Thus up to modifications induced by the different states of the outer heliosheath plasma, the mechanism of radiation will be similar to the generation of radiation from type II burst shocks. The main difference is that reconnection is involved here and that it takes over the responsibility for the production of intense electron beams along the reconnected spiral heliospheric and stretched interstellar magnetic fields. It is also responsible for further acceleration of the electrons and most important, for liberating them from being globally enslaved by the completely perpendicular GMIR shock at the heliopause position.

12.5 Conclusions

The main result of this review of the generation of the 2-3 kHz radiation in the outer heliosphere is somewhat sobering. Even though in the past theories have been offered that explain the generation of radiation, we have concluded that none of them draws a picture that is sufficiently convincing. The state of the art today is that the original claim of Gurnett et al. [1993], repeated by Kurth and Gurnett [2003], still holds. The outer heliosphere is incapable of producing the radiation. Electron beams and the more sophisticated lower-hybrid mechanisms for producing an outer heliosheath plasma "primed" with electron beams seem to be doubtful even though the intensities estimated are in the right range. Nowhere in the accessible space plasmas have in-situ measurements ever found lower hybrid waves to be strong enough to become important in plasma dynamics. It is hard to believe that this should be different in the heliosheath. Lower-hybrid wave theories, including our own [Pottelette et al., 1992], have never ever been confirmed by observation.

The radiation mechanism thus seems to be unknown. It poses a challenge to theorists and simulationists. After the recently obtained more precise knowledge [Lallement et al., 2005] about the direction of the interstellar magnetic field, however, theory or simulation must take into account the presence of this field. We have speculated about the role of such a field. Its most important contribution is not so much the slight deformation of the heliopause, but more the possibility of reconnecting with the spiral interplanetary heliospheric field. A few of the effects happening during such a reconnection have been mentioned in this chapter. One is the reordering of the fields, another the production of (slow) plasma jets along the heliopause.

The most important effect for the generation of radiation is the required acceleration of electrons. Electrons being accelerated in reconnection are a promising candidate. They escape from the reconnection site along the reconnected magnetic fields to both sides, forming beams and causing important effects. Radiation efficiencies are relatively low, however. For instance, from the reconnection in the Earth's tail no radiation has ever been detected because the "emission measure" is too small, i.e. the involved volume is simply too small for emitting sufficient energy in the form of radiation. This volume is of the order of the electron inertial lengths only! Radiation from the solar corona has sometimes been interpreted as coming from reconnection. One does not expect that under quiet conditions much radiation would be produced in the heliopause. Its intensity will not exceed the instrumental detection limit of Voyager. The situation may change when a fast GMIR interacts with the heliopause. We have suggested a scenario for generation of radiation in this case.

Acknowledgements

This research has benefitted from a Gay-Lussac-Humboldt award by the French Government, which is gratefully acknowledged. Part of this study was performed during a period as a Visiting Scientist at the International Space Science Institute in Bern. The quiet environment created by the ISSI staff has been instrumental in completing this work. The generosity of the directors of ISSI, R. Bonnet, R. von Steiger, and A. Balogh, is grate-

fully acknowledged. We thank I. Cairns, J. Geiss, D. Gurnett, M. Hoshino, C. Jaroschek, R. Jokipii, R. Kallenbach, W. Kurth, J. LaBelle, R. Lallement, W. Macek, H.-R. Mueller, H. Rucker, R. Sagdeev, M. Scholer. P. Zarka and L. Zeleny for various discussions on radiation and the role of the termination shock, heliosheath, heliopause, and the importance of the neutral gas component.

Bibliography

Aschwanden, M.J., and Treumann, R.A., in Coronal Physics from Radio and Space Observations, G. Trottet (ed.), Springer, Lecture Notes in Physics, Vol. 483, p. 108, 1997.

Aschwanden, M.J., *Space Sci. Rev.* **101**, 1, 2002.

Axford, W.I., in Physics of the Outer Heliosphere, S. Grzedzielski and D. E. Page (eds.), COSPAR Colloquia Series vol. 1, Pergamon Press, Oxford, p. 7, 1990.

Baranov, V.B., and Malama, Y.G., *J. Geophys. Res.* **98**, 15157, 1993.

Burlaga, L.F., Ness, N.F., Acuña, M.H., Lepping, R.P., Connerney, J.E.P., Stone, E.C., and McDonald, F.B., *Science* **309**, 2027, 2005.

Cairns, I.H., in Physics of the Outer Heliosphere, V. Florinski et al. (eds.), AIP Conf. Proc. 719, Melville, N.Y., 2004, p. 381.

Cairns, I.H., in The Sun and the Heliosphere as an Integrated System, G. Poletto and S. Suess (eds.), Kluwer, Dordrecht, 2004.

Cairns, I.H., Kurth, W.S., and Gurnett, D.A., *J. Geophys. Res.* **97**, 6245, 1992.

Cairns, I.H., and Zank, G.P., in The Outer Heliosphere: the Next Frontiers, COSPAR Colloquia Series vol. 11, K. Scherer, H. Fichtner, H.-J. Fahr, and E. Marsch (eds.), Pergamon Press, Amsterdam, p. 253, 2001.

Cairns, I.H., and Zank, G.P., *Geophys. Res. Lett.* **29**, 47-1, 2002.

Cairns, I.H., Mitchell, J.J., Knock, S.A., and Robinson, P.A., *Adv. Space Res.*, in press, 2005.

Chalov, S.V., and Fahr, H.J., *Astron. Astrophys.* **326**, 860, 1997.

Cravens, T.E., *Astrophys. J.* **532**, L153, 2000.

Cummings, A.C., Stone, E.C., and Steenberg, C.D., *Astrophys. J.* **578**, 194, 2002.

Czechowski, A., and Grzedzielski, S., *Nature* **344**, 640, 1990.

Czechowski, A., Grzedzielski, S., and Macek, W.M., *Adv. Space Sci.* **16**, 297, 1995.

Davidson, R.C., Nonlinear Plasma Theory, Academic Press, New York, 1973.

Decker, R.B., Krimigis, S.M., Roelof, E.C., Hill, M.E., Armstrong, T.P., Gloeckler, G., Hamilton, D.C., and Lanzerotti, L.J., *Science* **309**, 2020, 2005.

Drake, J.F., Swisdak, M., Cattell, C., Shay, M.A., Rogers, B.N., and Zeiler, A., *Science* **299**, 873, 2003.

Dubouloz, N., Pottelette, R., Malingre, M., and Treumann, R.A., *Geophys. Res. Lett.* **18**, 155, 1991.

Dubouloz, N., Treumann, R.A., Pottelette, R., and Malingre, M., *J. Geophys. Res.* **98**, 17415, 1993.

Dubouloz, N., Treumann, R.A., Pottelette, R., and Lynch, K., *Geophys. Res. Lett.* **22**, 2969, 1995.

Eastwood, J.P., Lucek, E.A., Mazelle, C., Meziane, K., Narita, Y., Pickett, J., and Treumann, R.A., in Outer Magnetospheric Boundaries: Cluster Results, G. Paschmann, S. J. Schwartz, C. P. Escoubet, and S. Haaland (eds.), Space Sciences Series of ISSI, Vol. 20, Ch. 2, and *Space Sci. Rev.* **118**, 41, 2005.

Fisk, L., *Science* **309**, 2016, 2005.

Florinski, V., Pogorelov, N.V., and Zank, G.P. (eds.), Physics of the Outer Heliosphere, AIP Conference Proceedings 719, AIP, Melville, N,Y., 2004.

Forbush, S.E., *Phys. Rev.* **51**, 1108, 1937.
Frisch, P.C., *J. Geophys. Res.* **111**, in press, 2006.
Grzedzielski, S., and Page, D.E. (eds.), The Outer Heliosphere, COSPAR Colloquia Series vol. 1, Pergamon Press, Oxford, 1990.
Gurnett, D.A., *Space Sci. Rev.* **72**, 243, 1995.
Gurnett, D.A., and Kurth, W.S., *Geophys. Res. Lett.* **21**, 1571, 1994.
Gurnett, D.A., and Kurth, W.S., *Space Sci. Rev.* **78**, 53, 1996.
Gurnett, D.A., and Kurth, W.S., *Science* **309**, 2025, 2005a.
Gurnett, D.A., and Kurth, W.S., AGU Spring Meeting 2005, abstract No. SH22A-05, 2005AGUSMSH22A, 2005b.
Gurnett, D.A., Kurth, W.S., Allendorf, S.C., and Poynter, R.L., *Science* **262**, 199, 1993.
Gurnett, D.A., Kurth, W.S., and Stone, E.C., *Geophys. Res. Lett.* **30**, 2209, 2003.
Jokipii, J.R., *Science* **307**, 1424, 2005.
Izmodenov, V., Gloeckler, G., and Malama, Y., *Geophys. Res. Lett.* **30**, 1351, 2003a.
Izmodenov, V., Malama. Y., Gloeckler, G., and Geiss, J., *Astrophys. J.* **594**, L59, 2003b.
Izmodenov, V., Wood, B.E., and Lallement, R., *J. Geophys. Res.* **107**, 1308, 2002.
Izmodenov, V., Alexashov, D., and Myasnikov, A., *Astron. Astrophys.* **437**, L35, 2005.
Jaroschek, C.H., Treumann, R.A., Lesch, H., and Scholer, M., *Phys. Plasmas* **11**, 1151, 2004.
Kerr, R.A., *Science* **308**, 1237, 2005.
Krimigis, S.M., Decker, R.B., Hill, M.E., Armstrong, T.P., Gloeckler, G., Hamilton, D.C., Lanzerotti, L.J., and Roelof, E.C., *Nature* **426**, 45, 2003.
Kurth, W.S., and Gurnett, D.A., *Geophys. Res. Lett.* **18**, 1801, 1991.
Kurth, W.S., and Gurnett, D.A., *J. Geophys. Res.* **98**, 15129, 1993.
Kurth, W.S., Gurnett, D.A., Scarf, F.L., and Poynter, R.L., *Nature* **312**, 27, 1984.
Kurth, W.S., Gurnett, D. A., Scarf, F. L., & Poynter, R. L., *Geophys. Res. Lett.* **14**, 49, 1987.
Kurth, W.S., and Gurnett, D.A., *J. Geophys. Res.* **108**, LIS 2-1, 2003.
Labrum, N.R. (ed.), *Solar Radiophysics*, Cambridge Univ. Press, 1985.
Lallement, R., Bertaux, and Clarke, J.T., *Science* **260**, 1095, 1993.
Lallement, R., Quémerais, E., Bertaux, J. L., Ferron, S., Koutroumpa, D., and Pellinen, R., *Science* **307**, 1441, 2005.
Macek, W.M., Cairns, I.H., Kurth, W.S., and Gurnett, D. A., *Geophys. Res. Lett.* **18**, 357, 1991.
Macek, W.M., *Space Sci. Rev.* **76**, 231, 1996.
McDonald, F.B., and Burlaga, L.F., in Cosmic Winds and the Heliosphere, J. R. Jokipii, C. P. Sonnett, and M. S. Giampapa (eds.), Univ. Arizona Press, Tucson, 1994.
McDonald, F.B., Cummings, A.C., Stone, E.C., Heikkila, B., Lal, N., and Webber, W.R., *Nature* **416**, 48, 2003.
McNutt, R.L., *Geophys. Res. Lett.* **15**, 1307, 1988.
Mitchell, J.J., Cairns, I.H., and Robinson, P.A., *J. Geophys. Res.* **109**, A06108, 2004.
Mitchell, J.J., Cairns, I.H., and Robinson, P.A., *Phys. Plasmas* **10**, 3315, 2003.
Mitchell, J.J., Cairns, I.H., and Robinson, P.A., *J. Geophys. Res.* **110**, A11101, 2005.
Mueller, H.-R., Zank, G.P., and Lipatov, A.S., *J. Geophys. Res.* **105**, 27419, 2000.
Nelson, G.J., and Melrose, D.A., in D.J. McLean and N.R. Labrum (eds.), Solar Radiophysics, Cambridge Univ. Press, Cambridge, p. 331, 1985.
Øieroset, M., Lin, R.P., Phan, T.D., Larson, D.E., and Bale, S. D., *Phys. Rev. Lett.*, **89**, 195001, 2002.
Pogorelov, N.V., and Zank, G.P., *Adv. Space Res.* **35**, 2055, 2005.
Pottelette, R., Treumann, R.A., and Dubouloz, N., *J. Geophys. Res.* **97**, 12, 1992.
Pottelette, R., Treumann, R.A., and Berthomier, M., *J. Geophys. Res.* **106**, 8465, 2001.

Quémerais, E., Bertaux, J.-L., Lallement, R., Sandel, B.R., and Izmodenov, V., *J. Geophys. Res.* **108**, 8029, 2003.
Rand, J.D., and Lyne, A.G., *MNRAS* **268**, 497, 1994.
Reipurt, B., Bally, J., Fesen, R.A., and Devine, D., *Nature* **396**, 334, 1998.
Richardson, R.J., and Smith, C.W., *Geophys. Res. Lett.* **30**, 1206, 2003.
Richardson, J.D., McDonald, F.B., Stone, E.C., Wang, C., and Ashmall, J., *J. Geophys. Res.* **110**, A09106, 2005.
Robinson, P.A., Cairns, I.H., and Willes, A.J., *Astrophys. J.* **422**, 870, 1994.
Scherer, K., Fichtner, H., Fahr, H.-J., and Marsch, E. (eds.), The Outer Heliosphere: The Next Frontiers, COSPAR Colloquia Series 11, Pergamon Press, Amsterdam, 2001.
Schwadron, N.A., and McComas, D.J., *Geophys. Res. Lett.* **30**, 1587, 2003.
Stone, E.C., Cummings, A.C., McDonald, F.B., Heikilla, B., Lal, N., and Webber, W.R., *Science* **309**, 2017, 2005.
Suess, S.T., *Rev. Geophys. Space Phys.* **28**, 97, 1990.
Thomas, G.E., *Ann. Rev. Earth. Planet. Sci.* **6**, 173–204, 1978.
Treumann, R.A., *Astron. Astrophys. Rev.*, in press, 2006.
Treumann, R.A., and LaBelle, J., *Astrophys. J.* **399**, L167, 1992.
Treumann, R.A., Macek, W.M., and Izmodenov, V., *Astron. Astrophys.* **336**, L45, 1998.
Wang, C., and Richardson, J.D., *Geophys. Res. Lett.* **29**, doi:10.1029/2001GL014472, 2002.
Wang, C., and Richardson, J.D., *J. Geophys. Res.* **108**, doi:10.1029/2002JA009322, 2003.
Webber, W.R., *J. Geophys. Res.* **110**, A10103, 2005.
Wood, B.E., Mueller, H.-R., and Zank, G.P., *Astrophys. J.* **542**, 493, 2000.
Zank, G.P., *Space Sci. Rev.* **89**, 413, 1999.
Zank, G., and Mueller, H.-R., *J. Geophys. Res.* **108**, 1240, 2003.
Zank, G., Li, G., Florinski, V., Hu, Q., Lario, D., and Smith, C.W., *J. Geophys. Res.* **111**, A06108, 2006.

— 13 —

Summary of the Results of INTAS Project WP 01-270: Physics of the Heliosheath Plasma Flow and Structure of the Termination Shock

Reinald Kallenbach[1]
International Space Science Institute, Bern, Switzerland

Vladislav Izmodenov
Moscow State University, Moscow, Russia

The primary goals of the INTAS research programme 01-270 "Physics of the Heliosheath Plasma Flow and Structure of the Termination Shock", were:

- to study theoretically the transport, acceleration, and interaction mechanisms of the distant heliospheric plasma components – solar wind protons and electrons, pickup ions, anomalous cosmic rays, and (energetic) neutral atoms – which determine the properties of the heliosheath plasma flow as well as the location, the structure, and the shape of the solar wind termination shock, and

- to verify the model predictions by currently available observations such as remote diagnostics of the heliosheath plasma and gas properties from the SWICS instruments onboard Ulysses and ACE, the CELIAS and SWAN instruments onboard SOHO, the GHRS and STIS instruments of the HST, and the radio wave experiment on board the Voyager 1 and 2 spacecraft, as well as in-situ measurements by the anomalous cosmic ray (ACR) and plasma instruments onboard the Voyager spacecraft, which provide all present experimental information on the properties of the distant solar wind at the heliospheric boundary to the local interstellar medium (LISM).

In this volume the members of the INTAS team 01-270 have reported on the results of their studies during the period 2001 to 2005. The following report underlines the main results obtained in the frame of the project and verifies that all objectives identified in the INTAS Work Programme 01-270 were fulfilled. The report consists of four sections, which address (1) global models of the heliospheric interface, (2) the "microphysics" of the distant solar wind plasma (note that the

[1]in *The Physics of the Heliospheric Boundaries*, V. Izmodenov and R. Kallenbach (eds.), ISSI Scientific Report No. 5, pp. 391 - 413, ESA-ESTEC, Paris 2006

"microscales" may be of order 1000 km), (3) the results from optical remote diagnostic methods, and (4) the conclusions drawn from the studies in the frame of this INTAS project and new challenges and problems for future studies.

13.1 Global models of the heliospheric interface

The main difficulties in the modelling of the heliosphere are connected with the multi-component nature of both the local interstellar medium (LISM) and the solar wind (SW). The LISM consists of the charged components, neutral components, cosmic rays, and the magnetic field. The charged LISM component is mainly hydrogen plasma, but ions of helium make a significant contribution to the total pressure of the LISM (helium is ionized by about 30-40% in the LISM). The solar wind consists of the dynamically important protons, electrons and alpha particles. Everywhere in the heliosphere, the charged component also includes pickup protons created from interstellar H (and heavier) atoms by ionization and the anomalous cosmic rays, which are pickup ions accelerated in the outer heliosphere.

Modelling the different components requires us to use different approaches and to solve different types of partial differential equations self-consistently. Very often their solution requires different mathematical techniques. For example, the kinetic equation for interstellar H atoms can be effectively solved by the Monte-Carlo method with splitting of trajectories (Malama, 1991), the Euler or MHD equations for the charged component require a Godunov-type numerical scheme, the while the Fokker-Planck type equation that describes the evolution of pick-up ion spectra can be effectively solved by using the method of stochastic differential equations. Combining all these methods in the frame of one numerical model requires the development of special numerical grids and algorithms.

Significant progress in the multi-component modelling of the heliospheric interface was achieved during the INTAS project. All numerical models developed in the frame of the project can be classified as kinetic-continuum models and be considered as an extension of the Baranov-Malama model of the heliospheric interface (Baranov and Malama, 1993). The latter is an axisymmetric two-component (plasma and atoms) model. The interstellar H atoms are described kinetically in the frame of the model, while the hydrodynamic approach was used for the plasma component. A detailed mathematical formulation of the model is given in Chapter 4 of this volume by Izmodenov and Baranov. The multi-component models that were developed in the frame of the INTAS project are summarized in the following subsections.

13.1.1 Three-dimensional kinetic-MHD models: Effect of the interstellar magnetic field

In order to study an effect of the interstellar magnetic field on the plasma flow and on the distribution of H atom parameters in the interface, Izmodenov et al. (2005a) have developed a self-consistent kinetic-MHD model of the heliospheric interface. The closed system of ideal magnetohydrodynamic (MHD) equations for the plasma component and the Boltzmann equation for interstellar H atoms were

solved numerically. One-fluid MHD equations were considered for the plasma component. Details of the model are given in Section 4.6 of Chapter 4 of this book. We summarize some of the results here.

Izmodenov et al. (2005a), Izmodenov and Alexashov (2005a, 2006) have studied the problem assuming that the interstellar magnetic field (IsMF) is inclined to the direction of the interstellar flow. In this case the SW/LIC interaction region becomes asymmetric and the flow pattern becomes essentially three-dimensional (see Figures 4.6 and 4.7 in Chapter 4). The basic conclusions of the study can be summarized as follows:

- The inclined interstellar magnetic field causes asymmetries in the shapes of the termination shock (TS), the bow shock (BS), and the heliopause (HP).
- The stagnation point, i.e. the point of zero velocity, for the interstellar plasma deviates from the direction of the undisturbed interstellar flow.
- Since the interstellar H atoms are coupled to the plasma, the velocity of the secondary H atom component (the component that has undergone two charge exchange processes in the heliospheric interface region: H atom → proton → H atom) is deviated from the direction of the interstellar flow.

The deviation of the secondary H atom flow is in fact observed by SOHO/-SWAN as will be discussed later. The comparison of the theory prediction with the SOHO/SWAN, data allows one to use the direction of interstellar H atoms as a compass to determine interstellar magnetic field (Lallement et al., 2005; Izmodenov et al., 2005a). Pogorelov and Zank (2006) pointed out that the deflection of the interstellar H atom flow could be also due to the influence of the heliospheric magnetic field. This potential difficulty was discussed in Izmodenov and Alexashov (2006) (see, also, section 4.6). It was shown that the heliospheric asymmetries may deflect the direction of interstellar atoms, but the deflection is less than the IsMF-driven deflection.

13.1.2 The influence of interstellar and solar ionized helium

Recent measurements of interstellar helium atoms (Witte et al., 1996; Witte, 2004) and interstellar He pickup ions (Gloeckler and Geiss, 2001; Gloeckler et al., 2004) inside the heliosphere, as well as of the interstellar helium ionization (Wolff et al., 1999) allow us to estimate the number density of interstellar helium ions to be 0.008-0.01 cm^{-3}. Current estimates of the proton number density in the LIC fall in the range 0.04 - 0.07 cm^{-3}. Since helium ions are four times heavier than protons, the dynamic pressure of the ionized helium component is comparable to the dynamic pressure of the ionized hydrogen component. Therefore, interstellar ionized helium cannot be ignored in models of the heliospheric interface. The model of the SW/LIC interaction that studied the effects of interstellar ionized helium was developed by Izmodenov et al. (2003b). Simultaneously with interstellar ionized helium, the model took into account solar wind alpha particles, which constitute 2.5 - 5% of the solar wind and, therefore, produce 10 - 20% of the solar wind dynamic pressure. The model considers all plasma components (electrons, protons,

pickup ions, interstellar helium ions, and solar wind α particles) as one fluid with total density ρ and bulk velocity $\mathbf{V}$. This one-fluid approximation assumes that all ionized components have the same temperature T. Details of the model are given in Section 4.4 of Chapter 4.

The results of the study can be briefly summarized as follows:

- Under the influence of interstellar helium ions the HP, the TS, and the interstellar BS move closer to the Sun.
- This effect is partially compensated by the additional solar wind α-particle pressure that we also took into account in our model.
- The net shift of the HP, the TS, and the BS locations are $\sim$12, $\sim$2, and $\sim$30 AU, respectively, inward to the Sun.

It was also found that both interstellar ionized helium and solar wind α-particles do not influence the filtration of the interstellar H atoms through the heliospheric interface.

13.1.3 Non-stationary model: Solar cycle effects

More than 30 years (three solar cycles) of observations of the solar wind show that its momentum flux varies by a factor of $\sim$2 from solar maximum to solar minimum (Gazis, 1996; Richardson, 1997). Such variations in the solar wind momentum flux strongly influence the structure of the heliospheric interface. A non-stationary self-consistent model of the heliospheric interface was developed by Izmodenov et al. (2003a), Izmodenov and Malama (2004a, b), Izmodenov et al. (2005b). This model is a non-stationary version of the axisymmetric two-component Baranov-Malama model (see Section 4.3 in Chapter 4). In addition to the classical Baranov-Malama two-component Ansatz, interstellar ions of helium and the solar wind alpha particles were taken into account. Detailed information on the non-stationary model is given in Section 4.7 in Chapter 4 of this book.

Izmodenov et al. (2005b) obtained the periodic solution of the system of governing equations with the periodic boundary conditions for the solar wind at the Earth's orbit. The period of the solution was the same as of the boundary conditions, i.e. 11 years. The basic results for the plasma component are:

- The solar cycle variation of the TS location is $\pm$7 AU around its mean value.
- The heliopause varies by $\pm$2 AU around its mean value.
- The variation of the bow shock location is negligible.
- There is a sequence of additional weak shocks and rarefaction waves in the region between the heliopause and the bow shock. The additional heat of the plasma in the outer heliosheath induced by the shock waves is small and not observable in our calculations.
- Our numerical results in the region between the HP and BS are confirmed by an analytical solution based on the WKB approximation.

For the interstellar H atom component the following results have been obtained:

- The variation in the number density of the H atoms in the outer heliosphere is within 10%. The variation increases at 5 AU up to 30% due to strong ionization processes in the vicinity of the Sun.
- The variations in the number densities of three populations of H atoms – primary and secondary interstellar atoms, and atoms created in the inner heliosheath – are coherent in the entire supersonic solar wind region and determined by loss due to charge exchange. The coherent behaviour of fluctuations disappears in the regions where the production process is dominant.
- There is no significant variation of the temperature and bulk velocity of the primary and secondary interstellar H atoms with the solar cycle. However, the bulk velocity and kinetic temperature of atoms created in the inner heliosheath vary with the solar cycle by 10-12%. It is shown that this variation reflects the plasma properties at the heliopause.
- There is a qualitative difference between our results and the results obtained by using the fluid or multi-fluid description for the interstellar H atoms. It was shown that the multifluid description is less appropriate for the time-dependent case than for the stationary case because the Knudsen number is larger for the time-dependent problem.

13.1.4 Multi-component plasma model

The Baranov-Malama model and more recent models described above assume immediate assimilation of pickup protons into the solar wind plasma and consider the mixture of solar wind and pickup protons as a single component. However, it is clear from observations (e.g. Gloeckler and Geiss, 2004; Chapter 5 of this volume) that the pickup ions are thermally decoupled from the solar wind protons and should be considered as a separate population. Moreover, measured spectra of pickup ions show that their velocity distributions are not Maxwellian. Therefore, a kinetic approach should be used for this component. Theoretical kinetic models of pickup ion transport, stochastic acceleration and evolution of their velocity distribution function can be found in the literature. However, these models are (1) restricted to the supersonic solar wind region, and (2) do not consider the back reaction of pickup protons on the solar wind flow pattern, i.e. pickup protons are considered as test particles.

Malama et al. (2006) have developed a new kinetic-continuum model of the heliospheric interface. The new model retains the main advantage of the previous models, namely a rigorous kinetic description of the interstellar H atom component. In addition, it considers pickup protons as a separate kinetic component. A detailed description of the model is given in Chapter 4. The model is very flexible and allows one to test different scenarios for the pickup component inside, outside, and at the termination shock. The model allows one to treat electrons as a separate component and to consider different scenarios for this component. A new tool for the interpretation of pickup ions and ENAs as well as all diagnostics, which are

connected with the interstellar H-atom component, was created. The new model requires a more exact description of the physical processes involved than the previous models, which were not self-consistent. As a main result, it was shown that

- the heliosheath becomes thinner and the termination shock is further from the Sun in the new model than in the Baranov-Malama model; the heliopause, however, is closer.

The main methodological advances made in the reported model, which were not discussed here, is that we successfully applied the Monte Carlo method with splitting of trajectories (Malama, 1991) to non-Maxwellian velocity distribution functions of pickup protons. The splitting of trajectories allows us to essentially improve the statistics of our method and to calculate differential fluxes of ENAs at 1 AU with a high level of accuracy. We have shown that ENAs created from different types of pickup protons dominate in different energy ranges. This allows us to analyze the nature of the heliosheath plasma flow with ENA observations.

13.1.5 The heliotail model

The plasma and H atom distributions in the tail of the LIC/SW interaction region were not of interest until recently. However, modelling of the heliospheric interface gives answers to the two fundamental questions:

- Where is the edge of the Solar System plasma?
- How far downstream does the solar wind influence the surrounding interstellar medium?

To supply an answer to the first question one needs to define the solar plasma system boundary. It is natural to assume that the heliospheric boundary is the heliopause that separates the solar wind and interstellar plasmas. This definition is not completely correct, because the heliopause is an open surface and, therefore, the heliosphere ends at infinity. To resolve the problem, and to address the second question, detailed specific modelling of the structure of the tail region up to 50000 AU was performed by Izmodenov and Alexashov (2003), Alexashov and Izmodenov (2003), Alexashov et al. (2004b). Their main results are:

- The charge exchange process qualitatively changes the solar wind - interstellar wind interaction in the tail region. The termination shock becomes more spherical and the Mach disk, reflected shock, and tangential discontinuity disappear.
- At $\sim$ 40000 - 50000 AU the solar wind gas-dynamic parameters become undistinguishable from undisturbed interstellar parameters.

The first result was obtained previously by Baranov and Malama (1993), who performed calculations out to 700 AU in the heliotail. In addition, however, Alexashov et al. (2004b) found that the jumps in density and tangential velocity across the heliopause become smaller in the heliotail and disappear at about 3000 AU. The parameters of the solar wind plasma and the interstellar H atoms approach

their interstellar values at large heliocentric distances. This allows an estimation of the influence of the solar wind, and, therefore, the Solar System size in the downwind direction to about 20000 - 40000 AU. The solar wind plasma has a velocity ~ 100 km/s and a temperature of $\sim 1.5 \times 10^6$ K immediately after passing the TS. Then the velocity becomes smaller due to new protons injected by charge exchange, and approaches the value of interstellar velocity. Since the interstellar H atoms are effectively cooler when compared to post-shocked protons, the solar wind also becomes cooler. This causes the Mach number to increase. At distances of ~ 4000 AU the solar wind again becomes supersonic and, then, the Mach number approaches its interstellar value at $\sim$ 40000 - 50000 AU, where the solar wind gas-dynamic parameters become undistinguishable from undisturbed interstellar parameters. This result cannot be obtained in the absence of H atoms because the solar wind flow in the heliotail remains subsonic in that case.

13.1.6 The effect of ACRs

The dynamical influence of ACRs on the solar wind flow in the outer heliosphere and on the structure of the termination shock has been studied by Alexashov et al. (2004a). The mathematical formulation of the model is given in Section 4.5 of Chapter 4. The results can be briefly summarized as follows:

- The effect of ACRs on the solar wind flow near the termination shock leads to the formation of a smooth precursor, followed by the subshock, and to a shifting of the subshock towards larger distances in the upwind direction. Both the intensity of the subshock and the magnitude of the shift depend on the value of the diffusion coefficient, with the largest shift (about 4 AU) occurring at medium values of $\kappa_{\rm CR}$. The precursor of the termination shock is rather pronounced except the case with large $\kappa_{\rm CR}$.

- The post-shock temperature of the solar wind plasma is lower in the case of the cosmic-ray-modified termination shock when compared to the shock without ACRs. The decrease in the temperature results in a decrease in the number density of hydrogen atoms originating in the region between the termination shock and heliopause.

- The cosmic-ray pressure downstream of the termination shock is comparable to the thermal plasma pressure for small $\kappa_{\rm CR}$ when the diffusive length scale is much smaller than the distance to the shock. On the other hand, at large $\kappa_{\rm CR}$ the post-shock cosmic-ray pressure is negligible when compared to the thermal plasma pressure.

- There is pronounced upwind-downwind asymmetry in the cosmic-ray energy distribution due to a difference in the amount of energy injected into ACRs in the up- and downwind parts of the termination shock. This difference is connected with the fact that the thermal plasma pressure is lower in the downwind part of the shock when compared with the upwind part.

13.1.7 Interaction of the termination shock with interplanetary shocks (MHD approach)

The problem of the termination shock interaction with interplanetary shocks (IS) has been studied by Baranov and Pushkar' (2004) in a 2D-magnetohydrodynamic approach. The problem was investigated numerically at different magnitudes of determining parameters such as the TS and IS Mach numbers, the angles between the interacting shocks and between the interplanetary magnetic field (IMF) and the normal to the IS, respectively. In doing so we used the results of the axisymmetric model of the solar wind interaction with the LISM by Baranov and Malama (1993) and the solution of the classical 2D MHD problem of two interacting shocks obtained by Pushkar (1995). The result of the study is that:

- the interaction of interplanetary reverse shock waves with the TS can give rise to the formation of a new TS. The velocity of the new TS in the heliocentric frame of reference can be directed towards the Sun.

The comprehensive calculations of all parameters downstream of the new TS may help in interpreting the Voyager 1 and 2 measurements.

13.1.8 Generalized Ohm's law in the outer heliosheath

To advance the global heliospheric models further, Baranov and Fahr (2003a,b) used the classical form of the generalized Ohm's law for a partially ionized gas obtained by Cowling (1976) and Kulikovskii and Lyubimov (1965) to estimate the effects of interstellar H-atoms on the outer heliosheath structure taking into account the interstellar magnetic field. In particular, it was shown that the magnetic field "freezing" in protons does not exclude the ion current (motion of H-atoms relative to protons) dissipation due to proton gyration in the interstellar magnetic field. This dissipation was not taken into account in previous models. The estimations by Baranov and Fahr showed that this effect is important in the problem considered and it can give rise to revision of the theoretical outer heliosheath structure. However, a new MHD model must be constructed on the basis of a kinetic approximation for describing the trajectories of H-atoms, rather than on the basis of MHD equations for partially ionized plasma.

13.2 Plasma processes in the outer heliosphere

In contrast to the previous section, where the global structure of the heliosphere and its boundaries has been discussed, this section summarizes the results of our studies on "microphysical" plasma processes such as ion transport and acceleration, the "microstructure" of the termination shock, and radio wave emission from accelerated electrons at the heliopause. "Microstructure" scale sizes of astrophysical plasma systems can, of course, be quite large. They are given by plasma parameters such as the proton or electron gyroradius or inertial length, which may be of the order of 1000 km or even larger.

13.2.1 Pick-up ion transport and acceleration in the supersonic solar wind

The study of pickup ion transport and acceleration throughout the heliosphere is a particularly important task because pre-accelerated pickup ions form the seed population for the anomalous cosmic rays (Fisk et al., 1974). This task included addressing:

- stochastic acceleration of pickup ions by turbulence in the supersonic and subsonic (heliosheath) solar wind,
- acceleration of pickup ions at forward and reverse shocks in co-rotating interaction regions,
- acceleration of pickup ions at interplanetary travelling shocks.

The results are published in Chalov et al. (2003; 2004a), Chalov (2005), and Kallenbach et al. (2004; 2005b), as well as in Chapters 7 and 8 by Kallenbach et al. and Chalov in this volume.

Here, we mainly discuss stochastic acceleration, while the results on acceleration at quasi-perpendicular shocks are referred to in the next subsection, where the termination shock is discussed. In order to predict the efficiency of stochastic acceleration in the supersonic solar wind, the evolution of turbulent power over heliocentric distances must be known. Both Alfvénic and compressional fluctuations originating at the Sun and amplified by energetic-particle anisotropies, by stream-stream interactions, and by the decay of merged interaction regions (Chapter 6 by Ness in this volume) have been modelled (see Chapter 7 by Kallenbach et al. and references therein). It has been shown that:

- stochastic acceleration in Alfvénic turbulence is not sufficient to compensate for the effect of adiabatic cooling on the suprathermal tails of pick-up ions convected in the expanding slow or fast supersonic solar wind
- the ubiquitous suprathermal tails observed in the solar wind by the SWICS instrument on board Ulysses and ACE (Chapter 5, this volume) and in fact also in Voyager 1 LECP data (Chapter 7, this volume) can be maintained out to the termination shock due to compressional (mainly large-scale magnetosonic) fluctuations
- ion-acoustic fluctuations may play a role in the turbulence regions downstream of interplanetary shocks and in the inner heliosheath near the termination shock.

The spectral indices of the phase space densities of suprathermal tails observed in the supersonic solar wind of about 8 (soft spectra) in the fast wind and of about 5 (rather hard spectra) in the slow wind are consistent with the fact that the fast solar wind fluctuations are predominantly Alfvénic, while the slow solar wind fluctuations are very compressional due to the much stronger sources of compressional turbulence such as stream-stream interactions, e.g. co-rotating interaction regions and merged interaction regions.

13.2.2 Termination shock structure

This task was aimed at analyzing two characteristic scale sizes of the termination shock:

- The microscopic scale of the magnetic field shock ramp has implications for the injection efficiency into first-order Fermi acceleration and thus on the efficiency of the production of the Anomalous Cosmic Rays (ACRs).

- The build-up of the ACR pressure has in turn an influence on the macroscopic pre-cursor scale size and the actual position, i.e. the heliocentric distance of the termination shock.

Results can be found in Alexashov et al. (2004), Chapter 5 by Izmodenov and Baranov, this volume, Kallenbach et al. (2004; 2005), Ksenofontov and Berezhko (2003), Scholer (2004), and Scholer and Matsukiyo (2004).

The shock ramp scale size

If the scale size of the shock ramp of a quasi-perpendicular shock is of the order of the electron inertial length, the pick-up ions may undergo acceleration in the convective electric field of the shock front during multiple reflections at the electric cross-shock potential. Scholer et al. (2003) have performed one-dimensional (1-D) full particle simulations of almost perpendicular supercritical collisionless shocks. Due to the accumulation of specularly reflected ions upstream of the shock, ramp shocks can reform on time scales of the gyro period in the ramp magnetic field. At times during the reformation process the cross shock potential can occur over a length scale of several electron inertial lengths. This scale may be just small enough for shock surfing to occur intermittently. Shock surfing could preaccelerate pickup ions to energies of up to hundreds of keV/amu, from where a second, first-order Fermi-type acceleration process could take over. The typical shock ramp scale size may be much larger at most times, of the order of the ion (proton) inertial length or of the order of the gyro radius (Larmor radius). The latter scale size would be most plausible as an average scale size of a quasi-perpendicular shock. Still, the short times of sharp shock ramps could allow for some injection, and the injection threshold into the first-order Fermi process is only of order 10 keV/amu (Chapter 7 by Kallenbach et al., this volume).

Voyager 1 observations near the termination shock and in the heliosheath show two particle populations (Stone et al., 2005):

- Termination Shock Energetic Particles (TSPs) close to the termination shock with a H/He abundance ratio of about 10,

- and a still higher-intensity ACR component further in the heliosheath with a H/He abundance ratio of about 5.

From our theoretical considerations, we propose the following interpretation (Chapter 7 by Kallenbach et al., this volume):

- TSPs are ions that are multiply reflected at the shock potential and injected into first-order Fermi acceleration, which has an injection threshold much lower than often assumed (Chapter 7). The TSPs do not undergo mass-per-charge fractionation during shock surfing, and thus basically represent interstellar abundances (Chapter 5 by Geiss et al., this volume).

- ACRs are suprathermal ions directly transmitted through the electric potential of the termination shock, a process that prefers a high mass-per-charge ratio. The transmitted ions undergo stochastic acceleration in the heliosheath. A fraction of the reflected ions, preferentially the ions with low mass-per-charge ratio, is thermalized into the bulk plasma of the heliosheath plasma.

This scenario would match the observation that the H/He ratio is about 10 for TSPs and about 5 for ACRs (Stone et al., 2005). If further stochastic acceleration of the transmitted ions occurs due to compressional fluctuations in the heliosheath, these ions may eventually return to the termination shock at higher energies – when they have reached the injection threshold – and may undergo first-order Fermi acceleration.

The shock precursor

Energetic particles with a mean free path much larger than the shock ramp scale size can influence the structure of the termination shock. While they are scattered in the upstream supersonic solar wind region, they transfer momentum to the bulk plasma. If their pressure is comparable to the bulk plasma pressure, the energetic particles slow down the upstream supersonic solar wind, a shock precursor is formed, and the subshock compression ratio is reduced (Alexashov et al., 2004; Chapter 7, this volume).

Solar wind speed data derived from the energetic particle anisotropies observed in Voyager 1 LECP data (Stone et al., 2005) seem to support the idea that the solar wind termination shock is a cosmic-ray (energetic-particle) mediated shock. Upstream of the termination shock, the solar wind seems to be slowed down much below the speed of about 250–300 km/s, which corresponds to the maximum slow-down of the solar wind due to the mass loading of interstellar pick-up protons in the outer heliosphere. However, the energetic particle pressure gradient in the upstream solar wind plasma is not in the form of a smooth precursor, but rather spiky and intermittent.

Although not confirmed unambiguously by observations, the result of this study can be stated as follows (see Chapter 7):

- For realistic mean free paths of ACRs based on observations in the heliosphere and on our model for the evolution of turbulent power in the solar wind, the scale size of the shock precursor upstream of the TS is of order 3-10 AU based on realistic mean free paths for the region upstream of the TS.

In additional studies we have found (Kallenbach et al., 2005b; Chapter 7) that, in a self-consistent manner, energetic particles (TSPs and ACRs) may influence their own intensity. Whenever there is a spatial gradient in energetic particle distributions, there is an anisotropy in the distribution observed in the plasma frame.

These anisotropies lead to the generation of plasma waves. These plasma waves, when generated in the solar wind plasma upstream of the termination shock, cascade and convect over the shock to the downstream region and, consequently, increase the injection threshold for first-order Fermi acceleration and thus limit the energetic particle intensity. It seems that it may be hard to reach the ACR flux levels by first-order Fermi acceleration at a completely homogeneous termination shock (i.e. termination shock with the same shock normal angle, energetic particle flux and shock normal angle everywhere). Perhaps, additional stochastic acceleration in the heliosheath is necessary to reach the unmodulated ACR level. Another scenario for a termination shock with varying shock normal angle and varying turbulence levels convected into the shock is that there are areas of *injection* at *low turbulence* levels and other areas of *acceleration* at *high turbulence* levels causing short acceleration time scales. This way, the unmodulated ACR flux may be reachable by the first-order Fermi process at the termination shock (McComas and Schwadron, 2006).

13.2.3 Postshock spectra of pickup ions, anomalous cosmic rays, and energetic neutral atoms in the heliosheath

Voyager 1 magnetic field data (Chapter 6 by Ness in this volume) revealed that the compressional fluctuations in the heliosheath are much stronger than in the upstream solar wind. Furthermore, Decker et al. (2005) have suggested that the increase of intensity in the suprathermal tails of pickup ions may be entirely the consequence of a compression like an ideal gas of the suprathermal ions when passing the TS, rather than being caused by first-order Fermi acceleration. In addition it has been observed that the flux of suprathermal and energetic ions still rises towards the expected level of the unmodulated ACR flux, while Voyager 1 cruises in the heliosheath.

Downstream of the TS, the transmitted and compressed suprathermal tails may be continuously further accelerated in the compressional fluctuations of the heliosheath to become ACRs. This is possibly the main acceleration process of ACRs. It would match the observed spectral index of about -5 in the phase space density of ACRs (Fisk et al., 2006; Chapter 5 by Geiss et al., this volume). Stochastic acceleration would well explain the power-law up to high energies because the momentum diffusion term $v^{-2}\partial_v \left[v^4 \partial_v f\,(v)\right]$, describing acceleration in compressional fluctuations, is scale invariant and produces, if dominant in the transport equation, a phase space density $f\,(v) \propto v^{-5}$.

We conclude from our studies that:

- The compressional fluctuations in the heliosheath are sufficiently strong to account for stochastic (second-order Fermi) acceleration of ACRs as the dominant acceleration mechanism (Chapter 7, this volume).

- Furthermore, it had been shown that even the Alfvénic fluctuations in the heliosheath may be strong enough to stochastically accelerate pickup ions up to about 10 keV/amu, if the Alfvénic fluctuations are amplified by about factor 4 at the termination shock layer; additional amplification by upstream

energetic particles may allow for acceleration up to 100 keV/amu, an explanation that has been invoked by Kallenbach et al. (2005b) to account for the flux of Energetic Neutral Atoms (ENAs) observed by SOHO/CELIAS/HSTOF (Hilchenbach et al., 1998).

At lower energies, not detectable by LECP on Voyager 1 in the heliosheath, there may be additional higher fluxes of pick-up ions, which cannot be explained by compression and further stochastic acceleration of suprathermal tails transmitted from the supersonic solar wind. Chalov et al. (2003, 2004) have shown that pickup protons constitute the major portion of suprathermal protons in the upwind part of the inner heliosheath (see also Chapter 8 by Chalov in this volume). Furthermore, they have suggested that the total pickup proton population consists of particles with different regions of origin. The high-energy part of pickup proton spectra consists of protons originating in the supersonic solar wind, corresponding to the particles at energies above 10 keV in Figure 7.12 in this volume. Pickup protons originating in the inner heliosheath form the low-energy population (particles below 10 keV in Figure 8.9). This low-energy population has presumably been observed as neutral atoms by Mars Aspera-3 in the inner heliosphere (Figure 7.12, this volume). However, the spectral gap between the low-energy and the high-energy part of pickup ions in the heliosheath has not been observed (compare Figures 7.12 and 8.9). This gap may be smoothed out by momentum diffusion in the rather high level of compressional fluctuations in the heliosheath.

To interpret observations by SOHO/CELIAS/HSTOF and by Mars-Aspera-3, calculations of fluxes of energetic neutral atoms (ENAs) originating in the heliosheath through charge exchange between interstellar atoms and accelerated pickup ions, TSPs, and ACRs, respectively, as observed by Voyager 1, have been performed. The results can be found in Chapters 7-9 of this volume and in the publications by Czechowski *et al.* (2005), and Kallenbach *et al.* (2004, 2005b). There is general agreement between the model calculations and observations.

Summarizing, our models show, in accordance with observations, that:

- the energetic neutral atoms at energies above about 10 keV/amu are anomalous cosmic ray ions, which originate from suprathermal pickup ions in the supersonic solar wind and are subsequently accelerated and neutralized by charge exchange in the heliosheath. An additional component at energies below about 10 keV/amu with a softer spectrum is created inside the heliosheath from freshly ionized and pre-accelerated pickup ions.

13.2.4 Filtration of interstellar atoms through the heliospheric interface

Onboard the Ulysses spacecraft, the pickup ions of other chemical elements were also measured (see Chapter 5 by Geiss et al., this volume). Using these measurements, the information on the cosmic abundance of different elements in the local interstellar medium, independent of astronomical observations, can be obtained using the theoretical description of the filtration of different atoms due to their interaction with the plasmas of the outer and inner heliosheaths. The most effective filtration process for hydrogen and oxygen is charge exchange with the

interstellar protons in the outer heliosheath (Izmodenov et al., 1997), but electron impact ionization may also produce noticeable filtration in the outer heliosheath (Izmodenov et al., 1999b; 2004). In Izmodenov et al. (2004) a comparative analysis of the penetration of interstellar hydrogen, oxygen and nitrogen atoms through the interface was drawn. It was shown that (81 ± 2)% and (89 ± 1)% of the interstellar oxygen and nitrogen, respectively, penetrate into the heliosphere through the interface. Using the calculated filtration coefficients, together with data from the Ulysses measurements of pick-up ions, the oxygen and nitrogen atom number densities in the LIC were determined and turned out to be equal to $n_{\mathrm{O\,I,LIC}} = (7.8 \pm 1.3) \times 10^{-5}$ cm^{-3} and $n_{\mathrm{N\,I,LIC}} = (1.1 \pm 0.2) \times 10^{-5}$ cm^{-3}. Having estimates for the number densities of different elements, their relative cosmic abundances can be evaluated: $(n_{\mathrm{O\,I}}/n_{\mathrm{H\,I}})_{\mathrm{LIC}} = (4.3 \pm 0.5) \times 10^{-4}$ and $(n_{\mathrm{N\,I}}/n_{\mathrm{O\,I}})_{\mathrm{LIC}} = 0.13 \pm 0.01$. The ratio $(n_{\mathrm{O\,I}}/n_{\mathrm{H\,I}})_{\mathrm{LIC}}$ thus obtained is only slightly different from the value $(4.8 \pm 0.48) \times 10^{-4}$ obtained on the basis of spectroscopic observations of absorption lines in stellar spectra (Linsky et al., 1995).

13.2.5 A novel scenario for the generation of the heliopause radio emission

An additional result of this project is the proposal of a novel scenario for the generation of the heliopause radio emission (Chapter 12 by Treumann et al., this volume). The shock of a Global Merged Interaction Region (GMIR) carries a layer of energetic reflected electrons in front of it that cannot escape into the upstream medium. These electrons, if faster than the electron thermal speed, drive the Bernstein-Green-Kruskal (BGK) instability and radiate at the fundamental plasma frequency. This radiation is invisible as the GMIR piston plasma screens it from the heliosphere. However, when the GMIR reaches the heliopause, reconnection between the compressed heliospheric magnetic field and the interstellar magnetic field occurs. The electrons are set free by this reconnection and leave the shock as energetic beams into the inner and outer heliosheath. Here they immediately become involved into the radiation process. When the electron beams run up the density gradient in the heliopause the emission frequency exceeds the piston threshold and the radiation is no longer screened from the heliosphere. This scenario matches Voyager 1 and 2 observations (Gurnett et al., 1993) that heliopause radio emission is correlated with strong Forbush decreases, and the directions of the emissions, i.e. the locations of preferred reconnection sites, match the interstellar magnetic field direction recently determined by Lallement et al. (2005).

13.3 Optical remote diagnostics

13.3.1 Backscattered Lyman-α radiation: models and observations

The major source of observational information on the properties of the interstellar atoms of hydrogen is the measurements of backscattered solar Lyman-α radiation. The interplanetary Lyman-α glow was first observed in the late 1960s

and identified as an interplanetary emission in the early 1970s (Thomas and Krassa, 1971; Bertaux and Blamont, 1971). Since the wavelength of the scattered (by moving atoms of hydrogen) photon is Doppler-shifted, the spectra of backscattered photons reflects the velocity distribution function of the interstellar H atoms.

Models

Quémerais and Izmodenov (2002) presented multiple scattering computations of interplanetary background line profiles using Angle Dependent Partial Frequency Redistribution to model the scattering process. The density and velocity distribution of hydrogen atoms in the heliosphere were computed using a self-consistent model of the solar wind interaction with the two-component (H atoms and plasma) interstellar plasma (Izmodenov et al., 2001). The details of the computations and results are given in Chapter 9 of this book.

It was shown that the main difference in the heliospheric interface model compared to the classical hot model lies in the existence of three populations of H atoms in the heliosphere. These populations are primary interstellar atoms, secondary interstellar atoms created by charge exchange in the outer heliosheath and a hot component (around 150 000 K) created in the inner heliosheath. The two interstellar components provide additional asymmetry in the backscattered Lyman-α profile at 1 AU, which is not expected from the classical hot model. At the Earth orbit in the upwind direction, the hot component of the backscattered intensity represents less than 5% of the total intensity. It reaches 15% in the downwind direction. Although the heliospheric interface has some effect on the upwind to downwind ratio of total backscattered Lyman-α intensity, on the apparent velocity and apparent temperature of interplanetary line profiles, they are difficult to discriminate from the results of the variations of the solar parameters. Therefore it was pointed out that future models should include time-dependence effects on the interplanetary hydrogen distribution. Finally, it is concluded that measurements of interplanetary Lyman-α profiles in the inner heliosphere may serve as a good diagnostic for the heliospheric interface. The existence of a faint hot component in the Lyman-α backscattered profiles would serve as a new tool to study the heliospheric interface.

Observations

Modern observations of backscattered solar Lyman-α radiation can be divided into two types: (a) spectroscopic observations at 1 AU (SOHO/SWAN, Hubble Space Telescope); (b) photometric observations beyond 1 AU (Voyager 1, Voyager 2,Pioneer 10).

- **SOHO/SWAN results:** Analysis of SOHO/SWAN observations of backscattered solar Lyman-α radiation has shown an important effect that has not been discovered before (Lallement et al., 2005). Namely, it was shown that the direction of the flow of interstellar neutral hydrogen in the heliosphere is deflected by about 4 degrees from the direction of the pristine local interstellar gas flow. Such a deviation could be explained by the interstellar magnetic field being inclined to the direction of the interstellar gas flow. This scenario

was explored quantitatively (Izmodenov et al., 2005a; see, also, Chapter 4, this volume). The result demonstrates that the 3D kinetic-MHD model of the solar wind interaction with the magnetized interstellar plasma (discussed above) is able to produce the measured deviation in the case of a rather strong interstellar magnetic field of about 2.5 μG inclined by 45 degrees to the direction of interstellar flow.

- **Voyager 1, Voyager 2 and Pioneer 10 observations:** Quémerais et al. (2003) reported the study of the UVS/Voyager 1 Lyman-α data obtained between 1993 and 2003. These data show that the radial variation of the intensities measured close to the upwind direction changed abruptly at the end of 1997 when the spacecraft was at a distance of more than 70 AU from the Sun. The coefficient a of the power law describing the intensity as a function of solar distance has changed from a value of -1.58 ± 0.02 between 1993 to 1997 to a value of -0.22 ± 0.07 after 1998. This change is not compatible with current stationary models of the hydrogen distribution whether they include the effects of the heliospheric interface or not. A possible cause for this change is the temporal variations in the hydrogen distribution near the heliopause as discussed in Izmodenov et al. (2005b).

  Two data sets, the P10 Lyman-α data obtained between 20 and 45 AU and the V2 data obtained between 39 and 55 AU, have been used to estimate the local interstellar neutral hydrogen and proton densities. State of the art neutral-plasma and radiative transfer models have been used to interpret the extreme ultraviolet data. It has been found that the VLISM neutral hydrogen density of 0.15 cm^{-3} and an ionization ratio of about 0.3 fit the spacecraft data best. The present calculation suggests that for the best fit density model the P10 photometer derived intensities (Rayleighs) need to be increased by a factor of about 2, and the V2 spectrometer intensities (R) need to be scaled down by a factor of 0.5. (Gangopadhyay et al., 2004, 2005, 2006).

13.3.2 Observation of interstellar absorptions toward nearby stars

Possible constraints on the heliosheath plasma flow from measurements of interstellar absorptions toward nearby stars are summarized in Izmodenov et al. (2002, 2003c), Wood et al. (2004).

The Lyman-α transition of atomic H is the strongest absorption line in stellar spectra. Thus, the heated and decelerated atomic hydrogen within the heliosphere produces a substantial amount of Lyman-α absorption. This absorption, which must be present in all stellar spectra since all lines of sight go through the heliosphere, has been unrecognized until recently, because it is undetectable in the case of distant objects characterized by extremely broad interstellar Lyman-α absorption lines that hide the heliospheric absorption. We know now that in the case of nearby objects with small interstellar column densities, it is detected in a number of directions (see Chapter 11 of this book). The heliospheric absorption will be very broad, thanks to the high temperature of the heliospheric H, and its centroid will also generally be shifted away from that of the interstellar absorption due to the

deceleration, allowing its presence to be detected despite the fact that it remains blended with the interstellar absorption. The hydrogen wall absorption was first detected by Linsky and Wood (1996) in Lyman-α absorption spectra of the very nearby star a Cen taken by the Goddard High Resolution Spectrograph (GHRS) instrument onboard the Hubble Space Telescope (HST). Since that time, it has been realized that the absorption can serve as a remote diagnostic of the heliospheric interface, and for stars in general, their "astrospheric" interfaces.

Izmodenov et al. (2002, 2003c) have compared H I Lyman-α absorption profiles toward six nearby stars observed by HST with theoretical profiles computed using BaranovMalama model of the heliospheric interface with six different sets of model parameters. The results are summarized as follows:

1. It has been shown that the absorption produced by the hydrogen wall does not depend significantly on local interstellar H atom and proton number densities for upwind and crosswind directions. In downwind directions the hydrogen wall absorption is sensitive to interstellar densities, but this absorption component is most easily detected in upwind directions. In crosswind and downwind directions, the hydrogen wall absorption is hidden in the saturated interstellar absorption and cannot be observed.

2. The heliosheath absorption varies significantly with interstellar proton and H atom number densities. For all models, the heliosheath absorption is more pronounced in the crosswind and downwind directions. The heliosheath absorption is redshifted in crosswind directions compared with the interstellar and hydrogen wall absorption components.

3. Comparison of computations and data shows that all available absorption spectra, except that of Sirius, can be explained by taking into account the hydrogen wall absorption only. Considering heliosheath absorption, we find that all models have a tendency to overpredict heliosheath absorption in the downwind directions. Toward upwind and crosswind stars the small differences between model predictions and the data can be corrected by small alterations of the assumed stellar Lyman-α profile. However, the downwind ϵ Eri line of sight is a problem, as the models predict too much heliosheath absorption in that direction, and for many, if not most, of the models the discrepancy with the data is too great to be resolved by reasonable alterations of the stellar profile.

4. It is puzzling that a model that provides the best fit to the absorption profile towards Sirius provides the worst fit to the other lines of sight. This may be due to our models underestimating heliosheath absorption in the downwind directions due to limited grid size, or perhaps the detected excess absorption towards Sirius is not really heliospheric in origin, as suggested by previous authors. It is also possible that the difficulties the models have with the downwind lines of sight towards Sirius and ϵ Eri might be resolved by modifications to the models, perhaps by taking into account the multi-component nature of the heliosheath plasma flow. Further details of the study of heliospheric absorption are given in Chapter 11 of this book.

13.4 Conclusions and future perspective in exploration of the heliospheric interface

The interaction between the supersonic flow of partially ionized plasma of the local interstellar medium and the solar wind produces heliospheric boundaries consisting of two shock waves (the heliospheric termination shock and the bow shock) and contact discontinuity, the heliopause. Due to the charge exchange process, the region between the two shocks (heliospheric interface) separating these flows plays the role of a filter for the penetration of interstellar H, O, N, and other atoms into the Solar System.

From a theoretical point of view, the interaction should be considered in the frame of kinetic-continuum models when the interstellar H atom component is described in the framework of the kinetic theory, since for hydrogen atoms the Knudsen number with respect to charge exchange is Kn ~ 1. The first self-consistent model of the SW/LIC interaction was developed by Baranov and Malama (1993). Since that time, the set of kinetic-continuum models was developed. The models developed in the frame of INTAS project are reviewed in Section 13.1. These kinetic-continuum models take into account the following physical components/effects:

- ionized interstellar helium component and solar wind alpha particles;
- anomalous and galactic cosmic rays;
- interstellar magnetic field;
- solar cycle variations of the solar cycle parameters;
- the heliotail;
- filtration of interstellar oxygen and nitrogen;
- multi-component natured of the heliospheric plasma.

A large effort on modelling the heliospheric interface was also made by other groups (e.g. Zank, 1999). Nevertheless, the complete time-dependent multi-component kinetic-continuum model that includes all effects above (plus interplanetary magnetic field) simultaneously has not been developed yet. This constitutes a challenge for future theoretical and modelling studies.

The numerical kinetic-continuum modelling of the heliospheric interface in the frame of the Baranov-Malama model led firstly to the prediction of the many physical phenomena discovered later onboard spacecraft, and secondly to the interpretation of previously obtained experimental data. This was discussed in previous sections. In December 2004 an event awaited for more than 30 years took place, namely, the Voyager 1 spacecraft finally crossed the heliospheric termination shock at a distance of 94 AU. This was predicted (with 10% accuracy) more than 25 years ago (Baranov et al., 1981; Baranov, 1990; Baranov, 2002).

The topicality of the heliospheric interface studies is dictated by several factors:

- It is expected that the Voyager 1 and 2 spacecraft will transmit information up to the year 2020.

- In 2008 NASA plans to launch the IBEX spacecraft, which will measure the fluxes of energetic neutral atoms arriving from the inner interface at Earth's orbit.
- NASA and ESA are discussing plans to launch the Interstellar Probe spacecraft which for 10 to 15 years will be at a distance of the order of 200 AU.
- The development of technologies that would make it possible to launch a spacecraft to α Centauri, the star nearest to the Sun, is planned.

Bibliography

Alexashov, D.B., and Izmodenov, V.V.: 2003, 'Modeling of the tail region of the heliospheric interface', Proc. of the 10th Int. Solar Wind Conf., AIP Conf. Proc. **679**, 218–221.

Alexashov, D.B., Chalov, S.V., Myasnikov, A.V., Izmodenov, V.V., and Kallenbach, R.: 2004a, 'The dynamical role of anomalous cosmic rays in the outer heliosphere', *Astron. Astrophys.* **420**, 729–736.

Alexashov, D.B., Izmodenov, V.V., Grzedzielski, S., 2004b: 'Effects of charge exchange in the tail of the heliosphere', *Advances in Space Research* **34**, 109-114.

Baranov, V.B., Ermakov, M.K., Lebedev, M.G., 1981: 'A Three-Component Model of Solar Wind - Interstellar Medium Interaction - Some Numerical Results', *Soviet Astron. Lett.* **7**, 206.

Baranov, V.B., and Malama, Yu.G.: 1993, 'The model of the solar wind interaction with the local interstellar medium: Numerical solution of selfconsistent problem', *J. Geophys. Res.*, 98(A9), 1515715163.

Baranov, V.B., Fahr, H.J., 2003a: 'On nonideal MHD properties of the partially ionized interstellar gas', *J. Geophys. Res.* **108**, 1110, DOI 10.1029/2001JA009221.

Baranov, V.B., and Fahr, H.J.: 2003b, 'Reply to comment by V. Florinski and G.P. Zank on nonideal MHD properties of the partially ionized interstellar gas', *J. Geophys. Res.* **108**, 1439, DOI 10.1029/2003 JA010118.

Baranov, V.B., and Pushkar', E.A.: 2004, 'Possible crossing of the termination shock in the solar wind by the Voyager-1 spacecraft', *Astron. Lett.* **30**, 170–186.

Bertaux, J.L., and Blamont, J.E.: 1971, 'Evidence for a Source of an Extraterrestrial Hydrogen Lyman-alpha Emission', *Astron. Astrophys.* **11**, 200.

Chalov, S.V.: 2005, 'Acceleration of interplanetary pick-up ions and anomalous cosmic rays', *Adv. Space Res.* **35**, 2106–2114.

Chalov, S., Fahr, H.J., and Izmodenov, V.V.: 2003, 'Evolution of pickup proton spectra in the inner heliosheath and their diagnostics by energetic neutral atom fluxes', *J. Geophys. Res.* **108**, CiteID10.1029/2002JA009492.

Chalov, S.V., Alexashov, D.B., and Fahr, H.J.: 2004a, 'Reabsorption of self-generated turbulent energy by pick-up protons in the outer heliosphere', *Astron. Astrophys.* **416**, L31–L34.

Chalov, S.V., Izmodenov, V.V. and Fahr, H.J.: 2004b, 'Spatial variations of pickup proton energy spectra in the inner heliosheath and fluxes of energetic atoms', *Adv. Space Res.* **34**, 99–103.

Cowling, T. G., *Magnetohydrodynamics*, Adam Hilger, London, U. K., 1976.

Czechowski, A., Hilchenbach, M., and Hsieh, K.C.: 2005, 'Heliospheric energetic neutral atoms as a means to determine the anomalous cosmic ray spectrum at the termination shock', *Astron. Astrophys.* **431**, 1061–1068.

Decker, R.B., Krimigis, S.M., Roelof, E.C., Hill, M.E., Armstrong, T.P., Gloeckler, G., Hamilton, D.C., and Lanzerotti, L.J.: 2005, 'Voyager 1 in the foreshock, termination shock, and heliosheath', *Science* **309**, 2020–2024.

Fisk, L.A., Kozlovsky, B., and Ramaty, R.: 1974, 'An interpretation of the observed oxygen and nitrogen enhancements in low-energy cosmic rays', *Astrophys. J.* **190**, L35.

Fisk, L.A., Gloeckler, G., and Zurbuchen, T.H.: 2006, *Astrophys. J.*, in press.

Gangopadhyay, P., Izmodenov, V.V., Quemerais, E., Gruntman, M. A., 2004: 'Interpretation of Pioneer 10 and Voyager 2 Lyman Alpha data: first results', *Adv. in Space Res.* **34**, 94-98.

Gangopadhyay, P., Izmodenov, V.V., Shemansky, D., Gruntman, M., Judge, D. L., 2005: 'Reappraisal of the Pioneer 10 and Voyager 2 Lyman-alpha intensity measurements', *Astrophys. J.*, **628** 514519.

Gangopadhyay, P., Izmodenov, V.V., Gruntman, M., Judge. D. L., 2006: 'Voyager 1, Voyager 2 and Pioneer 10 Lyman-alpha data and their interpretation', *Astrophys. J.* **637**, 786-790.

Gazis, P.R., 1996: 'Long-term enhancements in solar wind speed' *Rev. Geophys.* **34**, 379–402.

Gloeckler, G., Geiss, J.: 2001, 'Composition of the Local Interstellar Cloud from Observations of Interstellar Pickup Ions' *AIP Conf. Proc.* **598** 281-289.

Gloeckler, G., Geiss, J., 2004: 'Composition of the local interstellar medium as diagnosed with pickup ions', *Adv. Space Res.* **34**, 53–60.

Gloeckler, G., Moebius, E., Geiss, J., et al., 2004: 'Observations of the helium focusing cone with pickup ions', *Astron. Astrophys.* **426**, 845-854.

Gurnett, D.A., Kurth, W.S., Allendorf, S.C., and Poynter, R.L., *Science* **262**, 199, 1993.

Hilchenbach, M., Hsieh, K.C., Hovestadt, D., Klecker, B., Grünwaldt, H., et al.: 1998, 'Detection of 55-80 keV hydrogen atoms of heliospheric origin by CELIAS/HSTOF on SOHO', *Astrophys. J.* **503**, 916.

Izmodenov, V.V., and Alexashov, D.: 2003, 'A Model for the tail region of the heliospheric interface', *Astron. Lett.* **29**, 58–63.

Izmodenov, V.V., and Malama, Yu. G.: 2004a, 'Kinetic modeling of the H atoms in the heliospheric interface: solar cycle effects', AIP Conf. Proc. **719**, 47–52.

Izmodenov, V.V. and Malama, Yu.G.: 2004b, 'Variations of interstellar H atom parameters in the outer heliosphere: solar cycle effects', *Adv. Space Res.* **34**, 74–78.

Izmodenov, V.V., Alexashov, D.: 2005a, 'Role of the interstellar magnetic field on direction of the interstellar H atom inflow in the heliosphere', in Proc. Solar Wind 11 / SOHO 16 Conf. (Eds. B. Fleck, T.H. Zurbuchen, H. Lacoste), ESA SP-592, Published on CDROM, p.55.1.

Izmodenov, V.V., Alexashov, D.: 2006, 'Multi-component 3D modeling of the heliospheric interface: effects of interstellar magnetic field', *AIP Conf. Proc.***858**, 14–19.

Izmodenov V., Lallement R., Malama Yu.G., 1997: 'Interstellar neutral oxygen in the heliosphere: two-shocks model, Astron. Astrophys.', bf 317, 193-202.

Izmodenov, V.V., Lallement, R., Geiss, J., 1999b: 'Interstellar oxygen in the heliospheric interface: influence of electron impact ionization', *Astron. Astrophys.* **344**, 317- 321.

Izmodenov, V.V., Gruntman, M., Malama, Yu.G., 'Interstellar Hydrogen Atom Distribution Function in the Outer Heliosphere', *J. Geophys. Res.* **106**, 10,681-10,690.

Izmodenov, V., Wood, B., Lallement, R., 2002: 'Hydrogen wall and heliosheath Lyman-alpha absorption toward nearby stars: possible constraints on the heliospheric interface plasma flow', *J. Geophys. Res.* **107**, doi: 10.1029/2002JA009394.

Izmodenov, V.V., Gloeckler, G., and Malama, Y.: 2003a: 'When will Voyager 1 and 2 encounter the termination shock?', *Geophys. Res. Lett.* **30**, Issue 7, 3-1, CiteID 1351, DOI 10.1029/2002GL016127.

Izmodenov, V.V., Malama, Yu.G., Gloeckler, G., and Geiss, J.: 2003b, 'Effects of interstellar and solar wind ionized helium on the interaction of the solar wind with the local interstellar medium', *Ap. J. Let.* **954**, L59-L62.

Izmodenov, V., Wood, B., Lallement, R., 2003c: 'HST Lyman-alpha absorption spectra toward nearby stars as a remote diagnostics of the heliosheath plasma properties', *AIP Conf. Proc.* **679**,63-66.

Izmodenov, V., Malama, Y., Gloeckler, G., Geiss, J., 'Filtration of interstellar H, O, N atoms through the heliospheric interface: Inferences on local interstellar abundances of the elements', *Astron. Astrophys.* **414**, L29-L32.

Izmodenov, V., Alexashov, D., Myasnikov, A.: 2005a, 'Direction of the interstellar H atom inflow in the heliosphere: Role of the interstellar magnetic field', *Astron. Astrophys.* **437**, L35–L38.

Izmodenov, V.V., Malama, Y.G., and Ruderman, M.S.: 2005b, 'Solar cycle influence on the interaction of the solar wind with Local Interstellar Cloud', *Astron. Astrophys.* **429**, 1069–1080.

Kallenbach, R., Hilchenbach, M., Chalov, S.V., and Bamert, K.: 2004, 'On the origin of energetic neutral atoms detected by the SOHO/CELIAS/HSTOF sensor', Proc. 3rd IGPP Conf. on Astrophysics – Physics of the Outer Heliosphere, Riverside, California, 8-13 February 2004, AIP Conf. Proc. **719**, 229–236.

Kallenbach, R., Hilchenbach, M., Chalov, S.V., and Bamert, K.: 2005a, 'Observations of turbulence near interplanetary shocks', Proc. 4th IGPP Conf. on Astrophysics - Physics of Collisionless Shocks, University of California Riverside, Palm Springs, USA, 26 February – 3 March 2005, AIP Conf. Proc. **781**, 129–134.

Kallenbach, R., Hilchenbach, M., Chalov, S.V., le Roux, J.A., and Bamert, K.: 2005b, 'On the injection problem at the solar wind termination shock', *Astron. Astrophys.* **439**, 1–22.

Ksenofontov, L.T., and Berezhko, E.G.: 2003, 'Particle acceleration at the solar wind termination shock', Proc. 28th Int. Cosmic Ray Conf., 31 July - 7 August, 2003, p. 3761.

Kulikovskii, A. G., and G. A. Lyubimov, *Magnetohydrodynamics*, Addison-Wesley-Longman, Reading, Mass., 1965.

Lallement, R., Quémerais, E., Bertaux, J.-L., Ferron, S., Koutroumpa, D., and Pellinen, R.: 2005, 'Deflection of the interstellar neutral hydrogen flow across the

heliospheric interface', *Science* **307**, 1447–1449.
Linsky, J., Wood, B., 1996: 'The alpha Centauri Line of Sight: D/H Ratio, Physical Properties of Local Interstellar Gas, and Measurement of Heated Hydrogen (The 'Hydrogen Wall') Near the Heliopause', *Astrophys. J.* **463**, 254-270.
Linsky J.L., Diplas A., Wood B.E., et al., 1995: 'Deuterium and the Local Interstellar Medium Properties for the Procyon and Capella Lines of Sight', *Astrophys. J.* **451**, 335-351.
Malama, Yu.G.: 1991, 'Monte Carlo simulation of neutral atom trajectories in the solar system', *Astrophys. Space Sci.* **176**, 21–46, 1991.
Malama, Y. G., Izmodenov, V. V., Chalov, S. V., 2006: 'Modeling of the heliospheric interface: multi-component nature of the heliospheric plasma', *Astron. Astrophys.* **445**, 693-701.
McComas, D.J., and Schwadron, N.A.: 2006, 'An explanation of the Voyager paradox: Particle acceleration at a blunt termination shock', *Geophys. Res. Lett.* **33**, CiteID L04102.
Pogorelov, N.V., and Zank, G.P.: 2006, 'The Direction of the Neutral Hydrogen Velocity in the Inner Heliosphere as a Possible Interstellar Magnetic Field Compass', *Astrophys. J.* **636**, L161-L164.
Pushkar', E.A., 1995: 'Regular oblique interaction between shock waves coming from the same direction in a conducting medium with magnetic field', *Fluid Dynamics*, **30**, 912-925.
Quémerais, E., and Izmodenov, V.: 2002, 'Effects of the heliospheric interface on the interplanetary Lyman-α glow at 1 AU from the Sun', *Astron. Astrophys.* **396**, 269–281.
Quémerais, E., Bertaux, J. L., Lallement, R., Sandel, B. R., Izmodenov, V., 2003: 'Voyager 1/UVS Lyman α glow data from 1993 to 2003: Hydrogen distribution in the upwind outer heliosphere', *J. Geophys. Res.* **108**, LIS 4-1, CiteID 8029, DOI 10.1029/2003JA009871.
Richardson, J.D., 1997: The heliosphere-interstellar medium interaction: One shock or two? *Geophys. Res. Lett.* **24**, 2889–2892.
Scholer, M.: 2004, 'Kinetic structure of the heliospheric termination shock and implications for pickup ion injection', *Physics of the Outer Heliosphere*, AIP Conf. Proc. **719**, 311–316.
Scholer, M., and Matsukiyo, S.: 2004, 'Nonstationarity of quasi-perpendicular shocks: a comparison of full particle simulations with different ion to electron mass ratio', *Annales Geophysicae* **22**, 2345–2353.
Scholer, M., Shinohara, I., and Matsukiyo, S.: 2003, 'Quasi-perpendicular shocks: Length scale of the cross-shock potential, shock reformation, and implication for shock surfing', *J. Geophys. Res.* **108**, 1014, doi:10.1029/2002JA009515.
Stone, E.C., Cummings, A.C., McDonald, F.B., Heikkila, B.C., Lal, N., and Webber, W.R.: 2005, 'Voyager 1 explores the termination shock region and the heliosheath beyond', *Science* **309**, 2017–2020.
Thomas, G.E.; Krassa, R. F., 'OGO 5 Measurements of the Lyman Alpha Sky Background', *Astron. Astrophys.* **11**, 218-233.
Witte, M., Banaszkiewicz, M., Rosenbauer, H., 1996: 'Recent Results on the Parameters of the Interstellar Helium from the Ulysses/Gas Experiment', *Space Sci. Rev.* **78**, 289-296.

Witte, M., 2004: 'Kinetic parameters of interstellar neutral helium. Review of results obtained during one solar cycle with the Ulysses/GAS-instrument', *Astron. Astrophys.* **426**, 835-844.

Wolff, B., Koester, D., Lallement, R., 1999: 'Evidence for an ionization gradient in the local interstellar medium: EUVE observations of white dwarfs', *Astron. Astrophys.* **346**, 969-978.

Wood, B. E., Mueller, H.-R., Zank, G. P., Izmodenov, V. V., Linsky, J. L., 2004: 'The heliospheric hydrogen wall and astrospheres', *Adv. in Space Res.*, **34**, 66-73.

Zank, G. P., 1999: 'Interaction of the solar wind with the local interstellar medium: a theoretical perspective', *Space Sci. Rev.* **89**, 413-688.